Academic Press is an imprint of Elsevier
Linacre House, Jordan Hill, Oxford OX2 8DP, UK
84 Theobald's Road, London WC1X 8RR, UK
Radarweg 29, PO Box 211, 1000 AE Amsterdam, The Netherlands
30 Corporate Drive, Suite 400, Burlington, MA 01803, USA
525 B Street, Suite 1900, San Diego, CA 92101-4495, USA

First edition 2009

British Library Cataloguing in Publication Data
A catalogue record for this book is available from the British Library

Library of Congress Cataloging-in-Publication Data
A catalog record for this book is available from the Library of Congress

ISBN: 978-0-12-374737-2
ISSN: 0066-4103

For information on all Academic Press publications visit our web site at books.elsevier.com

Printed and bound in Great Britain
09 10 11 12 10 9 8 7 6 5 4 3 2 1

CONTRIBUTORS

David L. Bryce
Department of Chemistry and Centre for Catalysis Research and Innovation, University of Ottawa, Ottawa, Ontario, Canada K1N 6N5

Rebecca P. Chapman
Department of Chemistry and Centre for Catalysis Research and Innovation, University of Ottawa, Ottawa, Ontario, Canada K1N 6N5

Martin Goez
Institut für Chemie, Martin–Luther-Universität Halle–Wittenberg, Kurt–Mothes-Str. 2, D-06120 Halle/Saale, Germany

Harri Koskela
Finnish Institute for Verification of the Chemical Weapons Convention (VERIFIN), University of Helsinki, A.I. Virtasen aukio 1, FIN-00014, Finland

Ryan T. McKay
National High Field Nuclear Magnetic Resonance Centre (NANUC), University of Alberta, Edmonton, AB, Canada T6G 2E1

V. Mikhaltsevitch
Qrsciences Ltd., Cannington WA 6107, Australia

Cory M. Widdifield
Department of Chemistry and Centre for Catalysis Research and Innovation, University of Ottawa, Ottawa, Ontario, Canada K1N 6N5

PREFACE

It is my pleasure to introduce Volume 66 of *Annual Reports on NMR Spectroscopy*. As is usual with this series of reports, a number of diverse areas of science are covered in the contributions found in the present volume.

The first contribution is on 'Quantitative 2D NMR Studies' by H. Koskela; this is followed by an account from R. T. McKay on 'Recent Advances in Solvent Suppression for Solution NMR: A Practical Reference'; the third chapter is on 'Photo-CIDNP Spectroscopy' by M. Goez; this is followed by a discussion of 'Techniques Used in 14N NQR Studies' by V. Mikhaltsevitch; finally, there is a review of 'Chlorine, Bromine and Iodine Solid-State NMR Spectroscopy' by C. M. Widdifield, R. P. Chapman and D. L. Bryce.

It gives me great pleasure to thank all of these authors for their interesting and timely contributions.

G. A. Webb
Royal Society of Chemistry
Burlington House
Post Room
Piccadilly
London, WIJ OBA
England

CHAPTER 1

Quantitative 2D NMR Studies

Harri Koskela

Contents

Abstract

Nuclear magnetic resonance (NMR) spectroscopy is regarded as one of the most important analytical techniques in chemistry for characterization of molecular structure. In addition to the structural information, NMR spectroscopy also gives quantitative information about the sample constituent. The induced current in the coil can be regarded as linearly dependent on the concentration of the nucleus in the sample. Therefore the resonance integrals in a simple one-dimensional spectrum measured with the excitation–acquisition scheme offer a way to measure absolute amounts of the chemicals present in the sample. Recently, the need for quantitative analysis of highly complex samples has led to a situation where resonance overlap in

Finnish Institute for Verification of the Chemical Weapons Convention (VERIFIN), University of Helsinki, A.I. Virtasen aukio 1, FIN-00014, Finland

Annual Reports on NMR Spectroscopy, Volume 66
ISSN 0066-4103, DOI: 10.1016/S0066-4103(08)00401-8

one-dimensional spectra can compromise or even prevent accurate quantification of sample compounds. Two-dimensional NMR offers improved resolution of resonances, and therefore the use of two-dimensional NMR experiments in determination of sample constituent has gained interest in many fields of research where quantification of compounds in complex samples is needed. Concepts of the quantitative two-dimensional NMR and recent applications are discussed.

Key Words: Quantitative 2D NMR, 2D *J*-resolved NMR, COSY, TOCSY, HSQC, 2D INEPT, Natural products, Metabolomics, Oil fractions, Food analysis.

1. INTRODUCTION

There are several analytical instrumentation techniques which offer qualitative details about the sample. Some of those use electromagnetic radiation to measure absorption of energy on electron orbitals (visible and ultraviolet spectroscopy[1]) or bond vibrations (infrared spectroscopy[2]). Mass spectrometry, which can be used to determine the mass/charge ratio of ions, is recognized as a technique that can give accurate data from the molecular ions and fragments.[3] While these techniques can also be applied to extract quantitative information of the constituent of a sample, only one technique, nuclear magnetic resonance (NMR) spectroscopy, can give a detailed view to the molecular structure as well as intrinsically quantitative information.

The use of ^{1}H NMR spectroscopy in quantification has extended in many fields of chemistry. Most important field of application is in synthetic organic chemistry, where ^{1}H NMR experiment is used in structural analysis for determination of the number of protons in a molecule, and further to study mixture samples with high precision and accuracy.[4] Application of quantitative ^{1}H NMR has also taken its place in new, emerging fields of research, like metabolomics.[5]

The experimental set-up for quantitative ^{1}H NMR is quite straightforward, which has made its use so widespread. A typical procedure is to use a 90° excitation pulse, and the repetition delay is set equal to or more than five times the longest T_1 of protons to ensure sufficient relaxation of the magnetization before the next scan.[6] The peak integrals in the obtained ^{1}H NMR spectrum can then be used to determine the analyte concentrations with high accuracy. The principle of reciprocity, which states that the NMR signal strength is inversely proportional to the 90° pulse length,[7] offers also ways to accurately compare constituents of separate samples. This approach has been applied in ^{1}H NMR quantification of algal toxins[8] and protein concentrations[9] with external standards.

The quantification is not restricted to proton detection, as there are number of other NMR observable nuclei, like carbon which is common in organic molecules. While the major isotope, carbon-12, is not usable by NMR, the carbon-13 with 1.1% natural abundance can be observed with NMR spectroscopy. When the sample concentration is not the limiting factor for the analysis, quantitative ^{13}C{^{1}H} NMR is very useful in analysis of organic compounds. The advantage of quantitative

$^{13}C\{^{1}H\}$ NMR is the wider chemical shift range, which makes it less likely that the resonances of interest are overlapping. A typical procedure for quantification with $^{13}C\{^{1}H\}$ NMR spectroscopy is to use inverse-gated proton decoupling[10] to avoid the uneven nuclear Overhauser effect (NOE) contribution to the signal intensity.[11] Also, a shorter excitation pulse angle (30°–45°) can be applied so that adequate recovery of magnetization can be achieved in a shorter time period than five times the longest carbon-13 T_1. This approach provides no significant advantage in total acquisition time for a required signal-to-noise ratio, as discussed by Traficante.[12] However, since the excitation range of the radiofrequency (RF) pulse is the reciprocal of its length, the use of short pulses is valuable for nuclei with a wide spectral range to minimize the offset effects to the signal intensities.[13] Another common approach for keeping the repetition delays reasonably short is to use relaxation reagents.[14–18] A new quantitative $^{13}C\{^{1}H\}$ NMR experiment which applies a precise analysis of NOE enhancement and T_1 relaxation to speed up the acquisition has also been recently reported by Giraudeau and Baguet.[19]

Inverse-gated $^{13}C\{^{1}H\}$ NMR lacks sensitivity due to the absence of NOE. Therefore, polarization transfer experiments, such as distortionless enhancement by polarization transfer (DEPT) and insensitive nuclei enhanced by polarization transfer (INEPT), which offer higher sensitivity in carbon detection, have also been adapted for quantification[20–22]. Moreover, since these methods detect proton polarization transferred to carbon, the repetition rate is dictated by the T_1 relaxation of protons, not carbons. The drawback of polarization transfer methods is that quaternary carbons are not usually visible in the spectrum. However, a DEPT-based pulse sequence dubbed as DEPTQ[23,24] has been proposed that enables the detection of quaternary carbons in the spectrum. The study of evolution of magnetization during DEPTQ by Özdogan and Orbay[25] revealed a good agreement between theoretical and experimental results, suggesting that the experiment has potential in quantification.

Overlapping of signals often hampers reliable quantification with one-dimensional (1D) NMR experiments. In liquids the resonances are narrow due to the isotropic medium, but the complexity of the sample may still result in insufficient resolution of signals. Some experimental set-ups are reported to diminish the instrumental contribution of $^{13}C\{^{1}H\}$ NMR linewidths below 0.003 Hz,[26–28] which can help analysis of complex mixture samples. Several processing methods for the analysis of spectra with overlapping resonances, such as deconvolution[29,30] and singular value decomposition,[31] can help quantification to some degree, but even these methods have their limits with highly crowded spectra.

The idea of two-dimensional (2D) NMR spectroscopy was introduced in 1971 by Jeener,[32] and several experimental demonstrations were soon reported by Ernst and co-workers.[33–36] Since then many new 2D NMR experiments have been designed to give higher resolution of the resonances and information about the spectral parameters, and therefore the structural details, that would be inaccessible or at least more laborious to determine with 1D NMR experiments. The improved resolution in 2D NMR experiments has paved the way for general acceptance that NMR spectroscopy is a valid analytical technique in analysis of complex samples.[37,38]

2D NMR is, however, still comprehended more of qualitative than quantitative technique. If quantitativity is associated with 2D NMR, it is usually in contexts of measurement of exchange of magnetization through chemical exchange or cross relaxation. 2D exchange spectroscopy (EXSY) experiment[39,40] is useful in mapping exchange networks and rate constants in molecules.[41] With a different mixing time, the same experiment can be used also to study NOE mediated via cross relaxation. The 2D nuclear Overhauser effect spectroscopy (NOESY) spectrum[39,42] can be used to establish intra- and intermolecular spatial arrangements. One important application of this type of experiments is in determination of three-dimensional structure of biological macromolecules.[43,44] As the research of increasingly complex systems has gained interest, quantification of chemicals present in these samples has become a difficult task to perform just with 1D NMR experiments. In recent years more and more publications have emerged where the 2D NMR spectroscopy has been applied not only in structural elucidation but also in quantification of the concentration of the studied chemicals. The following sections concern with concepts of the quantitative 2D NMR, i.e. 2D NMR in quantification of the amount of analytes, and in some recent applications where 2D NMR has given significantly higher accuracy compared to quantitative 1D NMR.

2. CONCEPTS

Quantification by 2D NMR is not straightforward, as the factors that contribute to the volume of correlation peaks are numerous (e.g. relaxation rates, multiplicity and magnitude of coupling constants). However, the key issue in the use of 2D NMR experiments in quantification is that the observed cross peak volume can be regarded as linear with respect to the concentration of the analyte. Therefore, the quantification of chemicals can be based on determination of a calibration curve which has been defined by several standard samples containing known amounts of analytes within the expected concentration range. This calibration curve can then be used with the real samples to correlate the cross peak volume with the actual concentration of the analyte(s). A more universal and accurate quantification can be obtained, if the coherence pathways and polarization transfer efficiencies of the applied 2D NMR experiment are understood. The efficiency of the polarization transfer can be estimated by inspecting the function of the pulse sequence theoretically. Product operator formalism,[45–49] a concise version of density matrix calculations, provides tools to follow magnetization evolution through pulse sequences by simple transformations of spin operators. The density functions of the magnetization give information of the polarization transfer efficiency, and by that, offer a way to correct integration data so that observed cross peak volumes can be directly used to estimate the concentration of analytes. In the following sections, the polarization transfer in some 2D homo- and heteronuclear shift correlation experiments is demonstrated with product operator calculations. Additional aspects that affect the cross peak volume, like RF pulse imperfections and relaxation, are also discussed.

2.1. Homonuclear experiments

The simplest 2D NMR experiment, which offers enhanced resolution, is the homonuclear *J*-resolved experiment.[50] The experiment is basically a spin-echo sequence,[51,52] where the echo period is incremented. During this t_1 period the chemical shift evolution is refocused with a 180° pulse, but homonuclear *J* couplings are evolved. If we consider a proton *H* coupled to proton(s) *H*′, the density function of the observed proton magnetization is modulated by these couplings accordingly

$$\sigma(H) \propto \prod_{k=1}^{n} \cos\left(\pi J_{HH'_k} t_1\right) \tag{1}$$

The result is that the lines in a proton resonance multiplet are dispersed along both the F_1 and F_2 dimension, giving a tilted shape to the cross peak. With further processing the tilt can be straightened, so that the F_2 projection of the spectrum shows only single line for each resonance, and the multiplet structure is given in the F_1 dimension. In this way partially overlapping resonances can be separated, and integration is easier to accomplish. The *J*-resolved spectra are typically processed in magnitude mode, but there are also many reports of various approaches how a phase-sensitive spectrum can be obtained.[53–58] A F_2 projection of the 2D *J*-resolved spectrum can also be used to produce a quantitative ''proton-decoupled'' 1D spectrum.[59]

The second way to improve the resolution of proton resonances is with homonuclear correlation spectroscopy, or COSY, experiment.[36,60–63] In the basic form of the experiment the magnetization is excited with a 90° pulse. During the consequent t_1 period the chemical shift and homonuclear *J* couplings evolve, until a second 90° pulse is applied prior to acquisition. This pulse causes polarization transfer to take place between protons that are coupled to each other. If we consider a proton *H* coupled to another proton *H*′, then the observable terms of the proton *H* magnetization for the COSY experiments are

$$\sigma(H) \propto H_x \sin(\omega_H t_1) \cos\left(\pi J_{HH'} t_1\right) - H_y H'_z \sin\left(\omega_{H'} t_1\right) \sin\left(\pi J_{HH'} t_1\right) \tag{2}$$

The term H_x gives the diagonal peak, whereas the term $H_y H'_z$ corresponds the polarization transferred from the remote proton *H*′ with coupling $J_{HH'}$ to the observed proton. This term is responsible of the off-diagonal cross peak. Two resonances that are overlapping in the 1D spectrum can be separated by their off-diagonal cross peaks if they are coupled to separate protons with distinctly different chemical shifts. However, the nature of the off-diagonal term results in several implications. First of all, the splitting of the active *J* coupling is in anti-phase, i.e. the lines appear with 180° phase difference. If the line separation is comparable to the linewidth, self-cancellation[64] of lines will take place, diminishing the absolute-value cross peak volume. This can also introduce significant variation of the cross peak absolute-value volume, if the linewidths vary between the spectra. If COSY is performed in phase-sensitive mode,[65] or COSY is acquired with double-quantum filtering (DQF-COSY),[66–69] the total volume (the sum of

positive and negative lines) of any off-diagonal cross peak is, by default, zero. This can be of course circumvented by integrating only either positive or negative part of the cross peak volume. Due to aforementioned reasons, quantification with the COSY-type experiments is best to do using a calibration curve which has been defined by several standard samples. This approach can still give very accurate results as demonstrated by Giraudeau et al.[70] They made a comparative study of quantitativity between DQF-COSY and 2D *J*-resolved NMR with tropine–nortropine mixtures. The authors found a slightly better accuracy for DQF-COSY over 2D *J*-resolved NMR (errors were 2 and 3%, respectively), with standard deviation under 1%. There are also some reports on how a COSY-type spectrum can be acquired with in-phase cross peaks,[71–74] which should be much easier to integrate. It should be noted, that the evolution of magnetization is more complex in these experiments, and additional lineshape distortions or other limitations might be introduced.

Another related 2D NMR experiment, total correlation spectroscopy, or TOCSY,[75,76] can be applied to obtain in-phase off-diagonal cross peaks. In this experiment the chemical shift evolves during the t_1 period. The following spin-lock period t_m, which can be produced with e.g. composite pulse trains,[77–79] leads to an isotropic mixing condition bringing about homonuclear Hartmann–Hahn transfer of magnetization through *J* couplings.[80] If we consider a proton *H* coupled to another proton *H′*, the observable *in-phase* terms of the *H* proton magnetization are as follow[75]

$$\begin{aligned}\sigma(H) \propto\ & 1/2H_x \sin\left(\omega_H t_1\right)\left[1+\cos\left(2\pi J_{HH'} t_m\right)\right] \\ & + 1/2H_x \sin\left(\omega_{H'} t_1\right)\left[1-\cos\left(2\pi J_{HH'} t_m\right)\right]\end{aligned} \tag{3}$$

The first half of the equation gives the diagonal cross peak, whereas the second half produces the cross peak. With two-spin system the highest intensity for the cross-peak term is obtained when t_m is set for $1/(2J_{HH'})$. When more complex spin systems are involved, the setting of the optimal mixing time needs some trade-off to give a satisfactory intensity for cross peaks. This also means that quantification with TOCSY is best to do using a calibration curve which has been defined by several standard samples. Zero-quantum coherences are also produced during the mixing time,[75] which are responsible of distortions observed in the lineshapes. A number of techniques have been proposed to eliminate these zero-quantum distortions[81–84] which should enable more accurate integration.

2.2. Proton detected heteronuclear experiments

Methyl (CH_3), methylene (CH_2) or methine (CH) groups are common in organic chemicals. Compared to proton, carbon has a much larger chemical shift range, so higher separation of the CH_n proton resonances is achieved with ^1H–^{13}C heteronuclear correlation spectroscopy.[85] Therefore this approach can facilitate quantification even with highly complex mixtures.

Bodenhausen and Ruben reported in 1980 a 2D shift-correlated experiment designated as heteronuclear single-quantum coherence, or HSQC[86] (Figure 1).

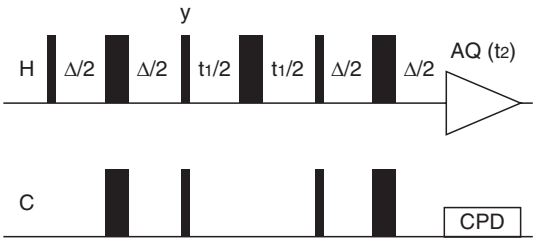

Figure 1 A basic pulse sequence for HSQC experiment. Narrow and wide bars represent 90° and 180° RF pulses, respectively. Pulse phase is *x*, if not stated otherwise.

The method employs inverse detection, thus giving superior sensitivity over the 2D methods with direct detection.[87]

HSQC starts with an INEPT step[88] which transfers the proton polarization to carbon. Then the polarization is modulated by the carbon chemical shift during the t_1 evolution period. Finally, a reverse-INEPT step[89] returns the polarization back to proton for observation. Pulsed field gradients can also be incorporated into HSQC[90] for coherence selection. Due to single-quantum coherence states, evolution of homonuclear coupling during t_1 evolution period has no effect to cross peak shape in HSQC. The evolution of polarization during the HSQC experiment is easy to predict, facilitating quantitative use of the experiment. The evolution period itself should only give the carbon chemical shift modulation to the signal, and therefore should not affect the quantitativity. The product operator analysis can be started with evolution time $t_1 = 0$ and then calculate what is the magnetization state after INEPT and reverse-INEPT steps. The density function after the pulse sequence is

$$\sigma(\mathrm{CH_3}, \mathrm{CH_2}, \mathrm{CH}) \propto \sin^2(\pi J_{\mathrm{CH}} \Delta) \tag{4}$$

As can be seen, the density function is the same for all CH_n groups. The cross peak volume is naturally dependent on proton number in the CH_n group, i.e. the $\mathrm{CH_3}$ cross peak is generally three times more intense than CH group. The $\mathrm{CH_2}$ cross peak intensity follows also the number of protons present, so if the protons are equivalent, the cross peak intensity is twice the intensity of the CH cross peak. The magnetization intensity is maximum whenever Δ equals $1/(n|J|)$, where n is a positive *even* integer. From the point of relaxation, the first solution, $\Delta = 1/(2|J|)$, is the most practical one. The effect of INEPT optimization can be more easily followed if the polarization transfer delay Δ is defined as $1/(2J_{\mathrm{opt}})$

$$\sigma(\mathrm{CH_3}, \mathrm{CH_2}, \mathrm{CH}) \propto \sin^2\left(\frac{\pi}{2}\frac{J_{\mathrm{CH}}}{J_{\mathrm{opt}}}\right) \tag{5}$$

The maximum intensity is met when the $J_{\mathrm{CH}}/J_{\mathrm{opt}}$ ratio equals 1, and the intensity decreases if the $J_{\mathrm{CH}}/J_{\mathrm{opt}}$ ratio is higher or lower than 1 (Figure 2). From the point of sensitivity it is best to set J_{opt} to the average of J_{CH}s of the sample. When the difference of J_{CH}s is exceptionally large, e.g. with a sample containing both alkane ($^1J_{\mathrm{CH}} \approx 125$ Hz) and alkyne ($^1J_{\mathrm{CH}} \approx 250$ Hz)[91] functionality, the cross peak

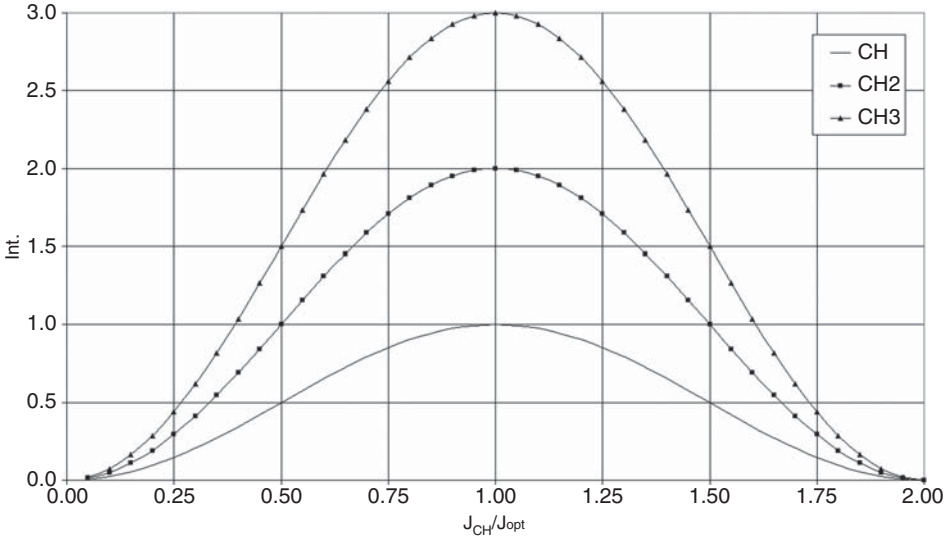

Figure 2 Relation of signal intensity and ratio J_{CH}/J_{opt} in the HSQC (see Equation (5)). The maximum intensities for CH_3, CH_2 and CH groups are 3, 2, and 1, respectively.

volumes for these protons will be 75% from the maximum attainable if the J_{opt} is set for average of the couplings. When the J_{CH}s of the sample are known, suitable coefficients can be formulated to correct the volumes to take this effect into account, and by that improve the accuracy of quantification.

As always, homonuclear coupling evolution during the pulse sequence affects the polarization transfer to the desired coherence and therefore affects the quantitativity. Homonuclear coupling evolution is active in HSQC experiment during both INEPT and reverse-INEPT periods. We can consider a CH group, with one remote proton H' coupled to the CH group proton. During both the INEPT and reverse-INEPT period a part of the polarization from the CH group proton ends up to the H' through a COSY-type transfer. Therefore, the density function for this spin system is

$$\sigma\left(\mathrm{CH}-H'\right) \propto \sin^2\left(\frac{\pi}{2}\frac{J_{\mathrm{CH}}}{J_{\mathrm{opt}}}\right)\cos^2\left(\frac{\pi}{2}\frac{J_{HH'}}{J_{\mathrm{opt}}}\right) \tag{6}$$

The loss of polarization is illustrated in Figure 3.

The loss of intensity can be significant, when the $J_{HH'}$ approaches the value of J_{CH}. Therefore HSQC experiment is most effective in detecting $^1J_{CH}$ correlations, whereas its usefulness in detecting $^{2-3}J_{CH}$ correlations is limited. If there are a large number of coupled protons, the general density function for a CH group with n remote coupled protons is

$$\sigma\left(\mathrm{CH}-nH'\right) \propto \sin^2\left(\frac{\pi}{2}\frac{J_{\mathrm{CH}}}{J_{\mathrm{opt}}}\right)\prod_{k=1}^{n}\cos^2\left(\frac{\pi}{2}\frac{J_{HH'_k}}{J_{\mathrm{opt}}}\right) \tag{7}$$

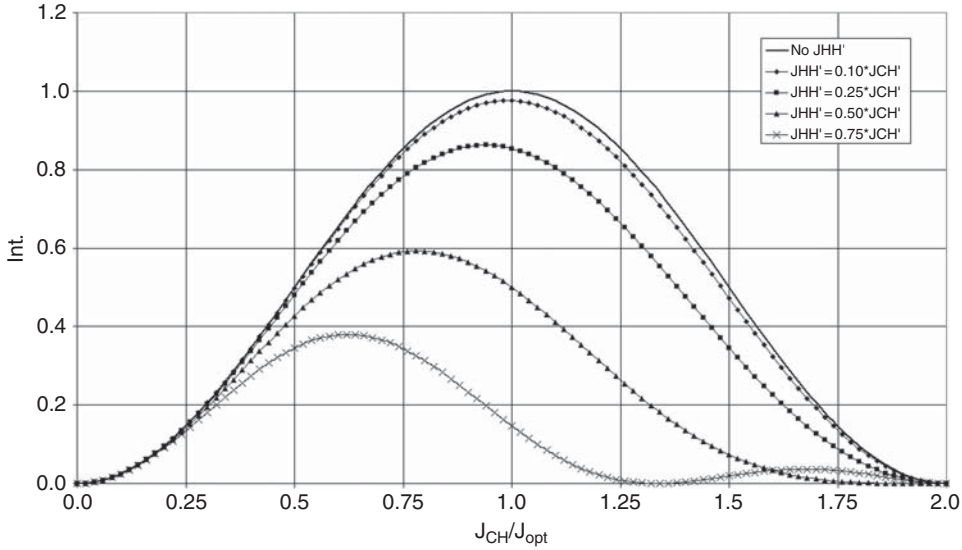

Figure 3 Signal loss in respect of homonuclear coupling evolution in the HSQC (see Equation (6)).

If $J_{HH'}$ is about 5% of J_{CH} (corresponds roughly to the typical values of $^3J_{HH}$ versus $^1J_{CH}$), the intensity loss is insignificant if only few protons are coupled (Figure 4). However, e.g. the methine group in the isobutyl fragment can have eight coupled protons, leading to 5% loss of intensity. More importantly, the cross peak would be split to nine lines (if equal J_{HH}s are assumed), which makes reliable integration of the cross peak difficult. If high accuracy in quantification is needed, these factors must be taken into account.

Recently, there have been attempts to refine the HSQC experiment to improve the quantitativity. Heikkinen et al.[92] reported an interesting variation of the experiment called as Q-HSQC. In this experiment, uniform polarization transfer over a range of J_{CH} couplings was accomplished with use of constant-time INEPT periods with varied J_{CH} evolution times. In the subsequent paper the lineshape problems associated with the J_{HH} coupling evolution during the long constant-time INEPT periods were corrected by Q-CAHSQC using the CPMG-INEPT approach, and the effects of carbon pulse offset were also discussed.[93] A solution to the necessity in Q-HSQC and Q-CAHSQC to measure a multiple of four scans per transient was proposed by Peterson and Loening.[94] Their QQ-HSQC experiment elegantly exploited localized manipulation of the sample volume in a way that the different parts of the sample were optimized for different polarization transfer evolutions, resulting reduced number of scans per transient and shorter total acquisition time. The principle concerning the spatial encoding of the sample volume with pulsed field gradients has also been employed in a number of applications, e.g. for measuring diffusion coefficients, homonuclear correlations and longitudinal relaxation rates.[95–97]

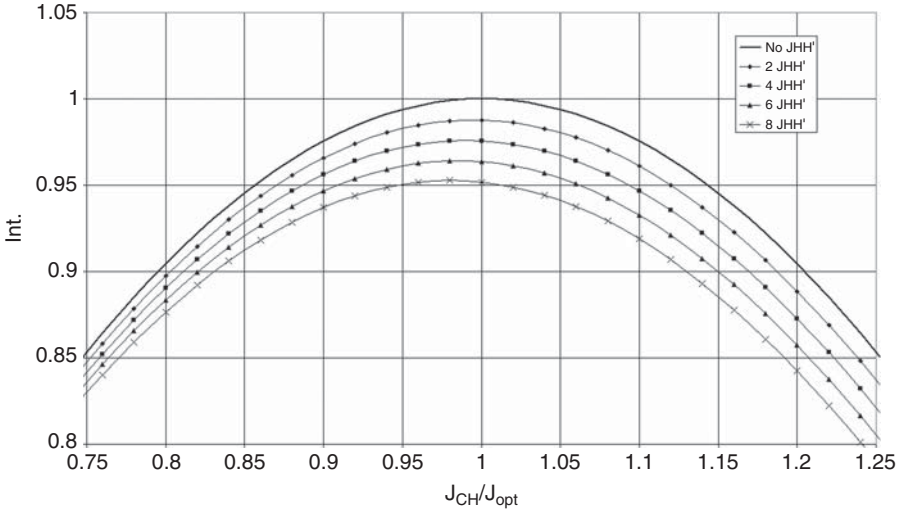

Figure 4 Signal loss in respect of multiple homonuclear couplings in the HSQC when $J_{HH'}$ is presumed to be 5% of the J_{CH} (see Equation (7)).

The other common inverse-detection method, heteronuclear multiple quantum coherence (HMQC)[98–101] relies on multiple-quantum coherence transitions during the pulse sequence. Due to the multiple-quantum coherence transitions it is more laborious to theoretically follow the course of magnetization, and the cross peak will be broader in the F_1 dimension due to the J_{HH} evolution.[102,103] Unlike HSQC, HMQC can also be optimized for[2–3] J_{CH} couplings. This heteronuclear multiple bond correlation experiment, or HMBC,[104,105] has lower sensitivity than HMQC/HSQC experiments, and the $^1J_{CH}$ correlations can appear as artefacts in the spectrum. However, the cross peak volume should follow the concentration of analyte, so with proper method validation HMQC and HMBC should also be applicable for quantification.

2.3. Carbon-detected heteronuclear experiments

INEPT[88] is used in multinuclear NMR spectroscopy to enhance sensitivity of nuclei with low gyromagnetic ratio and/or low natural abundance.[106–108] When used in direct observation of an insensitive heteronucleus like carbon, the standard INEPT has some shortcomings. The most prominent is the anti-phase multiplet structure of the resonances, which prevents proton decoupling during acquisition. These shortcomings have been addressed in several papers, and some improvements like possibility for multiplicity editing have been published.[109–112] There are also several examples how the INEPT experiment can be expanded to a 2D heteronuclear shift correlation experiment called as 2D INEPT.[113–115] Bendall et al.[113] have presented a thorough Heisenberg vector analysis how polarization is transferred in various versions of the 2D INEPT

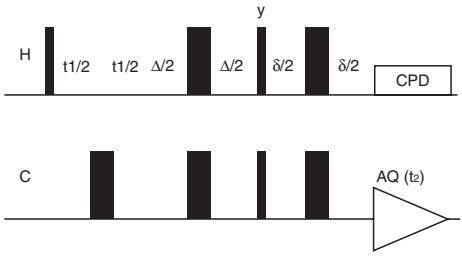

Figure 5 A pulse sequence for 2D INEPT.

experiment. The coherence pathways are thus well known, and the experiment is as such applicable for quantitative analysis. The basic version of the 2D INEPT (Figure 5) consists of the refocused INEPT[109,110] experiment with the extra t_1 period for proton chemical shift evolution.

Again, the evolution period itself should only give the proton chemical shift modulation to the signal and therefore should not affect the quantitativity. The analysis can be started with evolution time $t_1 = 0$. The INEPT period with the duration Δ transfers the proton polarization to carbon, and after INEPT the magnetization is in anti-phase with respect to proton(s), giving a typical anti-phase multiplet when the carbon signal is recorded.[112] The density function calculated using product operators shows that the intensity of the desired polarization (when effects of relaxation and pulse imperfections are neglected) is the same for all CH_n groups

$$\sigma(CH_3, CH_2, CH) \propto \sin(\pi J_{CH}\Delta) \tag{8}$$

If we define that the delay Δ equals $1/(2J_{opt})$, we can rewrite the proportionality as

$$\sigma(CH_3, CH_2, CH) \propto \sin\left(\frac{\pi}{2}\frac{J_{CH}}{J_{opt}}\right) \tag{9}$$

The above equation describes how the signal intensity changes with respect to the J_{opt} and the true J_{CH} coupling magnitude (Figure 6).

In the following refocusing period with duration δ the anti-phase carbon magnetization is refocused to in-phase magnetization. The intensity of the detected carbon magnetization depends on the multiplicity of the CH_n group, which must be taken into account. The density functions for each CH_n group[109,112] are

$$\begin{aligned} \sigma(CH_3) &\propto \frac{3}{4}[\sin(3\pi J_{CH}\delta) + \sin(\pi J_{CH}\delta)] \\ \sigma(CH_2) &\propto \sin(2\pi J_{CH}\delta) \\ \sigma(CH) &\propto \sin(\pi J_{CH}\delta) \end{aligned} \tag{10}$$

It can be seen that the refocusing period δ affects CH, CH_2 and CH_3 groups differently, hence offering possibility for multiplicity editing (Figure 7).

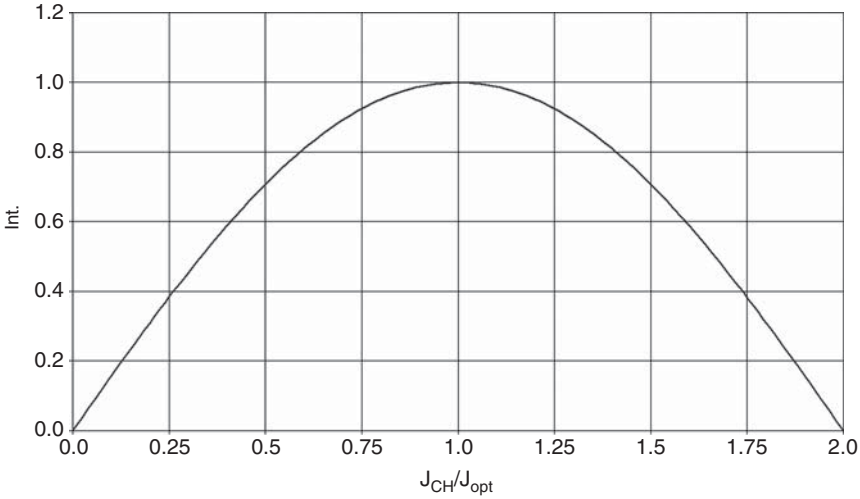

Figure 6 Relation of signal intensity and mismatch between J_{CH} and J_{opt} for the INEPT period (see Equation (9)).

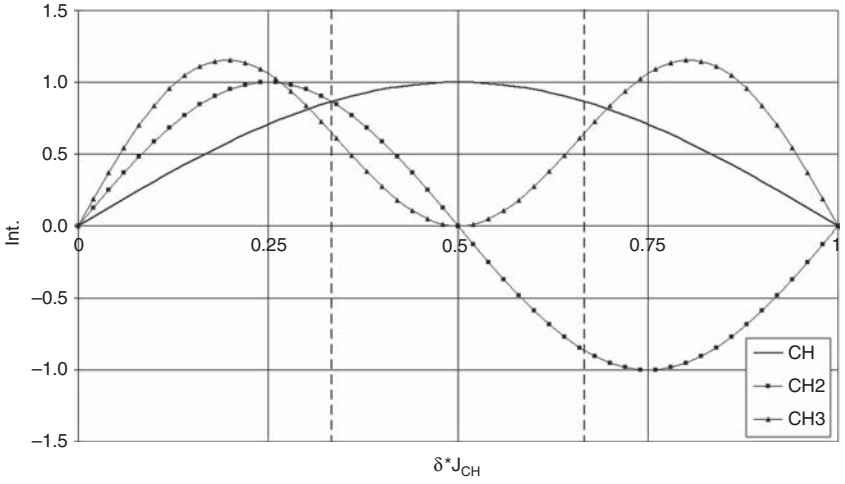

Figure 7 Relation of magnetization intensity and product of J_{CH} and δ for the INEPT refocusing period (see Equation (10)). The points where δJ_{CH} is 1/3 and 2/3 are marked with dashed lines.

It is common to use value $1/(3J_{opt})$ for the delay δ to have all the signals positive. If we look what the polarization transfer efficiency is for the whole refocused INEPT period with $\Delta = 1/(2J_{opt})$ and $\delta = 1/(3J_{opt})$, we can formulate

$$\begin{aligned}
\sigma(CH_3) &\propto \frac{3}{4}\sin\left(\frac{\pi}{2}\frac{J_{CH}}{J_{opt}}\right)\left[\sin\left(\pi\frac{J_{CH}}{J_{opt}}\right) + \sin\left(\frac{\pi}{3}\frac{J_{CH}}{J_{opt}}\right)\right] \\
\sigma(CH_2) &\propto \sin\left(\frac{\pi}{2}\frac{J_{CH}}{J_{opt}}\right)\sin\left(\frac{2\pi}{3}\frac{J_{CH}}{J_{opt}}\right) \\
\sigma(CH) &\propto \sin\left(\frac{\pi}{2}\frac{J_{CH}}{J_{opt}}\right)\sin\left(\frac{\pi}{3}\frac{J_{CH}}{J_{opt}}\right)
\end{aligned} \tag{11}$$

It is now possible to follow what is the polarization transfer efficiency from proton to carbon for each CH_n group, and also how the mismatch between true J_{CH} and the J_{opt} used for polarization transfer delay calculation affects the signal intensity (Figure 8). When the J_{CH}s of the sample are known, suitable coefficients can be formulated to correct the cross peak volumes.

The intensity curves show that the CH_3 and CH_2 group intensities drop rapidly when the J_{CH}/J_{opt} ratio exceeds 1. Sensitivity-wise, it is best to set J_{opt} higher than average of $^1J_{CH}$ of aliphatic hydrocarbons (typically 125 Hz), if the analyte has any, e.g. electronegative heteroatoms or other structural features that result considerably higher $^1J_{CH}$ couplings.[91] On the other hand, it is favourable to set $J_{opt} < J_{CH}$ when optimizing sensitivity for CH groups with high J_{CH}.

Homonuclear coupling evolution during the pulse sequence gives its own effect to the polarization transfer to the desired coherence and therefore affects the quantitativity. For 2D INEPT the crucial point in this respect is the INEPT period.

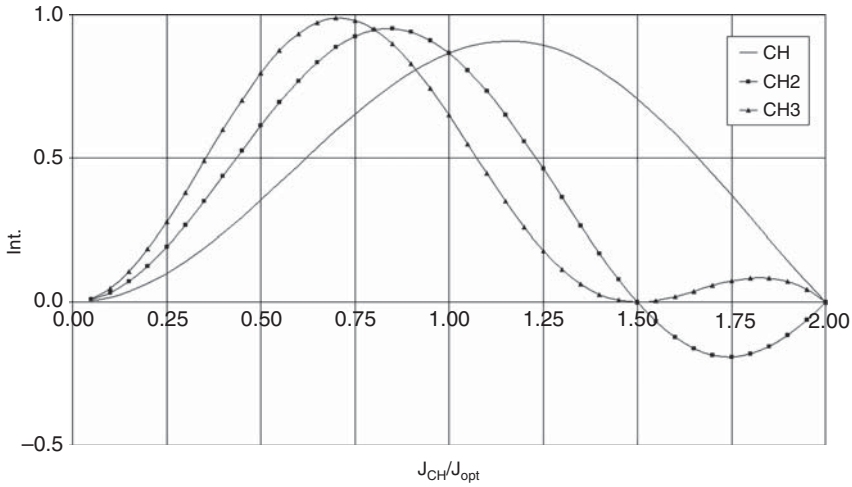

Figure 8 Relation of signal intensity and J_{CH}/J_{opt} ratio in the refocused INEPT (see Equation (11)).

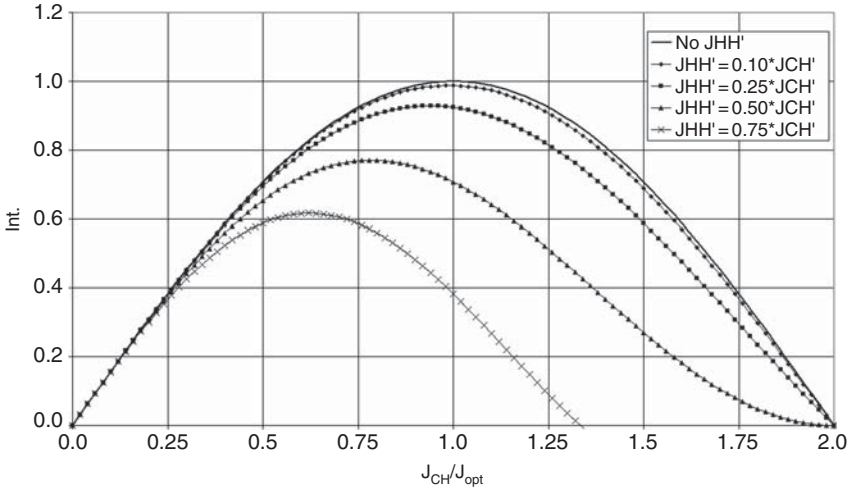

Figure 9 Signal loss with respect to homonuclear coupling evolution in INEPT (see Equation (12)).

We can consider a CH group with one remote proton H' coupled to the CH proton. During the INEPT period this homonuclear coupling evolves, and a part of the polarization from the CH group proton ends up to the H' through a COSY-type transfer. Therefore, the density function for this spin system is

$$\sigma\left(\mathrm{CH}-\mathrm{H}'\right) \propto \sin\left(\frac{\pi}{2}\frac{J_{\mathrm{CH}}}{J_{\mathrm{opt}}}\right)\cos\left(\frac{\pi}{2}\frac{J_{HH'}}{J_{\mathrm{opt}}}\right) \tag{12}$$

Depending on the ratio between the homonuclear coupling and heteronuclear coupling some polarization that would have ended during the following refocusing period as the in-phase carbon magnetization is lost (Figure 9).

The loss of polarization is less severe in 2D INEPT compared to HSQC (cf. Figure 3). As J_{HH} seldom exceeds 10% of the $^1J_{\mathrm{CH}}$, the effect of homonuclear coupling evolution to the quantitativity can be regarded as negligible in this particular case, but the error from this source should be understood when high precision in quantification is needed.

2.4. Sensitivity considerations

The amount of the analyte gives restrictions what types of experiments are applicable. With quantitative 2D NMR it must be considered which kind of spectrum delivers the needed information with best sensitivity.[116,117] The overall sensitivity of a pulse experiment can be calculated according to following equation[87]

$$S/N \propto \gamma_{\mathrm{exc}}\gamma_{\mathrm{obs}}^{3/2}\left\{1-\exp\left(-\frac{t_{\mathrm{recycle}}}{T_1^{\mathrm{exc}}}\right)\right\} \tag{13}$$

where γ_{exc} and γ_{obs} are the gyromagnetic ratios of the excited and observed nucleus, respectively, $t_{recycle}$ is the recycle time of the pulse sequence, and T_1^{exc} is the longitudinal relaxation time of the excited nucleus. The decisive factors in the sensitivity are the gyromagnetic ratios of the excited nuclei and the observed nuclei. In this regard, the most sensitive are the homonuclear 2D NMR experiments where the high gyromagnetic ratio of proton can be employed both in excitation and observation. In inverse-detected heteronuclear $^{1}H–^{13}C$ correlation experiments we can also employ proton both in excitation and observation. However, as the natural abundance of carbon-13 is 1.1%, only the same portion of the proton magnetization will contribute to observable signal. The advantage of inverse detection over the direct observation in $^{1}H–^{13}C$ correlation experiments is its eight-fold higher sensitivity. Therefore, if we need to analyze and quantify samples that contain the chemicals of interest in small amounts or if the chemicals are minor components, the best option from the sensitivity point of view is to employ 2D homonuclear correlation experiments. The inverse-detected $^{1}H–^{13}C$ correlation experiments are recommended when better resolution is wished without sacrificing too much the sensitivity. When the amount of the analyte is not the issue, the best resolution can be achieved using carbon-detected $^{1}H–^{13}C$ correlation experiment.

2.5. RF pulse imperfections

Preceding product operator examinations rely on assumption of perfect RF pulses. When RF pulse does not deliver magnetization transform as perfectly as intended, the result is loss of magnetization that gives the observable signal. In addition, unintended coherences may develop giving spurious artefacts to the spectrum. Usual source of pulse imperfections, and also the easiest to correct, is miscalibration of pulses. The source of the pulse imperfections can be also hardware related; the probe head coil can give inhomogeneous B_1 field, or the RF pulse synthesizer can give inconsistent RF pulse frequency, duration, phase or power. Nowadays hardware-related problems are in minor role due to digitalization of the RF pulse synthesis. However, there is also one aspect intrinsically related to the principle of pulse-Fourier NMR spectroscopy that can cause imperfect nutation of magnetization. An RF pulse with a finite amplitude delivers the intended nutation of magnetization when the transmitter frequency is on-resonance. When the resonance offset increases, the nutation of magnetization will deviate from the optimum. Development of high-field NMR spectrometers has made this off-resonance effect[118,119] quite common phenomenon. Proton with sufficiently narrow chemical shift range can be excited uniformly using standard RF amplifiers, but excitation of other nuclei with larger chemical shift dispersion, like carbon, can suffer heavily from this effect. Also, loss of signal intensity with polarization transfer experiments[120] can be significant due to off-resonance effects. Therefore, while the 2D homonuclear correlation experiments can be applied to quantification without further consideration of the offset effects, these effects can be a significant source of error when 2D $^{1}H–^{13}C$ correlation experiments are utilized.[93]

The importance of the problem has raised significant interest in the development of techniques aimed to improve the performance of the RF pulses with finite amplitude. The problem can be addressed by using a sequence of pulse elements, so-called composite pulses,[121,122] that are designed to fulfil either inversion,[123–125] refocusing,[126–28] excitation[129,130] or even arbitrary nutation[131] of magnetization. The other technique that can fulfil the need for uniform manipulation of magnetization over wide chemical shift range utilizes adiabatic fast passages[132,133]. There have been some intriguing demonstrations how the off-resonance effect can be compensated with broadband composite or adiabatic pulses thus giving a more uniform polarization transfer between proton and carbon over the whole chemical shift range.[134–136] These techniques can be utilized in development of suitable quantitative 2D ^{1}H–^{13}C correlation experiments with a better tolerance of offset effects.

2.6. Relaxation

When a spin system under a strong homogenous magnetic field is perturbed with a RF pulse from its thermodynamic equilibrium, it will tend to return back to the energetically favoured equilibrium state. This process is called as longitudinal or spin–lattice relaxation,[137] and the time constant for this exponentially occurring progress is marked with symbol T_1. Each spin in the spin system has its own unique rate of longitudinal relaxation, and by that its own T_1 time. The second relaxation process is also taking place when magnetization is tilted from the thermodynamic equilibrium to transverse plane. Due to, e.g. various spin interactions causing small magnetic field fluctuations the magnetization loses its coherence and therefore its intensity. This process is called as transverse or spin–spin relaxation,[138] and the time constant for this also exponentially occurring progress is marked with symbol T_2. Classically, these relaxation processes can be described with Bloch equations.[139,140]

In repetitive pulse experiments the magnetization recovers back towards the thermodynamic equilibrium during the acquisition time and the following relaxation delay with rate determined by the T_1 relaxation. If the magnetization has no time to fully recover during these delays, the magnetization gets saturated, and only a part of the magnetization can be excited with the next pulse. As a result, the signal intensity does not represent the full equilibrium magnetization of the given nucleus, and therefore the quantitativity of the spectrum is compromised. The recovered magnetization on the z-axis (the external magnetic field axis) in repetitive pulse experiments[141] is

$$M_z^{\mathrm{rep}} = M_0 \frac{1 - \exp\left(-\frac{t_\mathrm{r}}{T_1}\right)}{1 - \exp\left(-\frac{t_\mathrm{r}}{T_1}\right)\cos(\alpha)}, \tag{14}$$

where M_0 is the thermodynamic equilibrium magnetization, t_r is the repetition time, i.e. the sum of the acquisition time and the relaxation delay, and α is the

excitation pulse angle. In 2D NMR experiments the polarization of the observed nucleus is transferred usually completely on the transverse plane, so for the magnetization recovery considerations α is 90°. In 1D NMR experiments the excitation pulse angle can be adjusted quite freely, but is frequently also set for 90°. Theoretically, a 100% recovery of the magnetization takes infinitely long. Therefore a recovery that exceeds 99% is considered sufficient to guarantee quantitativity of the spectrum. With 90° excitation pulse this corresponds repetition time that is five times the longest T_1 of the excited nuclei. This means that in carbon-detected heteronuclear experiments, where the polarization is transferred from excited protons to carbons, we only need to consider proton T_1s when optimizing repetition times (see Equation (13)).

If the T_1 relaxation times are long, measurement of fully quantitative 2D NMR spectrum can take exceedingly long time. However, the quantitativity of the spectrum can also be considered from the point of the relative difference of peak volumes in the spectrum, and how it is affected by the partial saturation of magnetization due to insufficient repetition time. Consider two cross peaks, representing two chemicals of interest with longitudinal relaxation times of ${T_1}^0$ and ${T_1}^1$, in a 2D NMR spectrum. If the repetition time is set shorter than $5{T_1}^{0,1}$, ${M_z}^{\mathrm{rep}0,1} < {M_0}^{0,1}$ through saturation of the magnetization, and the signal intensity is decreased for both chemicals. If ${T_1}^0 = {T_1}^1$, and we assume that T_2 effects are negligible, we can hypothesize that the ratio ${M_z}^{\mathrm{rep}1}/{M_z}^{\mathrm{rep}0}$ is the same regardless of the repetition time t_r (Figure 10). Therefore, we can set the repetition time $1.269{T_1}^{0,1}$ to get the optimal sensitivity for given measurement time[142], while the integrals from the two chemicals can be used to accurately determine their relative amounts in the sample. A situation where the T_1s are identical is very rarely encountered with real samples. If the T_1 times of the excited nuclei are relatively close to each other and the best possible quantitativity is not needed, shorter repetition time than five times the T_1 can be used. For example, if the ratio of the shortest T_1 time (${T_1}^1$) and the longest T_1 time (${T_1}^0$) equals 3/5, we can set the repetition time to correspond $3{T_1}^0$ and still get the amount of the chemical with ${T_1}^1$ under 5% margin of error (Figure 10).

If the duration of the pulse sequence is long, the magnetization can also attenuate between the first pulse and the beginning of the acquisition time. The relaxation rate of the magnetization will vary during the pulse sequence depending on its coherence order. For a rigorous analysis of the dynamics of the spin system and the relaxation parameters a more elaborate mathematical treatment should be used.[143] However, in most cases the transverse relaxation of the excited nucleus is the dominant factor that attenuates the magnetization, and an approximate result can be obtained with Bloch equations.[139,140] The attenuation of magnetization during the pulse sequence can be approximated as

$$M_{x,y} = \exp\left(-t_\mathrm{ps}/T_2\right), \tag{15}$$

where t_ps is the time magnetization spends on transverse plane during the pulse sequence, i.e. where T_2 relaxation takes place (normally the time between the first pulse and the beginning of the acquisition time). We can again consider two cross

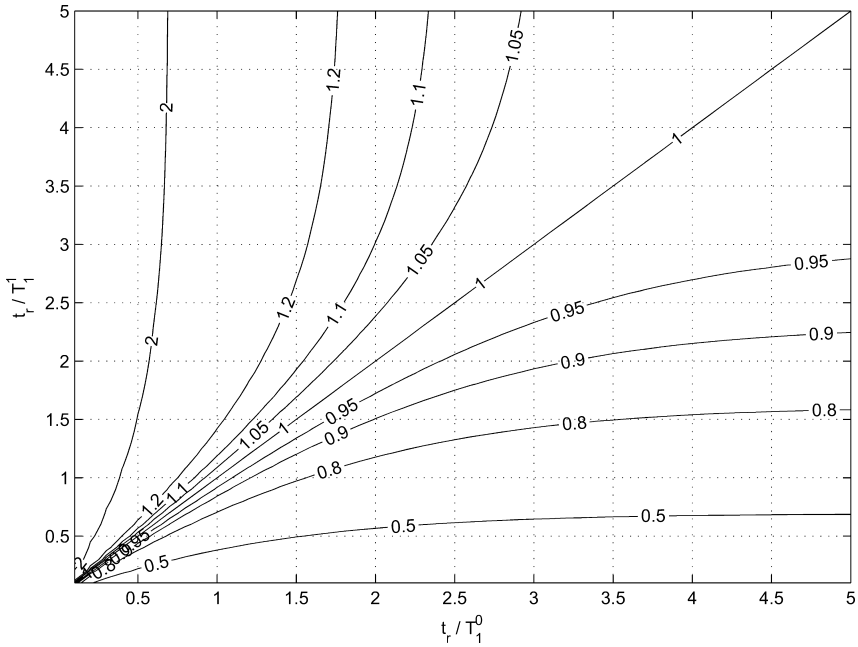

Figure 10 Intensity ratio for two resonances with different T_1 times (T_1^1 and T_1^0) with respect to the t_r/T_1^1 and t_r/T_1^0 ratios (cf. Equation (14)). The delay t_r is the repetition time of a 2D pulse experiment.

peaks representing two chemicals of interest with transverse relaxation times of T_2^0 and T_2^1 in a 2D NMR spectrum. If the pulse sequence duration is longer than 0.05 times $T_2^{0,1}$, the magnetization has lost over 5% its intensity through transverse relaxation, and the signal intensity recorded during the acquisition time is decreased. However, if $T_2^0 = T_2^1$, we can hypothesize that the ratio $M_{x,y}{}^1/M_{x,y}{}^0$ is the same regardless of the duration of the pulse sequence t_{ps} (Figure 11).

Furthermore, Figure 11 shows that if the difference of ratios t_{ps}/T_2^0 and t_{ps}/T_2^1 remains under 0.05, the intensities of the magnetization will not deviate more than 5% regardless of the values of t_{ps}, T_2^0 or T_2^1. For example, a HSQC experiment optimized for 125 Hz $^1J_{CH}$ couplings will have t_{ps} of 8 ms. For small molecules the T_2s can be in range of 1–3s, so the differences of signal intensities in the HSQC spectrum due to attenuation of magnetization through T_2 during the pulse sequence should be negligible.[92] The attenuation of magnetization in larger molecules with short T_2s can have a significant effect to the quantitativity.[144]

2.7. Processing

Processing of the NMR data has significant contribution to the quantitativity of the spectrum. To achieve a 2D NMR spectrum where cross peaks can be integrated with confidence, several factors that affect the spectrum must be considered. In the 1D pulse-Fourier NMR spectroscopy the excited magnetization

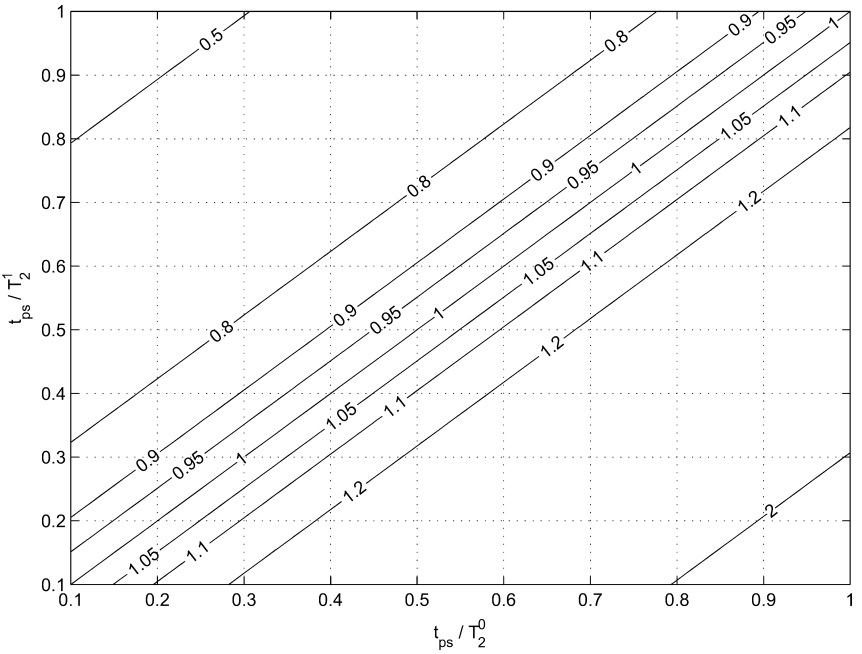

Figure 11 Intensity ratio for two resonances with different T_2 times (T_2^1 and T_2^0) with respect to the t_{ps}/T_2^1 and t_{ps}/T_2^0 ratios (cf. Equation (15)). The delay t_{ps} is the time in the pulse sequence where the T_2 relaxation takes place in a 2D pulse experiment.

induces the current to the receiver coil, and this current is sampled by the analog–digital converter at evenly spaced points with respect to time as the free-induction decay data. These data are transformed with discrete Fourier transform to the frequency-domain spectrum, where Lorentzian peaks are shown with respect to their resonance frequency. In 2D NMR spectroscopy, we have the same acquisition time period marked as t_2, which is sampled with respect to time. Additionally, we measure the t_2 data with different t_1 evolution times. The t_1 evolution time is also linearly incremented, so after discrete Fourier transform of the acquired data with respect to t_2 dimension, we can also perform the discrete Fourier transform along t_1 dimension of the 2D matrix. Ideally, after 2D Fourier transform of the 2D data matrix each peak in this 2D NMR spectrum should be with fully Lorentzian shape starting from the zero level of the 2D NMR spectrum. In practice, the quality of the 2D NMR spectrum can differ greatly from this ideal case, making reliable integration of the cross peaks more difficult.

One artefact that may appear in the 2D NMR spectrum has its origins in the nature of the data sampling. The spectrum can contain constant ridges along both F_1 and F_2 dimensions that start from the base of the cross peaks.[145] The reason of this artefact is improper weighting of the cosine-modulated time-domain data.[146] A solution to this problem, according to the theory of the discrete Fourier transform,[146] is to multiply the first time-domain point by 0.5. This correction is typically a default setting in spectrum processing software, but there can be

situations due to analogue filtering or receiver gating that the intensity of the first point is attenuated. In these cases the correct multiplication constant can be found empirically. Other possible solution for this problem is to modify the data acquisition so that sine-modulated data are recorded during t_2 and t_1 periods. This would mean that the first point of sine-modulated data should be zero, and in this way the weighting error would be negligible.[146]

The spectrum can also contain noise strands that go through the peak bases along F_1 dimension. The level of the noise is proportional to the intensity of the cross peak. This t_1 noise[147] is caused by general hardware instabilities like inconsistencies in RF pulse synthesis and pulse sequence timing.[148] Introduction of pulsed field gradients[149] together with digitalized RF pulse synthesizers has significantly reduced the level of this artefact, but this can still be a problem in analysis of minor components in a mixture sample containing intense background signals. The level of t_1 noise can not be reduced in the spectrum through processing of the acquired data. Baseline correction can be used to shift the middle point of the noise,[150] but this can also affect the volume of cross peaks that appear on this t_1 noise ridge. Such cross peaks should be cautiously used for quantification.

The number of acquired points should be sufficient to give a good digital resolution to the spectrum.[151] With 2D NMR experiments the number of data points in the indirect dimension is limited in order to keep the total acquisition time reasonable. Therefore the acquired data will need zero filling to provide the aimed digital resolution. The same rules apply to the 2D NMR spectra as to 1D NMR spectra; if the digital resolution is too small, the line shapes will be too coarse to accurately describe the resonance, and the peak volume will be biased.

Apodization or weighting of the acquired 2D data has a major effect to the appearance of the spectrum. Apodization is used either for enhanced signal-to-noise ratio or enhanced resolution. It can be also used to smooth a truncated acquisition data to avoid distortions that appear on the base of peaks.[151] Truncated data can be also corrected with linear prediction,[152–154] and it is useful to apply linear prediction to the indirect dimension to enhance resolution. In case of HSQC data, apodization that mimics the natural decay of the signal (i.e. exponential windowing) should guarantee the best quantitativity. Exponential windowing may not always be the best option if good resolution is aspired, and then a good compromise is to use apodization with a small resolution enhancement, like squared cosine windowing. Effects of apodization and linear prediction on the quantitativity of the spectrum have been discussed in literature by several authors.[155–158] Validation tests are naturally recommended in selection of the optimal apodization and linear prediction in the used 2D NMR experiment and the samples.

Integration of the cross peak can be performed in two ways: by direct summation of the spectral data points or by peak parameter search by curve fitting.[159] Direct summation is computationally fast method to acquire the peak volume, but may be affected by baseplane roll, t_1 noise, or tails of other peaks, whereas curve fitting, when successful, can reveal the true volume of the peak.[160–162] Usually the peak volume integration method is, however, chosen on the basis of availability, i.e. which integration tool is incorporated in the spectrometer's operating software. There are several third-party NMR processing software packages available

featuring some advanced NMR data processing tools[163–165] which offer more flexibility in processing of the spectra. When quantitative analysis is conducted for a large set of samples, the recorded spectra must be processed in identical manner, preferably by the same operator. This ensures that the processing deviations between the spectra are minimized and quantitative comparison between the samples should be straightforward.

2.8. Reference in quantification

In quantitative NMR spectroscopy the concentration of the analyte is typically determined by comparing the analyte resonance integral to an inert, internal reference with known concentration. In quantitative 2D NMR the relation between the cross peak integrals of the reference and the analyte can be established ether by calibration curve and/or correction coefficients derived from theoretical calculations. It is then quite straightforward to calculate the analyte concentration in the sample. In some cases there are no inert references available that could be applied internally to the sample. In these cases a reference chemical in a coaxial glass insert within the NMR sample tube can be used, so that no contact will take place between the sample and the reference chemical. Other possibility is to use external standard in a separate NMR tube.[8]

The referencing can also be done by employing an artificial reference resonance. The electronic reference to access in vivo concentrations also known as the (ERETIC)[166] method provides a reference signal, synthesized by an electronic device, which can be used for the determination of absolute concentrations. The ERETIC approach has been applied to 1D NMR quantification with high accuracy; the standard deviation has been reported to remain under 1%.[167,168] Michel and Akoka[169] have also adopted this technique to produce an artificial reference cross peak in 2D homonuclear and heteronuclear correlation spectra. This approach shows potential as a universal reference in quantification.

3. APPLICATIONS

A survey of literature gave over 20 papers where 2D NMR experiments was successfully applied in quantification of complex samples. The selection of the used experiments was also quite diverse; all typical 2D homo- and heteronuclear correlation experiments were among them. Many of the authors also compared the 2D NMR results against 1D NMR quantification or quantification with other analytical technique. In overall, 2D NMR quantification offered a better linearity and accuracy in these comparisons due to better resolved peaks. Additionally, the approach often facilitated analysis of minor components that were not distinguishable from 1D NMR spectra. The main part of the papers that demonstrated 2D NMR quantification focused on the analysis of natural products like animal and plant metabolites. Some articles were also found where quantitative 2D NMR was applied to quality control in food industry, and on characterization of the products of oil industry. The following sections give a short summary of the quantitative 2D NMR on the aforementioned topics.

3.1. Metabolic profiling

Study of natural products, biological systems and processes taking place in living organisms has become a major research. NMR spectroscopy has been an important technique in characterization and quantification of single natural products in plant extracts, dietary materials, and materials representing different metabolic stages of organisms.[170] A more comprehensive approach to follow the metabolic fluxes and metabolism with NMR spectroscopy, often referred as metabonomics,[171] is a new emerging research field, and many new methods in this research are under development. There are number of excellent review articles and text books that discuss the concepts and applications of metabolomics/metabonomics,[172–175] and the reader interested in this topic is encouraged to familiarize oneself with the literature.

2D *J*-resolved NMR has been applied to metabolomics to enhance resolution of the overlapping resonances and facilitate identification of the sample components.[176,177] Viant[178] used this approach to achieve quantitative 1D F_2-projections which were analysed using principal component analysis to evaluate metabolites citrate, taurine and alanine in embryogenesis of fish *Oryzias latipes*. In comparison to conventional ^{1}H NMR quantification the author stated that the likelihood that a peak in the projection spectrum contains more than one resonance is significantly smaller, thus providing additional accuracy for summarizing and interpreting the metabolomic data. The same combination of 2D *J*-resolved NMR and statistical analysis has been used by Viant et al. in subsequent studies,[179,180] and also by other research groups in studies of, e.g. liver tissue[181] and plant metabolism.[182–184]

Tiziani et al.[158] reported an extensive study on the comparison of two weighting functions, sine-bell and sine-bell combined with exponential, and their effects on the 2D *J*-resolved spectrum resolution and reproducibility. Their tests with dog urine, fish liver extract and leukaemia cell extract samples indicated that combined use of sine-bell and exponential apodization resulted in a better resolution and reproducibility, which should be beneficial in quantitative studies.

There are several reports dating from the 1980s where metabolic analyses were performed with COSY.[185–191] In a study by Alonso et al.[192] absolute-value COSY spectra were used to identify lactate in samples of intact frog muscle. The paper also demonstrated the quantification of the lactate levels on the basis of lactate cross peak volumes. The authors reported a good linear correlation (R^2 0.996) when the cross peak volume of lactate in varied concentration was compared against a cross peak volume of the internal reference, carnosine. Based on that finding the authors were able to follow the changes of lactate level in *gastrochemius* frog muscles during the 18 h observation time.

Nouaille et al.[193] studied occurrence of maltodextrins in a strain of *Fibrobacter succinogenes* using DQF-COSY. They were able to identify, and also quantify, the presence of maltodextrin-1-phosphate in this rumen bacterium. Massou et al.[194] applied both absolute-value DQF-COSY and phase-sensitive TOCSY experiments to quantification of ^{13}C-enriched glucose metabolites and carbon fluxes in *Escherichia coli*. In their comparison they observed that TOCSY delivered a better quantitativity in this application. The in-phase coherences obtained with zero-quantum filtering[83] gave only positive signals in the phase-sensitive TOCSY spectrum,

which enabled easier 2D integration. The magnitude calculations with the DQF-COSY caused broad lines, making the integration more difficult; other implications were also discussed. It was also noted that the heteronuclear scalar couplings were averaged to zero with TOCSY during the isotropic mixing period, and the effects related to long-range heteronuclear couplings were avoided. TOCSY experiment was also used by Van et al.[195] in comparison of global metabolic profiles of mouse urine. They reported that the improved resolution facilitated detection of minor metabolic components in urine giving more accurate and statistically relevant analysis of changes in the metabolic fluxes.

In the study by Dumas et al.[196] 2D ^{1}H–^{13}C correlation spectroscopy was validated in analysis of metabolism in cattle treated with anabolic steroids. Urine samples were analyzed with HMBC, where polarization transfer was optimized for $^{2-3}J_{CH}$ couplings. They applied linear discriminant analysis to extract quantitative variables from the spectra in order to reveal metabolism involved in endocrine disruption processes. Guerrini et al.[197] adopted also 2D ^{1}H–^{13}C correlation spectroscopy, in this case HSQC, in analysis of differently substituted monosaccharide components of heparan sulphate and other glycosaminoglycans obtained by chemical modification of the *E. coli* K5 polysaccharide. The authors discussed the implications to the quantitativity of the integrals with respect to the differences between polarization transfer optimization and the true $^{1}J_{CH}$ couplings. They stated that when variation among true $^{1}J_{CH}$ values was in range 5–8 Hz, as obtained for uronic acid residues, it did not affect to a significant degree to the calculated content in glycosaminoglycan individual residues. However, there were cases where observed couplings of certain groups differed 25 Hz, and differences of these magnitudes, according to the authors, can generate significant errors in the compositional analysis. HSQC was also applied by Lewis et al.[198] in their study. They reported identification and quantification of ca. 40 most abundant metabolites in extracts from *Arabidopsis thaliana*, *Saccharomyces cerevisiae* and *Medicago sativa* with their proposed fast metabolite quantification, or FMQ, method. The FMQ by NMR demonstrated excellent linearity (R^2 0.99, slope 0.97), and the average error was smaller in the FMQ by NMR compared to ^{1}H NMR quantification (2.7 and 16.2%, respectively).

3.2. Lignin chemistry

While a large part of natural product studies is focused on plant extracts containing small molecules, a significant amount of research is also going on with polymers of the flora. Pulp industry that uses cellulose of wood in paper making[199] has also carried out research on the other major polymer of the plant kingdom known as lignin.[200] Lignin is heterogeneous and lacks defined primary structure, and therefore various models of lignin structure have been proposed.[201–205] NMR as a powerful structural elucidation technique has also been employed in characterization of lignin both in solution and solid state.[206,207]

Heikkinen et al.[92] presented an application of the Q-HSQC experiment with uniform polarization transfer over a range of J_{CH} couplings in quantification. This study with a mixture of lignin model compounds demonstrated comparative

results against 1D ^{1}H and ^{13}C quantification, and the relative standard deviation remained below 3% in all cases. Zang and Gellersted[144] presented an extensive study on the influence of T_2 relaxation in quantification with HSQC experiment. They proposed an approach where cross peaks with the same T_2 relaxation profiles were analyzed as individual groups, so that the T_2 errors in quantification could be minimized. Their results in quantification of milled wood lignin of *Picea abies* agree well with the literature values[202,204,208,209] acquired with chemical analysis or 1D NMR methods.

Natural degradation of lignin has also been under interest. Lignin degradation products form a large part of humic substances in soil as well as in river and lake waters. NMR spectroscopy has been used in several studies to characterize these highly complex samples.[210–213] A report by Haiber et al.[214] described analysis of humic and fulvic acids in river water reference samples. They used HETCOR, a version of the 2D INEPT experiment, in identification of lignin degradation products. The size-exclusion fractioned sample with high molecular weight compounds (>100 kDa) was not analyzable with HETCOR due to relaxation losses, but the method was applicable in quantification of lower molecular weight fractions. Information was used to interpret the processes of lignin degradation.

3.3. Food analysis and quality control

Food production for human and animal consumption is an important branch of industry. The production, processing, as well as storage, is controlled by national and international legislation. This legislation is aimed to assure that the food is safe for human or animal consumption by regulating, e.g. what are the acceptable limits of bacteria growth and related toxins, pesticide and herbicide remnants, preservatives and additives. There is also need to verify the origin of the foodstuff (e.g. gene manipulated grain and vegetables) and to prevent counterfeit food products (e.g. wines and liqueurs) to end up on the market. Many of these regulations need verification by methods of analytical chemistry. NMR spectroscopy has also been applied to food analysis, and there are some excellent reviews on this topic.[215,216]

A report where quantitative 2D NMR was applied to differentiation of beer brands was published by Khatib et al.[217] They used 2D *J*-resolved NMR to improve resolution of components present in 2-butanol extracts of several beer brands. With application of principal component analysis they distinguished six lagers from each other based on their amino acid contents. They also discussed how the amount of compounds that have an important effect to the taste, like tyrosol, can be estimated with the method.

Hu et al.[218] demonstrated how organic compounds could be quantified in whole milk by HSQC. A relaxation reagent was used in the milk samples to speed up the acquisition. Calibration curves for sodium citrate, acetylglucosamine, tributyrin, triolein, trilinolein and lecithin measured against an external reference (1,1,2,2-tetrachloroethane) in a coaxial glass insert showed a good linearity; R^2 was above 0.98 in all cases. The amounts of the chemicals in milk were in accordance with the reference values determined by gas chromatography.

Use of quantitative 2D NMR spectroscopy is still quite rare in food analysis and quality control. A possible reason can be that experimental set-up, acquisition and processing of 2D NMR experiments are considered to be too difficult or time-consuming compared to 1D NMR experiments. Also, restrictions and regulations from the laboratory environment (quality systems, standards) can hinder application of new methodology in quantification. Considering the challenging sample matrices the 2D NMR methods would be excellent tools in quantification.

3.4. Product properties of oil fractions

Oil industry has a long history of application of NMR spectroscopy for characterization of crude oils, products and oil fractions. The methodology has been mainly 1D proton- or carbon-detected experiments. Quantitative ^{1}H NMR and ^{13}C{^{1}H} NMR experiments have been used in estimation of aromatic, olefin, naphtene and paraffin proportions in the samples.[219,220] A more detailed characterization has been obtained using various 1D carbon-detected experiments, like GASPE, CSE, QUAT and DEPT to obtain quantitative CH_n sub-spectra.[221–224] The goal of characterization of the oil fractions and quantification of certain structural features has been to find correlation between these features and the product properties (e.g. viscosity index, pour point). Due to environmental concerns oil companies are nowadays more interested in development of lubricant base oils that have low aromatic and olefin contents. Hydrogenation of unsaturated components also improves the stability of the base oils, which is an important property for the end-product. Quantitative analysis of a saturated oil fraction with NMR is a major challenge. When the oil fraction contains only aliphatic compounds, the spectrum width that contains the resonances narrows to ca. 1 ppm in the ^{1}H NMR spectrum and ca. 50 ppm in ^{13}C{^{1}H} NMR spectrum. This causes excessive resonance overlap in the 1D NMR spectra, thus rendering their usefulness in characterization of oil fractions quite limited. Therefore, elevated interest in 2D NMR spectroscopy for characterization and quantification of oil fraction components has risen. 2D NMR spectroscopy has been used by several research groups to characterize the average structure of the oil fractions.[225–229] Quantitativity studies of certain 2D NMR experiments like TOCSY[230] and 2D INEPT[231] have also been reported. In addition, there have been attempts to make statistical models how the quantitative information derived from 2D NMR spectra can be used to predict oil product properties. Peng et al.[232] applied 2D ^{13}C *J*-resolved NMR data to estimate the molar concentration of the different CH_n (n = 0, 1, 2, 3) spin systems in the sample, and by that to predict the density and viscosity of the crude oils. Väänänen et al.[233] used the artificial neural network analysis to correlate HSQC data from a set of hydrogenated oil fractions to their viscosity indexes. The part of the spectra containing methyl cross peaks, i.e. the part that contained most of the information about the hydrocarbon chain branching, was processed with the artificial neural network analysis. The analysis predicted viscosity indexes of the oil fractions with correlation coefficient 0.903, indicating that the hydrocarbon chain branching is an important factor in determination of the

viscosity index. The analysis also indicated what kind of branching in the hydrocarbons most likely promoted the desired high viscosity index.

While there is a limited number of publications about application of quantitative 2D NMR in oil fractions, they still demonstrate how much more details 2D NMR can offer. The reason for the low number of papers can be also explained by the nature of the business; oil companies might feel to lose an advantage in the markets if they publish their latest analytical methodologies. The industry itself is now on the verge of changes due to depleting oil resources and general concerns of environmental pollution. Motor oils and other oil products will be needed also in the future, but the oil consumption need to be controlled and reduced. Development of new oil products fulfilling these new requirements needs tools of analytical chemistry, and by that, NMR spectroscopy.

4. CONCLUSIONS

Quantitative 2D NMR has shown its applicability as well as validity on several fields of research. Compared to quantitative 1D NMR, quantitative 2D NMR is more demanding with respect to experimental set-up, processing and cost of measurement time, but with the invested effort, 2D NMR offers significant improvement in resolution, and therefore challenges 1D NMR techniques in quantification of complex samples. Combination of sophisticated statistical analysis and the quantitative 2D NMR is an approach that has found a fertile ground in, e.g. metabolomics and may demonstrate its value also in new fields of research. While 1D NMR will remain the most used NMR technique for quantification, use of 2D NMR will find growing interest in quantitative studies of complex samples.

ACKNOWLEDGMENTS

I would like to express my gratitude to Sami Heikkinen, Taito Väänänen and Outi Heikkinen for their comments on the manuscript.

REFERENCES

1. M. J. K. Thomas and D. J. Ando, *Ultraviolet and Visible Spectroscopy: Analytical Chemistry by Open Learning*. Second Edition, Wiley, Chichester, 1996.
2. B. H. Stuart, *Infrared Spectroscopy: Fundamentals and Applications*. Wiley, Chichester, 2004.
3. E. De Hoffmann and V. Stroobant, *Mass Spectrometry: Principles and Applications*. Third Edition, Wiley, Chichester, 2007.
4. V. Rizzo and V. Pinciroli, *J. Pharmaceut. Biomed.*, 2005, **38,** 851.
5. N. J. Serkova and C. U. Niemann, *Expert Rev. Mol. Diagn.*, 2006, **6,** 717.
6. M. L. Martin, G. L. Martin and J. J. Delpuech, *Practical NMR Spectroscopy*. Heyden, London, 1980, Chapter 9.
7. D. I. Hoult and R. E. Richards, *J. Magn. Reson.*, 1976, **24,** 71.
8. I. W. Burton, M.A Quilliam and J. A. Walter, *Anal. Chem.*, 2005, **77,** 3123.
9. G. Wider and L. Dreier, *J. Am. Chem. Soc.*, 2006, **128,** 2571.
10. R. Freeman, H. D. W. Hill and R. Kaptein, *J. Magn. Reson.*, 1972, **7,** 327.
11. J. N. Shoolery, *Prog. Nucl. Magn. Reson. Spectrosc.*, 1977, **11,** 79.
12. D. D. Traficante, *Concepts Magn. Reson.*, 1992, **4,** 153.

13. M. L. Martin, G. L. Martin and J. J. Delpuech, *Practical NMR Spectroscopy*. Heyden, London, 1980, Chapter 4.
14. D. J. Cookson and B. E. Smith, *J. Magn. Reson.*, 1984, **57,** 355.
15. M. Bouquet and A. Bailleul, *Fuel*, 1986, **65,** 1240.
16. N. H. Low, T. Brisbane, G. Bigam and P. Sporns, *J. Agric. Food Chem.*, 1988, **36,** 953.
17. H. H. Fischer, M. Seiler, T. S. Ertl, U. Eberhardinger, H. Bertagnolli, H. Schmitt-Willich and K. Albert, *J. Phys. Chem. B*, 2003, **107,** 4879.
18. E. Caytan, G. S. Remaud, E. Tenailleau and S. Akoka, *Talanta*, 2007, **71,** 1016.
19. P. Giraudeau and E. Baguet, *J. Magn. Reson.*, 2006, **180,** 110.
20. D. A. Netzel, *Anal. Chem.*, 1987, **59,** 1775.
21. M. Hamaguchi and T. Nishizawa, *Fuel*, 1992, **71,** 747.
22. L. Pouységu, B. De Jéso, J.-L. Lartigue, M. Pétraud and M. Ratier, *Chem. Pharm. Bull.*, 2002, **50,** 1114.
23. R. Burger and P. Bigler, *J. Magn. Reson.*, 1998, **135,** 529.
24. P. Bigler, R. Kümmerle and W. Bermel, *Magn. Reson. Chem.*, 2007, **45,** 469.
25. T. Özdoğan and M. Orbay, *Spectr. Lett.*, 2002, **35,** 447.
26. A. Allerhand, R. E. Addleman and D. J. Osman, *J. Am. Chem. Soc.*, 1985, **107,** 5809.
27. A. Allerhand and M. Dohrenwend, *J. Am. Chem. Soc.*, 1985, **107,** 6684.
28. A. Allerhand and S. R. Maple, *Anal Chem.*, 1987, **59,** 441A.
29. G. A. Pearson and R. I. Walter, *J. Magn. Reson.*, 1977, **16,** 348.
30. J. Mahler and A. Sebald, *Solid State Nucl. Magn. Reson.*, 1995, **5,** 63.
31. M. Uike and T. Uchiyama, *J. Magn. Reson.*, 1992, **99,** 363.
32. J. Jeener, *Ampére International Summer School*. Basko Pojke, 1971.
33. R. R. Ernst, *VI International Conference on Magnetic Resonance in Biological Systems*. Kandersteg, 1974.
34. R. R. Ernst, *Chimia*, 1975, **29,** 179.
35. L. Müller, A. Kumar and R. R. Ernst, *J. Chem. Phys.*, 1975, **63,** 5490.
36. W. P. Aue, E. Bartoli and R. R. Ernst, *J. Chem. Phys.*, 1976, **64,** 2229.
37. M. Lin and M. J. Shapiro, *Anal. Chem.*, 1997, **69,** 4731.
38. W. Eisenreich and A. Bacher, *Phytochemistry*, 2007, **68,** 2799.
39. J. Jeener, B. H. Meier, P. Bachmann and R. R. Ernst, *J. Chem. Phys.*, 1979, **71,** 4546.
40. B. H. Meier and R. R. Ernst, *J. Am. Chem. Soc.*, 1979, **101,** 6441.
41. C. L. Perrin and T. J. Dwyer, *Chem. Rev.*, 1990, **90,** 935.
42. S. Macura and R. R. Ernst, *Mol. Phys.*, 1980, **41,** 95.
43. A. Kumar, R. R. Ernst and K. Wüthrich, *Biochem. Biophys. Res. Commun.*, 1980, **95,** 1.
44. K. Wüthrich, *NMR of Proteins and Nucleic Acids*. Wiley, New York, 1986.
45. O. W. Sørensen, G. W. Eich, M. H. Levitt, G. Bodenhausen and R. R. Ernst, *Prog. Nucl. Magn. Reson. Spectrosc.*, 1983, **16,** 163.
46. G. D. Mateescu and A. Valeriu, *2D NMR: Density Matrix and Product Operator Treatment*. Prentice Hall, New Jersey, 1993.
47. F. J. M. Van de Ven, *Multidimensional NMR in Liquids: Basic Principles and Experimental Methods*. VCH, New York, 1995, Chapter 2.6.
48. J. Shriver, *Concepts Magn. Reson.*, 1992, **4,** 1.
49. I. S. Podkorytov, *Concepts Magn. Reson.*, 1997, **9,** 117.
50. W. P. Aue, J. Karhan and R. R. Ernst, *J. Chem. Phys.*, 1976, **64,** 4226.
51. H. Y. Carr and E. M. Purcell, *Phys. Rev.*, 1954, **94,** 630.
52. S. Meiboom and D. Gill, *Rev. Sci. Instrum.*, 1958, **29,** 688.
53. K. Nagayama, *J. Chem. Phys.*, 1979, **71,** 4404.
54. P. Xu, X. L. Wu and R. Freeman, *J. Am. Chem. Soc.*, 1991, **113,** 3596.
55. M. Woodley and R. Freeman, *J. Magn. Reson. A*, 1994, **109,** 103.
56. J. M. Nuzillard, *J. Magn. Reson. A*, 1996, **118,** 132.
57. S. Simova, H. Sengstschmid and R. Freeman, *J. Magn. Reson.*, 1997, **124,** 104.
58. V. A. Mandelshtam, H. S. Taylor and A. J. Shaka, *J. Magn. Reson.*, 1998, **133,** 304.
59. P. Mutzenhardt, F. Guenneau and D. Canet, *J. Magn. Reson.*, 1999, **141,** 312.
60. A. Bax, R. Freeman and G. Morris, *J. Magn. Reson.*, 1981, **42,** 164.
61. A. Bax and R. Freeman, *J. Magn. Reson.*, 1981, **44,** 542.
62. R. E. Hurd, *J. Magn. Reson.*, 1990, **87,** 422.

63. M. von Kienlin, C. T. W. Moonen, A. van der Toorn and P. C. M. van Zijl, *J. Magn. Reson.*, 1991, **93,** 423.
64. J. Cavanagh, W. J. Fairbrother, A. G. Palmer, III, M. Rance and N. J. Skelton, *Protein NMR Spectroscopy: Principles and Practice*. Second Edition, Academic Press, San Diego, 2007, Chapter 6.2.1.5.
65. D. Marion and K. Wüthrich, *Biochem. Biophys. Res. Commun.*, 1983, **113,** 967.
66. U. Piantini, O. W. Sørensen and R. R. Ernst, *J. Am. Chem. Soc.*, 1982, **104,** 6800.
67. M. Rance, O. W. Sørensen, G. Bodenhausen, G. Wagner, R. R. Ernst and K. Wüthrich, *Biochem. Biophys. Res. Commun.*, 1983, **117,** 479.
68. I. M. Brereton, S. Crozier, J. Field and D. M. Doddrell, *J. Magn. Reson.*, 1991, **93,** 54.
69. A. L. Davis, E. D. Laue, J. Keeler, D. Moskau and J. Lohman, *J. Magn. Reson.*, 1991, **94,** 637.
70. P. Giraudeau, N. Guignard, E. Hillion, E. Baguet and S. Akoka, *J. Pharm. Biomed. Anal.*, 2007, **43,** 1243.
71. A. Kumar, R. V. Hosur and K. Chandrasekhar, *J. Magn. Reson.*, 1984, **60,** 143.
72. R. V. Hosur, K. V. R. Chary, A. Kumar and G. Govil, *J. Magn. Reson.*, 1985, **62,** 123.
73. S. Talluri and H. A. Scheraga, *J. Magn. Reson.*, 1990, **86,** 1.
74. Y. Xia, G. Legge, K.-Y. Jun, Y. Qi, H. Lee and X. Gao, *Magn. Reson. Chem.*, 2005, **43,** 372.
75. L. Braunschweiler and R. R. Ernst, *J. Magn. Reson.*, 1983, **53,** 521.
76. D. G. Davis and A. Bax, *J. Am. Chem. Soc.*, 1985, **107,** 2820.
77. A. Bax and D. G. Davis, *J. Magn. Reson.*, 1985, **65,** 355.
78. A. J. Shaka, C. J. Lee and A. Pines, *J. Magn. Reson.*, 1988, **77,** 274.
79. F. Kramer, W. Peti, C. Griesinger and S. J. Glaser, *J. Magn. Reson.*, 2001, **149,** 58.
80. R. P. Hicks, J. K. Young and D. Moskau, *Concepts Magn. Reson.*, 1994, **6,** 115.
81. M. Rance, *J. Magn. Reson.*, 1987, **74,** 557.
82. A. L. Davis, G. Estcourt, J. Keeler, E. D. Laue and J. J. Titman, *J. Magn. Reson. A*, 1993, **105,** 167.
83. M. J. Thrippleton and J. Keeler, *Angew. Chem. Int. Ed.*, 2003, **42,** 3938.
84. K. E. Cano, M. J. Thrippleton, J. Keeler and A. J. Shaka, *J. Magn. Reson.*, 2004, **167,** 291.
85. T. T. Nakashima and R. E. D. McClung, *in: Encyclopedia of NMR*, D. M. Grant and R. K. Harris, eds., Wiley, New York, 1996.
86. G. Bodenhausen and D. J. Ruben, *Chem. Phys. Lett.*, 1980, **69,** 185.
87. R. R. Ernst, G. Bodenhausen and A. Wokaun, *Principles of Nuclear Magnetic Resonance in One and Two Dimensions*. Clarendon Press, Oxford, 1990, Chapter 8.5.
88. G. A. Morris and R. Freeman, *J. Am. Chem. Soc.*, 1979, **101,** 760.
89. R. Freeman, T. H. Mareci and G. A. Morris, *J. Magn. Reson.*, 1981, **42,** 341.
90. L. E. Kay, P. Keifer and T. Saarinen, *J. Am. Chem. Soc.*, 1992, **114,** 10663.
91. H.-O. Kalinowski, S. Berger and S. Braun, *Carbon 13 NMR Spectroscopy*. Wiley.
92. S. Heikkinen, M. M. Toikka, P. T. Karhunen and I. Kilpeläinen, *J. Am. Chem. Soc.*, 2003, **125,** 4362.
93. H. Koskela, I. Kilpeläinen and S. Heikkinen, *J. Magn. Reson.*, 2005, **174,** 237.
94. D. J. Peterson and N. M. Loening, *Magn. Reson. Chem.*, 2007, **45,** 937.
95. N. M. Loening, J. Keeler and G. A. Morris, *J. Magn. Reson.*, 2001, **153,** 103.
96. L. Frydman, T. Scherf and A. Lupulescu, *Proc. Natl. Acad. Sci. U.S.A.*, 2002, **99,** 15858.
97. N. M. Loening, M. J. Thrippleton, J. Keeler and R. G. Griffin, *J. Magn. Reson.*, 2003, **164,** 321.
98. L. Müller, *J. Am. Chem. Soc.*, 1979, **101,** 4481.
99. A. Bax and S. Subramanian, *J. Magn. Reson.*, 1986, **67,** 565.
100. R. E. Hurd and B. K. John, *J. Magn. Reson.*, 1991, **91,** 648.
101. J. Ruiz-Cabello, G. W. Vuister, C. T. W. Moonen, P. van Gelderen, J. S. Cohen and P. C. M. van Zijl, *J. Magn. Reson.*, 1992, **100,** 282.
102. A. Bax, M. Ikura, L. E. Kay, D. A. Torchia and R. Tschudin, *J. Magn. Reson.*, 1990, **86,** 304.
103. W. F. Reynolds, S. McLean, L. L. Tay, M. Yu, R. G. Enriquez, D. M. Estwick and K. O. Pascoe, *Magn. Reson. Chem.*, 1997, **35,** 455.
104. A. Bax and M. F. Summers, *J. Am. Chem. Soc.*, 1986, **108,** 2093.
105. W. Willker, D. Leibfritz, R. Kerssebaum and W. Bermel, *Magn. Reson. Chem.*, 1993, **31,** 287.
106. D. M. Doddrell, H. Bergen, D. Thomas, D. T. Pegg and M. R. Bendall, *J. Magn. Reson.*, 1980, **40,** 591.
107. D. M. Doddrell, D. T. Pegg, M. R. Bendall, W. M. Brooks and D. M. Thomas, *J. Magn. Reson.*, 1980, **41,** 492.

108. C. Brevard, G. C. van Stein and G. van Koten, *J. Am. Chem. Soc.*, 1981, **103,** 6746.
109. D. P. Burum and R. R. Ernst, *J. Magn. Reson.*, 1980, **39,** 163.
110. G. A. Morris, *J. Am. Chem. Soc.*, 1980, **102,** 428.
111. D. M. Doddrell and D. T. Pegg, *J. Am. Chem. Soc.*, 1980, **102,** 6388.
112. O. W. Sørensen and R. R. Ernst, *J. Magn. Reson.*, 1983, **51,** 477.
113. M. R. Bendall, D. T. Pegg and D. M. Doddrell, *J. Magn. Reson.*, 1981, **45,** 8.
114. A. Bax and S. K. Sarkar, *J. Magn. Reson.*, 1984, **60,** 170.
115. K. Ding, *J. Magn. Reson.*, 1999, **140,** 495.
116. W. P. Aue, P. Bachmann, A. Wokaun and R. R. Ernst, *J. Magn. Reson.*, 1978, **29,** 523.
117. M. H. Levitt, G. Bodenhausen and R. R. Ernst, *J. Magn. Reson.*, 1984, **58,** 462.
118. F. J. M. Van de Ven, *Multidimensional NMR in Liquids: Basic Principles and Experimental Methods*. VCH, New York, 1995, Chapter 1.5.
119. R. R. Ernst, G. Bodenhausen and A. Wokaun, *Principles of Nuclear Magnetic Resonance in One and Two Dimensions*. Clarendon Press, Oxford, 1990, Chapter 4.2.3.
120. K. V. Schenker and W. Von Philipsborn, *J. Magn. Reson.*, 1986, **66,** 219.
121. M. H. Levitt, *Prog. Nucl. Magn. Reson. Spectrosc.*, 1986, **18,** 61.
122. M. H. Levitt, *in:* Encyclopedia of NMR, D. M. Grant and R. K. Harris, eds., Wiley, New York, 1996.
123. M. H. Levitt and R. Freeman, *J. Magn. Reson.*, 1979, **33,** 473.
124. D. J. Lurie, *J. Magn. Reson.*, 1986, **70,** 11.
125. M. H. Levitt, *J. Magn. Reson.*, 1982, **48,** 234.
126. M. H. Levitt and R. Freeman, *J. Magn. Reson.*, 1981, **43,** 65.
127. H. P. Hetherington and D. L. Rothman, *J. Magn. Reson.*, 1985, **65,** 348.
128. C. S. Poon and R. M. Henkelman, *J. Magn. Reson.*, 1992, **99,** 45.
129. R. Tycko, H. M. Cho, E. Schneider and A. Pines, *J. Magn. Reson.*, 1985, **61,** 90.
130. R. Freeman, J. Friedrich and W. Xi-li, *J. Magn. Reson.*, 1988, **79,** 561.
131. M. H. Levitt and R. R. Ernst, *J. Magn. Reson.*, 1983, **55,** 247.
132. M. Garwood and L. DelaBarre, *J. Magn. Reson.*, 2001, **153,** 155.
133. E. Kupče, *Methods Enzymol.*, 2002, **338,** 82.
134. J. Bunkenborg, N. C. Nielsen and O. W. Sørensen, *Magn. Reson. Chem.*, 2000, **38,** 58.
135. R. D. Boyer, R. Johnson and K. Krishnamurthy, *J. Magn. Reson.*, 2003, **165,** 253.
136. E. Kupče and R. Freeman, *J. Magn. Reson.*, 2007, **187,** 258.
137. M. H. Levitt, *Spin Dynamics. Basics of Nuclear Magnetic Resonance*. Wiley, Chichester, 2001, Chapter 2.3.
138. M. H. Levitt, *Spin Dynamics. Basics of Nuclear Magnetic Resonance*. Wiley, Chichester, 2001, Chapter 2.4.
139. F. Bloch, *Phys. Rev.*, 1946, **70,** 460.
140. J. D. Roberts, *Concepts Magn. Reson.*, 1991, **3,** 27.
141. R. R. Ernst, G. Bodenhausen and A. Wokaun, *Principles of Nuclear Magnetic Resonance in One and Two Dimensions*. Clarendon Press, Oxford, 1990, Chapter 4.2.4.
142. R. R. Ernst, G. Bodenhausen and A. Wokaun, *Principles of Nuclear Magnetic Resonance in One and Two Dimensions*. Clarendon Press, Oxford, 1990, Chapter 4.3.
143. D. Canet, *Nuclear Magnetic Resonance: Concepts and Methods*. Wiley, Chichester, 1996, Chapter 4.
144. L. Zhang and G. Gellerstedt, *Magn. Reson. Chem.*, 2007, **45,** 37.
145. W. Denk, G. Wagner, M. Rance and K. Wüthrich, *J. Magn. Reson.*, 1985, **62,** 350.
146. G. Otting, H. Widmer, G. Wagner and K. Wüthrich, *J. Magn. Reson.*, 1986, **66,** 187.
147. K. Nagayama, P. Bachmann, K. Wüthrich and R. R. Ernst, *J. Magn. Reson.*, 1978, **31,** 133.
148. A. F. Mehlkopf, D. Korbee, T. A. Tiggelman and R. Freeman, *J. Magn. Reson.*, 1984, **58,** 315.
149. R. E. Hurd, *in:* Encyclopedia of NMR, D. M. Grant and R. K. Harris, eds., Wiley, New York, 1996.
150. R. E. Klevit, *J. Magn. Reson.*, 1985, **62,** 551, 1985.
151. J. K. M. Sanders and B. K. Hunter, Modern NMR Spectroscopy. A Guide for Chemists, *Second Edition*. Oxford University Press, New York, 1993.
152. H. Barkhuijsen, R. de Beer, W. M. M. J. Bovée and D. van Ormondt, *J. Magn. Reson.*, 1985, **61,** 465.
153. A. E. Schussheim and D. Cowbur, *J. Magn. Reson.*, 1987, **71,** 371.
154. C. F. Tirendi and J. F. Martin, *J. Magn. Reson.*, 1989, **81,** 577.
155. G. H. Weiss, J. E. Kiefer and J. A. Ferretti, *Chemometr. Intell. Lab. Syst.*, 1988, **4,** 223.

156. H. Gesmar, J. J. Led and F. Abildgaard, *Prog. Nucl. Magn. Reson. Spectrosc.*, 1990, **22,** 255.
157. D. M. Babcook, P. V. Sahasrabudhe and W. H. Gmeiner, *Magn. Reson. Chem.*, 1996, **34,** 851.
158. S. Tiziani, A. Lodi, C. Ludwig, H. M. Parsons and M. R. Viant, *Anal. Chim. Acta*, 2008, **610,** 80.
159. J. J. Led and H. Gesmar, *Methods Enzymol.*, 1994, **239,** 318.
160. G. W. Jeong, P. N. Borer, S. S. Wang and G. C. Levy, *J. Magn. Reson. A*, 1993, **103,** 123.
161. K. H. Sze, I. L. Barsukov and G. C. K. Roberts, *J. Magn. Reson. A*, 1995, **113,** 185.
162. R. Romano, D. Paris, F. Acernese, F. Barone and A. Motta, *J. Magn. Reson.*, 2008, **192,** 294.
163. T. D. Goddard and D. G. Kneller, SPARKY 3, University of California, San Francisco.
164. F. Delaglio, S. Grzesiek, G. W. Vuister, G. Zhu, J. Pfeifer and A. Bax, *J. Biomol. NMR*, 1995, **6,** 277.
165. J. L. Pons, T. E. Malliavin and M. A. Delsuc, *J. Biomol. NMR*, 1996, **8,** 445.
166. L. Barantin, S. Akoka and A. Le Pape, *Dispositif d'analyse quantitative par resonance magnétique nucléaire*. French Patent CNRS no. 95 07651, 1995.
167. S. Akoka, L. Barantin and M. Trierweiler, *Anal. Chem.*, 1999, **71,** 2554.
168. V. Silvestre, S. Goupry, M. Trierweiler, R. Robins and S. Akoka, *Anal. Chem.*, 2001, **73,** 1862.
169. N. Michel and S. Akoka, *J. Magn. Reson.*, 2004, **168,** 118.
170. G. F. Pauli, B. U. Jaki and D. C. Lankin, *J. Nat. Prod.*, 2005, **68,** 133.
171. J. K. Nicholson, J. C. Lindon and E. Holmes, *Xenobiotica*, 1999, **29,** 1181.
172. J. C. Lindon, J. K. Nicholson and J. R. Everett, *Ann. Rep. NMR Spectrosc.*, 1999, **38,** 1.
173. J. C. Lindon, E. Holmes and J. K. Nicholson, *Anal. Chem.*, 2003, **75,** 384A.
174. M. T. H. Khan and A. Ather, *Advances in Phytomedicine*, 2006, **2,** 411.
175. W., A. Weckwerth (ed. (2007). *In* Metabolomics: Methods and Protocols, 2007Humana Press Inc., Totowa.
176. P. J. D. Foxall, J. A. Parkinson, I. H. Sadler, J. C. Lindon and J. K. Nicholson, *J. Pharm. Biomed. Anal.*, 1993, **11,** 21.
177. P. J. D. Foxall, M. Spraul, R. D. Farrant, L. C. Lindon, G. H. Neild and J. K. Nicholson, *J. Pharm. Biomed. Anal.*, 1993, **11,** 267.
178. M. R. Viant, *Biochem. Biophys. Res. Commun.*, 2003, **310,** 943.
179. M. R. Viant, J. G. Bundy, C. A. Pincetich, J. S. de Ropp and R. S. Tjeerdema, *Metabolomics*, 2005, **1,** 149.
180. C. Y. Lin, H. Wu, R. S. Tjeerdema and M. R. Viant, *Metabolomics*, 2007, **3,** 55.
181. Y. Wang, M. E. Bollard, H. Keun, H. Antti, O. Beckonert, T. M. Ebbels, J. C. Lindon, E. Holmes, H. Tang and J. K. Nicholson, *Anal. Biochem.*, 2003, **323,** 26.
182. O. Hendrawati, Q. Yao, H. K. Kim, H. J. M. Linthorst, C. Erkelens, A. W. M. Lefeber, Y. H. Choi and R. Verpoorte, *Plant Sci.*, 2006, **170,** 1118.
183. H. T. Widarto, E. Van der Meijden, A. W. M. Lefeber, C. Erkelens, H. K. Kim, Y. H. Choi and R. Verpoorte, *J. Chem. Ecol.*, 2006, **32,** 2417.
184. A. Sánchez-Sampedro, H. K. Kim, Y. H. Choi, R. Verpoorte and P. Corchete, *J. Biotech.*, 2007, **130,** 133.
185. K. J. Cross, K. T. Holmes, C. E. Mountford and P. E. Wright, *Biochemistry*, 1984, **23,** 5895.
186. G. L. May, L. C. Wright, K. T. Holmes, P. G. Williams, I. C. P. Smith, P. E. Wright, R. M. Fox and C. E. Mountford, *J. Biol. Chem.*, 1986, **261,** 3048.
187. P. G. Williams, M. A. Helmer, L. C. Wright, M. Dyne, R. M. Fox, K. T. Holmes, G. L. May and C. E. Mountford, *FEBS Lett.*, 1985, **192,** 159.
188. K. T. Holmes, P. G. Williams, G. L. May, P. Gregory, L. C. Wright, M. Dyne and C. E. Mountford, *FEBS Lett.*, 1986, **202,** 122.
189. R. A. Iles, J. R. Jago, S. R. Williams and R. A. Chalmers, *FEBS Lett.*, 1986, **203,** 49.
190. L. C. Wright, G. L. May, M. Dyne and C. E. Mountford, *FEBS Lett.*, 1986, **203,** 164.
191. J. R. Bales, J. D. Bell, J. K. Nicholson, P. J. Sadler, J. A. Timbrell, R. D. Hughes, P. N. Bennett and R. Williams, *Magn. Reson. Med.*, 1988, **6,** 300.
192. J. Alonso, C. Arús, W. M. Westler and J. L. Markley, *Magn. Reson. Med.*, 1989, **11,** 316.
193. R. Nouaille, M. Matulova, A.-M. Delort and E. Forano, *FEBS Lett.*, 2004, **576,** 226.
194. S. Massou, C. Nicolas, F. Letisse and J.-C. Portais, *Phytochemistry*, 2007, **68,** 2330.
195. Q. N. Van, H. J. Issaq, Q. Jiang, Q. Li, G. M. Muschik, T. J. Waybright, H. Lou, M. Dean, J. Uitto and T. D. Veenstra, *J. Proteome Res.*, 2008, **7,** 630.
196. M.-E. Dumas, C. Canlet, F. André, J. Vercauteren and A. Paris, *Anal. Chem.*, 2002, **74,** 2261.

197. M. Guerrini, A. Naggi, S. Guglieri, R. Santarsiero and G. Torri, *Anal. Biochem.*, 2005, **337,** 35.
198. I. A. Lewis, S. C. Schommer, B. Hodis, K. A. Robb, M. Tonelli, W. M. Westler, M. R. Sussman and J. L. Markley, *Anal. Chem.*, 2007, **79,** 9385.
199. E. Sjöström, *Wood Chemistry. Fundamentals and Applications*, Second Edition. Academic Press, San Diego, 1993.
200. F. E. Brauns, *The Chemistry of Lignin*. Academic Press, New York, 1952.
201. K. Freudenberg, *Mol. Biol. Biochem. Biophys.*, 1968, **2,** 47.
202. E. Adler, *Wood Sci. Technol.*, 1977, **11,** 169.
203. Y. Z. Lai and K. V. Sarkanen, *in: Lignins. Occurrence, Formation, Structure and Reactions*, K. V. Sarkanen and C. H. Ludvig, eds., Wiley, New York, 1971.
204. A. Sakakibara, *in: Wood and Cellulose Chemistry*, D. N. -S. Hon and N. Shiraishi, eds., Marcel Dekker Inc., New York, 1991.
205. C. -L. Chen, *in: Wood Structure and Composition*, M. Lewis and I. S. Goldstein, eds., Marcel Dekker Inc., New York, 1991.
206. J. Ralph, J. M. Marita, S. A. Ralph, R. D. Hatfield, F. Lu, R. M. Ede, J. Peng, S. Quideau, R. F. Helm, J. H. Grabber, H. Kim G. Jimenez-Monteon, *et al*., *in: Advances in Lignocellulosics Characterization*, D. S. Argyropoulos, ed. TAPPI Press, Atlanta, 1999.
207. S. L. Maunu, *Prog. Nucl. Magn. Reson. Spectrosc.*, 2002, **40,** 151.
208. D. Robert, *in: Methods in Lignin Chemistry*, S. Y. Lin and C. V. Dence, eds., Springer-Verlag, Berlin, 1992.
209. E. A. Capanema, M. Y. Balakshin and J. F. Kadla, *J. Agric. Food Chem.*, 2004, **52,** 1850.
210. A. M. Dixon and C. K. Larive, *Anal. Chem.*, 1997, **69,** 2122.
211. S. Haiber, P. Burba, H. Herzog and J. Lambert, *Fresenius J. Anal. Chem.*, 1999, **364,** 215.
212. W. L. Kingery, A. J. Simpson, M. H. B. Hayes, M. A. Locke and R. P. Hicks, *Soil Sci.*, 2000, **165,** 483.
213. T. W. -M. Fan, R. M. Higashi and A. N. Lane, *Environ. Sci. Technol.*, 2000, **34,** 1636.
214. S. Haiber, H. Herzog, P. Burba, B. Gosciniak and J. Lambert, *Environ. Sci. Technol.*, 2001, **35,** 4289–4294.
215. S. Divakar, *J. Food Sci. Tech.*, 1998, **35,** 469.
216. M. J. McCarthy, P. N. Gambhir and A. G. Goloshevsky, *in: NMR Imaging in Chemical Engineering*, S. Stapf and S. -I. Han, eds., Wiley-VCH, Weinheim, 2006.
217. A. Khatib, E. G. Wilson, H. K. Kim, A. W. M. Lefeber, C. Erkelens, Y. H. Choi and R. Verpoorte, *Anal. Chim. Acta*, 2006, **559,** 264.
218. F. Hu, K. Furihata, Y. Kato and M. Tanokura, *J. Agric. Food Chem.*, 2007, **55,** 4307.
219. D. A. Netzel, D. R. McKay, R. A. Heppner, F. D. Guffey, S. D. Cooke, D. L. Varie and D. E. Linn, *Fuel*, 1981, **60,** 307.
220. L. Petrakis, D. T. Allen, G. R. Gavalas and B. C. Gates, *Anal. Chem.*, 1983, **55,** 1557.
221. D. J. Cookson and B. E. Smith, *Org. Magn. Reson.*, 1981, **16,** 111.
222. D. J. Cookson and B. E. Smith, *Fuel*, 1983, **62,** 34.
223. P. F. Barron, M. R. Bendall, L. G. Armstrong and A. R. Atkins, *Fuel*, 1984, **63,** 1276.
224. D. J. Cookson and B. E. Smith, *Anal. Chem.*, 1985, **57,** 864.
225. D. J. Cookson and B. E. Smith, *Energy Fuels*, 1987, **1,** 111.
226. F. Abu-Dagga and H. Rüegger, *Fuel*, 1988, **67,** 1255.
227. G. Dosseh, B. Rousseau and A. H. Fuchs, *Fuel*, 1991, **70,** 641.
228. V. Bansal, G. S. Kapur, A. S. Sarpal, V. Kagdiyal, S. K. Jain, S. P. Srivastava and A. K. Bhatnagar, *Energy Fuels*, 1998, **12,** 1223.
229. B. Behera, S. S. Ray and I. D. Singh, *Fuel*, 2008, **87,** 2322.
230. B.-T. Doan, B. Gillet, B. Blondel and J.-C. Beloeil, *Fuel*, 1995, **74,** 1806.
231. H. Koskela and T. Väänänen, *Magn. Reson. Chem.*, 2002, **40,** 705.
232. S. Peng, C. Ye and M. Liu, *Appl. Spectrosc.*, 2003, **57,** 1190.
233. T. Väänänen, H. Koskela, Y. Hiltunen and M. Ala-Korpela, *J. Chem. Inf. Comput. Sci.*, 2002, **42,** 1343.

CHAPTER 2

Recent Advances in Solvent Suppression for Solution NMR: A Practical Reference

Ryan T. McKay

Contents

Abstract

Recent advances in solvent suppression for liquids based NMR spectroscopy are explored. An emphasis on techniques developed over the past 10 years is

National High Field Nuclear Magnetic Resonance Centre (NANUC), University of Alberta, Edmonton, AB, Canada T6G 2E1

Annual Reports on NMR Spectroscopy, Volume 66
ISSN 0066-4103, DOI: 10.1016/S0066-4103(08)00402-X

provided including recommendations on sample preparation and spectrometer optimization. In addition, biologically relevant samples were used to demonstrate and compare the relative strengths/weaknesses of described techniques. This publication attempts to provide practical background and general knowledge for both novice and experienced users seeking to select and optimize the most appropriate tools for their NMR challenges.

Key Words: Nuclear magnetic resonance spectroscopy, Solvent, Water suppression, Radiation damping, Demagnetization field, Bulk susceptibility effect, Presaturation, Watergate, Purge, Metabonomics.

1. RATIONALE

1.1. Objectives

There are a fantastic number of exploratory manuscripts and reviews thoroughly covering aspects of biomolecular NMR and the relationship with solvent suppression over the last 30 years. Biochemically[a] focused NMR spectroscopy has been developing for well over a half century.[1] Originally we had planned to cover all aspects of solvent suppression but were quickly forced to re-evaluate this position for two reasons. The first was the overwhelming volume of material to cover in order to perform a comprehensive review. The second and perhaps more important reason was the quality of reviews completed by other authors and (at best) the redundancy that any comprehensive work on our part would necessarily encounter. Interestingly, larger reviews on solvent suppression seem to cover approximately 10-years of the literature, and the timing of this review is no exception. For example, a review by Hore[2] was published in 1989, while Coron et al.,[3] Gueron et al.,[4] Lui and Mao,[5] and the Price[6] reviews were published between 1999 and 2001. Other excellent reviews have emphasized integral techniques such as the incorporation of pulsed field gradients.[7,8] An extensive review already mentioned contains a unique focus on the mathematical theory behind solvent signals[4] and is highly recommended for anyone seeking insights in that aspect of spectroscopy.

During the past few years there have been three developments necessitating an updated review. The first is a recent resurgence of active development in the field of solvent suppression. The second is the rapid incorporation of cryogenically cooled probes into biomolecular NMR laboratories and the related challenges of increased signal to noise.[b] Lastly there has been an expansion of NMR into non-traditional fields (e.g. metabonomics[9–12]) and by researchers self-described as non-NMR experts. As result, there is a need for a review of recent advances and a practical guide to assist non-NMR focused investigators who are beginning to

[a] A simple PubMed search for 'NMR' in title yields some 78 000 references, with 180 000 hits for 'NMR' as a keyword.
[b] This is an interesting point as most spectroscopists would never think of increased signal to noise ratios as a challenge. Do not forget that the solvent signal gets more intense as do artefacts. In addition, as the noise floor drops any previously hidden problem tends to stand out.

consider the advantages that NMR can provide. Even researchers experienced with NMR may not be familiar with all the subtleties of optimizing solvent suppression. Therefore we will attempt to reference the excellent previous works wherever possible and only re-address similar topics in the cases where a review will facilitate a better understanding of a new development or where we can yield directed assistance for less experienced users. This publication will attempt to tackle the limitations and robustness of techniques on identical, biologically relevant samples to facilitate direct comparison and evaluation for the potential user. Best of luck and let us begin.

1.2. Why suppress solvent?

There are many reasons behind the need for solvent suppression. The most obvious is the occlusion of ^{1}H containing peaks of interest (solute) in the background of a massive solvent signal such as 90% $^{1}H_2O$ containing 10% $^{2}H_2O$ (also shown as D_2O) for an internal lock reference. We also always add 2,2-dimethyl-2-silapentane-5-sulfonic acid (DSS)[13] for internal referencing of biological samples. Just like trying to see something in the sky close to the sun, small peaks next to, or on top of the solvent peak are obscured and distorted. Attempting any type of quantitation is next to impossible due to a non-linear baseline and/or distortions from the overwhelming solvent resonance (Figure 1A).

Common spectral errors obtained by not suppressing the solvent were shown in Figure 1B and C. The errors in measurement of the FID caused by overloading the receiver yield problems with the discrete Fourier transform resulting in artefactual signals and large baseline 'wiggles'. None of the spectra were particularly useful.

While it may be easy to suggest and visualize the physical removal of ^{1}H solvent resonances from the sample by the full substitution of a maximally deuterated solvent (e.g. 99.99% $^{2}H_2O$ or suitable organic solvent such as deuterated chloroform), this choice removes resonances of interest[14] or calls into question the biological relevance of subsequent studies. For proteins, the use of exchangeable solvent deuterons would result in the eventual loss of all exchangeable hydrogen atom signals from the protein[15–20] with a rate determined proportional to exposure/regional instability (e.g. lack of hydrogen bonding or other tight secondary structural elements).

The concentration of ^{1}H resonances in fully protonated water samples is on the order of 110 M, which vastly exceeds even the most optimistic biological samples. Even if the solubility of a subject protein were such that solute signal could be on par with the solvent, any subsequent work would be hindered by concerns of non-specific binding, dimerization (or higher order polymerization), and functional relevance in any of these cases. Of course the more obvious problem would be the difficulty in obtaining and purifying enough sample (see Appendix), often labelled via expression in expensive ^{13}C, ^{15}N, and possibly even ^{2}H-enriched media, to create such a hypothetical sample. As the solubility of almost any sample can never come close to these concentrations, suppression of the solvent becomes inescapable.

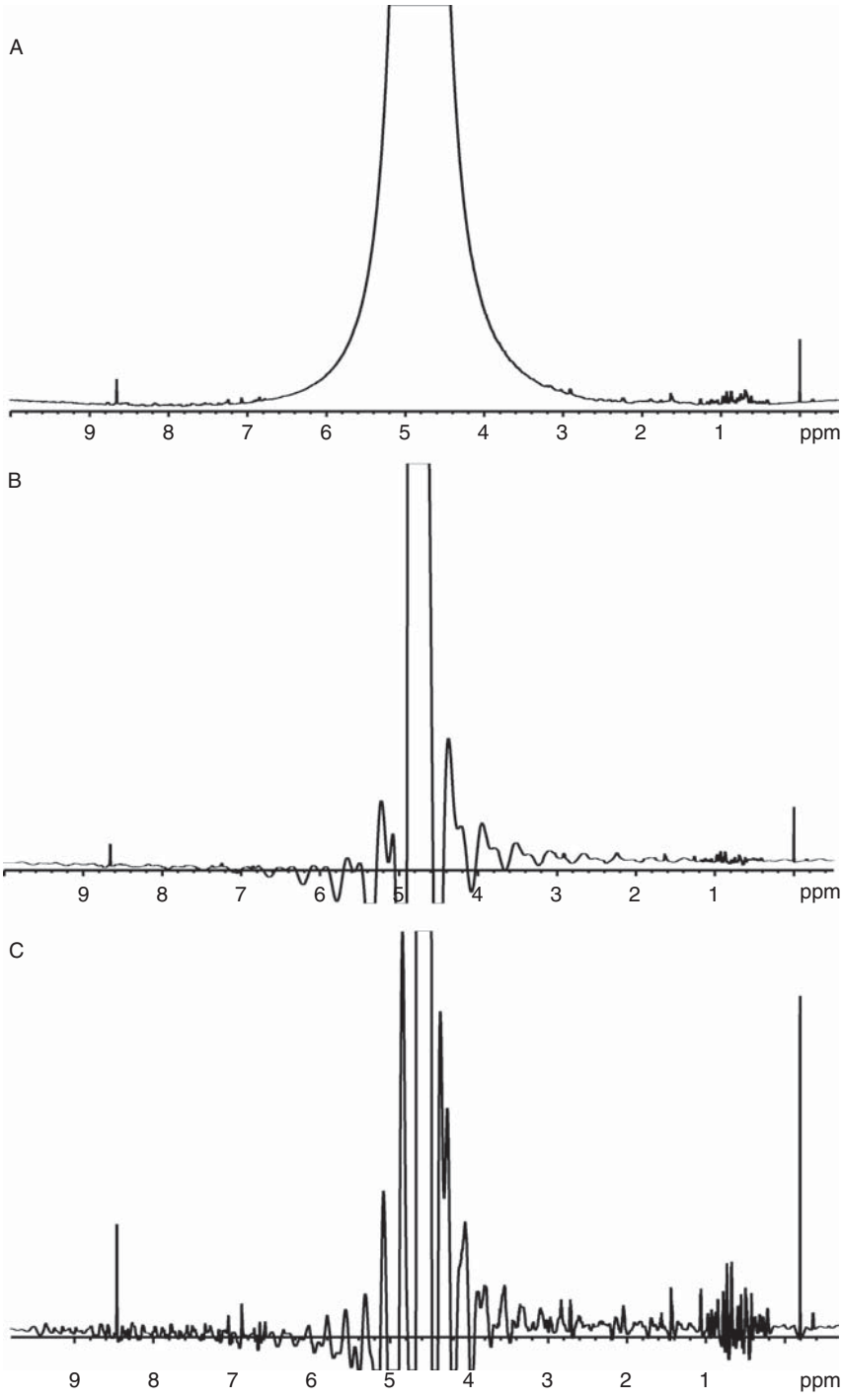
A
9 8 7 6 5 4 3 2 1 ppm
B
9 8 7 6 5 4 3 2 1 ppm
C
9 8 7 6 5 4 3 2 1 ppm

1.3. Problems with ignoring solvent signals

1.3.1. Receiver and analogue to digital converter errors

We have seen what happens if we simply ignore suppression concerns for the moment and acquire a spectrum (Figure 1). A receiver overflow occurs when the intensity of the receiver voltage exceeds the maximum that can be accurately read. Otherwise the start of the FID (that should show precession of a sinusoid) contains only maximum values until enough signal decay has occurred to bring the intensity back into scale (Figure 2). Until then, no accurate amplitudes can be measured. One solution is to turn down the amplification of that signal (and any other weaker signals that might be of interest). By turning down the signal amplification and/or by only exciting a fraction of the sample, we can bring the recorded voltage back into scale and the digital conversion back into a feasible solution (Figure 1A). This means that the maximum water signal amplitude fits inside the largest number possible for the digital converter, and the receiver can record the voltage levels in the coil.

However this does not mean the solute is being measured correctly, only that the largest signal is within the scale range. In most modern instruments a 16-bit converter (able to create a range of 2^{16} values) is used allowing definition of $\pm 32\,768$ points. This may seem like a lot, but if the water signal is 100 000 times larger than the signals of interest (i.e. 110 M H_2O peak compared to a 1 mM protein) there remains less than one digital point to define the entire signal of the solute (impossible as multiple interfering sinusoids cannot be accurately described by only ± 1 s and 0 s). Some newer consoles now contain 20-bit ADCs but this does not solve receiver overflows, or other distortions occurring due to the massive solvent signal.

1.3.1.1. Digitization noise Digitization noise can most easily be described as mistakes in the measured voltage when translated to a digital number. Essentially there are not enough points to accurately describe the voltage, and the nearest digital number is selected somewhat similar to simple rounding errors. Effective digitization of a signal intensity less than the smallest value has been discussed,[21] although the reasoning that noise levels should theoretically increase solute signals into a relatively detectable scale is certainly not the most palatable argument. Digital noise errors should be most common when extremely weak signals are sought after in the presence of very strong ones and everything has to fit in a limited range of values. While receiver overloads occur when intensities are too

Figure 1 *Effect of solvent*. (A)–(C) show the NMR spectra for a 600 uL sample of 1 mM ubiquitin and 0.5 mM DSS dissolved in 90% H_2O with 10% D_2O at pH 7 containing 0.1% NaN_3 (for inhibition of bacterial growth). All were run with a simple one pulse-read sequence containing no pre- or post-acquisition solvent suppression. Spectra were recorded on an Oxford 2.2K pumped non-shielded 18.8 T (800 MHz ^1H) magnet coupled to a four channel Varian Inova console and cryogenically cooled HCN-5 mm probe with Z-gradient coil. (A) Single high power pulse of 1 μs (approximately an 11° pulse) and no water suppression and the gain set to minimum. The short pulse was necessary to reduce the water signal intensity sufficiently to avoid receiver overflow. The effect of a full 90° pulse on the same sample with (B) minimal, and (C) normal gain settings show the resulting distortions in the processed FID due to ADC and receiver over flow errors. Even with minimal gain the water signal was sufficient to overload the receiver.

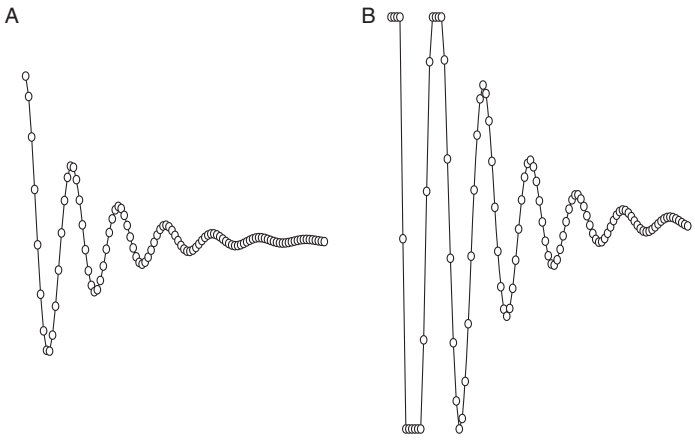

Figure 2 *Signal overload*. Two simple carton FIDs are shown. The left FID amplitude (A) is within scale and shows accurate measurements for each recorded point of acquisition. The right FID (B) shows a signal recorded with the gain set too high and the first series of points off scale. These points can only be incorrectly recorded by the hardware as maximum values.

high, digitization noise is the opposite extreme when signals are small but the amplification (gain) cannot be increased due to overpowering signals on the verge of being 'clipped' (overloaded and set to 100% by default). Ray Freeman's book 'Spin Choreography'[22] (Figure 10.1, p. 317) demonstrates this concept very nicely.[c] Even the versatility of increasing the resolution of the ADC (e.g. 20 bit digitization hardware) would easily be eclipsed by the conceptually simple act of removing the intense undesired signals to start with, and hence our discussion.

2. SOLVENT SUPPRESSION

2.1. Practicalities

The following sections attempt to quickly express some general NMR 'rules of thumb' that we have adopted. They are not meant to imply hard and fast rules or requirements to be imposed on all samples and spectroscopists (though some are certainly required at our facility), but instead simply methods we have found to effectively acquire consistent data in the most reasonable amount of time. As the saying goes, 'Your mileage may vary'.

2.1.1. Samples

The first rule of NMR is 'Crap in equals crap out'.[d] It does not matter how many millions you spend on a super conducting magnet, nor how carefully you isolate vibrations, eliminate electromagnetic noise, stabilize temperatures, train your

[c] All of Ray Freeman's books are scientifically excellent, a pleasure to read, and highly recommended for anyone interested in further NMR readings.
[d] Taken from *The 4 Rules of NMR* by Brian D. Sykes. 1. Crap in equals Crap out (censored version for our younger readers), 2. Cleanliness is next to Godliness, 3. Ain't broke do not fix it, and 4. Use the simplest experiment to answer the question.

spectroscopist, or cool your probe because if you have a bad sample you will undoubtedly obtain a poor result. We recommend a 600 uL sample (i.e. 5 mm NMR tube) resulting in a 44.5 mm sample length (measured from the bottom of the meniscus to the bottom of the tube). While spectrometer vendors recommend volumes as high as 700 uL, we have found that 500 uL is the practical minimum with 600 uL giving excellent results via a reasonable amount of shimming (see Section 2.1.5). The sample length is important because modern biomolecular-oriented NMR probes (i.e. ^{1}H coil on the inside closest to the sample) use longer receiver coils (e.g. 18 mm instead of older 16 mm) incorporating more coil wire turns in order to increase sensitivity. A 600 uL sample can be carefully centred in even 18 mm long cryogenically cooled receiver coils and yield good results. We have seen that 500 uL samples can be run, but the sacrifices in terms of final shim quality begin to outweigh the advantages gained by not diluting the solute concentration. For example, it is better to dilute a sample up to at least 500 uL (or even better to 600 uL) than it is to run it at 400 uL. The 400 uL sample suffers from overall inhomogeneity (lineshape) and solvent suppression problems that remove any expected advantages of higher concentration.

It is easy to imagine that the best overall magnetic field homogeneity should be achievable on a consistent cylinder of infinite length passing through perfect rotations of coil wiring. While we certainly cannot achieve infinite length samples, it is our experience that 10–11 mm of sample on either end of the receiver coil is sufficient in order to properly shim a sample. Achieving higher quality shims will make all peaks in the spectra sharper (thus signal/noise increases) and greatly facilitate any solvent suppression scheme improving baseline performance and sensitivity. When the amount of available sample is the limiting factor (not solubility), we have turned quite successfully to susceptibility-matched plugs such as those supplied by Shigemi NMR Tubes Inc. Shigemi manufactures tubes with solvent-matched plugs in the bottom of the NMR tube and a top plug that can be lowered to the surface of the sample. Using these tubes we have found that 325–350 uL fills the receiver coils to 20 mm of length and maintains enough material in the top reservoir to avoid refluxing of the solvent into the upper tube areas. Refluxing and subsequent capillary action can result in micro-bubbles forming in the receiver area. Bubbles are very disruptive to any resulting spectra as they form directly inside the receiver coils causing a drop of the lock level (indicative of a disruption to the homogeneity of the magnetic field) over several hours. For example, samples that are shipped for studies from sea level to higher altitudes often degas during (or shortly after) transportation. A simple way to check for bubbles (or any other non-soluble contaminant) without removing the sample from the magnet is by the observation of a distortion in the gradient profile (Figure 3).

Bubbles can be removed from Shigemi tubes by tilting the NMR tube to about 45° from vertical and carefully, but rapidly, depressing the top plunger a millimetre or two. A short but strong 'tap' on the plunger causing a small depth change will usually force the bubbles out. This can be repeated if necessary until all bubbles are removed, though some patience and care may be essential. When clear of bubbles, the plunger position can be readjusted and secured in place. Once

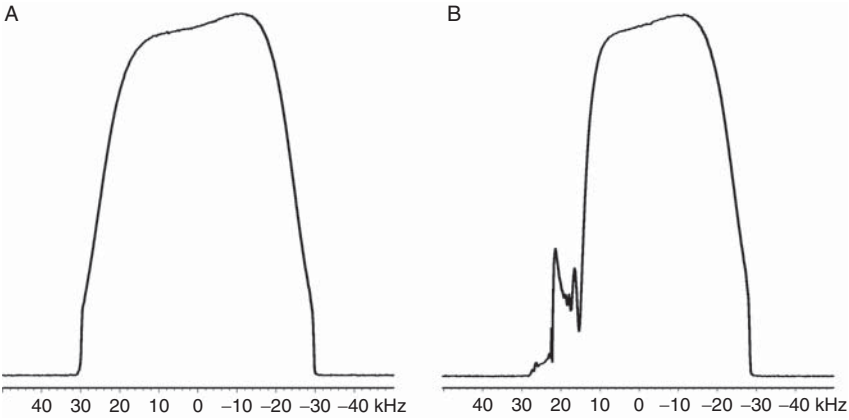

Figure 3 *Micro-bubbles present during Z-gradient profile acquisition.* Shown above is the Z-gradient profile of a 90/10 H_2O/D_2O sample in a Shigemi BMS-005V NMR tube (A) lacking and (B) containing small micro-bubbles. A sample yielding the gradient profile seen in (B) would be very difficult to shim to satisfactory levels and water suppression efforts would certainly suffer.

removed air bubbles rarely form again unless the volume of solvent in the upper well is too small and refluxes further up the tube drawing volume out of the receiver area by capillary action. The gradient profile of Figure 3A should confirm the result once temperature equilibrium has been re-established.

2.1.2. Tubes

Many researchers are seduced into saving money by buying cheap NMR tubes. These tubes are not only inexpensive but also poorly manufactured with relatively high error tolerances that deliver inconsistent results. In the past, when liquid samples were routinely spun at 15–20 Hz, the quality and precision of the tube manufacturing was critical to reduce artefacts such as spinning side bands. Today most spectrometer users do not spin their samples as the use of pulsed field gradients for coherence selection prohibits the physical rotation of the sample. This does not mean that consistent, high accuracy tube manufacturing is not important or that simple 1D-^{1}H experiments that do not commonly use coherence transfer selection via gradients would not benefit from spinning. On the contrary, for reproducible results and reducing the need for shimming adjustments from sample to sample, high quality precision tubes are ideal. Research groups focusing on high throughput (e.g. metabonomics) logically seek to minimize set up time between acquisitions. Unfortunately these same projects are faced with high initial costs associated with large (or massive) numbers of NMR tubes that are subsequently either reused (i.e. washed by hand) or even discarded. Our experience has been that cheaper tubes disrupt routine operation more often. These 'bad' tubes are far more difficult to shim and never yield the quality of results achievable with other tubes in the same production batch. Relatively good quality tubes can even go 'bad' during washing if they become scratched during handling.

We have found tubes equal to the quality of a Wilmad 535P NMR (Wilmad Glass, SP-Industries, Inc.) or Shigemi (Shigemi Inc., Allison Park, PA, USA) BMS-005V (V or B depending on your probe manufacturer) sufficient for biomolecular studies on spectrometers from 500 to 800 MHz. Admittedly, we have used Wilmad 541P (or equivalent) for facility standard samples (e.g. establishment of reference shim sets, see Section 2.1.5) but the costs preclude routine incorporation.

2.1.3. Lock

Many spectrometer users do not fully appreciate the importance or functionality of spectrometer 'lock'. The frequency of the internal deuterated solvent is continuously followed by the spectrometer hardware as a reference point, and a small magnetic field is applied to bring the reference frequency back to a preset static position. If the main magnetic field drifts far enough away from the set point, then the lock field generator will no longer be able to compensate, and the set point must be re-established in the new range. If external influences, such as large metal bodies, cryogen Dewars, temperature changes, vibrations, pressure changes, and so on, affect the magnet, then the lock circuitry must quickly compensate to maintain the position of the deuterium resonance. Like any signal, the phase of the observed resonance can be critical in the ability to evaluate the actual frequency. For example, being 90° out of phase with the deuterium signal would make the resonance appear as a null and only noise would be observed. Conversely, searching for the lock frequency when far off resonance would be difficult and time consuming regardless of the accuracy of the phase of measurement.

We have found that it is very important to set the lock position and phase prior to acquiring high field and high-resolution data. Incorrect settings of the lock phase by even a few degrees can cause distortions originating from intense peaks, especially when gradients are utilized on cold probes. As another saying goes, 'Every little bit helps' and having the lock correctly phased and positioned prior to and after shimming can increase the efficiency of subsequent solvent suppression efforts and reduce artefacts.

2.1.4. Temperature equalization

One of the most commonly encountered questions is ''How long do I have to wait until my sample reaches equilibrium?'' This is just as important for high throughput studies such as metabonomics and medical diagnostics that use only a few scans as it is for multidimensional biomolecular studies where a single experiment can last up to 6 days. The answer (and solvent suppression method) depends on the application.

Initial thermal equilibrium, often based on the lock level stability, can be reached quickly taking as little as a few minutes (e.g. a room temperature sample inserted into a regulated magnet at 25 °C). Increasing the airflow to the variable temperature controller can speed this equilibrium process but unfortunately can easily introduce microphonics in the resulting spectra due to minute vibrations (i.e. wiggling of the sample in the probe). This is of course deleterious, and a compromise between temperature stability and positional stability must be reached for each spectrometer. For cryogenically cooled probes this becomes

more complicated as the receiver coils are mere millimetres away at 25 K while the sample must be stable at 25 °C. Increased airflows are often required to minimize temperature gradients throughout (*X*-, *Y*-axis) or along (*Z*-axis) the sample.

For samples requiring runs of seconds or minutes, thermal equilibrium may be all that is required. This can be determined by the stability of the lineshape during shimming of the sample. For long-term experiments, equilibrium of the refluxing solvent must also be reached. As the solvent refluxes and condenses higher in the tube the volume of the sample in the receiver coil is reduced. The sample is no longer centred in the receiver coils and the lineshape degrades. We have found that aqueous solvents take about 18 hours to reach equilibrium depending on the cleanliness of the tube. To accommodate this finding we often insert a sample in the magnet the night before experiments are due to begin. This assists with overall shim stability and solvent suppression.

2.1.5. Shimming

Shimming is often called the 'art' of NMR. Everyone develops a routine or a method that they have evolved from practice and/or watching others. We have found that each spectrometer behaves differently: sometimes subtle, other times different enough that a method that works for one system may not be appropriate for another.

Each magnet, and perhaps even each probe, can have a distinct response to different shims. For example our 800 MHz system using the room temperature 5 mm HCN probe always had a −32 unit Z_1 adjustment (accompanied with a slight drop in the lock level) that needed to be made after either shimming for maximum lock response or after *Z*-gradient shimming. While counterintuitive, the overall homogeneity and lineshape improves despite the reduction in the relative lock level (more on this below). The adjustment is not nearly so pronounced on the 5 mm cold probe, but is still present and appropriate. Now whether this is a compensation for a lengthwise temperature gradient through the sample or an idiosyncrasy of our particular probe coil design is uncertain, but it is merely a fact and is performed almost without thought by experienced users on that particular instrument (and always results in better lineshape). None of the other magnets that we manage has this peculiarity (or at least that has the same magnitude of lock drop). We hypothesize that the lock drop is due to deuterated lock solvent at the edges of the coil moving out of resonance as the field inside the receiver coil is improved. The overall amount of lock solvent on resonance therefore decreases even though the lineshape is improving for the solute.

So why is it so important to learn the requirements for your system? The long and short of shimming is that the better the overall quality of shimming the narrower and more symmetric all resonances will be in the spectra. This is always a desired aspect for any form of solvent suppression no matter how good the pulse sequence may be. There are of course many methods to shim based on iterative manual shimming, shimming to obtain the highest lock level, automatic shimming on the lock via a pre-programmed algorithm, *Z*-gradient-based autoshimming, full three-dimensional shimming using *Z*-gradients and the *X* and *Y*

shim coils (capable of properly shimming a magnet from installation), or any combination of the previously mentioned techniques.

To minimize the time taken to shim, we have adopted a weekly routine on an ideal standard sample, and users are supplied an updated optimal shim set upon which to start their experiments. Users are strongly encouraged to use moderate to high quality NMR tubes with exactly 600 uL of sample volume (reproducing the volume used in the standard samples) and to centre the NMR tube in the spinner carefully in relation to the receiver coils. Users are often able to interactively shim on the resulting lineshape requiring only slight corrections to the Z_1, Z_2, X_1, and Y_1 shims.

Spectroscopists can also utilize Z-gradient shimming that typically yields reasonable results. Even in the worst cases, Z-gradient shimming should bring a researcher into the 'ballpark' of optimal sample shims (for an interesting discussion see Jerschow and Bodenhausen's paper[23]). It is our experience that short samples of 500 uL or less go vastly astray in the iterative portion of Z-gradient shimming with the Z_5 and Z_6 shims quickly moving out of range, seemingly overcompensating for one another. On normal or long samples, gradient shimming and subsequent interactive manual shimming of the spectra (in an interactive manner usually requiring less than 5 min) will result in acceptable lineshape and solvent suppression characteristics (Figure 4).

Conversely if a user ignores the facility recommendations (e.g. using a 475 uL sample volume in a low quality tube) they can spend several minutes to hours attempting to reproduce the homogeneity a standard sample can provide with the standard shim set.

For any type of high-throughput experimentation we cannot emphasize enough the utility and efficiency of having a set length of sample (with established content and supplied routine shims), consistently centred via the sample spinner for delivery into a well-maintained magnet. Anything less is most certainly a waste of one's precious human resources.

2.1.6. Pulse width calibrations

The proper calibration of the 90° pulse width (i.e. M_o vector model considered in the rotating frame) is one of the easiest and most dramatic optimizations that can be applied to an NMR sample. Any error in the determination of the effective 90° pulse length has an immediate effect on the quality of the solvent suppression and obtained data. Paul Keifer has carefully reviewed the fundamental technique of arraying the pulse length to include a 360° null for a given static power and by simple inspection, determining the appropriate 90° pulse without needing compensation for radiation damping or relaxation effects.[24] Also discussed was how a single array can be used to identify common problems such as radiation damping, RF homogeneity, probe arcing, and off-resonance effects (among others). The paper is therefore highly recommended.

2.1.6.1. Nutation frequency measurement Peter Wu and Gottfried Otting have recently described a technique that can quickly and accurately yield the 90° pulse width via a single acquired transient.[25] The concept is to measure the

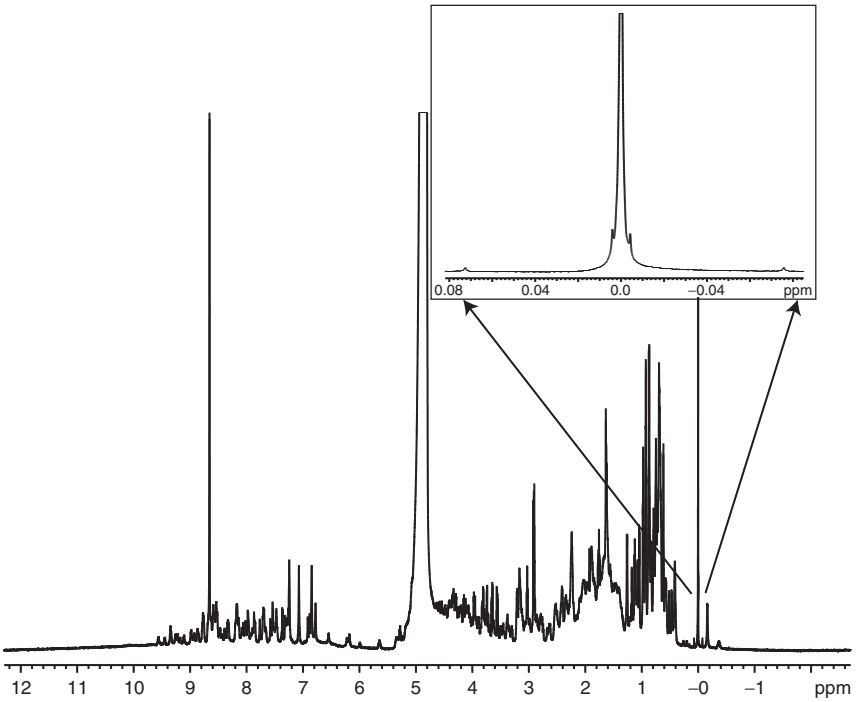

Figure 4 *Shimmed example*. The resulting spectra of a shimmed 550 uL 1 mM unlabelled ubiquitin sample containing 1 mM DSS (inset shows expansion of the DSS methyl peak) in 90/10 H_2O/D_2O is shown. Presaturation (91 Hz B_1 field) was applied for 2.5 s and a calibrated 90° pulse (8.6 us) was inserted directly after saturation. A total of four steady state pulses were used prior to the 32 acquired transients. The sweep width was 12 000 Hz (48k complex points for a 4 s acquisition time and 20× oversampling), data were zero filled to twice the acquired data size and no other weighting or post-acquisition modification was performed. The DSS methyl peak shows the natural abundance ^{13}C splitting (∼118 Hz) and the ^{29}Si satellites ∼7 Hz. This was the sample used for sequence comparisons.

spectral response while the sample is actively experiencing the B_1 induced field. This requires controlled gating of the ^1H amplifier while the receiver circuitry is open otherwise harm may befall the instrumentation. The frequency of nutation (in this case the magnitude of the observed splitting) of the observed resonance is the B_1 field strength and therefore one can easily determine the correct pulse width for the sample.[e] The most recent (i.e. ca. 2007 or newer) digital spectrometers have this capacity included with the software while older and more common consoles (e.g. Varian Inova) require a pulse sequence utilizing explicit acquisition periods.

[e] Frequency of nutation = γB_1, therefore the 90° pulse length = $(4\gamma B_1)^{-1}$. Also note that the authors used a 32-fold oversampling that appeared in their calculations, and users need to replace this with their own value (if applicable).

2.1.7. Carrier position

The last easily optimized parameter is the carrier position of the spectrometer. The carrier is often set using the lock frequency (based on solvent tables), or after a single pulse read experiment. We have found that a simultaneous array of both the high power carrier position and lower power presaturation frequency (if applicable) on the actual sample works best. As will be discussed later (see Section 2.2.4), the array of the carrier (and presaturation) frequency compensates for several properties of various solvents and provides the best frequency for the majority of the spins that will be involved in subsequent suppression techniques (e.g. poor shims resulting in an asymmetric solvent peak can require a slight offset from the mean to provide the best suppression). As solvent peaks are actively suppressed (resulting in asymmetric residual signals) and move depending on aspects such as sample temperature/stability or pH, it is not recommended to use a solvent resonance as a reference point.[13,26]

2.1.8. Summary

Each high quality sample (or group of similar samples) needs to be carefully shimmed and locked. As a minimum set of optimizations the pulse width and carrier position should be accurately established. These simple parameters should provide the background for at least manageable suppression. More complicated sequences may require further optimizations that will be discussed in greater detail in the following sections.

2.2. Understanding water

In biological systems the interaction of aqueous solvents with amino acids and polypeptide chains has been examined[27] and even exploited[28] for decades. Two brilliant papers were written by John Edsall and Hugh McKenzie, regarding how proteins might fold and thereby interact with water.[29,30] These papers were written at a time when eloquent scientific discussions were conducted through published manuscripts. They are a unique joy to read in today's application oriented environment and are recommended for anyone interested in the thought processes that evolved into modern protein folding theory and biomolecular spectroscopy.

2.2.1. Solvent in exchange

While most researchers first experience NMR incorporating organic solvents such as deuterochloroform ($CDCl_3$) or deuterated-benzene (C_6D_6), relevant biomolecular NMR often requires an electrostatic solvent such as water. Besides the hydrophobicity difference of organic solvents, one of the most obvious differences is the exchangeable nature of water. Since protons in H_2O can easily exchange in a pH dependent manner,[31,32] the complexity of residual solvent signal suppression vastly increases. Also the desire to avoid inadvertently suppressing exchangeable solute signals is evident. When the protons in water are actively suppressed (e.g. presaturation) and then allowed enough time to exchange into positions in the

solute, not only are the exchange sites themselves removed but also the immediate neighbours of the solute can show bleaching effects.[4,33]

2.2.2. Water 'Hump'

Perhaps the greatest problem with suppressing water is the width of the peak. The water peak is not only broad due to exchange but also depends on the stability and homogeneity of the main magnetic field B_o. Again we see the need for careful shimming of the sample once equilibrium has been reached (Section 2.1.5). Interestingly the regions of the sample slightly outside the probe's receiver coil have come under suspicion. Several groups use the term 'far-away' or 'distant' water to refer to this region. Solvent in this portion of the sample experiences different homogeneity of the main field as well as reduced induced fields (B_1) from hard and soft pulses. All of this results in resonances skewed away from the central resonance frequency and experiencing little or no suppression (more on this later).

2.2.3. Radiation damping

The entire utility of NMR is the ability to record the magnitude and phase information of precessing nuclei in a large (hopefully static) external field. Cumulative precession is digitized from a carefully nurtured voltage in the receiver circuitry. However, any oscillating signal will generate an electromagnetic field. Radiation damping occurs when large coherent precessing resonances (like the massive solvent signal) produce a current in the hardware of the receiver coil such that an effective field (B_{RD}) counter to the induced field (B_1) is generated.[34] Radiation damping effects[35] and suppression techniques have been extensively discussed and reviewed.[2,4–6,22,36–38] The result of B_{RD} is to tip signals, on or close to resonance with the solvent, back to the $+Z$-axis creating a faster apparent relaxation rate than would normally be expected. Water can relax on the order of seconds in the absence of radiation damping, but will only require 100–200 μs when radiation damping is in effect (Equation (1)).[6]

$$T_{1RD} = (2\pi\eta Q\gamma M)^{-1} \tag{1}$$

Essentially any attempt to move the bulk magnetization of the solvent into the XY-plane will be fought against while any manipulation of the spins back to the $+Z$-axis will be accelerated. One cannot rely on a single optimized calculation, based on off-resonance peaks (e.g. DSS methyl peak), for solvent either in the 'flipdown' or 'flipback' cases.

The solvent relaxes not with the expected T_1 time constant (i.e. small rate constant), but instead with a much smaller observed time constant T_{1RD} that is proportional to the quality factor (Q), filing factor (η, ratio of sample volume over coil volume),[39,40] and the magnetization (equilibrium being M_o). Room temperature probes typically have a Q of perhaps a few hundred units but cryogenically cooled probes can push this value to 1500[f] (or even upwards of 40 000 is possible though not applied in biomolecular probes). The increased rate of relaxation due to radiation dampening is immediately evident.

[f] Knut Mehr (Probe Designer, Varian Inc.) personal communication.

Interestingly RD causes different spin behaviour than expected for typical T_1 or T_2 relaxation. One can usually consider vector theory and models with coherent magnetization in the XY-plane precessing after a hard 90° pulse (e.g. $+X$ hard pulse). We usually think of T_2 relaxation leading to a reduction of the resulting vector magnitude in the XY-plane, followed by the longer T_1 period with the zero net magnetization slowly climbing up the Z-axis to equilibrium. Radiation damping results from an induced field (B_{RD}) caused by the solvent spins. In this case, the induced field B_{RD} causes the same effect as a weak $-X$ pulse tilting any XY magnetization back along the outside of the vector sphere towards $+Z$. For example during a 180° inversion pulse, any error in the pulse length resulting in some magnetization in the XY-plane will cause RD to build and induce spins away from the $-Z$-axis. This in turns yields a greater induced effect until all net magnetization is moved off the $-Z$-axis and full RD is achieved. Errors in pulse lengths become common when one remembers that RD fights the initial pulse B_1 (e.g. flipdown) and helps any subsequent pulse (e.g. flipback) returning magnetization towards the $+Z$-axis. There is an excellent description of this in Figure 4 of William Price's review.[6] It is important to appreciate the effects of radiation damping, as we shall see later on.

2.2.4. Demagnetization field effects

2.2.4.1. Identifying the problem For over a decade several groups have identified small chemical shift changes during particular 2D experiments. The assumption of all NMR experiments is that the primary field of the magnet is stable during the course of the experiment, or at least that any changes are compensated for via the lock circuitry and associated field(s) applied to bring the lock signal back to a set point. This assumption allows all calculations to be done on a non-time dependent B_o field. Malcolm Levitt published an excellent full review on this subject in 1996.[41] Prof. Levitt uses the term 'demagnetization field effect' (as will we) but terms such as 'bulk nuclear-paramagnetic-susceptibility-induced transients',[42] 'dipolar field', or 'bulk susceptibility effects'[43] have also been used.

The effect has arguably been attributed to other phenomena (e.g. Bloch–Siegert shifts[43] and intermolecular multiple-quantum cross peaks[44]). While these arguments are compelling, we will work with the results of Malcolm Levitt's study. For example, it was originally hypothesized that multiple-quantum peaks could be generated between water and solute accounting for artefacts in multidimensional spectra.[44] However Lix, Sonnichsen, and Sykes[42] resolved this question quite convincingly using ^{19}F–^{1}H heteronuclear Overhauser (commonly termed HOESY) measurements showing that perturbing the ^{1}H resonances altered the main magnetic field experienced by ^{19}F nuclei.

We now know that demagnetization can be thought of as a field created by the presence of a large number of spins such as an aqueous solvent. The perturbation caused by such a large number of spins affects the magnetic field experienced by the remaining nuclei in solution.[41] Therefore removing the spins using a solvent suppression technique changes B_o for a short period of time until equilibrium can be re-established. Every other resonance (including residual solvent resonances) proceeds under a slightly different magnetic field and their frequencies of

precession are correspondingly altered. This begs the question: if you are attempting to suppress a solvent, where are you doing it from and when is the best time considering your target is now moving around? A technique fully optimized on an organic solvent may fail on an aqueous sample for precisely this reason. Even presaturation, one of the simplest solvent suppression techniques depends strongly on the saturation pulse position. If water starts out resonating at one frequency but moves once suppression is initiated, then either the frequency of saturation must be changed during the saturation pulse to compensate, or a compromise intermediate position must be used that can be established by arraying the carrier frequency of the saturating pulse.

2.2.4.2. Understanding the effect on cold probes Levitt's review showed convincingly that demagnetization effects are real though relatively small in magnitude.[41] However, this study was done in 1996 prior to the wide spread use of cold probes.[40] Alexej Jershow has reported more recently on demagnetization field effects during his investigation of excitation sculpting,[45] but these studies were at 300 MHz and on a room temperature probe. In the simplest case flipback pulses that return the bulk solvent magnetization to the $+Z$-axis remove the field perturbation caused by demagnetization during the acquisition period, but the flipback pulses might not remove the disturbance during the indirectly detected dimensions (of course this is usually coupled with heteronuclear coherence pathway selection which has its own inherent solvent suppression[46,47]). We believe that demagnetization has a much larger effect than has been previously considered or reported.

While investigating what we thought to be hardware lock instability on our 800 MHz spectrometer we discovered what we now suggest is a large demagnetization effect on cold probes. What we found was a noticeable change in lock levels during presaturation periods (i.e. 2 s at an induced field strength of ~90 Hz) even when the lock circuitry was active (Figure 5).

The change was occurring despite the sample being locked perfectly on resonance and the lock resonance carefully phased, shown in Figure 5A and B region (iii). Turning the lock compensation off (Figure 5 iv) resulted in large changes when the same presaturation pulses were used. Conversely the lock changes were substantially reduced (both while locked and unlocked) when a 98% D_2O sample was used as shown in Figure 5B corresponding to the decrease in ^1H concentration. The lock circuitry was not able to completely compensate for the field disturbance in the H_2O sample as shown in Figure 5A.

To confirm the demagnetization field hypothesis, we repeated the same experiments with presaturation pulses both on and off resonance for both samples (off-resonance pulses had no effect), and then proceeded to repeat all tests on a 500 MHz spectrometer equipped with a room temperature probe. Finally we moved to a different 500 MHz spectrometer located in a different building equipped with a 5 mm cold probe and repeated the experiments (data not shown). The tests on the 500 MHz spectrometers confirmed that the lock perturbations were proportional to the spectrometer magnetic field strength, the presence of a high Q cooled-probe, and the concentration of ^1H in the sample. Future examinations will

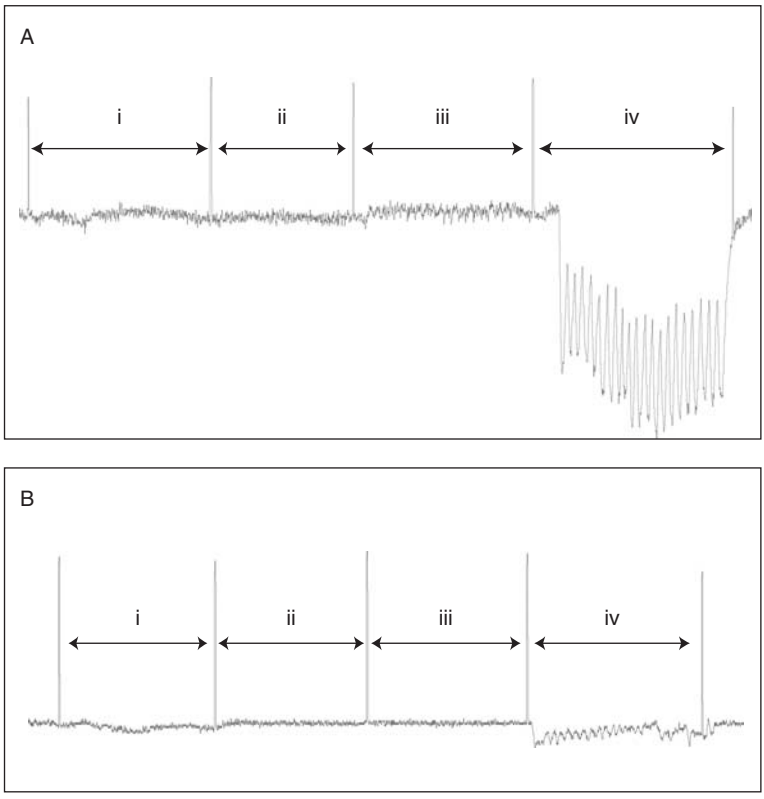

Figure 5 *Cold probe demagnetization field effects.* (A) shows the lock responses of a 90/10 H_2O/D_2O sample while (B) shows the lock of a 98% D_2O sample. The marked intervals correlate to: (i) equilibrium unlocked as a control, (ii) equilibrium with lock circuit active, (iii) locked while repeatedly pulsing with a 2.5 s ~90 Hz presaturation pulse and a 4 s recycle time, and (iv) the same repeating presaturation sequence as shown in (iii) but with an inactive lock circuit. Results are from an 800 MHz spectrometer with a 5 mm HCN cryogenically cooled probe.

undoubtedly clarify the magnitude of the demagnetization effect on cryogenically cooled probes, possible ways to compensate, and improve solvent suppression techniques.

2.3. How to suppress solvent?

There are only so many ways to distinguish one NMR signal from another (e.g. chemical shifts, relaxation, diffusion, and scalar couplings).[22,48–50] The ability to isolate and remove a solvent resonance carries all the resolution limitations that any other NMR study would incorporate, along with a few new ones due to the solvent signal magnitude and chemical nature. Water is especially irritating due to exchange characteristics when compared with highly deuterated common organic solvents like dichloromethane (CD_2Cl_2) or benzene (C_6D_6).

The spectroscopist requires a rapid technique that can isolate the solvent resonance(s) while causing little or no perturbation to the solvent or the quantum mechanical manipulation applied to the solute during the course of the experiment. We shall now briefly review a few of the more common methods (for more detailed reviews, see References 2, 4–7).

2.3.1. Coherence destruction/selection

Destructive methods often depend on exploiting or creating a time dependent function of the sample resonances such as diffusion rates (e.g. DRYCLEAN[51] and others[52]), B_1 inhomogeneity (e.g. presat) or gradients (e.g. WATERGATE, DANTE[53]) to isolate and destroy coherence of the solvent resonance(s).[54,55] The techniques most often depend on a chemical shift difference between the solvent and solute though solute resonances are often inadvertently suppressed (i.e. bandwidth issues). Methods in this category require multiple careful optimizations, and compromises must commonly be made in terms of overall suppression amplitude and bandwidth of effect. Refocusing of the solvent coherence must be avoided but is quite often overlooked.

The coherence pathway selection aspect applies most to heteronuclear systems. A great example is the common and extremely useful 2D-^{1}H,^{15}N-HSQC that can depend solely on pulsed field gradients (i.e. sensitivity enhancement[56,57] to select magnetization (both the P and N type) pertaining to the single quantum transitions of a ^{1}H^{15}N pair (e.g. amides in protein backbones). The coherence order is selected without the need for phase cycling. Solvent resonances cannot meet the heteronuclear selection criteria and are drastically suppressed though not entirely removed. Coherence selection against solvent can be improved with moderate solvent suppression techniques (e.g. flipback pulses) in order to further reduce residual solvent information and to improve the signal intensity of exchangeable solute signals.

2.3.2. Selective pulses

Selective pulses, also called shaped or soft pulses, can be used to isolate the response of solvent resonances exploiting chemical shift differences.[22,58–63] Shaped pulses are most often coupled with refocusing periods and gradients such as the water suppression by gradient-tailored excitation (WATERGATE) and Excitation Sculpting methods (see Section 3). Shaped pulses utilize altered phase, frequency, or amplitude (or any combination thereof) to mould the frequency response. Typical 'hard' pulses are square waves (or as square a wave as the hardware can deliver) that can be thought of as the amplifier in an 'off–on–off' sequence. Presaturation response is shaped by the extreme length (several seconds) of the pulse at relatively low power. Shaped pulses attempt to also achieve efficient selection, but in a far shorter period of time (typically hundreds of microseconds to a few milliseconds).

Modern spectrometers and the accompanying software usually supply the user with a graphic interface for the design and selection of a wide range of shaped pulses optimized for excitation, decoupling, inversion, and refocusing

(to name but a few). Combinations of shaped pulses resulting in the simultaneous selectivity of multiple resonances are possible and becoming common.[22,48,64,65]

2.3.3. Non-invasive flipbacks

As mentioned, non-invasive or passive techniques have been added to many multidimensional and multinuclear pulse sequences such as the 2D ^{1}H,^{15}N-edited-HSQC up to more complicated 3D and 4D heteronuclear-based NOESYs. The basic principle is to use a relatively long selective pulse to manipulate water.

Unlike the previous section, however, these pulses are used to return solvent (most often water) resonances back to the $+Z$-axis without the need for selection or coherence destruction, effectively removing much of the echo refocusing, radiation damping, demagnetization, and alternate suppression concerns.[14,66] The pulses require optimization (especially on higher field systems) but can yield excellent results.

2.3.4. Evaluation criteria for suppression

It has always been desirable to have an analytical process for the evaluation of solvent suppression methods. One of the first attempts at quantitation was done by Peter Hore in his review of solvent suppression.[2] However, it has been difficult to establish a method for the same reasons that solvent suppression is difficult in the first place. Each solvent behaves differently in terms of relaxation, coupling, and chemical shift (among other properties). In addition, each spectrometer has different characteristics and each user individually evaluates the quality of shimming to be used and the time available for optimizations. This makes establishing a standard sample to work on and how any pulse sequence will be evaluated challenging (to say the least).

2.3.4.1. Residual solvent amplitude Residual solvent amplitude is perhaps the most obvious parameter when judging the effectiveness of a suppression sequence. The magnitude of the remaining solvent resonance(s) is easily identified in the spectra and can be judged in comparison to the solute present in the sample. While certainly not the only criterion, it is indeed important and most sequences realize the need to suppress solvents such as water by a factor of 10^4 or 10^5 to bring samples into dynamic range.

2.3.4.2. Suppression bandwidth This is another important criterion that is easily overlooked. When judging the pulse sequence simply by the value of remaining solvent signal, one forgets that there is often a price to be paid via the suppression range. Peaks that are close to or under the solvent resonance may be fully or partially suppressed by any selective technique. The goal of all solvent suppression techniques of course is to be as effective as possible, in a region as narrow as possible, and not require too much time to execute.

2.3.4.3. Pulse sequence length This leads us to the third criterion of sequence performance. A method that requires too much time either runs into problems with radiation damping and/or exchange with atoms of interest in the solute

(e.g. H_N backbone or side chain atoms), or can add an unacceptable amount of time to the acquisition. This can occur from individual pulse sequence lengths, or from the requirement of multiple acquisitions via extensive phase cycling and subsequent cancellation, to delays required for full relaxation before the next FID can be acquired. An ideal suppression technique will therefore need to be powerful, selective, and quick, but are there additional characteristics?

2.3.4.4. Artefacts Any technique can inadvertently introduce changes to the rest of the spectra. For example, baseline distortions are timing errors in the first few acquisition points. Another common problem involves phase changes (linear and non-linear) introduced throughout the spectrum (both 1D and higher dimensionality) that easily occur depending on the method used. Homonuclear couplings develop during spin-echo sequences and are not easily suppressed interfering with quantitative analysis. A good suppression sequence must not create these problems or should attempt to compensate in some other way.

2.3.4.5. Calibrations and tolerance Now we add one more level of complication. Not only will the sequence need the characteristics described above (i.e. powerful, selective, quick, and clean), but we also seek methods that are easy to use and tolerant of mistakes. All NMR users, regardless of experience, would undoubtedly appreciate a pulse sequence that is easy to conceptualize, requires the least number of experimental parameters to be optimized, and yields simple reproducible results for efficient optimization. If a pulse sequence takes hours to optimize (e.g. full equilibrium must be reached between transients) with multiple interdependent parameters and must subsequently be re-optimized for each sample, then the sequence will need exceptional performance in every other aspect of evaluation to be adopted. Alternatively, a pulse sequence that gives only average suppression but requires little or no optimization will likely receive enthusiastic usage even though the overall performance may not meet that of other suppression choices. While neither extreme is likely we are often faced with several comparable choices and must evaluate the experimental needs and the robustness of the chosen suppression method(s).

3. SUPPRESSION PULSE SEQUENCES

The order of review was intended to be alphabetical with the exception of presaturation and water-eliminated Fourier transform (WEFT)/NOESY due to the importance of these sequences and comparisons to subsequent developments. Presaturation and WEFT (commonly referred to as 1D-NOESY) remain, for many groups, the 'gold standard' to which all other forms of suppression are compared. Suppression techniques prior to or during acquisition are considered. Suppression in the solid state[67] and post-acquisition mathematical suppression techniques (e.g. WAVEWAT[68] and others[3,69,70]) are beyond the scope of this review.

3.1. Presaturation

Selective presaturation (presat), with 'pre' referring to implementation prior to execution of the nearly limitless range of pulse sequences (Figure 6A), depends on the inhomogeneity of the induced field (B_1) to result in a loss of coherence (saturation) for the selected resonance.[71–73]

This is most often the water resonance for biomolecular samples but can be any resonance or even multiple[64,65] simultaneous resonances requiring suppression.

Selectivity is achieved by elongating the pulse so that an extremely narrow effective bandwidth ensues. Even the most modern spectrometers, with ever increasing RF pulse and field performance, cannot deliver identical signals for an indefinite period of time, and the inhomogeneity causes an eventual loss of coherence in the water signal. Since the selectivity is proportional to the pulse duration, one naturally considers increasing the pulse length hopefully resulting in perfectly selective solvent suppression.

While a wonderful idea, this can never be the result. Thinking about establishing equilibrium in the real spectral world, one can easily envision a situation where longer and longer pulses have an ever-decreasing improvement on the quality of suppression (i.e. equilibrium is achieved), and that the overall shimming quality of the sample comes into play. For example, a broad or asymmetric water peak resulting from a moderately shimmed sample (or inhomogeneous/unstable magnet) cannot be effectively eliminated by a narrow band of suppression and extending the saturation period would only make matters worse. The efficacy of presaturation depends on the power delivered, the extent of pulse length, and the position at which this power is delivered to the sample.

A broad asymmetric peak makes the selection of the carrier position difficult since a compromise frequency must be selected to immediately saturate the greatest number of spins and then again during exchange with the other resonances. As the symmetry of the resonances in the sample improves (most likely through shimming) and the peaks become taller and narrower, the ideal presaturation position becomes evident.

Once the shims have been optimized yielding the narrowest peak possible and the best carrier position has been selected (see Section 2.1), the only parameters left to optimize are the power levels and duration of the saturation pulse. Unfortunately, as noted by Wu and Otting,[74] presaturation becomes more problematic on higher field instruments equipped with cold probes and the amplifier powers associated with overcoming radiation damping become so intense that 'bleaching' (i.e. saturation transfer) of nearby resonances is unavoidable. Radiation damping fights the induced saturation field requiring more power than initially surmised by simple extrapolation from higher power levels (even on non-compressing amplifiers). Increasing the power yields better water suppression but a larger effective suppression band that reduces the intensity of neighbouring peaks. Mao and Yi have reported a very simple modification to the standard presaturation sequence where they introduce 90° phase shift (Presat90) into the later part of the saturation pulse.[75] The concept was to remove any spin-lock effect of the

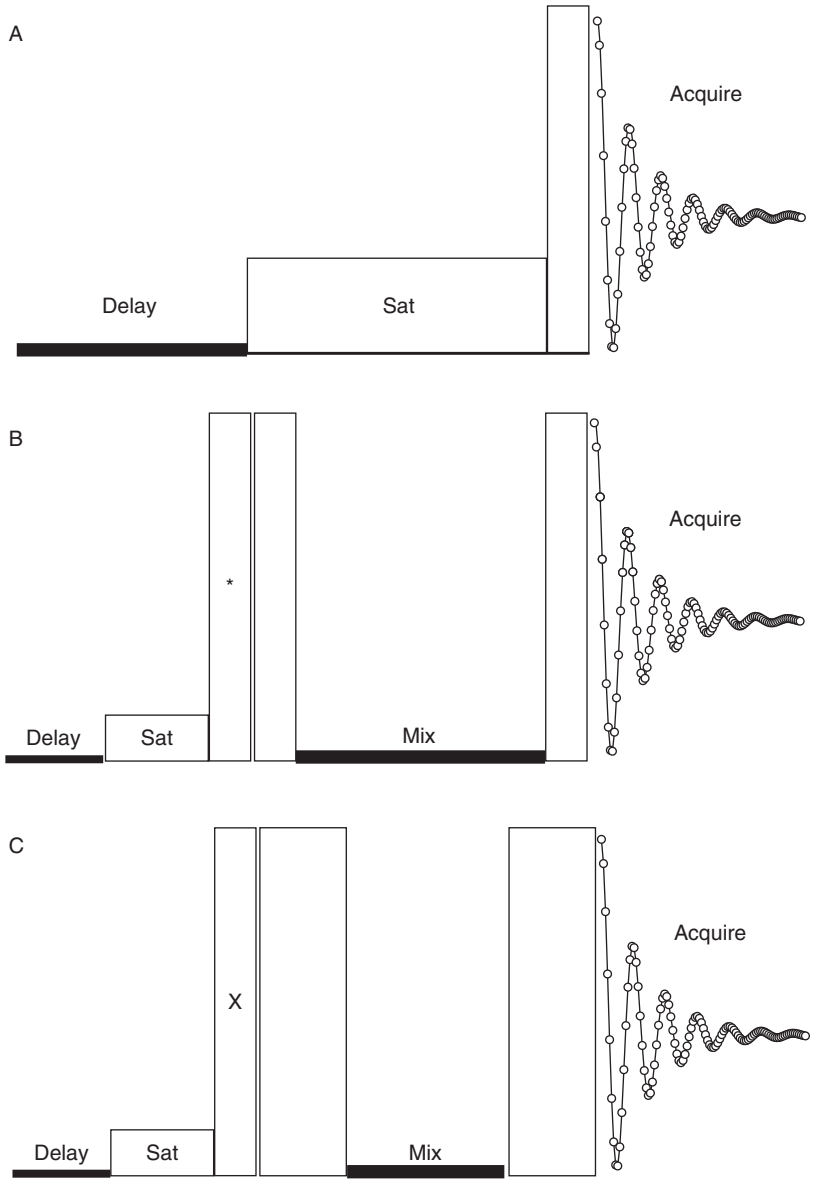

Figure 6 *Presat, WEFT/NOESY, and FLIPSY*. The typical (A) presat, (B) WEFT/NOESY and (C) FLIPSY. Any 90° and 180° hard pulses are identified, respectively, by narrow and wide hollow rectangles, respectively, with relative phases indicated inside the shape (where appropriate). Outlined Gaussian shapes indicate selective pulses while gradients are represented on their own horizontal line by filled shapes. For full phase cycle discussions please refer to the referenced manuscripts. The 45° phase shifted pulse discussed in the text is indicated by the asterisk in the NOESY sequence and an 'x' in the FLIPSY shows the variable flip angle pulse. The modified FLIPSY contains a homo-spoil gradient just after the presaturation period.

principle saturation pulse. However at higher fields equipped with a cold probe we did not find this modification to be entirely distinct from the original presat (see Figure 11).

3.2. Using T_1

3.2.1. WEFT/NOESY

The 1D version of the 2D-^{1}H,^{1}H-NOESY sequence[76] shown in Figure 6B is perhaps one of the most widely chosen suppression schemes. The first increment of the 2D is acquired while the delay increments, phase cycles, and quadrature detection related to the indirectly detected dimension are not used (Exorcyle[77] and other phase cycling is still performed[g]). This sequence also seems to be the present method of choice for metabonomics studies.[11,78,79]

This family of solvent suppression techniques really began with WEFT[80] and later related sequences.[50,81] The pulse sequence originally depended upon the T_1 relaxation time of the solvent being much greater than the solute. In this case after the initial 180° inversion pulse, as the solvent has relaxed to a net zero M_o, the solute should have returned to equilibrium (or close to it) and therefore be ready for the final 90° excitation pulse. The solute would be observed at full intensity while the solvent would have little or no signal to contribute. This method is one of the few sequences that allows resonances to be observed in proteins close to or even under the water peak.[54]

For cases where RD comes into play causing water to relax at a rate similar to the solute, the related Water-Press sequence[82] applies gradients inside the delay to suppress RD. Water then relaxes at a normal slow rate allowing the solute to reach equilibrium before the solvent. Super-WEFT[81] uses a series of dummy-scans to explicitly establish an equilibrium using much shorter delays than are required for full relaxation. Instead of waiting for equilibrium between each FID, the steady state is achieved producing far faster repetition though suppression can be a bit more challenging to optimize.

Modern usage of the 1D-NOESY pulse sequence is essentially a WEFT experiment with much shorter delays in a steady-state equilibrium exactly as initially described by Patt and Sykes and later detailed by Inubushi and Becker. Optimization of the 'mixing' time allows selection of the equilibrium null for the solvent though some groups do not optimize choosing to instead run a consistent delay for all spectra.

3.2.2. Volume selection

William Price was one of the first to explicitly state in the literature that the additional suppression afforded some sequences was due to the 'volume selection'[37,53,83] of the phase cycle.[6] Volume selection certainly does seem to be playing

[g] Exorcyle was appropriately and humorously named in reference to the ''ghosts'' and ''phantoms'' that were removed from the spectra.

a key role in recent suppression developments, especially considering the wider coils and additional difficulties involved in cooled probes. Modern NMR tubes with susceptibility-matched plugs make it easier to select the physical region to be recorded. A very recent paper has suggested a method for physically restricting the sample volume to the receiver coils using immiscible layers.[84]

The WEFT/NOESY style experiment provides substantially better water suppression than simple presaturation with four transients, which is the minimum for the phase cycle to take effect. With proper optimization of the mixing period the WEFT/NOESY still yields suppression even when considering only the first transient, and before pulsed field gradients were used in the mixing period. Therefore, while important, volume selection alone cannot be the sole answer.

At first glance there is little difference between the sequences (Figure 6). They all depend on the difference in relaxation time between the quickly relaxing solute and the presumably much longer solvent. The delay time (i.e. mixing time in the NOESY) is empirically selected to coincide with the solvent magnetization reaching net zero along the *Z*-axis, and gradients (in more modern versions) are used to eliminate any pulse width errors. The gradients should therefore be placed at the end of the mixing period in the cases where radiation dampening would be used to assist the relaxation process, that is when the spin–lattice relaxation time of the solute is relatively long. When the solute relaxation rates are actually slower then the solvent (e.g. RD on solvent), then the null of the solvent occurs before the solute (i.e. negative solute peaks). The resulting inverted amplitude spectra are typically phased 180° to be positive without the realization that a steady state has been achieved, though with decreased signal.

A recent modification to the WEFT/NOESY involves the use of a 45° phase shift to the excitation pulse in relation to the receiver coil.[7] This modification is not well documented in the literature, but the purpose of the change results in 1/2 the signal to noise in the first increment, and the apparent lost signal intensity is recovered on the second transient. The original version had an initial full signal read pulse parallel and a zero signal second FID anti-parallel to the receiver coil. The actual effectiveness of this change maybe somewhat elusive, but the logic behind it is to balance the real and imaginary signal intensities when considering radiation damping.

The main drawback to the original WEFT/NOESY experiments was the dependence on T_1 relaxation times. The optimal case was to wait for 3–5 times T_1, re-establishing equilibrium between each transient. As noted above this need not be the case and a steady-state using much shorter delays can still be used with good results.

Lastly, it is commonly assumed that the relaxation rate of all solute atoms is consistent, which is not the case for multiple compounds in a single sample (e.g. metabonomics). Calibrations must be applied to any standard database for identification based on relative rates of relaxation, and therefore intensity of peaks. Different functional groups in the same molecule can have different spin–lattice relaxation rates as would more flexible regions of large molecules. For extremely accurate measurements the calibration of signal loss is also frequency dependent (i.e. distance to carrier position is proportional to intensity variation) due to the profile of the hard pulses.

3.2.3. FLIPSY and modified FLIPSY

Neuhaus et al. first introduced FLIPSY[85] (flip angle adjustable one-dimensional NOESY) in 1996 and re-evaluated the pulse sequence in 2008 for use with metabonomics projects.[79] The modified FLIPSY is similar to the original (Figure 6C) with the exception of a small homospoil gradient prior to the flip-angle controlled pulse and just after the presaturation period.

The concept is to remove any transverse magnetization that may remain or has developed due to the weak spin-locking effect of the presaturation pulse (similar to the idea of the 90° phase shift added to the original presat, see Section 3.1). As stated by the authors, the water suppression should be identical to WEFT/NOESY with the added advantage of using a variable flip angle for Ernst angle calculations resulting in signal to noise improvements and reduced recycle delays.

3.3. Selective excitation family

3.3.1. Double-pulsed field gradient spin echo

Excitation sculpting (Figure 7) is a popular water suppression technique[86–88] originally reported by A. J. Shaka's group in 1995. The sculpting aspect comes from the gradient–delay–($180^{-x}_{\text{selective}}$–$180^{x}_{\text{hard}}$)–delay–gradient (pulse field gradient spin echo or PFGSE) refocusing period common to many suppression and spectroscopic techniques.

The key is that refocusing was achieved by a 180° pulse selective for the solvent, and a hard non-selective pulse. This resulted in either a net 0° pulse (i.e. $-x$ selective and $+x$ hard as reported by the authors) or net 360° pulse (i.e. $+x$ selective with $+x$ hard) on the solvent which, as a result, experiences two dephasing gradients while the solute is defocused and refocused by the two equivalent gradients. This refocusing module can be doubled (hence double PFGSE or DPFGSE) with differing gradient pairs (e.g. G_1–refocus–G_1–G_2–refocus–G_2) resulting in suppression and baseline quality improvements. Interestingly, the authors emphasize that the DPFGSE style experiments are not necessarily twice the duration of an equivalent double WATERGATE sequence (see Section 3.6). Their discussion does not, however, indicate why the 180° selective pulse is necessarily the same duration as each of the 90° soft pulses used in WATERGATE other than perhaps to compare shape performance at similar pulse lengths (even this is not necessarily convincing as one is comparing a 90° to a 180° pulse performance). Depending on the power levels or type of pulses chosen, the duration of these pulses could change dramatically, and the purpose of the distinction and conclusion is not absolutely clear. In addition, there is no discussion about the refocusing period lengths (all the delays are displayed as gradient lengths only). The authors also mention how the DPFGSE sequence is inherently more robust when dealing with even the small phase errors of modern spectrometers that are associated with large attenuator differences between hard and soft pulses.[89] In our experience, the difference is quite small as the WATERGATE experiments only have minor phase sensitivities of 1° or 2° corrections at most, though this may depend on the type of hardware available.

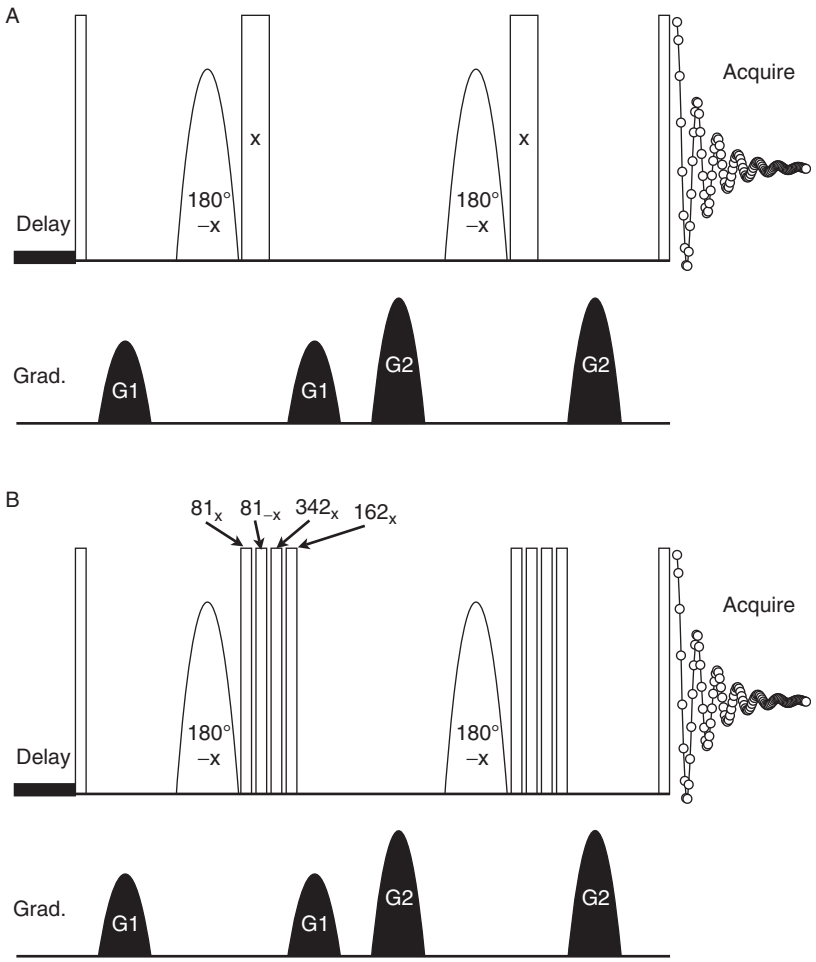

Figure 7 *Excitation sculpting and SOGGY pulse sequence.* (A) shows a cartoon representation of the basic DPFGSE module while (B) shows the SOGGY sequence. Cartoon sequence components are the same as described previously.

3.3.2. SOGGY

Solvent-optimized gradient–gradient spectroscopy (SOGGY)[89] is an improvement on the already effective excitation sculpting pulse sequence. The non-selective 180° pulse in the middle of the refocusing periods was replaced with a 'phase-alternating composite pulse' designed to compensate for B_1-field inhomogeneity (Figure 7B), and selection criteria for the composite pulse were quite strict. The replacement pulse had to compensate for any imperfections of the selective 180° pulse, closely approximate the performance of the hard pulse on resonance, and outperform the original 180° pulse in the off-resonance cases. A key was that the composite pulse should only counteract off-resonance inhomogeneity. Final selection criteria for the composite pulse included that the pulse should not add to the

total experimental length, be too difficult to create, or require specialized hardware. After several pulses were tried and improved upon, the authors reported the final $81^\circ_{(x)}$ $81^\circ_{(-x)}$ $342^\circ_{(x)}$ $162^\circ_{(-x)}$ SOGGY composite pulse best met the desired criteria.

Interestingly, the authors showed a comparison of SOGGY against several other recent suppression sequences such as WATERGATE and PURGE. They noted the off-resonance 'undulations' caused by the SOGGY suppression technique, but did not comment on the implications for high-resolution quantitative metabonomics measurements where baseline performance is critical. While SOGGY has some advantages, this was certainly one disadvantage when compared to some of the other sequences.[h]

SOGGY has average coding requirements, excellent solvent suppression performance, and good solute retention. The compact preparatory nature of the sequence makes it easy to apply to existing pulse sequences. SOGGY is certainly one of the best solvent suppression techniques available and does not come with the high number of parameters requiring optimization that other sequences contain.

3.4. Presat-180

The Presat-180 (presaturation with Adiabatic Toggling of 180 degree pulse inversion) sequence[90] attempts to directly address the 'faraway water' existing at the edges of the receiver coil detection limit. The sequence begins with standard presaturation that removes the bulk of the water resonances. Any 'distant' or 'far-away' solvent resonances (and solute) do not experience the full effect of saturation. At this point, an inversion pulse is applied, resulting in a relatively reduced effective pulse flip angle to resonances on the edges of the sample. The inversion pulse is toggled on and off in subsequent transients resulting in alternating $-Z$ and $+Z$ solute magnetization. The difference is taken, and therefore each scan allows the solute to increase while the far-away water and imperfect pulse results are cancelled. An adiabatic inversion pulse can easily be used to increase the sequence tolerance to B_1-inhomogeneity. Unlike refocusing style experiments, there are no losses due to diffusion or development of homonuclear scalar couplings. Also, there is no loss due to the inversion-recovery T_1 dependence seen the in the WEFT/NOESY style experiments (i.e. T_1 rates must be calibrated and compensated for in the WEFT/NOESY experiments for metabonomics work).

The Presat-180 is: simple, easy to implement with a short phase cycle, relatively insensitive to miscalibration, does not add significantly to the length of pulse sequences or introduce artefacts, and is adequately effective (Figure 11C).

[h] The use of 125 Hz presaturation pulse for 3 s in the relaxation delay was perhaps not the fairest comparison for intensity measurements.

3.5. PURGE

Presaturation utilizing relaxation gradients and echoes (PURGE, shown in Figure 8)[91] is a relatively new pulse sequence by Andre Simpson and Sarah Brown from the Chemistry department at the University of Toronto.

PURGE relies upon both presaturation and repeated refocusing cassettes (i.e. 90°–delay–180°–delay) interspersed with gradients. Initial presaturation removes the bulk of the solvent resonances while weak presat pulses (200 us) during the refocusing delays move portions of any remaining solvent resonances off the *XY*-plane. The final 90° pulse returns magnetization to the *Z*-axis, except for those solvent spins which were slightly off the *XY*-plane due to the saturation pulses. Off-axis spins are removed by the gradients, and the cassettes are repeated with different gradient strengths to avoid refocusing solvent signals.

The pulse sequence yielded surprising solvent suppression given the few parameters (i.e. pulse width and maybe the refocusing delay Δ) that needed to be adjusted. The sequence is efficient, selective, yields flat baselines, and executes quickly. However, the sequence and phase cycle are certainly not trivial in terms of being incorporated into already complex pulse sequences. The authors point out that theoretically any 90° pulse could be replaced by the PURGE sequence, but implementing this could prove a challenge. An extensive phase cycle was reported and condensed in Figure 8, but it was noted that suppression could be achieved with as few as four steps.

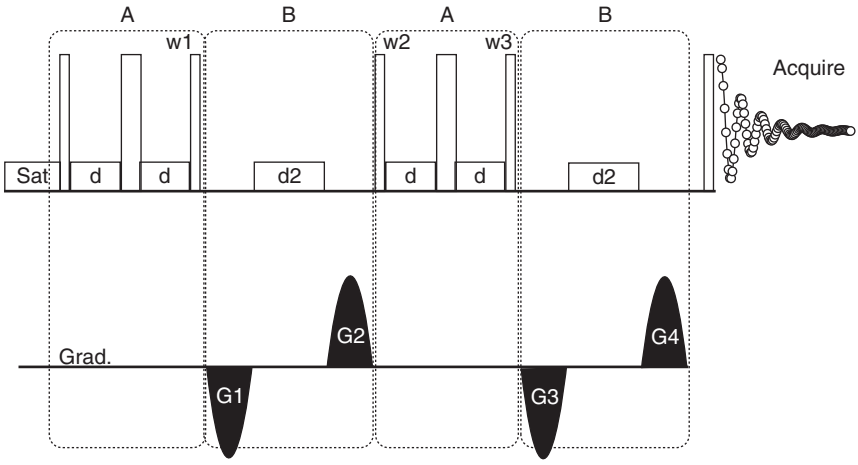

Figure 8 *PURGE pulse sequence*. A cartoon representation of the PURGE pulse sequence is shown. The delay d and d_2 were reported to be 200 us (d was reported between 3 us to 15 ms with little change to solvent suppression). Gradients (G/cm) were empirically optimized to $G_1 = -7.3$, $G_2 = 29.2$, $G_3 = -9.5$, $G_4 = 38.0$ and the phase cycles were reported to be: $w_1 = 2(x)$, $2(-x)$; $w_2 = 4(x)$, $4(-x)$, $-y$, $3(y)$, $4(-y)$; $w_3 = 2(x, -x)$, $2(-x, x)$, $2(y, -y)$, $2(-y, y)$; receiver $= x$, $2(-x)$, x, $-x$, $2(x)$, $-x$, $-y$, $2(y)$, $-y$. Cartoon components are as described previously.

3.6. WATERGATE family

3.6.1. WATERGATE

WATERGATE[92] (water suppression by gradient tailored excitation, Figure 9A) comprises some form of selective inversion pulse[61,93] surrounded by two gradients of equal magnitude and duration. The only specification for the inversion unit is that it results in full inversion of the solute, while leaving the solvent resonance(s) unaffected and dephased by the isocromats of the pulse field gradients.[54] In this way the intensity of the solvent coherence destruction is directly proportional to the applied gradient amplitudes. However, the refocusing period allows T_2 relaxation, diffusion, and scalar coupling to evolve with some concomitant solute intensity losses. In addition, extremely intense gradients can take unacceptably long periods of time to settle delaying acquisition or resulting in spectral distortions. A compromise always has to be reached between solvent suppression and system stability.

The original pulse sequence comprised of an initial 90° bringing all magnetization into the *XY*-plane. A gradient was used to encode the coherences, and refocusing was employed by a non-selective 180° hard pulse surrounded by two 90° shaped pulses of opposite phase. After the refocusing pulses, another identical time period was used containing a final gradient of equal amplitude. Solute was effectively encoded by the first gradient, reversed, and decoded by the final gradient. The type of selective pulses, amplitudes, and durations determined the efficacy and selectivity of the solvent suppression. Optimization could be achieved by modifying the type of shaped pulse and duration, then arraying the fine attenuator (or course attenuator if more applicable on your system) to find a minimum. Any effects due to miscalibration and/or radiation damping could therefore be compensated for empirically. Other components requiring optimization include the hard 180-pulse width, carrier position, and phase of the two soft pulses.

3.6.2. The 3919 WATERGATE

A modification to the original WATERGATE was proposed by Sklenar et al. in 1993. The selective portion of the pulse sequence comprised a 3α–d–9α–d–19α–d–19α–d–9α–d–3α (with $26\alpha = 180°$ pulse and d being a short delay, usually in the few hundred microseconds range, Figure 9B).[94] The sequence was called a W3 due to the three pulse components making up the selective portion of the WATERGATE suppression, but is more commonly referred to as a 3919 WATERGATE.

This sequence did not suffer from any phase problems associated with rapid attenuator switching (i.e. lower power shaped pulses to high power square pulses and vice versa)[89] as all pulse were high power square waves, and no optimizations were required as only the inter-pulse delay can be altered. The inter-pulse delay (τ, see Equation (2)) controls the bandwidth of suppression (i.e. the longer the delay the narrower the suppression region) and the frequency of higher order notches.[i]

[i] A second version of the 3919 for off resonance selective excitation was reported with notches at $\pm(2n + 1)/2\tau$ and required a slightly different phase cycle.

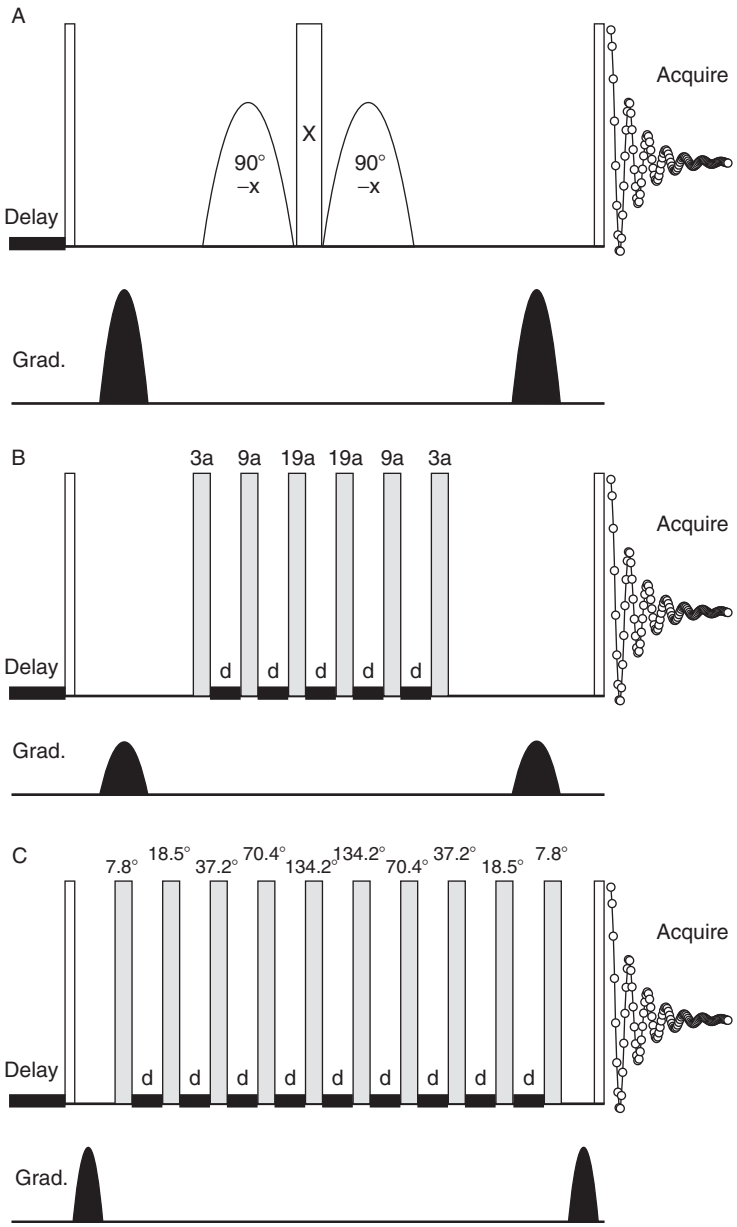

Figure 9 *WATERGATE pulse sequences.* The various evolutions of the WATERGATE sequences are shown. (A) shows the original WATERGATE, while (B) shows the 3919 modification, and (C) the W5. The pulse components used are described in Figure 6 except that the specific length pulses are shaded gray.

$$\Delta\nu_{sup} = \pm n\frac{1}{\tau}, \quad n = 0, 1, 2, 3 \ldots \tag{2}$$

One must take care not to bring the secondary notches into the solute spectra, and this limits the control over the selectivity of the solvent suppression that can be obtained (i.e. a compromise between suppression efficiency and solute detection). One can make the solvent suppression extremely selective, however the off-resonance notches will move closer to the carrier frequency, in from the edges, removing valuable solute information. The notches can be moved well outside the frequency range of desired resonances, but the central notch widens removing information close to the carrier.

The 3919 WATERGATE sequence is very effective and requires little optimization. Once a suitable delay is determined for a spectrometer frequency it can simply be used as a standard setting and requires no further attention. Coding the appropriate phase cycles into an existing sequence is not difficult though care should be taken on complex experiments. The exclusive use of hard pulses makes power calibration far simpler, and the use of a vector simulation program such as PJNMR[j] can make visualizing the necessary phase alterations or the effect of gradients and pulses much easier when designing the experiment.

3.6.3. W5 WATERGATE

In 1998, Liu et al. introduced modifications to the 3919 sequence to reduce the width of the on-resonance suppression notch while moving the secondary notches further out. The two new pulses were termed W4 and W5 (Figure 9C).[95] It is important to note that there is a typo in the first paragraph incorrectly stating that the 3919 uses '$62\alpha = 180°$'. The value in the abstract and the original 3919 paper is correct (i.e. $26\alpha = 180°$). Like the 3919 sequence, W5 involves a series of explicit pulses (i.e. 5) interspersed with delays that control the solvent suppression width and where the secondary suppression notches occur. It is important to remember that these types of suppression schemes have a net zero effect on solvent (solvent resonances are moved off the $+Z$-axis but return, while solute is inverted) so radiation damping can certainly cause problems. Additional power may be required.

3.6.4. RECUR-NMR

Recovery of underwater resonances by magnetization transfer NMR (RECUR-NMR)[96] was reported by Liu et al. in 2001. The sequence uses a double WATERGATE, followed by a TOCSY or ROESY transfer of magnetization (either through dipolar coupling or through space via the ROE) to resonances that would have otherwise been removed, as they fall inside the suppression region of the WATERGATE shaped pulses. The sequence was therefore modified from the others in the family to include a spin-lock at the end, just before acquisition. Not only did this allow transfer of magnetization back on to otherwise suppressed atoms but it could also suppress resonances from large molecular fragments, such as membrane

[j] Pure Java NMR (PJNMR) $ written by Paul-Jean Letourneau, Robert Boyko, and Brian Sykes, $ Department of Biochemistry at the University of Alberta. Available for free download at the NANUC website (http://www.nanuc.ca).

fragments, glyco-proteins, and anti-bodies in binding studies. Resonances from large molecules can cause baseline roll making quantitation difficult. In all other aspects this method should perform similarly to a normal WATERGATE.

3.6.5. Modified binomials

Zheng, Torres, and Price have recently introduced phase-modulated binomial six-pulse sequences applicable to Excitation Sculpting or WATERGATE.[97] The phase modulation was designed to avoid the introduction of artefacts into the spectra, and the pulses to have a net zero effect on resonance (solvent). The binomials were supposed to quickly progress to full inversion with the most consistent phase and amplitude across as wide an effective bandwidth as possible. The newer sequences had a steeper climb slope angle from the on-resonance minimum to the maximum inversion point and were reported to have ~10% better bandwidth than W5. Also the entire sequence was shorter in duration than the W5. The sequence is only slightly more difficult to code than the original excitation sculpting or WATERGATE though accurate phase reproduction would be required to execute this suppression method. The pulse sequence was not coded at the time of testing and was therefore not included in the comparisons, however we expect similar performance on our instrumentation to that of the W5 sequence (with reported improvements of course).

3.7. WET series

The original concept was reported by Ogg, Kingsley, and Taylor in 1994 and was designed for *in vivo* studies.[98] Ogg et al. were attempting to use frequency selective pulses (Section 2.3.2) and gradients in a longitudinal relaxation time (T_1) and induced field (B_1) independent manner. They also desired efficient suppression of the solvent signal on the first set of pulses (no signal averaging over separate transients) and without subsequent water refocusing echoes (echoes can begin to develop once the gradients cease). This means that they were attempting to discern a way to suppress different solvents on different instruments with the same method yet without the need for major recalibration by the spectroscopist. This was, and still is, a very challenging objective even with today's advances in software and hardware. They settled on the use of four different variable pulse tip angles, four gradients, and four identical inter-pulse delays (t) initially determined using the Bloch equations (Figure 10). They explored different pulse lengths and inter-pulse delays monitoring off resonance, B_1 and T_1 dependencies.

The initial technique was built upon by Smallcombe, Patt, and Keifer[99] in 1995 who settled on the sequence shown in Figure 10A with each subsequent gradient amplitude 1/2 the intensity of the preceding member (e.g. 1×, 0.5×, 0.25×, 0.125×). The reduction in the gradient strengths was done to reduce solvent echoes, and a short delay (d_z) was included to allow minimization of the small negative residual solvent.

The researchers also noted the ability to select solvent peaks away from the carrier using shifted and/or composite laminar pulses (SLP).[100] Modern spectrometer software makes creating these types of shaped pulses quite easy. One of the

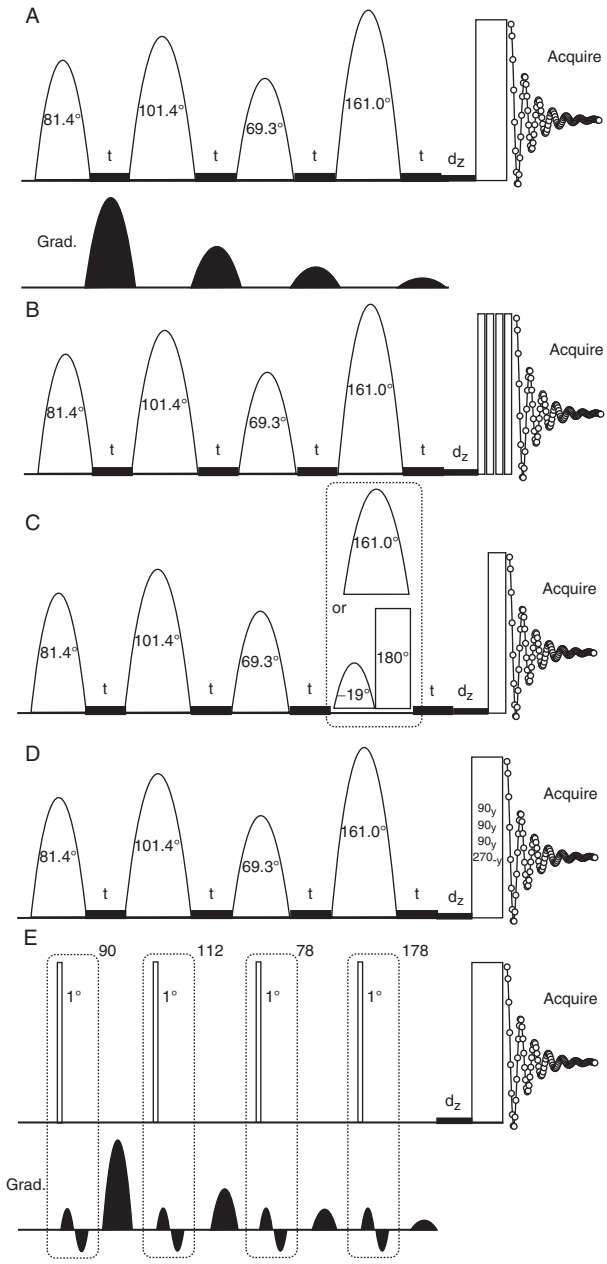

Figure 10 *Wet pulse sequences.* Cartoon representations of the (A) basic WET, (B) WET with composite ($90_x90_y90_{-x}90_{-y}$) read pulse, (C) WET180, (D) WET270, and (E) SWET pulse sequences. See Figure 6 for pulse descriptions and text for details. WET gradients were the same for all sequences and are described in text.

primary advantages of WET sequences was the rapid nature of the suppression, making it ideal for application in flow cell spectrometers where the solvent signal was rapidly and consistently replenished with unsuppressed material. These experiments can also make the 1% natural abundance ^{13}C splitting from organic solvents a nuisance and the authors reported a method to decouple these peaks during the selective ^{1}H pulses. The preparatory nature of the sequence also makes incorporation into multidimensional experiments easier.

3.7.1. WET180

The WET180 sequence[101] was introduced by Hauping Mo and Daniel Raftery this year. A toggled inversion pulse is inserted into the final selective WET shaped pulse (Figure 10C). Originally they had attempted to include the alternating 180° pulse after the four selective pulses, but this interfered with the optimized performance of the WET selective sequence. Instead they inserted a $180^\circ_{(y)}$ adiabatic pulse into the final shape and maintained the total pulse performance by changing the shaped pulse into a $19^\circ_{(-y)}$; therefore the total effect of the shaped and adiabatic pulse was the required $161^\circ_{(y)}$. Solvent on the edge of the receiver coils does not properly respond to the 180° pulses and therefore should be suppressed by the subsequent toggling and associated subtractive phase cycle.

Unfortunately, a version of the pulse sequence was not available for our spectrometer and the sequence could not be included in our tests.[k] The authors did show comparisons to the other WET style experiments. A unique observation was that WET270 on their instrumentation had a phase and calibration difficulty that required the 90° and 270° components to be separately acquired and phased before addition.[102]

3.7.2. WET270

Zhang et al. published the WET270 (Figure 10D) modification[102] of the original WET water suppression scheme in 2000. They were focusing on the 'far-away' water problem similar to that attempted by other sequences and tested a composite volume selective pulse pioneered by Ad Bax[53] instead of the final read pulse (Figure 10D). They felt that the original $90_x90_y90_{-x}90_{-y}$ volume selective pulse was too limiting (bandwidth secondary nulls at −0.8080 and 0.5475 γB_1 and a nonlinear phase distortion) and opted for an alternative approach. They collected the standard WET sequence, but on the fourth acquired transient they swapped the final 90° pulse for a 270° pulse with opposite phase. The result was that any resonances that experienced the full B_1 field would see four equal full additions (remember that a 270° pulse with opposite phase should be equivalent to the previous 90° pulses). However, the important part is that any spins experiencing less than the full B_1 field will not add, but instead be subtracted on the fourth acquisition. For example, if the effective B_1 field experienced by the 'far-away' water at the fringes of the ^{1}H coils was 30% then the total accumulation over four transients would be $30\% + 30\% + 30\% + 3\times(-30\%) = 0$. It is possible that the 270° pulse may produce some concerns regarding receiver overflow or inconsistent pulse response yielding less than optimal subtraction. This may account for the

[k] A version of the sequence is expected very soon for Varian spectrometers.

unusual acquisition and processing mentioned in the WET180 manuscript comparisons.[101] This sequence was unfortunately not available at the time of writing.

3.7.3. SWET

The purpose of the Secure Water Suppression (SWET)[74] pulse sequence (Figure 10E) was to eliminate the effects of radiation damping (see Section 2.2.3) while still using the WET pulse-gradient method for water suppression. As noted in the RD section, this is especially important on modern high field magnets equipped with high *Q*-factor cold probes (remember that RD is proportional to B_o and probe *Q*-factor). The effects of RD make shape pulse calibration problematic, and a high power pulse calibration cannot be used (even assuming linear amplifier response) to determine the optimal WET selective pulses. SWET combats RD by incorporating a bipolar gradient pair in the delay between subsequent selective pulses thus causing the destruction of solvent coherence. The water suppression components are identical to the original WET sequence.

4. COMPARISONS, CONCLUSIONS, AND ADVICE

All the suppression techniques worked well in reducing solvent by many orders of magnitude. Solvent suppression has become so effective that improvements on the order of only a few percent can be the deciding factor when trying to determine the 'best' method during comparisons.

We selected two samples for the sequence comparisons. The first sample was a 1 mM ubiquitin protein dissolved in 90% H_2O with 10% D_2O with 1 mM DSS as an internal reference. The sample was deliberatively shortened to 550 uL to make the shimming less effective. The sample was symmetrically shimmed, but only down to a linewidth (50% height) of ~1 Hz. This sample was used to evaluate the solvent amplitude after suppression and to give insight into the relative effect (if any) of the solute signals on an 800 MHz instrument equipped with 5 mm HCN cold probe. The results of the tests were discussed in Section 4.1. The second sample was a 10 mM *N*-acetyl-asparagine in 98% D_2O (600 uL) also symmetrically shimmed with a final width at 50% height of 0.77 Hz. This sample was ideal in terms of efficient solvent suppression and was used to compare and evaluate the baseline characteristics and off-resonance effects of the sequences on solute suppression (Section 4.2).

4.1. Comparison of suppression

All the spectra were collected sequentially on the ubiquitin sample with each experiment taking approximately 2.5 min to complete. The results are shown in Figure 11A–L.

Each of the sequences was optimized with appropriate parameters (see figure legend) and presented at the same vertical scale for direct comparison. Standard parameters such as the 90° pulse width, sweep width, acquisition times, presaturation periods and powers, carrier positions and so on were maintained for each

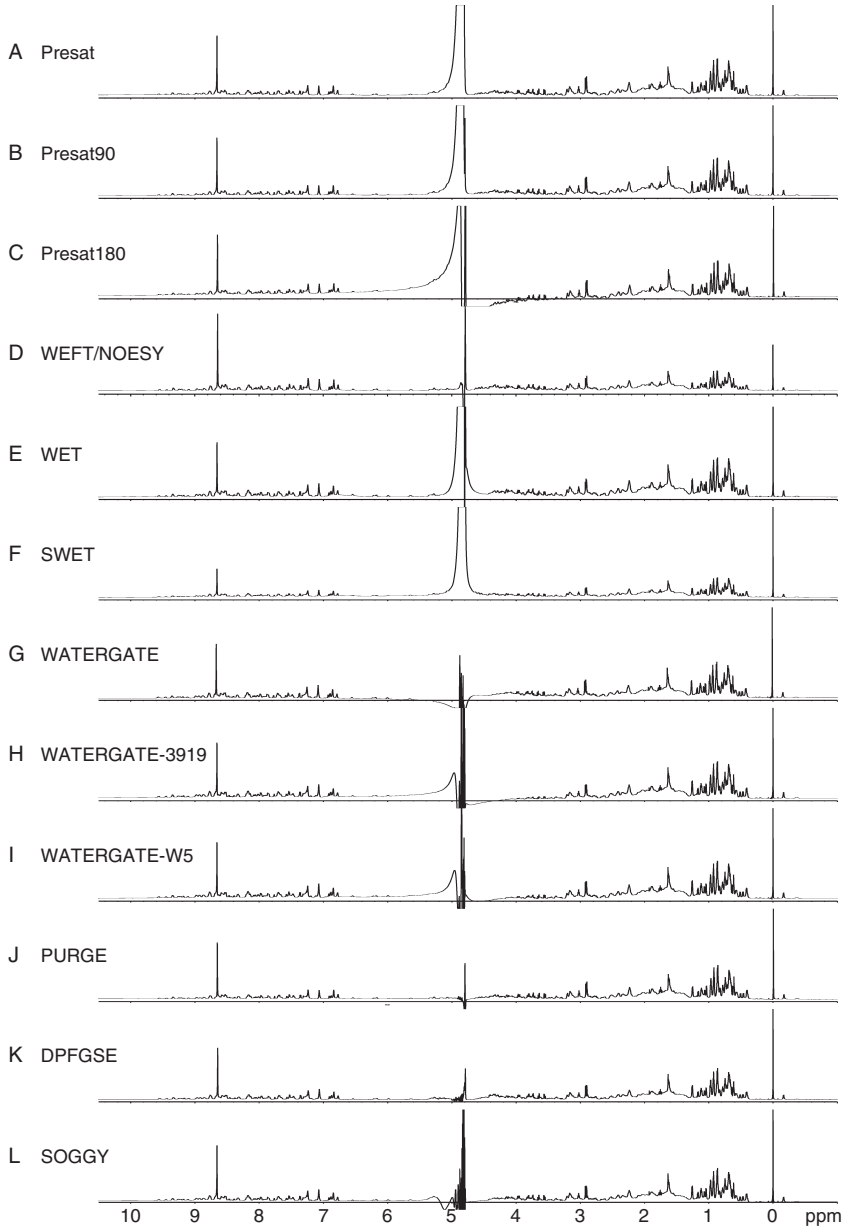

Figure 11 *Suppression comparison on a ubiquitin sample.* The figure shows consecutively acquired spectra collected on the ubiquitin sample (see text). All spectra were acquired with 32 transients after 4 steady-state pulses. The acquisition time was 2 s with 2.5 s of preparation (e.g. presaturation, recycle delay, etc.). Spectra were zero-filled to twice the number of acquired points.
(A) Presaturation with optimized carrier position and pulse width that was used for all subsequent hard pulses, (B) Presat90 with the same parameters, (C) Presat180 with an independently optimized 180° pulse length, (D) WEFT/NOESY with the same carrier and pulse width as optimized in the previous experiments and a 100 ms mixing time, (E) WET (118 us inter-pulse delay) with optimized

experiment type. Presat (Figure 11A) and WEFT/NOESY (Figure 11D) are the spectra most often used for suppression comparisons. All sequences yielded acceptable to superb suppression of the water preventing both receiver overflow and ADC problems (WET/SWET exception detailed below). The amplitudes of both the amide and aliphatic regions were very similar with the exception of WEFT. While the amides were almost equally as intense, the aliphatic and the DSS reference peak show a marked reduction. This is most likely due to the loss of signal from using shorter than optimal delays (i.e. incomplete relaxation between FIDs) as discussed in Section 3.2.1. Another immediate observation is the stunning suppression performance of the WATERGATE, excitation sculpting (DFGPSE), and PURGE sequences compared to the more traditional sequences. Even the WEFT/NOESY had difficulty competing with the PURGE and SOGGY sequences for overall amplitude solvent suppression and was at least a factor of 2 behind in solute signal to noise. The WATEGATE 3919 and W5 sequences did not suppress water as well, but required far fewer parameter optimizations, especially compared to the original WATERGATE.

Most of the sequences performed well even on this short and moderately shimmed sample. Despite not optimizing the shims, almost every sequence was able to suppress sufficiently to acquire useful spectra with minimal baseline distortions even close to the solvent. The exception occurred for the WET style sequences. The WET family did not suppress nearly as well and required the gain to be reduced by 6 dB (vertical scale in the figure was increased to compensate) to prevent a receiver overflow and ADC error. However, WET and SWET are very easy to include in pulse sequences (e.g. during the recycle delay or mixing periods) and allow simple suppression of multiple frequencies using composite shaped pulses. The poor results may come from several sources (e.g. coding error, optimization error, etc.) and therefore may not represent a limitation of the pulse sequences. Alternatively, as a real world example, some sequences simply perform better on some spectrometers and users must be prepared to adapt when necessary. We have typically found WET to be extremely reliable and robust, but certainly not on this particular sample.

4.2. Bandwidth, artefacts, and baseline

Residual solvent signal amplitude is only one of the many criteria for evaluating suppression techniques. As spectroscopists, we are certainly interested in any baseline corruption that may result, as this will deter the ability to properly integrate and automatically interpret spectra. We also do not want the inclusion of spurious peaks, or the removal of actual information close to the solvent signal.

---

d_z delay shaped pulse length, (F) SWET (118 us inter-pulse delay) with optimized 1° pulse width (1.8 us), (G) WATERGATE with optimized: carrier frequency, independent suppression frequency, phase correction (1°) for low attenuator pulses, shaped pulse power, independent flipdown and flipback pulse lengths, and 180° inversion pulse length, (H) WATERGATE-3919 without further optimization, (I) WATERGATE-W5 without further optimization, (J) PURGE without optimization, (K) DPFGSE with optimized shaped pulse length, and finally (L) SOGGY without further optimization.

Therefore to evaluate the pulse sequences more closely, we selected a different sample that contained far fewer peaks than ubiquitin, a large intense peak in order to evaluate baseline performance, and a set of peaks very close to the solvent to check the bandwidth of suppression. We selected a synthetic sample of *N*-acetyl-asparagine (kindly donated by Daniels Fine Chemicals Ltd. of Redwater, Alberta) that contained all the peaks of interest. Figure 12 shows a similar comparison of all the sequences reviewed previously, but run on the synthetic sample. All the methods performed well on the amide (~6–8 ppm, eightfold higher scale) and the aliphatic (~1–5.5 ppm) regions. The downfield H_α peaks however did reveal some notable differences in the bandwidth of suppression. The WET (using 3 ms SINC pulse lengths), WATERGATE (1.6 ms selective pulses), 3919, and W5 versions all demonstrated that nearby resonances can also be drastically suppressed during solvent elimination. To a lesser degree SOGGY also showed some reduction of the nearby peaks. The larger bandwidth of reduction for the 3919 and W5 sequences was due to the very short inter-pulse delay (89 us) resulting from automatic software optimizations. An initial value of 160 us was manually selected but the software program determined that the maximum suppression occurred at 89 us. For our tests, the automated results were maintained to show what a typical user might encounter, and what the highest level of suppression could achieve. This may however not be the fairest comparison in terms of suppression bandwidth, and readers are encouraged to experiment on their systems with different delay settings.

None of the sequences introduced large artefacts, and the baseline performance was quite good with some small imperfections close to the water peak (e.g. Figure 12E–I). However, upon close examination we did find a very interesting small distortion. There was a distinct weak distortion associated with the intense resonance of the acetyl group (Figure 13).

The error was an 's' shaped bend (Figure 13A) in the baseline that could not be removed with any combination of non-linear or linear phase corrections. We had previously noted this type of error when the lock phase was incorrectly set, but this was not the culprit in this case. The lock position and phase were optimal and even altering these parameters away from the optimal value did not modulate the distortion. The 's' shape did not appear in non-gradient sequences such as presat and was quite small (compared to the two 0.5% natural abundance ^{13}C coupled peaks on either side of the main signal). The distortion was only noticed due to the very intense amplitude of the source acetyl peak and the fact that we were looking specifically for distortions when comparing sequences (if you look closely you can see the distortion in Figure 12). We did find that the error had a gradient strength dependency. Low gradient strengths resulted in inconsistent baseline problems while very high gradients (e.g. 30 g/cm or higher) yielded consistent baseline problems with amplitudes proportional to the gradient strength applied. Even during intermediate gradients (e.g. 3–8 g/cm) the distortions were consistent but reduced in amplitude. We have been able to track down the problem to a gradient hardware issue previously undiagnosed on our system. By reversing the amplitude of the applied gradients in every other acquired FID the problem was completely resolved (e.g. DPFGSE sequence with alternating gradients result in

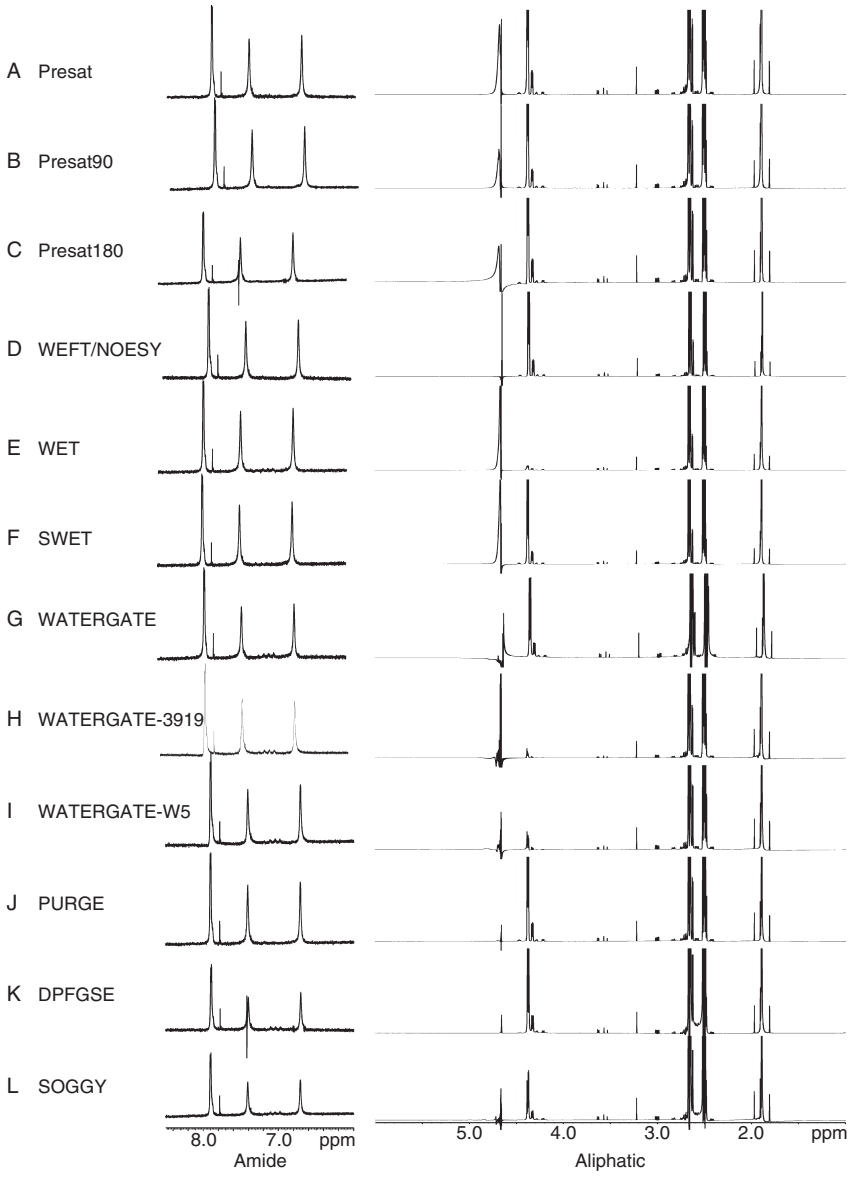

Figure 12 *Bandwidth, artefacts, and baseline.* Pulse sequences previously tested in Figure 11 were applied to a sample of 10 mM *N*-acetyl-asparagine (98% D_2O) in order to evaluate the effects of the various suppression methods on exchangeable atoms (amides), resonances close to the solvent (H_αs), and extremely intense peaks (acetyl group).

Figure 13B). We have begun to explore which other sequences may require this gradient compensation.

Finally, a comparison of the solvent suppression pulse sequences was performed with purposeful errors in pulse width (−10%) or carrier position (−4 Hz).

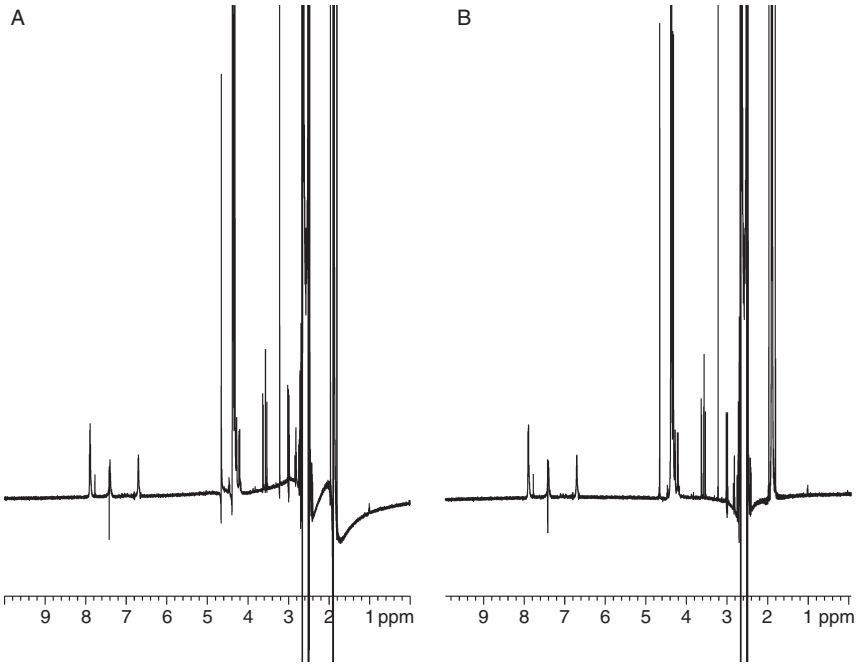

Figure 13 *Baseline distortion.* (A) shows an expanded view including the upfield *N*-acetyl peak region and the typical distortion seen in all suppression experiments utilizing gradients. (B) shows the same experiment but utilizing alternate amplitude gradients. The CH2s show homonuclear coupling evolution. Note that the natural abundance ^{13}C couplings are almost off scale indicating the relative magnitude of the problem.

While definite problems were seen with single scans, once a full phase cycle was applied all the sequences performed amazingly well, and therefore the data were not included. Our experience is that even common small errors can result in usable (though certainly not ideal) spectra when utilizing any of these modern, robust, suppression methods.

4.3. Conclusion

Every suppression sequence covered in this review provides at least adequate (often excellent) suppression of a single solvent resonance with several sequences providing astounding performance. In addition, many of the sequences are capable of suppressing multiple resonances simultaneously in very short experimental times. Some sequences provided poorer overall suppression performance such as presat or the WET family, but the presat and WET methods are the easiest to implement and optimize. The WATERGATE sequences are more difficult to code, but provided very good suppression with little or no optimization (e.g. 3919 or W5). The best suppression undoubtedly was provided by the WATEGATE, PURGE, and Excitation Sculpting (DPFGSE and SOGGY) sequences. Unfortunately WATERGATE and DPFGSE require the most optimizations to attain the

highest levels of solvent suppression and solute retention. Luckily modern spectrometers often come with automation software to optimize the suppression sequences relieving the obvious tedium (and common errors). The NMR user has many choices and fortunately none of them are a 'bad' choice. In most cases whichever suppression sequence is most familiar and/or pre-coded on your system should yield satisfactory results providing at least minimal optimization is performed. In the cases of the most difficult samples, the addition of moderate presaturation at the beginning of any existing suppression sequence should remove enough solvent signal to eliminate any remaining receiver or ADC problems. There are certainly no bad sequences, and therefore we recommend first use what is available, then code what may be needed. All the best of luck.

ACKNOWLEDGMENTS

I would like to thank Kent Dixon for critical reading, Trent Bjorndahl (D. Wishart research group, Univ. of Alberta) for assistance and access to a cryogenically cooled probe on an 11.74T spectrometer to confirm the demagnetization field effects, John C. Lindon and David Neuhaus for correspondence over the years regarding solvent suppression developments, Frank Delaglio for discussions and patience on so many NMR techniques, George Gray for assistance with Varian's BioPack pulse sequences, Eberhard Hoffman for discussions on common 1D-NOESY phase cycles and 45° phase shift, Eriks Kupče on shaped pulses, Peter Sandor for suggestions on the use of reversed gradients and coding of the DPFGSE sequences, Daniels Fine Chemicals Ltd. (Edmonton, AB) for donation of the *N*-acetyl-asparagine sample used for evaluations of pulse sequence performance, and the Vice-President of Research (University of Alberta) for financial support of my position. NANUC is funded by the Natural Science and Engineering Research Council of Canada (NSERC).

While attempting to perform as thorough a literature search as possible, I apologize in advance to any authors whose work I may have overlooked. The error was purely my own and is not meant to imply any selectivity. Thanks to all the researchers whose work I have had the pleasure of reading for this review. Special thanks to Ray Freeman, Malcolm Levitt, William Price, Peter Hore, and Maurice Guéron (and co-authors) whose reviews, books, and articles were an inspiration for this work.

Special thanks to Elizabeth, Mark, and Kathryn McKay for allowing me time to work on this manuscript and putting up with me during the writing.

Finally, I am greatly indebted to Brian D. Sykes for invaluable discussions, insights, and inspirations on all aspects of scientific investigation.

APPENDIX

If attempting to increase the solute concentration.
A simplified example:
(Remember that a 10 kD protein = 10 000 g/mol)

$$1\text{mM} = 1 \times 10^{-3}\text{mol} \times 10000\ \text{g/mol} \times 600 \times 10^{-6}\text{L} = 6\ \text{mg}$$

To make a solute concentration equivalent to solvent:
(Remember that water is ~18 g/mol therefore 1000 g/L×1 mol/18 g = 55 M water = 110 M ^{1}H)

$$110\ \text{mol/L} \times 600 \times 10^{-6}\text{L} \times 10000\ \text{g/mol} = 660\ \text{g}$$

Therefore a 10 kDa protein would require 660 g of material to be dissolved in a 600 uL sample to be equal to the signal of the solvent. This is not possible, nor would even a sample at 1/100th the concentration be moderately feasible. The alternative is to reduce the solute signal and work with a realistic solute concentration often around 1 mM.

REFERENCES

1. A. Abragam, *Principles of Nuclear Magnetism* (Oxford University Press, Toronto, 1961), pp. 599.
2. P. J. Hore, *Methods Enzymol.*, 1989, **176,** 64–77.
3. A. Coron, L. Vanhamme, J. P. Antoine, P. Van Hecke and S. Van Huffel, *J. Magn. Reson.*, 2001, **152,** 26–40.
4. M. Gueron, P. Plateau and M. Decops, *Progress in NMR Spectroscopy*, 1991, **23,** 135–209.
5. M. Liu and X.-A Mao, *Solvent Suppression Methods in NMR Spectroscopy* (Elsevier, Ltd, 1999), pp. 2145–2152.
6. W. S. Price, *Annual Reports on NMR Spectroscopy*, 1999, **38,** 289–354.
7. A. Altieri, K. Miller and A. Byrd, *Magnetic Resonance Review*, 1996, **17,** 27–82.
8. J. Keeler, R. T. Clowes, A. L. Davis and E. D. Laue, *Methods in Enzymology*, 1994, **239,** 145–207.
9. E. J. Saude, C. M. Slupsky and B. D. Sykes, *Metabolomics*, 2006, **2,** 113–123.
10. B. C. Potts, A. J. Deese, G. J. Stevens, M. D. Reily, D. G. Robertson and J. Theiss, *J. Pharm. Biomed. Anal.*, 2001, **26,** 463–476.
11. R. H. Barton, J. K. Nicholson, P. Elliott and E. Holmes, *Int. J. Epidemiol.*, 2008, **37,** 31–40.
12. J. K. Nicholson and I. D. Wilson, *Progress in NMR Spectroscopy*, 1989, **21,** 449–501.
13. D. S. Wishart, C. G. Bigam, J. Yao, F. Abildgaard, H. J. Dyson, E. Oldfield, J. L. Markley and B. D. Sykes, *Journal of Biomolecular NMR*, 1995, **6,** 135–140.
14. S. Grzesiek and A. Bax, *J. Am. Chem. Soc.*, 1993, **115,** 12593–12594.
15. R. L. Smith and E. Oldfield, *Science*, 1984, **225,** 280–288.
16. B. M. Fung and M. C. Peden, *Biochim. Biophys. Acta*, 1976, **437,** 273–279.
17. G. Arvidson, G. Lindblom and T. Drakenberg, *FEBS Lett.*, 1975, **54,** 249–252.
18. S. R. Heller, *Biochem. Biophys. Res. Commun.*, 1968, **32,** 998–1001.
19. K. Wüthrich, *NMR of proteins and nucleic acids*. (John Wiley & Sons, New York, 1986), pp. 1–292.
20. J. Cavanagh, W. J. Fairbrother, A. G. Palmer III and N. J. Skelton, *Protein NMR Spectroscopy: Principles and Practice* (Academic Press, Toronto, ed. 2nd, 2006), pp. 1–885.
21. P. J. Hore, *Journal of Magnetic Resonance*, 1983, **55,** 283–300.
22. R. Freeman, *Spin Choreography: Basic Steps in High Resolution NMR* (Oxford University Press, Oxford, 1997), pp. 1–391.
23. A. Jerschow and G. Bodenhausen, *J. Magn. Reson.*, 1999, **137,** 108–115.
24. P. A. Keifer, *Concepts in Magnetic Resonance*, 1999, **11,** 165–180.
25. P. S. Wu and G. Otting, *J. Magn. Reson.*, 2005, **176,** 115–119.
26. J. L. Markley, A. Bax, Y. Arata, C. W. Hilbers, R. Kaptein, B. D. Sykes, P. E. Wright and K. Wuthrich, *J. Biomol. NMR*, 1998, **12,** 1–23.
27. G. Otting, *Progress in NMR Spectroscopy*, 1997, **31,** 259–285.
28. C. Dalvit, P. Pevarello, M. Tato, M. Veronesi, A. Vulpetti and M. Sundstrom, *J. Biomol. NMR*, 2000, **18,** 65–68.
29. J. T. Edsall and H. A. McKenzie, *Adv. Biophys.*, 1978, **10,** 137–207.
30. J. T. Edsall and H. A. McKenzie, *Adv. Biophys.*, 1983, **16,** 53–183.
31. S. Englander and N. Kallenbach, *Q. Rev. Biophys.*, 1983, **16,** 521–655.
32. O. K. Baryshnikova, T. C. Williams and B. D. Sykes, *J. Biomol. NMR*, 2008, **41,** 5–7.
33. C. M. Slupsky, *Thesis*., University of Alberta (1995), pp. 1–352.
34. N. Bloembergen and R. V. Pound, *Physical Review*, 1954, **95,** 8–12.
35. C. Szantay and A. Demeter, *Concepts in Magnetic Resonance*, 1999, **11,** 121–145.
36. X. Mao and J. Chen, *Chemical Physics*, 1996, **202,** 357–366.

37. C. Szantay, *J. Magn. Reson.*, 1998, **135,** 334–352.
38. S. Warren, S. Hammes and J. Bates, *J. Chem. Phys.*, 1989, **91,** 5895–5904.
39. H. Kovacs, D. Moskau and M. Spraul, *Progress in NMR Spectroscopy*, 2005, **46,** 131–155.
40. A. G. Webb, *Annual Reports on NMR Spectroscopy*, 2006, **58,** 1–50.
41. M. H. Levitt, *Concepts in Magnetic Resonance*, 1996, **8,** 77–103.
42. B. Lix, F. D. Sonnichsen and B. D. Sykes, *Journal of Magnetic Resonance*, 1996, **A121,** 83–87.
43. M. Augustine and K. Zilm, *Journal of Magnetic Resonance*, 1996, **A123,** 145–156.
44. W. S. Warren, W. Richter, A. H. Andreotti and B. T. N. Farmer, *Science*, 1993, **262,** 2005–2009.
45. A. Jerschow, *J. Magn. Reson.*, 1999, **137,** 206–214.
46. L. E. Kay, *Curr. Opin. Struct. Biol.*, 1995, **5,** 674–681.
47. D. J. Thomas, L. Mitschang, B. Simon and H. Oschkinat, *J. Magn. Reson.*, 1999, **137,** 10–24.
48. R. Freeman, *Progress in NMR Spectroscopy*, 1998, **32,** 59–106.
49. D. Canet, J. Brondeau, E. Mischler and F. Humbert, *Journal of Magnetic Resonance*, 1993, **A105,** 239–244.
50. C. Haasnoot, *Journal of Magnetic Resonance*, 1983, **52,** 153–158.
51. P. Zijl and C. Moonen, *Journal of Magnetic Resonance*, 1990, **87,** 18–25.
52. G. Zheng, T. Stait-Gardner, P. G. Anil Kumar, A. M. Torres and W. S. Price, *J. Magn. Reson.*, 2008, **191,** 159–163.
53. A. Bax, *Journal of Magnetic Resonance*, 1985, **65,** 142–145.
54. A. S. Altieri and R. A. Byrd, *J. Magn. Reson. B*, 1995, **107,** 260–266.
55. R. Sarkar, D. Moskau, F. Ferrage, P. R. Vasos and G. Bodenhausen, *J. Magn. Reson.*, 2008, **193,** 110–118.
56. L. E. Kay, P. Keifer and T. Saarinen, *Journal of the American Chemical Society*, 1992, **114,** 10663–10665.
57. A. G. Palmer III, J. Cavanagh, P. E. Wright and M. Rance, *Journal of Magnetic Resonance*, 1991, **93,** 151–170.
58. A. Böckmann and E. Guittet, *Journal of Biomolecular NMR*, 1996, **8,** 87–92.
59. B. Cutting, J. H. Chen, D. Moskau and G. Bodenhausen, *J. Biomol. NMR*, 2000, **17,** 323–330.
60. L. Emsley and G. Bodenhausen, *Journal of Magnetic Resonance*, 1990, **87,** 1–17.
61. M. Mescher, A. Tannus, M. O. N. Johnson and M. Garwood, *Journal of Magnetic Resonance*, 1996, **A123,** 226–229.
62. G. A. Morris and R. Freeman, *Journal of Magnetic Resonance*, 1978, **29,** 433–462.
63. K. Zangger, M. Oberer and H. Sterk, *J. Magn. Reson.*, 2001, **152,** 48–56.
64. E. Kupce and R. Freeman, *Journal of Magnetic Resonance*, 1993, **A105,** 234–238.
65. E. Kupce and R. Freeman, *Journal of Magnetic Resonance*, 1995, **112A,** 216–264.
66. L. E. Kay, D. Marion and A. Bax, *J. Magn. Reson.*, 1989, **84,** 72–84.
67. D. H. Zhou and C. M. Rienstra, *J. Magn. Reson.*, 2008, **192,** 167–172.
68. U. L. Gunther, C. Ludwig and H. Ruterjans, *J. Magn. Reson.*, 2002, **156,** 19–25.
69. Y. Chen, F. Zhang and R. Bruschweiler, *Magn. Reson. Chem.*, 2007, **45,** 925–928.
70. D. Marion, M. Ikura and A. Bax, *Journal of Magnetic Resonance*, 1989, **84,** 425–430.
71. I. D. Campbell, C. Dobson, G. Jeminet and R. Williams, *FEBS Lett.*, 1974, **49,** 115–119.
72. D. I. Hoult, *Journal of Magnetic Resonance*, 1976, **21,** 337–347.
73. A. G. Redfield and R. K. Gupta, *Pulsed-Fourier-Transform Nuclear Magnetic Resonanec Spectrometer*, J. S. Waugh, ed. (Academic Press, New York, 1971), pp. 81–115.
74. P. S. Wu and G. Otting, *J. Biomol. NMR*, 2005, **32,** 243–250.
75. X. Mao and C. Ye, *Chemical Physics Letters*, 1994, **227,** 645–650.
76. A. Kumar, R. R. Ernst and K. Wuthrich, *Biochem. Biophys. Res. Commun.*, 1980, **95,** 1–6.
77. G. Bodenhausen, R. Freeman and D. L. Turner, *Journal of Magnetic Resonance*, 1977, **27,** 511–514.
78. M. E. Dumas, E. C. Maibaum, C. Teague, H. Ueshima, B. Zhou, J. C. Lindon, J. K. Nicholson, J. Stamler, P. Elliott, Q. Chan and E. Holmes, *Anal. Chem.*, 2006, **78,** 2199–2208.
79. M. Lauridsen, A. D. Maher, H. Keun, J. C. Lindon, J. K. Nicholson, N. T. Nyberg, S. H. Hansen, C. Cornett and J. W. Jaroszewski, *Anal. Chem.*, 2008, **80,** 3365–3371.
80. S. L. Patt and B. D. Sykes, *Journal of Chemical Physics*, 1972, **56,** 3182–3184.
81. T. Inubushi and E. D. Becker, *Journal of Magnetic Resonance*, 1983, **51,** 128–133.
82. W. S. Price, K. Hayamizu and Y. Arata, *J. Magn. Reson.*, 1997, **126,** 256–265.
83. S.-I. Tate and F. Inagaki, *Journal of Magnetic Resonance*, 1992, **96,** 635–643.

84. J. M. Wieruszeski, B. Fritzinger, X. Hanoulle, J. C. Martins and G. Lippens, *J. Magn. Reson.*, 2008, **193,** 37–40.
85. D. Neuhaus, I. M. Ismail and C.-W. Chung, *Journal of Magnetic Resonance*, 1996, **118 Series A,** 256–263.
86. D. Callihan, J. West, S. Kumar, B. I. Schweitzer and T. M. Logan, *J. Magn. Reson. B*, 1996, **112,** 82–85.
87. T. Hwang and A. Shaka, *Journal of Magnetic Resonance*, 1995, **112A,** 275–279.
88. B. D. Nguyen, X. Meng, K. J. Donovan and A. J. Shaka, *J. Magn. Reson.*, 2007, **184,** 263–274.
89. H. Mo and D. Raftery, *J. Magn. Reson.*, 2008, **190,** 1–6.
90. A. J. Simpson and S. A. Brown, *J. Magn. Reson.*, 2005, **175,** 340–346.
91. M. Piotto, V. Saudek and V. Sklenár, *Journal of Biomolecular NMR*, 1992, **2,** 661–665.
92. A. L. Davis, *Journal of Magnetic Resonance*, 1989, **84,** 620–626.
93. V. Sklenar, M. Piotto, R. Leppik and V. Saudek, *Journal of Magnetic Resonance*, 1993, **102,** 241–245.
94. M. Liu, X. Mao, C. Ye, H. Huang, J. Nicholson and J. C. Lindon, *J. Magn. Reson.*, 1998, **132,** 125–129.
95. M. Liu, H. Tang, J. K. Nicholson and J. C. Lindon, *J. Magn. Reson.*, 2001, **153,** 133–137.
96. G. Zheng, A. M. Torres and W. S. Price, *J. Magn. Reson.*, 2008, **194,** 108–114.
97. R. Ogg, P. Kingsley and J. Taylor, *Journal of Magnetic Resonance*, 1994, **B104,** 1–10.
98. S. Smallcombe, S. L. Patt and P. Keifer, *Journal of magnetic Resonance*, 1995, **A117,** 295–303.
99. S. L. Patt, *Journal of Magnetic Resonance*, 1992, **96,** 94–102.
100. H. Mo and D. Raftery, *J. Biomol. NMR*, 2008, **41,** 105–111.
101. S. Zhang, X. Yang and D. G. Gorenstein, *J. Magn. Reson.*, 2000, **143,** 382–386.

CHAPTER 3

Photo-CIDNP Spectroscopy

Martin Goez

Contents

Institut für Chemie, Martin–Luther-Universität Halle–Wittenberg, Kurt–Mothes-Str. 2, D-06120 Halle/Saale, Germany

Annual Reports on NMR Spectroscopy, Volume 66
ISSN 0066-4103, DOI: 10.1016/S0066-4103(08)00403-1

Abstract Photo-CIDNP spectroscopy relies on a unique interplay of magnetic interactions, diffusion, and chemical reactivity; it possesses all the advantages of NMR spectroscopy but responds to processes on a nanosecond timescale. This very powerful method can be used to investigate short-lived intermediates, the mechanisms of complex photoreactions, structures and folding of proteins, and processes in photosynthetic reaction centres. This chapter provides an introduction to the theory, explains the instrumentation and techniques with emphasis on new developments, uses a series of case studies to illustrate the information that a chemist can obtain from photo-CIDNP, and reviews recent applications of photo-CIDNP spectroscopy to chemical and biochemical problems. The literature from 1996 to mid-2008 is covered.

Key Words: Chemically induced dynamic nuclear polarization, Photochemistry, Paramagnetic NMR, NMR in reacting systems.

1. INTRODUCTION

NMR spectra recorded during the course of certain chemical reactions exhibit anomalous signal intensities, namely, enhanced absorption or emission of individual lines, or whole multiplets. This was discovered independently by Bargon, Fischer, and Johnsen,[1] and by Ward and Lawler[2] in 1967. It is not surprising that spectrometer artefacts were originally thought to be responsible. The exciting atmosphere of those days has been recalled by Bargon[3] in a recent paper dedicated to the memory of Hanns Fischer, who died in 2005.

From the start, these phenomena were recognized as spin polarizations (deviations of the populations of the nuclear spin states from the Boltzmann distribution) caused by radical reactions. As the first attempts to understand their generation erroneously focussed on Overhauser effects, they were christened ''chemically induced dynamic nuclear polarizations''. Although only partially correct, that name has stuck, possibly because its acronym CIDNP (usually pronounced ''kidnap'') evokes the picture of radical scavenging. However, only 2 years later the now universally accepted quite different explanation, the hitherto unknown radical-pair mechanism, was found, again by two groups independently.[4,5]

The radical-pair mechanism relies on a complex interplay of nuclear–spin dependent intersystem crossing of radical pairs, modulated by the dynamics of

interdiffusion, and electron-spin dependent chemical reactivity of the pairs at reencounters. Hence, CIDNP experiments can yield very detailed information about the intermediates and the pathways of their formation and decay, information that is often difficult or impossible to obtain in other ways. Yet, this power comes at a price: Although they can be performed with standard equipment, CIDNP experiments are slightly more difficult to plan and interpret than are ordinary NMR measurements, and some expertise is needed to make the most of that powerful method. The present review has been written with the purpose of bridging that gap by including a detailed explanation of the principles, the experimental techniques, and the kind of information that can be routinely obtained with CIDNP spectroscopy; it aims at NMR spectroscopists with a chemical background.

Although CIDNP was first observed in thermal reactions, its true potential lies in the field of photochemistry, and over the years the interest of the community has shifted more and more towards photo-CIDNP; in the last 10 years, thermal reactions have accounted for less than 15% of all CIDNP work reported. A histogram of published papers shows a levelling off of publication frequency in the last decade, so the field has reached maturity by now, the decrease in publication numbers being mainly caused by a lower number of studies dealing with the effect as such, not with its application to chemical problems. Reflecting general trends, mechanistic and kinetic studies of organic photoreactions by CIDNP have been slightly decreasing in frequency over the last years, which is compensated by a growing interest in applying photo-CIDNP to systems of biochemical interest, most notably proteins and the photosynthetic reaction centre.

Exhaustive coverage of both background and applications of photo-CIDNP up to 1988 is provided by Steiner's review,[6] and the literature from that point of time up to mid-1996 has been extensively reviewed by the present author.[7] Since then, only a number of shorter reviews concerned with specific aspects of photo-CIDNP have appeared, which will be dealt with in the pertaining sections below. The review section of this chapter, therefore, concentrates on the period from 1996 to mid-2008, and will go into details of earlier work only where necessary.

Writing about a method that is not so commonly used (in the author's opinion, less frequently than it deserves), one faces the problem that readers will have very diverse motives and questions, ranging from the applicability to a given chemical problem over the optimization of experimental parameters and protocols to quantitative calculations of the effects. Bearing that in mind, a structured approach is taken. Sections 2–3.3 provide the qualitative framework while Section 3.4 is only needed by those who are interested in a quantitative treatment. Section 3.5 deals with recent research focussed on the CIDNP effect itself. Experimental aspects, including new developments, are comprehensively covered in Section 4. In a series of case studies, Section 5 describes the kind of information CIDNP experiments yield; this should enable a chemist to judge whether his or her problem could benefit from investigating it by this method. Finally, recent applications of photo-CIDNP to chemical and/or biochemical problems are reviewed in Section 6, which is grouped by reaction types on one hand and classes of substances on the other.

2. CIDNP PHENOMENA

2.1. Net and multiplet effects

For the very common case of a weakly coupled spin system, any nonequilibrium population such as caused by CIDNP can be decomposed into longitudinal one-spin order I_{1z}, two-spin order $2I_{1z}I_{2z}$, and so forth. While the basis of that decomposition, the product operator formalism,[8] was unknown at the time when CIDNP was discovered, the characteristic signal patterns associated with one- and two-spin orders were immediately recognized, and given the names ''net effect'' and ''multiplet effect''. Their phases (i.e. signs) depend in a simple way on the structures of the paramagnetic intermediates and the reaction mechanism, as explained in Section 3.2, which is probably the most frequently exploited feature of CIDNP. Figure 1 displays examples of these two effects.

NMR spectrometers of the late 1960s did not permit the detection of higher spin orders for sensitivity reasons, so no new name was coined for them; the term used today is ''higher multiplet effects''. More importantly, with the cw instruments ubiquitous at that time a separation of different spin orders n was principally impossible. The advent of pulsed and Fourier transform spectrometers reduced that to a trivial task: Because for a weakly coupled spin system the amplitude of the detectable signal is proportional to $\sin\vartheta\ \cos^{n-1}\vartheta$, one simply has to acquire spectra with different flip angles ϑ and form suitable linear combinations (e.g. one- and two-spin orders are separated by adding and subtracting two spectra acquired with $\vartheta = 45°$ and $\vartheta = 135°$).[9]

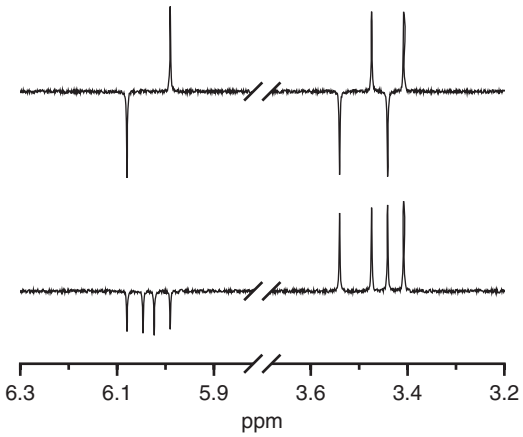

Figure 1 *CIDNP net effects* (bottom trace) *and multiplet effects* (top trace) for the olefinic protons of *N*, *N*-diethylvinylamine V (for the formula, see Chart 5) formed in the photoreaction of xanthone with triethylamine in acetonitrile. Net and multiplet effects were separated by their flip angle dependence, as described in the text. Left: X part (α proton) of the ABX spectrum; right: AB part (β protons). The reason for the missing two inner lines from the multiplet of the α protons in the upper spectrum is explained in Ref. 114.

As will be explained in Section 3.2, multiplet and higher multiplet effects are much more prominent at low fields. For that reason, CIDNP net effects prevail on today's high-field spectrometers.

2.2. Time-resolved photo-CIDNP

The processes generating the spin polarizations are typically completed within a few nanoseconds after the birth of the radical pairs. While this feature is lost when radical-pair generation is continuous, as in thermal reactions or photoreactions brought about by cw illumination, radical-pair formation can easily be made fast on that timescale when a pulsed laser is used as the light source.

To become observable by NMR, the polarizations next have to find their way into diamagnetic products. This depends on the chemistry of the system and on the concentrations, but very often occurs on a timescale of several tens of microseconds. If an rf pulse is applied at some point of time during that period, it converts the polarizations present at that very moment into coherences and isolates them from the further development of the polarizations, which are longitudinal magnetizations only; hence, these coherences decay in the same way as any normal NMR signal.

By varying the time between the laser flash and the rf pulse in a series of scans, a temporal profile of the reaction is thus obtained. This technique was introduced on a millisecond timescale[10] within less than a decade after the discovery of the CIDNP effect, and soon afterwards extended to the microsecond[11] and submicrosecond[12] range. Figure 2 shows an example of such an experiment. Because the durations of hard pulses for protons on modern spectrometers are in the microsecond range, a time resolution on that order is routinely accessible; deconvolution methods[13] allow a reduction by another factor of 10.

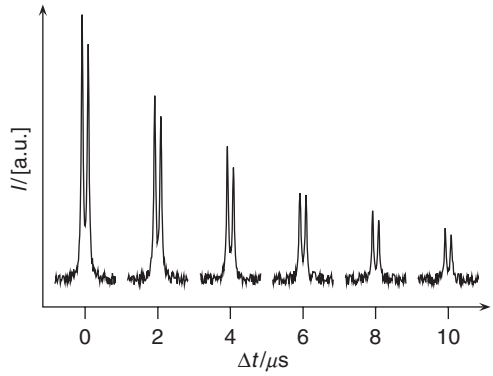

Figure 2 *Time-resolved CIDNP experiment* on the system xanthone/triisopropylamine in acetonitrile at 294 K; amine concentration 10 mM. Shown are the CIDNP signals of the terminal protons of the amine as functions of the delay Δt between the laser flash and the sampling rf pulse (duration, 1.0 μs).

3. CIDNP THEORY

3.1. The radical-pair mechanism[4,5]

Radical pairs are the key intermediates for CIDNP effects. From the way chemistry is taught, most scientists would regard single radicals as something natural and radical pairs as something exotic. Yet, that is a misconception from the start because all reactions that produce radicals from non-radical precursors (bond cleavage or electron transfer) produce them in pairs.

Even more pertinent to the character of a radical pair as an entity is the idea of a cage. Intuitively, that word evokes the picture of the pair being kept together by surrounding solvent molecules, which would make a cage a region of space. However, CIDNP and related effects could not arise if the two radicals did not easily and rapidly separate to distances where there is no interaction between them. What makes them still a pair under these conditions is a correlation of their electron spins, which persists despite their separation and despite the absence of any interaction between them, and provides a memory of each other (a slowly fading one, because of relaxation). That correlation does not manifest itself as long as the radicals are separated; its detection is only possible if the two radicals—meaning the *same* two, not just chemically equivalent others—reencounter at some later point of time. As is probably not common knowledge, the probability that that happens is quite substantial, even approaching unity if there is a Coulombic attraction between them. At the moment of reencounter, the question of whether the radicals have remained in the cage can be determined in retrospect: They have if their spin correlation has not been lost during the preceding diffusive excursion. Hence, a cage is a much more abstract notion, a region of time during which the joint electron-spin state keeps the radicals from becoming independent despite the absence of interactions between them.

An overline is normally used to symbolize a spin-correlated, or ''geminate'', radical pair $\overline{\mathrm{R_1^\bullet\ R_2^\bullet}}$ and to distinguish it from single, or ''free'', radicals $\mathrm{R_1^\bullet}$ and $\mathrm{R_2^\bullet}$. Additionally, the electron spin multiplicity of the pair is specified at the top left of the overline.

3.1.1. Electron-spin states of a radical pair

When the radicals of a pair are in contact, i.e. at the moment the pair is born or at a later reencounter, the spin Hamiltonian is completely dominated by the exchange interaction. In consequence, the two unpaired electrons are indistinguishable, and wave functions such as $|\alpha\beta\rangle$ are inacceptable because they violate the Pauli principle. The correct eigenstates are singlet and triplet,

$$|S\rangle = \frac{1}{\sqrt{2}}(|\alpha\beta\rangle - |\beta\alpha\rangle) \tag{1}$$

$$|T_{-1}\rangle = |\beta\beta\rangle,\ |T_0\rangle = \frac{1}{\sqrt{2}}(|\alpha\beta\rangle + |\beta\alpha\rangle),\ |T_{+1}\rangle = |\alpha\alpha\rangle \tag{2}$$

On the other hand, when the radicals are far apart the exchange interaction is zero, so the unpaired electrons can now be distinguished (e.g. by an EPR experiment or by scavenging), and the eigenstates are the four doublet functions

$$\begin{aligned} |D_{-\frac{1}{2},-\frac{1}{2}}\rangle &= |\beta\beta\rangle \ (\equiv |T_{-1}\rangle), \ |D_{-\frac{1}{2},+\frac{1}{2}}\rangle = |\beta\alpha\rangle \\ |D_{+\frac{1}{2},+\frac{1}{2}}\rangle &= |\alpha\alpha\rangle \ (\equiv |T_{+1}\rangle), \ |D_{+\frac{1}{2},-\frac{1}{2}}\rangle = |\alpha\beta\rangle \end{aligned} \tag{3}$$

It is seen that $|\alpha\alpha\rangle$ and $|\beta\beta\rangle$ always remain eigenfunctions regardless of the interradical separation.

Although the other two functions are only eigenfunctions in special situations (contact, singlet and triplet; infinite separation, two doublets), each set is nevertheless a valid set of basis functions that can be used to describe the spin state. $|S\rangle$ and $|T_0\rangle$ are most useful for that purpose because they are eigenfunctions at the start and at the end of a diffusive excursion. At in-between times, the spin state $|X\rangle(t)$, which will usually be time dependent, is always describable by a linear combination

$$|X\rangle(t) = c_S(t)|S\rangle + c_{T_0}(t)|T_0\rangle \tag{4}$$

with time dependent coefficients c_S and c_{T_0}.

This opens up the possibility of intersystem crossing of a radical pair. Let the pair be born, e.g. in state $|T_0\rangle$, and then enter on a diffusive excursion during which the spin state evolves under the spin Hamiltonian. If c_S is no longer zero at reencounter, the pair has acquired some singlet character. But at that moment, the exchange interaction is operative again and forces the pair into one of its eigenstates, meaning that in an ensemble of radical pairs a certain fraction will produce singlet pairs upon reencounter, i.e. will have undergone intersystem crossing.

3.1.2. Intersystem crossing of radical pairs

The distance dependence of the exchange interaction J is crucial for the evolution of the spin state of a pair. An exponential decrease with the interradical separation r is usually assumed.[14] Typical potential energy curves of singlet and triplet states are displayed in Figure 3. In a magnetic field, the Zeeman energy causes an additional splitting of the triplet sublevels, as shown in the inset.

There are two situations when J vanishes, and when intersystem crossing is thus most efficient. First, for r larger than a certain value, not more than a few molecular diameters, $|S\rangle$ and $|T_0\rangle$ become degenerate. This condition holds for most of a diffusive excursion unless diffusion is restricted (as would be the case, e.g. in a micelle), so processes of type $|S\rangle \leftrightarrow |T_0\rangle$ provide the most efficient, and most common, pathway of intersystem crossing of radical pairs. Second, at some critical distance there exists a level crossing between $|S\rangle$ and either $|T_{-1}\rangle$ or, in the rare case of a positive exchange interaction, $|T_{+1}\rangle$. Because intersystem crossing is

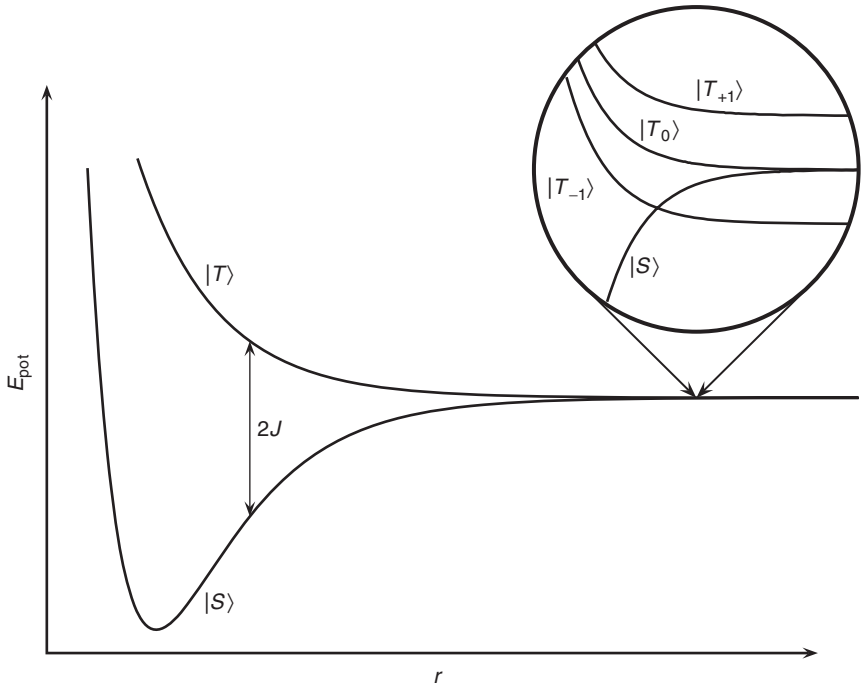

Figure 3 *Potential energy E_{pot} of a radical pair as a function of the interradical separation r.* The exchange integral *J* is one-half the vertical separation of the singlet and triplet functions. The inset shows the splitting of the triplet levels in a magnetic field. Further explanation, see text.

a slow process, the system has to spend a considerable time in a region of $J \approx 0$, and intersystem crossing by $|S\rangle \leftrightarrow |T_{\pm 1}\rangle$ pathways is normally only relevant for biradicals or in micelles. Its efficiency increases with decreasing angle of intersection of the two potential curves, so it is also more efficient if the magnetic field is low.

Vector diagrams[15] (Figure 4) allow a very convenient visualization of the mechanism of intersystem crossing between $|S\rangle$ and $|T_0\rangle$. The electron spin of each radical is drawn as an arrow. This allows a correct representation in the case of two individual radicals but violates the Pauli principle for the singlet and the $|T_0\rangle$ state; despite this limitation, the diagrams lead to correct conclusions. The singlet state has no magnetic moment, so the two vectors have to be antiparallel. $|T_0\rangle$ does possess a non-zero magnetic moment but zero *z* component, so the two vectors have to be drawn as shown on the r.h.s. of Figure 4. In a situation where the two radicals do not interact, their electron spins precess independently, and, unless the two radicals are absolutely identical—not only as far as their chemical constitution is concerned but also with respect to the spin state of each nucleus they contain—in general with different precession frequencies. Hence, if the system starts out in state $|S\rangle$, the two arrows will get out of phase, as displayed in the centre

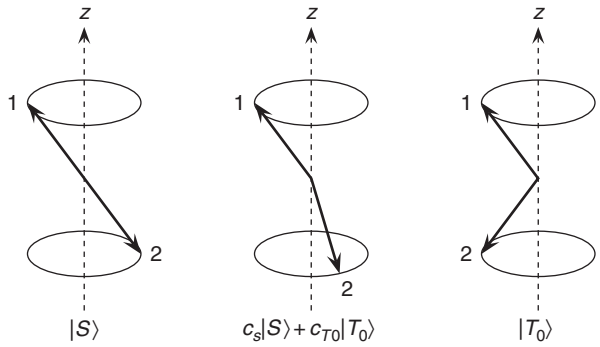

Figure 4 *Vector model visualization of intersystem crossing of radical pairs in high fields.* Left: singlet state; centre: superposition state; right: state $|T_0\rangle$. Further explanation, see text.

of Figure 4, eventually reach state $|T_0\rangle$, then gradually revert to state $|S\rangle$, and so forth. Intersystem crossing between $|S\rangle$ and $|T_0\rangle$ is thus a coherent oscillation caused by different precession frequencies of the non-interacting radicals.

In high fields, where electron and nuclear spin states can be specified independently, this picture can easily be cast into a formula for the angular frequency ω_{ST_0} of intersystem crossing. One has to consider the differences of the Zeeman interaction (g_1 and g_2, g-values of the two radicals; β, Bohr magneton; B_0, field of the NMR magnet) and of the hyperfine interactions (a_n and m_n, hyperfine coupling constant and z spin projection of nucleus n; positive sign and index i for the nuclei in the first radical, negative sign and index j for those in the second), so

$$\omega_{ST_0} = \frac{1}{2\hbar}\left\{(g_1 - g_2)\beta B_0 + \sum_i a_i m_i - \sum_j a_j m_j\right\} \tag{5}$$

A characteristic of intersystem crossing between $|S\rangle$ and $|T_0\rangle$ is that the nuclear spin state does not change. The situation is different for intersystem crossing between $|S\rangle$ and $|T_{\pm1}\rangle$: This requires a concomitant spin flip of a nucleus because the z component of the total electron spin changes. Neither the Zeeman interaction nor the secular terms of the hyperfine interaction mix $|S\rangle$ with $|T_{\pm1}\rangle$. However, the non-secular terms of the hyperfine interaction, which are completely non-diagonal and have zero matrix elements between $|S\rangle$ and $|T_0\rangle$ for any nuclear spin configuration, cause transitions between $|S\rangle$ and $|T_{-1}\rangle$ and $|T_{+1}\rangle$ that are accompanied by a change of the nuclear spin state. The angular frequency of intersystem crossing $\omega_{ST_{\pm1}}$ is

$$\omega_{ST_{\pm1}} = \frac{1}{\hbar}\left\{\sum_i a_i(\mathbf{S}_{1x}\mathbf{I}_{ix} + \mathbf{S}_{1y}\mathbf{I}_{iy}) + \sum_j a_j(\mathbf{S}_{2x}\mathbf{I}_{jx} + \mathbf{S}_{2y}\mathbf{I}_{jy})\right\}. \tag{6}$$

A comparison of Equations (5) and (6) shows that the intersystem crossing frequencies are of comparable magnitudes.

3.1.3. Mechanism of CIDNP generation in high fields (S–T_0-type CIDNP)

The radical-pair mechanism is displayed in Chart 1. Its main ingredients are that spin is conserved during chemical processes; that radical pairs are formed, diffuse apart and reencounter; and that the eigenstates of their electron spins are different when the radicals are in contact or when they are far apart, leading to an evolution of the electron-spin state under the spin Hamiltonian during a diffusive excursion.

The mechanism can be broken down into three steps:

1. Birth of the radical pair in the singlet or triplet state
   (As follows from Section 3.1.2, only the $|T_0\rangle$ state is relevant, and molecules born in one of the other two triplet states can be ignored because they do not lead to any CIDNP effects of the S–T_0-type; as this is tacitly assumed, only the multiplicity of the pair is specified in the scheme.) That state is the same as that of the radical-pair precursor, in other words its multiplicity is that of the excited state from which the photoreaction starts.

   For completeness, it should be mentioned that a radical pair can also be formed by a chance encounter of two free (i.e. uncorrelated) radicals. Because this produces all four spin states with equal probability but a significant fraction of the resulting singlet pairs will immediately combine to give diamagnetic products before CIDNP can arise, these so-called F-pairs behave qualitatively like triplet-born pairs.

   The mechanism is thus entered from the top, either by the left branch or the right branch, producing either the radical pair on the left or that on the right. Looking at an ensemble, the radical pairs initially all have the same electron spin multiplicity, and all nuclear spin states are populated according to the Boltzmann distribution (i.e. are populated practically equally).

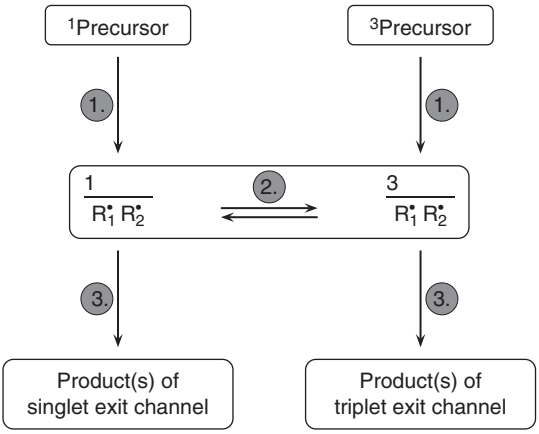

Chart 1

2. Nuclear–spin selective intersystem crossing of the spin correlated pairs (''nuclear spin sorting'')
   During the life of the pairs intersystem crossing between $|S\rangle$ and $|T_0\rangle$ occurs with a frequency that depends on the g-value difference and on the nuclear spin state of each individual pair (Equation 5). Because of the ''leaks'' provided by step 3 it is permissible, at least for a qualitative description, to equate those frequencies with rates. Each configuration of the nuclear spins thus causes a specific intersystem crossing rate of the radical pairs containing it; those configurations that decrease the rate are enriched in the pairs of the starting multiplicity, those that increase it in the pairs of the other multiplicity. Hence, the nuclear spins are sorted between the two multiplicities, i.e. opposite nuclear spin polarizations are generated in the paramagnetic intermediates (but are not yet observable by NMR). Because of the symmetry of nuclear energy levels, the sorting is also symmetrical, i.e. these opposite polarizations are exactly identical in magnitude.
3. Electron-spin selective reactions of the radical pairs
   This feature is again due to spin conservation in chemical reactions. The typical case is a combination of the two radicals of the pair to give a product (''geminate'' reaction). A singlet pair must yield a singlet product and a triplet pair a triplet product. Very often, though not always, the first alternative is thermodynamically allowed and the second forbidden. Radical pairs that cannot react will undergo another diffusive excursion but eventually lose their spin correlation and form free radicals (''escape'' from the cage) that react individually, with other reaction partners than with each other.

   Not only is the electron-spin state conserved in all these reactions but also the nuclear spin state. Hence, the nuclear spin polarizations present in the pairs are transferred into the diamagnetic products, where they can be detected. Those nuclear spin configurations that slowed down intersystem crossing are overpopulated in the product(s) of the exit channel on the same side as the entry channel of the scheme; those that accelerated it are overpopulated in the product(s) of the exit channel on the other side.

   The importance of different exit channels can hardly be overstressed. If both exit channels lead to the same product, the spin sorting is undone, and no S–T_0-type CIDNP results. However, a difference of reaction probabilities suffices for some CIDNP to remain. Another important factor avoiding a cancellation that would otherwise be perfect is nuclear spin relaxation in longer-lived paramagnetic intermediates, free radicals or triplet molecules. Even if there is a complete cancellation of the polarizations at long times but an imbalance of reaction rates, CIDNP occurs as a transient effect and can be detected in a time-resolved experiment.

3.1.4. S–$T_{\pm1}$-type CIDNP

The different operating principle of generating nuclear spin polarizations, by electron–nuclear flip-flop transitions instead of by spin sorting, reduces the mechanism to a two-step scheme.

1. Birth of the radical pair in the singlet or the triplet state (which in this case usually means $|T_{-1}\rangle$, rarely $|T_{+1}\rangle$)
   Flip-flop transitions are bidirectional, so the precursor multiplicity is a key prerequisite, in the same way as for S–T_0-type CIDNP.
   For an ensemble of radical pairs, the same initial condition as before holds, i.e. each pair again starts out with the same electron-spin state, and the nuclear spins are unpolarized.
2. Development of nuclear polarizations in the spin-correlated pairs or biradicals
   Because Equation (6) couples the nuclear spin motion and the electron-spin motion, not only the electron-spin state of each pair oscillates but also the nuclear spin state. Over the ensemble, however, the oscillation is not symmetrical because flip–flop transitions are only possible for one-half of the pairs. Consider, for example, an ensemble of biradicals with one proton, and let the biradicals be born in state $|T_{-1}\rangle$. Taking into account also the nuclear spin, one-half of the biradicals are thus born in state $|T_{-1}\alpha\rangle$ and the other half in state $|T_{-1}\beta\rangle$. The latter cannot undergo flip-flop transitions to the singlet state, so have to remain in the state they were born. The others oscillate between $|T_{-1}\alpha\rangle$ and $|S\beta\rangle$. If a fraction n of them has reached the singlet state, the total number of biradicals with nuclear spin $|\alpha\rangle$ is $(1–n)/2$, and the total number of biradicals with spin $|\beta\rangle$ is $n/2+1/2$. The difference between the number of molecules with nuclear spin $|\alpha\rangle$ and $|\beta\rangle$ is thus $–n$, in other words the system oscillates between zero polarization ($n = 0$) and complete polarization of one sort ($n = –1$, i.e. all nuclear spins in state $|\beta\rangle$ in the example) but can never develop a nuclear spin polarization of the other sort (a surplus of nuclear spins $|\alpha\rangle$ in the example) because n cannot be negative.

   Looking at the singlet and the triplet state separately, the difference between the number of molecules with nuclear spin $|\alpha\rangle$ and $|\beta\rangle$ is $–n/2$ for the singlet state in the example because $|S\alpha\rangle$ is never formed, and $(1–n)/2–1/2$, i.e. $–n/2$ for the triplet state. Hence, at any time the nuclear spin polarizations of the singlet and the triplet state are seen to be equal.

The polarization generation by flip-flop transitions instead of by spin sorting thus causes S–$T_{\pm1}$-type CIDNP to differ from S–T_0-type CIDNP in three main aspects. First, different exit channels are not needed. Second, even in cases when they are available, the polarizations from them are exactly equal. Third, the polarizations are always of one sort (one sign).

3.2. Qualitative rules

Much of the attractivity of CIDNP for chemical investigations stems from the fact that simple qualitative rules[16] can be formulated that relate the phases (signs) of the observed polarizations to the reaction mechanism and the magnetic parameters of the radical pairs.

From the discussion of Chart 1 it has emerged that one can only distinguish whether the pathway from the precursor to an observed product traverses the diagram diagonally or whether entry and exit channel lie on the same side. This

can be described by assigning a parameter μ to the entry channel ($\mu = +1$, triplet precursor; $\mu = -1$, singlet precursor), and a parameter ϵ to the exit channel, which is +1 if product formation occurs from singlet pairs and –1 for product formation from triplet pairs, including the case that the route to the observed product is via free radicals. (Older publications use the nomenclature ''cage'' and ''escape'' products, which is less fortunate because a triplet pair can react to give a triplet product *in the cage*). Multiplying μ and ε yields +1 for a diagonal pathway through the diagram, and –1 for a vertical one.

A connection with the magnetic parameters can be established with the aid of Equation (5) and the vector diagrams of Figure 4. To see the effects more clearly, projections of the vectors onto the xy plane are advantageous. As, furthermore, only differential precession effects intersystem crossing, that coordinate system is taken to rotate with the average frequency ω_{av},

$$\omega_{av} = \frac{1}{2\hbar}\left\{(g_1 + g_2)\beta B_0 + \sum_i a_i m_i + \sum_j a_j m_j\right\} \tag{7}$$

To avoid an ambiguity, it is necessary to choose radical 1 as the radical containing the observed nucleus. The vectors of the initial state define an axis. At any time during the evolution, the contribution of that state, and that of the other state, to the superposition of Equation (4) is then obtained by projecting the vectors onto that axis, and onto the axis perpendicular to it.

Figure 5 shows an example for a radical pair with one nucleus of spin 1/2, e.g. a proton, and a triplet precursor. Assume that radical 1 has the higher g-value, that the hyperfine coupling constant of the nucleus is positive, and that the sense of precession is clockwise. The action of the g-value difference is first shown separately. It is seen to cause a symmetrical displacement of the two vectors from their initial positions. Next, the effect of the hyperfine interaction for the nucleus having spin α and spin β is superimposed on that. The resulting displacements are again symmetrical, but with respect to the positions of the vectors after rotation by the g-value difference. Obviously, the Zeeman and hyperfine terms add constructively

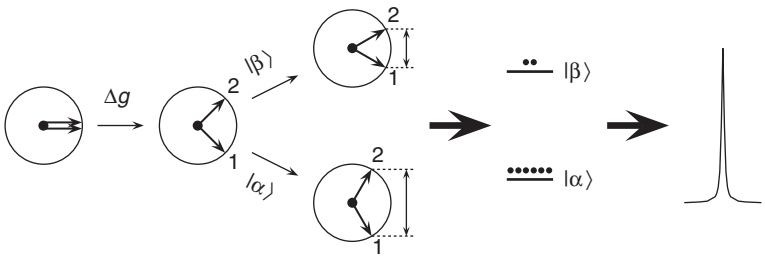

Figure 5 *Phase of a CIDNP net effect explained with vector models (projections).* From left to right, starting state; influence of the g-value difference; influence of the nuclear spin state through the hyperfine coupling constant; resulting population difference of the nuclear spin states in the product; resulting CIDNP signal. The labels on the vector models denote the electron spin of radical 1 or 2. Further explanation, see text.

when the spin state of the nucleus is α but oppose each other when it is β. Hence, in the singlet pairs and their subsequent products, the α spins are enriched while the β spins are depleted, so the resulting NMR signal appears in enhanced absorption.

The opposite signal would be obtained if the g-value difference Δg were made negative, or if the hyperfine coupling constant a were made negative; however, no change would be result if both Δg and a were made negative.

All these regularities are summed up by Kaptein's rule[16] for the phase (sign) Γ_i of a CIDNP net effect ($\Gamma_i = +1$, enhanced absorption of nucleus i; $\Gamma_i = -1$, emission),

$$\Gamma_i = \mu \times \varepsilon \times \text{sign}(\Delta g) \times \text{sign}\ a_i \tag{8}$$

From the discussion of Figure 5 it also emerges that a CIDNP net effect can only arise if both Δg and a are non-zero because either interaction on its own causes a symmetrical displacement around the starting axis, so no spin sorting takes place.

CIDNP multiplet effects can be rationalized in the same way. The simplest case is that of a radical pair with two spin-1/2 nuclei A and X. Let both be contained in radical 1 and have positive hyperfine coupling constants a_A and a_X; as in Figure 5 let the precursor multiplicity be triplet and the product be formed via the singlet exit channel; let the coupling constant J in the observed product have a positive sign. The treatment can be greatly simplified by setting Δg to zero. Not only does that remove all net effects but the precession differences caused by the spin state of nucleus 1 then have the same effect as the Δg term in the preceding example. Assuming that a_A is larger than a_X, one arrives at the vector model and population diagram displayed in Figure 6, which shows that a so-called E/A multiplet (emission of the low-field line, absorption of the high-field line of each doublet) results.

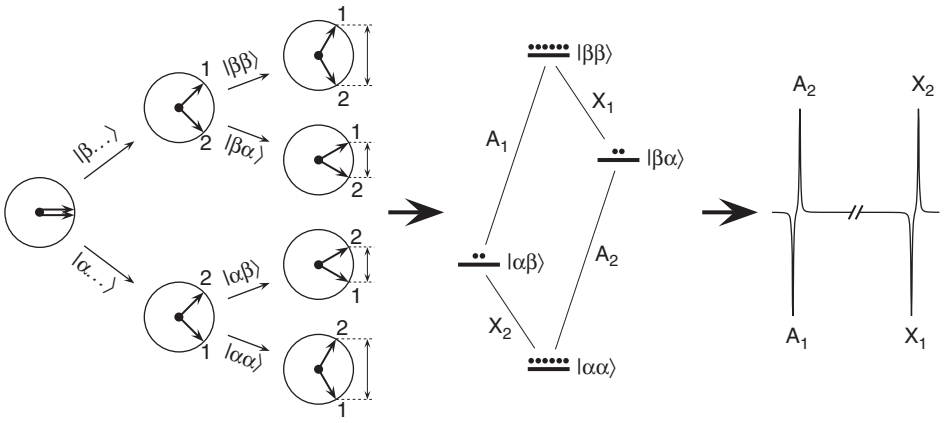

Figure 6 *Explanation of a CIDNP multiplet effect with vector models (projections).* From left to right, starting state; influence of the first nuclear spin (A) only; influence of the second nuclear spin; population differences; resulting spectrum. The labels on the vector models denote the electron spin of radical 1 or 2, the labels in the NMR spectrum the nuclear transitions. Further explanation, see text.

Making a_A smaller than a_X only permutes vectors within diagrams, so has no influence on the CIDNP spectrum. Modifying the other parameters has the following effects: Inverting the sign of either a_A or a_X interchanges the populations of all spin states connected by a transition, so inverts the signal pattern (A/E instead of E/A); putting either A or X into radical 2 has the same consequence; changing the sign of J permutes the two lines of each doublet, so again inverts the multiplet pattern. Combining all these factors, one arrives at Kaptein's rule[16] for a CIDNP multiplet effect Γ_{ij} of two nuclei i and j ($\Gamma_{ij} = +1$, E/A; $\Gamma_{ij} = -1$, A/E),

$$\Gamma_{ij} = \mu \times \varepsilon \times \text{sign}\, a_i \times \text{sign}\, a_j \times \sigma_{ij} \times \text{sign}\, J_{ij} \tag{9}$$

where the additional parameter σ_{ij} is $+1$ when the two nuclei are contained in the same radical and -1 when they are not.

These vector models also show that the multiplet effects decrease when the Zeeman interaction has to be taken into account, because the additional rotation causes the projections onto the singlet state to differ less. This explains why multiplet effects are much more important in low fields and for radical pairs with small g-value differences.

The reliability of Equations (8) and (9) is almost surprising when one considers that they represent the radical-pair mechanism in a simplified form only. The most important situation where they are known to predict wrong phases is for the polarizations of nuclei with small hyperfine coupling constants in the presence of other nuclei with very large hyperfine coupling constants, as is the case, for instance, if ^{1}H-CIDNP is investigated in ^{13}C labelled molecules.[17] A recent example has been reported for ^{13}C-polarizations stemming from phosphorous-centred radicals.[18]

A sign rule can also be formulated for the phases of S–$T_{\pm1}$-type CIDNP. As Section 3.1.4 has shown, neither the magnetic parameters nor the exit channel have any relevance for the polarizations. What decides their phase is only the intersystem crossing pathway, that is, whether intersystem crossing occurs between $|T_{-1}\rangle$ and $|S\rangle$ or between $|T_{+1}\rangle$ and $|S\rangle$, because each pathway cannot flip nuclear spins of one kind (β in the first case, α in the second). That pathway is in turn determined by which triplet curve in Figure 3 crosses the singlet curve: It is between $|T_{-1}\rangle$ and $|S\rangle$ for a negative exchange interaction J (the normal case), or between $|T_{+1}\rangle$ and $|S\rangle$ if J is positive. In other words, the sign of J is the only relevant quantity apart from the parameter μ, which has the same meaning as before. This leads to an even simpler rule for the phase γ of an S–$T_{\pm1}$-type net effect ($\gamma = +1$, absorption; $\gamma = -1$, emission),

$$\gamma = \mu \times \text{sign}\, J \tag{10}$$

Multiplet effects cannot arise in S–$T_{\pm1}$-type CIDNP.

3.3. Pair substitution

Transformations of radical pairs into others also leave there imprint on the polarizations if they occur on a timescale comparable to the radical-pair life.[19–21] These processes are called pair substitution. At the moment of such a transformation of the first pair into the second, the intersystem crossing frequency of

Equation (5) or (6) abruptly changes because the second pair will in general have different Δg and/or different hyperfine coupling constants. The resulting CIDNP effects are, therefore, not simply the sum of CIDNP from the first pair, if that pair had an infinite life, and from the second, if that pair were the only one present. Instead, they can be regarded as arising from a hypothetical pair, for which Δg and each hyperfine coupling constant is a weighted average of the respective parameter for the first and second pair, with the weighting factors given by the two lifetimes. Examples have been reported[20] where neither pair on its own develops a CIDNP net effect, one because of negligible hyperfine couplings and the other because of zero Δg, but where pair substitution causes CIDNP to appear. This can easily be visualized by Figure 5 where these two interactions, which normally work simultaneously, have been separated for clarity. If the magnetic properties of each pair are known or can be estimated, the transformation rate can be obtained from the CIDNP signals. This extends the timescale of NMR to the sub-nanosecond range. Examples are given below.

3.4. Calculations of CIDNP intensities

As usual in quantum mechanics, the formulation of the problem is comparatively simple but the calculational difficulties can be formidable.

The time evolution of the density matrix ϱ of the system under the joint influence of the spin Hamiltonian $\mathbf{H}$ comprising also the exchange interaction, of diffusion (operator $\mathbf{\Gamma}$), of the chemical reaction (operator $\mathbf{K}$), and of relaxation (operator $\mathbf{R}$) is given by the so-called stochastic Liouville equation,[22]

$$\frac{\partial}{\partial t}\varrho = -\frac{i}{\hbar}[\mathbf{H}, \varrho] + D\Gamma\varrho + \mathbf{K}\varrho + \mathbf{R}\varrho \tag{11}$$

NMR spectroscopists are normally familiar with the first and last term on the r.h.s. of Equation (11), the second term is a partial differential operator known from classical physics, and the third term is simply a projection operator onto each reacting multiplicity times the respective reaction rate.

It is at this point that S–T_0-type CIDNP and S–$T_{\pm1}$-type CIDNP diverge. Because there are no flip-flop transitions in the first case, a separation of nuclear and electronic subspaces is possible and leads to a drastic simplification of the problem, since only four elements of the density matrix have to be retained. This even affords a closed-form analytical solution if some simplifying assumptions are introduced. In the second case, no such separation is possible, and numerical solutions of the stochastic Liouville equation are the only feasible procedure; this subject is obviously beyond the scope of this review.

For S–T_0-type CIDNP, the relevant density matrix is, in explicit notation,

$$\varrho = \begin{pmatrix} \varrho_{SS} & \varrho_{ST_0} \\ \varrho_{T_0S} & \varrho_{T_0T_0} \end{pmatrix} \tag{12}$$

and the Hamiltonian **H** of the system is

$$\mathbf{H} = \begin{pmatrix} +E & Q \\ Q & -E \end{pmatrix} \tag{13}$$

with Q being the matrix element of intersystem crossing (see, Equation (5)) and E being the sum of the magnetic energy (see, Equation (7)) and of the exchange integral J; through the latter, E is distance dependent.

Carrying out the matrix multiplications of the commutator in Equation (11), and rewriting the result as a vector equation one gets

$$\frac{\partial}{\partial t}\begin{pmatrix} \varrho_{SS} \\ \varrho_{ST_0} \\ \varrho_{T_0S} \\ \varrho_{T_0T_0} \end{pmatrix} = -\frac{i}{\hbar}\begin{pmatrix} 0 & -Q & Q & 0 \\ -Q & 2E & 0 & Q \\ Q & 0 & -2E & -Q \\ 0 & Q & -Q & 0 \end{pmatrix}\begin{pmatrix} \varrho_{SS} \\ \varrho_{ST_0} \\ \varrho_{T_0S} \\ \varrho_{T_0T_0} \end{pmatrix} \tag{14}$$

Because the density matrix is Hermitian, and because its trace is 1 in the absence of a chemical reaction (which will be considered at a later stage), a change of variables allows a further simplification of Equation (14),[23]

$$\frac{\partial}{\partial t}\begin{pmatrix} \varrho_{SS} - \varrho_{T_0T_0} \\ 2\mathrm{Im}\ (\varrho_{ST_0}) \\ 2\mathrm{Re}\ (\varrho_{ST_0}) \end{pmatrix} = \frac{2}{\hbar}\begin{pmatrix} 0 & -Q & 0 \\ Q & 0 & -E \\ 0 & E & 0 \end{pmatrix}\begin{pmatrix} \varrho_{SS} - \varrho_{T_0T_0} \\ 2\mathrm{Im}\ (\varrho_{ST_0}) \\ 2\mathrm{Re}\ (\varrho_{ST_0}) \end{pmatrix} \tag{15}$$

The purpose of this change of variables is threefold. First, the size of the matrix is reduced to three. Second, all variables are now real quantities. Third, and most importantly, two of the variables now correspond to physical observables: The first is the *population difference between* $|S\rangle$ *and* $|T_0\rangle$, which is directly related to the product yields, and the third is an *opposite polarization of both electron spins* of the radicals. The second component, a *phase correlation*, is not directly observable.

The solution of 15 is obtained by standard methods. It is

$$\begin{pmatrix} \varrho_{SS} - \varrho_{T_0T_0} \\ 2\mathrm{Im}(\varrho_{ST_0}) \\ 2\mathrm{Re}(\varrho_{ST_0}) \end{pmatrix} = \begin{pmatrix} \frac{E^2}{V^2} + \frac{Q^2}{V^2}\cos(\Omega t) & -\frac{Q}{V}\sin(\Omega t) & \frac{QE}{V^2}[1-\cos(\Omega t)] \\ \frac{Q}{V}\sin(\Omega t) & \cos(\Omega t) & -\frac{E}{V}\sin(\Omega t) \\ \frac{QE}{V^2}[1-\cos(\Omega t)] & \frac{E}{V}\sin(\Omega t) & \frac{Q^2}{V^2} + \frac{E^2}{V^2}\cos(\Omega t) \end{pmatrix}\begin{pmatrix} \varrho_{SS} - \varrho_{T_0T_0} \\ 2\mathrm{Im}(\varrho_{ST_0}) \\ 2\mathrm{Re}(\varrho_{ST_0}) \end{pmatrix}_{t=0} \tag{16}$$

with the abbreviations

$$V = \sqrt{Q^2 + E^2}, \quad \Omega = \frac{2V}{\hbar}$$

The distance dependence of the exchange integral J couples spin evolution and diffusive motion of the radical pair. However, J is such a strongly varying function that during a diffusive excursion there are almost instantaneous transitions

between an inner region (called the exchange region, with a diameter of only a few times the sum of the molecular radii of the radicals) where the spin Hamiltonian is totally dominated by J and an outer region stretching to infinity where J is negligible compared to Q. This dichotomy permits the following approximate treatment,[24] which leads to a closed-form solution.

Within the exchange region, only electron-spin polarization and phase correlation are mixed, as can be seen by setting Q to zero in Equation (15); Equation (16) shows the mixing to be a rotation through an angle $2Jt$. As $1/J$ falls into the subpicosecond range in this region, the angle of rotation is much larger than 2π, so the different lengths of the trajectories until a reencounter and above all the distance-dependent size of J cause a complete randomization of these two components of the density matrix,[23] whereas the population difference is unaffected.

Outside the exchange region, phase correlation and population difference are mixed while the electron-spin polarization remains constant. Because there is no distance dependence in this region, the amount of mixing is only governed by the duration of the diffusive excursion until the boundary of the exchange region is reached again. Assuming that a diffusive excursion starts and stops at that boundary, and neglecting relaxation, one can thus average over the ensemble using the reencounter function $f(t, d, d)$, which is the conditional probability density that two radicals initially separated by distance d re-approach to distance d in the period of time between t and $t+\mathrm{d}t$. The resulting averaged density matrix $\bar{\vec{\varrho}}$ is

$$\bar{\vec{\varrho}} = \begin{pmatrix} c & -s & 0 \\ s & c & 0 \\ 0 & 0 & p \end{pmatrix} \cdot \vec{\varrho}(0) \tag{17}$$

It is seen that c and s are the Fourier cosine and sine transforms of $f(t, d, d)$ at the angular frequency of intersystem crossing $2Q/\hbar$ and p is the total probability of reencounter,

$$c = \int_0^\infty \cos(2Qt/\hbar) f(t,d,d)\mathrm{d}t \tag{18}$$

$$s = \int_0^\infty \sin(2Qt/\hbar) f(t,d,d)\mathrm{d}t \tag{19}$$

$$p = \int_0^\infty f(t,d,d)\mathrm{d}t \tag{20}$$

The Noyes reencounter function[25]

$$f(t,d,d) = \frac{p(1-p)d}{\sqrt{4\pi D}} t^{-3/2} \exp\left[-\frac{(1-p)^2 d^2}{4Dt}\right] \tag{21}$$

where D is the interdiffusion coefficient, is frequently used. Equation (21) is valid for diffusion occurring by steps of length λ_D ($\lambda_D < d$) and in the absence of attractive or repulsive forces between the radicals. With this model, the probability p is, to a very good approximation, given by[26]

$$p \approx 1/\left(1 + \frac{2\lambda_D}{3d}\right) \tag{22}$$

and the Fourier transforms are

$$c = \cos[(1-p)\delta]\exp[-(1-p)\delta] \tag{23}$$

$$s = \text{sign}\, Q\, \sin[(1-p)\delta]\exp[-(1-p)\delta] \tag{24}$$

with

$$\delta = \sqrt{\frac{2|Q|d^2}{D}} \tag{25}$$

For small mixing matrix element Q and large diffusion coefficient (i.e. non-viscous solvents) an expansion of Equations (23) and (24) to first order is possible and leads to the very simple results that c and s are approximately given by 1–(1–p)δ and sign Q·(1–p)δ.

To describe chemical reactions upon reencounter, which in general will occur with different probabilities for the singlet and triplet states, one has to separate the variables ϱ_{SS} and $\varrho_{T_0T_0}$ again. However, because electron-spin polarization does not arise during a diffusive excursion and is randomized in the approach of the radicals to their contact distance, it suffices to retain the component $2\text{Im}(\varrho_{ST_0})$ in the density matrix; the component $2\text{Re}(\varrho_{ST_0})$ is not needed. In this new basis, the mixing matrix $\hat{\mathbf{M}}$ of Equation (17) becomes

$$\hat{\mathbf{M}} = \begin{pmatrix} (1+c)/2 & (1-c)/2 - s/2 & 0 \\ (1-c)/2 & (1+c)/2 + s/2 & 0 \\ s & -s & c \end{pmatrix} \tag{26}$$

Assuming that only singlets react at a reencounter, and with a probability λ, one gets the amount of geminate product formed by applying the projection operator (λ 0 0) to the density matrix of that moment. Pairs that have not reacted will undergo a new diffusive excursion. For the density matrix at the start of that excursion, one has to take into account that molecules were removed by the reaction and that the phase correlation was destroyed in the approach to the contact distance, hence one obtains it by applying the matrix $\hat{\mathbf{R}}$, $\hat{\mathbf{R}} = \text{diag}(1-\lambda, 1, 0)$, to the density matrix before the reencounter.

This allows an easy description of multiple reencounters:[24] From encounter n to encounter $n+1$, the change of the density matrix is given by

$$\bar{\bar{\varrho}}_{n+1} = \hat{\mathbf{M}}\,\hat{\mathbf{R}}\,\bar{\bar{\varrho}}_n \tag{27}$$

Multiplying the density matrix at each reencounter with the projection operator, and summing up the series yields the total amount F^* of product formed from a triplet precursor and via the singlet exit channel,

$$F^* = \begin{pmatrix} \lambda & 0 & 0 \end{pmatrix} \left[\sum_{k=0}^{\infty} (\hat{\mathbf{M}}\,\hat{\mathbf{R}})^k \right] \begin{pmatrix} 0 \\ 1 \\ 0 \end{pmatrix} = \begin{pmatrix} \lambda & 0 & 0 \end{pmatrix} [\hat{\mathbf{E}} - \hat{\mathbf{M}}\,\hat{\mathbf{R}}]^{-1} \begin{pmatrix} 0 \\ 1 \\ 0 \end{pmatrix} \tag{28}$$

where $\hat{\mathbf{E}}$ is the unit matrix and the exponent –1 denotes matrix inversion. It has been shown[24] that the product yields for singlet or F-pair precursors can all be expressed with the key quantity F^*. Carrying out the tedious calculations of Equation (28), one obtains the very compact result

$$F^* = \frac{p(1-c)}{2-p(1+c)} \tag{29}$$

which is independent of the diffusion model used. When c and s are given by Equations (23–25), an expansion to first order, which is permissible in solvents of low viscosity, leads to an even simpler expression,

$$F^* = \frac{p\delta}{2} \tag{30}$$

With Equations (5), (25), and (30) one can also deduce approximate rules for the dependences of the CIDNP intensities on the strength of the magnetic interactions and on the field B_0. For the simple model system of a radical pair with one proton in the first radical, the population difference of the nuclear spin states $|\alpha\rangle$ and $|\beta\rangle$ is seen to be

$$P_\alpha - P_\beta \propto \sqrt{|Q_\alpha|} - \sqrt{|Q_\beta|} \quad \propto \quad \sqrt{|\Delta g \beta B_0 + a/2|} - \sqrt{|\Delta g \beta B_0 - a/2|} \tag{31}$$

For high fields and sufficiently large Δg, the Δg term can be factored out. When one assumes both Δg and a to be positive to simplify the procedure, one gets by expanding to first order

$$\begin{aligned} P_\alpha - P_\beta &\propto \sqrt{\Delta g \beta B_0} \times [\sqrt{1 + a/(2\Delta g \beta B_0)} - \sqrt{1 - a/(2\Delta g \beta B_0)}] \\ &\approx (\Delta g \beta B_0)^{-1/2} \times a/2 \end{aligned} \tag{32}$$

The decrease of the polarization with increasing field is in strong contrast to normal NMR, where the Boltzmann population differences increase linearly with B_0. The approximate proportionality between hyperfine coupling constant and polarization intensity forms the basis of identifying paramagnetic

intermediates by CIDNP, since the CIDNP spectrum thus carries practically the same information as the EPR spectrum.

3.5. Recent studies of the CIDNP effect as such

This section lists theoretical and experimental investigations where the focus has been predominantly on the CIDNP effect itself; instrumentation, techniques and applications are covered in later sections.

Diffusion is intricately linked with all aspects of the radical-pair mechanism. The CIDNP kinetics for the reaction of a sensitizer with a large spherical molecule that has only a small reactive spot on its surface were studied theoretically.[27] This situation is typical for protein CIDNP, where only three amino acids are readily polarizable, and where such a polarizable amino acid must be exposed to the bulk solution to be able to react with a photoexcited dye. Goez and Heun carried out Monte Carlo simulations of diffusion for radical ion pairs both in homogeneous phase[28] and in micelles.[29] The advantage of this approach compared to numerical solutions of the diffusion equation is that it can easily accommodate arbitrary boundary conditions, such as non-spherical symmetry, as opposed to the commonly used ''model of the microreactor''[30] where a diffusive excursion starts at the micelle centre and one radical is kept fixed there.

CIDNP experiments are almost invariably carried out in (homogeneous or heterogeneous) liquid phase, first because those media are most relevant for chemical reactions and biological processes, and second because the diffusion properties in gases and solids are expected to make the radical-pair mechanism ineffective. However, a few groups have ventured onto this terrain. Salikhov et al. compared gas-phase and liquid-phase CIDNP of cyclic ketones.[31] The fact that the paramagnetic intermediates in these reactions are biradicals avoids the reencounter problem normally present in a gas. The exchange interaction was found to be much stronger in the gas phase, which was explained by a more compact configuration of the biradical. CIDNP of cyclic and acyclic ketones was investigated in plastic[32,33] and crystalline[33] cyclohexane. No polarizations were found in the crystalline medium, emphasizing the necessity of molecular mobility for CIDNP.

In systems with unrestricted diffusion, the ubiquitous variant of CIDNP is the S–T_0-type, and reports of S–T_{-1}-type CIDNP under these conditions are very rare, even in low fields. All recent examples[34–38] involve radical pairs with very large hyperfine coupling constants caused by an inorganic nucleus (^{31}P or ^{119}Sn). Even then, diffusion must favour longer dwell times around the level crossing, as is seen by the observation that low-field net CIDNP of ^{31}P from the radical-pair trimethylbenzoyl/dimethoxyphosphonyl still arises to 60–70% through S–T_0-type CIDNP in the less viscous solvent acetonitrile, while in the more viscous solvent dioxane the contribution of this intersystem crossing pathway decreases to 20–50%.[37]

Much experimental and theoretical work has been done on flexible biradicals obtained by the photolysis of cyclododecanones.[39–45] Field-dependent CIDNP

measurements in low fields,[39,40,42–44] including the temperature dependence,[39,44] and time-resolved experiments in high fields on the CIDNP net[40,41] and multiplet[43] effects were complemented by measurements of stimulated nuclear polarization[39,44] and time-resolved EPR.[41,42] The competition of intersystem crossing by spin–orbit coupling and by hyperfine interactions was addressed by comparing the acyl-ketyl and bis(ketyl) biradicals formed during photolysis of a 2-hydroxy and a 2,12-dihydroxy substituted cyclododecanone;[42] spin–orbit coupling dominates for the former type of biradical whereas intersystem crossing occurs primarily by hyperfine interactions and relaxation in the latter. Numerical solutions of the stochastic Liouville equation are the only feasible way of taking into account the complicated dynamics of the polymethylene chain. The numerical calculations have been refined in such a way that good agreement between experiment and theory is now reached for the CIDNP phenomena in these systems including the effects of added scavengers.[45]

Other polarization mechanisms sporadically appear in the literature. Anomalous (with respect to S–T_0-type CIDNP) polarization phases in the photoinitiated oxidation of NADH catalysed by horseradish peroxidase have been ascribed to quartet-doublet transitions.[46] The influence of the free radical TEMPO on CIDNP during photolysis of diisopropylketone was interpreted by spin exchange,[47] whereas other authors came to the conclusion that for the very similar substrate dibenzylketone all effects can be explained by the increased relaxation rate caused by the paramagnetic reagent.[48] Earlier observations of unusual polarizations in the photolysis of acetone in isopropanol (e.g. net CIDNP although the radical pair consists of two identical radicals), which seemed to point to a cross-relaxation or cross-correlation mechanism of CIDNP,[49,50] were later found to be due to secondary chemistry and a strong solvent dependence of relaxation.[51] However, such mechanisms exist for nuclei with a strong anisotropy of the hyperfine coupling, most notably ^{19}F, and were shown to be the reason for inversions of CIDNP phases in a protein when the rotational correlation times are increased.[52]

The influence of relaxation in different species on the CIDNP signals has been considered by several authors. In a theoretical study it was concluded that even in a confined environment (micelle) and low fields relaxation in the radical pairs affects only the amplitude but not the shape of the field dependence.[53] For macromolecular systems, relaxation is much faster than for small molecules, which leads to a loss of CIDNP. In the very important case of biopolymers this cannot be avoided by raising the experimental temperature until a region of more favourable correlation times is reached because irreversible destruction of the structure would occur. To explore how serious the influence of relaxation is, Kuhn and Bargon investigated ketones with a macromolecular side chain.[54] It was found that CIDNP in products of low molecular weights can be observed with good sensitivity even if these products arise from a radical pair with a macromolecular character, but the observation of CIDNP in macromolecular products is much less sensitive. In other words, the molecular weight does not interfere with CIDNP generation but only with CIDNP detection. Relaxation in the products is, however, not always detrimental. Kuprov and Hore[55] analysed cross-relaxation (NOE transfer) in 3-fluorotyrosine from the strongly polarized ^{19}F

nuclei to the less strongly polarized protons and concluded that if this modified amino acid is incorporated in a protein, a detectable NOE enhancement of an unpolarized nearby proton could still result at distances of about 7Å.

Most chemical applications of CIDNP rely on identifying an intermediate and/or a reaction pathway by the polarization phases through Equations (8) and (9), and intensities through Equation (32), for which the relationship between polarizations and hyperfine coupling constants a is the crucial link. The reliability of CIDNP for determining hyperfine coupling constants was investigated by comparing the values extracted from the CIDNP spectra with EPR data and the results of DFT calculations; good agreement was found.[56] ''Anti-Kaptein'' net effects on nuclei with small a in the presence of others with a large a had previously only been observed in ^{1}H-CIDNP of ^{13}C labelled compounds,[17] but ^{13}C nuclei in the presence of ^{31}P nuclei can suffer the same fate, as was recently reported for acylphosphine oxide photoinitiators.[18]

Pair substitution continues to attract the attention of CIDNP spectroscopists. The analysis is mostly carried out by numerical simulations based on the standard theory; a general formalism that treats pair substitution through quadrature of Green functions was developed.[57] However, a closed-form solution has been reported for reversible pair substitution,[58] i.e. processes of the type $RP_1 \rightleftarrows RP_2$. All calculations of pair substitutions need the magnetic parameters as their input, but these quantities are frequently not known very well. Adjusting them by a fit is the usual remedy but problematic, as it introduces at least four more adjustable fit parameters because each pair has its specific Δg and hyperfine coupling constant of the observed nucleus. Starting from the recognition that precisely these parameters determine the polarizations in the limits of no pair substitution and of infinitely fast pair substitution, and that these two limiting cases can be measured separately if pair substitution occurs by a bimolecular reaction, the theory was recast in a form that its inputs are the limiting polarizations instead of the magnetic parameters, which are thus contained implicitly.[59] In a pair substitution, the abrupt change of the spin Hamiltonian usually takes place at an arbitrary time during a diffusive excursion. Quite distinct from that is the case that a radical pair is transformed into another radical pair at the moment of an encounter. For that scenario, a closed-form solution that again contains the magnetic parameters implicitly was developed (compare Chart 5 and Figure 21 below).[60]

Experiments in low magnetic fields yield very valuable information, in particular because CIDNP is then only affected by the hyperfine coupling constants but not the Δg term. However, in spin systems with a scalar coupling there is a danger that CIDNP is redistibuted, so nuclei that are not actually polarized by CIDNP because of insufficient hyperfine coupling acquire polarization indirectly through this redistribution. This was analysed theoretically and experimentally, and it was concluded that it is not sufficient to consider only the coupling but that the duration of the irradiation, the waiting times, and the time for transferring the sample to the high field for observation play a very important role.[61,62]

With CIDNP, sudden perturbations of a spin system are normally only applied for detection purposes, as in time-resolved experiments where an rf pulse converts polarizations into coherences. A direct perturbation of the radical pairs can

be achieved by rapidly switching the magnetic field during their life. This method (switched external magnetic field, SEMF)[63] has been applied successfully to study the kinetics of micellized radical pairs,[64,65] the lifetime of short-lived radicals in solution,[66] degenerate electron exchange[67,68] hydrogen abstraction,[69] and radical coupling.[70]

4. INSTRUMENTATION AND TECHNIQUES

4.1. Standard hardware

All Photo-CIDNP experiments need an NMR spectrometer and a light source.

Although even a cw instrument would be capable of recording CIDNP spectra, a pulsed and FT one is indispensable for all experimental schemes described in the next sections. No hardware modifications are necessary. The field strength is only dictated by resolution requirements (or spectrometer availability) because the sensitivity of CIDNP measurements is field-independent.[7] Pulsed field gradients are more than helpful for CIDNP work. On one hand, some of the illumination methods explained in the following can distort the field so severely that shimming without gradients is almost impossible or at least extremely time-consuming. On the other hand, some of the pulse sequences given below rely on gradients or are greatly improved in performance by them.

As the light source, a cw or pulsed laser is mostly used today. The high power of a laser is particularly advantageous because the photo-CIDNP signal is directly proportional to the photochemical turnover. As a consequence of the high photon flux, however, illumination of the sample has to be off at all times except for a short duration before an acquisition, otherwise quick decomposition would occur. Hence, a shutter is an essential add-on for a cw laser while a pulsed laser allows not only single-pulse (i.e. time-resolved) experiments but also quasi-continuous illumination, if a train of pulses with a high repetition rate is applied for some time; the simplest way to achieve the latter is by letting the laser run freely and controlling the duration of the illumination with a shutter. Another benefit of gated illumination is that advanced pulse schemes (see below) for background suppression in experiments without time resolution become possible.

The synchronization of the NMR pulse sequence and the timing of the illumination poses little problems because modern spectrometers usually have one or several spare lines; alternatively, unused transmitter or decoupler channels can serve for that purpose. A recent, fairly typical software implementation for a pulsed Nd:YAG laser, which requires one trigger signal for its flash lamp and another for its Q-switch, is discussed in Ref. 71.

More challenging is the question of how to get the light into the sample with good efficiency. Different methods have been compared in Ref. 72. In the early times of CIDNP, the NMR probe was frequently modified as to allow the insertion of a quartz rod from below, which was either orientated in line with the NMR tube or off-axis. In the first case, the light entered through the bottom of the tube; in the second, a prism on top of the quartz rod effected side-on illumination of the region

between the coils. Today's probes not only are too expensive for such modifications but also would lose part of their functionality and specifications, so with them illumination from the top, through the NMR tube, seems to be mandatory. The conflicting requirements are

– The absorption by the solution above the coil region should be minimized because it both reduces the observed CIDNP signal and decreases the stability of the sample.
– Field distortions caused by any inserts must be kept to a level that can be compensated by the shim set.

The relatively small photon flux of a cw laser is easily accommodated by an optical fibre. When this is pushed down the tube to a few millimetres above the top of the coils, as shown in Figure 7A, both criteria are met satisfactorily as long as the samples are optically thin. The problem with strongly absorbing samples was recently solved by etching the fibre in a stepwise manner;[72] the very thin end can then be inserted completely into the coil region (Figure 7B) without unmanageable field distortions while the steps greatly improve the homogeneity of the illumination.

The high peak powers of a pulsed laser are incompatible with fibres. Instead, as Figure 7C illustrates, a tightly fitting quartz rod acting as a light guide can be inserted into the tube. Shimming presents no problems if the end of this rod is not lower than the optical fibre in Figure 7A but some care has to be taken to avoid air

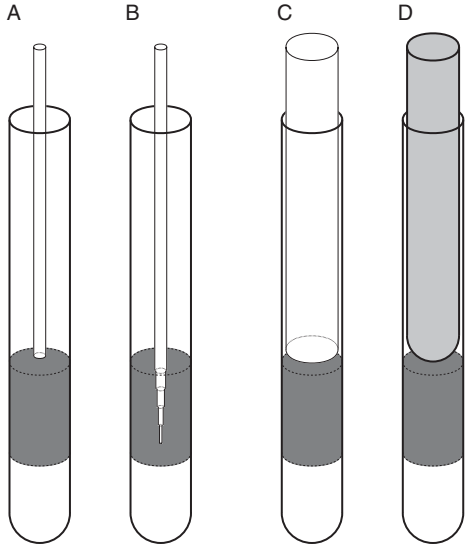

Figure 7 *Illumination methods for photo-CIDNP spectroscopy*. The coil area has been shaded. Inserts from left to right, (A) normal optical fibre; (B) stepwise etched optical fibre; (C) quartz rod; (D) inserted smaller NMR tube. In (A) and (B), the diameter of the fibre relative to that of the tube has been exaggerated for better visibility. Further explanation, see text.

bubbles at the quartz–air interface. The poor man's version of this is the insertion of a tightly fitting NMR tube filled with the solvent used, or with D_2O; see, Figure 7D. Up to the top end of the light guide in Figure 7C or D, the light is best transmitted though the air using high-reflectance mirrors or prisms. When the last of these optical elements sits on an adjustable mount positioned above the magnet and on its *z*-axis, aligning the optical path is very easy if the probe is temporarily removed. However, any tilting of the magnet deteriorates the alignment, so great care has to be exercised during reinsertion of the probe and insertion of the samples because the air bearings of a modern superconducting magnet do not return to exactly the same position after mechanical movement.

4.2. Pulse sequences for standard CIDNP measurements

There are two basic variants of photo-CIDNP experiments.

Experiments without time resolution are very valuable for mechanistic studies. Because their essence is simply prefacing any pulse sequence of interest with an illumination period (compare Figure 8), they are extremely easy to implement. They also have a high sensitivity because the number of absorbed photons can be made very high. Limitations arise in two respects. Relaxation of the observed diamagnetic products causes deviations of the signals from the true polarizations for illumination durations longer than about $0.1T_1$; however, this can be overcome fairly easily by shortening the illumination and using a proportionally higher intensity. More of a challenge is the suppression of the Boltzmann signals of unreacted, hence unpolarized molecules (the ''background''), which can totally obscure small polarizations, especially in biochemical systems where experiments are often carried out in mostly undeuterated water or in the presence of high concentrations of denaturants. Even if presaturation is used to destroy these background signals before the start of the experiment, recovery during the illumination period can be considerable in those cases.

Time-resolved experiments are indispensable for kinetic work. Their basic idea is illustrated by Figure 9. It consists of recording a series of traces with different delays Δt between a laser flash and an acquisition pulse; the signal intensities as functions of Δt yield the time dependence. Background problems are absent as the delays are much shorter than T_1, so recovery during them is negligible. However, because the chemical turnover is typically quite low, sensitivity is the central issue with time-resolved experiments.

Despite the fact that CIDNP spectroscopy has reached 40 years of age, novel pulse sequences were devised only recently[73–75] that greatly improve the performance of these two classes of photo-CIDNP experiments with respect to their specific key problems.

4.2.1. New pulse sequences for experiments without time resolution

A long-known solution to the background problem is to record alternating spectra with and without illumination, and then subtract them. Apart from the degradation of the sensitivity by a factor of $\sqrt{2}$ because CIDNP is only acquired in one-half of the spectra but the noise in all of them, this is plagued by the usual artefacts of

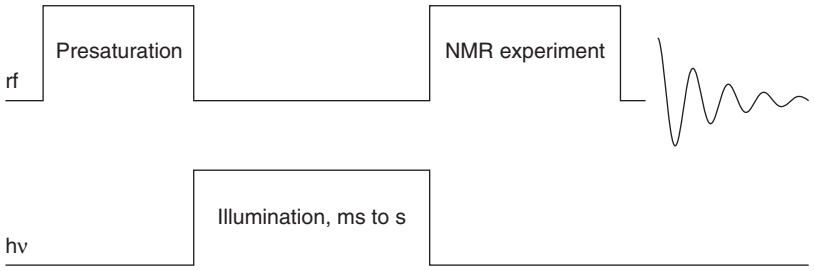

Figure 8 *Principle of a photo-CIDNP experiment without time resolution.* Further explanation, see text.

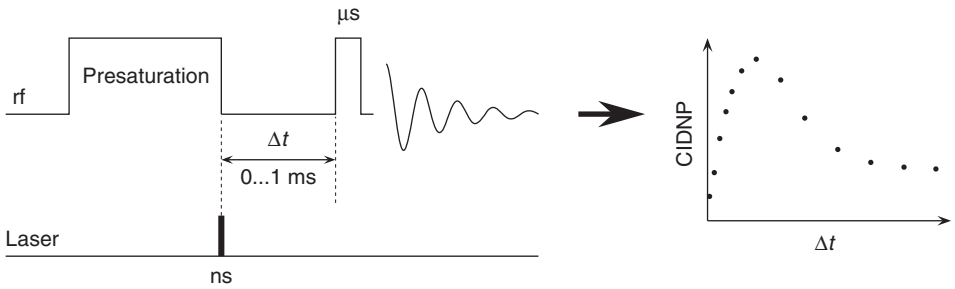

Figure 9 *A time-resolved photo-CIDNP experiment*. Further explanation, see text. Adapted from Ref. 75 with permission; copyright (2006) Taylor & Francis Ltd, http://www.tandf.co.uk/journals.

difference spectroscopy, which can be very pronounced because the illumination causes the temperature in the two measurements to be unequal.

A completely different approach to solve the background problem[73] is illustrated by the one-dimensional COSY sequence displayed in Figure 10, where the background is assumed to have been destroyed before the start of the experiment proper. The key to background suppression is provided by the recognition that only the $\pi/2$ pulses of the example can convert the background into an observable whereas the π pulses cannot. Nor does the background play any role during the rest of the sequence. So, in general the background is only detrimental at those moments of a pulse sequence when coherence is generated or transferred, that is, when pulses with flip angles other than an integer multiple of π are applied. Exploiting this, one can make the background oscillate around zero, by using a grid of inversion pulses, such that it is zero at the crucial moments.

In general, the nuclei of the background will have (possibly widely) different T_1. However, the elementary building block of the described background-nulling grid, a π pulse sandwiched between two delays, has a self-compensating property, as is also shown in Figure 10. If the timing is chosen such that the magnetization of the background nuclei with the shortest T_1 exactly crosses zero at the crucial moment, the zero crossings of all other background nuclei occur almost at the

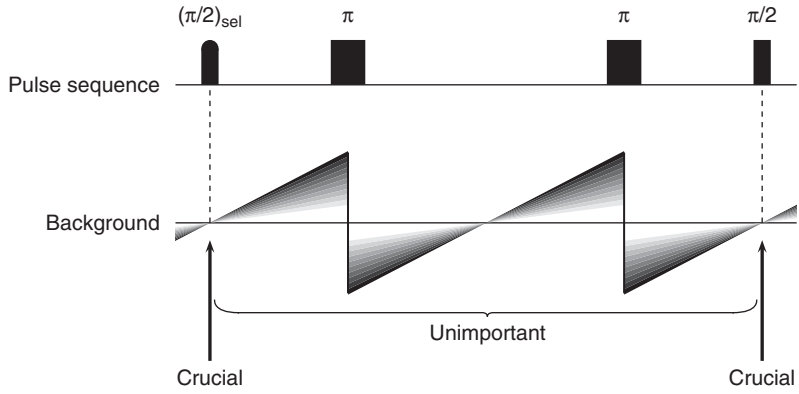

Figure 10 *Operating principle of a background-nulling grid explained by a one-dimensional COSY sequence*. At the moment of the first pulse, the background passes zero while the CIDNP signal is non-zero. The crucial points of time when the background would be converted into a signal have been marked with arrows; at all other times the magnitude of the background is of no consequence. The background oscillations for nuclei with different T_1 are colour-coded, a longer T_1 corresponding to a lighter shade of gray. Further explanation, see text.

same point of time. The reason for this self-compensation is that a more slowly relaxing nucleus regains a smaller fraction of its equilibrium magnetization during the first part of the block, so starts out with a less negative value at the beginning of the second part. The self-compensation further improves when n such blocks are used in succession. Also, for even n it is considerably better than for odd n, which is a fortunate coincidence because an even number of π pulses also avoids artefacts such as incomplete refocussing of chemical shifts and coherence transfer in strongly coupled spin systems or with CIDNP multiplet effects.[75]

A great many pulse sequences contain π pulses as an integral part (such as the 1D COSY sequence of the example) or will tolerate the insertion of additional ones. For those that do not, an independent background reduction method by a phase cycle was developed,[73] which is shown in Figure 11. To avoid a cancellation of CIDNP signals generated during a background-nulling grid, gated illumination during alternate delays has to be applied. The rf pulse scheme is always kept the same, but the illumination periods are inserted at different points of the pulse sequence on successive scans. With the illumination timing displayed for scan 1, 3, . . ., CIDNP experiences an even number of inversions, so does not change sign, but when illumination is done as shown for scan 2, 4, . . ., the number of inversions is odd, and CIDNP is inverted. In contrast, the background magnetization remains unchanged by the illumination timing. Co-adding the two transients with opposite receiver phase will thus retain CIDNP, but strongly suppress the background. With every multi-pulse experiment used in modern NMR, the detected signal will change phase when the input is inverted, so the described phase cycle is generally applicable.

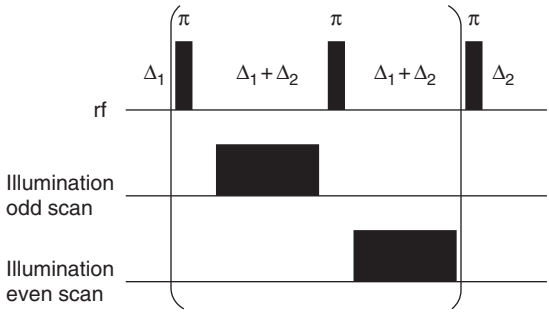

Figure 11 *Background suppression by a phase cycle in a photo-CIDNP experiment with gated illumination*. The actual pulse sequence, for example that of Figure 10 follows directly after the final delay Δ_2. On the even scans, the receiver phase is inverted. The block in parentheses can be repeated as desired. Further explanation, see text. Adapted from Ref. 73 with permission; copyright (2005) Elsevier Inc.

That approach has three further attractive features. First, it is completely independent from the previously described background-nulling grid during the pulse sequence proper, so can be used on its own or can be combined with that method. Second, no artefacts caused by different temperatures during the two acquisitions are to be expected because the illumination conditions are very similar. Third, each scan yields a CIDNP signal, so the sensitivity does not deteriorate.

Figure 12 illustrates the joint application of both methods to a protein CIDNP spectrum in 90% undeuterated water; additionally a denaturant and a buffer were present in high concentration. The water peak was suppressed by a DPFGSE sequence,[76] which can accommodate a background-nulling grid. While it would have been possible to suppress the denaturant and buffer signals in the same way by properly shaped pulses in the DPFGSE sequence, this would have worked by eliminating the respective frequency range from the spectrum and would thus have rendered unobservable all CIDNP signals in that range. However, with the described background suppression schemes, CIDNP signals in the spectral region of background signals (see the tyrosine β protons) can be observed, because these schemes differentiate z magnetization by virtue of its source, Boltzmann magnetization or CIDNP.

4.2.2. New pulse sequences for time-resolved experiments

Signal co-addition is the traditional method to increase the signal-to-noise ratio of any NMR experiment. However, in the context of photo-CIDNP this collides with the problem of sample decomposition because chemical turnover is a prerequisite for polarization generation; the achievable improvement is thus always smaller than the theoretical limit for n acquisitions, i.e. smaller than $\sqrt{n}$. Since the CIDNP signal is proportional to the number of reacting molecules and each acquisition incurs the same noise penalty, the only room for improvement left with a given chemical system (i.e. fixed amount of polarization per photon) and a given

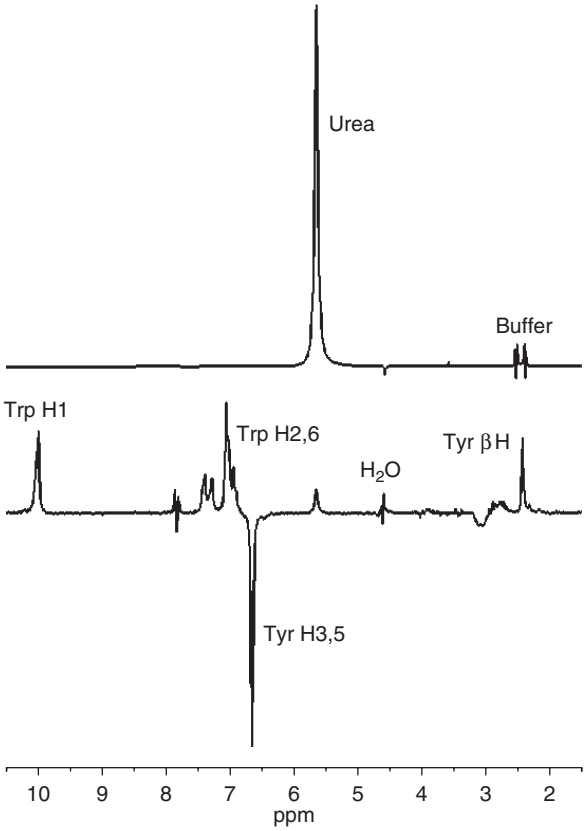

Figure 12 *Application of the described background suppression schemes to a protein in water*. In both spectra, the water peak was eliminated by a DPFGSE sequence. Proteine, bovine α-lactalbumine; buffer, sodium citrate; denaturant, 6 M urea; photosensitizer flavin mononucleotide. Top trace: spectrum without illumination; the resonances of the buffer are distorted by the DPFGSE water suppression sequence. Bottom trace: photo-CIDNP spectrum recorded with the background-nulling grid of Figure 10 and the phase cycle of Figure 11. The very small remaining urea signal shows the degree of suppression. The buffer signal is completely suppressed, and the polarized signal of the tyrosine β protons is not obscured by it. Further explanation, see text. Reproduced from Ref. 73 with permission; copyright (2005) Elsevier Inc.

spectrometer (i.e. fixed amount of electronic noise per acquisition) is to minimize the number of acquisitions while keeping constant the number of photons absorbed.

Increasing the laser power would be the simplest means to achieve that end but problems of cost, of damage to the optical components needed to transport the light to the sample, and above all of two-photon processes that can open up completely new reaction channels, put a limit to that. A completely different approach was recently reported,[74,75] which relies on carrying out a co-addition of the CIDNP signals not in the acquisition computer but in the spin system itself,

where no electronic noise arises. After the desired number of flashes, the co-added signal is then read out, with the spectrometer noise being acquired only once.

The principle of storing the CIDNP signal in the spin system at a certain point of time after a laser flash, and superimposing on it the CIDNP signal present at the same point of time after the next flash, is illustrated in Figure 13. It exploits the fact that CIDNP is longitudinal magnetization only. By sampling it with an rf pulse at a given moment, it is converted into coherences. Subsequently, CIDNP develops further under the influence of the chemical reaction, but there is no coupling whatsoever between the newly formed CIDNP and the one converted into coherences. Hence, the sampled CIDNP signal can be regarded as being stored in the transverse plane. After, usually, much less than 500 μs CIDNP generation has come to an end, and the stored signal is transferred to the z-axis, where it is kept until the laser is ready to fire again (typically, for tens of milliseconds with affordable lasers). Finally, a sampling pulse applied at the same time after the new laser flash as before captures both the time-dependent CIDNP signal caused by this flash and the stored signal of the preceding flash. This procedure can be repeated as often as desired. The actual pulse sequence is much more complex than Figure 13 suggests: Chemical shift evolution during transverse storage is

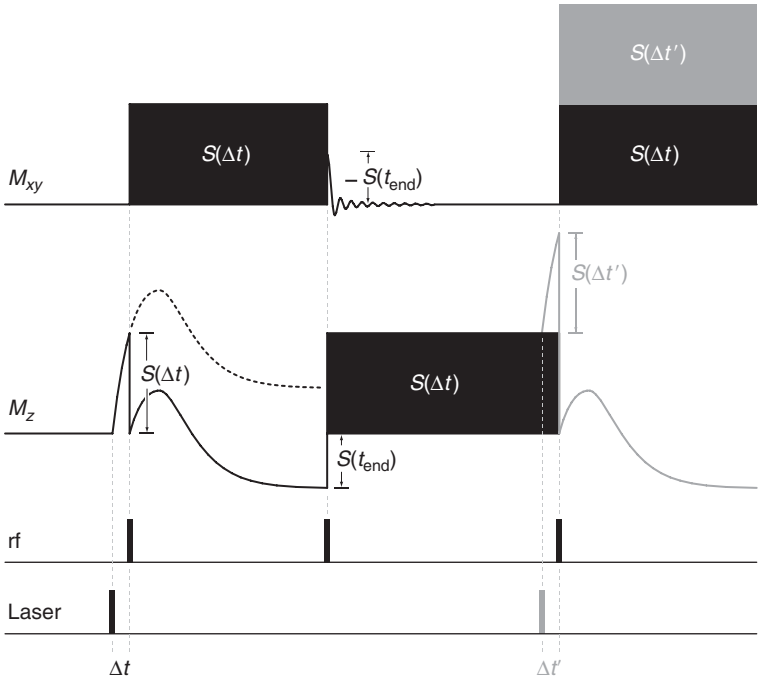

Figure 13 *Storage and accumulation of a time-resolved CIDNP signal in a spin system.* The picture displays the timing of the laser and the spectrometer, and the time dependence of longitudinal and transverse magnetization. Further explanation, see text. Reproduced from Ref. 75 with permission; copyright (2006) Taylor & Francis Ltd, http://www.tandf.co.uk/journals.

suppressed by double spin echoes, background recovery between flashes is precluded by double inversion sandwiches as in Figure 10, and storage of CIDNP at unwanted times is barred by gradients; further modifications serve to accommodate sampling pulses of flip angles other than $\pi/2$.[74,75]

Figure 14 demonstrates the sensitivity improvement that is obtained by the described co-addition in the spin system, and shows that the method is applicable without distortions to strongly coupled spin systems and to CIDNP multiplet effects.

The time resolution of such experiments is not limited by the rf pulse width. Pulses can be staggered from scan to scan by less than their duration, yet by deconvolution the time dependence can be recovered with a resolution equal to the stagger interval, but this incurs a reduction of the signal-to-noise ratio. As compared to conventional NMR, both flip angle and acquisition time must be optimized in a quite different manner to achieve maximum sensitivity.[77]

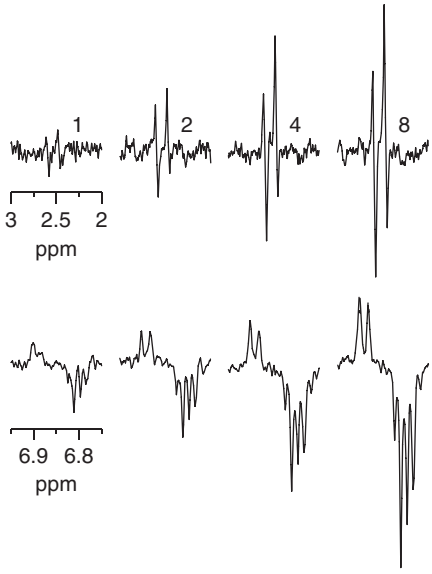

Figure 14 *Signal improvement by multi-flash CIDNP experiments with storage and accumulation in the spin system*. Delay Δt (see, Figure 13) between laser flash and sampling rf pulse, 0 μs. *Bottom trace*: absorptive doublet and emissive AB spin system of 3-fluoro-DL-tyrosine. *Top trace*: multiplet effect in β-NADH. The number of flashes accumulated before one acquisition is given at the upper spectra, "1" denoting the control experiment with the standard sequence of Figure 9. It is seen that neither multiplet signals nor CIDNP multiplet effects are distorted by the method. Further explanation, see text. Adapted from Ref. 75 with permission; copyright (2006) Taylor & Francis Ltd, http://www.tandf.co.uk/journals.

4.3. Special hardware

It can safely be stated that flow or transfer devices are the most frequent add-ons to the conventional hardware a routine CIDNP experiment needs, for two reasons. First, CIDNP relies on chemical turnover, so a depletion of the reactants or a build-up of unwanted products are commonly encountered problems a flow system can help avoid. Second, CIDNP in low and variable magnetic fields is very attractive because valuable information can be obtained; however, spectral resolution would be totally lost if the low field inducing the polarizations were also used for acquiring the free induction decay, so a means of transferring the sample between different magnets, or at least different field regions, is indispensable.

A pneumatically driven syringe that repeatedly injects the solution into the NMR tube and draws it back into a reservoir located in the bore of the magnet, thus efficiently mixing depleted and fresh portions of the sample between scans, was successfully used in protein work.[78] A much more sophisticated pneumatic injector with a dead time as low as a few tens of milliseconds has been described in Ref. 79; its performance was assessed using digital video measurements, rapid-acquisition NMR measurements following a pH jump, and NMR imaging.

The first of these injection devices has also found application in variable field CIDNP. Because CIDNP generation is not very sensitive to field inhomogeneities (as opposed to CIDNP detection through the NMR spectrum), Hore et al. generated CIDNP by illuminating the sample in a small cell placed at a variable height in the magnet bore above the probe, and then injected it into an NMR tube in the probe for observation.[80] Compared to CIDNP generation in an external magnet, a much lower transfer time is achievable because the solution has to travel through a short distance only.

Another concept for variable-field CIDNP and field-cycling experiments involves transporting the whole probe with a stepper motor.[81,82] Transfer times are obviously much longer, but continuous sample rotation during the transfer is possible.

Switching the magnetic field during the life of the radical pairs is an experimentally much more demanding extension of CIDNP. A specially built external magnet and controller are needed; experimental details for single[64,67] and double switching[69] can be found in the literature.

4.4. Special pulse sequences

The CIDNP effect has been employed to boost the sensitivity of Frydman's ''ultrafast'' NMR experiments, which record a two-dimensional spectrum in one scan through spatially encoding the indirect dimension by gradients and reading out the spectrum with an echo-planar imaging sequence.[83] Another unusual combination of CIDNP with an imaging technique has been employed to study the spatial distribution of the reaction products during photolysis.[84]

As has long been known, CIDNP net effects, multiplet effects, and higher multiplet effects (i.e. 1-spin order, 2-spin order, etc.) can be separated through their dependence on the flip angle ϑ.[9] This is normally done by recording spectra

with pre-calculated values of ϑ and taking appropriate linear combinations. The same result can be obtained more efficiently by a Fourier analysis of the measured intensity dependence of each line on ϑ;[85,86] a separation through the refocussing properties of spin echoes on odd and even spin orders is also possible.[87]

5. CHEMICAL INFORMATION OBTAINABLE BY HIGH-FIELD CIDNP

5.1. Absence or occurrence of CIDNP in a reaction

The failure to observe CIDNP effects is sometimes used as evidence for a mechanism that does not involve radicals. While non-radical reactions indeed cannot give rise to CIDNP, a simple reversal of that argument is dangerous because there are many reasons that can cause CIDNP to be unobservable in a radical reaction. Most important are unfavourable magnetic parameters: If the g-value difference of the radicals is nearly zero, CIDNP will be negligible except in the comparatively rare case of a multiplet effect; if the hyperfine coupling constants are too small, both net and multiplet effects will be insignificant. However, suppression of CIDNP can also occur by cancellation, either if radical pairs are formed from both singlet and triplet precursors (compare the region around room temperature of Figure 16) or if singlet and triplet exit channels lead to the same product (see the bottom trace of Figure 15, or the intermediate concentration regime of Figure 17). Hence, the absence of CIDNP should be regarded as rather weak evidence unless control experiments have been performed that rule out these factors.

In contrast, the observation of a CIDNP effect clearly indicates a reaction via radical pairs. In such a situation, however, the question is often raised—in particular by reviewers less familiar with CIDNP—whether that pathway via radicals is the only pathway, or if it is only a minor side reaction that is detected nevertheless because of the signal amplification by the polarizations while the greater part of the reaction proceeds via non-radical routes. Much of this worry is due to a misconception as to the size of the signal enhancements, which were indeed very large in the early days of CIDNP but are much smaller on modern high-field instruments (e.g. at 300 MHz, the Boltzmann population differences are five times larger than at 60 MHz but the polarizations are smaller by a factor of about $\sqrt{5}$, so the enhancements are lower by an order of magnitude). Yet, the objection is partly valid because CIDNP would indeed not capture any parallel non-radical route. That issue can be addressed in the same way as in classical mechanistic chemistry: When a reaction is believed to involve X as a key intermediate, one prepares X by an independent route; if X so obtained decays to the same products and with the same yields as before, the reaction does occur exclusively via X.

For electron-transfer induced reactions, this strategy has been applied to CIDNP.[59,88,89] An example is provided by Chart 2 and Figure 15. Irradiation (308 nm) of the donor *trans*-anthole D in the presence of the acceptor fumarodinitrile A in a polar solvent leads to isomerization of both olefins and to cycloaddition. The direct photoreaction proceeds via the excited donor D* because A does not absorb at the wavelength used and energy transfer to A is not feasible

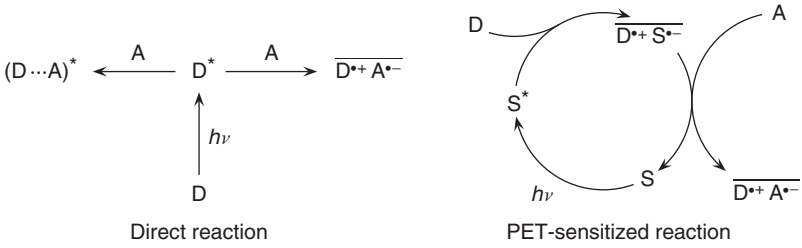

Chart 2

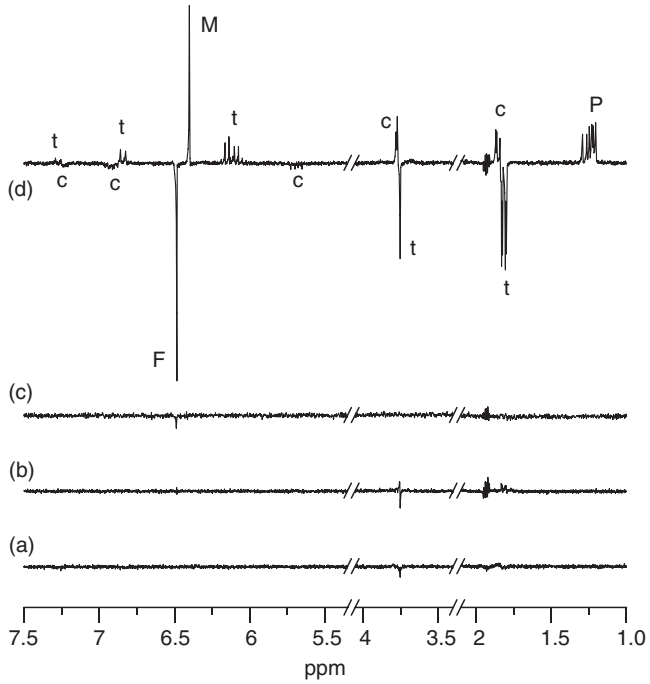

Figure 15 CIDNP spectra in the system 9-cyanoanthracene S (1 mM), *trans*-anethole D (20 mM), and fumarodinitrile A (90 mM) in acetonitrile upon excitation with 388 nm (all four spectra) or 308 nm (spectrum (d)). Spectrum (a), only S and D present; spectrum (b), only D and A present; spectrum (c), only S and A present; spectrum (d), *either* all three species present, excitation with 388 nm (the PET-sensitized reaction) *or* only D and A present but excitation with 308 nm (the direct reaction). Further explanation, see text and Chart 2. Reproduced from Ref. 59 with permission; copyright (2006) the PCCP Owner Societies.

thermodynamically. The strong and manifold polarizations (see, top trace of Figure 15) unambiguously show that CIDNP arises in radical-pairs $\overline{D^{\bullet+}A^{\bullet-}}$. However, by itself this does not rule out that isomerization and cycloadduct formation via exciplexes $(D...A)^*$ might occur as a parallel pathway, in particular as this has frequently been postulated in the literature for similar systems.

To exclude that, photoinduced electron transfer (PET) sensitization was employed to prepare the radical-pair $\overline{D^{\bullet+}A^{\bullet-}}$ by a route that bypasses D* and thus renders an exciplex impossible. PET sensitization works by generating a first radical pair through PET involving an auxiliary sensitizer S, and then replacing (in this case) the radical anion $S^{\bullet-}$ by a thermal electron transfer to a molecule of A; the conditions are chosen such that this exchange takes place in the cage, i.e., fast on the CIDNP timescale. The desired radical ion pair $\overline{D^{\bullet+}A^{\bullet-}}$ is thus obtained indirectly, as Chart 2 shows. For the system in question, 9-cyanoanthracene is very well suited as the sensitizer. The excitation wavelength was set to 388 nm to preclude the direct photoreaction between D and A.

As Figure 15B proves, CIDNP in the original system, D and A, indeed no longer arises upon 388 nm excitation because neither molecule absorbs. Nor do polarizations result when the sensitizer S is illuminated in the presence of the acceptor A only (Figure 15C) because no quenching is possible for thermodynamic reasons. When only D is added to S, again no polarizations are detected (Figure 15A) although it can be shown that radical-pairs $\overline{D^{\bullet+}S^{\bullet-}}$ are formed in high yield. This absence of CIDNP is due to the very low triplet energy of S, which makes electron return of singlet and triplet pairs equally likely, and thus leads to a complete cancellation of their polarizations. Because none of the two-component systems, for different reasons, produces any CIDNP whatsoever, the strong polarizations in the three-component system, which occur through the PET-sensitization mechanism of Chart 2, are very striking. A comparison of the CIDNP signals and intensities in this PET-sensitized experiment and in the direct experiment shows that the pathway via radical ion pairs is the only pathway to the products in that system; a participation of the exciplex route can be excluded.

5.2. Precursor multiplicity

As Platt[90] put it ''. . .you can catch phenomena in a logical box or in a mathematical box. The logical box is coarse but strong. The mathematical box is fine-grained but flimsy. The mathematical box is a beautiful way of wrapping up a problem but it will not hold the phenomena unless they have been caught in a logical box to begin with''. The sign relationship of Equation (8), which connects the polarization phase with the precursor multiplicity, provides such a logical box and is probably one of the most valuable assets of photo-CIDNP. Because it influences all signals of a product in the same way, it is practically proof against artefacts. The small ambiguity sometimes caused by the involvement of other parameters in Equation (8), in particular concerning the signs of Δg and the hyperfine coupling constants, can be removed by a control experiment using a triplet photosensitizer. If the polarization phases of a product remain the same in that sensitized experiment the precursor multiplicity in the unsensitized photoreaction leading to that product is also triplet.

One has to bear in mind, however, that the CIDNP effect responds to the concentration difference between singlet and triplet precursors, so the ''logical box'' captures the prevailing multiplicity. If a variation of the experimental conditions affects the balance between these two entry channels to the radical-pair

mechanism, the ''logical box'' evolves into a ''mathematical box'' that allows a separation of the contributions of singlet and triplet precursors.

A spectacular example of that has been reported[91] for the β-cleavage of (*N*-methylanilino)acetone (Chart 3). The radical pair formed upon excitation at 308 nm yields a variety of products. The analysis concentrates on the regenerated starting material (cage product via the singlet exit channel) and on 2,5-hexanedione (escape product via the triplet exit channel). Figure 16 displays the background-free CIDNP signals of the CH_2-groups in both compounds as functions of the temperature during photolysis. Clearly, one precursor multiplicity—triplet, as follows from a sensitization experiment—dominates at low temperature and the other at high temperature. (Because both multiplicities accidentally balance near room temperature, CIDNP becomes zero under these conditions although there is no decrease in radical-pair yield; this illustrates the caveat given in Section 5.1 that the absence of CIDNP does not necessarily indicate a non-radical mechanism.)

Because the illumination first produces the singlet excited state, which then undergoes temperature-independent intersystem crossing to the much longer lived triplet state, the temperature dependence of Figure 16, as a ''logical box'', is very clear evidence that there is an activation barrier for cleavage of the singlet state. The ''mathematical box'' is rather difficult to handle reliably in that case because absolute CIDNP intensities are also temperature-dependent through diffusion, but still allows an estimation of the activation barrier (15–20 kJ mol^{-1}).[91]

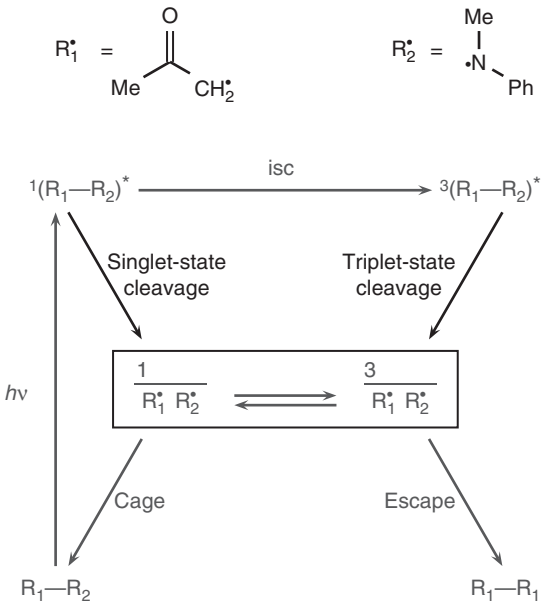

Chart 3

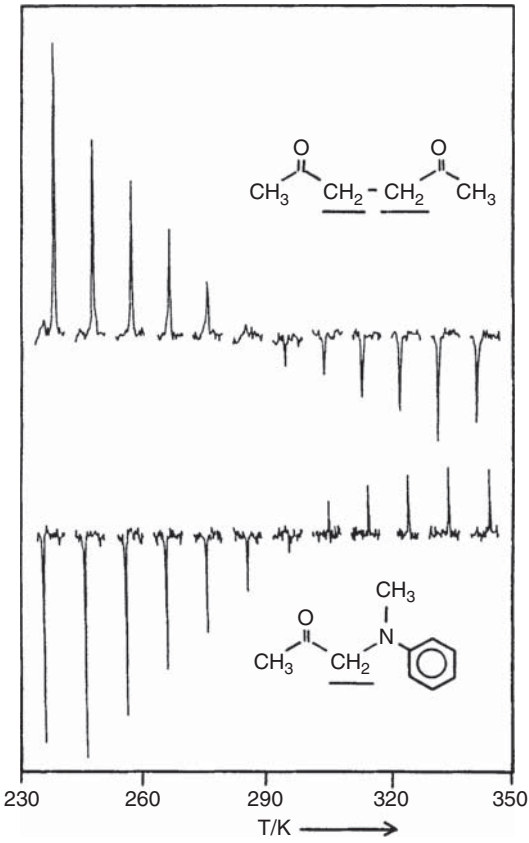

Figure 16 *Temperature-dependent photo-CIDNP signals in the photoreaction of (N-methylanilino)-acetone*. Top trace: escape product; bottom trace: cage product. Further explanation, see text. Reproduced from Ref. 91 with permission; copyright (1992) Elsevier Sequoia.

5.3. Exit channel

Through Equation (8), the exit channel is related to the CIDNP signals in an analogous manner as the precursor multiplicity is. However, employing the polarization phase as a ''logical box'' to determinate the exit channel is very rarely necessary in practice because it can usually be predicted with certainty on the basis of thermodynamic data. In the majority of cases, the triplet exit channel is tantamount to escape, i.e. formation of free radicals. Exceptions only occur for pairs of radical ions, for which reverse electron transfer or biradical formation can be feasible geminate reactions in the triplet state; because these processes are obviously also possible for the singlet pairs and lead to the same products, though possibly with a different efficiency, cancellation effects are unavoidable.

In an ingenious experiment, Schaffner and Fischer[92,93] were able to control the degree of that cancellation, and to separate singlet and triplet reverse electron transfer of a radical ion pair (Figure 17). Excited *N*,*N*-dimethyl-1-naphthylamine

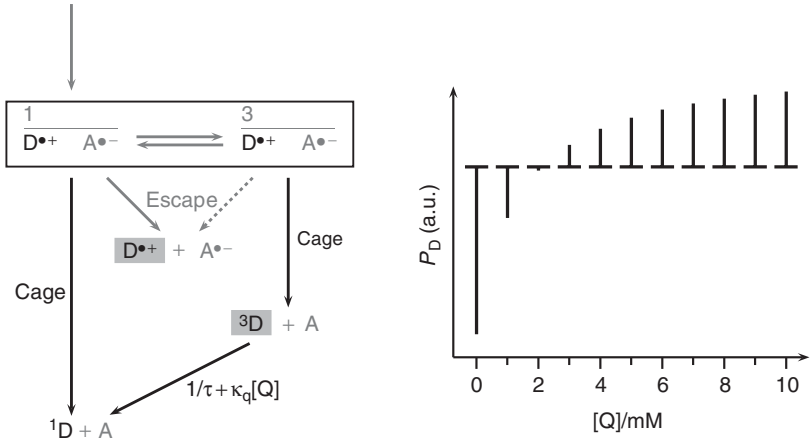

Figure 17 Photoreaction of *N*, *N*-dimethyl-1-naphthylamine (D) with benzonitrile (A) in the presence of variable amounts of the triplet quencher 1,3-cyclohexadiene (Q). Displayed are the relevant parts of the reaction mechanism (left) and the schematic concentration dependence of the CIDNP signals as functions of the quencher concentration (right); these signals are not experimental data but were calculated from the kinetic parameters of Ref. 93 to show the effect more clearly. The donor species underlayed with gray in the scheme are not observable by NMR, but store polarizations. Further explanation, see text.

is quenched by benzonitrile to give the radical cation $D^{\bullet+}$ of the amine and the radical anion $A^{\bullet-}$ of the nitrile; the radical pair is formed in the singlet state. The spin sorting mechanism of CIDNP produces an emissive polarization of the dimethylamino protons in the singlet pairs and an absorptive one in the triplet pairs. Reverse electron transfer of the singlet pairs regenerates the starting amine in its ground state, so the emissive polarization appears in the CIDNP spectrum. Reverse electron transfer of the triplet pairs to give the amine in the triplet state is also possible, and even preferred kinetically, but the associated absorptive polarization is hidden for a time on the order of 10 μs in the triplet molecule, which is not observable by NMR. A time-resolved experiment with a short rf pulse applied immediately after the laser flash thus detects all the emissive polarization from the singlet exit channel, and practically none of the absorptive one from the triplet exit channel (see, right-hand side of Figure 17). However, the transfer of this absorptive polarization into the observed diamagnetic molecule can be accelerated by adding the triplet quencher 1,3-cyclohexadiene, which quenches so efficiently that the transfer can be made essentially complete by using an easily accessible concentration.

It might be thought that a total cancellation of CIDNP would occur in that case, but electron return in the singlet state is fairly slow because it falls into the Marcus inverted region, so a substantial fraction of the emissive polarization ends up in escaping radicals, which are not captured by the short-time detection scheme. Hence, in the limit of complete triplet quenching the absorptive polarizations dominate, as can be seen on the right-hand side of Figure 17.

In the example, the phase inversion once more served as a ''logical box'', this time to catch a change of the exit channel. With that as the starting point, a transformation into a ''mathematical box'' is again possible: In between the extremes, the CIDNP intensity follows a Stern–Volmer-type behaviour when the quencher concentration is varied. From an analysis of the polarizations including their time dependence, which is complicated by exchange processes between triplet-state and ground-state molecules as well as between radical cations and ground-state molecules, the kinetic parameters were determined.[93]

5.4. Time-resolved experiments

The preceding example was unusual in that the two exit channels from the radical pair (singlet or triplet) did not correspond to the two exit modes, geminate reaction or escape; in the majority of cases the singlet channel is synonymous with a geminate reaction and the triplet channel with escape. Despite this difference, it was an instance of the not infrequently encountered situation that the same product is formed via the two exit channels. This would undo the spin sorting and destroy all polarizations. However, the triplet exit channel by necessity leads to a paramagnetic species, which is not observable by NMR. To manifest themselves in the NMR spectrum, the polarizations first have to find their way into a diamagnetic molecule, so a secondary chemical transformation of the paramagnetic species into a diamagnetic one has to occur.

Depending on the conditions, this chain of events can take much longer than the life of a radical pair, so by time-resolved CIDNP one can separate the polarizations of the singlet geminate reaction, which are quasi-instantaneous on the timescale of the experiment, from the polarizations of a triplet geminate reaction or escape from the cage followed by a secondary process. Even if complete cancellation of CIDNP eventually occurs because the polarization stored in the paramagnetic species is quantitatively transferred, the time-resolved experiment will capture the transient polarizations and, through their time dependence, allow a determination of the rate of the secondary processes. Nuclear spin relaxation in the paramagnetic species will usually destroy part of the polarizations, so a small residual signal will remain in an experiment without time resolution.

The described scenario is usually realized in PET, where the geminate reaction of the radical ion pair regenerates the reactants with polarizations of one phase, and escape produces free radical ions bearing polarizations of the opposite phase. Degenerate electron exchange between a radical ion and a neutral molecule effects no chemical change but equilibrates the spin polarizations of the radicals and the ground-state molecules (''exchange cancellation''), e.g. for a donor D

$$^{*}D^{\bullet+} + D \rightleftharpoons {}^{*}D + D^{\bullet+} \tag{33}$$

where an asterisk symbolizes spin polarization.

Figure 18 shows an example.[89] Photoexcited triphenylamine is quenched by fumarodinitrile to give a pair consisting of the amine radical cation and the olefin radical anion. A CIDNP spectrum acquired with zero delay between the laser flash and the sampling rf pulse exhibits quite strong polarizations of both

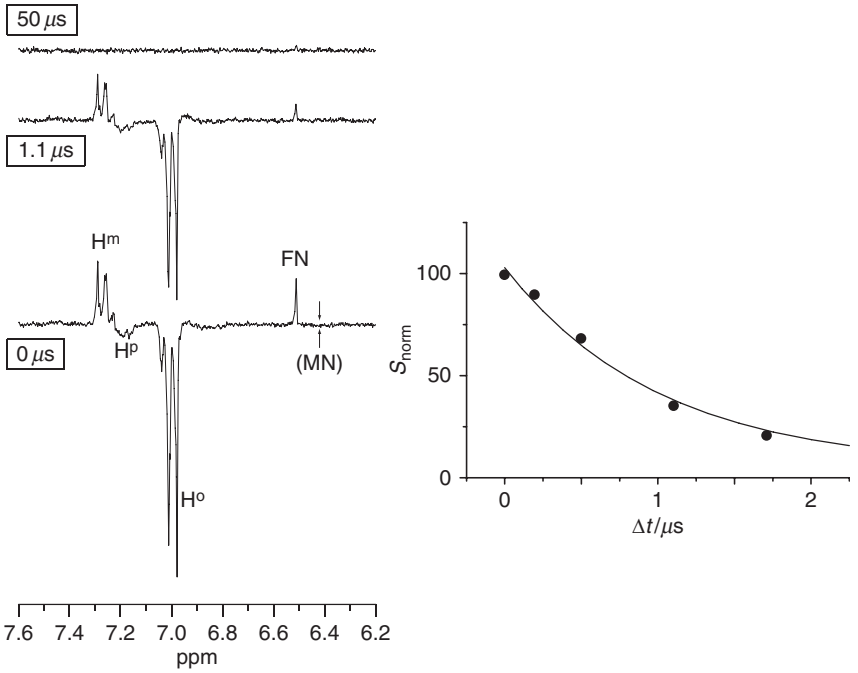

Figure 18 *Time-resolved CIDNP in the system triphenylamine/fumarodinitrile*. Left: example spectra taken at three different delays between laser flash and rf pulse. H^o, H^m, H^p are the signals of the aromatic protons of the amine, FN and MN those of the protons of the starting olefin and the isomerized olefin (which are not observed). Right: time dependence of the CIDNP signals of FN. Further explanation, see text. Reproduced from Ref. 89 with permission; copyright (2006) Verlag Helvetica Chimica Acta AG.

reactants, which result from reverse electron transfer of singlet pairs (cage reaction). When the delay is increased, the polarizations become weaker; at long delays they are practically zero. Analysis of the signal intensities as functions of the delay yields the exchange rates, which despite the uselessness of a degenerate reaction to a synthetic chemist are of fundamental importance for the kinetic description of an electron transfer. More important to an organic chemist is the observation that no signal of the isomerized olefin maleodinitrile appears, which means that the radical anion is configurationally stable.

5.5. Identification of intermediates

There is a direct correspondence (often, approximate proportionality) between the polarization a nucleus picks up in the radical pairs and its hyperfine coupling constant. The so-called polarization pattern[94]—the relative polarization intensities of the nuclei in a product—may thus be regarded as a frozen EPR spectrum of the intermediates, although the obtained values of the coupling constants are only relative ones, i.e. scaled by a constant factor. Hence, the paramagnetic intermediates can be identified and characterized by photo-CIDNP spectroscopy in a

similar way as by EPR spectroscopy. But why should one, for that purpose, resort to photo-CIDNP, which is not only a less common but also an indirect method, instead of using EPR, which is certainly much more mainstream and allows a direct observation of the radicals? There are three points in favour of CIDNP spectroscopy:

First, an EPR spectrum only yields a set of hyperfine coupling constants, but which of these constants belongs to which nucleus has to be determined by an assignment that can be quite time-consuming, e.g. requiring isotope substitution; in contrast, the CIDNP effect always connects each hyperfine coupling constant unambiguously with a nucleus.[95] Second, the signs of the hyperfine coupling constants, which provide valuable information about the radical structure, cannot be obtained from an EPR spectrum; however, they can be read directly from a CIDNP spectrum. Third, short-lived radicals frequently escape EPR detection, whereas the CIDNP effect captures their signature even on a sub-nanosecond timescale.

The radical cation of cysteine, $Cys^{\bullet+}$, serves as an example of the first and third point.[96] This amino acid contains two potential donor sites, sulphur and nitrogen, so electron transfer to an excited sensitizer could result in a sulphur-centred or a nitrogen-centred radical cation. Decarboxylation of $Cys^{\bullet+}$ to give an α-amino alkyl radical occurs on a timescale slightly faster than 1 ns, so a direct observation by EPR is not feasible. However, the CIDNP spectrum with 4-carboxybenzophenone CB as the sensitizer exhibits polarizations of the starting amino acid, which can only be the product of reverse electron transfer of pairs $\overline{Cys^{\bullet+}CB^{\bullet-}}$ but obviously not in any way the product of the radical pairs formed by the decarboxylation. Concentrating on the cysteine polarizations thus avoids all complication due to the rich secondary chemistry.[96]

Because it is well established that radical cations of monoamines and monosulphides have substantial hyperfine couplings only for the protons at carbon atoms adjacent to the radical centre,[94] nitrogen-centred $Cys^{\bullet+}$ can develop polarizations only for H_α of the substrate, while sulphur-centred $Cys^{\bullet+}$ must cause both H_β and H_γ to be polarized, but not H_α. As can be seen in Figure 19, H_α is completely unpolarized while H_β and H_γ are strongly polarized, so it can be concluded umambiguously that electron transfer occurs exclusively from sulphur.

Numerous radical cations eluding EPR detection have been studied in a similar way (and exploiting also the signs of the hyperfine couplings) over the years, and in many cases unusual structures have been found. Perhaps one of the most striking recent examples of this application of CIDNP to characterize paramagnetic intermediates is the biradical formed from benzoquinone and quadricyclane (see Section 5.6), which is also most unusual because short-chain biradicals do not normally produce CIDNP of the S–T_0-type.[97] The change in the polarization pattern brought about by pair substitution can be used in a similar way to trace radical transformations. An example is provided by Chart 5 and Figure 21.

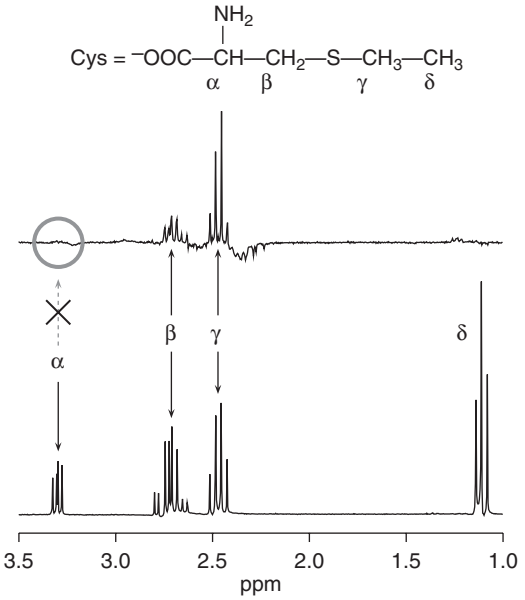

Figure 19 *Polarization pattern in the photoreaction of S-ethylcysteine Cys with 4-carboxybenzophenone at pH 11.* Bottom trace: spectrum in the dark; top trace: photo-CIDNP spectrum. The assignment of the resonances refers to the formula given at the top. The α proton is unpolarized, the β and γ protons are polarized, so the radical cation is seen to be sulphur-centred. Further explanation, see text.

5.6. Polarizations as labels

That each nucleus picks up its specific CIDNP intensity in the radical pairs has a much more far-reaching consequence than the described ''self-assignment'' of hyperfine coupling constants: It means that the polarization of a nucleus can be regarded as a label that is affixed at the paramagnetic stage and then persists, apart from relaxation. Because the magnetic energies are so tiny, this labelling is nearly ideal, affecting neither the energetics nor the kinetics of a chemical reaction.

Not only does the observation of such a label in a product mean that that product had the radical pair as a precursor, but the distribution of the labels between different products affords relative reaction rates (see, e.g. Figure 17), and time-resolved CIDNP experiments that probe how fast the labels appear in the products even yield absolute rates (compare Figure 18).

As an even more valuable asset for mechanistic investigations, any structural changes during product formation can be unravelled by analysing where in the product the labels show up. Figure 20 provides a nontrivial example. In the photoreaction of benzoquinone with quadricyclane, the polarizations arise from the 1,5-biradical BR_1. The singlet exit channel leads to the oxolane P_1, the triplet channel to the oxetane P_2. The structure of the quadricyclane-derived moiety in BR_1 is identical to that in P_1 but quite different from that in P_2, so obviously P_1 is formed by a simple combination of the radical centres whereas an extensive skeleton

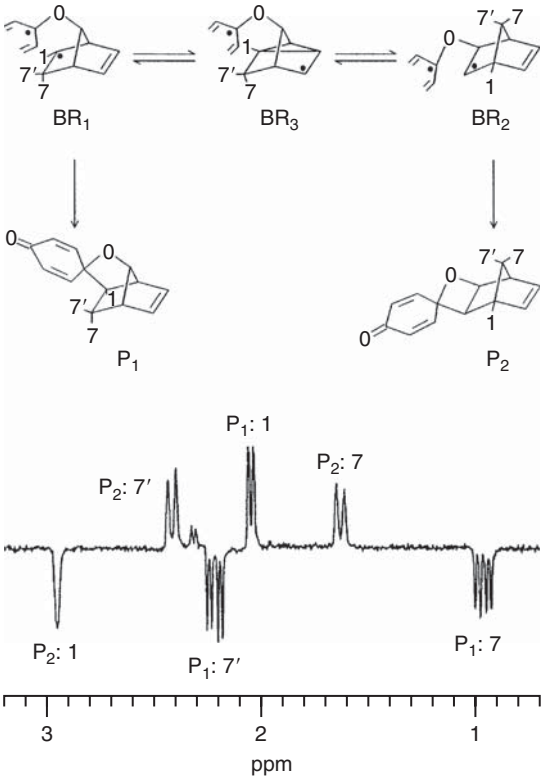

Figure 20 *Polarizations of protons 1, 7, and 7′ as labels in the sensitized photoreaction of quadricyclane with benzoquinone*. The polarizations arise in biradical BR_1. Ring closure of BR_1 yields the product P_1, rearrangement the biradicals BR_3 and BR_2; from the latter, the product P_2 is formed. The CIDNP spectrum is shown at the bottom. Further explanation, see text.

rearrangement occurs on the route from BR_1 to P_2. It is natural to assume that the carbon–hydrogen bonds remain intact in that process, so the CIDNP signal of each proton serves as a label for the carbon atom to which that proton is attached.

All proton hyperfine coupling constants in BR_1 are large enough to give detectable polarizations, but some of the CIDNP signals of P_1 and P_2 overlap and others are best used for corroboration only because of their smallness. Concentrating on the very large ones of H_1, H_7 and $H_{7'}$, the ratios of which are about –2 to +3 to +2.5, one finds that the rearrangement takes H_1, hence the carbon bearing the unpaired electron in BR_1, to a bridgehead position, and the methylene group (H_7 and $H_{7'}$) to the bridge; the less strongly polarized protons (not shown in the spectrum) occupy adjacent positions of the cyclobutane ring in P_2. By tracing the structural changes in such detail, one can immediately identify them as a cyclopropylmethyl-homoallyl rearrangement.

It is seen that a semi-quantitative knowledge of the hyperfine coupling constants (large, medium, or small; positive or negative) suffices for such an analysis even in a case as complex as this. Essentially, all CIDNP investigations of reactions

occurring after the radical-pair stage are based on the principle of using the polarizations as labels, and it would not be overstating the case that this feature of CIDNP is the most frequently exploited one in mechanistic work.

6. RECENT APPLICATIONS OF CIDNP TO CHEMICAL AND BIOCHEMICAL PROBLEMS

6.1. Electron transfer

Electron-transfer induced secondary reactions are included in the respective sections below. Selected examples have been discussed in Ref. 98.

For pairs of neutral radicals, the singlet exit channel is usually the only viable geminate pathway. The situation is very different for radical ion pairs, which frequently undergo geminate reactions such as electron return or biradical formation in the triplet state, and the importance of the triplet exit channel in electron transfer reactions has been emphasized in several recent reviews.[99–102]

Time-resolved CIDNP experiments have been used to measure the rates of the degenerate electron exchange between the radical cation of 1,6-diphenylhexa-1,3,5-triene and its parent compound.[103] A similar study on the 2,2′-dipyridyl radical anion compared the exchange in water and in *β*-cyclodextrin cavities, and came to the conclusion that the rate of nuclear spin relaxation in the free radical ions is significantly enhanced in these microreactors.[104]

PET is the most convenient way to prepare radical ions and use CIDNP to obtain information about their structure. The basis of the identification and structural characterization of intermediates, through the polarization pattern, has been explained above (Section 5.5). Unusual radical cations have continued to attract the attention of CIDNP spectroscopists (Chart 4).

Roth et al.[102, 105–107] concentrated on (mostly rigid) cyclopropane systems. One striking observation has been[105] that the radical cations of *syn*- and *anti*-tricyclo [5.1.0.0^{2,4}] octanes **1**$^{\bullet+}$ exhibit very different polarization patterns. With the *syn*-isomer, spin and charge are delocalized through the lateral bonds of the cyclopropane rings, which are lengthened and weakened, while with the *anti*-isomer the evidence seems to indicate a structure with spin and charge localized in the inner bonds. Even more unusual are the radical cations of phenylcyclopropanes **2**$^{\bullet+}$, which are characterized by the two bonds connected to the benzylic position being weakened, i.e. resemble a π complex.[107]

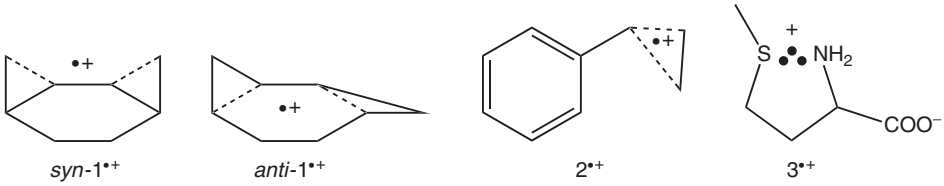

syn-1$^{\bullet+}$ *anti*-1$^{\bullet+}$ 2$^{\bullet+}$ 3$^{\bullet+}$

Chart 4

At least in liquid solution, the radical cation of methionine $\mathbf{3}^{\bullet+}$ is too short-lived for EPR detection. Photo-CIDNP experiments allowed the first characterization of the spin-density distribution in this elusive species.[108] The polarization pattern provides direct evidence for the two-centre three-electron bond between sulphur and nitrogen.

Photo-CIDNP experiments have also been used as additional evidence for the intermediacy of the radical cation of bicyclo[4.2.0]octa-2,4,7-triene upon oxidation of *anti*-tricyclooctadiene,[109] and for σ-bishomoconjugation in the four-centre three-electron radical cation of a [1.1.1.1] pagodane.[110,111]

6.2. Hydrogen abstraction

Sensitized hydrogen abstractions from tertiary aliphatic amines DH (for two recent reviews, see Refs. 112 and 113) were the first application of the polarization pattern to the identification of intermediates.[94] This approach revealed the involvement of amine radical cations $DH^{\bullet+}$, e.g. $>N^{\bullet+}-CH_2-CH_3$ and α-amino alkyl radicals D, e.g. $>N-CH^{\bullet}-CH_3$ in the reactions. Their distinction by ^{1}H-CIDNP net effects is extremely clear-cut even without knowledge of the precursor multiplicity, the exit channel, and the sign of Δg: The radical cations have significant hyperfine couplings only for the α protons, so only the α protons acquire polarizations while the β protons remain unpolarized; the neutral radicals exhibit large hyperfine coupling constants of opposite signs for the α and β protons, so an up/down or down/up pattern results for those two sorts of protons.

The radical cation and the neutral radical form an acid/base pair. Even if only the radical-cation polarization pattern is observed, deprotonation is an essential step because the neutral radical is the direct precursor to the products. Two parallel deprotonation pathways were identified.[114] The proton is removed from the radical cation either within the cage, i.e. by the sensitizer radical anion, or outside the cage, the base in this case being surplus amine. The latter assumption was corroborated by EPR measurements.[115] The second pathway involves only free radicals, so cannot produce new CIDNP but transfers existing CIDNP (of the radical-ion type) to the neutral radicals and their subsequent products. However, the first pathway yields a new radical pair, in which polarizations of the neutral-radical type can be generated in addition to the already existing ones of the radical-ion type. For triethylamine, the whole mechanism is displayed in Chart 5. Observation most conveniently focuses on the very characteristic signals (see, bottom trace of Figure 1) of *N*,*N*-diethylvinylamine **V.**

There is a pronounced dependence of the polarization pattern on the sensitizer[114] and the solvent,[116] which runs in parallel with the free enthalpy of the in-cage deprotonation and shows a threshold behaviour. Within a range from about –90 to about –130 kJ mol^{-1} a complete changeover of the polarization pattern occurs. On the negative side of this transition regime the neutral-radical pattern is exclusively observed, on the positive side exclusively the radical-cation pattern. This was rationalized by the kinetic window for CIDNP generation in the radical ion pair, which is set by the rates of intersystem crossing and escape. If the rate of in-cage deprotonation falls outside this window on the slow side, the radical ion pairs

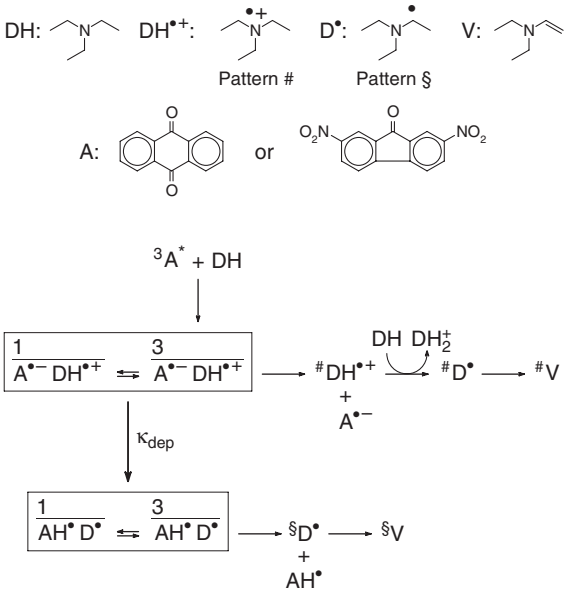

Chart 5

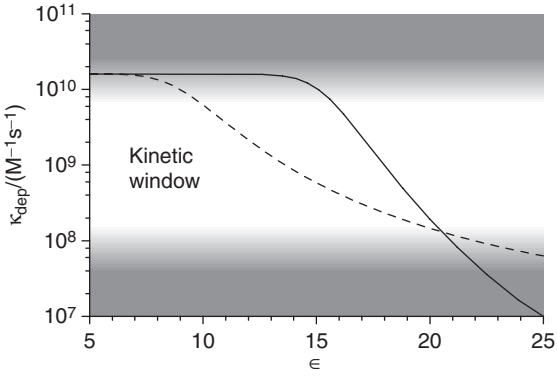

Figure 21 *CIDNP investigation of the in-cage deprotonation of the triethylamine radical cation by the radical anion of 9,10-anthraquinone (solid line) and 2,7-dinitrofluorenone (broken line).* The graph shows the deprotonation rate constant k_{dep} as function of the relative permittivity of the solvent. The shaded areas denote the approximate boundaries of the kinetic window accessible by the CIDNP experiments. Further explanation, see text and Chart 5. Reproduced from Ref. 60 with permission; copyright (2003) American Chemical Society.

either undergo reverse electron transfer or escape before the radical cation can be deprotonated by the radical anion, so no polarizations other than of the radical-ion type can arise; if that rate is on the fast side on the window, the radical ions are deprotonated so rapidly that they cannot acquire polarizations before their

conversion into a pair of neutral radicals, and during the life of those secondary radical-pairs polarizations of the neutral-radical type are then generated.

A quantitative theory describing these processes was developed and applied to the photoreactions of triethylamine with the sensitizers 9,10-anthraquinone and 2,7-dinitrofluorenone.[60] Rate constants of the in-cage deprotonation were extracted from the solvent dependence of the polarization pattern. Figure 21 displays the results and reveals the influence of the solvent polarity and the sensitizer, through its redox potential. The kinetic window accessible with this method is seen to span about two orders of magnitude in a chemically very important range, namely, near diffusion control.

The radical cations of aliphatic sulphides are more acidic than are those of tertiary aliphatic amine, so in-cage deprotonation is faster with the sulphur compounds. Hence, the rate of this key process is shifted outside the kinetic window of CIDNP, and polarizations in sensitized hydrogen abstractions from sulphides usually only exhibit the pattern of the α-thio alkyl radical; only if the energy of the radical ion pair is made very low by choosing a sensitizer that is very easily reducible (benzoquinone) and a very polar solvent (water) can the pattern of the radical cation be observed.[117] Hydrogen abstraction from steroids by substituted benzoquinones also proceeds through electron transfer to the excited triplet state of the sensitizer as the first step,[118] whereas the CIDNP signals only respond to the pair of neutral radicals in the photoreactions of 1-acetylindole-2,3-dione with several hydrogen donors.[119]

Isotope effects in hydrogen abstractions from cyclohexane were studied by the concentration dependence of CIDNP for mixtures of protiated and perdeuterated

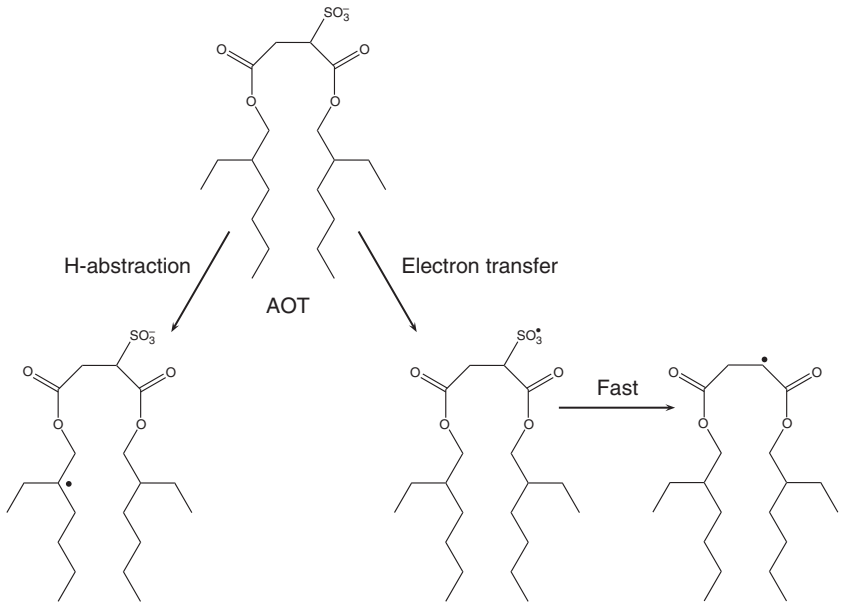

Chart 6

benzophenones, and explained by energy transfer between the two isotopologues.[120]

The rich photochemistry of the surfactant AOT (see Chart 6) with the sensitizer 2,6-anthraquinone disulphonate has been unravelled[121] by the combined use of time-resolved EPR and CIDNP experiments, the motive for that investigation being that AOT is frequently used in industrial applications of photoredoxreactions carried out in microemulsions. The polarization patterns gave clear evidence for the competition of hydrogen abstraction from the tertiary carbons on one hand and dissociative electron transfer from the sulphonate group on the other hand; the elimination of SO_3 from the primarily formed sulphur-centred radical is fast on the CIDNP timescale, hence the polarizations of that reaction channel are exclusively generated in the resulting alkyl radical. CIDNP results also indicate hydrogen abstraction by 2,6-anthraquinone disulphonate from another microreactor, *β*-cyclodextrin.[122]

6.3. Fragmentations

Applications of CIDNP to the study of photoinitiators have recently been reviewed.[123,124]

6.3.1. α-Cleavage of carbonyl compounds

Carboxylic esters of α-hydroxymethylbenzoin[125] and *O*-acyl 2-oximinoketones[126] were investigated by photo-CIDNP. These two classes of polymerization initiators were found to undergo α-cleavage through the triplet state of the carbonyl and the carbonyl-analogous functional group, respectively, as the first step. A variety of other radical pairs was identified in these reactions, most of which have to be ascribed to the secondary photochemistry of the products rather than to pair substitution because continuous illumination with a 1000 W high pressure arc lamp was used.

Mono- and bisacylphosphine oxides **4** and **5** (Chart 7) are efficient photoinitiators for radical polymerizations. Their photochemistry was studied by ^{1}H-, ^{13}C-, and ^{31}P-CIDNP spectroscopy.[18] The primary step is the breaking of the bond between the carbonyl group and phosphorous in a triplet state; for the bisacylphosphine oxides, a stepwise cleavage occurs.

An interesting stereo-electronic effect was found for the two isomeric ketones *endo*-**6** and *exo*-**6** (Chart 7).[127] With the *exo*-isomer, the carbonyl and alkene moieties are isolated from each other, the compound undergoes α-cleavage accompanied by CIDNP effects, and is a good initiator for radical polymerizations. In contrast, the

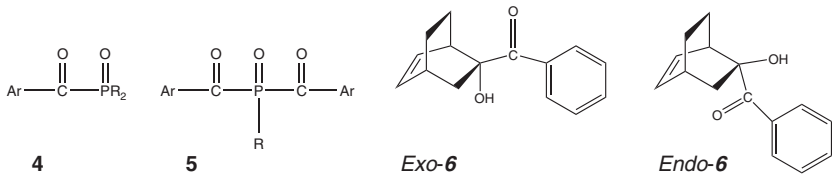

4 **5** *Exo*-***6*** *Endo*-***6***

Chart 7

geometry of *endo*-**6** leads to preferential deactivation by an intramolecular Paterno–Büchi reaction. This strongly suppresses α-cleavage, so this isomer exhibits no polarizations and a poor curing efficiency.

The photochemistry of three thioxanthone-initiator dyads with carbonyl functions in the initiator moieties was compared by CIDNP and complementary techniques.[128] Expectedly, the triplet–triplet energy gap determines the readiness of the molecule to undergo α-cleavage after intramolecular energy transfer. However, intramolecular electron transfer can also occur as a competing reaction and leads to dehydrogenation of the initiator part.

In the α-cleavage of dibenzyl ketone, twice as low polarizations of the escape product $(PhCH_2)_2$ were found in *β*-cyclodextrin microreactors as compared to homogeneous phase.[129] The authors explained this in the same way as for the 2,2′-dipyridyl radical anion[104] (see Section 6.1), by a significantly higher relaxation rate in the inclusion complex.

6.3.2. *β*-Cleavage and related reactions

The classification as πσ* photodissociations of such seemingly unrelated reactions as the *β*-cleavage of aromatic ketones (see the example of Section 5.2), the photo-Fries rearrangement, and the photo-Claisen rearrangement is a relatively new concept in photochemistry.[130] In striking contrast to the α-cleavage of carbonyl compounds, these photodissociations depend neither on the orbital character nor on the multiplicity of the excited state. The ability to deduce the reacting state from the polarization phase makes CIDNP very valuable for addressing the latter issue. A corroborative photo-CIDNP investigation of the photodissociation of arylethers and arylthioethers, which was complemented by sensitization, triplet quenching, and radical scavenging experiments, showed that cleavage of the carbon–oxygen and carbon–sulphur bond invariably is the first step of the photoreaction and occurs for both multiplicities, with the singlet gaining preference at elevated temperatures.[131]

Another study,[132] on the photo-Fries rearrangement of 1-naphthylacetate, gave a contradiction between the results of laser flash photolysis and measurements of quantum yields, which revealed cleavage from the singlet state to be dominant, and photo-CIDNP experiments, which displayed polarizations resulting from triplet radical pairs; furthermore, the addition of a triplet quencher decreased the polarizations much more than the quantum yields of product formation. The authors resolved that puzzle by assuming the involvement of a higher triplet state that is populated by a two-photon process under the intense illumination of the CIDNP experiment, and yields intrinsically stronger polarizations than the singlet precursor. In a later reinvestigation, they explained their findings by intersystem crossing from the first excited singlet state to a higher excited triplet state which has a lifetime of a few nanoseconds.[133]

6.3.3. Peroxides

CIDNP results have also been taken as evidence for the participation of different electronic states in the photolysis of acetylpropionyl peroxide,[134–136] while the polarizations in the photoreaction of 3-*tert*-butylperoxy-3-methyl-1-butyne were

explained by a singlet precursor only.[137] From CIDNP data and product yields, the decarboxylation rates of the intermediate acyloxy radicals were determined.[134]

6.3.4. Dissociative electron transfer

Sulfonium cations Ar_3S^+ and iodonium cations Ar_2I^+ are technically relevant initiators both for radical and cationic polymerizations. CIDNP and other methods were used to study the solvent dependence of their electron-transfer induced cleavage.[138–141] In contrast to usual photoredox systems, electron transfer from an excited sensitizer to these compounds is feasible also in non-polar solvents because it is not a charge separation but a charge shift. Although, therefore, their quantum yields of disappearance were found not to depend very strongly on the solvent, dramatic changes of the CIDNP spectra were observed for the iodonium compounds.[138,140,141] This was explained by pair substitution effects: These reduced initiators cleave to give phenyl radicals and a diamagnetic species (see, Chart 8), and the solvent causes a shift of the rate of this fragmentation with respect to the kinetic window of CIDNP whereas cleavage of the sulfonium salts is intrinsically faster, so falls outside this window at all polarities.[138]

The most peculiar phenomena occurring in the system Ph_2I^+/naphthalene are inversions of all polarizations when (a) the solvent is changed from diethyleneglycol dimethyl ether to chloroform or (b) experiments in dioxane are performed at magnetic fields of 5.9 and 11.7T.[140] The described pair substitution was found to rationalize all the polarization effects within the framework of S–T_0-type CIDNP; invoking S–T_{-1}-type CIDNP as a mechanism of their generation[142] is unnecessary.

Although for sulfonium systems CIDNP experiments cannot capture the radical-pair transformations, they have been instrumental in unravelling the diverse decay pathways of the phenyl radical contained in the second pair.[139]

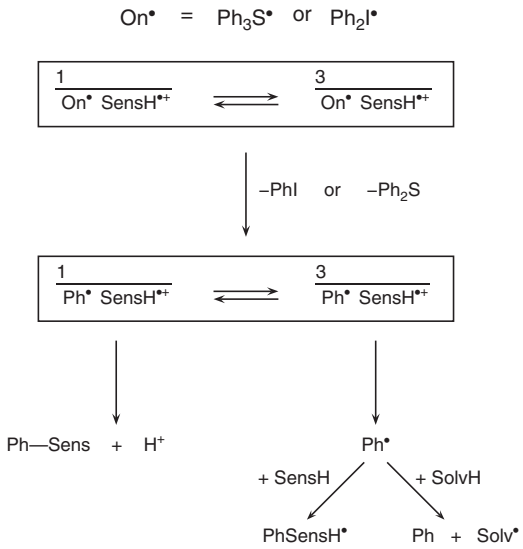

Chart 8

Most important for practical purposes is the result that protic acids, which initiate a cationic polymerization, are efficiently formed by geminate combination of the phenyl radical with the sensitizer radical cation, i.e. via the singlet exit channel, whereas escaping phenyl radicals, the initiators of a radical polymerization, are scavenged very efficiently by surplus sensitizer and less efficiently by the solvent (which is the monomer in a technical application). This suggests that for cationic polymerizations onium salts should be sensitized by singlet sensitizers that are capable of donating a hydrogen atom after oxidation and are employed in high concentration. In contrast, for a radical polymerization triplet sensitizers should be used in low concentration.

Other examples of dissociative electron transfers investigated by CIDNP include one of the two reaction pathways in the reaction of AOT with a quinone[121] (see Chart 6) and the cleavage of 4-(*N*,*N*-dimethylamino)phenyl pinacol in chloroform,[143] which is thought to start with a PET from the substrate to the solvent.

6.4. *cis–trans* Isomerizations and cycloadditions

Geometric isomerizations that occur direct upon excitation or after intersystem crossing are transparent to CIDNP because no radical pairs are involved; the same holds for photocycloadditions of an excited singlet state with a ground-state molecule. The short-chain triplet biradicals that are formed in Paterno–Büchi reactions or their analogues are also extremely unlikely to develop CIDNP because of the large value of the exchange integral, although one clear case of strong S–T_0-type CIDNP from a 1,5-biradical in the photocycloadditions of quinones with quadricyclane or norbornadiene is known.[97] This leaves pathways via radical ion pairs as the only pathways from which CIDNP can be expected in isomerizations and cycloadditions.

Three types of species are potential candidates for the isomerization proper[99]:

1. Free radical cations or radical anions of the olefins formed by escape
2. Olefin triplets formed by reverse electron transfer
3. Triplet biradicals formed by a geminate reaction

Although the first case puts no demands on the energetics because escape is always a feasible process, no direct observation by a time-resolved CIDNP experiment seems to have been successful so far; instead, it has repeatedly been reported that time-resolved photo-CIDNP experiments showed olefin radical cations or anions to be configurationally stable.[89,116,144,145] The second and third cases are obviously only possible if the energy of the olefin triplet or the biradical lies below the energy of the radical ion pair.

Following ideas originally put forward by Roth et al.,[146,147] the different types of CIDNP effects that systems composed of an olefin M and a sensitizer S can produce in the absence of biradical formation have recently been classified systematically as a function of the energetics (see, Chart 9), and examples for each category have been provided.[89] Only transient polarizations occur for class Ia and Ib because of exchange cancellation (Figure 18 is an example of class Ia); such systems can be used to probe by time-resolved CIDNP experiments whether or

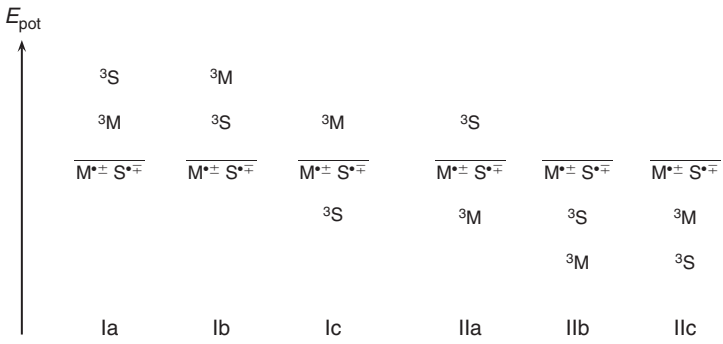

Chart 9

not the radical ions of the olefin isomerize. Neither permanent nor transient polarizations result for class Ic because a geminate reaction is possible for the singlet and the triplet pairs; since this regenerates the olefin in its ground state through both exit channels, the polarizations cancel on the timescale of the radical-pair life, so are not detectable even by a time-dependent CIDNP experiment.

Class IIa produces strong permanent polarizations of opposite phase but equal magnitude for the *cis*- and the *trans*-olefin even if the isomerization of the triplet state does not give both isomers in equal yields: The isomerized olefin receives a fraction x of the polarization of the triplet exit channel, the starting olefin receives both a fraction $1 - x$ through this channel and the complete polarization of the singlet exit channel (i.e. –1), which partly compensates and leaves a polarization $-x$ for it. This characteristic feature of the olefin polarizations remains with classes IIb and IIc but a part of the polarizations is now lost through the same process as in class Ic. Systems of class IIb can be used to study the competition between reverse electron transfer regenerating the olefin or regenerating the sensitizer; class IIc is particularly useful for PET sensitization experiments, as no polarizations are detectable if the sensitizer has a very low-lying triplet state but can be made visible upon addition of a third component (compare, Figure 15).

Other recent examples of CIDNP studies on olefin isomerizations via reverse electron transfer populating the triplet, which all fall into class IIa, concerned all-*trans* retinal with stilbene as donor or a quinone as an acceptor,[148] and α, β unsaturated ketones with triphenylamine or triphenylphosphine as donors[149,150] or pyrene as acceptor.[151]

As a rule, isomerizations via the triplet state are bidirectional, i.e. lead to similar amounts of the *cis* and the *trans* olefin regardless of what the configuration of the starting olefin was, because the reduction of the bond order to 1 in the triplet causes the substituents to adopt a perpendicular orientation to minimize steric strain. This is in sharp contrast to isomerization via formation of a triplet biradical followed by intersystem crossing and scission of the singlet biradical, which occurs in competition with cycloadduct formation. In this case, steric interactions in the biradical will normally favour a configuration that yields the *trans* olefin.

By photo-CIDNP experiments, the interplay of isomerization and cycloaddition in the system *trans*-anethole/fumarodinitrile has been unravelled.[144] In this system, both isomerization pathways are operative, but can be separated by CIDNP. The results show that the efficiency of biradical formation is about twice as high as that of reverse electron transfer of triplet pairs, which was explained by the low driving force of the latter reaction, and that there is no strong preference for ring closure of the singlet biradicals as opposed to scission. CIDNP experiments with variation of the fumarodinitrile concentration and the light intensity unexpectedly revealed the presence of a parallel isomerization pathway via a second radical pair, which was identified as stemming from a photoionization of the anethole. This example illustrates the power of CIDNP to obtain both mechanistic and quantitative information on a complex reaction.

Isomerization via biradicals was also inferred from the CIDNP effects in the photoreaction of β-ionone with chloranil or other electron-deficient quinones,[152] whereas other CIDNP studies concentrated on cycloadduct formation, between 1,1-diarylethenes and chloranil[153] and between arylacetylenes and quinones.[154]

6.5. Other reactions

6.5.1. Substitution reactions

^{15}N-CIDNP was used to investigate photoinduced nitrations of aromatic compounds ArH with tetranitromethane.[155,156] The polarizations invariably arise from radical pairs $\overline{\mathrm{ArH}^{\bullet+}\mathrm{NO}_2^{\bullet}}$, but the experiments reveal different pathways of formation of these pairs. With a substrate such as 1,2-dimethoxybenzene, the precursor multiplicity is triplet and the pairs are produced by a dissociative electron transfer from the aromatic compound to tetranitromethane, which then cleaves into an $\mathrm{NO}_2^{\bullet}$ radical and $\mathrm{C(NO_2)_3^-}$. In contrast, the very similar substrate anisole (methoxybenzene) exhibits polarizations indicating a singlet precursor, and the radical pair is thought to be formed by decomposition of a preceding unstable diamagnetic intermediate, most probably a nitro-trinitromethyl adduct.[156]

6.5.2. Addition reactions

To study the addition of 2-hydroxy-2-propyl radicals to alkenes, Batchelor and Fischer[157] employed a ketone as the source of these radicals, which then develop multiplet polarizations from F-pairs; the normal reaction product is isopropanol. The addition of an alkene scavenges some part of the radicals and thus decreases the isopropanol polarizations. Time-resolved CIDNP experiments yield the addition rate. The advantage of analysing multiplet CIDNP instead of net CIDNP is that relaxation effects are avoided. The method was reported to be applicable for scavenging rate constants between $10^5\,\mathrm{M^{-1}\,s^{-1}}$ and $10^9\,\mathrm{M^{-1}\,s^{-1}}$.

Older work on reversible radical additions to aromatic systems has been reviewed in Ref. 158.

CIDNP was used as additional evidence in investigations of the photooxygenation of acenaphthenone sensitized by dicyanoanthracene.[159,160] The authors proposed that a radical ion pair is formed as the first step, then undergoes

a keto-enol tautomerization, and finally recombines with $O_2^{-\bullet}$ produced by electron transfer from the sensitizer radical anion.

6.5.3. Photoionizations

The CIDNP phases and polarization pattern in the photoionization of the 5-sulfosalicylic acid dianion in aqueous solution indicate a singlet precursor and are consistent with a radical pair consisting of the hydrated electron and the monoanion (i.e. radical anion) of the substrate.[161]

Photoionization also occurs in the already mentioned photoreactions between *trans*-anthole and fumarodinitrile.[144] In this case, the electron is immediately scavenged by the solvent to give a monomeric or dimeric anion of acetonitrile, which constitutes the second radical of the pair. The precursor multiplicity is again singlet, and CIDNP experiments with varying laser intensity show the ionization to be a two-photon process.

6.5.4. Radical–radical reactions

Scavenging of a spin-polarized escaping radical by a stable radical has received some attention.

A ''persistent radical effect'' is found if the cleavage of a molecule yields two radicals of which only one undergoes self-termination (i.e. recombination with a like radical) while the other does not and only decays by cross-termination (i.e. recombination with the other radical). As a consequence of this behaviour, there is a self-regulating effect on the reaction rates, and unusual kinetics result.

In the photoinduced cleavage of *N*-alkoxyamines, where the transient and the persistent radical are an alkyl and an aminoxyl radical, Fischer et al. used time-resolved CIDNP to clarify the mechanism of cross-termination and to determine the rate constant of the recombination.[162] They concluded that disproportionation plays no role in this system, and that no unknown side reactions occur. Later, Ananchenko and Fischer compared the recombinations of the transient *tert*-butyl and 2-hydroxy-2-propyl radicals with the stable radical TEMPO.[163] They were able to show that the former radical reacts by a simple coupling while the latter reacts by an electron transfer followed by a proton transfer. Disproportionation was also found to be absent in reactions of ester-substituted alkyl radicals with nitroxides.[164,165]

6.6. Biradicals

Flexible biradicals have been discussed in Section 3.5 because the pertaining investigations were predominantly concerned with the CIDNP effect *per se.*

The semi-flexible 1,5-biradical BR_1 (see Figure 20), which is the key intermediate in Paterno–Büchi photocycloadditions of benzoquinone with norbornadiene or quadricyclane, is very unusual as it exhibits strong and exclusive S–T_0-type CIDNP. Although this might partly be due to a reduction of the exchange interaction because of the perpendicular orientation of the orbitals bearing the unpaired spins, the main reason is the existence of an escape reaction:[97] The rearrangement of BR_1 to the 1,4-biradical BR_2 via the intermediate BR_3 is spin-independent, and BR_2, being a Paterno–Büchi biradical, undergoes extremely fast intersystem crossing by

spin–orbit coupling followed by collapse of the singlet biradical to give an oxetane; hence, BR_2 acts as a multiplicity-independent chemical sink. The ratio of the nuclear spin polarizations in the oxolane P_1 (singlet exit channel) and in the oxetane P_2 (multiplicity-independent exit channel) strongly depends on temperature, which was interpreted by the competition of the rearrangement with nuclear spin relaxation in BR_1. By a kinetic treatment, a closed-form expression for the polarization ratio was obtained, and the activation energy of the cyclopropylmethyl-homoallyl rearrangement was determined.[166]

Fischer et al.[167–169] investigated rigid biradicals resulting from photoinduced intramolecular charge separation[170] in dyads D–spacer$_n$–A (see, Chart 10). The reaction scheme is extremely similar to the intermolecular analogue shown in Figure 17. Excitation of the donor moiety (dimethoxynaphthalene) followed by quenching by the acceptor moiety (dicyanoethylene) produces a singlet biradical$^{+\bullet}$D–spacer$_n$–A$^{\bullet-}$. Reverse electron transfer is feasible for both multiplicities of the biradical, the singlet exit channel regenerating the ground-state dyad D–spacer$_n$–A direct, and the triplet exit channel indirect by first producing a locally excited triplet state D–spacer$_n$–^{3}A which then deactivates to the ground state. Nevertheless, in high fields S–T_0-type transient polarizations are observable because the polarizations of the triplet exit channel are hidden in D–spacer$_n$–^{3}A for a time on the order of 10μs, so a time-resolved CIDNP experiment can be used to probe the instantaneous polarizations of the singlet exit channel and their gradual disappearance by cancellation. The fact that the reactions are intramolecular even facilitates the kinetic analysis,[167] as no free radical ions can be formed.

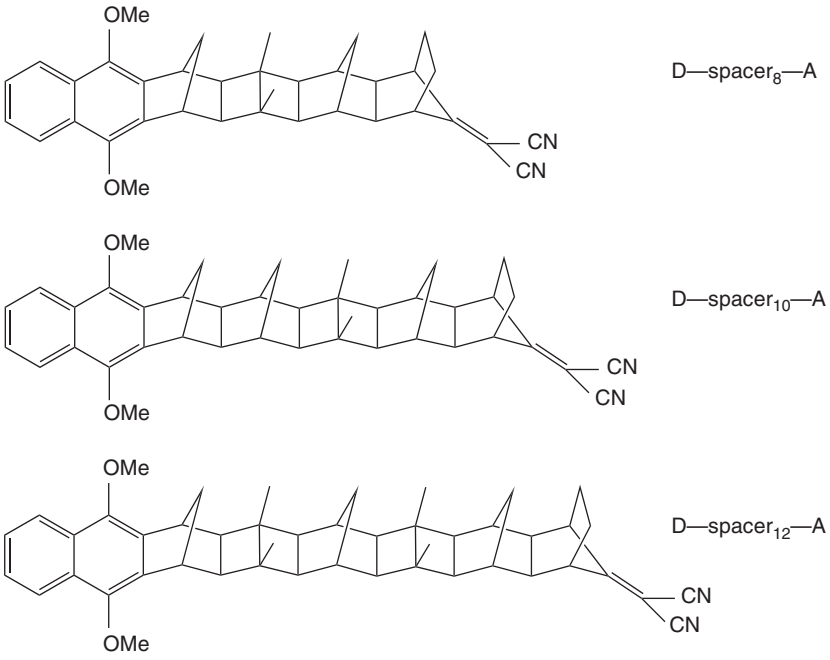

Chart 10

Field-dependent CIDNP experiments in low magnetic fields[168,169] reveal that CIDNP is of the comparatively rare S–T_{+1}-type. The curves exhibit the bell-shaped behaviour typical for intersystem crossing at a level intersection, which has long been known for biradicals with a polymethylene chain. However, the rigidity of the dyads removes a complication present in flexible biradicals, namely, that the CIDNP experiment weighs certain conformations and distances between the radical termini more heavily than others.[171] Hence, in the dyad experiments the value B_0 at which the extremum of the field-dependence occurs corresponds directly to the condition $g\beta B_0 = 2|J|$. An exponential dependence of J on the spacer length n was found with a damping factor of about $0.75 Å^{-1}$, which is comparable to that in other biradical systems.

CIDNP was also used as additional evidence for the characterization of the photoprocesses in a steroid-linked norbornadiene-carbazol dyad.[172]

6.7. Inorganic and metal organic substrates

Most efforts in this relatively narrow area have focussed on the reactions of the heavier carbene analogues Me_2Si and Me_2Ge, which are conveniently obtained by photolysis of sila- and germanorbornadienes **7** (Chart 11). Typical reactions of them producing CIDNP effects are chlorine abstractions from a suitable substrate such as CCl_4 to give a radical pair,[173–179] or attack to surplus molecules **7**.[175–179] The polarizations in the latter case are thought to arise from a 1,6-biradical of structure **8**, which can also be prepared by cleavage of the reaction product 7,8-digermabicyclo[2.2.2]octadiene **9**.[177] Most studies conclude that the precursor multiplicity is triplet[175–179] although a singlet precursor to the radical pairs was also reported.[173]

CIDNP was observed in the halophosphination of phenylacetylenes and diphenylethylenes;[180] other studies of phosphorous-containing compounds were concerned with the polarization mechanism rather than with the chemistry (see Section 3.5).

Norrish-I cleavage of 2-methylpropanoyltripropylstannane $Pr_3SnC(O)iPr$ affords the expected spin-polarized products.[181] A much more complex

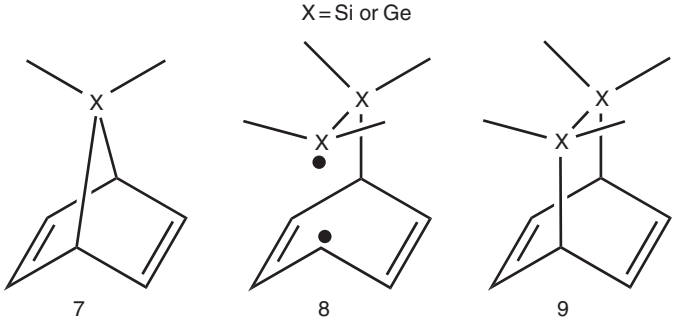

Chart 11

secondary chemistry occurs in the reactions of *N*-bromohexamethyldisilazane $(Me_3Si)_2NBr$ with substrates of the type $R_3MCH_2CH{=}CH_2$ (M=Si or Sn). The primary step is fragmentation of the N–Br-bond, the polarizations are thought to originate in F-pairs, and product formation by chain reactions has been discussed.[182,183] In contrast, the photoreaction of dodecamethyl-cyclohexasilane $(Me_2Si)_6$ with 9,10-phenanthraquinone was shown to proceed by a simple electron transfer to give radical ion pairs in a triplet state.[184]

6.8. Amino acids

There has been a strong but very selective interest in CIDNP on amino acids, strong because of the importance for the application of CIDNP to proteins (see Section 6.9), and very selective because only three amino acids (tryptophan **10**, tyrosine **11**, and histidine **12**, compare Chart 12; for their CIDNP spectra, see Ref.185) are routinely useable for that purpose while two others, cysteine **13** and methionine **14**, have received attention because of their putative role for long-range electron transfer across cell membranes or oxidative damage of cell components.

The complex photochemistry of cysteine derivatives sensitized by 4-carboxybenzophenone **15** has been unravelled by CIDNP.[96] The initially formed sulphur-centred (see, Figure 19) radical decarboxylates rapidly to give an α-amino alkyl radical, which in turn cleaves into a thiyl radical R–S$^\bullet$ and a vinylamine in competition with being oxidized to an imine by surplus sensitizer; all these resulting species are unstable themselves and undergo further reactions. The rates of the radical fragmentations and the radical oxidation were obtained from the CIDNP experiments.

Methionine adds another degree of complexity because the radical cation, which is formed by the same pathway as in the cysteine case, namely, by exclusive electron transfer from sulphur, can stabilize by the formation of a cyclic structure with a two-centre three-electron bond between sulphur and nitrogen. CIDNP has provided unequivocal evidence for this species and allowed to probe its spin distribution, through the polarization pattern.[108] Only an unprotonated amino group can function as a donor and effect the cyclic stabilization, so there is a pronounced dependence of the polarization pattern on the pH.[58,108] This pH-dependence was explained by a reversible pair substitution of the open-chain and cyclic radical cations,[58] but later reinterpreted as arising from a fast (on the CIDNP timescale) equilibrium between the different forms in conjunction with degenerate electron exchange.[186]

The chemistry underlying the polarization processes of tryptophan, tyrosine, and histidine (electron transfer for the first two amino acids, hydrogen transfer for the third) has long been known.[187] For the frequently used sensitizer 2, 2′-dipyridyl **16**, the kinetics of the quenching by tryptophan,[188] tyrosine,[189] and histidine[190] have recently been studied in detail by time-resolved CIDNP experiments; the effects of added surfactants on the polarizations of tyrosine with flavins **17** or other sensitizers have been investigated.[191] Several low-field CIDNP investigations of the field-dependence have been carried out, with a view to optimizing

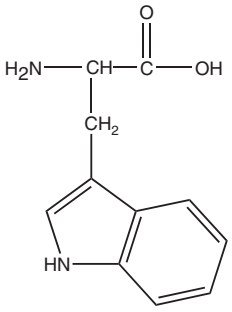

10

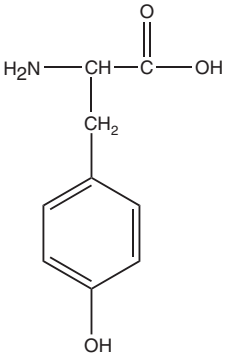

11

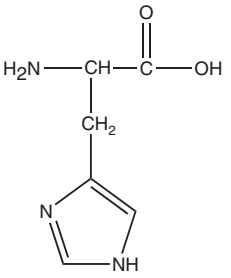

12

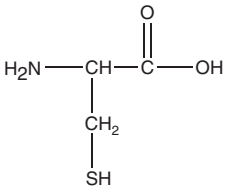

13

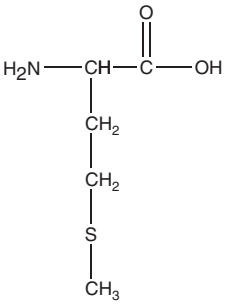

14

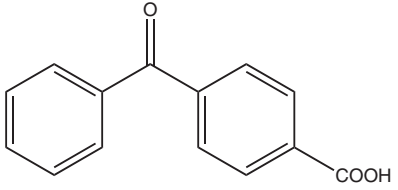

15

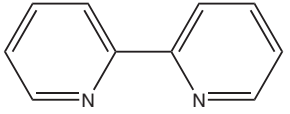

16

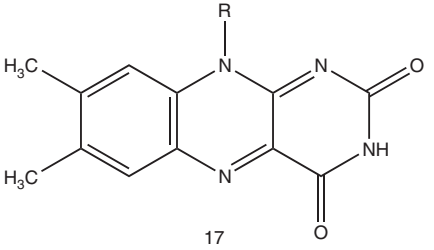

17

Chart 12

the conditions for protein CIDNP,[82,192] to determining the magnetic parameters of the amino-acid derived radicals,[80] and to refining the calculational procedures.[86,193]

6.9. Proteins

The determination of surface accessibilities in a protein is by now a well-established application of photo-CIDNP. Its operating principle is that a sensitizer in the bulk solution is photoexcited, forms a radical pair with an amino acid that is exposed to the solution, and so causes CIDNP to arise; amino acids not accessible to the dye remain unpolarized. To avoid disruptions of the structure the photoreaction(s) must be cyclic. As this leads to exchange cancellation, one either observes the polarizations that remain because of relaxation in the free radicals or samples the geminate polarizations in a time-resolved CIDNP experiment. The latter appears preferable for quantitative conclusions as it also removes other artefacts,[194,195] but cannot be applied to the pulse-labelling and related experiments described below. Commonly employed dyes are 2, 2′-dipyridyl **16** or flavins **17**. As already mentioned in the preceding section, only tryptophan **10**, tyrosine **11**, and histidine **12** are polarizable. However, the reduction of the information content in a crowded protein spectrum by this selectivity is a much desired blessing rather than a drawback.

There are three caveats when one forms structural hypotheses on the basis of the observed CIDNP signals. First, the polarization intensity of a residue is not simply a constant that is specific for that particular amino acid but is subject to a Stern-Volmer competition of all accessible residues for the excited dye molecules,[196] so CIDNP of an accessible amino acid can be suppressed by other accessible amino acids that are more reactive; that problem is most pronounced for histidine. Second, in one study surface accessibility as detected by CIDNP was found to depend not only on the location of the amino acid but also to some extent on the nature of the dye;[194] no systematic investigation of this effect with a range of known protein structures has yet been attempted. Third, the radical cation of a tryptophan or tyrosine residue could undergo electron transfer with a nearby tyrosine or tryptophan that is located in the interior of the protein. If this pair substitution causes polarizations of the inner residue to develop, misinterpretations as to the protein structure might obviously result. This problem has attracted considerable attention.[195,197–201] For lysozyme, such an intramolecular electron transfer appears to be more important in the denatured state than in the native state.[195]

Solution structures from CIDNP experiments were compared with crystallographically determined structural parameters,[202,203] and CIDNP, in conjunction with other methods, was used to characterize several unmodified[204–207] and chemically modified[207–212] peptides and proteins in their native states. Structural changes during carbohydrate binding[213–220] or binding of other ligands[221–223] were investigated by CIDNP.

With protein CIDNP now being a universally accepted technique, the interest in its application is shifting more and more towards the denatured state of proteins and towards folding processes. A recent review is provided by Ref.185.

For real-time studies, the protein is subjected to a sudden perturbation that causes refolding, and CIDNP spectra are acquired in rapid succession to monitor the ensuing changes; a very short period of background suppression and laser irradiation (a few milliseconds in total) precedes each acquisition. The time resolution is thus determined by the acquisition time (typically, on the order of a hundred milliseconds). An ingenious combination of two lasers has been employed where a uv laser first releases Ca^{2+} ions from a photolabile chelator, thus inducing refolding, and a visible laser then generates CIDNP in the repetitive acquisition scheme.[224] Despite the great promise of this in situ approach, at present faster perturbations of the protein state can be achieved with the more common stopped-flow injector devices, which have frequently been used for real-time folding studies.[78,225–227]

Several direct CIDNP investigations on denatured proteins have been performed,[205,212,228,229] but there is the general problem of broad peaks and poor spectral dispersion caused by conformational exchange. To circumvent this, a method that uses the polarizations as labels to detect the accessibility in the denatured state indirectly, through observation of the refolded state, has been devised.[230] For this ''pulse labelling'', the denatured protein is illuminated to develop polarizations, and then a refolding solution is injected rapidly (or, alternatively, the illumination is performed in the injector, which is placed directly above the NMR tube in the bore of the magnet, and the polarized protein then injected into a refolding solution in the NMR tube). Only amino acids that were exposed to the solvent in the denatured state now appear polarized in the spectrum of the native state; their assignment is comparatively easy because that spectrum is much better resolved than that of the denatured state. Several applications of this technique have been reported.[79,230,231]

As an extension, this method was coupled with cross-relaxation (NOE transfer of magnetization) to gain much deeper insight into the structure of the denatured state of an ultrafast folding synthetic miniprotein, TC5b.[232] The experiment is illustrated by Figure 22. The side chain Trp6 is solvent-exposed in the denatured state and acquires CIDNP. Cross-relaxation transfers these polarizations to nearby unpolarized amino acids with an efficiency that depends on the inverse sixth power of the distance. Subsequent injection into a buffer causes complete refolding within the injection time, 50ms, i.e. on a timescale faster than T_1. The signal intensities of the other, normally unpolarizable amino acids in the well-resolved spectrum of the native TC5b are the observables, and allow a quantification of the distances to Trp6 in the denatured state. The method is expected to be generally applicable, provided that a polarizable side chain is present in the denatured state and that refolding of the protein is faster than spin–lattice relaxation of the polarizations.

6.10. Other biologically relevant molecules

Giese et al. investigated the α-cleavage of ketone **18** (Chart 13) as a model of 4′-DNA radical strand cleavage.[233] The observed polarization pattern can only accommodate a radical cation **20**, so the initially formed radical **19** must eliminate $-(EtO)_2PO_2^-$ fast on the CIDNP timescale. This is evidence that anaerobic scission

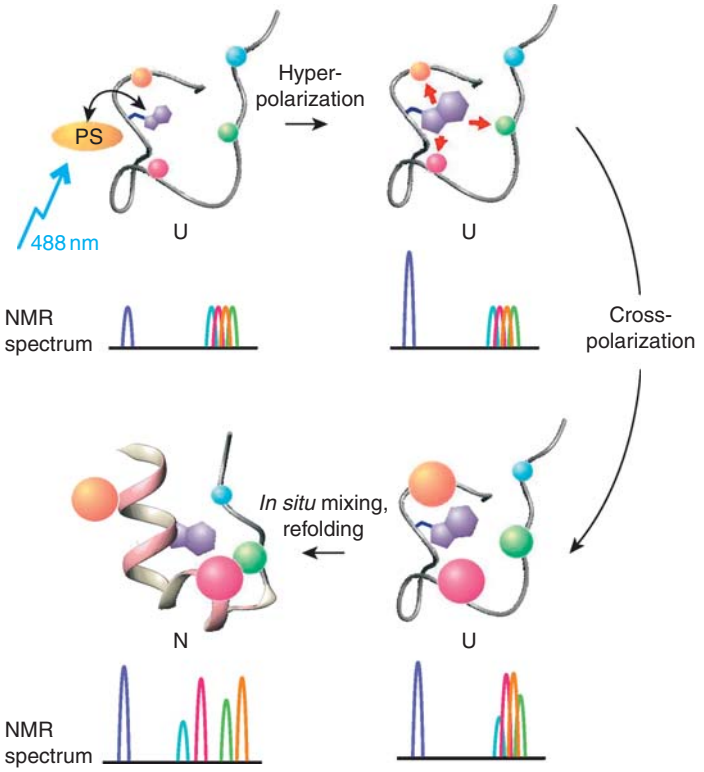

Figure 22 *Schematic description of a structure determination of a denatured protein by combining pulse labelling with NOE*. In the denatured state U, hyperpolarization (CIDNP) is generated in a tryptophan residue by the reaction with a sensitizer PS, transferred to nearby amino acids by cross-relaxation (NOE), and then transferred to the native protein N by fast refolding, where it is observed. Further explanation, see text. Reproduced from Ref. 232 with permission; copyright (2007) Nature publishing group.

of 4′-DNA radicals proceeds by an S_N1-type mechanism. Quenching of triplet tryptophan by several nucleotides was found not to involve radical pairs, the only exception being uridine-5′-monophosphate.[234] As a model of chemical DNA repair, electron transfer from tryptophan and tyrosine to the radical of guanosin monophosphate **21** (Chart 13) was studied.[235–237] Because CIDNP is a much more specific detection method than is optical spectroscopy, the rate constants for the differently protonated radical species derived from **21** could be separated. CIDNP was further used to probe whether the anti-tumour drug UCH9 binds to the major or minor groove of DNA.[238]

Other efforts centred on cobalt complexes modelling coenzyme B_{12},[239,240] photooxidations of NADH analogues **22** (Chart 13),[46,241–243] with emphasis on the calcium antagonist nifedipine (R_1 = 2-nitrophenyl, $R_2 = R_3$ = Me, R_4 = H),[244,245] and photoredox reactions of the natural alkaloid lappaconitin, a sodium channel blocker, or its synthetic analogue anthranilic acid,[246–248] as well as the complexation of these compounds with glycyrrhicic acid,[245,247,249] which increases their therapeutic activity while reducing the toxicity.

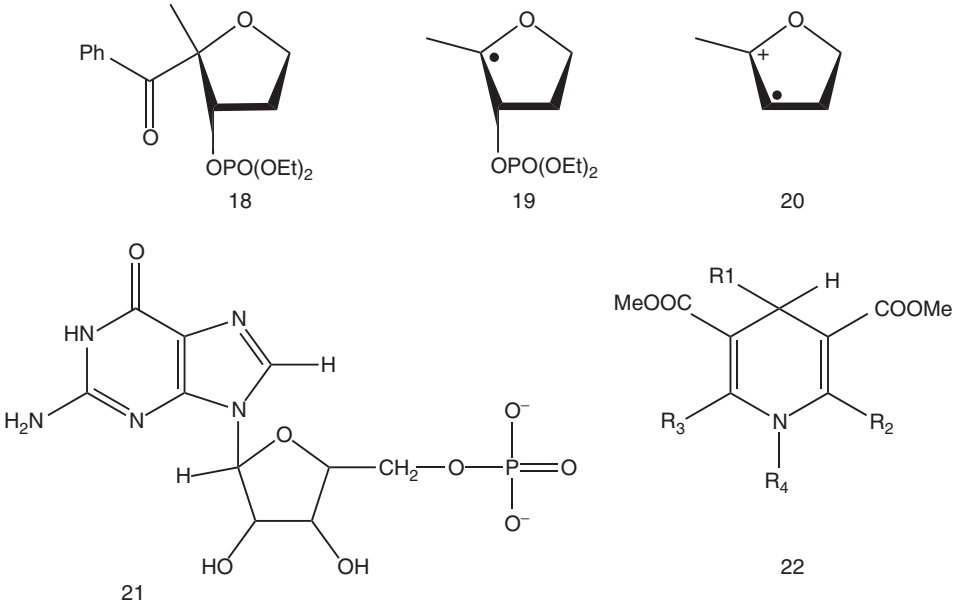

Chart 13

6.11. CIDNP on photosynthetic reaction centres

This field was opened up in 1994 when Zysmilich and McDermott reported strong nuclear spin polarizations in solid-state ^{15}N spectra from photosynthetic reaction centres in which the forward electron transfer from the primary charge-separated state to the accepting quinone had been blocked.[250] It has been rapidly expanding since 1996 when they published two further accounts of their results elucidating the phenomena in more detail,[251,252] and when a group at Leiden University took up that line of research.[253–269]

These reactions are cyclic electron transfers, with the same reaction scheme as in Figure 17 except that no escape (no separation of the radical ions by diffusion) is possible; D corresponds to the special pair and A to a pheophytin. In all cases, CIDNP is of the S–T_0 type but there are three competing mechanisms of CIDNP generation, the relative amounts of which strongly depend on the chemical and magnetic parameters of the system:

1. The differential relaxation mechanism[270]
   This is basically the mechanism described for the dyads of Section 6.6. Spin sorting occurs in the usual way but would be undone by the fact that singlet and triplet exit channels lead to the same product. If, however, the triplet is long lived (e.g. some 100μs in reaction centres of *Rhodobacter sphaeroides* P26), a part of its nuclear spin polarizations is destroyed by relaxation, so the cancellation is not perfect, and CIDNP of the singlet exit channel dominates.

2. The three-spin mixing mechanism[271,272]
   This has no equivalent in CIDNP in solution. With this mechanism, electron-spin polarization is first generated, and then converted into a net nuclear spin polarization by the anisotropy of the hyperfine interaction.
3. The differential decay mechanism[273]
   This again has no parallel in liquid-phase CIDNP. It is based on a coherent process in correlated radical pairs, without the involvement of electron-spin polarizations but again with the anisotropy of the hyperfine interaction playing a major role; different lifetimes of the singlet and triplet pairs break the symmetry of the spin evolution.

An in-depth comparison of the last two mechanisms has been given, and sign rules similar to Kaptein's rules have been formulated for them.[274]

A more detailed discussion of this still young branch of CIDNP is outside the scope of this review but its great potential and promise for the study of photosynthetic reaction centres at the atomic and molecular level are obvious.

7. CONCLUSIONS

Although photo-CIDNP spectroscopy has come of age by now, new applications still arise. As has emerged, the CIDNP effect connects diffusion, chemical reactivity, and spin evolution in a unique way; it also combines the analytical potential of NMR spectroscopy with a sensitivity to species as short-lived as a nanosecond or even less. Hence, photo-CIDNP spectroscopy provides very diverse and deep insight into both chemical and physical processes, and yields information that is often inaccessible by other techniques. A method as powerful and versatile as this certainly deserves to be more widely known, and more frequently applied.

REFERENCES

1. J. Bargon, H. Fischer and U. Johnsen, *Z. Naturforsch. A*, 1967, **22,** 1551–1555.
2. H. R. Ward and R. G. Lawler, *J. Am. Chem. Soc.*, 1967, **89,** 5518–5519.
3. J. Bargon, *Helv. Chim. Acta*, 2006, **89,** 2082–2102.
4. R. Kaptein and L. J. Oosterhoff, *Chem. Phys. Lett.*, 1969, **4,** 195–197.
5. G. L. Closs, *J. Am. Chem. Soc.*, 1969, **91,** 4552–4554.
6. U. E. Steiner and T. Ulrich, *Chem. Rev.*, 1989, **89,** 51–147.
7. M. Goez, *Adv. Photochem.*, 1997, **23,** 63–163.
8. O. W. Sørensen, G. W. Eich, M. H. Levitt, G. Bodenhausen and R. R. Ernst, *Prog. NMR Spectrosc.*, 1983, **16,** 163–192.
9. R. Hany, J. -K. Vollenweider and H. Fischer, *Chem. Phys.*, 1988, **120,** 169–175.
10. S. Schäublin, A. Wokaun and R. R. Ernst, *Chem. Phys.*, 1976, **14,** 285–293.
11. G. L. Closs and R. J. Miller, *J. Am. Chem. Soc.*, 1979, **101,** 1639–1641.
12. R. J. Miller and G. L. Closs, *Rev. Sci. Instrum.*, 1981, **52,** 1876–1885.
13. M. Goez, *Chem. Phys. Lett.*, 1990, **165,** 11–14.
14. F. J. Adrian, *J. Chem. Phys.*, 1972, **57,** 5107–5113.
15. H. R. Ward, *Acc. Chem. Res.*, 1972, **5,** 18–24.
16. R. Kaptein, *J. Chem. Soc., Chem. Commun.*, 1971, 732–733.

17. H. D. Roth, K. C. Hwang, R. S. Hutton, N. J. Turro and K. M. Welsh, *J. Phys. Chem.*, 1989, **93,** 5697–5701.
18. U. Kolczak, G. Rist, K. Dietliker and J. Wirz, *J. Am. Chem. Soc.*, 1996, **118,** 6477–6489.
19. J. A. den Hollander, *J. Chem. Soc., Chem. Commun.*, 1975, 352–353.
20. J. A. Den Hollander, *Chem. Phys.*, 1975, **10,** 167–184.
21. J. A. Den Hollander and R. Kaptein, *Chem. Phys. Lett.*, 1976, **41,** 257–263.
22. J. H. Freed and J. B. Pedersen, *Adv. Magn. Reson.*, 1976, **8,** 1–84.
23. L. Monchick and F. J. Adrian, *J. Chem. Phys.*, 1978, **68,** 4376–4383.
24. J. B. Pedersen, *J. Chem. Phys.*, 1977, **67,** 4097–4102.
25. R. M. Noyes, *J. Am. Chem. Soc.*, 1956, **78,** 5486–5490.
26. L. Monchick, *J. Chem. Phys.*, 1956, **24,** 381–385.
27. K. L. Ivanov, A. V. Yurkovskaya, P. J. Hore and N. N. Lukzen, *Mol. Phys.*, 2006, **104,** 1687–1702.
28. M. Goez and R. Heun, *J. Phys Chem. A*, 2001, **105,** 10446–10453.
29. M. Goez and R. Heun, *Phys. Chem. Chem. Phys.*, 2002, **4,** 5531–5538.
30. V. F. Tarasov, E. G. Bagryanskaya, I. A. Shkrob, N. I. Avdievich, N. D. Ghatlia, N. N. Lukzen, N.J. Turro and R. Z. Sagdeev, *J. Am. Chem. Soc.*, 1995, **117,** 110–118.
31. A. A. Obynochnyi, P. A. Purtov and K. M. Salikhov, *Russ. J. Phys. Chem. A*, 2008, **82,** 298–302.
32. A. A. Obynochny, A. G. Maryasov, P. A. Purtov and K. M. Salikhov, *Appl. Magn. Res.*, 1998, **15,** 259–268.
33. K. Miesel, A. V. Yurkovskaya and H. -M. Vieth, *Appl. Magn. Res.*, 2004, **26,** 51–64.
34. I. V. Koptyug, G. W. Sluggett, N. D. Ghatlia, M. S. Landis, N. J. Turro, S. Ganapathy and W. G. Bentrude, *J. Phys. Chem.*, 1996, **100,** 14581–14583.
35. A. I. Kruppa, M. B. Taraban, N. V. Shokhirev, S. A. Svarovsky and T. V. Leshina, *Chem. Phys. Lett.*, 1996, **258,** 316–322.
36. G. S. Ananchenko, P. A. Purtov, E. G. Bagryanskaya and R. Z. Sagdeev, *J. Phys. Chem. A*, 1997, **101,** 3848–3854.
37. G. S. Ananchenko, P. A. Purtov, E. G. Bagryanskaya and R. Z. Sagdeev, *J. Phys. Chem. A*, 1999, **103,** 3430–3437.
38. G. S. Ananchenko, D. I. Potapenko, P. A. Purtov, E. G. Bagryanskaya and R. Z. Sagdeev, *Appl. Magn. Res.*, 2004, **26,** 65–82.
39. S. V. Dvinskikh, A. V. Egorov and H. M. Vieth, *Appl. Magn. Res.*, 1997, **12,** 465–476.
40. O. B. Morozova, A. V. Yurkovskaya, Y. P. Tsentalovich and H. Vieth, *J. Phys. Chem. A*, 1997, **101,** 399–406.
41. O. B. Morozova, A. V. Yurkovskaya, Y. P. Tsentalovich, R. Z. Sagdeev, T. Wu and M. D. E. Forbes, *J. Phys. Chem. A*, 1997, **101,** 8803–8808.
42. Y. P. Tsentalovich, O. B. Morozova, N. I. Avdievich, G. S. Ananchenko, A. V. Yurkovskaya, J. D. Ball and M. D. E. Forbes, *J. Phys. Chem. A*, 1997, **101,** 8809–8816.
43. O. B. Morozova, Y. P. Tsentalovich, A. V. Yurkovskaya and R. Z. Sagdeev, *J. Phys. Chem. A*, 1998, **102,** 3492–3497.
44. A. Yurkovskaya, S. Grosse, S. Dvinskikh, O. Morozova and H. Vieth, *J. Phys. Chem. A*, 1999, **103,** 980–988.
45. A. V. Popov, P. A. Purtov and A. V. Yurkovskaya, *Chem. Phys.*, 2000, **252,** 83–95.
46. M. S. Afanasyeva, P. A. Purtov, M. B. Taraban, T. V. Leshina and C. B. Grissom, *Russ. Chem. Bull.*, 2006, **55,** 1132–1136.
47. I. M. Magin, V. S. Shevel'kov, A. A. Obynochny, A. I. Kruppa and T. V. Leshina, *Chem. Phys. Lett.*, 2002, **357,** 351–357.
48. S. R. Shakirov, N. V. Lebedeva, V. R. Gorelik, V. F. Tarasov and E. G. Bagryanskaya, *Appl. Magn. Res.*, 2006, **30,** 535–548.
49. Y. P. Tsentalovich, A. A. Frantsev, A. B. Doktorov, A. V. Yurkovskaya and R. Z. Sagdeev, *J. Phys. Chem.*, 1993, **97,** 8900–8908.
50. O. B. Morozova, Y. P. Tsentalovich, A. V. Yurkovskaya and R. Z. Sagdeev, *Chem. Phys. Lett.*, 1995, **246,** 499–505.
51. S. N. Batchelor and H. Fischer, *J. Phys. Chem.*, 1996, **100,** 556–564.
52. I. Kuprov, T. D. Craggs, S. E. Jackson and P. J. Hore, *J. Am. Chem. Soc.*, 2007, **129,** 9004–9013.
53. M. V. Fedin, P. A. Purtov and E. G. Bagryanskaya, *Chem. Phys. Lett.*, 2001, **339,** 395–404.

54. J. Bargon and L. T. Kuhn, *Helv. Chim. Acta*, 2006, **89,** 2522–2532.
55. I. Kuprov and P. J. Hore, *J. Magn. Reson.*, 2004, **168,** 1–7.
56. A. S. Kiryutin, O. B. Morozova, L. T. Kuhn, A. V. Yurkovskaya and P. J. Hore, *J. Phys. Chem. B*, 2007, **111,** 11221–11227.
57. A. V. Popov, P. A. Purtov and A. B. Doktorov, *Appl. Magn. Res.*, 2002, **23,** 149–170.
58. M. Goez and J. Rozwadowski, *J. Phys. Chem. A*, 1998, **102,** 7945–7953.
59. M. Goez and G. Eckert, *Phys. Chem. Chem. Phys.*, 2006, **8,** 5294–5303.
60. M. Goez and I. Sartorius, *J. Phys. Chem. A*, 2003, **107,** 8539–8546.
61. K. L. Ivanov, K. Miesel, A. V. Yurkovskaya, S. E. Korchak, A. S. Kiryutin and H. -M. Vieth, *Appl. Magn. Res.*, 2006, **30,** 513–534.
62. K. Miesel, K. L. Ivanov, A. V. Yurkovskaya and H. -M. Vieth, *Chem. Phys. Lett.*, 2006, **425,** 71–76.
63. A. Parnachev, P. Purtov, E. Bagryanskaya and R. Sagdeev, *J. Chem. Phys.*, 1997, **107,** 9942–9953.
64. M. V. Fedin, E. G. Bagryanskaya and P. A. Purtov, *J. Chem. Phys.*, 1999, **111,** 5491–5502.
65. E. G. Bagraynskaya, N. V. Lebedeva, M. V. Fedin and R. Z. Sagdeev, *NATO Sci. Ser. II*, 2002, **76,** 173–184.
66. M. V. Fedin, E. G. Bagryanskaya, P. A. Purtov, T. N. Makarov and H. Paul, *J. Chem. Phys.*, 2002, **117,** 6148–6156.
67. E. G. Bagryanskaya, V. R. Gorelik and R. Z. Sagdeev, *Chem. Phys. Lett.*, 1997, **264,** 655–661.
68. S. R. Shakirov, T. N. Makarov, E. G. Bagryanskaya and R. Z. Sagdeev, *Phys. Chem. Chem. Phys.*, 2001, **3,** 3672–3676.
69. T. N. Makarov, E. G. Bagryanskaya, S. R. Shakirov, N. N. Lukzen and R. Z. Sagdeev, *Chem. Phys. Lett.*, 2000, **317,** 252–259.
70. N. V. Lebedeva, D. P. Zubenko, E. G. Bagryanskaya, R. Z. Sagdeev, G. S. Ananchenko, S. Marque, D. Bertin and P. Tordo, *Phys. Chem. Chem. Phys.*, 2004, **6,** 2254–2259.
71. I. Kuprov, M. Goez, P. A. Abbott and P. J. Hore, *Rev. Sci. Instrum.*, 2005, **76,** 084103/1–084103/7.
72. I. Kuprov and P. J. Hore, *J. Magn. Reson.*, 2004, **171,** 171–175.
73. M. Goez, K. H. Mok and P. J. Hore, *J. Magn. Reson.*, 2005, **177,** 236–246.
74. M. Goez, I. Kuprov and P. J. Hore, *J. Magn. Reson.*, 2005, **177,** 139–145.
75. M. Goez, I. Kuprov, K. H. Mok and P. J. Hore, *Mol. Phys.*, 2006, **104,** 1675–1686.
76. T. -L. Hwang and A. J. Shaka, *J. Magn. Reson. A*, 1995, **112,** 275–279.
77. M. Goez, *J. Magn. Reson. A*, 1996, **123,** 161–167.
78. K. Maeda, C. E. Lyon, J. J. Lopez, M. Cemazar, C. M. Dobson and P. J. Hore, *J. Biomol. NMR*, 2000, **16,** 235–244.
79. K. H. Mok, T. Nagashima, I. J. Day, J. A. Jones, C. J. V. Jones, C. M. Dobson and P. J. Hore, *J. Am. Chem. Soc.*, 2003, **125,** 12484–12492.
80. C. E. Lyon, J. J. Lopez, B. Cho and P. J. Hore, *Mol. Phys.*, 2002, **100,** 1261–1269.
81. S. Grosse, F. Gubaydullin, H. Scheelken, H. -M. Vieth and A. V. Yurkovskaya, *Appl. Magn. Res.*, 1999, **17,** 211–225.
82. S. Grosse, A. V. Yurkovskaya, J. Lopez and H. Vieth, *J. Phys. Chem. A*, 2001, **105,** 6311–6319.
83. B. Shapira, E. Morris, K. A. Muszkat and L. Frydman, *J. Am. Chem. Soc.*, 2004, **126,** 11756–11757.
84. A. A. Obynochny, A. G. Maryasov, K. A. Il'yasov, O. I. Gnezdilov and K. M. Salikhov, *Appl. Magn. Res.*, 1999, **17,** 609–614.
85. K. L. Ivanov, K. Miesel, H. -M. Vieth, A. V. Yurkovskaya and R. Z. Sagdeev, *Z. Phys. Chem.*, 2003, **217,** 1641–1659.
86. K. L. Ivanov, H. Vieth, K. Miesel, A. V. Yurkovskaya and R. Z. Sagdeev, *Phys. Chem. Chem. Phys.*, 2003, **5,** 3470–3480.
87. K. L. Ivanov and R. Z. Sagdeev, *Doklady Phys. Chem.*, 2006, **409,** 221–223.
88. G. Eckert and M. Goez, *J. Am. Chem. Soc.*, 1994, **116,** 11999–12009.
89. M. Goez and G. Eckert, *Helv. Chim. Acta*, 2006, **89,** 2183–2199.
90. J. R. Platt, *Science*, 1964, **146,** 347–353.
91. S. Grimme and H. Dreeskamp, *J. Photochem. Photobiol. A*, 1992, **65,** 371–382.
92. E. Schaffner and H. Fischer, *J. Phys. Chem.*, 1995, **99,** 102–104.
93. E. Schaffner and H. Fischer, *J. Phys. Chem.*, 1996, **100,** 1657–1665.
94. H. D. Roth and M. L. Manion, *J. Am. Chem. Soc.*, 1975, **97,** 6886–6888.
95. H. D. Roth, *Z. Phys. Chem.*, 1993, **180,** 135–158.

96. M. Goez, J. Rozwadowski and B. Marciniak, *J. Am. Chem. Soc.*, 1996, **118,** 2882–2891.
97. M. Goez and I. Frisch, *J. Am. Chem. Soc.*, 1995, **117,** 10486–10502.
98. M. Goez, *J. Inf. Rec.*, 1998, **24,** 9–22.
99. H. D. Roth, *J. Photochem. Photobiol. C*, 2001, **2,** 93–116.
100. H. D. Roth, *J. Phys. Chem. A*, 2003, **107,** 3432–3437.
101. J. Bargon, *Photochem. Photobiol. Sci.*, 2006, **5,** 970–978.
102. H. D. Roth, *Photochem. Photobiol. Sci.*, 2008, **7,** 540–546.
103. F. Schael and H. -G. Loehmannsroeben, *Chem. Phys.*, 1996, **206,** 193–210.
104. S. S. Petrova, A. I. Kruppa and T. V. Leshina, *Chem. Phys. Lett.*, 2007, **434,** 245–250.
105. T. Herbertz and H. D. Roth, *J. Am. Chem. Soc.*, 1997, **119,** 9574–9575.
106. H. D. Roth, H. Weng and T. Herbertz, *Tetrahedron*, 1997, **53,** 10051–10070.
107. H. D. Roth, T. Herbertz, P. S. Lakkaraju, G. Sluggett and N. J. Turro, *J. Phys. Chem. A*, 1999, **103,** 11350–11354.
108. M. Goez, J. Rozwadowski and B. Marciniak, *Ang. Chem. Int. Ed.*, 1998, **37,** 628–630.
109. T. Bally, S. Bernhard, S. Matzinger, L. Truttmann, Z. Zhu, J. Roulin, A. Marcinek, J. Gebicki, F. Williams, G. Chen, H. D. Roth and T. Herbertz, *Chemistry*, 2000, **6,** 849–857.
110. H. Prinzbach, J. Reinbold, M. Bertau, T. Voss, H. Martin, B. Mayer, J. Heinze, D. Neschchadin, G. Gescheidt, G. K. S. Prakash and G. A. Olah, *Ang. Chem. Int. Ed.*, 2001, **40,** 911–914.
111. J. Reinbold, M. Bertau, T. Voss, D. Hunkler, L. Knothe, H. Prinzbach, D. Neschchadin, G. Gescheidt, B. Mayer, H. Martin, J. Heinze G. K. S. Prakash, et al., *Helv. Chim. Acta*, 2001, **84,** 1518–1560.
112. M. Goez, *Recent Res. Dev. Chem. Sci.*, 1997, **1,** 59–68.
113. H. D. Roth, *Helv. Chim. Acta*, 2006, **89,** 2847–2860.
114. M. Goez and I. Sartorius, *J. Am. Chem. Soc.*, 1993, **115,** 11123–11133.
115. J. Lu and D. Beckert, *Res. Chem. Intermed.*, 2000, **26,** 621–641.
116. M. Goez and I. Sartorius, *Chem. Ber.*, 1994, **127,** 2273–2276.
117. M. Vogtherr and M. Goez, *J. Inf. Rec.*, 1998, **24,** 23–27.
118. C. Yang, Z. Jiang, D. Zhu, S. Wu, L. Yang and L. Wu, *Chin. J. Chem.*, 2001, **19,** 1211–1216.
119. H. Guo, B. Yan, X. Wang and T. Wang, *Sci. China B*, 2005, **48,** 115–121.
120. A. A. Obynochny, P. A. Purtov and S. G. Fedorenko, *Appl. Magn. Res.*, 1998, **14,** 115–130.
121. R. C. White, V. Gorelik, E. G. Bagryanskaya and M. D. E. Forbes, *Langmuir*, 2007, **23,** 4183–4191.
122. S. S. Petrova, A. I. Kruppa and T. V. Leshina, *Chem. Phys. Lett.*, 2005, **407,** 260–265.
123. A. Liegard, K. Dietliker, P. Dubs, G. Knobloch, U. Kolczak, D. Leppard, R. Martin, H. R. Meier, P. Rzadek and G. Rist, *Appl. Magn. Res.*, 1996, **10,** 395–412.
124. I. V. Khudyakov, N. Arsu, S. Jockusch and N. J. Turro, *Design. Monomers Poly.*, 2003, **6,** 91–101.
125. C. J. Groenenboom, H. J. Hageman, P. Oosterhoff, T. Overeem and J. Verbeek, *J. Photochem. Photobiol. A*, 1997, **107,** 253–259.
126. C. J. Groenenboom, H. J. Hageman, P. Oosterhoff, T. Overeem and J. Verbeek, *J. Photochem. Photobiol. A*, 1997, **107,** 261–269.
127. G. Gescheidt, D. Neshchadin, G. Rist, A. Borer, K. Dietliker and K. Misteli, *Phys. Chem. Chem. Phys.*, 2003, **5,** 1071–1077.
128. K. Dietliker, S. Broillet, B. Hellrung, P. Rzadek, G. Rist, J. Wirz, D. Neshchadin and G. Gescheidt, *Helv. Chim. Acta*, 2006, **89,** 2211–2225.
129. S. S. Petrova, A. I. Kruppa and T. V. Leshina, *Chem. Phys. Lett.*, 2004, **385,** 40–44.
130. S. Grimme, *Chem. Phys.*, 1992, **163,** 313–330.
131. G. Pohlers, H. Dreeskamp and S. Grimme, *J. Photochem. Photobiol. A*, 1996, **95,** 41–49.
132. N. P. Gritsan, Y. P. Tsentalovich, A. V. Yurkovskaya and R. Z. Sagdeev, *J. Phys. Chem.*, 1996, **100,** 4448–4458.
133. I. F. Molokov, Yu. P. Tsentalovich, A. V. Yurkovskaya and R. Z. Sagdeev, *J. Photochem. Photobiol. A*, 1997, **110,** 159–165.
134. E. D. Skakovskii, S. A. Lamotkin and L. Yu. Tychinskaya, *J. Appl. Spectrosc.*, 1997, **64,** 319–324.
135. E. D. Skakovskii, S. A. Lamotkin, A. I. Stankevich, L. Yu. Tychinskaya and S. V. Rykov, *Russ. J. Gen. Chem.*, 1998, **68,** 979–984.
136. E. D. Skakovskii, A. I. Stankevich, S. A. Lamotkin, L. Yu. Tychinskaya, G. S. Avrinskii and S. V. Rykov, *J. Appl. Spectrosc.*, 2000, **67,** 770–777.

137. T. G. Shutova, E. D. Skakovskii, V. E. Agabekov, V. L. Murashko and E. A. Dikusar, *Russ. J. Gen. Chem.*, 2001, **71,** 627–632.
138. G. Eckert, M. Goez, B. Maiwald and U. Mueller, *Ber. Bunsen-Ges.*, 1996, **100,** 1191–1198.
139. G. Eckert and M. Goez, *J. Am. Chem. Soc.*, 1999, **121,** 2274–2280.
140. M. Goez, G. Eckert and U. Mueller, *J. Phys. Chem. A*, 1999, **103,** 5714–5721.
141. M. Goez and G. Eckert, *J. Inf. Rec.*, 2000, **25,** 281–285.
142. R. J. DeVoe, M. R. V. Sahyun and E. Schmidt, *Can. J. Chem.*, 1988, **66,** 319–324.
143. W. Zhang, L. Yang, L. Wu, Y. Liu and Z. Liu, *J. Chem. Soc., Perkin Trans.*, 1998, **2,** 1189–1194.
144. M. Goez and G. Eckert, *J. Am. Chem. Soc.*, 1996, **118,** 140–154.
145. N. Polyakov, T. Leshina and L. Kispert, *RIKEN Rev.*, 2002, **44,** 140–143.
146. H. D. Roth and M. L. Manion-Schilling, *J. Am. Chem. Soc.*, 1979, **101,** 1898–1900.
147. H. D. Roth and M. L. Manion-Schilling, *J. Am. Chem. Soc.*, 1980, **102,** 4303–4310.
148. N. E. Polyakov, V. S. Bashurova, P. V. Schastnev and T. V. Leshina, *J. Photochem. Photobiol. A*, 1997, **107,** 55–62.
149. N. E. Polyakov, V. S. Bashurova, T. V. Leshina, O. A. Luzina and N. F. Salakhutdinov, *J. Photochem. Photobiol. A*, 2002, **153,** 77–82.
150. N. E. Polyakov, A. I. Kruppa, V. S. Bashurova, T. V. Leshina and L. D. Kispert, *J. Photochem. Photobiol. A*, 2002, **153,** 113–119.
151. N. E. Polyakov and T. V. Leshina, *Mol Phys.*, 2002, **100,** 1297–1302.
152. N. E. Polyakov, A. I. Kruppa, V. S. Bashurova, R. N. Musin, T. V. Leshina and L. D. Kispert, *J. Photochem. Photobiol. A*, 1999, **128,** 65–74.
153. J. Xue, J. Xu, L. Yang and J. Xu, *J. Org. Chem.*, 2000, **65,** 30–40.
154. X. Y. Wang, B. Z. Yan and T. Wang, *Chin. Chem. Lett.*, 2003, **14,** 270–273.
155. M. Lehnig and K. Schuermann, *Eur. J. Org. Chem.*, 1998, 913–918.
156. K. Schurmann and M. Lehnig, *Appl. Magn. Res.*, 2000, **18,** 375–384.
157. S. N. Batchelor and H. Fischer, *J. Phys. Chem.*, 1996, **100,** 9794–9799.
158. L. T. Kuhn and J. Bargon, *Top. Curr. Chem.*, 2007, **276,** 125–154.
159. S. Wu, J. Liu and Z. Jiang, *Sci. China B*, 1996, **39,** 171–178.
160. S. Wu, J. Liu and Z. Jiang, *Chem. Comm.*, 493–494.
161. I. P. Pozdnyakov, V. F. Plyusnin, V. P. Grivin, D. Y. Vorobyev, A. I. Kruppa and H. Lemmetyinen, *J. Photochem. Photobiol. A*, 2004, **162**.
162. T. Kothe, S. Marque, R. Martschke, M. Popov and H. Fischer, *J. Chem. Soc., Perkin Trans.*, 1998, **2,** 1553–1559.
163. G. Ananchenko and H. Fischer, *J. Chem. Soc., Perkin Trans.*, 2001, **2,** 1887–1889.
164. D. Zubenko, I. Kirilyuk, G. Roshchupkina, I. Zhurko, V. Reznikov, S. R. A. Marque and E. Bagryanskaya, *Helv. Chim. Acta*, 2006, **89,** 2341–2353.
165. D. Zubenko, Y. Tsentalovich, N. Lebedeva, I. Kirilyuk, G. Roshchupkina, I. Zhurko, V. Reznikov, S. R. A. Marque and E. Bagryanskaya, *J. Org. Chem.*, 2006, **71,** 6044–6052.
166. M. Goez and I. Frisch, *J. Phys. Chem. A*, 2002, **106,** 8079–8084.
167. M. Wegner, H. Fischer, M. Koeberg, J. W. Verhoeven, A. M. Oliver and M. N. Paddon-Row, *Chem. Phys.*, 1999, **242,** 227–234.
168. M. Wegner, H. Fischer, S. Grosse, H. -M. Vieth, A. M. Oliver and M. N. Paddon-Row, *Chem. Phys.*, 2001, **264,** 341–353.
169. S. Grosse, M. Onnen, H. Vieth, M. Wegner, H. Fischer, A. Oliver and M. Paddon-Row, *RIKEN Rev.*, 2002, **44,** 137–139.
170. J. W. Verhoeven, *J. Photochem. Photobiol. C*, 2006, **7,** 40–60.
171. G. L. Closs, M. D. E. Forbes and P. Piotrowiak, *J. Am. Chem. Soc.*, 1992, **114,** 3285–3294.
172. L. Zhang, B. Chen, L. Wu, C. Tung, H. Cao and Y. Tanimoto, *Chemistry*, 2003, **9,** 2763–2769.
173. H. Goerner, M. Lehnig and M. Weisbeck, *J. Photochem. Photobiol. A*, 1996, **94,** 157–162.
174. M. Adachi, K. Mochida, M. Wakasa and H. Hayashi, *Main Group Metal Chem.*, 1999, **22,** 227–230.
175. M. B. Taraban, O. S. Volkova, A. I. Kruppa, V. F. Plyusnin, V. P. Grivin, Yu. V. Ivanov, T. V. Leshina, M. P. Egorov and O. M. Nefedov, *J. Organomet. Chem.*, 1998, **566,** 73–83.
176. T. V. Leshina, M. B. Taraban, V. F. Plyusnin, O. S. Volkova and M. P. Egorov, *Russ. Chem. Bull.*, 2000, **49,** 421–426.

177. M. B. Taraban, O. S. Volkova, V. F. Plyusnin, Y. V. Ivanov, T. V. Leshina, M. P. Egorov, O. M. Nefedov, T. Kayamori and K. Mochida, *J. Organomet. Chem.*, 2000, **601,** 324–329.
178. T. V. Leshina, O. S. Volkova and M. B. Taraban, *Russ. Chem. Bull.*, 2001, **50,** 1916–1928.
179. M. B. Taraban, O. S. Volkova, V. F. Plyusnin, A. I. Kruppa, T. V. Leshina, M. P. Egorov and O. M. Nefedov, *J. Phys. Chem. A*, 2003, **107,** 4096–4102.
180. M. V. Sendyurev, E. I. Gol'dfarb, B. I. Ionin and A. L. Buchachenko, *Russ. J. Gen. Chem.*, 1999, **69,** 1184–1185.
181. A. I. Kruppa, M. B. Taraban, S. A. Svarovsky and T. V. Leshina, *J. Chem. Soc., Perkin Trans.*, 1996, **2,** 2151–2155.
182. M. B. Taraban, A. I. Kruppa, V. I. Rakhlin, S. I. Grigor'ev, O. S. Volkova, R. G. Mirskov and T. V. Leshina, *J. Organomet. Chem.*, 2001, **636,** 12–16.
183. M. B. Taraban, A. I. Kruppa, N. E. Polyakov, M. G. Voronkov, V. I. Rakhlin, S. V. Grigor'ev, O. S. Volkova, R. G. Mirskov and T. V. Leshina, *J. Organomet. Chem.*, 2002, **658,** 228–234.
184. M. B. Taraban, N. E. Polyakov, O. S. Volkova, L. V. Kuibida, T. V. Leshina, M. P. Egorov and O. M. Nefedov, *J. Organomet. Chem.*, 2006, **691,** 1411–1418.
185. K. H. Mok and P. J. Hore, *Methods*, 2004, **34,** 75–87.
186. O. B. Morozova, S. E. Korchak, R. Z. Sagdeev and A. V. Yurkovskaya, *J. Phys. Chem. A*, 2005, **109,** 10459–10466.
187. J. J. Hore and R. W. Broadhurst, *Prog. NMR Spectrosc.*, 1993, **25,** 345–402.
188. Y. P. Tsentalovich, O. B. Morozova, A. V. Yurkovskaya and P. J. Hore, *J. Phys. Chem. A*, 1999, **103,** 5362–5368.
189. Y. P. Tsentalovich and O. B. Morozova, *J. Photochem. Photobiol. A*, 2000, **131,** 33–40.
190. Y. P. Tsentalovich, O. B. Morozova, A. V. Yurkovskaya, P. J. Hore and R. Z. Sagdeev, *J. Phys. Chem. A*, 2000, **104,** 6912–6916.
191. J. J. Lopez, M. A. G. Carter, Yu. P. Tsentalovich, O. B. Morozova, A. V. Yurkovskaya and P. J. Hore, *Photochem. Photobiol.*, 2002, **75,** 6–10.
192. H. Fabian, S. Grosse, M. Onnen, H. Vieth and A. Yurkovskaya, *RIKEN Rev.*, 2002, **44,** 134–136.
193. K. L. Ivanov, N. N. Lukzen, H. -M. Vieth, S. Grosse, A. V. Yurkovskaya and R. Z. Sagdeev, *Mol. Phys.*, 2002, **100,** 1197–1208.
194. O. B. Morozova, A. V. Yurkovskaya, R. Z. Sagdeev, K. H. Mok and P. J. Hore, *J. Phys. Chem. B*, 2004, **108,** 15355–15363.
195. O. B. Morozova, P. J. Hore, R. Z. Sagdeev and A. V. Yurkovskaya, *J. Phys. Chem. B*, 2005, **109,** 21971–21978.
196. S. L. Winder, R. W. Broadhurst and P. J. Hore, *Spectrochim. Acta A*, 1995, **51,** 1755–1761.
197. O. B. Morozova, A. V. Yurkovskaya, Yu. P. Tsentalovich, M. D. E. Forbes, P. J. Hore and R. Z. Sagdeev, *Mol. Phys.*, 2002, **100,** 1187–1195.
198. O. Morozova, A. Yurkovskaya, Y. Tsentalovich and R. Sagdeev, *RIKEN Rev.*, 2002, **44,** 131–133.
199. O. B. Morozova, A. V. Yurkovskaya, Y. P. Tsentalovich, M. D. E. Forbes and R. Z. Sagdeev, *J. Phys. Chem. B*, 2002, **106,** 1455–1460.
200. O. B. Morozova, A. V. Yurkovskaya, H. Vieth and R. Z. Sagdeev, *J. Phys. Chem. B*, 2003, **107,** 1088–1096.
201. O. B. Morozova, A. V. Yurkovskaya and R. Z. Sagdeev, *J. Phys. Chem. B*, 2005, **109,** 3668–3675.
202. H. Siebert, C. von der Lieth, R. Kaptein, U. M. S. Soedjanaatmadja, J. F. G. Vliegenthart, C. S. Wright and H. Gabius, *J. Mol. Model.*, 1996, **2,** 351–353.
203. P. F. Varela, D. Solis, T. Diaz-Maurino, H. Kaltner, H. Gabius and A. Romero, *J. Mol. Biol.*, 1999, **294,** 537–549.
204. A. Nordmann, M. J. J. Blommers, H. Fretz, T. Arvinte and A. F. Drake, *Eur. J. Biochem.*, 1999, **261,** 216–226.
205. C. E. Lyon, J. A. Jones, C. Redfield, C. M. Dobson and P. J. Hore, *J. Am. Chem. Soc.*, 1999, **121,** 6505–6506.
206. H. Takashima, H. Tamaoki, N. Teno, Y. Nishi, S. Uchiyama, K. Fukui and Y. Kobayashi, *Biochem.*, 2004, **43,** 13932–13936.
207. I. J. Day, R. Wain, K. Tozawa, L. J. Smith and P. J. Hore, *J. Magn. Reson.*, 2005, **175,** 330–335.
208. H. Siebert, E. Tajkhorshid, C. von der Lieth, R. G. Kleineidam, S. Kruse, R. Schauer, R. Kaptein, H. Gabius and J. F. G. Vliiegenthart, *J. Mol. Model.*, 1996, **2,** 446–455.

209. H. Siebert, S. Andre, G. Reuter, R. Kaptein, J. F. G. Vliegenthart and H. Gabius, *Glycoconjugate J.*, 1997, **14,** 945–949.
210. G. Richter, S. Weber, W. Roemisch, A. Bacher, M. Fischer and W. Eisenreich, *J. Am. Chem. Soc.*, 2005, **127,** 17245–17252.
211. G. Richter, S. Weber, W. Roemisch, A. Bacher, M. Fischer and W. Eisenreich, *J. Am. Chem. Soc.*, 2008, **130,** 7166–7166.
212. F. Khan, I. Kuprov, T. D. Craggs, P. J. Hore and S. E. Jackson, *J. Am. Chem. Soc.*, 2006, **128,** 10729–10737.
213. H. Siebert, C. von der Lieth, R. Kaptein, J. J. Beintema, K. Dijkstra, N. van Nuland, U. M. S. Soedjanaatmadja, A. Rice, J. F. G. Vliegenthart, C. S. Wright and H. Gabius, *Proteins*, 1997, **28,** 268–284.
214. H. Siebert, R. Adar, R. Arango, M. Burchert, H. Kaltner, G. Kayser, E. Tajkhorshid, C. Von Der Lieth, R. Kaptein, N. Sharon, J. F. G. Vliegenthart and H. Gabius, *Eur. J. Biochem.*, 1997, **249,** 27–38.
215. H. Siebert, R. Kaptein, J. J. Beintema, U. M. Soedjanaatmadja, C. S. Wright, A. Rice, R. G. Kleineidam, S. Kruse, R. Schauer, P. J. W. Pouwels, J. P. Kamerling H. Gabius, et al., *Glycoconjugate J.*, 1997, **14,** 531–534.
216. E. Tajkhorshid, H. Siebert, M. Burchert, H. Kaltner, G. Kayser, C. von der Lieth, R. Kaptein, J. F. G. Vliegenthart and H. Gabius, *J. Mol. Model.*, 1997, **3,** 325–331.
217. J. F. G. Vliegenthart and H. Siebert, *Carbohydrates*, 2000, **2,** 1025–1044.
218. H. Siebert, S. Lue, M. Frank, J. Kramer, R. Wechselberger, J. Joosten, S. Andre, K. Rittenhouse-Olson, R. Roy, C. von Lieth, R. Kaptein J. F. G. Vliegenthart, et al., *Biochemistry*, 2002, **41,** 9707–9717.
219. M. Jimenez, S. Andre, H. Siebert, H. Gabius and D. Solis, *Glycobiology*, 2006, **16,** 926–937.
220. H. Siebert, E. Tajkhorshid, J. F. G. Vliegenthart, C. von der Lieth, S. Andre and H. Gabius, *ACS Symp. Ser.*, 2006, **930,** 81–113.
221. H. Vis, O. Vageli, J. Nagel, C. E. Vorgias, K. S. Wilson, R. Kaptein and R. Boelens, *Magn. Reson. Chem.*, 1996, **34,** S81–S86.
222. T. Neufeld, M. Eisenstein, K. A. Muszkat and G. Fleminger, *J. Mol. Recognit.*, 1998, **11,** 20–24.
223. A. J. Mason, J. J. Lopez, M. Beyermann and C. Glaubitz, *Biochim. Biophys. Acta*, 2005, **1714,** 1–10.
224. J. Wirmer, T. Kuhn and H. Schwalbe, *Ang. Chem. Int. Ed.*, 2001, **40,** 4248–4251.
225. P. J. Hore, S. L. Winder, C. H. Roberts and C. M. Dobson, *J. Am. Chem. Soc.*, 1997, **119,** 5049–5050.
226. D. Canet, C. E. Lyon, R. M. Scheek, G. T. Robillard, C. M. Dobson, P. J. Hore and N. A. J. van Nuland, *J. Mol. Biol.*, 2003, **330,** 397–407.
227. M. Cemazar, S. Zahariev, S. Pongor and P. J. Hore, *J. Biol. Chem.*, 2004, **279,** 16697–16705.
228. O. B. Morozova, P. J. Hore, V. E. Bychkova, R. Z. Sagdeev and A. V. Yurkovskaya, *J. Phys. Chem. B*, 2005, **109,** 5912–5918.
229. C. Schloerb, S. Mensch, C. Richter and H. Schwalbe, *J. Am. Chem. Soc.*, 2006, **128,** 1802–1803.
230. C. E. Lyon, E. Suh, C. M. Dobson and P. J. Hore, *J. Am. Chem. Soc.*, 2002, **124,** 13018–13024.
231. K. H. Mok, T. Nagashima, I. J. Day, P. J. Hore and C. M. Dobson, *Proc. Natl. Acad. Sci.*, 2005, **102,** 8899–8904.
232. K. H. Mok, L. T. Kuhn, M. Goez, I. J. Day, J. C. Lin, N. H. Andersen and P. J. Hore, *Nature*, 2007, **447,** 106–109.
233. A. Gugger, R. Batra, P. Rzadek, G. Rist and B. Giese, *J. Am. Chem. Soc.*, 1997, **119,** 8740–8741.
234. O. A. Snytnikova, Y. P. Tsentalovich and R. Z. Sagdeev, *Appl. Magn. Res.*, 2004, **26,** 183–195.
235. A. V. Yurkovskaya, O. A. Snytnikova, O. B. Morozova, Y. P. Tsentalovich and R. Z. Sagdeev, *Phys. Chem. Chem. Phys.*, 2003, **5,** 3653–3659.
236. O. B. Morozova, A. S. Kiryutin, R. Z. Sagdeev and A. V. Yurkovskaya, *J. Phys. Chem. B*, 2007, **111,** 7439–7448.
237. O. B. Morozova, A. S. Kiryutin and A. V. Yurkovskaya, *J. Phys. Chem. B*, 2008, **112,** 2747–2754.
238. R. Katahira, M. Katahira, Y. Yamashita, H. Ogawa, Y. Kyogoku and M. Yoshida, *Nucleic Acids Res.*, 1998, **26,** 744–755.
239. A. I. Kruppa, M. B. Taraban, T. V. Leshina, E. Natarajan and C. B. Grissom, *Inorg. Chem.*, 1997, **36,** 758–759.
240. J. L. Male, D. A. Braden and D. R. Tyler, *Chemtracts*, 1997, **10,** 908–912.
241. T. V. Leshina, *Kin. Catal.*, 1996, **37,** 620–626.

242. N. E. Polyakov, A. I. Kruppa, T. V. Leshina, V. Lusis, D. Muceniece and G. Duburs, *J. Photochem. Photobiol. A*, 1997, **111,** 61–64.
243. I. M. Magin, A. I. Kruppa, T. V. Leshina, V. Lusis and D. Muceniece, *J. Photochem. Photobiol. A*, 2003, **155,** 119–126.
244. N. E. Polyakov, M. B. Taraban and T. V. Leshina, *Photochem. Photobiol.*, 2004, **80,** 565–571.
245. N. E. Polyakov, V. K. Khan, M. B. Taraban and T. V. Leshina, *J. Phys. Chem. B*, 2008, **112,** 4435–4440.
246. N. E. Polyakov, V. K. Khan, M. B. Taraban, T. V. Leshina, O. A. Luzina, N. F. Salakhutdinov and G. A. Tolstikov, *Org. Biomol. Chem.*, 2005, **3,** 881–885.
247. V. S. Kornievskaya, A. I. Kruppa, N. E. Polyakov and T. V. Leshina, *J. Phys. Chem. B*, 2007, **111,** 11447–11452.
248. N. E. Polyakov and T. V. Leshina, *Russ. Chem. Bull.*, 2007, **56,** 631–642.
249. V. S. Kornievskaya, A. I. Kruppa and T. V. Leshina, *J. Inclusion Phen.*, 2008, **60,** 123–130.
250. M. G. Zysmilich and A. McDermott, *J. Am. Chem. Soc.*, 1994, **116,** 8362–8363.
251. M. G. Zysmilich and A. McDermott, *J. Am. Chem. Soc.*, 1996, **118,** 5867–5873.
252. M. G. Zysmilich and A. McDermott, *Proc. Natl. Acad. Sci*, 1996, **93,** 6857–6860.
253. H. J. M. de Groot, *Adv. Photosynth.*, 1996, **3,** 299–313.
254. J. Matysik, A. Alia, J. G. Hollander, T. Egorova-Zachernyuk, P. Gast and H. J. M. De Groot, *Indian J. Biochem. Biophys.*, 2000, **37,** 418–423.
255. J. Matysik, A. Alia, P. Gast, H. J. Van Gorkom, A. J. Hoff and H. J. M. De Groot, *Proc. Natl. Acad. Sci.*, 2000, **97,** 9865–9870.
256. J. Matysik, E. Schulten, A. Alia, P. Gast, J. Raap, J. Lugtenburg, A. J. Hoff and H. J. M. De Groot, *Biol. Chem.*, 2001, **382,** 1271–1276.
257. J. Matysik, A. Alia, P. Gast, J. Lugtenburg, A. J. Hoff and H. J. M. De Groot, *Focus Struct. Biol.*, 2001, **1,** 215–225.
258. E. A. M. Schulten, J. Matysik, A. Alia, S. Kiihne, J. Raap, J. Lugtenburg, P. Gast, A. J. Hoff and H. J. M. de Groot, *Biochem.*, 2002, **41,** 8708–8717.
259. S. Prakash, A. Alia, P. Gast, G. Jeschke, H. J. M. de Groot and J. Matysik, *J. Mol. Struct.*, 625–633.
260. A. Alia, E. Roy, P. Gast, H. J. Van Gorkom, H. J. M. De Groot, G. Jeschke and J. Matysik, *J. Am. Chem. Soc.*, 2004, **126,** 12819–12826.
261. A. Diller, A. Alia, E. Roy, P. Gast, H. J. van Gorkom, J. Zaanen, H. J. M. de Groot, C. Glaubitz and J. Matysik, *Photosynth. Res.*, 2005, **84,** 303–308.
262. S. Prakash, A. Alia, P. Gast, H. J. M. de Groot, G. Jeschke and J. Matysik, *J. Am. Chem. Soc.*, 2005, **127,** 14290–14298.
263. S. Prakash, A. Alia, P. Gast, I. I. J. M. de Groot, J. Matysik and G. Jeschke, *J. Am. Chem. Soc.*, 2006, **128,** 12794–12799.
264. A. Diller, S. Prakash, A. Alia, P. Gast, J. Matysik and G. Jeschke, *J. Phys. Chem. B*, 2007, **111,** 10606–10614.
265. A. Diller, E. Roy, P. Gast, H. J. van Gorkom, H. J. M. de Groot, C. Glaubitz, G. Jeschke, J. Matysik and A. Alia, *Proc. Natl. Acad. Sci.*, 2007, **104,** 12767–12771.
266. S. Prakash, A. Alia, P. Gast, H. J. M. De Groot, G. Jeschke and J. Matysik, *Biochem.*, 2007, **46,** 8953–8960.
267. E. Roy, A. Diller, A. Alia, P. Gast, H. J. van Gorkom, H. J. M. de Groot, G. Jeschke and J. Matysik, *Appl. Magn. Res.*, 2007, **31,** 193–204.
268. E. Daviso, A. Diller, A. Alia, J. Matysik and G. Jeschke, *J. Magn. Reson.*, 2008, **190,** 43–51.
269. E. Roy, T. Rohmer, P. Gast, G. Jeschke, A. Alia and J. Matysik, *Biochem.*, 2008, **47,** 4629–4635.
270. A. McDermott, M. G. Zysmilich and T. Polenova, *Solid State Nucl. Magn. Reson.*, 1998, **11,** 21–47.
271. G. Jeschke, *J. Chem. Phys.*, 1997, **106,** 10072–10086.
272. G. Jeschke, *J. Am. Chem. Soc.*, 1998, **120,** 4425–4429.
273. T. Polenova and A. McDermott, *J. Phys. Chem. B*, 1999, **103,** 535–548.
274. G. Jeschke and J. Matysik, *Chem. Phys.*, 2003, **294,** 239–255.

CHAPTER 4

Techniques Used for ^{14}N NQR Studies

V. Mikhaltsevitch[1]

Contents

Abstract

Experimental and theoretical aspects of using direct multi-pulse techniques in ^{14}N nuclear quadrupole resonance (NQR) are considered. The optimum correlations between the parameters of multi-pulse sequences and the relaxation characteristics of the substances under investigation are discussed. A number of methods for cancelling magneto-acoustic and piezo-electric ringing signals in the spectroscopy of NQR are also considered.

Key Words: NQR, Nitrogen, Multi-pulse sequence, Explosive detection, Magneto-acoustic ringing, Polarization enhancement.

Qrsciences Ltd., Cannington WA 6107, Australia
[1] Corresponding author: 4A Higham Court, Leeming 6149, WA, Australia, Email: vmikhaltsevitch@gmail.com

Annual Reports on NMR Spectroscopy, Volume 66
ISSN 0066-4103, DOI: 10.1016/S0066-4103(08)00404-3

1. INTRODUCTION

The history of the detection of nitrogen-containing substances with the NQR method, originating in 1960s and in details described in a number of publications,[1–3] gives a convincing substantiation to the fact that the NQR of nitrogen is considered by the majority of experts as first of all a very convenient and relatively inexpensive tool for explosive detection. The detection of explosives and, since recently, narcotic substances, will remain, apparently, a priority task in this area of spectroscopy for a long time.

Despite the large number of modern techniques developed in the NQR of nitrogen, such as imaging,[4] two-frequency spectroscopy,[5–7] two-dimensional methods,[8] quantum computing,[9] double NQR–NMR[10–12] and cross-relaxation spectroscopy,[13,14] direct multi-pulse methods for some decades maintain the central position in this section of NQR. The latter relates to the fact that a whole range of unresolved technical problems does not permit considering highly sensitive indirect methods like double NQR–NMR and cross-relaxation spectroscopy as serious competitors to direct methods for most practical applications, especially in the frequency range above 1 MHz. But in spite of the concernment of direct methods there is no review article devoted to this subject published so far. Therefore, the main attention in this chapter is focused on direct multi-pulse methods of the detection of nitrogenous compounds as priority methods in this field of NQR spectroscopy.

The chapter consists of four sections, which are devoted to theoretical and practical issues of the detection of nitrogen-containing substances. Section 2 deals with theoretical aspects of the two most popular multi-pulse sequences: multi-pulse spin-locking—MW-4 and ''strong off-resonant comb''—SORC. In spite of the fact that the development of these sequences has enabled a dramatic increase in the sensitivity of NQR methods, until recently a number of theoretical and experimental peculiarities of these sequences have not been studied adequately. The primary issue concerns the sequence SORC, and also behaviour of both sequences in case of close times of spin–lattice and dipolar relaxations, which is especially important for the detection of such a popular explosive as hexogen (RDX). There are also demonstrated some experimental techniques for the detection of some other explosives (PETN and trinitrotoluene (TNT)).

In Section 3 the Zeeman polarization-enhanced method is discussed. The method demonstrates its efficiency when spin–lattice relaxation time of the NQR spin-system is long enough to ensure the feasibility of the adiabatic demagnetization process.

Section 4 is devoted to multi-pulse methods of removing magneto-acoustic and piezo-electric ringing (MAPER), generated by numerous objects containing metallic, ferrite, ferro- and piezo-electric components, when detecting explosives with NQR landmine detectors and luggage scanners.

Section 5 deals with the theoretical and experimental analysis of the effect of time-dependent transient nutations in the effective field of multiple-pulse sequences (TNEFMS) in NQR ^{14}N, which was first established in 1991,[15] and the nature of which is still not clearly understood. Experimental results indicate that

the TNEFMS effect, manifested in the generation of the inductance and echo on the NQR envelope, is of a very general nature and is observed in the field of a great number of multi-pulse sequences. It was theoretically proven that the inductance and echo are generated by the perturbing factors that disrupt the regularity of the multi-pulse sequence and create the spin-locking effect.[16] Such factors can be created by introducing additional pulses or by changing pulse parameters of a sequence, e.g. phase switching. The practical applications of this effect are yet unclear and require additional research.

2. SHORT-REPETITION TIME SEQUENCES IN NQR OF NITROGEN

The application of various multi-pulse methods in NQR requires a clear theoretical understanding of physical processes first of all behind the simplest ''basic'' multi-pulse sequences which include such a popular sequence as multi-pulse spin locking—MW-4,[17] and a sequence of identically spaced coherent radio frequency (RF) pulses with intervals between them less than the time constant of free induction decay (FID) T_2^* —strong off-resonance comb—SORC.[18]

Though fundamental articles on the theoretical study of this type of sequences (first of all SLS) were published comparatively long ago,[19–21] detailed experimental research works on the correspondence of theoretical results to experimental data have not been numerous.[22–24]

In the theoretical part of the chapter we follow paper[16] to obtain analytical expressions for the magnetisation of quadrupole nuclei in quasi-stationary and stationary states that take into account the frequency offset of the carrier frequency in relation to the resonant frequency of the irradiated transition during the effect of the pulses.

The following scheme is used.

In accordance with the works[19–21,25] we assume that for analysing the effect of RF pulses on the quadrupolar spin system, it is sufficient to consider only three types of interactions: quadrupolar interaction, homonuclear dipole–dipole interaction and the nuclear–spin interaction with the magnetic component of the RF field. Before the initiation of the multi-pulse sequence the quadrupolar system is described by two Hamiltonians: quadrupolar H_Q and the part of the homonuclear dipole–dipole Hamiltonian H_d secular in relation to the quadrupole Hamiltonian, the sum of which can be regarded as the effective Hamiltonian of the spin system independent of the time factor.

If the carrier frequency of the RF pulses is close to one of the resonance transitions of the irradiated sample, the effect of the multi-pulse sequence leads to the establishment of a new time independent effective Hamiltonian H_{eff}, now also containing the interaction of nuclear–spins with the RF field (that the effective Hamiltonian is time independent should be understood that it is independent of the number of the pulse interval but not independent of the time inside the definite pulse interval). A part of the dipole Hamiltonian H_{d} no longer commutes with the new effective Hamiltonian, which after the T_2 time results in heat mixing of the quadrupole reservoir and the reservoir of the components of

dipole–dipole interactions non-secular in relation to H_{eff}. As a result of this process, quasi-stationary state is established. Its evolution at times $<T_{1e}$ is practically completely determined by the Hamiltonian H_{eff}.

The independence of H_{eff} on the time interval of the sequence under the condition that this interval lies between T_2 and T_{1e} can be used for determining proper H_{eff}. This approach was first used in multi-pulse nuclear magnetic resonance in paper,[26] and later, in NQR, for the analysis of quasi-stationary state in multi-pulse spin locking in the nuclear system with the spin of 5/2[27] at exact resonance. We extended this approach to the arbitrary offset of the pulse carrier frequency in relation to the resonance transition.

When analysing the stationary state we use the approach elaborated in articles.[28,16]

2.1. Quasi-stationary state

Let us consider a monocrystalline sample that contains chemically identical spin-1 nuclei. In our physical model it will be assumed that the quadrupole principal axes for each of the spins have the same orientation. The quadrupole Hamiltonian in the quadrupole principal axes frame is given as

$$H_Q = \frac{1}{3}\omega_Q[3I_z^2 - I^2 + \eta(I_x^2 - I_y^2)], \tag{1}$$

where $\omega_Q = 3e^2qQ/4$, e^2qQ is the nuclear quadrupole coupling constant, η is the asymmetry parameter of the electric-field gradient (EFG) tensor. In terms of the fictitious spin-1/2 operators H_Q has the form[29]

$$H_Q = \frac{2}{3}\omega_Q(I_{x,3} - I_{y,3} - \eta I_{z,3}) = \frac{2}{3}\omega_Q(I_{z,4} - \eta I_{z,3}) = \omega_p I_{p,3} + \omega_p^{'} I_{p,4} \tag{2}$$

with

$$\omega_x = \frac{1}{3}\omega_Q(\eta + 3), \omega_y = \frac{1}{3}\omega_Q(\eta - 3), \omega_z = -\frac{2}{3}\omega_Q\eta,\ \omega_p^{'} = \frac{1}{3}(\omega_q - \omega_r). \tag{3}$$

The Hamiltonian H_Q is written in frequency units ($\eta = 1$), $p, q, r = x, y, z$ or cyclic permutation; three parameters ω_x, ω_y and ω_z are connected with the three resonance frequencies of the quadrupolar nucleus ω_+, ω_- and ω_0 by equations $\omega_x = \omega_+$, $\omega_y = -\omega_-$, $\omega_z = -\omega_0$. Further on parameters $\omega_x, \omega_y, \omega_z$ will be treated as equivalent to resonant frequencies $\omega_+, \omega_-, \omega_0$. We consider one of these three transitions with arbitrary frequency ω_p.

If we neglect spin–lattice interactions the equation for a density matrix ρ may be expressed as follows

$$\frac{d\rho}{dt} = -i[H_Q + H_{rf}(t) + H_d + H_S + H_{IS}, \rho], \tag{4}$$

where H_d is the Hamiltonian of homonuclear dipolar interactions (HDI) of the like spin-1 nuclei; H_{IS} is the Hamiltonian of heteronuclear dipolar interactions of the spin-1 nuclei with the other sort nuclei S; H_S is the Hamiltonian which

describes the motion of the S-nuclei; $H_{\mathrm{rf}}(t)$ is the Hamiltonian of the interaction of a spin with the RF field. Let the carrier frequency of the RF pulses be $\omega = \omega_p - \Delta\omega$; $\Delta\omega$ is the resonance offset.

The RF Hamiltonian is obtained from:

$$\begin{aligned} H_{\mathrm{rf}}(t) &= -2\gamma \cdot H_1(\sin\,\vartheta_{\mathrm{L}} \cdot\cos\,\varphi_{\mathrm{L}} I_{x,1} + \sin\vartheta_{\mathrm{L}} \cdot\sin\varphi_{\mathrm{L}} I_{y,1} + \cos\vartheta_{\mathrm{L}} I_{z,1})\cos(\omega t + \phi) \\ &= -\cos(\omega t + \phi) \sum_{m=x,y,z} a_m I_{m,1}, \end{aligned} \tag{5}$$

where $a_x = \gamma H_1 \cdot\sin\,\vartheta_{\mathrm{L}} \cdot\cos\,\varphi_{\mathrm{L}}$, $a_y = \gamma H_1 \cdot\sin\,\vartheta_{\mathrm{L}} \cdot\sin\,\phi_{\mathrm{L}}$, $a_z = \gamma H_1 \cdot\cos\,\vartheta_{\mathrm{L}}$, γ is the gyromagnetic ratio, H_1 is the amplitude of the RF field, ϕ is its initial phase, ϑ_{L} and ϕ_{L} are the polar and azimuthal angles of the field vector in the principal axes frame, ω-carrier frequency of the RF pulses.

Now consider a transformation into the interaction representation with the Hamiltonian

$$H_0 = \omega \cdot I_{p,3} + \frac{1}{3}(\omega_q - \omega_r - \Delta\omega) I_{p,4} = \omega_q I_{q,3} + \frac{1}{3}(\omega_r - \omega + \Delta\omega) I_{q,4}. \tag{6}$$

The secular part of the RF Hamiltonian in the H_0 representation takes the form

$$H_{\mathrm{rf}}(t) = -\omega_1[\cos\phi \cdot I_{p,1} + \sin\phi \cdot I_{p,2}], \quad \omega_1 = a_p. \tag{7}$$

As it was pointed out in paper[19] the frequencies determined by H_{Q} and H_{S} are different and so the secular part of the Hamiltonian with respect to H_0 equals zero. As a consequence, the Hamiltonians H_{IS} and H_{S} are excluded out of our consideration.

The dipolar Hamiltonian can be written as follows[29]

$$H_{\mathrm{d}} = \sum_{i \neq j} \sum_{p,q=x,y,z} \Omega_{ij}^{pq} I_{p,1}^{i} I_{q,1}^{j}, \tag{8}$$

where $\Omega_{ij}^{pq} = \Omega_{ij}^{qp}$ is the tensor of the HDI of two like i and j spins in the quadrupole principal axes frame. The diagonal elements of this tensor are defined by[20]

$$\Omega_{ij}^{p} \equiv \Omega_{ij}^{pp} = \frac{\gamma^2}{r_{ij}^3}(1 - 3\,\cos^2\psi_{ij}), \tag{9}$$

ψ_{ij} is the angle between the vector r_{ij} and p-axis; r_{ij} is the internuclear distance between i and j nuclei.

Following[29] one finds that secular parts of H_{d}, which are determined with respect to H_0 and H_{Q}, are the same.

To calculate H_{d} in the representation of H_0 we must consider a bilinear operator $I_{p,1}^{i} I_{q,1}^{j}$ for two arbitrary spins i and j in this representation. Taking into account that $[I_{p,1}, I_{p,4}] = 0$ we get:

$$\begin{aligned}\tilde{I}^i_{p,1}(t)\cdot\tilde{I}^j_{q,1}(t) &\equiv [\exp(\mathrm{i}H_0t)I^i_{p,1}\exp(-\mathrm{i}H_0t)]\cdot[\exp(\mathrm{i}H_0t)I^j_{q,1}\exp(-\mathrm{i}H_0t)]\\ &= \exp(\mathrm{i}\omega tI^i_{p,3})I^i_{p,1}\exp(-\mathrm{i}\omega tI^i_{p,3})\exp(\mathrm{i}\omega_q tI^j_{q,3})I^j_{q,1}\exp(-\mathrm{i}\omega_q tI^j_{q,3}).\\ &= [I^i_{p,1}\cos\omega t - I^i_{p,2}\sin\omega t]\cdot[I^j_{q,1}\cos\omega_q t - I^j_{q,2}\sin\omega_q t]\end{aligned}$$

The time independent part of the operator $\tilde{I}^i_{p,1}\tilde{I}^j_{q,1}$ equals

$$\frac{1}{2}(I^i_{p,1}I^j_{p,1} + I^i_{p,2}I^j_{p,2})\delta_{\omega\omega_q}.$$

Therefore,

$$\tilde{H}_\mathrm{d} = \sum_{i\neq j}\sum_{p=x,y,z}\Omega^p_{ij}(I^i_{p,1}I^j_{p,1} + I^i_{p,2}I^j_{p,2}) \tag{10}$$

In the H_0 representation the evolution of the density matrix $\tilde{\rho}(\tilde{\rho}(t) = \exp(\mathrm{i}H_0t)\rho(t)\exp(-\mathrm{i}H_0t))$ is described by the equation

$$\frac{\mathrm{d}\tilde{\rho}}{\mathrm{d}t} = -\mathrm{i}[\Delta\omega I_{p,3} + \tilde{H}_\mathrm{rf} + \tilde{H}_\mathrm{d}, \tilde{\rho}] \tag{11}$$

during the effect of the RF pulses, and it is described by

$$\frac{\mathrm{d}\tilde{\rho}}{\mathrm{d}t} = -\mathrm{i}[\Delta\omega I_{p,3} + \tilde{H}_\mathrm{d}, \tilde{\rho}] \tag{12}$$

between the pulses.

Take into account that during the action of the RF pulse $||\Delta\omega I_{p,3} + \tilde{H}_\mathrm{rf}|| \ll ||\tilde{H}_\mathrm{d}||$, where $||\Delta\omega I_{p,3} + \tilde{H}_\mathrm{rf}||$ and $||\tilde{H}_\mathrm{d}||$ are the norms of the Hamiltonians $\Delta\omega I_{p,3} + \tilde{H}_\mathrm{rf}$ and $\tilde{H}_\mathrm{d}$, we can neglect $\tilde{H}_\mathrm{d}$ in the Equation (11) and write

$$\frac{\mathrm{d}\tilde{\rho}}{\mathrm{d}t} = -\mathrm{i}[\Delta\omega I_{p,3} + \tilde{H}_\mathrm{rf}, \tilde{\rho}]. \tag{13}$$

Here and further on all calculations and results will be done in H_0 representation, so that the tilde notation will be dropped.

The SRTS sequence consists of a preparatory pulse and an arbitrary long train of the phase-coherent RF pulses of the same flip angle applied with a constant short-repetition time. As was noted above, the ''short time'' in this case should be interpreted as the pulse spacing T within the sequence that meets the condition $T << T_2 \sim ||H_\mathrm{d}||^{-1}$. The state that is established in the spin system after the time, $\sim T_2$, is traditionally defined as the ''steady-state free precession'' (SSFP),[30] and includes two other states (or sub-states): quasi-stationary, that exists at times $T_2 < t < T_{1\mathrm{e}}$ ($T_{1\mathrm{e}}$—effective relaxation time) and stationary, that is established after the time $\sim 3T_{1\mathrm{e}}$ after the start of the sequence.[19–21] The SSFP is a very particular state which requires a specific mechanism for its description. This mechanism was devised in articles[31,32] on the basis of the effective field concept and canonical transformations. Later approaches on the basis of the average-Hamiltonian theory were developed.[33]

The quasi-stationary state, established at times $\sim T_2$, is characterised by two spin temperatures. One temperature corresponds to a common thermodynamic reservoir, which appears due to the thermal mixing of the quadrupole reservoir and the reservoir of components of the dipole–dipole interactions, non-secular in relation to the effective Hamiltonian. The second temperature corresponds to the reservoir of the secular part of the dipole–dipole interactions. At conditions to be determined further, both spin temperatures can coincide.

Note that we consider the case when the width of all pulses $t_w \ll \tau$.

Let us examine the effect of the preparatory RF pulse t_{w0} on the quadrupolar spin system.

The initial density matrix at the moment when $t = 0$, i.e. before the pulse excitation, in the high-temperature approximation can be written as

$$\rho(0) = \frac{1}{3}\{E - \alpha_0[\omega_p I_{p,3} + \omega_p^{'} I_{p,4}]\} = \frac{1}{3}\{E - \alpha_0 \omega_p \boldsymbol{n}_0 \boldsymbol{I}_p - \alpha_0 \omega_p^{'} I_{p,4}\}, \tag{14}$$

where α_0 is the reverse spin temperature, corresponding to the equilibrium state of the spin system; $n_0 = (n_{01}, n_{02}, n_{03})$ is the unit vector with components for the initial density matrix equalling $n_{01} = 0, n_{02} = 0, n_{03} = 1$.

The Equation (13) for the spin system density matrix during the effect of the RF pulse can be rewritten as follows:

$$\begin{aligned} \mathrm{i}\frac{\mathrm{d}\rho(t)}{\mathrm{d}t} = [\Delta\omega I_{p,3} + H_{\mathrm{rf}},\ \rho(t)] &= [\Delta\omega I_{p,3} - \omega_1 t_{w0}(I_{p,1}\cos\phi + \boldsymbol{I}_{p,2}\sin\phi), \rho(t)] \\ &= -[\boldsymbol{\omega}_e \cdot \boldsymbol{I}_p, \rho(t)]. \end{aligned} \tag{15}$$

Here $\boldsymbol{I}_p$ is the vector in the $I_{p,i}$-operator space.

$$\begin{aligned} &\omega_e = \omega_e \cdot \boldsymbol{k}(\phi); \quad \omega_e = \sqrt{\Delta\omega^2 + \omega_1}; \quad \boldsymbol{k}(\phi) \equiv (k_1, k_2, k_3); \quad k_1 = \frac{\omega_1}{\omega_e}\cos\phi; \\ &k_2 = \frac{\omega_1}{\omega_e}\sin\phi; \quad k_3 = -\frac{\Delta\omega}{\omega_e}. \end{aligned} \tag{16}$$

Its solution at the moment when $t = t_{w0}$ determines the density matrix of the spin system immediately after the preparatory pulse:

$$\rho_0 = R(t_{w0}) \cdot \rho(0) \cdot R(t_{w0})^{-1}, \tag{17}$$

where

$$R(t_{w0}) = \exp(-\mathrm{i} \cdot (\Delta\omega I_{p,3} + H_{\mathrm{rf}}) \cdot t_{w0}) = \exp(\mathrm{i}\varphi_0 \cdot \mathbf{k} \cdot \mathbf{I}_{\mathrm{p}})); \quad \varphi_0 \equiv \omega_e t_{w0}. \tag{18}$$

When we consider the effect that the difference of the phases of the carrier frequency of the preparatory pulse and the following pulses produces on the NQR signal, for the convenience of our calculations let us assume that $\phi = \pi/2$ for the preparatory pulse and $\phi = 0$ for the other pulses.

The evolution of the system set by Equation (17) is determined by the rotation of the angular momentum operator, in accordance with expression[34]

$$\begin{aligned} \boldsymbol{I}' &= \exp(\mathrm{i}\vartheta \boldsymbol{k}\boldsymbol{I})\boldsymbol{I}\exp(-\mathrm{i}\vartheta \boldsymbol{k}\boldsymbol{I}) \\ &= \boldsymbol{k}(\boldsymbol{k}\cdot\boldsymbol{I}) + (\boldsymbol{I} - \boldsymbol{k}(\boldsymbol{k}\cdot\boldsymbol{I}))\cos\,\vartheta + (\boldsymbol{k}\times\boldsymbol{I})\sin\,\vartheta \\ &= \boldsymbol{k}(\boldsymbol{k}\cdot\boldsymbol{I})(1-\cos\,\vartheta) + \boldsymbol{I}\cos\,\vartheta + (\boldsymbol{k}\times\boldsymbol{I})\sin\,\vartheta, \end{aligned} \tag{19}$$

where ϑ is an arbitrary rotation angle of the angular momentum $\boldsymbol{I} = (I_1, I_2, I_3)$ is an arbitrary rotation angle of the angular momentum about the direction predetermined by the unit vector $\boldsymbol{k}$.

Assuming that $\vartheta = \varphi_0$, considering Equations (17) and (14), and also taking into account that $\boldsymbol{n}_0 = (0, 0, 1)$, we obtain:

$$\begin{aligned} \rho_0 \equiv \rho(t_{\mathrm{w}0}) &= \exp(+\mathrm{i}\varphi_0\boldsymbol{k}(\phi)\cdot\boldsymbol{I}_p)\rho(0)\exp(-\mathrm{i}\varphi_0\boldsymbol{k}(\phi)\cdot\boldsymbol{I}_p) = \frac{1}{3}\{E - \alpha_0\omega_p\boldsymbol{n}_0\boldsymbol{I}'_p - \alpha_0\omega'_p I_{p,4}\} \\ &= \frac{1}{3}[E - \alpha_0\omega_p\Big\{I_{p,1}(k_3k_1(1-\cos\varphi_0) - k_2\sin\varphi_0) + I_{p,2}(k_3k_2(1-\cos\varphi_0) + k_1\sin\varphi_0) \\ &\quad + I_{p,3}(k_3^2 + (1-k_3^2)\cos\varphi_0)\Big\} - \alpha_0\omega'_p I_{p,4}] \end{aligned} \tag{20}$$

or

$$\rho_0 = \frac{1}{3}[E - \alpha_0\omega_p\boldsymbol{l}\cdot\boldsymbol{I}_{\mathrm{p}} - \alpha_0\omega'_p I_{p,4}], \tag{21}$$

where

$$\begin{aligned} &l = (l_1, l_2, l_3); l_1 = -\frac{\Delta\omega\cdot\omega_1}{\omega_e^2}[1-\cos\varphi_0]\cos\phi - \frac{\omega_1}{\omega_e}\sin\varphi_0\sin\phi; \\ &l_2 = -\frac{\Delta\omega\cdot\omega_1}{\omega_e^2}[1-\cos\varphi_0]\sin\phi + \frac{\omega_1}{\omega_e}\sin\varphi_0\cos\phi;\ l_3 = \frac{\Delta\omega^2}{\omega_e^2} + \frac{\omega_1^2}{\omega_e^2}\cos\varphi_0. \end{aligned} \tag{22}$$

After the time interval τ, the preparatory pulse is followed by the other sequence pulses with the pulse spacing of 2τ. The interaction of the nuclear–spin with these pulses, if we neglect their duration, can be presented as

$$H_{\mathrm{rf}} = -f(t)\boldsymbol{I}_{\mathrm{p}}, \tag{23}$$

where $f(t)$ is the pulsed function

$$f(t) = \omega_e\boldsymbol{k}(0)\sum_{m=0}^{\infty}\delta(\tau + 2m\cdot\tau - t). \tag{24}$$

Now two Equations (12) and (13) can be replaced with one

$$\mathrm{i}\frac{\mathrm{d}\rho(t)}{\mathrm{d}t} = [-\omega_e\boldsymbol{I}_p\sum_{m=0}^{\infty}\delta(\tau + 2m\cdot\tau - t) + H_{\mathrm{d}}, \rho(t)]. \tag{25}$$

Following[31] we define an effective field ω_{eff}, which substitutes the effect of the RF pulses and the resonance offset in the middle of the time interval between the two adjacent pulses of the sequence, by

$$\exp(-\mathrm{i}\omega_{\text{eff}}\boldsymbol{I}_p 2\tau) = \exp(-\mathrm{i}\Delta\omega\tau\boldsymbol{I}_{p,3})\exp(\mathrm{i}\omega_e t_{\text{w}} I_p)$$
$$\exp(-\mathrm{i}\Delta\omega\tau I_{p,3}) = \left(\cos\frac{\Delta\omega\tau}{2} - \mathrm{i}2I_{p,3}\sin\frac{\Delta\omega\tau}{2}\right)\left(\cos\frac{\omega_e t_{\text{w}}}{2} + \mathrm{i}2\boldsymbol{k}\boldsymbol{I}_p\sin\frac{\omega_e t_{\text{w}}}{2}\right) \quad (26)$$
$$\left(\cos\frac{\Delta\omega\tau}{2} - \mathrm{i}2I_{p,3}\sin\frac{\Delta\omega\tau}{2}\right).$$

Define a unit vector

$$\boldsymbol{\omega}_{\text{eff}} = \boldsymbol{n}(\tau)\omega_{\text{eff}};\ \boldsymbol{n}(\tau) = (n_1, n_2, n_3);\ \omega_{\text{eff}} = |\boldsymbol{\omega}_{\text{eff}}|.$$

Then from Equation (26) we get

$$\cos(\omega_{\text{eff}}\tau) = \cos\frac{\omega_e t_{\text{w}}}{2}\cos\Delta\omega\tau - \frac{\Delta\omega}{\omega_e}\sin\frac{\omega_e t_{\text{w}}}{2}\sin\Delta\omega\tau;$$
$$n_1 = \frac{\omega_1}{\omega_e}\frac{\sin\dfrac{\omega_e t_{\text{w}}}{2}}{\sin\omega_{\text{eff}}\tau};\ n_2 = 0;\ n_3 = -\frac{1}{\sin\omega_{\text{eff}}\tau}\left(\cos\frac{\omega_e t_{\text{w}}}{2}\sin\Delta\omega\tau + \frac{\Delta\omega}{\omega_e}\sin\frac{\omega_e t_{\text{w}}}{2}\cos\Delta\omega\tau\right) \quad (27)$$

Let us keep in mind that in the absence of HDI H_{d} the Hamiltonian $\omega_{\text{eff}}\boldsymbol{I}_p$ can be considered as an effective Hamiltonian H_{eff} of the spin system subjected to the irradiation of the sequence consisting of identical RF pulses where each of the pulses is determined by Equation (16) with the initial phase $\phi = 0$.

Here, neglecting as before the Hamiltonian H_{d} during the impact of the pulses, we however are trying to consider the influence of dipolar interactions on the spin system in the pulse spacing. For this purpose we define the effective Hamiltonian H_{eff} with the expression:

$$\exp(-\mathrm{i}H_{\text{eff}}2\tau) = \exp\Big(-\mathrm{i}(\Delta\omega I_{p,3} + H_{\text{d}})\tau\Big)\exp\Big(\mathrm{i}\omega_e\boldsymbol{k}(0)\boldsymbol{I}_p t_w\Big)\exp\Big(-\mathrm{i}(\Delta\omega I_{p,3} + H_{\text{d}})\tau\Big)$$
$$= \exp(-\mathrm{i}\tau H_{\text{d}})\exp(\mathrm{i}\omega_{\text{eff}} t_{\text{w}}\boldsymbol{I}_p)\exp(-\mathrm{i}\tau H_{\text{d}}). \quad (28)$$

In the latter expression we used the equation $[\Delta\omega I_{p,3}, H_{\text{d}}] = 0$.

At the time $> T_2$ after the beginning of the pulse sequence the processes in the spin system are sufficiently slow to be considered as quasi-equilibrium. Such state of the spin system may be described by the density matrix ρ_{qst}, which meets the condition of equilibrium:

$$\exp(-\mathrm{i}2\tau H_{\text{eff}})\rho_{\text{qst}}\exp(\mathrm{i}2\tau H_{\text{eff}}) = \rho_{\text{qst}}. \quad (29)$$

We assume that the usual condition $||H_\mathrm{d}||\tau \ll 1$ is experimentally realisable in our case and find one of the solutions for Equation (29) to the first order approximation with respect to the parameter $\varepsilon = ||H_\mathrm{d}||\tau$. Solution in the linear approximation is equivalent to neglecting a slow irreversible decay of magnetisation. At this approach the first solution ρ_qst for may be obtained as a linear combination of six operators: $H_\mathrm{d}^m (m = 0, \pm 1, \pm 2)$ and $\omega_e I_p 2\tau$. Here H_d^m are the parts of H_d which are defined by equations[20]:

$$H_\mathrm{d} = \sum_m H_\mathrm{d}^m, \ [\boldsymbol{n}\boldsymbol{I}_p, H_d^m] = mH_\mathrm{d}^m, \ m = 0, \pm 1, \pm 2. \tag{30}$$

Hence,

$$\rho_\mathrm{qst1} = \sum_{m=-2}^{2} c_m H_\mathrm{d}^m + 2\tau \cdot \omega_\mathrm{eff} \boldsymbol{I}_p \tag{31}$$

is assumed to be equal to 1. Using the expansion

$$\exp(\hat{L})\ \hat{a}\ \exp(-\hat{L}) = \hat{a} + \frac{1}{1!}[\hat{L}, \hat{a}] + \frac{1}{2!}[\hat{L}, [\hat{L}, \hat{a}]] + \ldots, \tag{32}$$

where $\hat{L}$ and a and are arbitrary operators.

Inserting Equation (31) in (29) and for three times in accordance with Equation (28) using (32), in linear approximation ε of we receive

$$c_m = m\varphi \cdot \tau \cot \frac{m\varphi}{2}, \tag{33}$$

where $\varphi = 2\omega_\mathrm{eff}\tau$.

The first and the second solutions of Equation (29) are obvious:

$$\rho_\mathrm{qst1} = E,$$

$$\rho_\mathrm{qst2} = 2\tau H_\mathrm{d}^0.$$

The third solution can be represented as:

$$\rho_\mathrm{qst3} = \boldsymbol{n}\boldsymbol{I}_p\varphi + 2\tau \sum_{\substack{m=-2 \\ m\neq 0}}^{m=2} \left(\frac{m\varphi}{2}\right) \cot \frac{m\varphi}{2} H_\mathrm{d}^m. \tag{34}$$

According to condition $\mathrm{Tr}\rho_\mathrm{qst} = 1$ the total solution is received from:

$$\rho_\mathrm{qst} = \left\{ E - \alpha_\mathrm{qst} \frac{1}{2\tau} \rho_\mathrm{qst3} - \beta_\mathrm{qst} \frac{1}{2\tau} \rho_\mathrm{qst2} \right\}, \tag{35}$$

where α_{qst} and β_{qst} are the inverse temperatures. Note that $\alpha_\mathrm{qst} = \beta_\mathrm{qst}$ for $\omega_\mathrm{eff} \leq \omega_\mathrm{loc}$ and $\beta_\mathrm{qst} = 0$ for $\omega_\mathrm{eff} > \omega_\mathrm{loc}$ ($\omega_\mathrm{loc}^2 \equiv \mathrm{Tr}(H_\mathrm{d})^2 / \mathrm{Tr}(I_{p,3})^2$). Therefore, we can rewrite Equation (35) as:

$$\rho_{\mathrm{qst}} = \frac{1}{3}\{E - \alpha_{\mathrm{qst}} H_{\mathrm{eff}}\}, \tag{36}$$

where

$$H_{\mathrm{eff}} = \frac{1}{2\tau}\rho_{\mathrm{qst3}} + \frac{P}{2\tau}\rho_{\mathrm{qst2}}, \tag{37}$$

$P = 1$ for $\omega_{\mathrm{eff}} \leq \omega_{\mathrm{loc}}$ and $P = 0$ for $\omega_{\mathrm{eff}} > \omega_{\mathrm{loc}}$.

Note that $H_{\mathrm{eff}} = H_{\mathrm{d}}$ for $\phi = 0$ and $H_{\mathrm{eff}} = \phi \cdot \boldsymbol{n} I_p$ for $H_{\mathrm{d}} = 0$. To obtain the inverse temperature α_{qst} we use the expressions

$$\mathrm{Tr}(\rho_{\mathrm{qst}} H_{\mathrm{eff}}) = \mathrm{Tr}(\rho_0 H_{\mathrm{eff}}) :$$

$$\alpha_{\mathrm{qst}} = \alpha_0 \omega_p \frac{\varphi}{2\tau} \frac{n_1 l_1 + n_3 l_3}{\frac{\varphi^2}{4\tau^2} + \sum\limits_{m \neq 0} \left(\frac{m\varphi}{2} \cot \frac{m\varphi}{2}\right)^2 \frac{\mathrm{Tr}\left(H_{\mathrm{d}}^{m}(\tau) H_{\mathrm{d}}^{-m}(\tau)\right)}{\mathrm{Tr}(I_{p,3})^2} + \frac{P\mathrm{Tr}\left(H_{\mathrm{d}}^{0}(\tau)\right)^2}{\mathrm{Tr}(I_{p,3})^2}}. \tag{38}$$

The traces $\mathrm{Tr}(H_{\mathrm{d}}^{m} H_{\mathrm{d}}^{-m})$for a two-spin system are given in paper.[35] The resulting magnetization has two components 90°-shifted in phase

$$M_{\mathrm{qst}k} = 2\mathrm{Tr}(\rho_{\mathrm{qst}} I_{p,k}) = -\alpha_{\mathrm{qst}} \frac{\varphi}{2\tau} n_k, \; k = 1, 2. \tag{39}$$

If the influence of dipolar interactions can be neglected, then in the case of the MW-4 sequence

$$M_{\mathrm{qst}}(\mathrm{MW}\ 4) = -\alpha_0 \omega_p (n_1 l_1 + n_3 l_3) n_1. \tag{40}$$

For the SORC sequence $l_1 = 0$, $l_3 = 1$ and relation

$$M_{\mathrm{qst}}(\mathrm{SORC}) = -\alpha_0 \omega_p n_3 n_1 \tag{41}$$

is true.

The maximum amplitude of the free induction decay signal M_{FID}, generated by a single pulse, is achieved immediately after the end of the pulse and can be determined from Equation (22)

$$M_{\mathrm{FID}} = 2\mathrm{Tr}(\rho_0 I_{p,1}) = -\alpha_0 \omega_p, \; \mathrm{if} \phi = \pi/2,$$

or

$$M_{\mathrm{FID}} = 2\mathrm{Tr}(\rho_0 I_{p,2}) = -\alpha_0 \omega_p, \; \mathrm{if} \phi = 0. \tag{42}$$

If we assume that the phase of the preparatory pulse $\phi = \pi/2$ and the resonance offset conforms to the $\Delta\omega << \omega_1$ condition, then from Equations (22), (40) and (41) we obtain

$$\frac{M_{qst}(MW4)}{M_{FID}} = -n_1^2 \sin\varphi_0 + n_3 n_1 \cos\varphi_0$$
$$= -\frac{\sin^2\frac{\varphi}{2}\cos^2\Delta\omega\tau}{1-\cos^2\frac{\varphi}{2}\cos^2\Delta\omega\tau}\sin\varphi_0 + \frac{1}{4}\frac{\sin\varphi\cdot\sin(2\Delta\omega\tau)}{1-\cos^2\frac{\varphi}{2}\cos^2\Delta\omega\tau}\cos\varphi_0; \quad (43)$$

$$\frac{M_{qst}(SORC)}{M_{FID}} = n_3 n_1 = \frac{1}{4}\frac{\sin\varphi\cdot\sin\ (2\Delta\omega\tau)}{1-\cos^2\frac{\varphi}{2}\cos^2\Delta\omega\tau}. \quad (44)$$

As was shown in articles,[36,37] the preparatory pulse effect is ''forgotten'' by the spin system after times of about several T_{2e} and, consequently, the spin-locking effect vanishes at the same time. If in Equation (43) we set $\varphi_0 = 0$, the result will be that ''forgetting'' the preparatory pulse leads to the disappearance of the differences between MW-4 and SORC.

It follows from Equation (43) that the maximum amplitude of the signal created by sequence MW-4 equals the maximum amplitude of the free induction decay signal M_{FID} and is achieved at

$$\varphi_0 = \frac{\pi}{2} \text{ or } \frac{3\pi}{2},\ \phi = \pm\frac{\pi}{2},\ \Delta\omega\tau = \pi k,\ k = 0,\ \pm 1,\ \pm 2, \ldots. \quad (45)$$

In case of SORC the maximum possible amplitude of the signal is determined by the maximum product of $n_3 n_1$ and equals half of the M_{FID} value. To achieve the maximum value of the value of $n_3 n_1$ the pulses flip angle φ and parameter $\Delta\omega\tau$ must equal

$$\varphi = \frac{\pi}{2} \text{ or } \frac{3\pi}{2}, \Delta\omega\tau = \pi/2 + \pi k, \quad k = 0, \pm 1, \pm 2, \ldots. \quad (46)$$

2.2. Stationary state

When considering the states of the spin system when irradiating it with a multipulse sequence at times $>T_1$ we proceed from the assumption that there are two mechanisms that ensure the existence of the stationary signal. The first mechanism is connected with the interaction between the quadrupole and the dipole–dipole reservoirs, hence when the resonance conditions are not met, part of the energy is transferred from the quadrupole to the dipole–dipole reservoir, preventing the saturation of the spin system and the attenuation of the signal.

The second mechanism as we see it can only occur in the case of strong spin–lattice relaxation, as in RDX, for example. In this case the exchange of energy between the quadrupole system and the spin–lattice can also lead to the establishment of the stationary state.

The first mechanism has been thoroughly analysed in articles[19–21] more than two decades ago, but the second mechanism was analysed relatively recently.[16]

Following paper[16] we shall give here the brief description of the second mechanism.

If the existence of the stationary signal at time $>T_1$ is not determined by the interactions between quadrupole and dipole–dipole reservoirs but by the spin–lattice relaxation, we can neglect processes in which the spins absorb the quanta of the dipole–dipole interaction modulated by the RF field and can omit corresponding terms in the total Hamiltonian of the spin system. Such reduced total Hamiltonian coincides with the effective Hamiltonian H_{eff} in Equation (37).

We consider the case when $P = 0$ in Equation (37) and limit analysis to the case T_2 when T_1 and are close.

The density matrix of the quasi-stationary state in the representation of the interaction H_0 looks as follows:

$$\tilde{\rho}_{\text{st}} = \frac{1}{3}\{E - \alpha_{\text{st}} H_{\text{eff}} - \beta_{\text{st}} \omega'_p I_{p,4}\}, \tag{47}$$

α_{st} and $\beta_{\text{st}} = \alpha_0$ are reverse spin temperatures of the parts of the spin system that respectively are and are not excited by the RF pulses.

In Equation (47) we resume using the tilde notation when determining operators in the representation of the interaction.

As the time of establishing the spin temperature ($\sim T_2$) coincides with the time of the spin–lattice relaxation T_1, than β_{st} practically does not deviate from its equilibrium value and remains a constant value equal to α_0. Consequently, a part of the density matrix $\beta_{\text{st}}\omega'_p I_{p,4}$ is the integral of the motion and can be excluded from our consideration.

Taking into account the Hamiltonian of the spin–lattice interactions H_{SL} at times $\sim T_1$ can be treated with the usual perturbation theory using the master equation.[38]

A complete operator set that permits to adequately describe the behaviour of the spin system has to contain $4I(I+1)$ independent operators, which constitutes eight operators for spin $I = 1$.[39] A set of operators of the fictitious spin-1/2 $I_{p,i}$ ($p = x, y, z$; $i = 1, 2, 3$) contains 12 operators, eight of which are independent and consequently form a complete basis set of the spin-1 system.

The fictitious spin-1/2 have to be determined in the basis set of eigenstates of operator H_{Q}. This choice permits the simplest way of linking the components of the magnetization of the nuclear–spin systems with the mean values of the operators of the fictitious spin-1/2.[39]

The total Hamiltonian of the spin system in our case in the representation of H_0 is $\tilde{H} = H_{\text{eff}} + \tilde{H}_{\text{SL}}$. Considering $\tilde{H}_{\text{SL}}$ as a perturbation, we can use the master equation for the density matrix[38]:

$$\frac{\mathrm{d}}{\mathrm{d}t}\tilde{\rho}(t) = -\int_0^t \overline{[\tilde{H}_{\text{SL}}(t), \tilde{H}_{\text{SL}}(t-t'), \rho(t) - \rho(0)]}\,\mathrm{d}t'. \tag{48}$$

In accordance with article[28] when using the complete basis of operators, Equation (48) can be transformed into a kinetic equation:

$$\frac{\mathrm{d}}{\mathrm{d}t}\langle\tilde{Q}\rangle = -\left[\frac{1}{T}\right](\langle\tilde{Q}\rangle - \langle Q\rangle_0), \tag{49}$$

where matrix $\left[\frac{1}{T}\right]$ determines the relaxation of any time indepentent observable Q like I_x, I_y, I_z in the representation of H_0; $\tilde{Q} = \exp(\mathrm{i}H_0t)Q\exp(-\mathrm{i}H_0t)$; $\langle\tilde{Q}\rangle = \mathrm{Tr}\Big(Q \cdot \tilde{\rho}(t)\Big)$; $\langle Q\rangle_0 = \mathrm{Tr}(Q \cdot \rho_0)$; $\rho_0 \equiv \rho(0)$.

In particular, at $Q \equiv I_{p,i}$ the following is true:

$$\frac{\mathrm{d}}{\mathrm{d}t}\langle\tilde{I}_{p,i}\rangle = \sum_q\sum_j \frac{1}{T_{(p,i)(q,j)}}(\langle\tilde{I}_{q,j}\rangle - \langle I_{q,j}\rangle_0), \tag{50}$$

$1/T_{(p,i)(q,j)}$ are the components of the matrix $\left[\frac{1}{T}\right]$.

Let us proceed to the rotating frame set by the transformation

$$Q^* = \exp(-\mathrm{i}H_{\mathrm{eff}}t)\tilde{Q}\exp(\mathrm{i}H_{\mathrm{eff}}t). \tag{51}$$

In this frame the density matrix equals

$$\rho^* = \exp(-\mathrm{i}H_{\mathrm{eff}}t)\tilde{\rho}\exp(\mathrm{i}H_{\mathrm{eff}}t) \tag{52}$$

and, consequently

$$\begin{aligned}\frac{\mathrm{d}}{\mathrm{d}t}\langle Q\rangle^* &= \mathrm{Tr}\left\{Q^*\frac{\mathrm{d}}{\mathrm{d}t}\rho^*\right\} = -\mathrm{i}\mathrm{Tr}\left\{[Q, H_{\mathrm{eff}}], \tilde{\rho}\right\} + \frac{\mathrm{d}}{\mathrm{d}t}\tilde{Q} \\ &= -\mathrm{i}\mathrm{Tr}\left\{[Q, H_{\mathrm{eff}}], \tilde{\rho}\right\} - \left[\frac{1}{T}\right](\langle\tilde{Q}\rangle - \langle Q > {}_0\rangle).\end{aligned} \tag{53}$$

As follows from,[28] in case of spin I= 1 the density matrix $\tilde{\rho}$ can be presented in form

$$\tilde{\rho} = \frac{1}{3}E + 2\sum_q\sum_j\langle\tilde{I}_{q,j}\rangle I_{q,j}, \quad \langle\tilde{I}_{q,j}\rangle = \mathrm{Tr}(I_{q,j}\cdot\tilde{\rho}). \tag{54}$$

Substituting (54) into (53) with $Q \equiv I_{p,i}$, one can get

$$\frac{\mathrm{d}}{\mathrm{d}t}\langle I_{p,i}\rangle^* = -\mathrm{i}\sum_q\sum_j\omega_{(p,i)(q,j)}\langle\tilde{I}_{q,j}\rangle + \sum_q\sum_j\frac{1}{T_{(p,i)(q,j)}}(\langle\tilde{I}_{q,j}\rangle - \langle I_{q,j}\rangle_0). \tag{55}$$

Here

$$\omega_{(p,i)(q,j)} = 2\mathrm{Tr}\{[I_{p,i}, H_{\mathrm{eff}}], I_{q,j}\}. \tag{56}$$

When calculating $\omega_{(p,i)(q,j)}$ it is necessary to take into account that $\mathrm{Tr}\{[I_{p,i}, H_d^m], I_{q,j}\} = 0$.[35]

Then, if for the stationary state we assume that $\frac{d}{dt}\langle I_{p,i}\rangle^* = 0$ and also take into account that $\langle I_{q,j}\rangle_0 = 0$ at $j \neq 3$ and that at relaxation times under consideration it is possible to neglect all members for which $p \neq q$, we shall receive a simple system consisting of three equations:

$$\begin{aligned} 0 &= \omega_{\text{eff}}(n_2\langle\tilde{I}_{p,3}\rangle - n_3\langle\tilde{I}_{p,2}\rangle) + \frac{\langle\tilde{I}_{p,1}\rangle}{T_{12}}, \\ 0 &= \omega_{\text{eff}}(n_3\langle\tilde{I}_{p,1}\rangle - n_1\langle\tilde{I}_{p,3}\rangle) + \frac{\langle\tilde{I}_{p,2}\rangle}{T_{12}}, \\ 0 &= \omega_{\text{eff}}(n_1\langle\tilde{I}_{p,2}\rangle - n_2\langle\tilde{I}_{p,1}\rangle) + \frac{\langle\tilde{I}_{p,3}\rangle - \langle I_{p,3}\rangle_0}{T_{11}}. \end{aligned} \tag{57}$$

the solution for which will look as follows:

$$\begin{aligned} \langle\tilde{I}_{p,1}\rangle &= \frac{1}{6}\alpha_0\omega_p \frac{\omega_{\text{eff}} n_2 T_{12} - \omega_{\text{eff}}^2 T_{12}^2 n_1 n_3}{1 + \omega_{\text{eff}}^2\{n_3^2 T_{12}^2 + (n_1^2 + n_2^2)T_{12}T_{11}\}}; \\ \langle\tilde{I}_{p,2}\rangle &= -\frac{1}{6}\alpha_0\omega_p \frac{\omega_{\text{eff}} T_{12} n_1 + \omega_{\text{eff}}^2 T_{12}^2 n_2 n_3}{1 + \omega_{\text{eff}}^2\{n_3^2 T_{12}^2 + (n_1^2 + n_2^2)T_{12}T_{11}\}}; \\ \langle\tilde{I}_{p,3}\rangle &= \frac{1}{6}\alpha_0\omega_p \frac{1 + \omega_{\text{eff}}^2 T_{12}^2 n_3^2}{1 + \omega_{\text{eff}}^2\{n_3^2 T_{12}^2 + (n_1^2 + n_2^2)T_{12}T_{11}\}}. \end{aligned} \tag{58}$$

T_{12} is a spin–lattice relaxation time for $I_{p,1}$ and $I_{p,2}$; T_{11} is a spin–lattice relaxation time for $I_{p,3}$.

It follows from (27) that for the multi-pulse spin-locking sequence $n_2 = 0$, so we shall obtain

$$\begin{aligned} \langle\tilde{I}_{p,1}\rangle &= -\frac{1}{6}\alpha_0\omega_p \frac{\omega_{\text{eff}}^2 T_{12}^2 n_1 n_3}{1 + \omega_{\text{eff}}^2\{n_3^2 T_{12}^2 + n_1^2 T_{12}T_{11}\}}; \\ \langle\tilde{I}_{p,2}\rangle &= -\frac{1}{6}\alpha_0\omega_p \frac{\omega_{\text{eff}} T_{12} n_1}{1 + \omega_{\text{eff}}^2\{n_3^2 T_{12}^2 + n_1^2 T_{12}T_{11}\}}; \\ \langle\tilde{I}_{p,3}\rangle &= \frac{1}{6}\alpha_0\omega_p \frac{1 + \omega_{\text{eff}}^2 T_{12}^2 n_3^2}{1 + \omega_{\text{eff}}^2\{n_3^2 T_{12}^2 + n_1^2 T_{12}T_{11}\}}. \end{aligned} \tag{59}$$

The expressions for the in-phase and the quadrature magnetisation components are:

$$\begin{aligned} M_1 &= 2\langle I_{p,1}\rangle = -\frac{1}{3}\alpha_0\omega_p \frac{\omega_{\text{eff}}^2 T_{12}^2 n_1 n_3}{1 + \omega_{\text{eff}}^2\{n_3^2 T_{12}^2 + n_1^2 T_{12}T_{11}\}}, \\ M_2 &= 2\langle I_{p,2}\rangle = -\frac{1}{3}\alpha_0\omega_p \frac{\omega_{\text{eff}} T_{12} n_1}{1 + \omega_{\text{eff}}^2\{n_3^2 T_{12}^2 + n_1^2 T_{12}T_{11}\}}. \end{aligned} \tag{60}$$

It should be noted that when substituting $T_{12} \to T_2$, $T_{11} \to T_1$, $\omega_{\text{eff}} n_1 \to \gamma H_1$ and $\omega_{\text{eff}} n_3 \to \Delta\omega$(γ is the gyromagnetic ratio of the nucleus, H_1 is the amplitude of the RF field, $\Delta\omega$ is the resonance offset of the carrier frequency), Equations (60) coincide completely with the expressions for the magnetisation obtained on the basis of the equations by Bloch[40] for a continuous RF irradiation of a substance.

Note that at $T_{12} \approx T_{11} \equiv T_1$

$$M_1 = -\frac{1}{3}\alpha_0\omega_p \frac{\omega_{eff}^2 \mathrm{T}_1^2 n_1 n_3}{1+\omega_{eff}^2 \mathrm{T}_1^2}, \quad M_2 = -\frac{1}{3}\alpha_0\omega_p \frac{\omega_{eff} \mathrm{T}_1 n_1}{1+\omega_{eff}^2 \mathrm{T}_1^2}. \tag{61}$$

2.3. Experiments with multi-pulse sequences

To determine the optimal correlation between pulse intervals in the MW-4 sequence and relaxation parameters of a substance, the dependence of the effective relaxation time T_{2e} on the pulse interval 2τ was studied in powder $NaNO_2$ at the ν_+ = 4.640 MHz resonance transition at 22 °C.[41] Flip angles of the pulses were 0.66 π (90° pulse in powder) and 0.33 π. Figure 1 shows the diagrams of the dependences of T_{2e} on 2τ.

As one can observe from the dependence at $2\tau \leq 2$ ms the T_{2e} time achieves its maximum value which is close to the time of spin–lattice relaxation T_1= 90 ms.[42] At the transition frequency ν_+ the inverse parameter of the line width T_2^* equals 2 ms[42] and therefore the condition of achieving the maximum value of T_{2e} and consequently the maximum intensity of the NQR signal can be written as $2\tau \leq T_2^*$.

The dependences of signal intensity for sequences MW-4 and SORC on the resonance offset $\Delta\omega/2\pi$ presented in Figure 2 confirm theoretical calculations that the maximum signal obtained with the MW-4 sequence is almost twice greater than the maximum signal achieved with the SORC sequence. The dependences also demonstrate the advantage of MW-4 over SORC under the conditions of exact resonance.

The advantage of the MW-4 sequence in intensity is preserved at times $\sim T_{2e}$ that allows to reduce considerably the detection time of the substances with the spin–lattice relaxation time T_1 exceeding several seconds (TNT, PETN, HMX, black powder, etc.).

Besides selecting the conditions for receiving the maximum signal amplitude with the minimum sample saturation, another important factor for successful detection with multi-pulse sequences is the irradiation power. Using high power when detecting such easily saturated samples as, for example, TNT can lead to the complete saturation of the sample even before the transition of the spin-system into the steady-state regime, i.e. during the time ~2–3 T_2. Therefore when establishing the power of the irradiating pulses it is necessary to consider the saturation factor $[1+(\gamma H_1/2\tau)^2 T_1 T_2^*]^{-1}$.[43] Obviously the value of $\gamma^2 H_1 T_1 T_2^*$ should not exceed 1 manifold.

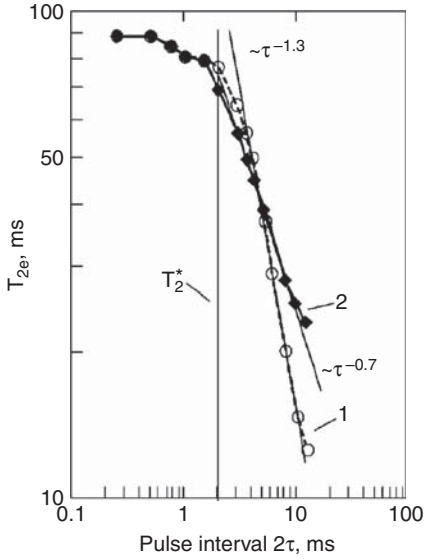

Figure 1 The dependences of the effective relaxation time T_{2e} on the pulse interval 2τ at 22 °C obtained with the sequence MW-4 $(\varphi_0)_y - (\tau - \varphi_x - \tau)_n$ at $\varphi = \varphi_0 = 0.66\pi$ (curve 1) and $\varphi = \varphi_0/2 = 0.33\pi$(curve 2).

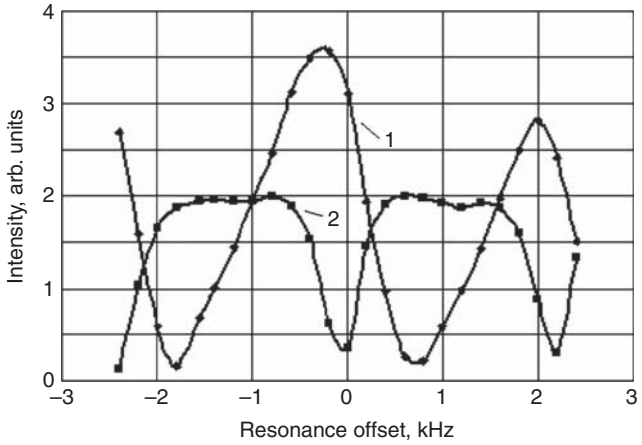

Figure 2 Diagrams of powdered $NaNO_2$ NQR quasi-stationary signal intensity as a function of the resonance offset at line $\nu_+ = 4.640$ MHz. Curves 1 and 2 are plotted for the signal obtained with sequences $(\varphi_0)_y - (\tau - \varphi_x - \tau)_n$ and $(\tau - \varphi_x - \tau)_n$ correspondingly. Sequence parameters are $\tau = 232$ μs; all pulse widths are 80 μs ($\varphi = \varphi_0 = 0.66$ π); the number of averages is 100. To avoid transient processes the averages were begun after first 10 cycles of the sequence.

Having touched upon the basic principles of multi-pulse detection, we will examine in more detail the issue of TNT detection.

Thus in Figure 3 we presented the TNT ν_- spectral line at 741.2 kHz, obtained in a 1-l coil from a 200 g sample after 0.5 s when irradiating with the MW-4

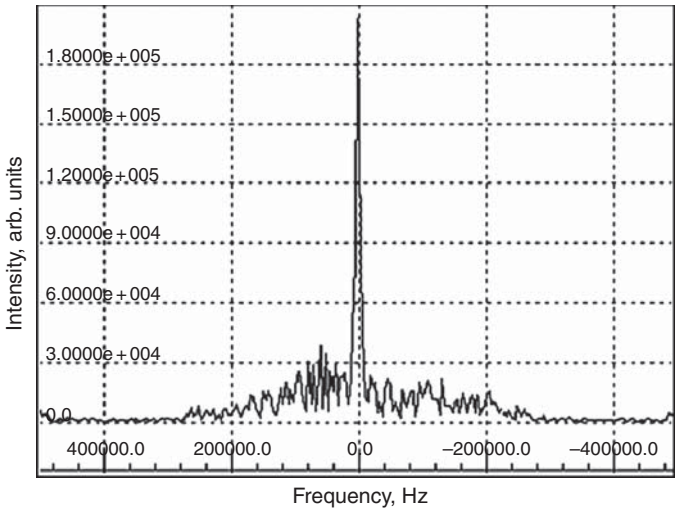

Figure 3 The spectral line at 741.2 kHz in TNT obtained at the temperature of 23 °C using multi-pulse spin-locking $(\varphi_0)_y - (\tau - \varphi_x - \tau)_n$ at $n = 2000$, $\tau = 120$ μs, all pulse widths are 80 μs.

sequence with the following parameters: $\tau = 120$ μs; $t_{w0} = t_w = 80$ μs; peak power of the transmitter was 100 W.

The measurements of the magnetisation behaviour in the centre of the pulse interval were taken as follows. At exact resonance one of the signal components (e.g., quadrature) was set for the minimum. At a small resonance offset we adjusted the choice of the point in the pulse interval where the signal was registered. The position of the point remained permanent for both the stationary and the quasi-stationary signal measurements.

When measuring the quasi-stationary signal in $NaNO_2$ and the stationary signal in RDX, during the first 10 cycles the signal was not registered, and after that during the following 100 cycles the averaging of the signal was performed.

When measuring the stationary signal in the same substance the first 400 cycles were left out and then during the following 100 the averaging was performed.

The results of measurements with the sequences $(\varphi_0)_y - (\tau - \varphi_x - \tau)_n$ and $(\tau - \varphi_x - \tau)_n$ in $NaNO_2$ for the signals in the quasi-stationary state are presented in Figure 4.

In Figure 5 the dependence of the stationary signal in RDX on the offset for the sequence $(\tau - \varphi_x - \tau)_n$ at resonance transition $\nu_- = 3.41$ MHz is presented.

In Figure 6 theoretical dependencies on the offset stationary magnetisation in sequence $(\tau - \varphi_x - \tau)_n$, obtained on the basis of Equations (61), are demonstrated.

In the case of long relaxation times T_1 ($NaNO_2$) the theory presented in article[20] quite adequately covers the experimental results.

Equations (39) and (60) for quasi-stationary and stationary magnetisation offer quite a simple description of the NQR system in multi-pulse experiments.

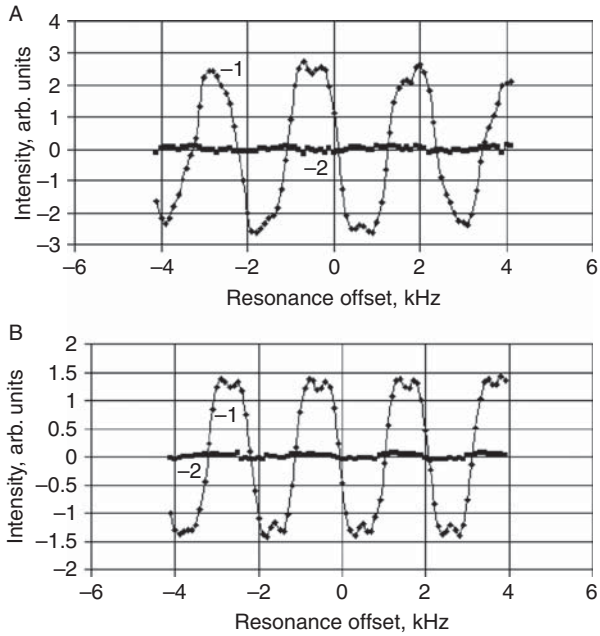

Figure 4 Diagrams of powdered $NaNO_2$ NQR signal intensity in the middle of the pulse spacing as a function of the resonance offset. Curves 1 and 2 are plotted correspondingly for the in-phase and quadrature components of the quasi-stationary signal obtained with sequences (A) $(\varphi_0)_y - (\tau - \varphi_x - \tau)_n$ and $(\tau - \varphi_x - \tau)_n$. Sequence parameters are $\tau = 490$ μs; all pulse widths are 62 μs; the number of averages is 10. Averages were begun after first 10 cycles of the sequence.

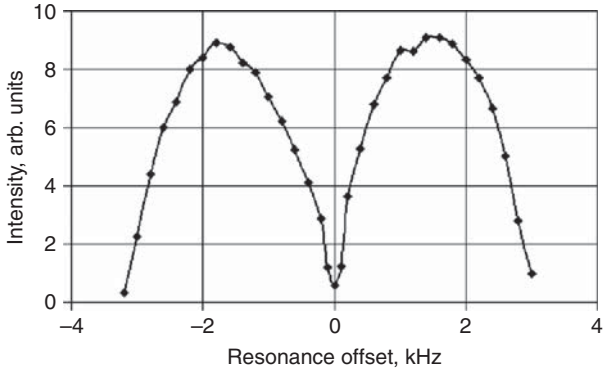

Figure 5 Diagrams of powdered RDX NQR signal intensity as a function of the resonance offset obtained with the sequence at $(\tau - \varphi_x - \tau)_n$ resonance line $\nu_- = 3.41$ MHz. Sequence parameters are $\tau = 168$ μs; all pulse widths are 62 μs; the number of averages is 100. Averages were begun after first 10 cycles of the sequence.

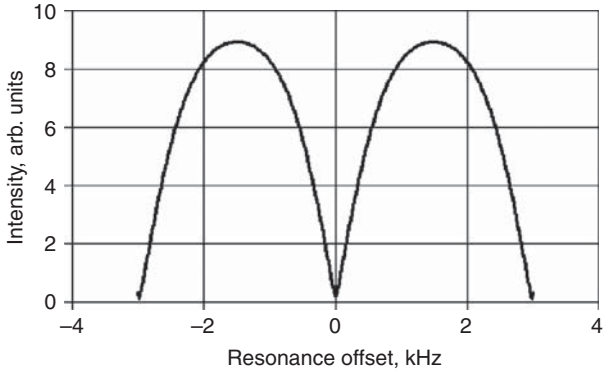

Figure 6 Theoretical dependence on the offset for quasi-stationary stationary magnetisation in sequence $(\tau - \varphi_x - \tau)_n$, obtained on the basis of expressions (61). Sequence parameters used for calculations are the same as in Figure 5.

Equation (39) is applicable for analysing the magnetisation behaviour of substances, for the detection of which the stationary state is practically not used, such as PETN, TNT and black powder. To analyse the magnetisation of substances with very short relaxation times, such as RDX, where quasi-stationary state is very short, Equations (60) and (61) can be used with satisfactory results.

3. POLARIZATION ENHANCEMENT OF NQR SIGNALS

The issue of methods for enhancing weak NQR signals in nitrogen-14 when detecting explosive substances is one of the central issues in applied NQR spectroscopy. It has been approached in a number of publications, e.g. Refs. 3, 10–12, 14, 44–48. The experiments described in papers[45,46] in polarization of quadrupolar nuclei through the thermal contact with the proton Zeeman system which was preliminarily polarized in an inhomogeneous magnetic field are the simplest to implement and therefore look the most promising for detecting explosive substances with low NQR frequencies such as PETN and TNT. In paper[49] the polarization method was used for the detection of plastics with 70% contents of PETN C $(CH_2ONO_2)_4$. The experiments were taking place at room temperature, and the signal was detected by a multi-pulse sequence MW-4.

The scheme of the experiment on polarization enhancement of NQR signals for PETN detection is shown in Figure 7. A PETN sample was placed for a fixed period of time between two identical ring magnets after which it was manually transferred inside the solenoidal coil of the detector of an NQR spectrometer where the signal from ^{14}N nuclei was detected using a multi-pulse spin-locking sequence MW-4 $\varphi_y - (\tau - \varphi_x - \tau)_n$.

The peak power achieved in every pulse of the MW-4 sequence when detecting an NQR signal from a PETN sample was low and did not exceed 20 W. The

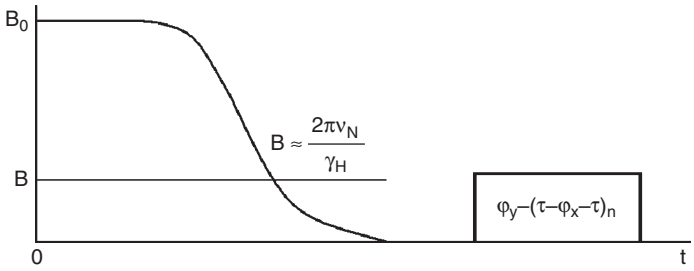

Figure 7 Scheme of the experiment on polarization enhancement of NQR signals for PETN detection. The experiment is conducted in three stages: polarization of the proton system of the sample in a permanent magnetic field B_0 (Zeeman proton system and quadrupole nitrogen nuclei system are isolated from each other); bringing the quadrupole and the Zeeman system in thermal contact when the ^{1}H NMR and ^{14}N NQR energy level splittings cross (at this stage polarization is transferred from the protons to the nitrogen nuclei); NQR signal detection with a multi-pulse sequence in a zero magnetic field (the Zeeman and the quadrupole systems of the sample are again thermally isolated from each other).

duration of all pulses in the MW-4 sequence including the preparatory pulse was 200 μs; the delay between the back edge of the RF pulse and the beginning of detection was 150 μs; the acquisition time was 512 μs. The number of pulses in the sequence coinciding with the number of averagings equalled $n = 4000$. The sample of the sheet plastic PETN was circle shaped with the thickness of ~1 cm, the mass of the sample was 160 g. The parameters of each magnet used in the experiment: external and internal diameters equal 5 and 2 cm, respectively, thickness equals 1.2 cm. The magnitude of the magnetic field on the surface of the magnets was ~170 mT. The averaged magnetic field for the sample volume was $B_0 \approx 80$ mT. All measurements were taken at the temperature of 20 °C.

Let us consider the experiment from the point of view of physics.

During the polarization of protons in the permanent magnets field B_0 (Figure 7) the spin temperature of the proton system approaches lattice temperature T_L. After the T_L temperature is reached, the entropy of the proton system equals[50]

$$S = \text{const} - \frac{1}{2k}\left(\frac{B_0}{T_L}\right)^2, \tag{62}$$

where k is the Boltzmann constant.

Then the sample is removed from the field of the magnets. To preserve the proton polarization, the demagnetization process is carried out adiabatically ($dB/dt < \gamma_H B_{loc}$, where γ_H is the gyromagnetic ratio for protons, B_{loc} is the mean local dipole field at the sites of protons). The value of the permanent magnetic field inside the sample slowly decreases finally reaching the value of $B \approx 2\pi\nu_N/\gamma_H$. The entropy of the Zeeman proton reservoir at this moment is determined by expression

$$S = \text{const} - \frac{1}{2k}\left(\frac{B}{T^*}\right)^2, \tag{63}$$

where T^* is the new spin temperature of the proton system. T^* can be found from the condition of preserving entropy in the adiabatic process and equals

$$T^* = \frac{B}{B_0}T_L = \frac{2\pi\nu_N}{\gamma_H B_0}T_L = \frac{\nu_N}{\nu_H(B_0)}T_L, \tag{64}$$

$\nu_H(B_0)$ is the frequency of the Larmor precession of protons in the B_0 field; ν_N is the resonance frequency the quadrupole nuclei of nitrogen.

It is obvious that the temperature of the subsystem of the sample consisting of nitrogen nuclei equals the lattice temperature T_L and for the case of $\nu_H \gg \nu_N$ it is true that $T_L \gg T^*$. Thus when the proton and quadrupolar systems get in thermal contact, the spin temperature of the proton system is much lower than the temperature of nitrogen system. After the splittings between the energy levels of both systems cross, a common spin temperature T is established due to the energy exchange through dipole–dipole interactions. It can be calculated based on the condition of conservation of energy:

$$\langle H\rangle_H + \langle H\rangle_N = \langle H\rangle_{H+N}, \tag{65}$$

where $\langle H\rangle_H$ and $\langle H\rangle_N$ are the energies of the Zeeman and quadrupole hermodynamic reservoirs, respectively, at the moment the energy levels were crossed $\nu_H(B) = \nu_N$; $\langle H\rangle_{H+N}$ is the energy of the common reservoir of protons and quadrupole nuclei after the common spin temperature was attained; and B is the value of the magnetic induction when the energy levels were crossed.

Note that the energy of the reservoir of dipole–dipole interactions was ignored. The values of energies $\langle H\rangle$ satisfy the relations

$$\langle H\rangle_N \sim \frac{\nu_N^2}{T_L}N_N,\ \langle H\rangle_H \sim \frac{\nu_H^2}{T^*}N_H,\ \langle H\rangle_{H+N} \sim \frac{1}{T}[N_N\nu_N^2 + N_H\nu_H^2]. \tag{66}$$

Here, N_H and N_N are the amounts of protons and nitrogen nuclei in the sample.

Substituting Equation (66) into Equation (65) and taking into account that when the splittings $\nu_p(B) = \nu_N$ cross, we get

$$\frac{\nu_N^2}{T_L}N_N + \frac{(\nu_H(B))^2}{T^*}N_H = \frac{1}{T}[N_N\nu_N^2 + N_H(\nu_H(B))^2]. \tag{67}$$

Keeping in mind that when the splittings cross $\nu_p(B) = \nu_N$, we get

$$\frac{1}{T_L}N_N + \frac{1}{T^*}N_H = \frac{1}{T}[N_N + N_H], \tag{68}$$

whence it follows that

$$F = \frac{1/T}{1/T_L} = \frac{\nu_N N_N + \nu_H(B_0)N_H}{\nu_N(N_N + N_H)} \approx \frac{\nu_H(B_0)}{\nu_N}\frac{N_H}{N_N + N_H}. \tag{69}$$

The value of F is proportional to the ratio of the population difference of the quadrupolar system energy levels before and after the splittings cross and consequently determines the gain in the amplitude of the NQR signal received as a result of transfer of polarization from the Zeeman to the quadrupolar subsystem.[46]

On the basis of the chemical formula of the PETN molecule $C(CH_2ONO_2)_4$, we obtain

$$\frac{N_H}{N_N + N_H} = \frac{2}{3}.$$

Thus, the gain is

$$F = \frac{2}{3}\frac{\nu_H(B_0)}{\nu_N} = \frac{2}{3}\frac{3.4\ \text{MHz}}{0.89\ \text{MHz}} \approx 2.6. \tag{70}$$

After the sample is removed from the magnetic field, the equation $\nu_H = \nu_N$ is no longer true, which leads to thermodynamic isolation between the Zeeman and the quadrupolar reservoirs. If the spin–lattice relaxation time of the quadrupole nuclei is sufficiently long (for the nitrogen nuclei of PETN spin relaxation time is 32 s at 20 °C[41]), then the polarization received by the nitrogen subsystem keeps long enough to be detected in the NQR signal amplitude by standard pulse methods.

Results of measurements are shown in Figures 8 and 9.

In Figure 8 one can see the graphic dependence of enhancement factor F on the time of proton polarization in the magnetic field B_0, measured as a ratio of NQR signals obtained before and after polarization.

In Figure 9 one can the dependence of the enhancement factor F on the resonance offset. Curve 1 was received without the sample polarization. Each point of the curve obtained after a 2-min polarization of the sample in the magnetic field B_0. Signal detection was performed using the same MW-4 sequence described above.

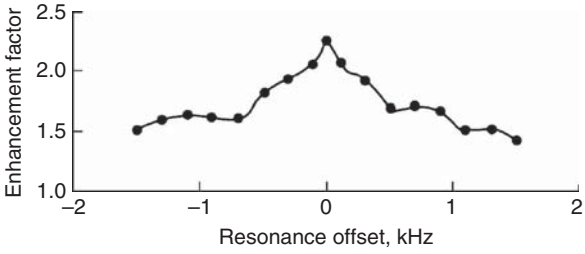

Figure 8 Dependence of enhancement factor F on the time of protons polarization in magnetic field $B_0 \approx 80$ mT, measured for NQR signals received before and after polarization. NQR signal detection was performed with multi-pulse spin locking sequence $\varphi_y - (\tau - \varphi_x - \tau)_n$ with the following parameters: $n = 4000$, duration of all pulses $= 200$ μs, pulse spacing $= 874$ μs, peak irradiation power $\sim$20 W.

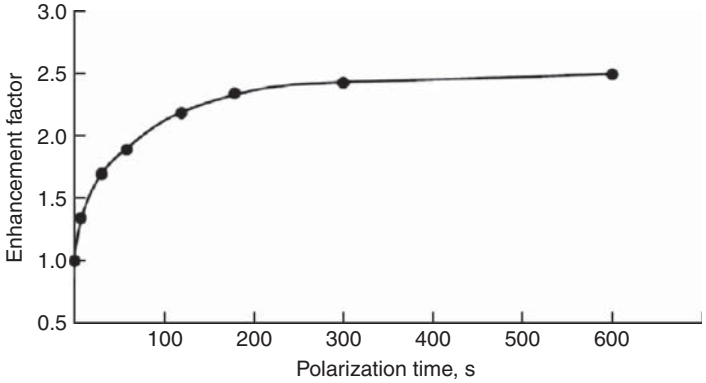

Figure 9 Enhancement factor *F* of the NQR signal obtained using the polarization enhancement technique, as a function of the resonance offset of the detecting sequence's carrier frequency. The parameters of the pulse sequence are given in Figure 8.

The results of measurements demonstrate that using Zeeman polarization enhancement of the NQR signal, considerable gain in the detection sensitivity can be achieved even though the magnets used have a comparatively weak magnetic field.

The obtained result is in reasonable accord with that expected based on Equation (70).

The experiments show at least twofold enhancement of the NQR signal from a PETN sample after the sample was subjected to a preliminary 2-min polarization in a strongly inhomogeneous field with the magnitude of ~80 mT averaged according to the sample volume. The experiments also demonstrate the efficiency of the method at room temperature which is very important for some applications. This method is unlikely to be suitable for NQR scanners intended for detecting explosives in hold stow or carry-on luggage in airports,[51–54] as there are strict time limitations for scanning each article, however, it could be used by small NQR scanners in postal, bank, embassy, office security, and so on.

4. MULTI-PULSE SEQUENCES UNDER CONDITIONS OF MAGNETO-ACOUSTIC AND PIEZO-ELECTRIC RINGING

One of the central problems that emerge while developing NQR devices for the detection of explosives in airport luggage is the issue of cancelling MAPER, generated by numerous objects containing metallic, ferrite, ferro- and piezo-electric components.

The MAPER problem in NQR spectroscopy became particularly urgent when the first NQR landmine detectors and luggage scanners started to be created[42,53,54] that was reflected mainly in patents[55–61] and, to a smaller extent, in journal and conference publications.[62,63]

In this article we follow paper[52] and deal only with multi-pulse sequences as the most powerful instrument for a critical increase in the signal-to-noise ratio while registering weak NQR ^{14}N signals produced by explosives. The sequences presented here according to Gerothanassis classification[64] refer to echo sequences and to sequences based on the linear properties of the distortions.

The methods suggested in paper[52] are based on using multi-pulse sequence of the following type:

$$(\varphi_0)_\phi - (\tau - \varphi_x - 2\tau - \varphi_y - 2\tau - \varphi_{-x} - 2\tau - \varphi_{-y} - \tau)_n \tag{71}$$

(subscripts indicate the phase of the carrier (RF) frequency), and also a multi-pulse analogue of the two-pulse Hahn sequence, where the first pulse is replaced by a short steady-state sequence.

We also suggest a new method of orthogonal effective fields (MOEF) for a fast saturation of the quadrupole spin system, which can be used for subtracting the MAPER component from the signal.

The techniques discussed in this paper can be used not only for solving the problem of magneto-acoustic or piezo-electric ringing, but also for cancelling the residual ringing in the coil, the secondary ringing caused by the Q-switch system or any other spurious signals.

4.1. Sequence $(\varphi_0)_\phi - (\tau - \varphi_x - 2\tau - \varphi_y - 2\tau - \varphi_{-x} - 2\tau - \varphi_{-y} - \tau)\eta$

For revealing the main peculiarities of the effect of the multi-pulse sequence (71) a simplified theoretical treatment was suggested[52] that does not include dipolar and spin–lattice interactions. Then the equation for a density matrix ρ of the spin-1 system may be expressed as follows:

$$\mathrm{i}\frac{\mathrm{d}\rho}{\mathrm{d}t} = [H_\mathrm{Q} + H_\mathrm{rf}(t), \rho], \tag{72}$$

where $H_\mathrm{rf}(t)$is the Hamiltonian of the interaction of a spin with the RF field.

The carrier frequency of the RF pulses is $\omega = \omega_p - \Delta\omega$; $\Delta\omega$ is the resonance offset.

The RF Hamiltonian for sequence (71) is

$$H_\mathrm{rf}(t) = -2I_{p,1}\{\varphi_0\delta(t)\cdot\cos(\omega t + \phi) + F_1(t)\cos\omega t - F_2(t)\sin\omega t\}, \tag{73}$$

where pulse functions $F_1(t)$ and $F_2(t)$equal

$$F_1(t) = \varphi\Big[\sum_{k=0}^{\infty}\delta(t - (1+8k)\tau) - \sum_{k=0}^{\infty}\delta(t - (5+8k)\tau)\{\}\Big], \tag{74a}$$

$$F_2(t) = \varphi[-\sum_{k=0}^{\infty}\delta(t - (3+8k)\tau) + \sum_{k=0}^{\infty}\delta(t - (7+8k)\tau)], \tag{74b}$$

and we also assume that the resonance offset meets the condition $\Delta\omega \ll \omega_1$.

In the interaction representation with the Hamiltonian H_0 determined by Equation (6) is described by the expression

$$\mathrm{i}\frac{\mathrm{d}\tilde{\rho}}{\mathrm{d}t} = [\Delta\omega I_{p,3} + \tilde{H}_{\mathrm{rf}}, \tilde{\rho}], \tag{75}$$

where the secular part of the RF Hamiltonian $\tilde{H}_{\mathrm{rf}}$ in the H_0 representation takes the form

$$\tilde{H}_{\mathrm{rf}} = -\varphi_0\delta(t)[\cos\phi\cdot I_{p,1} + \sin\phi\cdot I_{p,2}] - F_1(t)\cdot I_{p,1} - F_2(t)\cdot I_{p,2}. \tag{76}$$

Here and further on all calculations and results will be done in the H_0 representation, so that the tilde notation will be dropped.

The density matrix of the equilibrium state equals

$$\rho(0) = \frac{1}{3}[E - \alpha_0(\omega_p I_{p,3} + \omega'_p I_{p,4})]. \tag{77}$$

The initial density matrix formed by the preparatory pulse φ_0 is determined by the expression

$$\begin{aligned}\rho_0 &= \exp(\mathrm{i}\varphi_0(I_{p,1}\cos\phi + I_{p,2}\sin\phi))\rho(0)\exp(-\mathrm{i}\varphi_0(I_{p,1}\cos\phi + I_{p,2}\sin\phi)) \\ &= \frac{1}{3}[E - \alpha_0\omega_p \boldsymbol{I}_0\cdot\boldsymbol{I}_p - \alpha_0\omega_p \boldsymbol{I}_{p,4}],\end{aligned} \tag{78}$$

where $\boldsymbol{I}_p = (I_{p,1}, I_{p,2}, I_{p,3})$; E is the unit matrix;

$$\boldsymbol{I}_0 = (l_{01}, l_{02}, l_{03}); l_{01} = -\sin\varphi_0\ \sin\phi; l_{02} = \sin\varphi_0\cos\phi; l_{03} = \cos\varphi_0. \tag{79}$$

The equation for the density matrix of the spin system acted upon by pulse sequence (71), looks as follows:

$$\mathrm{i}\frac{\mathrm{d}\tilde{\rho}}{\mathrm{d}t} = [\Delta\omega I_{p,3} - \varphi_0\delta(t)[\cos\phi\cdot I_{p,1} + \sin\phi\cdot I_{p,2}] - F_1(t)\cdot I_{p,1} - F_2(t)\cdot I_{p,2}, \tilde{\rho}]. \tag{80}$$

After a canonical transformation of Equation (80)

$$\tilde{\rho}(t) = \exp\left(-\mathrm{i}\left[\frac{\pi}{4}\cdot\frac{t}{\tau} - \frac{\pi}{4}\right]I_{p,3}\right)\rho''\exp\left(\mathrm{i}\left[\frac{\pi}{4}\cdot\frac{t}{\tau} - \frac{\pi}{4}\right]I_{p,3}\right), \tag{81}$$

we obtain

$$\mathrm{i}\frac{\mathrm{d}\rho''}{\mathrm{d}t} = \left[\left(\Delta\omega - \frac{\pi}{4\tau}\right)I_{p,3} - \varphi_0\delta(t)\left[\cos\left(\phi + \frac{\pi}{4}\right)\cdot I_{p,1} + \sin\left(\phi + \frac{\pi}{4}\right)\cdot I_{p,2}\right] - F(t)\cdot I_{p,1}, \rho''\right], \tag{82}$$

where

$$F(t) = \varphi\sum_{k=0}^{\infty}\delta(t - (1+2k)\tau). \tag{83}$$

Equation (82) describes the spin system acted upon by multi-pulse spin-locking MW-4[20,21] with the pulses carrier frequency shifted off resonance by $\Delta\omega - \frac{\pi}{4\tau}$ and the preparatory pulse phase shifted off the initial value by $\frac{\pi}{4}$: $\phi \to \phi + \frac{\pi}{4}$.

As shown in Section 2.1 (Equations (26) and (27)), the propagator describing the evolution of the spin-system during one $(\tau - \varphi_x - \tau)$ cycle of the MW-4 sequence

$$U = \exp(-i\Delta\omega\tau I_{p,3})\exp(\varphi I_{p,1})\exp(-i\Delta\omega\tau I_{p,3}), \tag{84}$$

can be presented in the form ($\Delta\omega \ll \omega_1$)

$$U = \exp(-i2\tau\cdot\boldsymbol{\omega}'_{\text{eff}}\boldsymbol{I}_p), \tag{85}$$

while

$$\boldsymbol{\omega}'_{\text{eff}} = \boldsymbol{n}'\omega'_{\text{eff}}; \boldsymbol{n}' = (n'_1, \cdot n'_2, \cdot n'_3); \omega'_{\text{eff}} = |\boldsymbol{\omega}'_{\text{eff}}|.$$

$$\cos(\omega'_{\text{eff}}\tau) = \cos\frac{\varphi}{2}\cos\Delta\omega\tau; \tag{86a}$$

$$\boldsymbol{n}'_1 = \frac{\sin\frac{\varphi}{2}}{\sin\omega'_{\text{eff}}\tau}; \boldsymbol{n}'_2 = 0; \boldsymbol{n}'_3 = -\frac{\cos\frac{\varphi}{2}\sin\Delta\omega\tau}{\sin\omega'_{\text{eff}}\tau}. \tag{86b}$$

The $\boldsymbol{\omega}'_{\text{eff}} = \boldsymbol{n}'\boldsymbol{\omega}'_{\text{eff}}$ vector determines the effective field which substitutes the effect of the RF pulses and the resonance offset of the MW-4 sequence.

After making substitution $\Delta\omega \to \Delta\omega - \frac{\pi}{4\tau}$ in Equation (86) and a number of trivial simplifications we obtain an expression for effective field ω_{eff} of sequence (71) in the coordinate system determined by transformation (81):

$$\omega_{\text{eff}} = \boldsymbol{n}\omega_{\text{eff}};\ \boldsymbol{n} = (n_1, \cdot n_2, \cdot n_3);\ \omega_{\text{eff}} = |\boldsymbol{\omega}_{\text{eff}}|.$$

$$\cos(\omega_{\text{eff}}\tau) = \cos\frac{\varphi}{2}\cos\left(\Delta\omega\tau - \frac{\pi}{4}\right); \tag{87a}$$

$$n_1 = \frac{\sin\frac{\varphi}{2}}{\sin(\omega_{\text{eff}}\tau)}; n_2 = 0; n_3 = \frac{\cos\frac{\varphi}{2}\sin\left(\Delta\omega\tau - \frac{\pi}{4}\right)}{\sin(\omega_{\text{eff}}\tau)}. \tag{87b}$$

After transformation (81) the initial density matrix ρ_0 changes to

$$\rho''_0 = \frac{1}{3}[E - \alpha_0\omega_p\boldsymbol{l}\cdot\boldsymbol{I}_p - \alpha_0\omega'_p I_{p,4}], \tag{88}$$

$$\boldsymbol{l} = (l_1, l_2, l_3);\ l_1 = -\sin\varphi_0\ \sin\left(\phi + \frac{\pi}{4}\right); l_2 = \sin\varphi_0\cos\left(\phi + \frac{\pi}{4}\right); l_3 = \cos\varphi_0. \tag{89}$$

Density matrix ρ''_{qst} of the quasi-stationary state ($\rho'' = \rho''_{\text{qst}}$ when $\frac{d''\rho}{dt} = 0$), formed at times ~T_2 (T_2 being the time of the spin–spin relaxation) equals

$$\rho''_{\text{qst}} = \frac{1}{3}[E - \alpha_{\text{qst}}\, H_{\text{eff}} - \alpha_0\ \omega'_p I_{p,4}], \tag{90}$$

$$H_{\text{eff}} = \boldsymbol{\omega}_{\text{eff}}\boldsymbol{I}_p. \tag{91}$$

The inverse spin temperature α_{qst} is found on the basis of the law of conservation of energy

$$\mathrm{Tr}(\rho_0'' H_{\mathrm{eff}}) = \mathrm{Tr}(\rho_{qst}'' H_{\mathrm{eff}}) \tag{92}$$

and equals:

$$\alpha_{qst} = \alpha_0 \omega_p \frac{l_1 n_1 + l_3 n_3}{\omega_{\mathrm{eff}}}. \tag{93}$$

Quasi-stationary state magnetisation in the coordinate system set by Equation (81) is determined by expression:

$$M_{qst} = 2\mathrm{Tr}(\rho_{qst}'' I_{p,1}) = -\alpha_0 \omega_p (l_1 n_1 + l_3 n_3) n_1. \tag{94}$$

To experimentally get into the coordinate system determined by expression (81), it is sufficient to set the receiver phase after each pulse to be the same as the phase of the pulse.

When the preparatory pulse $\varphi_0 = \pi/2$

$$M_{st} = -\alpha_0 \omega_p l_1 n_1^2 = \alpha_0 \omega_p \frac{\sin^2 \frac{\varphi}{2} \sin\left(\phi + \frac{\pi}{4}\right)}{1 - \cos^2 \frac{\varphi}{2} \cos^2\left(\Delta\omega\tau - \frac{\pi}{4}\right)}. \tag{95}$$

It follows from (95) that the optimum phase of the preparatory pulse at $\varphi_0 = \pi/2$ is $\phi = \pi/4$ or $-3\pi/4$.

To summarise this short theoretical consideration, it should be said that sequence (71) $(\varphi_0)_\phi - (\tau - \varphi_x - 2\tau - \varphi_y - 2\tau - \varphi_{-x} - 2\tau - \varphi_{-y} - \tau)_n$with carrier frequency of RF pulses ω coincides in all its characteristics with sequence $(\varphi_0)_{\phi+\frac{\pi}{4}} - (\tau - \varphi_x - \tau)_{4n}$ that has carrier frequency of RF pulses $\omega + \frac{\pi}{4\tau}$.

To proceed, the terms ''SSFP type sequence'' and ''echo sequence'' should be clarified. The SSFP type sequence or simply ''SSFP sequence'' designates any sequence which under certain conditions depending on the pulse flip angle, pulse intervals and resonance offset create a phenomenon called the ''steady-state free precession'' and linked with two effects: (1) weak saturation of the spin system and (2) phase and intensity anomalies.[30] As was shown in Ref. 23 for a sequence of identical pulses $(\tau - \varphi - \tau)_n$, the SSFP phenomenon is observed when $2\tau < T_2^*$. Under the condition $2\tau < T_2^*$ all formal characteristics of the SSFP phenomenon (weak saturation of the spin system, and phase and intensity anomalies) remain even in such sequences creating spin-locking effect as MW-4 $(\varphi_0)_y - (\tau - \varphi_x - \tau)_n$, MW-2 $(\varphi_0)_x - (\tau - \varphi_x - 2\tau - \varphi_{-x} - \tau)_n$ and the just discussed sequence $(\varphi_0)_{\frac{\pi}{4}} - (\tau - \varphi_x - 2\tau - \varphi_y - 2\tau - \varphi_{-x} - 2\tau - \varphi_{-y} - \tau)_n$, which for the sake of convenience of further discussion will be included in the group of the SSFP type sequences.

The three sequences above can be regarded as echo sequences on condition of $T_1 \gg 2\tau > T_2^*$ which ensures the formation of echo signals. It will be demonstrated

further on with sequence $(\varphi_0)_{\frac{\pi}{4}} - (\tau - \varphi_x - 2\tau - \varphi_y - 2\tau - \varphi_{-x} - 2\tau - \varphi_{-y} - \tau)_n$ that at $2\tau > T_2^*$ intensity variations, which are a characteristic of SSFP, become negligible.

The term ''short SSFP sequence'' (SSS) will be also used to designate sequences with duration not exceeding the spin–spin relaxation time T_2. Sequences with duration less than T_2 do not result in any appreciable changes of the initial spin temperature, and therefore its constituent pulses can in this case be regarded as a group of individual pulses with its effect determined by the effect of each pulse in accordance with its sequence order in the group, as one can see in paper.[29] When condition $2\tau < T_2^*$ is also complied with, than all transients created by each pulse are added into one continuous signal.

Sequence (71) can be used to cancel spurious signals both when $2\tau < T_2^*$ and $2\tau > T_2^*$, however in each case it has certain specificity.

For cases when $2\tau < T_2^*$ the best results are achieved when using sequence (71) as a combination of the following type:

$$(\varphi_0)\frac{\pi}{4} - \tau - (\varphi_x - 2\tau[+x] - \varphi_y - 2\tau[+y] - \varphi_{-x} - 2\tau[-x] - \varphi_{-y} - 2\tau[-y])_n - T -$$

$$(\varphi_0)\frac{3\pi}{4} - \tau - (\varphi_x - 2\tau[-x] - \varphi_{-y} - 2\tau[+y] - \varphi_{-x} - 2\tau[+x] - \varphi_y - 2\tau[-y])_n, \quad (96)$$

where T is a time interval between two sequences which can be arbitrary; receiver phases are shown in square brackets. It is obvious that such arrangement of pulse phases and receiver phases results in complete cancelling of the MAPER signals if their duration does not exceed 2τ. The effective frequencies for the first and second sequences of combination (90) are $\omega + \frac{\pi}{4\tau}$ and $\omega - \frac{\pi}{4\tau}$, respectively. The difference between the effective frequencies equals $\pi/2\tau$. The width of the resonance line which has the Lorentzian shape in angular frequency units equals $2/T_2^*$ and complies with the inequation $\frac{\pi}{2\tau} > \frac{2}{T_2^*}$. In accordance with this inequation the effective frequency of only one of the two sequences (96) can coincide with the resonance line. Using two effective frequencies while applying combination (30) permits to diminish the problem of intensity variations, particularly significant when the temperature of the sample is unknown and the resonance frequency has a large temperature coefficient.

The sequence (71) is effective for cancelling the MAPER signals only when the duration of these signals does not exceed pulse interval 2τ. If the duration of the MAPER signals exceeds the T_2^* time than $2\tau > T_2^*$ and the condition of inequation $\frac{\pi}{2\tau} > \frac{2}{T_2^*}$ will not hold. In this case at some resonance offsets the second sequence of (96) can subtract the NQR signal received after irradiation with the first sequence. A combination of sequences (71) for the condition $2\tau > T_2^*$ is demonstrated below.

Now we demonstrate the use of sequence (71) in a case when pulse intervals 2τ are comparatively long $2\tau > T_2^*$ that is necessary for forming echo signal.[52] In this

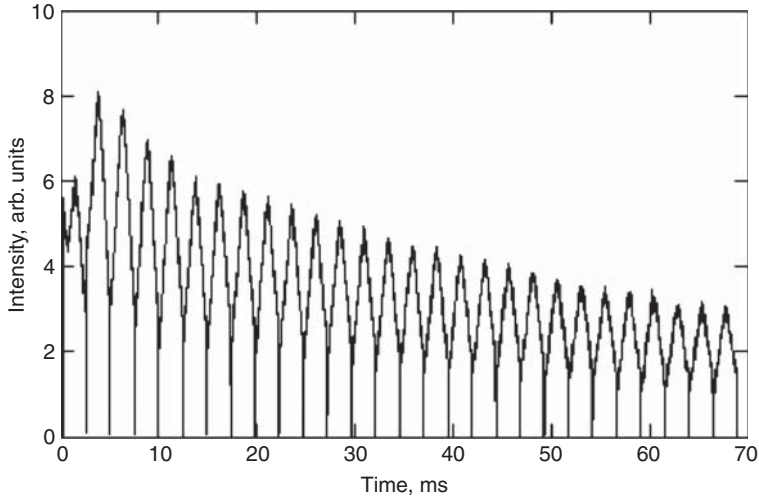

Figure 10 Spin-echo signals from ^{14}N in a powdered sample of sodium nitrite after the impact of sequence $(\varphi_0)_{\frac{\pi}{4}} - (\tau - \varphi_x - 2\tau - \varphi_y - 2\tau - \varphi_{-x} - 2\tau - \varphi_{-y} - \tau)_n$ at resonance frequency $\nu_+ = 4.642$ MHz. Sequence parameters are τ = 1200 μs; duration of all pulses is 80 μs; n = 28; delay between the end of RF pulse and beginning of detection is 120 μs. The number of averages is 200.

case if the preparatory signal phase is $\phi = \frac{\pi}{4}$, sequence (71) is similar to the spin-locking spin-echo multi-pulse sequence.[17] Figure 10 shows signals from sequence (71) at room temperature in powder $NaNO_2$ at resonance transition $\nu_+ = 4.642$ MHz and the following parameters: duration of all sequence pulses is 80 μs ($\varphi_0 = \varphi = 0.66\pi$), τ= 1.2 ms, total number of averages—200, mass of the sample—80 g.

Using echo sequences for cancelling MAPER has several important advantages. As was shown in Ref. 65 choosing pulse interval $\sim 3T_2^*$ leads to minimal distortions connected with intensity anomalies which is very important under the conditions when neither the exact sample temperature nor the exact resonance frequency of quadrupole nuclei is known. Another important advantage is a possibility to increase the delay between the trailing edge of sequence pulses and the acquisition time. It was demonstrated in Ref. 57 that many magneto-acoustic signals appearing at resonant transition frequencies ν_+ and ν_- of such explosive substances as RDX and HMX have a short decay time constant as compared with T_2^* and, consequently, an increase in the delay time can prove an effective means of cancelling such signals.

Sequence (71) with the preparatory pulse phase $\phi = -\frac{\pi}{4}$ does not create a spin-locking effect (Figure 11). Therefore using a combination of two sequences

$$(\varphi_0)_{\frac{\pi}{4}} - (\tau - \varphi_x - 2\tau - \varphi_y - 2\tau - \varphi_{-x} - 2\tau - \varphi_{-y} - \tau)_n \tag{97}$$

and

$$(\varphi_0)_{-\frac{\pi}{4}} - (\tau - \varphi_x - 2\tau - \varphi_y - 2\tau - \varphi_{-x} - 2\tau - \varphi_{-y} - \tau)_n \tag{98}$$

permits to remember both useful and spurious signals during the first sequence and then the spurious signal only during the second sequence. The pure NQR

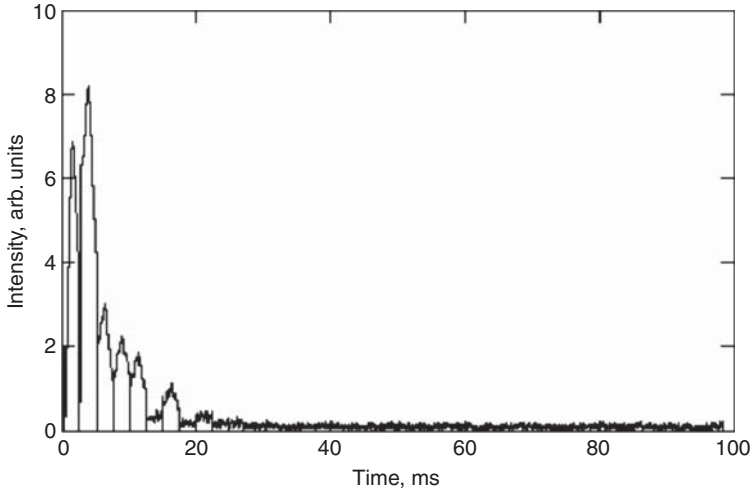

Figure 11 Spin-echo signals in a powdered sample of sodium nitrite after the impact of sequence $(\varphi_0)_{-\frac{\pi}{4}} - (\tau - \varphi_x - 2\tau - \varphi_y - 2\tau - \varphi_{-x} - 2\tau - \varphi_{-y} - \tau)_n$ at resonance frequency $\nu_+ = 4.642$ MHz. Sequence parameters are the same as in Figure 10.

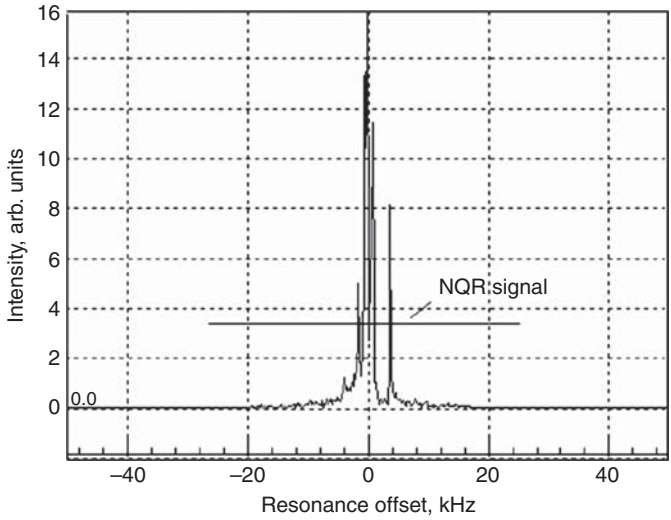

Figure 12 Signals received in a powdered sample of sodium nitrite (frequency $\nu_+ = 4.642$ MHz) in the presence of a nickel-plated washer after the impact of sequence $(\varphi_0)_{\frac{\pi}{4}} - (\tau - \varphi_x - 2\tau - \varphi_y - 2\tau - \varphi_{-x} - 2\tau - \varphi_{-y} - \tau)_n$ with τ = 1.2 ms; duration of all pulses is 80 μs; n = 100; delay between the end of RF pulse and beginning of detection is 0.6 ms. The sample mass is 30 g.

signal is received by subtracting the signals received after the second sequence from the signals received after the first one.

In Figure 12 one can see signals from sequence (97) at n = 100 from 30 g of $NaNO_2$ (frequency $\nu_+ = 4.642$ MHz) in the presence of a nickel-plated washer.

In Figure 13 one can see the subtraction result when the signal received after the effect of sequence (98) is subtracted from the signal presented in Figure 12 also at $n = 100$.

In Figure 14 the dependence of the NQR signal on the offset is presented. It was recorded after the effect of a combination of sequences (97) and (98) on the $NaNO_2$ sample, with the receiver phase in the first sequence coinciding with the previous pulse phase and in the second sequence being opposite to it.

Let us consider the advantages and disadvantages of using sequence (71) to cancel spurious signals. Its advantage for the case when $2\tau < T_2^*$ is the fact that it reduces the problem of intensity anomalies which is important for many practical purposes. We must also keep in mind that in the last discussed combination of sequence (71) one of the two sequences is used only for cancelling spurious signals and not for obtaining the NQR signal, and thus the overall NQR signal per unit time is reduced.

4.2. Multi-pulse analogue of the Hahn sequence

The fact that the duration of transient signals after SSFP type sequences can exceed T_2^* (T_2^* is a time constant of the free induction decay) can be used to eliminate spurious signals. The SSS can replace conventional pulses in the multiple-pulse sequences with intervals between pulses longer than T_2^* while detecting explosives at frequencies higher than 3 MHz (RDX, HMX, tetryl), where the duration of

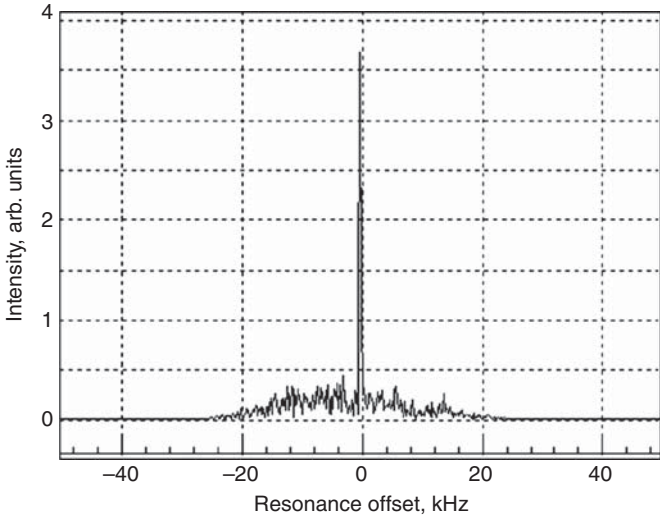

Figure 13 Result of subtracting the signal received after the impact of sequence $(\varphi_0)_{-\frac{\pi}{4}} - (\tau - \varphi_x - 2\tau - \varphi_y - 2\tau - \varphi_{-x} - 2\tau - \varphi_{-y} - \tau)_n$ from the signal presented in Figure 12. Sequence parameters are the same as in Figure 12.

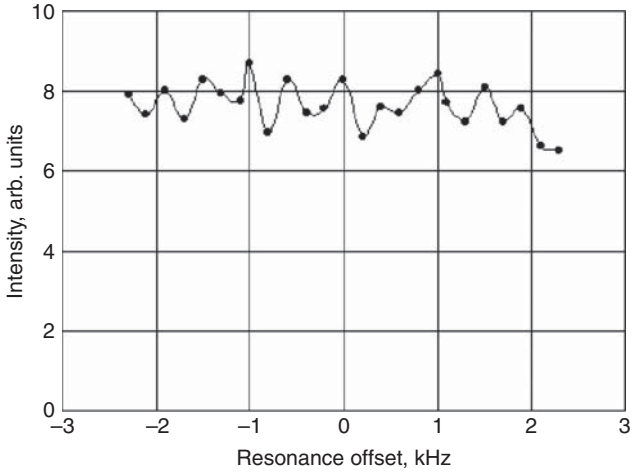

Figure 14 Dependence of the NQR signal on the offset received after irradiating a powdered sample of $NaNO_2$ with a combination of sequences $(\varphi_0)_{\frac{\pi}{4}} - (\tau - \varphi_x - 2\tau - \varphi_y - 2\tau - \varphi_{-x} - 2\tau - \varphi_{-y} - \tau)_n$ and $(\varphi_0)_{-\frac{\pi}{4}} - (\tau - \varphi_x - 2\tau - \varphi_y - 2\tau - \varphi_{-x} - 2\tau - \varphi_{-y} - \tau)_n$ with the phase of the receiver in the first sequence coinciding with the phase of the preceding pulse and opposite to it in the second sequence. Sequence parameters are τ = 1.2 ms; duration of all pulses = 80 μs; $n = 200$; delay between the end of RF pulse and beginning of detection is 120 μs. The sample mass is 80 g.

MAPER normally does not exceed 1.5–2 ms. In this case the delay between the SSS and the acquisition time can be considerably increased. As seen in Ref. 57 an increase in the delay is an effective measure against spurious signals.

The further improvement of the effectiveness of the spurious signal suppression can be achieved with a multi-pulse analogue of the two-pulse Hahn sequence, where the first pulse is replaced by SSS.[52]

In the example discussed in the experimental part of the chapter we use the following spin-locking type sequence as SSS $(\pi/2)_y - (\tau - \varphi_x - \tau)_n$. The use of this sequence can find theoretical substantiation in paper,[29] where the initial stage of multi-pulse spin locking preceding the establishment of quasi-stationary state was studied for the times$\leq T_2$. It was demonstrated in the paper that during the multi-pulse spin-locking a re-focusing of the spin-system magnetisation occurs even at the initial stage of the sequence effect. Such refocusing leads to the increase of the time of the transient decay.

Using SSS in combination with a 180° pulse separated from the SSS by an interval $\geq T_2^*$ reates a long echo signal that permits to increase the delay without losing the intensity of the registered signal.

To illustrate this, Figure 15 shows echo signals received from a powder sample of $NaNO_2$ at resonance frequency $\nu_- = 3.605$ MHz at room temperature after applying three sequences:

(1)

$$(\varphi_0)_x - \tau_l - (\varphi_1)_x - \text{delay} - \text{acquisition}[+x] \\ -T - (\varphi_0)_{-x} - \tau_l - (\varphi_1)_x - \text{delay} - \text{acquisition}[-x], \tag{99}$$

(2)

$$(\tau - \theta_x - \tau)_4 - \tau_l - (\varphi_1)_x - \text{delay} - \text{acquisition}[+x] \\ -T - (\tau - \theta_{-x} - \tau)_4 - \tau_l - (\varphi_1)_x - \text{delay} - \text{acquisition}[-x], \tag{100}$$

(3)

$$(\varphi_0)_y - (\tau - \vartheta_x - \tau)_4 - \tau_l - (\varphi_1)_x - \text{delay} - \text{acquisition}[+x] \\ -T - (\varphi_0)_{-y} - (\tau - \vartheta_{-x} - \tau)_4 - \tau_l - (\varphi_1)_x - \text{delay} - \text{acquisition}[-x], \tag{101}$$

which have the following parameters: T = 600 ms; τ = 140 μs; τ_l = 2 ms; $\varphi_0 = 0.66\pi$ (90° pulse in powder), $\varphi_1 = 1.43\pi$ (180° pulse in powder), $\theta = 0.22\pi$, $\vartheta = 0.13\pi$ which corresponds to pulse durations of 80, 172, 26 and 16 μs, respectively; delay is 400 μs.

As multiple signal accumulation from the combination of the SSS and the 180° pulse is only possible after time intervals $\geq T_1$, the accumulated NQR signal sufficient for a positive detection in an acceptable time period is possible only for RDX. Therefore all measurements referring to this method and described in the experimental part of this paper were done for this substance.

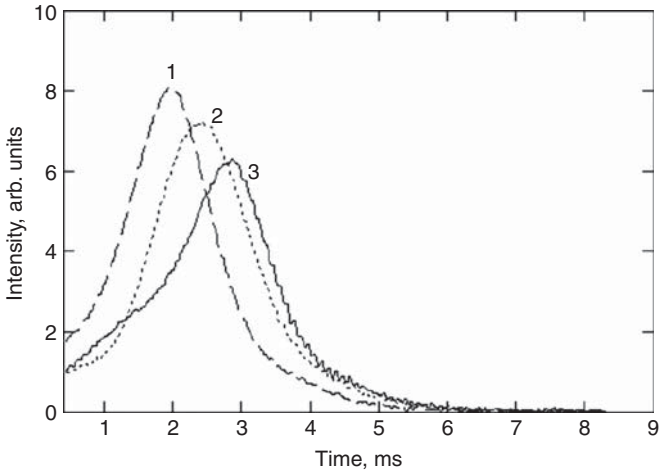

Figure 15 Echo signals from ^{14}N in a powdered sample of sodium nitrite ($NaNO_2$) at resonance frequency $\nu_- = 3.605$ MHz after the impact of sequences $(\varphi_0)_x - \tau_l - (\varphi_1)_x$ – delay– acquisition$[+x]$ – T – $(\varphi_0)_{-x} - \tau_l - (\varphi_1)_x$ –delay – acquisition$[-x]$ (line 1); $(\tau - \theta_x - \tau)4 - \tau_l$ $-(\varphi_1)_x$ – delay – acquisition$[+x]$ – T – $(\tau - \theta_{-x} - \tau)_4 - \tau_l - (\varphi_1)_x$ – delay – acquisition$[-x]$ (line 2); $(\varphi_0)y - (\tau - \vartheta_x - \tau)_4 - \tau_l - (\varphi_1)_x$ – delay – acquisition$[+x]$– T – $(\varphi_0)_{-y} - (\tau - \vartheta_{-x} - \tau)_4 - \tau_l - (\varphi_1)_x$ – delay – acquisition$[-x]$ (line 3). Sequence parameters are $\varphi_0 = 0.66\pi$ (pulse duration is 80 μs), $\varphi_1 = 1.43\pi$ (172 μs), $\theta = 0.22\pi$ (26 μs), $\vartheta = 0.13\pi$ (16 μs); T = 600 ms; τ= 140 μs; τ_l = 2 ms; delay is 400 μs. The number of averages is 20. The sample mass is 80 g.

When trying to cancel spurious signals while detecting NQR signals from substances that have short spin–lattice relaxation times T_1 it is advisable to use a sequence consisting of a SSS and an individual pulse, preferably a 180° one (as, e.g. in sequences (100) and (101)), separated from the last SSS pulse by the time $\geq T_2^*$. The sequence is applied repeatedly keeping the number of repetitions even and having intervals between the repetitions equal to or exceeding T_1. At the beginning of each sequence there is a preparatory 90° pulse and its phase varies by 180° in each consecutive repetition. Such sequence structure permitted detecting NQR signal with the suppression of MAPER by at least 45 dB.

Let us examine one of possible versions of the suggested sequence, when SSS is a sequence of the MW-4 type $(\varphi_0)_{\pm x} - (\tau - \varphi_y - \tau)_n$.

In the presented example $n = 4$; $\tau = 120$ μs; $\varphi_0 = 0.66\pi$, $\varphi = 0.22\pi$ which corresponds to pulse durations of 80 and 26 μs. The experiments were carried out for a powdered sample of RDX at resonance frequency $\nu_+ = 5.192$ MHz. The time interval between the last pulse of the SSS and the 180° ''registering'' pulse is 2.5 ms, which is greater than the value of T_2^*.[42] The detection of NQR signal occurs after the delay time that equals 1 ms. The acquisition time is 4096 μs. The time period from the end of one sequence to the beginning of the other equals 25 ms, which is approximately three times longer than the time of spin–lattice relaxation T_1.[42] The mass of the detected RDX is 30 g and the coil volume is 1 l. A nickel-plated washer with a diameter of 30 mm was used as a source of magneto-acoustic ringing. The result of the action of the sequence consisting of 200 such sets is presented in Figure 16. Whatever delays from 0.6 to 1.4 s were used between the 180° pulse and the acquisition time, the cancelling of MAPER was complete. To compare, in Figure 17 one can see the spectrum of the signal obtained after using sequence $(\tau - \varphi_y - \tau)_n$ with the pulse duration of 50 μs, $n = 200$ and $\tau = 1.2$ ms. Magneto-acoustic signal created by such sequence is greater than the NQR signal received after the same sequence.

4.3. Method of orthogonal effective fields

The MOEF achieves a fast saturation of the spin system and is convenient for subtracting spurious signals when detecting explosives with long times of spin–lattice relaxation T_1. MOEF can be used in combination with a block method suggested in Ref. 58, the essence of which is to use two identical sequences one after the other with a certain interval during which the spin system becomes saturated and then compare the signals received after each sequence.

Suppose both blocks consist of the SSFP type sequences. At the time $\geq T_2$ after the beginning of the first pulse sequence the process in the spin system can be considered as a quasi-stationary one. Such state of the spin system may be described by the density matrix ρ_{st}:

$$\rho_{qst} = \frac{1}{3}[E - \alpha_{qst} H_{eff}] = \frac{1}{3}[E - \alpha_{qst} \omega_{eff} \boldsymbol{n} \boldsymbol{I}_p], \tag{102}$$

α_{qst} is the inverse spin temperature of the spin system in the quasi-stationary state. A specific value of α_{qst} is not important for the further description. The $\alpha_0' \omega_p I_{p,4}$

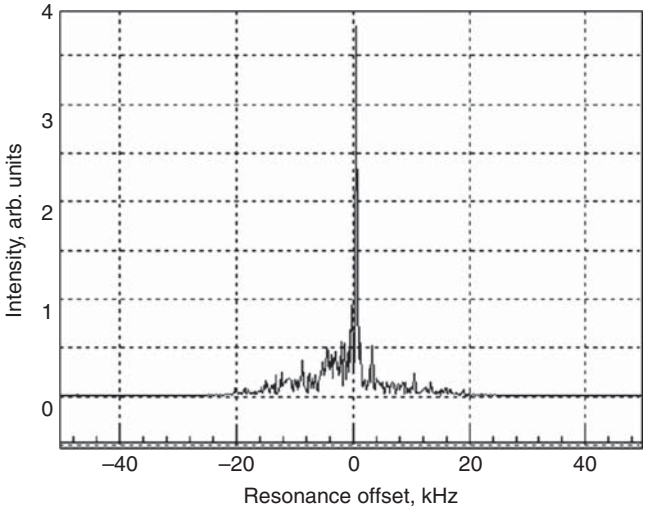

Figure 16 NQR signal received from 30 g of RDX (frequency $\nu_+ = 5.192$ MHz) in the presence of a nickel-plated washer after the impact of a multi-pulse analogue of Hahn sequence $(\varphi_0)_x - (\tau - \varphi_y - \tau)_4 -$ delay $- \varphi_1$, with $\tau = 120$ μs, delay $= 2.5$ ms, duration of pulses φ is 25 μs, duration of pulse φ_0 is 25 μs, duration of pulse φ_1 is 80 μs, and duration of pulse is 172 μs, delay between the end of pulse φ_1 and beginning of detection is 1 ms; number of averages is 200.

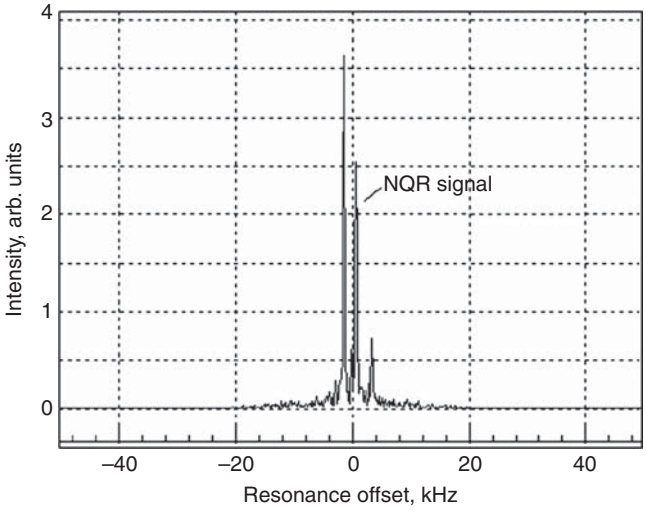

Figure 17 NQR signal received from 30 g of RDX (frequency $\nu_+ = 5.192$ MHz) in the presence of a nickel-plated washer, after the impact of $(\tau - \varphi_y - \tau)_n$. Sequence parameters are $\tau = 1.2$ ms, duration of all pulses is 50 μs, n = 200, delay between the end of pulse and beginning of detection is 1 ms.

member of the spin system that does not influence the behaviour of the spin system at times $<T_1$ is left out of the consideration.

Now if the sequence suddenly changes and the new effective field adopts the value of ω'_{eff} with the direction $\boldsymbol{n}' = (n'_1, n'_2, n'_3)$, then the Hamiltonian of the spin system looks as follows $H'_{\text{eff}} = \omega'_{\text{eff}} \boldsymbol{n}' \boldsymbol{I}_p$. However the density matrix of the spin system will preserve the former value ρ_{qst} (time $\sim T_2$ is required for its change), described with Equation (102). The energy of the system in this case equals $\text{Tr}(\rho_{\text{qst}} H'_{\text{eff}})$. After the time $\sim T_2$ the density matrix of the system will look as follows:

$$\rho'_{\text{eff}} = \frac{1}{3}[E - \alpha'_{\text{new}} H'_{\text{eff}}] = \frac{1}{3}[E - \alpha'_{\text{new}} \omega'_{\text{eff}} \boldsymbol{n}' \boldsymbol{I}_p]. \tag{103}$$

Further, as the energy of the spin system for times $\ll T_1$ stays the same, we receive

$$\text{Tr}(\rho_{\text{qst}} H'_{\text{eff}}) = \text{Tr}(\rho'_{\text{qst}} H'_{\text{eff}}), \tag{104}$$

which results in

$$\alpha'_{\text{new}} = \alpha_{\text{qst}} \frac{\omega_{\text{eff}}}{\omega'_{\text{eff}}} \boldsymbol{n} \cdot \boldsymbol{n}'. \tag{105}$$

If vectors n and $\boldsymbol{n}'$ are orthogonal, then their scalar product equals zero. Consequently, the reverse spin temperature α'_{new} also equals zero as well as the density matrix ρ'_{new} and the NQR signal, which in the general case has two M_k components, determined by expressions:

$$M_k = 2\text{Tr}(\rho'_{\text{new}} I_{p,k}) \sim (\boldsymbol{n} \cdot \boldsymbol{n}') n_k, k = 1, 2. \tag{106}$$

Let us assume that the spin system is subjected to the effect of two sequences in turn: first PAPS $(\tau - \psi_x - 2\tau - \psi_{-x} - \tau)_n$, and then SORC $(\tau - \varphi_x - \tau)_n$.

The effective field $\omega_{\text{eff}} = \boldsymbol{n}\omega_{\text{eff}}$ of the sequence $(\tau - \psi_x - 2\tau - \psi_{-x} - \tau)_n$ is as follows.[66]

$$\sin(\omega_{\text{eff}}\tau) = \cos\psi \sin(\Delta\omega\tau); \tag{107a}$$

$$n_1 = 0; n_2 = \frac{\sin\frac{\psi}{2}}{\cos(\omega_{\text{eff}}\tau)}; n_3 = \frac{\cos\frac{\psi}{2}\cos(\Delta\omega\tau)}{\cos(\omega_{\text{eff}}\tau)}. \tag{107b}$$

Vector $\boldsymbol{n}'$ for SORC is determined by expressions (86). Then $\boldsymbol{n} \cdot \boldsymbol{n}' = n_3 \cdot n'_3$ and the task of cancelling the NQR signal is limited to minimizing of the product of $n_3 \cdot n'_3$. In the case when the flip angle in SORC $\varphi = \pi$, for any flip angles ψ in PAPS $n_3 \cdot n'_3 = 0$, consequently the NQR signal is completely cancelled.

The experimental dependence of the NQR signal intensity on the time after a single change from PAPS $(\varphi = 0.44\pi)$ to SORC $(\psi = 0.66\pi)$ is presented in Figure 18.

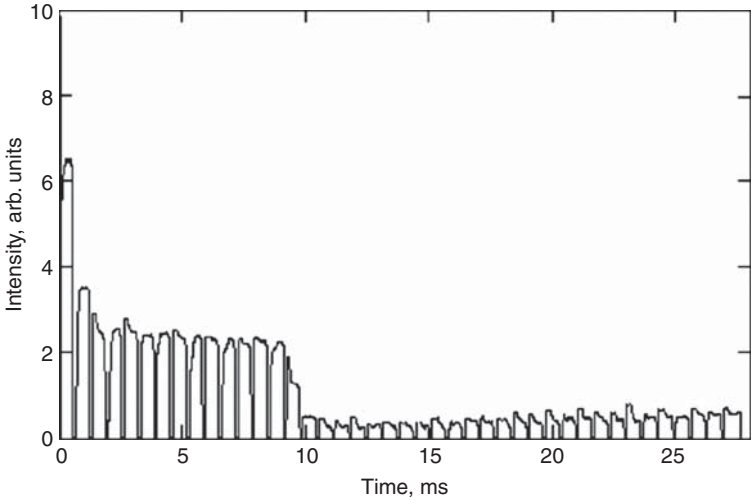

Figure 18 NQR signals in powdered $NaNO_2$ (frequency $\nu_+ = 4.642$ MHz) after the impact of two sequences activated one after the other: seven PAPS cycles $(\tau - \psi_x - 2\tau - \psi_{-x} - \tau)$ and 28 SORC $(\tau - \varphi_x - \tau)$ cycles; 200 accumulations; τ = 400 μs; pulse duration is 54 μs in PAPS and 80 μs in SORC. The sample mass is 80 g.

After the second change of the sequence, i.e. after the return to the initial sequence, the relation of the final signal M_2 to the initial signal M_1 is proportional already to $(\boldsymbol{n}\cdot\boldsymbol{n}')^2$. This circumstance permits using SSFP sequences with flip angles much smaller than 180° to completely eliminate the NQR signal. The experimental illustration for such double change of the sequences is shown in Figure 19.

Combining the MOEF with the method of blocks[58] permits achieving 40 dB of cancelling magneto-acoustic ringing at the PETN resonance frequency of 890 kHz (not shown).

The methods of cancelling the MAPER presented above encompass the whole range of spin–lattice relaxation times T_1 and are applicable for most explosive substances.

Although we mostly spoke about the MOEF under the steady-state conditions at $2\tau < T_2^*$, it should be noted that it can be used effectively for cancelling spurious signals also at $2\tau \geq T_2^*$.

5. EFFECT "TNEFMS" IN MULTI-PULSE ^{14}N NQR

Since 1991 there appeared a whole number of communications on experimental observations of non-stationary phenomena in the effective field of multi-pulse sequences in nitrogen-14 NQR,[37,66–72] which the authors of work[70] called TNEFMS—transient nutation in the effective field of multiple-pulse sequences.

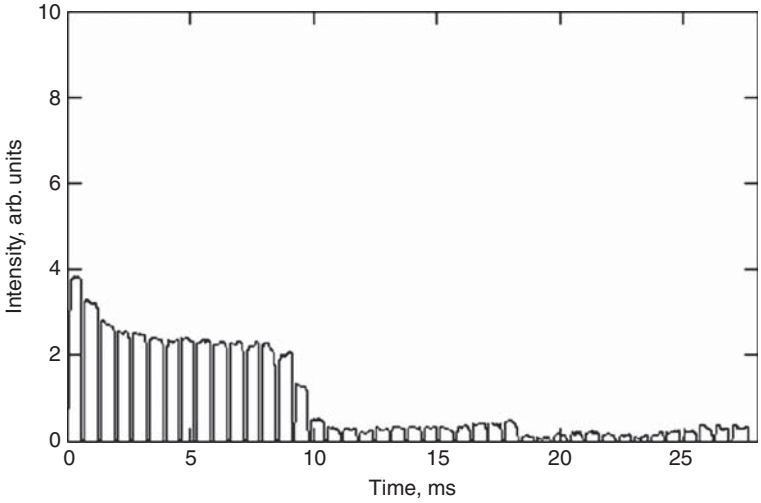

Figure 19 NQR signals in powdered $NaNO_2$ after the impact of two sequences activated one after the other: seven PAPS cycles $(\tau - \psi_x - 2\tau - \psi_{-x} - \tau)$, 14 SORC cycles $(\tau - \varphi_x - \tau)$ and then seven PAPS cycles again. All parameters are the same as in Figure 18.

The experiments described in the above articles had been carried out on a single crystal of $NaNO_2$ at frequency $\nu_+ = 4.93135$ MHz and at a temperature of 77 K with sequences

$$(\varphi_0)_x - (\tau - \varphi_y - 2\tau - \varphi_{-y} - \tau)_n - [(\tau - \varphi_{-y} - 2\tau - \varphi_y - \tau)_{2n} - (\tau - \varphi_y - 2\tau - \varphi_{-y} - \tau)_{2n}]_N, \quad (108)$$

and

$$(\varphi_0)_x - (\tau - \varphi_y - 2\tau - \varphi_{-y} - \tau)_n - [(\varphi_1)_{-y} - (\tau - \varphi_y - 2\tau - \varphi_{-y} - \tau)_{2n}]_N, \quad (109)$$

when the exact resonance conditions are met and $\varphi_0 = \pi/2$ or 0, $\varphi = \pi$. In all cases, the signal was detected at the end of each two-pulse cycle.

The observed effects manifest themselves in the appearance of induction and echo in the envelope of the NQR signals, with the number of echoes coinciding with the number N of supercycles in the sequence.

Osokin in article[71] made an attempt to formulate a theory for the above phenomenon. However, the attempt to explain the oscillating dependencies of signals by various deviations of neighbouring interacting spins from the median resonance frequency of the sample does not look convincing to us, and the resulting expressions for the magnetization of the spin system cannot describe the actual behaviour of the spin system.

In papers[71,72] we reported experimental evidence for the general character of the effects established in articles.[37,66–70] We obtained multiple echo signals in a number of powdered substances with substantially different relaxational constants and EFG asymmetry parameters $r\pi$ at room temperature (20 °C), in

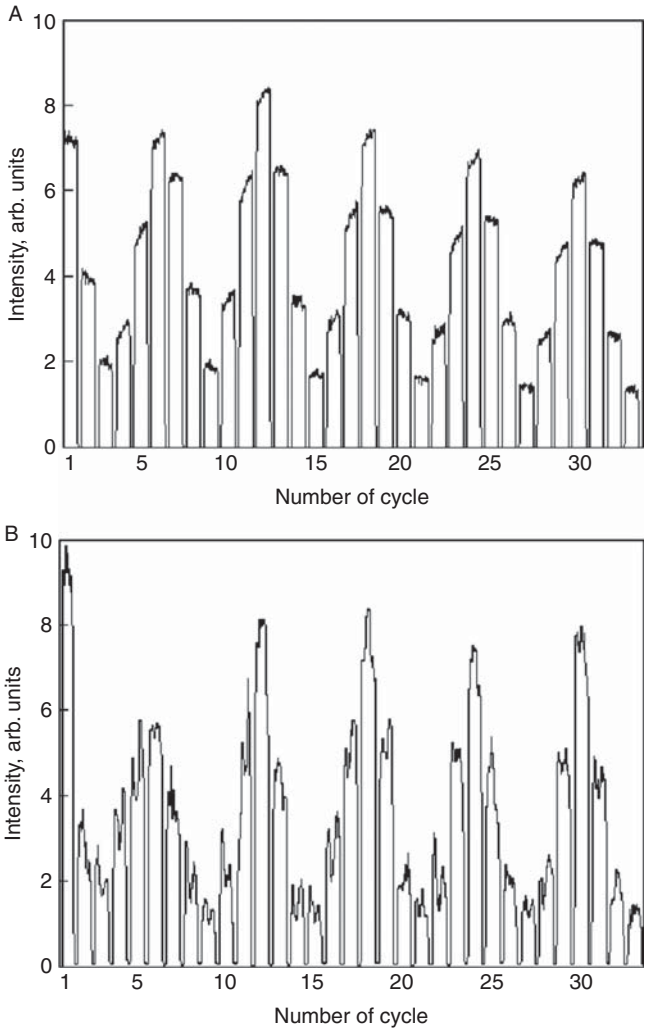

Figure 20 Induction and echo signals obtained upon the irradiation of powdered substances at 20 °C by sequence $(\varphi_0)_x - (\tau - \varphi_y - 2\tau - \varphi_{-y} - \tau)_n - [(\varphi_1)_{-y} - (\tau - \varphi_y - 2\tau - \varphi_{-y} - \tau)_{2n}]_N$ ($n = 3$, $\varphi_0 = \varphi = 0.66\pi$, $\varphi_1 = 1.32\pi$, $\tau = 128$ μs) with the preparatory pulse phase alternating every repetition. (A) Sodium nitrite $NaNO_2$, line $\nu_+ = 4.642$ MHz, and the number of supercycles $N = 5$. (B) Octogene $C_4H_8N_8O_8$, line $\nu_+ = 5.302$ MHz, and $N = 5$.

particular, at the $\nu_+ = 4.604$ MHz line in sodium nitrite $NaNO_2$ (Figure 20A) and at $\nu_+ = 5.302$ MHz in octogene $C_4H_8N_8O_8$ (Figure 20B).[72] Signals were detected using pulse sequences of the form (108) or (109) after averaging 200 pulses with the flip angles φ_0, φ and φ_1, varying in a broad range of their values. Examples of the NQR envelope as functions of the flip angle φ, and resonance offset are shown in Figure 21 for the sequence (109) with $\varphi_1 = 1.32\pi$ (doubled 90° pulse in powder) at the ν_+ transition in $NaNO_2$.

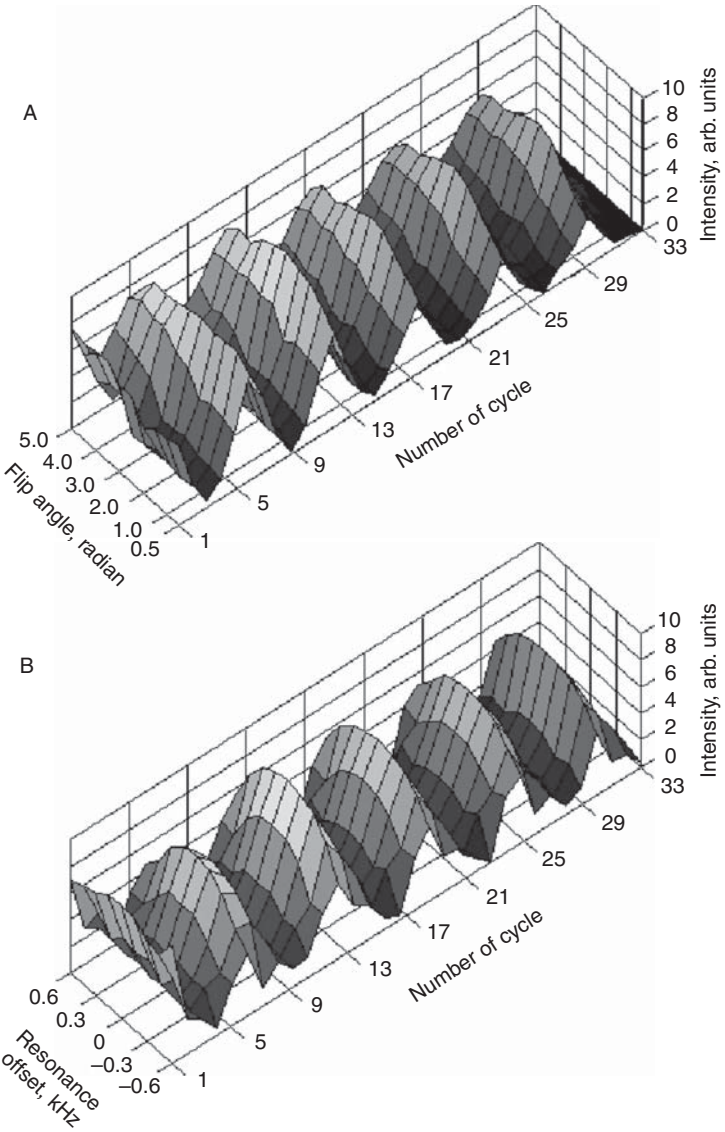

Figure 21 NQR-signal amplitudes in powdered $NaNO_2$ at $\nu_+ = 4.642$ MHz for sequence $(\varphi_0)_x - (\tau - \varphi_y - 2\tau - \varphi_{-y} - \tau)_n - [(\varphi_1)_{-y} - (\tau - \varphi_y - 2\tau - \varphi_{-y} - \tau)_{2n}]_N$ $n = 3$, $N = 5$, $\varphi_1 = 2\varphi_0 = 1.32\pi$), as functions of the flip angle (A) and resonance offset (B).

To separate signal components corresponding only to the preparatory pulse, the phases of the prepulse and of the detector reference voltage were reversed at each repetition of the multi-pulse sequence. In this scheme, all free-induction and echo-signal components generated by sequence pulses other than the preparatory pulse are subtracted, while the echo signals related to the preparatory pulse are summed.

Following the article[71] we briefly consider the TNEFMS effect theoretically by the example of a nitrogen-containing single-crystal sample with $\eta \neq 0$ subjected to the simplified sequence (109)

$$(\varphi_0)_x - (\tau - \varphi_y - 2\tau - \varphi_{-y} - \tau)_{n_1} - (\varphi_1)_{-y} - (\tau - \varphi_{-y} - 2\tau - \varphi_y - \tau)_{n_2} \qquad (110)$$

with flip angles of pulses $\varphi_0 = \pi/2$, $\varphi = \pi$.

The theoretical analysis[72] is based on a two-particle model.

Let sequence (110) irradiate the resonance transition $\omega_p/2\pi$. The quadrupole Hamiltonian H_Q of the two-spin system in terms of two-particle operators[72,73] looks as follows[72]

$$H_Q \sim \omega_p I_{p,3} = \omega_p(2K_1^r + L_3 + M_3). \qquad (111)$$

The secular part of the dipolar Hamiltonian with respect to H_Q according to the article[73] can be expressed the following form

$$H_d = 2\sum_{k=p,q,r} \Omega_k(I_{k,1}I_{k,1} + I_{k,2}I_{k,2}) \sim \Omega_p K_3^q + (\Omega_q - \Omega_r)(M_3 - L_3), \qquad (112)$$

where Ω_p are the tensor components of the Hamiltonian of HDI; and the two-particle operators K_3^q, M_3 and L_3 are related to three independent operator subspaces **K**, **M** and **L**. The operator commutation rules in the **L**-, and **M**-operator subspaces are the same and fully coincide with the analogous rules for the standard case of spin I= 1/2[74,73]. All relations for the operators K_l^λ are identical with those for the operator of effective spin 1/2 $I_{\lambda,l}$ with the same indices. Taking into account the relations[73]

$$I_{p,l} = 2K_1^{\lambda_l} + M_l + L_l (l = 1,2,3, \lambda_1 = p, \lambda_2 = q, \lambda_3 = r), \qquad (113)$$

one obtains for the initial density matrix after the action of preparatory pulse φ_0

$$\rho_0 \sim I_{p,2} = 2K_1^q + L_2 + M_2. \qquad (114)$$

According to the Waugh theory, the average Hamiltonian approximating the action of one cycle $(\tau - \varphi_y - 2\tau - \varphi_{-y} - \tau)$ is[74]

$$\begin{aligned} H_{av} = \frac{1}{2}(H_d + \tilde{H}_d) \sim \Omega_p(K_3^q \cos^2\varphi - K_2^q \sin\varphi \cos\varphi) \\ + (\Omega_q - \Omega_r)((M_3 - L_3)\cos^2(\varphi/2) - (M_2 - L_2)\sin(\varphi/2)\cos(\varphi/2)), \end{aligned} \qquad (115)$$

where $\tilde{H}_d = \exp(-i\varphi I_{p,2}\ H_d \exp(i\varphi I_{p,2})$.

The action of sequence (110) on the spin system is described by the density matrix of the form ($t_c = 4\tau$)

$$\begin{aligned} \rho((n_1 + n_2)t_c) = \exp(-in_2 t_c H_{av})\ \exp(iI_{p,2}\varphi_1)\ \exp(-in_1 t_c H_{av})\rho_0 \\ \times \exp(in_1 t_c H_{av})\ \exp(-iI_{p,2}\varphi_1)\ \exp(in_2 t_c H_{av}). \end{aligned} \qquad (116)$$

Setting $\varphi = \pi$, one obtains the following expression for the envelope of NQR signals

$$M \sim \mathrm{Tr}(\rho(n_1 t_c), S_x^p + iS_y^p) = \cos(n_1\Omega_p t_c)\cos(n_2\Omega_p t_c) - \cos(2\varphi_1)\sin(n_1\Omega_p t_c)\sin(n_2\Omega_p t_c). \quad (117)$$

For $\varphi_1 = \pi$ Equation (117) coincides with the expression for the signal envelopes observed upon the action of sequence (108) with $\varphi = \pi$.

Note also that, for the MW-2 sequence and its modification with $\varphi = \pi$ the contribution from the Hamiltonian of inhomogeneous broadening to the signal is virtually absent, much as this happens in NMR.[74]

Let us consider two particular cases for Equation (117). For $\varphi_1 = \pi$ the magnetization of the spin system is

$$M = M_1 \sim \alpha_0\omega_p\cos((n_1 + n_2)\Omega_p 4\tau)\sin\varphi_0. \quad (118)$$

and, for $\varphi_1 = \pi/2$

$$M = M_1 \sim \alpha_0\omega_p\cos((n_1 - n_2)\Omega_p 4\tau)\sin\varphi_0. \quad (119)$$

The action of sequence (109) on the powdered $NaNO_2$ is shown in Figure 22A for $n = 6$ and $\varphi = 2\varphi_1 = 1.32\pi$, and, in Figure 22B, for $\varphi = 2\varphi_1 = 1.32\pi$. One can see from these figures that the echo signals in the second case are more than 1.5 times more intense. Since the principal HDI tensor axes in the powder are arbitrarily oriented about the axis of the RF coil, a portion of spins, for which the condition $\Omega_p = \pi/n_1 t_c$ or $\exp(\Omega_p 2n_1 t_c) = 1$ is met with a relatively high accuracy, is also present if $1/t_c \ll ||H_d||$. These spins produce the signal in the first case. In the second case, the HDI is reversed in each sequence supercycle, so that the condition $\Omega_p = \pi/n_1 t_c$ is not necessary, and the signal is produced by a considerably larger number of spins. The second case can be considered as a certain analogue of magic echo in solid-state NMR.[75] In both examples, the effective decay time T_1 for the echo-signal envelope is approximately the same and equal to $T_{2e} = 45$ ms. Note, for comparison, that the spin–lattice relaxation time for the ν_+ line in a $NaNO_2$ powder is 90 ms at 20 °C.[42]

6. CONCLUSION

In as much as the problem of reduction of various interactions is not so relevant to NQR as it is to NMR, the multi-pulse sequences with complex cycles, which are so popular in NMR, did not find a wide utility in NQR spectroscopy. Therefore, the issues discussed in this chapter related to theoretical and applied aspects of the elementary multi-pulse sequences MW-4 and SORC are, perhaps, the most important and essential in the direct methods of ^{14}N NQR. Further improvement of the direct methods will be conditioned, above all, by introduction of the latest achievements of electronic technology into experiment.

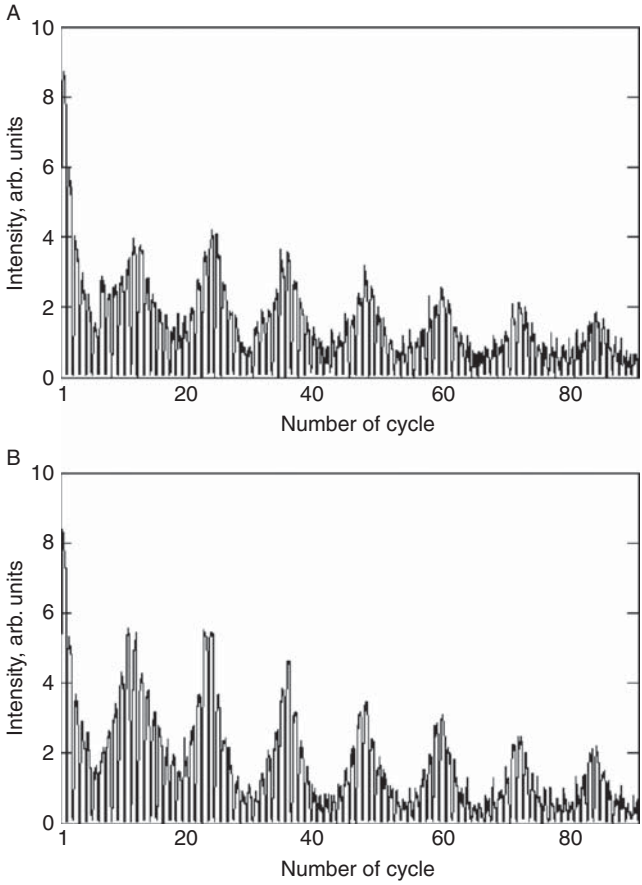

Figure 22 Induction and echo signals in powdered $NaNO_2$ at 20 °C, as obtained upon irradiation by sequence $(\varphi_0)_x - (\tau - \varphi_y - 2\tau - \varphi_{-y} - \tau)_n - [(\varphi_1)_{-y} - (\tau - \varphi_y - 2\tau - \varphi_{-y} - \tau)_{2n}]_N$ with $n = 6$, $\varphi_1 = 2\varphi_0 = 1.32\pi$ and (A) $\varphi_1 = 1.32\pi$ and (B) $\varphi_1 = 0.66\pi$.

REFERENCES

1. A. N. Garroway, M. L. Buess, J. B. Miller, B. H. Suits and A. D. Hibbs, *IEEE Trans. Geosci. Remote Sens.*, 2001, **39,** 1108.
2. J. Shaw, *The NQI Newslett.*, 1994, **1**(3), 29.
3. V. S. Grechishkin and N. Y. Sinjavskii, *Physics – Uspekhi*, 1997, **40,** 393.
4. S. Matsui, K. Kose and T. Inouye, *J. Magn. Reson.*, 1990, **88,** 186.
5. V. S. Grechishkin, V. P. Anferov and N. Y. Sinjavsky, *Adv. Nucl. Quadrupole Reson.*, 1983, **5,** 1.
6. K. L. Sauer, B. H. Suits, A. N. Garroway and J. B. Miller, *Chem. Phys. Lett.*, 2001, **342,** 362.
7. G. V. Mozjoukhine, *Appl. Mag. Reson.*, 2002, **22,** 31.
8. G. S. Harbison, A. Slokenbergs and T. M. Barbara, *J. Chem. Phys.*, 1989, **90,** 5292.
9. G. B. Furman and S. D. Goren, *Z. Naturforsch.*, 2002, **57a,** 315.
10. D. T. Edmonds, *Phys. Rep.*, 1977, **29,** 233.
11. R. Blinc, J. Seliger, D. Arčon, P. Cevc and V. Zagar, *Phys. Status Solidi A*, 2000, **180,** 541.
12. V. S. Grechishkin and A. Y. Shpilevoi, *Physics – Uspekhi*, 1996, **39,** 713.
13. F. Noack, *Prog. NMR Spectrosc.*, 1986, **18,** 171.

14. M. Nolte, A. Privalov, J. Altmann, V. Anferov and F. Fujara, *J. Phys. D: Appl. Phys.*, 2002, **35,** 939.
15. V. L. Ermakov, R. K. Kurbanov, D. Y. Osokin and V. A. Shagalov, *JETP Lett.*, 1991, **54,** 467.
16. V. T. Mikhaltsevitch and T. N. Rudakov, *Solid State Nucl. Magn. Reson.*, 2003, **24,** 263.
17. R. A. Marino and S. M. Klainer, *J. Chem. Phys.*, 1977, **67,** 3388.
18. T. B. Hirshfeld, S. M. Klainer and R. A. Marino, *In: Fourier, Hadamard and Hilbert Transforms in Chemistry*, A. G. Marshall, ed., , 1982 p. 147. Plenum, New York.
19. A. K. Hitrtin, G. E. Karnaukh and B. N. Provotorov, *Sov. Phys. JETP*, 1983, **57,** 91.
20. A. K. Hitrtin, G. E. Karnaukh and B. N. Provotorov, *J. Mol. Struct.*, 1982, **83,** 269.
21. M. M. Maricq, *Phys. Rev. B*, 1986, **33,** 4501.
22. D. Y. Osokin, *Zh. Eksp. Teor. Fiz.*, 1983, **84,** 118.
23. M. L. Buess, A. N. Garroway and J. B. Miller, *J. Magn. Reson.*, 1991, **92,** 348.
24. S. S. Kim, J. R. P. Jayacody and R. A. Marino, *Z. Naturforsch.*, 1992, **47a,** 415.
25. D. Y. Osokin, *J. Mol. Struct.*, 1982, **83,** 243.
26. L. N. Erofeev, B. A. Shumm and G. B. Manelis, *Fiz. Tverd. Tela (Leningrad)*, 1984, **26,** 277.
27. G. B. Furman, G. E. Kibrik, A. Yu. Poljakov and I. G. Shaposhnikov, *J. Mol. Struct.*, 1989, **192,** 207.
28. D. Petit and J.-P. Korb, *Phys. Rev. B*, 1988, **37,** 5761.
29. R. S. Cantor and J. S. Waugh, *J. Chem. Phys.*, 1980, **73,** 1054.
30. R. R. Ernst, G. Bodenhausen and A. Wokaun, *Principles of nuclear Magnetic Resonance in One and Two Dimensions*, 1987, Clarendon Press, Oxford.
31. L. N. Erofeev, B. A. Shumm and G. B. Manelis, *Sov. Phys. JETP*, 1978, **48,** 925.
32. Y. N. Ivanov, B. N. Provotorov and E. B. Fel'dman, *Sov. Phys. JETP*, 1978, **48,** 930.
33. M. M. Maricq, *Phys. Rev. B*, 1985, **31,** 127.
34. L. C. Bidenharn and J. D. Louck, *Angular Momentum in Quantum Physics, 1981*, Acklison-Wesley Publishing Company Reading, Massachusetts .
35. V. Mikhaltsevitch and T. Rudakov, *Solid State Nucl. Magn. Reson.*, 2004, **25,** 99.
36. D. Y. Osokin, *Mol. Phys.*, 1983, **48,** 283.
37. D. Y. Osokin, V. L. Ermakov, R. K. Kurbanov and V. A. Shagalov, *Z. Naturforsch.*, 1992, **47a,** 439.
38. A. Abragam, *The Principles of Nuclear Magnetism 1961*, Clarendon Press, Oxford .
39. S. Vega, *J. Chem. Phys.*, 1978, **68,** 5518.
40. F. Bloch, *Phys. Rev.*, 1946, **70,** 460.
41. V. Mikhaltsevitch and T. Rudakov, *Phys. Stat. Sol. (b)*, 2004, **241,** 411.
42. A. N. Garroway, M. L. Buess, J. P. Yesinowski and J. B. Miller, *SPIE Subst. Detect. Syst.*, 1993, **2092,** 318.
43. N. Bloembergen, E. M. Purcell and R. V. Pound, *Phys. Rev.*, 1948, **73,** 679.
44. R. Blinc, J. Seliger, D. Arčon, T. Apih, P. Cevc, Z. Trontelj, J. Luznik and V. Zagar, *In: International Meeting on the Advances in NQR Detection of Land Mines and Explosives*, p. 40. Ljubljana.
45. J. Luznik, J. Pirnat and Z. Trontelj, *Solid State Commun*, 2002, **121,** 653.
46. R. Blinc, T. Apih and J. Seliger, *Appl. Magn. Reson.*, 2004, **25,** 523.
47. J. B. Miller and A. N. Garroway, *Appl. Magn. Reson.*, 2004, **25,** 475.
48. M. D. Hürlimann, C. H. Pennington, N. Q. Fan, J. Clarke, A. Pines and E. L. Hahn, *Phys. Rev. Lett.*, 1992, **69,** 684.
49. V. Mikhaltsevich and A. Belyakov, *Instrum. Exp. Tech.*, 2005, **48,** 397.
50. R. Lenk, *Fluctuations, Diffusion and Spin Relaxation*, Elsevier, Amsterdam, 1986, p. 30.
51. J. H. Flexman, T. N. Rudakov, P. A. Hayes, N. Shanks, V. T. Mikhaltsevitch and W. P. Chisholm, in: *Detection of Bulk Explosives: Advanced Techniques Against Terrorism*, Volume 138, H. Shubert and A. Kuznetsov, eds., Kluwer Academic Publishers, NATO Science Series, Series II: Mathematics, Physics and Chemistry, 2004, p. 113.
52. V. T. Mikhaltsevitch, T. N. Rudakov, J. H. Flexman, P. A. Hayes and W. P. Chisholm, *Appl. Magn. Reson.*, 2004, **25,** 449.
53. T. Hirschfeld and S. M. Klainer, *J. Molec. Struct.*, 1980, **58,** 63.
54. A. N. Garroway, J. B. Miller and M. L. Buess, in: *Proc. First Int. Symp. Explosive Detection Technology*, Atlantic City, NJ, 1992 p. 435.
55. M. L. Buess, A. N. Garroway and J. P. Yesinowski, U.S. Patent 5 365 171, 1994.
56. J. A. S. Smith and N. F. Peirson, Patent Int. Publication No. WO 96/26453, 1996.
57. J. A. S. Smith, M. Blanz and N. F. Peirson, U. S. Patent 6246237, 2001.

58. N. F. Peirson, J. Barras and J. A. S. Smith, Patent Int. Publication No. WO 99/19740, 1999.
59. G. A. Barrall, L. J. Burnett and A. G. Sheldon, U. K. Patent GB 2 338 787, 1999.
60. A. V. Belyakov, T. N. Rudakov, V. T. Mikhaltsevitch and W. P. Chisholm, Patent US 6856133, 2005.
61. V. T. Mikhaltsevitch, T. N. Rudakov, J. H. Flexman, P. A. Hayes and W. P. Chisholm, Patent US 7250763, 2007.
62. A. N. Garroway, M. L. Buess, J. P. Yesinowski, J. B. Miller and R. A. Krauss, *SPIE Cargo Inspection Technol.*, 1994, **2276,** 139.
63. M. D. Rowe and J. A. S. Smith in: *Proc. EUREL Int. Conf. Detection of Abandoned Landmines*, Edinburgh, UK, 1996, pp. 62–66.
64. I. P. Gerothanassis, *Prog. NMR Spectrosc.*, 1987, **19,** 267.
65. R. R. Ernst and W. A. Anderson, *Rev. Sci. Instr.*, 1966, **37,** 93.
66. V. L. Ermakov, R. K. Kurbanov, D. Y. Osokin and V. A. Shagalov, *JETP Lett.*, 1991, **54,** 467.
67. D. Y. Osokin, V. L. Ermakov, R. K. Kurbanov and V. A. Shagalov, *Z. Naturforsch.*, 1992, **47a,** 439.
68. D. Y. Osokin, R. K. Kurbanov and V. A. Shagalov, *In:* Magnetic Resonance and Related Phenomena, K. M. Salikhov, ed., 1994 p. 835. Kazan, RussiaAbstracts of the XXVII-th Congress AMPERE.
69. D. Y. Osokin and V. A. Shagalov, *Solid State Nucl. Magn. Reson.*, 1997, **10,** 63.
70. D. Y. Osokin, *Sov. Phys. – JETP*, 1999, **88,** 868.
71. V. Mikhaltsevich and T. Rudakov, *JETP Lett.*, 2003, **77,** 175.
72. V. Mikhaltsevitch and T. Rudakov, *State Nucl. Magn. Reson.*, 2003, **24,** 263.
73. V. L. Ermakov and D. Y. Osokin, *Mol. Phys.*, 1984, **53,** 1335.
74. M. Mehring and V. A. Weberruβ, *In:* Object-Oriented Magnetic Resonance , 2001, p. 330. Academic, London.
75. W.-K. Rhim, A. Pines and J. S. Waugh, *Phys. Rev. Lett.*, 1970, **25,** 218.

CHAPTER 5

Chlorine, Bromine, and Iodine Solid-State NMR Spectroscopy

Cory M. Widdifield, Rebecca P. Chapman, and **David L. Bryce**[1]

Contents

Abstract

We review the solid-state NMR literature for the $^{35/37}$Cl, $^{79/81}$Br, and ^{127}I nuclides, with coverage up to August 2008. The theory related to NMR spectroscopy of half-integer quadrupolar nuclei in powdered samples is briefly summarized, as are the experimental methods for recording such spectra. The most recent experimental results demonstrate the increasing feasibility and utility of

Department of Chemistry and Centre for Catalysis Research and Innovation, University of Ottawa, Ottawa, Ontario, Canada K1N 6N5
[1] Corresponding author: Email: dbryce@uottawa.ca

Annual Reports on NMR Spectroscopy, Volume 66
ISSN 0066-4103, DOI: 10.1016/S0066-4103(08)00405-5

observing solid-state NMR spectra for these nuclei, particularly chlorine-35/37. Several chlorine chemical shift tensors have been measured recently, along with their orientation relative to the electric field gradient tensor. The increased availability of ultrahigh-field solid-state NMR spectrometers ($\mathbf{B}_0 \geq 18.8$ T) is the dominant factor responsible for the increased number of studies and increased amount of available information. For example, insights have been gained into the hydrogen bonding environment at the chlorine atoms in various organic hydrochloride salts by interpreting trends in the chlorine quadrupolar coupling and chemical shift tensors. The sensitivity of the $^{35/37}$Cl NMR parameters to polymorphism and pseudo-polymorphism has also been demonstrated. Important advances in quantum chemistry which are having an impact on the computation of quadrupolar and magnetic shielding tensors for these nuclei are also briefly discussed. Data available from gas-phase molecular beam and microwave spectroscopy experiments are presented. Finally, prospects for future studies of $^{35/37}$Cl, $^{79/81}$Br, and ^{127}I by solid-state NMR spectroscopy are presented.

Key Words: Chlorine-35, Chorine-37, Bromine-79, Bromine-81, Iodine-127, Quadrupolar nuclei, Zeeman-perturbed NQR, Solid-state NMR, Electric field gradient, Magnetic shielding tensor, Chemical shift tensor, Quantum chemical calculations, Ab initio calculations.

List of abbreviations

α, β, γ	Euler angles relating two principal axis systems
CP/MAS	Cross-polarization magic-angle spinning
C_Q	Nuclear quadrupolar coupling constant
CS	Chemical shift
CSA	Chemical shift anisotropy
CT	Central transition
δ_{11}, δ_{22}, δ_{33}	Principal components of the chemical shift tensor
DFT	Density functional theory
EFG	Electric field gradient
η_Q	Quadrupolar asymmetry parameter
GIAO	Gauge including atomic orbitals or Gauge independent atomic orbitals
GIPAW	Gauge-including projector-augmented wave
IUPAC	International union of pure and applied chemistry
κ	Skew of the magnetic shielding (or chemical shift) tensor
MAS	Magic-angle spinning
MQMAS	Multiple-quantum magic-angle spinning
NN	Nearest neighbour
NNN	Next nearest neighbour
NQR	Nuclear quadrupole resonance
PAS	Principal axis system
QI	Nuclear electric quadrupole interaction
σ_{11}, σ_{22}, σ_{33}	Principal components of the magnetic shielding tensor
SSNMR	Solid-state nuclear magnetic resonance

ST	Satellite transitions
STMAS	Satellite transition magic-angle spinning
V_{11}, V_{22}, V_{33}	Principal components of the electric field gradient tensor
Ω	Span of the magnetic shielding (or chemical shift) tensor

1. INTRODUCTION

Chlorine, bromine, and iodine are important elements in a wide variety of materials, catalysts, and biochemically important molecules. For example, inorganic catalysts,[1,2] biochemically vital chloride ion channels,[3–6] and industrially important X-ray storage phosphors and scintillation devices[7–10] all involve chloride, bromide, or iodide ions as ubiquitous components. Chlorine-35/37, bromine-79/81, and iodine-127 are quadrupolar nuclei ($I > 1/2$) and all possess a moderate to large nuclear electric quadrupole moment (Q). The nuclear spin properties of these nuclides are summarized in Table 1. All the nuclides have moderate to high natural abundances, ranging from 24.23% for ^{37}Cl to 100% for ^{127}I. Only chlorine-35/37 may be classified as low-γ (i.e. $\gamma < \gamma(^{15}\text{N})$); however, the resonance frequencies are not particularly low in the conventional magnetic fields used for NMR (e.g. for $\mathbf{B}_0 = 11.75$ T, $\nu(^{35}\text{Cl}) = 49.07$ MHz and $\nu(^{37}\text{Cl}) = 40.85$ MHz). The main challenges associated with recording solid-state NMR (SSNMR) spectra of these quadrupolar halogens in commercially available magnetic field strengths stem from the interaction between Q and the surrounding electric field gradient (EFG) tensor. In compounds where the nucleus of interest sits at a site of low symmetry, quadrupolar broadening will typically dominate the NMR spectrum of a powdered sample. In these cases only the central transition (CT, $m = 1/2 \leftrightarrow -1/2$) is likely to be observable, although even this may span spectral regions on the order of MHz (depending on the nuclide, the local environment, and the value of $\mathbf{B}_0$). Nevertheless, a CT perturbed by second-order quadrupolar effects provides a substantial amount of relevant information on the environment of the nucleus. Anisotropy of the nuclear magnetic shielding tensor, which can be of

TABLE 1 Selected NMR properties of the half-integer quadrupolar halogen nuclei

^{A}X	$\gamma / 10^7$ (rad T^{-1} s^{-1})	Ξ (%)	NA (%)	I	Q (mb)[323]	$\Delta\nu_{CT}$ (relative)[a]	Standard[b]
^{35}Cl	2.624198	9.797 909	75.78	3/2	–81.65(80)	1.340	0.1 M NaCl
^{37}Cl	2.184368	8.155 725	24.22	3/2	–64.35(64)	1.000	
^{79}Br	6.725616	25.053 980	50.69	3/2	313(3)	7.702	0.01 M NaBr
^{81}Br	7.249776	27.006 518	49.31	3/2	262(3)	5.006	
^{127}I	5.389573	20.007 486	100.0	5/2	–696(12)	11.445	0.01 M KI
^{211}At	–	–	0	9/2	–	–	–

[a] The value of η_Q is assumed to equal 0. The value of $\Delta\nu_{CT}(^{37}\text{Cl})$ has been arbitrarily normalized.
[b] As suggested by Harris et al.[34] (in D_2O).

comparable magnitude to the second-order quadrupolar interaction in some systems, can manifest itself as observable chemical shift anisotropy (CSA) in the SSNMR spectra of quadrupolar nuclei. To measure such anisotropy, it is advantageous to have $\mathbf{B}_0$ as large as possible. A large value for $\mathbf{B}_0$ will reduce the second-order quadrupolar broadening of the CT and enhance the observable effects of CSA.

In 2006, a review of chlorine-35/37, bromine-79/81, and iodine-127 SSNMR data was published, which covered the literature up to July 2005.[11] In the present contribution, we provide a fresh and more thorough perspective on this field, with an emphasis on the new developments in $^{35/37}$Cl SSNMR and expanded discussions on the historical importance of $^{79/81}$Br and ^{127}I SSNMR experiments. Effort has been made to cover the literature in its entirety, from the earliest days of NMR spectroscopy until August 2008. In the previous review, three general recommendations were made for further study and it is important to discuss the progress which has been made in these areas. These areas were, in general terms: (i) to more fully substantiate and understand the relationship between halogen NMR parameters and the local hydrogen bonding environment in organic hydrochlorides; (ii) to pursue the measurement of halogen chemical shift tensors with the goal of using this information to provide more insight into the local molecular and electronic structure; (iii) to take advantage of modern quantum chemical methods to calculate and interpret halogen NMR interaction tensors. Since 2005, significant progress has been made in each of the areas (*vide infra*).

Although the focus of this chapter will be on SSNMR spectroscopy of diamagnetic powdered samples, liquid-state NMR[12,13] and NQR[14] data may also provide complementary information; hence, selected results from both will also be discussed, where appropriate.

2. THEORETICAL BACKGROUND

The Hamiltonian operator (H) used to describe the SSNMR spectrum of a quadrupolar nucleus within a diamagnetic material is typically constructed by considering the electric quadrupole (H_Q) and nuclear magnetic shielding (H_σ) interactions as perturbations to the Zeeman Hamiltonian (H_Z). Although additional interactions are present (both direct dipolar and indirect spin–spin (J) coupling, for example), they are in many practical cases negligible for chlorine, bromine, and iodine, and we will therefore focus on the quadrupolar and shielding effects in the following discussion. The sections below provide a brief summary of the quadrupolar and shielding interactions, as well as their effects upon the observable SSNMR spectra of powdered diamagnetic samples. References will be made to single-crystal experiments in selected cases. For more complete theoretical treatments, the reader is referred elsewhere.[14–20]

2.1. The nuclear electric quadrupole interaction

The nuclear electric quadrupole interaction (QI) results from the coupling between Q and the EFG at the nuclear site. The EFG is a symmetric tensor quantity of zero trace and may be described by five independent parameters. When in its principal axis system (PAS), the off-diagonal matrix elements equal zero, and two parameters can fully describe the diagonal elements. The diagonal elements of a tensor in its PAS (V_{11}, V_{22}, and V_{33} in this case) are called the principal components. In practice, the SSNMR spectrum is usually described by the nuclear quadrupolar coupling constant, C_Q, and quadrupolar asymmetry parameter, η_Q, which are related to the principal components of the EFG tensor as follows:

$$C_Q = \frac{eV_{33}Q}{h}, \tag{1}$$

$$\eta_Q = \frac{V_{11} - V_{22}}{V_{33}}, \tag{2}$$

where $|V_{33}| \geq |V_{22}| \geq |V_{11}|$, h is Planck's constant and e is the elementary charge. When describing the orientation of the EFG PAS with respect to a secondary axis system (e.g., a second PAS, or a molecular or goniometer frame), three additional values are required to describe the angular relationship between the two frames (see Section 2.5).

Unless very high nuclear site symmetry (e.g. octahedral or tetrahedral) is present, the SSNMR line shape of a powdered sample will be broadened by the QI. Due to the moderate to large Q values associated with the quadrupolar halogens, first-order perturbation theory generally fails to describe the observed SSNMR lineshapes for most powdered samples and will not correctly predict the orientation dependence of the resonance signals in single crystals. However, there exist numerous situations where second-order perturbation theory provides an adequate representation of the observed SSNMR signal. When the QI is large enough such that second-order perturbation theory is required, the satellite transitions (ST) of a half-integer quadrupolar nucleus in a powdered solid are often broadened to such an extent that they are unobservable. The CT is not broadened to first order and is therefore observable in many situations. According to second-order perturbation theory, the breadth of the second-order CT line shape for a stationary powdered sample is dependent upon four parameters (C_Q, ν_0, I, and η_Q)[18]:

$$\Delta\nu_{CT} = \left[\frac{3C_Q}{2I(2I-1)}\right]^2 \frac{\left(\eta_Q^2 + 22\eta_Q + 25\right)\left(I(I+1) - \frac{3}{4}\right)}{144\nu_0}, \tag{3}$$

where ν_0 is the Larmor frequency. Increasing $\mathbf{B}_0$ will therefore reduce the quadrupolar broadening of the CT in Hz for a given EFG tensor. It is also seen that nuclides with higher nuclear spin quantum numbers will yield narrower spectra for a given value of C_Q as compared with nuclides of lower spin in the same environment. For the various halogen nuclei in a powder, relative ratios of the CT linewidth for a given EFG tensor are provided in Table 1.

2.2. The high-field approximation

Many half-integer quadrupolar nuclei possess properties and are in environments such that the inclusion of first- and second-order quadrupolar perturbations to the Zeeman eigenstates allows for the accurate modelling of the observed spectra at standard applied magnetic fields (i.e. $\mathbf{B}_0$ ranging from 7 to 12 T). For the quadrupolar halogen nuclei, it is often the case that the quadrupolar frequency, ν_Q,[a] becomes comparable (i.e. the same order of magnitude) to the Larmor frequency and it is therefore unclear if the high-field approximation is valid. Recently, an exact formulation of the combined Zeeman and quadrupolar interactions for arbitrary I and $\mathbf{B}_0$ was presented[21]; other exact solutions are also available.[22–26] Using the computational software developed by Prof. Bain (McMaster),[27] we have carried out several simulations which highlight the differences between the second-order and exact approaches. For the sake of discussion, the calculations assume that the sample under study is an ideal single crystal and that $\eta_Q = 0$. The value of θ represents the angle between $\mathbf{B}_0$ and V_{33}. As can be seen (see Figure 1 caption), for some applications the approximation is unquestionably valid (Figure 1A, representing a typical ^{23}Na nuclear environment). Other situations (Figures 1B and C) are less clear. For these cases, the differences between the second-order and exact approaches are now three orders of magnitude larger than in Figure 1A. However, it could be argued that the second-order approximation is still valid since the error resulting from the approximation remains under typical measurement errors. For example, the maximum absolute difference between the approximate and exact theories in Figure 1B is about 60 ppm (when $\theta = 54°$ and 126°). However, when simulating the *powder pattern* that corresponds to an axially symmetric EFG (neglecting CSA), only the edge discontinuities are of critical importance. At these points, the difference between the second-order and exact approaches would be 0 ppm for the high-frequency edge and about 32 ppm for the low-frequency edge. Thus, in this situation, for a powder pattern having a total breadth of about 7740 ppm, the error as a percentage is about 0.4%, which is within typical experimental error.[28] The result is much the same when considering the case in Figure 1C (∼1% error). The situation presented in Figure 1D highlights a potential scenario involving ^{127}I where the difference between the two approaches is slightly closer to expected measurement errors (∼1.3%).

Thus, when making quantitative comparisons between the second-order perturbation and exact approaches for a single crystal containing half-integer quadrupolar nuclei, it is seen that the difference in the expected transition frequencies for the CT at several crystal orientations is minor (< 1%), up to the point at which ν_Q and ν_0 become comparable (about a factor of 1/2 for spin-3/2 and 1/5 for spin-5/2). It is also clear that the CT of a powdered sample is somewhat less affected by the truncation. It seems therefore that a common rule-of-thumb regarding the extent to which the second-order approximation (and hence the high-field approximation) is valid (i.e. when $\nu_Q < 0.1\nu_0$) may in many practical cases be slightly conservative.

[a] For a given nuclear spin, I, $\nu_Q = 3C_Q\sqrt{1 + (\eta_Q^2/3)}/(2I(2I-1))$

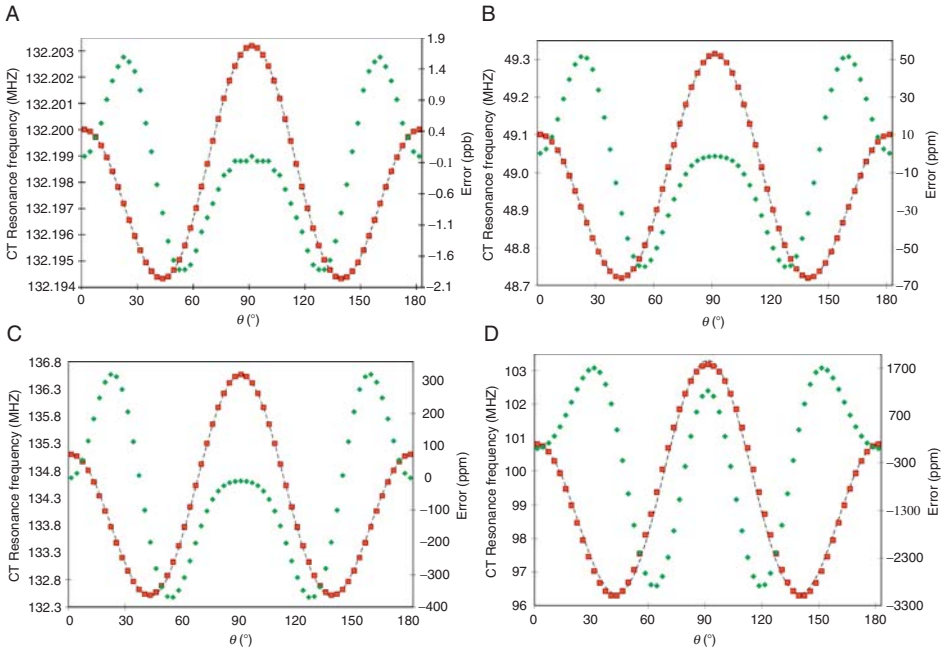

Figure 1 Comparison between the second-order perturbation (dashed line) and exact (squares) approaches for the calculation of a CT resonance frequency (left vertical axis), as V_{33} is rotated about an axis perpendicular to $\mathbf{B}_0$. The angle between V_{33} and $\mathbf{B}_0$ is represented by θ. The diamonds correspond to the difference (right vertical axis) between the two values for a particular orientation. The cases are as follows: (A) $C_Q = 3$ MHz, $\nu_0 = 132.2$ MHz; (B) $C_Q = 15$ MHz, $\nu_0 = 49.1$ MHz; (C) $C_Q = 65$ MHz, $\nu_0 = 135.1$ MHz; (D) $C_Q = 150$ MHz, $\nu_0 = 100.8$ MHz and are intended to model somewhat typical QI parameters for: (A) ^{23}Na; (B) ^{35}Cl; (C) ionic ^{81}Br; and (D) ionic ^{127}I. In all cases, $\mathbf{B}_0 = 11.7$ T, $\eta_Q = 0$ and CSA is neglected. Please note the right vertical scale change between (A) and (B)–(D).

2.3. Chemical shifts and absolute shielding

The magnetic shielding (σ) at a nucleus may constructively add to or destructively subtract from the applied magnetic field. Lamb[29] and Ramsey[30–33] have previously described the physical models for atomic and molecular systems, respectively. Although magnetic shielding is a fundamental atomic or molecular property, it is not measured directly when one conducts an NMR experiment. Rather, it is the chemical shift (δ), which results from the difference between the magnetic shielding of an unknown sample and a reference sample which is routinely measured. A recent recommendation,[34] endorsed by IUPAC, defines chemical shift in ppm, in terms of resonance frequencies rather than shielding constants:

$$\delta/\text{ppm} = \frac{\nu - \nu_{\text{ref}}}{\nu_{\text{ref}}}, \tag{4}$$

with ν and ν_{ref} representing the resonance frequency of the sample and the reference, respectively. Another convention, still in common use, defines the chemical shift in terms of magnetic shielding:

$$\delta/\text{ppm} = \frac{\sigma_{ref} - \sigma}{1 - \sigma_{ref}} \times 10^6, \tag{5}$$

with σ and σ_{ref} representing the magnetic shielding of the sample and the reference, respectively. As detailed later, shielding is a second-rank tensor quantity, but the preceding equation may also be used to determine each element of a chemical shift tensor (δ_{ij}), if the isotropic magnetic shielding constant (σ_{iso}) of the sample and reference are known.

The same IUPAC report recommended that a unified chemical shift scale (Ξ) be established for all nuclides.[34] The primary reference frequency used for the Ξ scale is the ^{1}H resonance of a maximally 1% (v/v) tetramethylsilane (TMS) in $CDCl_3$ solution (ν_{TMS}). The unified ''shift'' (it is recommended that Ξ values be expressed as percentages) is defined as the ratio between a secondary reference frequency and ν_{TMS} in the same $\mathbf{B}_0$:

$$\Xi = \frac{\nu}{\nu_{TMS}}. \tag{6}$$

Solution state standards for each of the quadrupolar halogen nuclei were also recommended (Table 1). As mentioned previously,[11] one should carefully note both the concentration and solvent when preparing solution state standards, as the measured shift values have been shown to depend significantly upon these two variables (see also Section 4.5). Typical solvent isotope effects[35,36] (expressed as the result of $\delta(X, H_2O) - \delta(X, D_2O)$, $X = $ Cl, Br, I) are ca. 5 ppm for chlorine, 8–10 ppm for bromine, and 13 ppm for $Na^{127}I$, and are one (in the case of Cs) to three (Li/Na) orders of magnitude greater than the corresponding solvent isotope shifts for the alkali metals in the alkali metal halides.

Temperature and pressure dependencies are expected to be minimal under typical lab conditions and will not be discussed further. As part of this review, we later discuss convenient standards for SSNMR experiments on the quadrupolar halogen nuclei (Section 4.5). Chlorine-35/37 are the only quadrupolar halogen nuclides for which a precise absolute shielding scale is available. Using a combined experimental and theoretical approach, a chloride ion in an infinitely dilute aqueous solution was determined to have an isotropic magnetic shielding constant (σ_{iso}) of 974(4) ppm.[37] This represents an improvement over previously suggested absolute shielding scales for chlorine.[38,39]

The absolute shielding scales for bromine and iodine are far less precisely determined and are not referenced with respect to the corresponding bare nuclei. For example, using a semi-quantitative theoretical model[40] along with experimental data,[41,42] Ikenberry and Das used Hartree–Fock methods to calculate the shift of the bromide anion with respect to the free anion and obtained –194 ppm.[43] On the basis of experimental solution state measurements, Itoh and Yamagata arrived at –600 ppm for I^- in dilute solution with respect to the free anion.[44] These calculations were expected to be rather crude estimates, even in the opinion of the original

authors[45] and therefore it is apparent that reliable absolute shielding scales for bromine and iodine remain to be established. The bromine shielding tensor of $CH_3Br(g)$ has been determined experimentally from spin-rotation data[46] and calculated using coupled Hartree–Fock theory.[47] This molecule could possibly serve as a candidate molecule for establishing the bromine absolute shielding scale (alternatively, gaseous HBr could also be used). Gaseous HI may be used to establish the absolute shielding scale iodine. For both gaseous HBr and HI, relativistic shielding parameters were recently calculated using the normalized elimination of the small component (NESC) theory under the second-order regular approximation (SORA),[48] both are commercially available and their spin-rotation parameters are precisely known. One of the issues to be addressed, however, is how relativistic effects influence the straightforward non-relativistic relationship[49,50] between the shielding and the spin-rotation constants.[51] A survey of available spin-rotation constants for halogen nuclides in diatomic molecules is presented in Section 4.6.

2.4. Magnetic shielding/chemical shift anisotropy

While isotropic chemical shifts are routinely measured, magnetic shielding is a tensor quantity. Hence, additional information may be obtained by characterizing the full tensor. Unlike the EFG tensor, the shielding tensor is, in general, asymmetric and has a non-zero trace; unless a certain degree of nuclear site symmetry is present,[52,53] the magnetic shielding interaction requires nine independent parameters to be fully described. Fortunately, the anti-symmetric portion may almost always be ignored, leaving the isotropic and symmetric contributions. In its PAS, three independent values are required to specify the magnitude of the interaction. Anet and O'Leary provide further discussion on the symmetry properties of the magnetic shielding tensor.[54]

Unlike the EFG tensor, there is currently no universally accepted way to go about describing the magnitude of an observed chemical shift tensor or a magnetic shielding tensor.[55,56] Recent IUPAC recommendations suggest the Haeberlen convention be adhered to when discussing shielding tensors, while chemical shift tensors may be expressed using either the Haeberlen or Herzfeld–Berger/Maryland convention. As noted in the IUPAC recommendations, the Haeberlen convention can suffer from an ''oddity [which] makes for difficulties in comparing tensor components or anisotropies for a series of related molecules and has sometimes led to misunderstandings.'' For these reasons, we prefer to use the principal components and/or the ''Herzfeld–Berger''[57]/''Maryland''[56] conventions where possible.

2.4.1. Haeberlen convention

The Haeberlen-Mehring-Spiess convention defines three parameters in terms of the three shielding tensor principal components, σ_{XX}, σ_{YY}, and σ_{ZZ}. The three parameters are the isotropic shielding value (σ_{iso}), the shielding anisotropy ($\Delta\sigma$), and the shielding asymmetry (η). Their definitions are provided below:

$$\sigma_{iso} = \frac{(\sigma_{XX} + \sigma_{YY} + \sigma_{ZZ})}{3}, \tag{7}$$

$$\Delta\sigma = \sigma_{ZZ} - \frac{(\sigma_{XX} + \sigma_{YY})}{2}, \tag{8}$$

$$\eta = \frac{3(\sigma_{YY} - \sigma_{XX})}{2\Delta\sigma}, \tag{9}$$

where $|\sigma_{ZZ} - \sigma_{iso}| \geq |\sigma_{XX} - \sigma_{iso}| \geq |\sigma_{YY} - \sigma_{iso}|$. Shielding anisotropy is positive if $\sigma_{ZZ} > \sigma_{iso}$ and negative if $\sigma_{ZZ} < \sigma_{iso}$, and the asymmetry takes on a positive value between 0 and 1.

2.4.2. "Herzfeld–Berger"/"Maryland" convention

This convention labels the three principal components of the shielding tensor as σ_{11}, σ_{22}, and σ_{33}, with $\sigma_{11} \leq \sigma_{22} \leq \sigma_{33}$. The isotropic shielding constant is therefore $(1/3)(\sigma_{11} + \sigma_{22} + \sigma_{33})$. The span ($\Omega$), and the skew ($\kappa$) are used to describe the breadth and asymmetry, respectively, of the shielding tensor:

$$\Omega = \sigma_{33} - \sigma_{11}, \tag{10}$$

$$\kappa = \frac{3(\sigma_{iso} - \sigma_{22})}{\Omega}. \tag{11}$$

The skew may range between -1 and $+1$, while Ω may take on any positive value. When discussing chemical shift tensors, the definitions in terms of the principal components $\delta_{11} \geq \delta_{22} \geq \delta_{33}$ are as follows, where the approximate equality is introduced due to the denominator in Equation (5).

$$\delta_{iso} = \frac{(\delta_{11} + \delta_{22} + \delta_{33})}{3}, \tag{12}$$

$$\Omega \approx \delta_{11} - \delta_{33}, \tag{13}$$

$$\kappa = \frac{3(\delta_{22} - \delta_{iso})}{\Omega}. \tag{14}$$

As long as $1 - \sigma_{ref}$ is close to unity, (13) is valid. Even in the case of ^{127}I, where the chemical shift range is on the order of 10^4 ppm, the approximations are still reasonable; for example, a very large span of 50 000 ppm (heretofore unknown for ^{127}I) would introduce an error of approximately 5%.

2.5. Tensor interplay

2.5.1. Static conditions: Contributions from quadrupolar and shielding tensors

In practice, the SSNMR spectra of the quadrupolar halogen nuclei in non-cubic environments are expected to be dominated by the QI. This is due to the moderately large Q associated with each nuclide, coupled with typically modest CSA contributions (typical CSAs are observed to be on the order of 10^1–10^2 ppm). However, recent work in particular (*vide infra*) has shown that there are in fact many examples, particularly for chlorine-35/37, where contributions from CSA

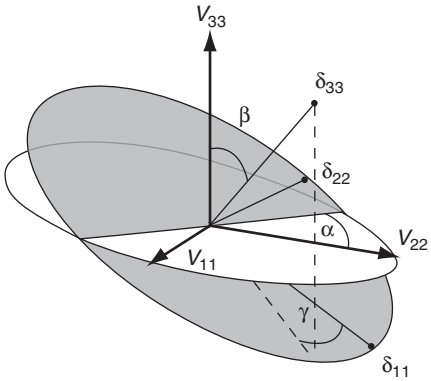

Figure 2 Euler angles relating the principal axis systems of the EFG and CS tensors, according to the "*z*–*y*–*z*" convention.

to the NMR spectrum of a stationary powdered sample can have a significant impact on spectral interpretation. When contributions from the anisotropic quadrupolar and shielding interactions are present, up to eight independent parameters are required to describe the line shape of the central transition: δ_{11}, δ_{22}, δ_{33}, C_Q, η_Q, α, β, γ. The angles α, β, and γ describe the rotations that are required to bring the EFG tensor into coincidence with the CS tensor, that is so that V_{33} and δ_{33}, V_{22} and δ_{22}, and V_{11} and δ_{11}, respectively, are collinear. In the Arfken convention,[58] the angles may be visualized as in Figure 2. Beginning with coincident PASs for the EFG and CS tensors, the CS tensor is rotated by an angle α about the direction of δ_{33}. Next, the CS tensor is rotated about the new (intermediate) direction of δ_{22} by an angle β, and finally the CS tensor is rotated about the new direction of δ_{33} by and angle γ. All rotations are counterclockwise. The angular relationship between the PASs of the EFG and CS tensors has a strong impact on the appearance of the NMR spectrum, provided that the magnitudes of the interactions are not too disparate. Examples of the types of lineshapes which can be expected for the CT under the influence of both quadrupolar and CS interactions are presented in Figure 3.

2.5.2. MAS conditions: Residual dipolar coupling

Quadrupolar halogen nuclei are most frequently characterized by SSNMR through the direct observation of their CT, either under stationary or MAS conditions. A well-known alternative method for obtaining insight into the EFG at a quadrupolar nucleus is to observe the MAS NMR spectrum of a spin-1/2 nucleus which is spin-coupled to the quadrupolar nucleus.[59] Since MAS does not entirely average to zero the dipolar coupling between a spin-1/2 and a quadrupolar nucleus, a ''residual'' dipolar coupling remains. Reports of residual dipolar coupling involving $^{35/37}$Cl, $^{79/81}$Br, or ^{127}I may be found in the literature.[60–83] The residual coupling is quantified by a parameter, d:

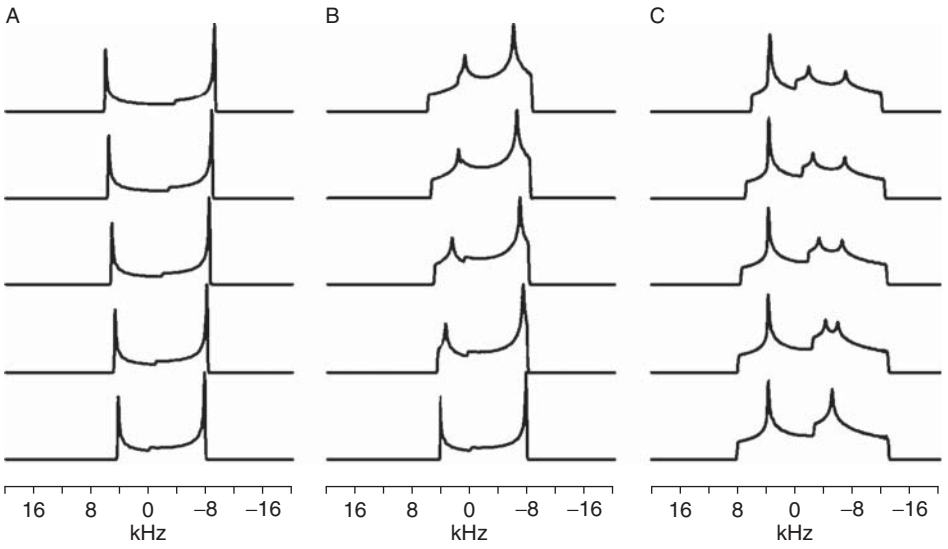

Figure 3 Select simulated spectra of the CT for a spin-3/2 nucleus ($C_Q = 3.2$ MHz) in a powdered sample. (A) Coincident EFG and CS tensor PASs ($\alpha = \beta = \gamma = 0°$), with $\kappa = +1$. The span of the CS tensor ranges from zero (bottom) to 40 ppm (top) in 10 ppm increments. (B) Same as (A), but $\beta = 90°$. (C) With $\kappa = 0.5$, $\alpha = \gamma = 0°$ and $\Omega = 40$ ppm, β is varied from 0° (bottom) to 40° (top) in steps of 10°.

$$d = -\frac{3C_Q R_{\text{eff}}}{20\nu_S}\left[\left(3\cos^2\beta_d - 1\right) + \eta_Q \sin\left(2\beta_d\right)\cos\left(2\alpha_d\right)\right]. \quad (15)$$

The spectrum of the spin-1/2 nucleus will depend on d and on $|J_{\text{iso}}|$, to first order. Here, α_d and β_d are the polar angles describing the orientation of the internuclear vector in the EFG PAS. As the observed spectrum depends on R_{eff}, internuclear distance information can also be obtained under favourable conditions. For example, shown in Figure 4 are the ^{13}C CPMAS spectra of the carbonyl carbon of 2-chloro-2-(phenylsulfonyl)-1-phenylpropanone, obtained at 2.35 and 4.7 T.[61] Residual dipolar coupling between ^{13}C and $^{35/37}$Cl causes the carbonyl resonance to split into a complicated multiplet. Due to the inverse dependence of the coupling parameter d on the Larmor frequency of the quadrupolar nucleus (ν_S), the splittings are more pronounced at 2.35 T. Spectral simulations result in a ^{13}C–^{35}Cl dipolar coupling constant of 135 Hz, a ^{35}Cl quadrupolar coupling constant of -73 ± 2 MHz and $\beta_d = 35°$. Analysis of the ^{13}C CP/MAS NMR spectra of this compound and of a related chloroketosulfone also provided the first direct measurement of $^1J(^{35/37}\text{Cl}, ^{13}\text{C})_{\text{iso}}$, -20 ± 5 Hz. Importantly, analysis of the NMR spectra of spin-1/2 nuclei coupled to quadrupolar nuclei has the potential to provide the *signs* of parameters such as C_Q and J_{iso}. The sign of C_Q is not available from the analysis of a simple one-dimensional NMR spectrum of the quadrupole.

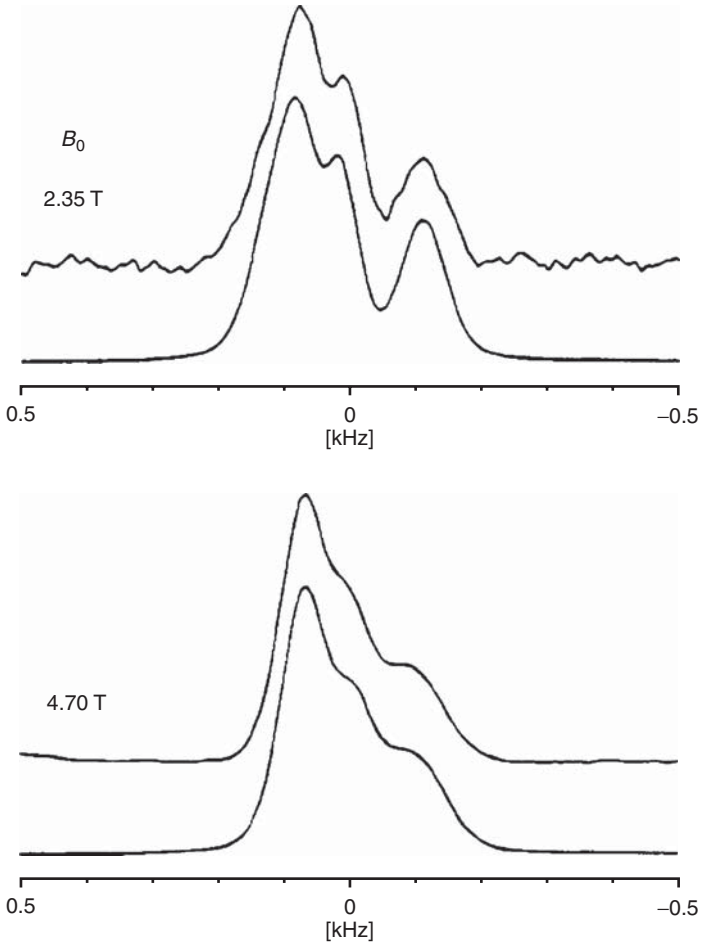

Figure 4 Experimental (upper traces) and simulated ^{13}C CPMAS NMR spectra of the carbonyl carbon of 2-chloro-2-(phenylsulfonyl)-1-phenylpropanone, showing evidence for residual dipolar coupling between ^{13}C and $^{35/37}Cl$. From Ref. 61. Reproduced by permission of the *American Chemical Society*.

3. EXPERIMENTAL AND COMPUTATIONAL METHODS

3.1. Single-crystal methods

Analysis of NMR spectra from the stepped rotation of a single-crystal sample is the most rigorous manner in which to characterize the tensor interactions associated with a particular nucleus. Particularly, the orientation of the PAS of an interaction tensor with respect to the molecular framework can be precisely determined. The methods of analysis of single-crystal NMR data have been reported elsewhere.[84–86] While once more common, single-crystal analyses of quadrupolar halogens in diamagnetic samples are no longer as frequently

reported; none have been reported in the past couple of decades, to our knowledge. For this reason we will not discuss single-crystal methods any further. We note that many single-crystal studies of chlorine, bromine, and iodine in magnetic materials have been reported in the 1950s to 1980s, particularly in the solid-state physics literature. Many Zeeman-perturbed NQR studies also use single-crystal analyses (*vide infra*). In the literature discussion which follows (Section 4), reference to single-crystal methods and results will be made where needed.

3.2. Powdered sample methods

Most modern SSNMR experiments on the quadrupolar halogen nuclei are carried out on powdered samples. We present briefly here an overview of the most commonly applicable methods to be used on stationary and MAS powdered samples.

If the broadening of the CT is small enough under a given $\mathbf{B}_0$, a MAS NMR spectrum will, under favourable conditions, provide the values of δ_{iso}, $C_{Q,}$ and η_Q through line shape simulations. Recent advances such as ultrafast MAS probes make it feasible to acquire MAS spectra for quadrupolar nuclei in an increasing number of compounds. Currently, the fastest-spinning commercially available MAS probes use 1.3 mm o.d. rotors, which offer stable MAS rotation frequencies of up to ca. 70 kHz. Over the past few years, several methods have been introduced to enhance the CT NMR signal of quadrupolar nuclei by transferring intensity from the ST through saturation or inversion.[87] These methods include rotor-assisted population transfer (RAPT),[88] double-frequency sweeps (DFS),[89] and hyperbolic secant pulses.[90] Thus far, these methods have not been applied extensively to chlorine, bromine, or iodine. However, a great potential for using these techniques exists, particularly in the case of chlorine because these nuclei have the least inherent sensitivity and the narrowest spectral lines for a given EFG.

The satellite transition spectroscopy (SATRAS) approach,[91–93] whereby the spectra of the satellite transitions are observed under MAS conditions and simulated to extract the relevant NMR information, is most generally applicable when the quadrupolar interaction is small. Shown in Figure 5 is an example of the spectra obtained by Trill et al. for a series of halide sodalites.[94] This method will also benefit from continued increases in available MAS rates.

The quadrupolar Carr–Purcell–Meiboom–Gill (QCPMG) pulse sequence[95] has begun to be applied to chlorine, iodine (*vide infra*) and bromine.[28] This method relies on a train of π pulses and a reasonably large T_2/T_2^* ratio to generate a time-domain system response which looks much like a series of spikes. Using the symmetry inherent to the Fourier-transformation, the frequency-domain spectrum of the transformed time-domain response creates a powder pattern that is split (under MAS or stationary conditions) into a manifold of so-called ''spikelets''. Not only is the experimental sensitivity enhanced by the multiple acquisition periods per relaxation delay, but signals are also more easily detected, since the total signal intensity is concentrated into the spikelets. Siegel et al. have demonstrated the QCPMG ^{127}I NMR experiment using KIO_4.[96] We have found that this is an excellent sample on which to set up ^{127}I QCPMG experiments.

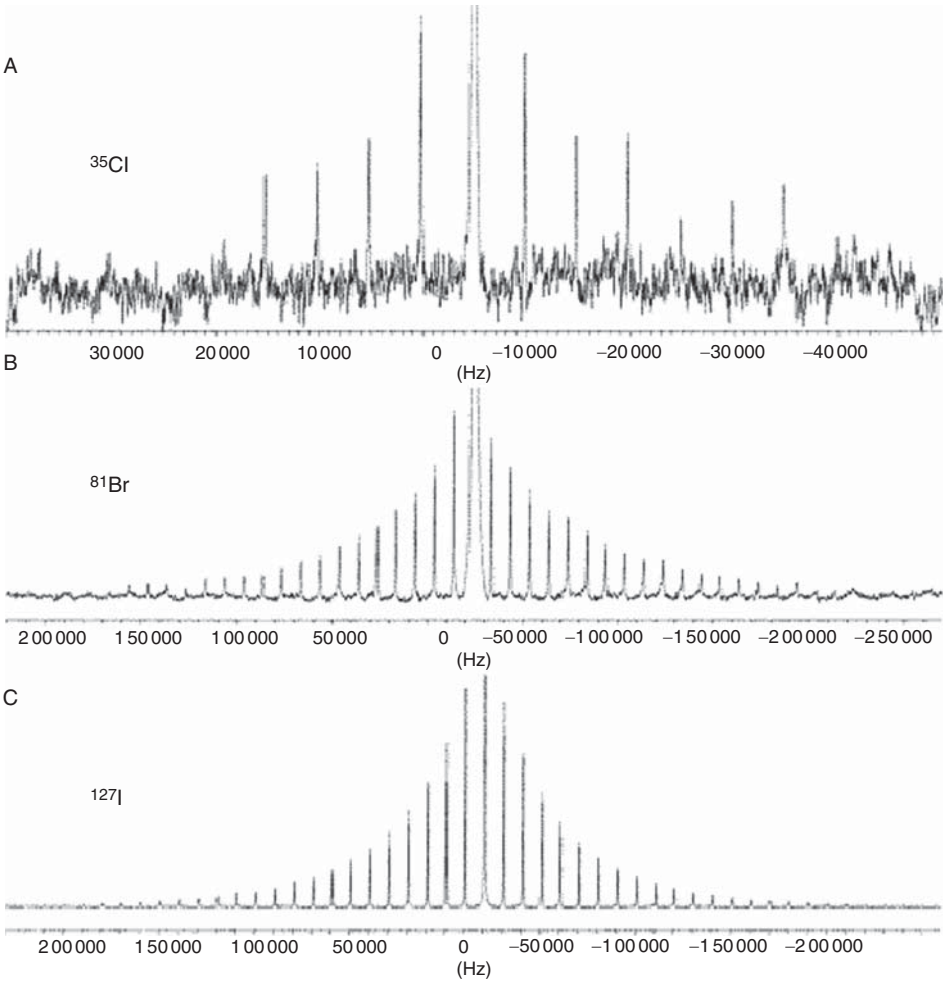

Figure 5 SATRAS NMR spectra of pure halide sodalites. From: Ref. 94. Reproduced by permission of the *American Chemical Society*.

The general strategy used to characterize both the EFG and CS tensors of quadrupolar halogen nuclei is to first acquire a MAS NMR spectrum (if possible) and by line shape analysis extract the values of δ_{iso}, C_Q, and η_Q. A spectrum of the stationary sample is then acquired. Ignoring the typically modest temperature increase due to the frictional heating of the sample while it is rotating, the values of δ_{iso}, C_Q, and η_Q are constant between experiments and hence may be fixed during the simulation of the spectrum of the stationary sample. This reduces the number of remaining parameters that are to be fit to five: Ω, κ, α, β, and γ. In many instances for $^{35/37}$Cl, $^{79/81}$Br, and ^{127}I, it is not possible to spin the sample fast enough to separate the rotational sidebands from the centreband and hence time-dependent numerical simulations involving up to eight adjustable parameters

would need to be carried out. The solution arrived at by this process is not necessarily unique; hence, it is of limited use. In situations of this nature, there is no (current) experimental method that can reduce the number of adjustable parameters and hence the spectrum of the stationary sample will depend on all eight unknown parameters. Fortunately for chlorine and bromine, there are two readily observable isotopes. By taking advantage of the known ratio of the quadrupole moments for each pair of isotopes ($^{35/37}$Cl or $^{79/81}$Br) and by assuming that isotope effects on the CS tensor are negligible, the spectra of both isotopes of the same element can be fit simultaneously. Further restraints on the eight unknowns are provided by acquiring spectra of both isotopes at more than one value of $\mathbf{B}_0$.

We note that Grandinetti and co-workers have recently reported a multiple-quantum two-dimensional method (correlation of anisotropies separated through echo refocusing, COASTER) for obtaining relative EFG and CS tensor orientations, which could prove to be useful for studies particularly of chlorine-35/37.[97]

In cases where the quadrupolar interaction is so large that the CT is broadened to the extent that it cannot be acquired without line shape distortion (due to a non-uniform excitation profile), the variable-offset frequency approach may be applied. We have found this procedure to be of substantial benefit for the acquisition of high-quality $^{79/81}$Br SSNMR spectra.[28] The method can be applied using an echo or QCPMG pulse sequence, and simply entails stepping the rf transmitter across the breadth of the CT spectrum and summing the individual sub-spectra to obtain the final undistorted spectrum. For example, Schurko and co-workers have applied the stepped-frequency QCPMG method to study the ^{27}Al resonances in three- and five-coordinate aluminium complexes, and discussed the optimal procedure for combining the ''sub-spectra'' such that distortions are minimized.[98] One could also potentially adjust the applied magnetic field while keeping the transmitter frequency fixed, as demonstrated by Smith and co-workers for aluminum-27.[99] O'Dell and Schurko[100] recently reported a QCPMG method which uses adiabatic pulses for faster acquisition of broad spectral patterns; this method will be useful for future studies of chlorine, bromine, and iodine.

Multiple-quantum magic-angle-spinning (MQMAS)[101] and satellite-transition magic-angle-spinning (STMAS)[102] have developed over the past decade into useful and widely applied tools for obtaining high-resolution ''isotropic'' spectra of half-integer spin quadrupolar nuclei. To our knowledge, only one report of MQMAS applied to a quadrupolar halogen is available. Trill et al. reported ^{35}Cl MQMAS results for a chloride-containing mixed sodalite; however, no spectrum was published.[94] We are not aware of any applications of STMAS to chlorine, bromine, or iodine. Since these nuclei are often subject to large quadrupolar interactions, it is not surprising that the high-resolution MAS methods have not been extensively applied to $^{35/37}$Cl, $^{79/81}$Br, or ^{127}I. First of all, the quadrupolar interaction must be small enough to enable a MAS NMR spectrum to be recorded. This is typically only the case for some chlorine compounds. Furthermore, even when MAS is possible, the quadrupole interactions remain large enough such that it is difficult to efficiently excite the proper coherences for the MQMAS or STMAS experiments to provide useful results. We have observed this first hand for barium chloride dihydrate, where only one of the two crystallographically

non-equivalent chloride sites was easily observable in the ^{35}Cl STMAS NMR spectrum obtained at 11.75 T (unpublished). In general, methods such as MQMAS and STMAS are not expected to become commonly used tools for the quadrupolar halogens; however, there may be specific classes of compounds which will benefit from these techniques, particularly when such experiments are carried out in the highest possible applied magnetic fields.

Persons and Harbison reported the ''slow turning reveals enormous anisotropic quadrupolar interactions'' (STREAQI) method in 2007, and applied it to several ^{79}Br containing samples.[103] This interesting 2D technique offers the possibility of characterizing sites with very large quadrupolar interactions (tens of MHz) using very slow (e.g. 300 Hz) sample rotation. One limitation of their reported analysis is that it currently does not account for chemical shift anisotropy. Nevertheless, the method holds promise for studying a range of samples containing Cl, Br, or I.

3.3. Calculations of NMR parameters

As mentioned, the quadrupolar and magnetic shielding interactions are frequently the most important contributors to the total SSNMR spectrum of the quadrupolar halogens. Some calculations of indirect nuclear spin–spin coupling tensors involving chlorine, bromine, and iodine have been performed, particularly for gaseous diatomic molecules.[104,105] However, we focus here on the parameters of current importance to the analysis of solid powdered samples (i.e. the EFG and σ tensors).

There are two aspects related to Cl, Br, and I which necessitate special attention when calculating their NMR parameters. First, many compounds of interest which can be studied by SSNMR feature these nuclei in predominantly ionic environments. As a result, it can often be challenging to obtain results from calculations which agree with experiment since an isolated molecular model does not describe the long range environment very well. For example, it was shown that the isolated molecular approach, as well as a self-consistent charge-field perturbation (SC-CFP) model[106] implemented using Gaussian software did not produce chlorine quadrupolar coupling constants and shielding tensors in good agreement with experiment for a series of alkaline earth chlorides and their hydrates.[107] The values of C_Q tended to slowly converge towards the experimental values as the size of the model considered in the calculation increased; however, the absolute value remained far from experiment.

The gauge-including projector-augmented wave (GIPAW) approach has found much success recently in the calculation of NMR parameters in solids. This approach allows the whole crystal lattice to be described in the calculation, which can be very important for the calculation of EFG tensors, since contributions to this vary inversely with respect to the cube of the distance between the nucleus of interest and other charges in the lattice. Clearly this becomes particularly important when the crystal under consideration is highly ionic versus being composed of neutral molecules. The implementation of the GIPAW approach for the calculation of NMR parameters in the CASTEP[108–110] software package has been used to

calculate chlorine NMR parameters in solids,[112] as has the Paratec code.[111] Other available plane-wave software includes, for example: VASP, Wien2k, CPMD, and abinit. Zwanziger and Torrent have recently implemented the calculation of EFGs in metals, semiconductors, and insulators using a projector-augmented wave approach in the abinit software package.[113] The ^{127}I C_Q and η_Q of CdI_2 were calculated ($C_Q = 91.656$ MHz; $\eta_Q = 0.0$) and, through comparison with the available data[114] from NQR spectroscopy ($C_Q \approx 97.6$ MHz; $\eta_Q = 0.0$), they assessed some of the limitations of the PAW method. It is noted that the PAW method provides excellent agreement with experiment despite the fact that the method treats the core electron distribution as a rigid sphere—this may be somewhat surprising given that Sternheimer effects[115] may be expected to play an important role in determining iodine EFGs. The calculated value was improved (93.502 MHz) relative to experiment after including $4d^{10}$ electrons in the valence space of an improved PAW.

The second potentially problematic issue when considering NMR calculations, particularly on bromine and iodine nuclides, is that of relativistic effects. It is known from quantum chemical calculations that these effects are often important for achieving correct results for NMR parameters in small halogen-containing molecules, including *J*-couplings,[105,116] EFGs,[117–119] and shielding constants.[120,121] The details of relativistic calculations of NMR parameters will not be discussed here; we refer the reader to the literature in this area.[122–124] Given the increasing activity in SSNMR of the quadrupolar halogens, one must nevertheless be aware of the potential impact of relativity on the NMR parameters of both the halogens and lighter nuclides which interact with the halogens. For example, in their study of ^{127}I–^{1}H and ^{127}I–^{13}C coupling constants and ^{1}H/^{13}C chemical shifts in iodo compounds, Kaupp et al. pointed out in 1998 that ''the importance of spin–orbit effects on NMR chemical shifts is still widely underestimated by the practical chemists and NMR spectroscopists''.[123]

4. SURVEY OF AVAILABLE EXPERIMENTAL DATA

Previous reviews of solution state chlorine, bromine, and iodine NMR were published by Lindman or Lindman and Forsén[13] in 1976, 1978, and 1983, by Forsén and Drakenberg in 1983,[12] and by Akitt in 1987.[125] The only previous review of solid-state halogen NMR appeared in 2006.[11] This section will begin with a detailed discussion of the SSNMR observations for the alkali metal halides. Subsequently, the SSNMR literature will be reviewed for all other relevant systems with separate sections being dedicated towards each element. All data are summarized in Tables 2–21, and selected results are discussed.

4.1. Alkali metal chlorides, bromides and iodides (MCl, MBr, MI)

A significant amount of SSNMR data has been acquired for the alkali metal halide systems, MX (M = Li, Na, K, Rb, Cs; X = Cl, Br, I). As the data for these systems are generally complementary in nature, this section combines the $^{35/37}$Cl, $^{79/81}$Br, and ^{127}I SSNMR observations for all the MX compounds.

TABLE 2 Chlorine-35 solid-state NMR data for chloride salts

Compound	$\delta_{iso}(\pm)$ (ppm)	$C_Q(\pm)$ (MHz)	References (condition)	Additional experiments/comments
NaCl	–	–	Kanda(M)[128]	Kanda's[128] early study reported trend in ^{35}Cl solid-state chemical shifts: TlCl > CsCl > AgCl > NaCl
	–	–	Yamagata(M)[133]	
	–	–	Kanert(S)[348]	
	–	–	Marsh Jr. and Casabella(S)[148]	
	−48[a]	–	Günther and Hultsch[175]	Trend in chemical shifts, relaxation times, and quadrupolar coupling reported by Yamagata[133]
	−46.1[b]	–	Weeding and Veeman(M)[135]	
	−42.0[c]			
	−49.73(0.03)[d]	–	Hayashi and Hayamizu(M)[137]	
	−47.4[e]	–	Lefebvre(M)[136]	Marsh[148] monitored elastic deformation and effect on ^{35}Cl SSNMR spectrum to 6.9 MPa; measurement of the gradient-elastic tensor
	−45.8[c]			
	–	–	Man(S)[347]	
	−44[h]	–	Jelinek et al.(M)[349]	
	–	–	Yamanishi et al.(S),[150,151] Michihiro et al.(S)[152]	
	−49.6[d]	–	Saito et al.(M)[350]	Man[347] performed a ^{37}Cl study of a single crystal to verify the density matrix determined evolution of a spin 3/2 system by a spin echo
	−46(1)[e]	–	Stebbins and Du(M)[190]	
	−46(1)[e]	0	Sandland et al.(M)[191]	Yamanishi et al.[150,151] and Michihiro et al.[152] reported the temperature dependence of T_1 used to determine the activation energy of defect migration

(*continued*)

TABLE 2 (*continued*)

Compound	$\delta_{iso}(\pm)$ (ppm)	$C_Q(\pm)$ (MHz)	References (condition)	Additional experiments/comments
NaCl/cement	–	–	Yun et al.(M)[351]	Signal tentatively assigned to Friedel's salt by Barberon et al.[352]
	~30[g] for solid/adsorbed chloride	–	Barberon et al.(M)[352]	
KCl	–	–	Yamagata(S)[133]	Trend in chemical shifts, relaxation times, and quadrupolar coupling reported by Yamagata[133]
	3.07[b]	–	Weeding and Veeman(S)[135]	
	2.8[c]			
	0[d]	–	Hayashi and Hayamizu(M)[137]	
	3.1[e]	–	Lefebvre(M)[136]	
	3.0[c]			
	0[d]	–	Saito et al.(M)[350]	
AgCl	−7[h]	–	Jelinek et al.(M)[349]	
	−12.82(0.05)[d] (at 294 K)	–	Hayashi and Hayamizu(M)[178]	
	Temperature dependence of chemical shift also reported: $\delta = (-0.054\ \text{ppm K}^{-1})(T/\text{K}) + 2.8$ ppm (over the range 160–320 K)			Yamanishi et al.[150,151], Kanashiro et al.[153] and Michihiro et al.[152] used T_1 temperature dependence to determine the activation energy of defect migration
	–	–	Yamanishi et al.(S)[150,151] Kanashiro et al.(S)[153] Michihiro et al.(S)[152]	
	–25(35)[b]	–	Kanda(M)[128]	
CsCl	110(1)[e]	–	Stebbins and Du(M)[190]	Trend in chemical shifts, relaxation times, and quadrupolar coupling reported by Yamagata[133]
	105.96(0.11)[d]	–	Hayashi and Hayamizu(M)[137]	
	109.4[b]	–	Weeding and Veeman(M)[135]	
	109.6[c]			
	–	–	Yamagata(S)[133]	
	30(35)[b]	–	Kanda(M)[128]	
	110.0[e]	–	Lefebvre(M)[136]	
	108.7[c]			

RbCl	–	–	Yamagata(S)[133]	Trend in chemical shifts, relaxation times, and quadrupolar coupling reported by Yamagata[133]
	–	–	Hackeloer and Kanert(S)[149]	
	44.7[b]	–	Weeding and Veeman(M)[135]	
	44.8[c]			
	41.13(0.09)[d]	–	Hayashi and Hayamizu(M)[137]	Hackeloer and Kanert[149] use gradient-elastic constants determined through monitoring change in spectrum with static elastic stress
	43.2[e]	–	Lefebvre(M)[136]	
	44.0[c]			
LiCl	–	–	Yamagata(S)[133]	Trend in chemical shifts, relaxation times, and quadrupolar coupling reported by Yamagata[133]
	–	–	Hackeloer and Kanert(S)[149]	
	1.31(0.06)[d]	–	Hayashi and Hayamizu(M)[137]	Hackeloer and Kanert[149] use gradient-elastic constants determined through monitoring change in spectrum with static elastic stress
	5.0[e]	–	Lefebvre(M)[136]	
	2.7[c]			
CuCl	–93[a]	–	Günther and Hultsch[175]	
	Chemical shifts measured as a function of temperature	–	Becker(M)[177]	
	−127.23(0.05)[d] (at 294 K) $\delta = (0.092\ \text{ppm K}^{-1})(T/\text{K}) - 154.8$ ppm (over the range 150–400 K)	–	Hayashi and Hayamizu(M)[178]	
	–	–	Kanashiro et al.(M)[353]	

(*continued*)

TABLE 2 (*continued*)

Compound		$\delta_{iso}(\pm)$ (ppm)	$C_Q(\pm)$ (MHz)	References (condition)	Additional experiments/comments
NH_4Cl		–	–	Ueda and Itoh(S)[173], Itoh[172], Ueda[174]	
		74.0[b]	–	Weeding and Veeman(M)[135]	
		73.8[c]			
		73.6[e]	–	Lefebvre(M)[136]	
		72.6[c]			
NH_4Cl	Phase 1	–	–	Itoh and Yamagata(S/M)[172]	
	Phase 2	76(10)[i]			
	Phase 3	–			
$CaCl_2$		–	–	Lefebvre(M)[136]	Second-order quadrupolar lineshape observed under MAS by Saito et al.[350]
		–	–	Saito et al.(M)[350]	
		122(5)[e]	2.1(0.1) ($\eta_Q = 0.7(0.1)$)	Sandland et al.(M)[191]	
tris Sarcosine calcium chloride		14.7(10.0)[b]	4.04(0.03) ($\eta_Q = 0.62(0.02)$)	Bryce et al.(M)[181]	Orientation of EFG tensor reported by Erge et al.[193–195] and Michel et al.[197]
		–	4.10 ($\eta_Q = 0.67$); (room temperature); errors in tensor elements are less than 5% Temperature dependence of ^{35}Cl signal was studied; quadrupolar frequency varies by 0.75 kHz K^{-1} (120–260 K) Paraelectric phase: 4.0 (0.4) ($\eta_Q = 0.65(0.05)$)	Erge et al.(S)[193–195] Michel et al.(S)[197] Engelke et al.(M)[196]	

$CaCl_2 \cdot 2H_2O$	–	–	Lefebvre(M)[136]	Chemical shifts reported by Lefebvre[136] were shown by Bryce et al.[112] to be peak maxima from two parts of second-order quadrupolar powder patterns and not true isotropic shifts
	110.0(2.0)[f]	4.26(0.03) ($\eta_Q = 0.75(0.03)$)	Bryce et al.(M)[112]	
$BaCl_2$	–	–	Lefebvre(M)[136]	
	Site 1: 124(5)[e]	Site 1: 3.5(0.1) ($\eta_Q = 0.15$ (0.05))	Stebbins and Du(M)[190]	
	Site 2: 219(5)[e]	Site 2: 3.95 ($\eta_Q = 0.1$)		
$BaCl_2 \cdot 2H_2O$	–	–	Lefebvre(M)[136]	Chemical shifts reported by Lefebvre[136] were shown by Bryce et al.[112] to be peak maxima from two parts of second-order quadrupolar powder patterns and not true isotropic shifts
	Site 1: 163.4(2.0)[f]	Site 1: 2.19(0.08) ($\eta_Q = 0$)	Bryce et al.(M)[112]	
	Site 2: 156.6(2.0)[f]	Site 2: 3.42(0.08) ($\eta_Q =$ 0.31(0.10))		
VCl_2	–	~4 MHz (two sites) ($\eta_Q = 0$; assumed)	Tabak et al.(M)[354]	Relaxation rates measured as a function of temperature
$AlCl_3$	–	9.4(0.2) ($\eta_Q = 0.40(0.05)$)	Sandland et al.(M)[191]	The reported chemical shift of 2880 ppm appears to be erroneous
$MgCl_2$	–	–	Lefebvre(M)[136]	
$MgCl_2 \cdot 6H_2O$	–	–	Lefebvre(M)[136]	Chemical shifts reported by Lefebvre[136] were shown by Bryce et al.[112] to be peak maxima from two parts of second-order quadrupolar powder patterns and not true isotropic shifts
	75.0(1.0)[f]	3.02(0.05) ($\eta_Q = 0.0$)	Bryce et al.(M)[112]	

(*continued*)

TABLE 2 (*continued*)

Compound	$\delta_{iso}(\pm)$ (ppm)	$C_Q(\pm)$ (MHz)	References (condition)	Additional experiments/comments
$SrCl_2$	140.8[e]	–	Lefebvre(M)[136]	
	188.2(1.0)[f]	~0	Bryce et al.(M)[112]	
$SrCl_2 \cdot 2H_2O$	142.1(1.0)[f]	1.41(0.02) ($\eta_Q = 0.80(0.10)$)	Bryce et al.(M)[112]	
$SrCl_2 \cdot 6H_2O$	–	–	Lefebvre(M)[136]	Chemical shifts reported by Lefebvre[136] were shown by Bryce et. al.[112] to be peak maxima from two parts of second-order quadrupolar powder patterns and not true isotropic shifts
	90.4(1.0)[f]	3.91(0.05) ($\eta_Q = 0$)	Bryce et al.(M)[112]	
$CoCl_2$	–	~5.2	Bragin and Ryabchenko[355]	
$CoCl_2$ in a graphite intercalation compound (GIC)	–	~11.2	Tsuda et al.[356,j]	
$CoCl_2 \cdot 2H_2O$	–	At 76 K (paramagnetic state): 9.866 (0.001) ($\eta_Q = 0.44(0.01)$) At 4 K (antiferromagnetic state): 9.855, 7.767[c]	Narath(S)[357]	Information on EFG orientation also obtained.
$CsNiCl_3$	–	16.698(0.010) ($\eta_Q = 0.387$ (0.0015)) (at 300 K) 16.978(0.012) ($\eta_Q = 0.387$ (0.0015)) (at 300 K) 16.57 ($\eta_Q = 0.472$) (at 1.4 K) 16.51 ($\eta_Q = 0.414$) (at 77 K) 16.30 ($\eta_Q = 0.387$) (at 300 K)	Rinneberg et al.(S)[358] Clark and Moulton(S)[359,360]	Paramagnetic shift tensor components also reported

$CsCoCl_3$	–	14.024(0.0050) ($\eta_Q = 0.4477(0.0005)$) (at 84 K) 13.983(0.0050) ($\eta_Q = 0.4421(0.0005)$) (at 120 K) 13.890(0.0030) ($\eta_Q = 0.4353(0.0005)$) (at 195 K) 13.75850(0.0002) ($\eta_Q = 0.4293(0.0005)$) (at 300 K)	Rinneberg and Hartmann(S)[361]	Paramagnetic shift tensor components also reported
$CsMgCl_3$	–	8.930(0.002) ($\eta_Q = 0.235$ (0.005)) (at 300 K)	Rinneberg and Hartmann(S)[361]	
$CsMnCl_3$	–	Site 1: 10.5290(0.0030) ($\eta_Q = 0.2683(0.0004)$) (at 300 K) Site 2: 18.3670(0.0030) ($\eta_Q = 0.0234(0.0004)$) (at 300 K)	Rinneberg and Hartmann(S)[361]	Paramagnetic shift tensor components also reported
$CsCuCl_3$	–	Site 1: 22.498(0.004) (at 300 K) 22.832(0.016) (at 77 K) ($\eta_Q = 0.389$ (0.0005)) (at 300 K and 77 K) Site 2: 21.402(0.010) (at 300 K) 21.858(0.016) (at 77 K) ($\eta_Q = 0.131$ (0.0005)) (at 300 K and 77 K)	Rinneberg et al.(S)[358]	

(*continued*)

TABLE 2 (*continued*)

Compound	$\delta_{iso}(\pm)$ (ppm)	$C_Q(\pm)$ (MHz)	References (condition)	Additional experiments/comments
$CsNiCl_3$	–	16.57 ($\eta_Q = 0.472$) (at 4.2 K) 16.51 ($\eta_Q = 0.414$) (at 77 K)	Euler et al.(S)[362]	
$RbNiCl_3$	–	15.95(0.004) ($\eta_Q = 0.488$ (0.006)) (at 4.2 K) 15.96(0.004) ($\eta_Q = 0.432$ (0.003)) (at 77 K)	Euler et al.(S)[362]	
$CsNiCl_3$	–	–	Clark and Moulton(S)[359]	
Betaine calcium chloride dihydrate ($(CH_3)_3NCH_2COO{\cdot}CaCl_2.2H_2O$)	–	4.871 ($\eta_Q = 0.882$) (ambient temperature "N phase") Site 1: 5.667 ($\eta_Q = 0.8$) Site 2: 4.875 ($\eta_Q = 0.726$) (38 K low-temperature phase)	Holzer et al.(S)[363]	Very small C_Q values determined from satellite transition frequencies. Tensor orientations also determined from single-crystal study
$Mn(CO)_5Cl$	–	36.07(0.01) ($\eta_Q = 0.050$ (0.005)) (at 303 K)	Spiess and Sheline(S)[269]	Partial EFG tensor orientation information was obtained
$ZnCu_3(OH)_6Cl_2$	–	–	Ofer et al.(M)[364]	Lineshape monitored as a function of temperature
	Shift monitored as a function of temperature	–	Imai et al.(M)[365]	Lineshape also monitored as a function of temperature
$GdCl_3$	–	–	Hessler[366]	
TlCl	251(45)[b]	–	Kanda(M)[128]	Activation energy of Cl vacancy diffusion determined through study of relaxation rates as a function of temperature by Samuelson and Ailion[176]
	250[a]	–	Günther and Hultsch[175]	
	–	–	Samuelson and Ailion[176]	

$CuCl_2 \cdot H_2O$	Paramagnetic	–	($\eta_Q = 0.42(0.07)$)	O'Sullivan(S)[367]	Single crystal study of the paramagnetic state between 5 and 76 K
	Antiferromagnetic				Zero-field measurements of the antiferromagnetic state between 1.3 and 4.2 K
$FeCl_2$		–	4.74(0.01)	Barnes and Segel(S,P)[368]	Jones and Segel studied both the paramagnetic and antiferromagnetic states[369]
		–	Paramagnetic State: 4.74 (0.02)	Jones and Segel(S)[369]	
Several *n*-alkylammonium chlorides	n-$C_5H_{11}NH_3Cl$	–	1.143(0.001) at 315 K	Honda(M)[189]	Temperature dependence of C_Q probed; Even-odd effect noted (see text)
	n-$C_7H_{15}NH_3Cl$		1.401(0.001) at 300 K		
	n-$C_8H_{17}NH_3Cl$		1.501(0.001) at 315 K		
	n-$C_9H_{19}NH_3Cl$		1.303(0.002) at 320 K		
	n-$C_{10}H_{21}NH_3Cl$		1.469(0.001) at 325 K		
	n-$C_7H_{15}ND_3Cl$		1.375(0.001) at 300 K		
	n-$C_9H_{19}ND_3Cl$		1.280(0.002) at 320 K		
	n-$C_{10}H_{21}ND_3Cl$		1.452(0.002) at 325 K		
$C_4H_9NH_3Cl$		–	~1.2–0.85 on heating from 300–480 K ($\eta_Q \approx 0$)	Hattori et al.(P)[188]	
$C_4H_9ND_3Cl$					
$K_2CuCl_4 \cdot 2H_2O$		–	4.2 K: Site 1: 18.98 ($\eta_Q = 0.1883$) Site 2: 3.490 ($\eta_Q = 0.877$) 77 K: Site 1: 19.07 ($\eta_Q = 0.1902$) Site 2: 3.434 ($\eta_Q = 0.895$) 295 K: Site 1: 19.05 ($\eta_Q = 0.183$)	Choh and Stager(S)[370]	

(*continued*)

TABLE 2 (*continued*)

Compound		$\delta_{iso}(\pm)$ (ppm)	$C_Q(\pm)$ (MHz)	References (condition)	Additional experiments/comments
			Site 2: 3.262 ($\eta_Q = 0.945$) 340 K: Site 2: 3.229 ($\eta_Q = 0.970$)		
BaFCl		–	2.38 ($\eta_Q = 0$)	Bastow et al.(M)[371]	
Ag_5Te_2Cl-polymorphs	α-form	−12.9(0.5)[e] (at 356 K)	–	Brinkmann et al.(M)[170]	
	β-form	−8.9[e] (at 296 K)			
	γ-form	−4.8(0.5)[e] (at 216 K)			
K_2IrCl_6		–	–	Brown et al.(S)[372]	Parallel and perpendicular components of the hyperfine shift are determined
K_2ReCl_6		–	–	Brown et al.(S)[372]	Parallel and perpendicular components of the hyperfine shift are determined by Brown et al.[372]
		–	27.66 ($\eta_Q = 0$)	Segel and Barnes[373]	

Within the references column, the condition of the solid-state sample will be denoted accordingly: S = single crystal, P = polycrystalline, M = microcrystalline powder; if the condition of the sample is unknown, it will not be specified.
[a] With respect to saturated NaCl(aq).
[b] With respect to infinitly dilute Cl^-.
[c] Refers to ^{37}Cl value.
[d] With respect to solid KCl.
[e] With respect to 1 M NaCl(aq).
[f] With respect to solid NaCl.
[g] With respect to NaCl(aq), concentration not specified.
[h] With respect to 0.1 M NaCl(aq).
[i] With respect to a dilute solution of alkali chlorides.
[j] Experiment done on five highly oriented pyrolytic graphite based $CoCl_2$-GIC specimens.

TABLE 3 Chlorine-35 solid-state NMR data for sodalites

Compound	$\delta_{iso}(\pm)$ (ppm)	P_Q[a] $(\pm)$ (MHz)	References (condition)	Additional experiments/ comments
$Na_8[Al_6Si_6O_{24}]$ $Cl_x \cdot (e^-)_{2-x}$ sodalite	–	–	Trill et al.(M)[374]	ESR hyperfine coupling constant, $A_0 = 85$ kHz
Mixed Cl/Br sodalites	−125.4(0.2)[b] (5% Cl) −125.2(0.2) (18% Cl) −124.7(0.2) (38% Cl) −124.3(0.2) (56% Cl) −124.1(0.2) (62% Cl) −123.8(0.2) (76% Cl) −123.6(0.2) (90% Cl) −123.2(0.2) (100%Cl)	0.2(0.1) For all Cl percentages from MAS; 55(5) kHz from ^{35}Cl SATRAS spectrum for 100% Cl sodalite	Trill et al.(M)[94]	
Mixed Cl/I sodalites	−128.2(0.3)[b] (5% Cl) −128.7(0.3) (6% Cl) −128.4(0.3) (10% Cl) −124.1(0.3) (22% Cl) −123.7(0.3) (89% Cl) −123.8(0.3) (90% Cl) −123.4(0.3) (97% Cl) −123.2(0.3) (100% Cl) −127.6 and −124.6 (50:50 Cl:I), from 3QMAS	0.2(0.1) for all Cl percentages from MAS	Trill et al.(M)[94]	

(*continued*)

TABLE 3 (*continued*)

Compound	$\delta_{iso}(\pm)$ (ppm)	P_Q[a] ($\pm$) (MHz)	References (condition)	Additional experiments/ comments
$Na_8(Al_6Si_6O_{24})Cl_2$ (sodalite)	−124(1)[b]	–	Stebbins and Du (M)[190]	
Na_8Cl_2–sodalite $Na_8Cl_{0.46}I_{1.54}$–sodalite Ag_8Cl_2–sodalite $Ag_8Cl_{0.46}I_{1.54}$–sodalite	–	–	Jelinek et al. (M)[349]	Peak maxima of −122 (Na_8Cl_2–sodalite), −125 ($Na_8Cl_{0.46}I_{1.54}$–sodalite), −310 (Ag_8Cl_2–sodalite), and −305 ppm ($Ag_8Cl_{0.46}I_{1.54}$–sodalite) (wrt 0.1 M NaCl) are reported for various chloride levels

Within the references column, the condition of the solid-state sample will be denoted accordingly: S = single crystal, P = polycrystalline, M = microcrystalline powder; if the condition of the sample is unknown, it will not be specified.

[a] $P_Q = C_Q(1 + \eta_Q^2/3)^{1/2}$.

[b] With respect to 1M NaCl(aq).

TABLE 4 Chlorine-35 solid-state NMR data for hydrochloride salts

Compound	$\delta_{iso}(\pm)$ (ppm)	$C_Q(\pm)$ (MHz)	References (condition)	Additional experiments/comments
Tyrosine hydrochloride	95(1)[a]	2.3(0.1) ($\eta_Q = 0.7(0.1)$)	Gervais et al.(M)[111]	
	94.7(0.5)[a]	2.23(0.02) ($\eta_Q = 0.72(0.03)$)	Bryce et al.(M)[179,181]	
Glycine hydrochloride	117(1)[a]	6.5(0.1) ($\eta_Q = 0.6(0.1)$)	Gervais et al.(M)[111]	
	101(5)[a]	6.42(0.05) ($\eta_Q = 0.61(0.03)$)	Bryce et al.(M)[179]	
L-Valine hydrochloride	114(1)[a]	6.0(0.1) ($\eta_Q = 0.5(0.1)$)	Gervais et al.(M)[111]	
	90(10)[a]	5.89(0.05) ($\eta_Q = 0.51(0.05)$)	Bryce et al.(M)[179]	
L-Glutamic acid hydrochloride	104(1)[a]	3.7(0.1) ($\eta_Q = 0.6(0.1)$)	Gervais et al.(M)[111]	
	102(1)[a]	3.61(0.01) ($\eta_Q = 0.65(0.02)$)	Bryce et al.(M)[179]	
Quinuclidine hydrochloride	9.7(10.0)[b]	5.25(0.02) ($\eta_Q = 0.05(0.01)$)	Bryce et al.(M)[181]	
L-Ornithine hydrochloride	–	–	Lupulescu et al.(M)[187]	A new method was proposed (RAS) to resolve different ^{35}Cl sites based on relaxation times
L-Lysine hydrochloride	–	–	Lupulescu et al.(M)[187]	A new method was proposed (RAS) to resolve different ^{35}Cl sites based on relaxation times
L-Cysteine ethyl ester hydrochloride	53.2(0.5)[b]	3.78(0.02) ($\eta_Q = 0.03(0.03)$)	Bryce et al.(M)[181]	
L-Cysteine methyl ester hydrochloride	48.2(0.7)[b]	2.37(0.01) ($\eta_Q = 0.81(0.03)$)	Bryce et al.(M)[181]	

(*continued*)

TABLE 4 (*continued*)

Compound	$\delta_{iso}(\pm)$ (ppm)	$C_Q(\pm)$ (MHz)	References (condition)	Additional experiments/comments
Cysteine hydrochloride monohydrate	104.2(0.5)[a]	3.92(0.01) ($\eta_Q = 0.47(0.02)$)	Chapman et al. (M)[182]	
Cocaine hydrochloride	~ 0[a]	5.027 ($\eta_Q = 0.2(0.05)$)	Yesinowski et al.(M)[184]	
L-Lysine hydrochloride	105(2)[a]	2.49(0.01) ($\eta_Q = 0.42(0.02)$)	Bryce et al.(M)[179]	
L-Serine hydrochloride	120(30)[a]	3.0(0.3) ($\eta_Q = 0.8(0.2)$)	Bryce et al.(M)[179]	
L-Proline hydrochloride	37(5)[a]	4.50(0.05) ($\eta_Q = 0.63(0.05)$)	Bryce et al.(M)[179]	
L-Isoleucine hydrochloride	96(20)[a]	4.39(0.05) ($\eta_Q = 0.25(0.03)$)	Bryce et al.(M)[179]	
L-Phenylalanine hydrochloride	96(5)[a]	6.08(0.05) ($\eta_Q = 0.52(0.03)$)	Bryce et al.(M)[179]	
L-Tryptophan hydrochloride	105.0(1.0)[a]	5.05(0.04) ($\eta_Q = 0.86(0.03)$)	Bryce et al.(M)[180]	
DL-Arginine hydrochloride monohydrate	91.5(1.0)[a]	2.035(0.020) ($\eta_Q = 0.98(0.02)$)	Bryce et al.(M)[179,180]	
Alanine hydrochloride	106(5)[a]	6.4(0.1) ($\eta_Q = 0.75(0.06)$)	Chapman et al.(M)[182]	
Aspartic Acid hydrochloride	102(5)[a]	7.1(0.1) ($\eta_Q = 0.42(0.05)$)	Chapman et al.(M)[182]	
Histidine hydrochloride monohydrate	93(1)[a]	4.59(0.03) ($\eta_Q = 0.46(0.02)$)	Chapman et al.(M)[182]	
Methionine hydrochloride	99(1)[a]	4.41 (0.02) ($\eta_Q = 0.35(0.03)$)	Chapman et al. (M)[182]	
Threonine hydrochloride	99(10)[a]	5.4(0.1) ($\eta_Q = 0.94(0.02)$)	Chapman et al.(M)[182]	
Procaine hydrochloride	96(6)[a]	4.87(0.07) ($\eta_Q = 0.28(0.04)$)	Hamaed et al.(M)[183]	
Tetracaine hydrochloride	71(6)[a]	6.00(0.10) ($\eta_Q = 0.27(0.04)$)	Hamaed et al.(M)[183]	

Lidocaine hydrochloride	100(4)[a]	4.67(0.07) ($\eta_Q = 0.77(0.03)$)	Hamaed et al.(M)[183]
Lidocaine hydrochloride polymorph[c]	Site 1: 85(10)[a]	Site 1: 2.52(0.12) ($\eta_Q = 0.95$ (0.05))	Hamaed et al. (M)[183]
	Site 2: 110(10)[a]	Site 2: 5.32(0.10) ($\eta_Q = 0.32(0.10)$)	
Bupivacaine hydrochloride	96(10)[a]	3.66(0.10) ($\eta_Q = 0.72(0.08)$)	Hamaed et al. (M)[183]
Bupivacaine hydrochloride heated to 120 °C	Site 1: 118(10)[a]	Site 1: 4.75(0.20) ($\eta_Q = 0.65$ (0.10))	Hamaed et al. (M)[183]
	Site 2: 95(10)[a]	Site 2: 5.85(0.20) ($\eta_Q = 0.26$ (0.04))	
Bupivacaine hydrochloride heated to 170 °C	118(5)[a]	4.58(0.05) ($\eta_Q = 0.56(0.06)$)	Hamaed et al.(M)[183]

Within the references column, the condition of the solid-state sample will be denoted accordingly: S = single crystal, P = polycrystalline, M = microcrystalline powder; if the condition of the sample is unknown, it will not be specified.

[a] With respect to solid NaCl.

[b] With respect to infinitely dilute NaCl(aq).

[c] See Ref. 183 for details on preparation.

TABLE 5 Chlorine-35 solid-state NMR data for glasses

Compound		$\delta_{iso}(\pm)$ (ppm)	$C_Q(\pm)$ (MHz)	References (condition)	Additional experiments/ comments
Several Cl-containing silicate and aluminosilicate glasses	*Silicates*			Sandland et al. (M)[191]	C_Q was determined with η_Q arbitrarily set to 0.7. Estimated mean values of C_Q could therefore vary by up to 15%.
	NS	−65(5)[a]	3.3(0.1)		
	N2CS	−67(10)[a]	3.0(0.2)		
	CNS	−35(15)[a]	3.2(0.4)		
	C2NS	−20(15)[a]	3.3(0.3)		
	CS	102(22)[a]	4.4(0.4)		
	Aluminosilicates				
	NAS1	−89(11)[a]	3.0(0.3)		
	NAS4	−65(7)[a]	2.9(0.2)		
	CAS1	52(38)[a]	3.5(0.9)		
	CAS3	62(45)[a]	3.6(1.0)		
	CAS4	79(42)[a]	4.0(0.9)		
$Na_2Si_3O_7$ + 5 wt% NaCl		−77(10)[a]	2.4–2.9	Stebbins and Du(M)[190]	(estimated)
$Na_3AlSi_6O_{15}$ + 5 wt% NaCl		–			
$NaAlSi_3O_8$ + 1.5 wt% NaCl		–			
$Cs_2Si_4O_9$ + 5 wt% CsCl		127(10)[a]			
$95Cs_2Si_4O_9 \cdot 5Al_2O_3$ + 5 wt% CsCl		–			
$BaSi_2O_5$ + 5 wt% $BaCl_2$		143(10)[a]			
$Na(CN)_xCl_{1-x}$ glasses		–	–	Elschner and Petersson(M)[375]	

Within the references column, the condition of the solid-state sample will be denoted accordingly: S = single crystal, P = polycrystalline, M = microcrystalline powder; if the condition of the sample is unknown, it will not be specified.

[a] With respect to 1 M NaCl(aq).

TABLE 6 Chlorine-35 solid-state NMR data for simple chlorates and perchlorates

Compound	$\delta_{iso}(\pm)$ (ppm)	$C_Q(\pm)$ (MHz)	References (condition)	Additional experiments/comments
$NaClO_3$	Chemical shifts reported for distinct crystal orientations	–	Kawamori and Itoh (S)[207]	
	–	–	Khasawneh et al. (S)[208]	Frequencies of several single- and multiple-quantum transitions; 17 of 24 possible transitions were observed
		~60 ($\eta_Q = 0$)	Segel and Barnes[373]	
$NaClO_4$	1044.3(0.5)[a]	0.887(0.014) (η_Q = 0.92(0.02))	Skibsted and Jakobsen(M)[202]	$^{35/37}$Cl data are used to assess the ratio of their quadrupole moments
$NaClO_4 \cdot H_2O$	1039.9(0.3)[a]; 1040.1(0.5)[b]	0.566(0.009) ($\eta_Q = 0.90(0.02)$); 0.459(0.012)[b] ($\eta_Q = 0.91(0.04)$)	Skibsted and Jakobsen(M)[202]	^{35}Cl and ^{37}Cl data are used to assess the ratio of their quadrupole moments
NH_4ClO_4	917.5(0.7)[c]	0.6949(0.0005) (η_Q = 0.7552(0.0012))	Bastow and Stuart (S)[376,a]	Orientation of EFG and CS tensors reported by Bastow and Stuart[376]
	–	0.640(0.040) ($\eta_Q = 0.80(0.10)$) at 300 K; ± 50 kHz at 4.2 K Temperature dependence of C_Q studied over the range 4–340 K	Segel et al.(S,M)[377]	

(*continued*)

TABLE 6 (*continued*)

Compound	$\delta_{iso}(\pm)$ (ppm)	$C_Q(\pm)$ (MHz)	References (condition)	Additional experiments/comments
NH_4ClO_4 ND_4ClO_4	930[c]	–	Bastow et al.(M)[376,b]	
(polyethylene glycol)$_x$$NH_4ClO_4$	–	–	Binesh and Bhat (M)[378]	Study of thin films
$LiClO_4$	1034.2(0.5)[c]; 1034.1(0.5)[b]	1.282(0.008); 1.010(0.012)[b] ($\eta_Q = 0.34(0.01)$) (^{35}Cl and ^{37}Cl)	Skibsted and Jakobsen(M)[202]	^{35}Cl and ^{37}Cl data are used to assess the ratio of their quadrupole moments
$LiClO_4 \cdot 3H_2O$	1045.9(0.5)[a]	0.695(0.004) (η_Q = 0.00(0.03))	Skibsted and Jakobsen(M)[202]	^{35}Cl and ^{37}Cl data are used to assess the ratio of their quadrupole moments
$KClO_4$	–	0.51 (at 296 K) ($\eta_Q = 0.52$) Temperature dependence of C_Q measured	Tarasov et al.(M)[201]	Skibsted and Jakobsen[202] use ^{35}Cl and ^{37}Cl data to assess the ratio of their quadrupole moments
	1049.2(0.3)[a]	0.440(0.006) (η_Q = 0.88(0.02))	Skibsted and Jakobsen(M)[202]	
$RbClO_4$	−3(5)[d]	~0.60 ($\eta_Q = 0.53$) Temperature dependence of C_Q monitored	Tarasov et al.(M)[201]	
	1049.4(0.3)[a]; 1049.1(0.3)[b]	0.537(0.015) ($\eta_Q = 0.87(0.03)$); 0.424(0.014)[b] ($\eta_Q = 0.86(0.02)$)	Skibsted and Jakobsen(M)[202]	Skibsted and Jakobsen[202] use ^{35}Cl and ^{37}Cl data to assess the ratio of their quadrupole moments

$CsClO_4$	–	~0.63 ($\eta_Q = 0.55$) Temperature dependence of C_Q and η_Q determined	Tarasov et al.(M)[200]	Skibsted and Jakobsen[202] use ^{35}Cl and ^{37}Cl data to assess the ratio of their quadrupole moments
	1047.7(0.3)[a]	0.585(0.008) ($\eta_Q = 0.86(0.02)$)	Skibsted and Jakobsen(M)[202]	
$Mg(ClO_4)_2$	1036.2(0.5)[a]	2.981(0.007) ($\eta_Q = 0.57(0.01)$)	Skibsted and Jakobsen(M)[202]	^{35}Cl and ^{37}Cl data are used to assess the ratio of their quadrupole moments
$Mg(ClO_4)_2 \cdot 6H_2O$	Site 1: 1046.6(0.3)[a] 1046.6(0.3)[b]	Site 1: 0.309(0.006) ($\eta_Q = 0.00$ (0.08)); 0.245(0.005)[b] ($\eta_Q =$ 0.00(0.10))	Skibsted and Jakobsen(M)[202]	^{35}Cl and ^{37}Cl data are used to assess the ratio of their quadrupole moments
	Site 2: 1045.5(0.3)[a] 1045.5(0.3)[b]	Site 2: 0.475(0.008) ($\eta_Q = 0.00$ (0.05)); 0.375(0.003)[b] ($\eta_Q = 0.00(0.07)$)		
$Ba(ClO_4)_2$	1029.6(0.5)[a]	2.256(0.008) ($\eta_Q = 0.58(0.01)$)	Skibsted and Jakobsen(M)[202]	^{35}Cl and ^{37}Cl data are used to assess the ratio of their quadrupole moments
$Ba(ClO_4)_2 \cdot 3H_2O$	1040.6(0.3)[a]; 1040.5(0.5)[b]	0.383(0.005) ($\eta_Q = 0.00(0.03)$); 0.299(0.004)[b] ($\eta_Q = 0.01$ (0.03))[b]	Skibsted and Jakobsen(M)[202]	^{35}Cl and ^{37}Cl data are used to assess the ratio of their quadrupole moments
$Cd(ClO_4)_2 \cdot 6H_2O$	1044.4(0.3)[a]	0.328(0.005) ($\eta_Q = 0.00(0.03)$)	Skibsted and Jakobsen(M)[202]	^{35}Cl and ^{37}Cl data are used to assess the ratio of their quadrupole moments

(*continued*)

TABLE 6 (*continued*)

Compound	$\delta_{iso}(\pm)$ (ppm)	$C_Q(\pm)$ (MHz)	References (condition)	Additional experiments/comments
$(CH_3)_4NClO_4$	1049.3(0.3)[a]	0.307(0.004) ($\eta_Q = 0.00(0.03)$)	Skibsted and Jakobsen(M)[202]	^{35}Cl and ^{37}Cl data are used to assess the ratio of their quadrupole moments
$[C_4H_8NH_2]ClO_4$ $[C_4H_8ND_2]ClO_4$	–	–	Ono et al.(M)[379]	Narrow spectra indicated rotation of the perchlorate anion at 315 and 400 K
Trimethylammonium perchlorate	–	0.370 (phase III; 303–355 K) (η_Q varies between 0.60 and 1); 0.318 (phase II; 400–460 K)	Jurga et al.(M)[198]	
Dimethylammonium perchlorate	1003[e] (phase I)	1.120 ($\eta_Q = 0$) (phase III); 0.238 ($\eta_Q = 0$) (phase II)	Jurga et al.(M)[198]	
Monomethylammonium perchlorate	–	1.016 ($\eta_Q = 0.75$) (phase III); 0.258 ($\eta_Q = 0$) (phase II)	Jurga et al.(M)[198]	
[2-CNPyH][ClO_4]	–	–	Czupiński et al. (M)[171]	Temperature dependant phase change monitored
Piperidinium perchlorate ($[C_5H_{10}NH_2]ClO_4$)	–	–	Ono et al.(M)[380]	Solid-solid phase transitions were investigated

Within the references column, the condition of the solid-state sample will be denoted accordingly: S = single crystal, P = polycrystalline, M = microcrystalline powder; if the condition of the sample is unknown, it will not be specified.

[a] With respect to solid NaCl.
[b] Refers to ^{37}Cl value.
[c] With respect to solid NH_4Cl.
[d] With respect to 0.1M $RbClO_4$(aq).
[e] With respect to solid KCl.

TABLE 7 Chlorine-35 solid-state NMR data for other compounds

Compound	$\delta_{iso}(\pm)$ (ppm)	$C_Q(\pm)$ (MHz)	References (condition)	Additional experiments/comments
bis(4-chlorophenyl)sulphone ($(ClC_6H_4)_2SO_2$)	–	68.7 ($\eta_Q = 0.1(0.03)$)	Taye et al.(S)[381–384]	Orientation of EFG tensor in crystal axis system determined
$Li_{0.48}(THF)_{0.3}HfNCl$	–	–	Tou et al.(M)[385]	Zero Knight shift; temperature dependence of shift measured from 4–150 K
$[Al_4(HPO_4)_4(C_2H_5OH)_{12}]Cl_4 \cdot 4\text{-}C_2H_5OH$	76(5)[a]	5.86(0.05) ($\eta_Q = 0.96$ (0.035))	Azaïs et al.(M)[386]	
$[Al_2(HC_6H_5PO_2)_2(C_4H_9OH)_8]Cl_4$	76(5)[a]	7.0(0.15) ($\eta_Q = 0.95$ (0.05))	Azaïs et al.(M)[386]	Two crystallographic sites are simulated with one set of parameters
$[Al_3(\mu_2\text{-}OH)(\mu_3\text{-}C_6H_5PO_3)_2(C_2H_5OH)_{10}]Cl_4 \cdot H_2O$	Site 1 (Cl2): 76[a]; Site 2 (Cl1 and Cl4): 70[a]; Site 3 (Cl3): 50[a]	Site 1 (Cl2): 5.8(0.15) ($\eta_Q = 0.96(0.04)$); Site 2 (Cl1 and Cl4): 7.0(0.15) ($\eta_Q = 0.96(0.04)$); Site 3 (Cl3): 7.8(0.15) ($\eta_Q = 0.96(0.04)$)	Azaïs et al.(M)[386]	Four crystallographic sites are simulated with three sets of parameters
$LiAl_2(OH)_6ClO_4 \cdot nH_2O$	997.2[b] (at 0% R.H.) 998.8[b] (at 11% R.H.) 997.8[b] (at 51% R.H.) ~999.3[b] (at 75% and 84% R.H.)	0.7 (and $\eta_Q = 0.1$) at 0% R.H.	Hou and Kirkpatrick(M)[387]	Spectra recorded at several relative humidities (R.H.)
$Mg_3Al(OH)_6ClO_4 \cdot nH_2O$	1001.2[b] (at 0% R.H.)		Hou and Kirkpatrick(M)[387]	Spectra recorded at several relative humidities (R.H.)

(*continued*)

TABLE 7 (*continued*)

Compound	$\delta_{iso}(\pm)$ (ppm)	$C_Q(\pm)$ (MHz)	References (condition)	Additional experiments/comments
$LiAl_2(OH)_6Cl{\cdot}nH_2O$ (''LiAlCl5''; ''LiAlCl6''; ''LiAlCl8'')	9.3[b] (at 0% R.H.) 5.3 (at room humidity and temperature, from static spectrum) 11 (at room humidity and temperature, from MAS)	0.9 ($\eta_Q = 0$) (at room humidity and temperature, from MAS)	Hou et al.(M)[388,389]	Spectra recorded at several relative humidities (R.H.) and temperatures
Coal A	−49.6[c]	–	Saito et al.(M)[350]	Peak assigned to NaCl(s)
$(CH_3)_4NCdCl_3$	–	Phase I (296 K): 13.48 ($\eta_Q = 0.16$) Phase I (120 K): 13.64 ($\eta_Q = 0.13$) Phase II (115 K, 3 sites): 14.98 ($\eta_Q = 0.12$) 14.02 ($\eta_Q = 0.22$) 12.64 ($\eta_Q = 0.27$) Phase III (98 K, 9 sites): 15.18 14.72 14.68 13.98 13.90 13.86 13.52 13.30	Mulla-Osman et al. (S)[390–392]	Data are in agreement with NQR results reported in the same paper Phase transitions investigated by ^{35}Cl NMR

		13.04		
$Sr_2CuO_2Cl_2$	–	–	Suh et al.(S)[393,394]	
$YBa_2Cu_3O_{6.7}Cl_{0.2}$ (Cl-doped YBCO)	–	~2 ($\eta_Q = 1$)	Goren et al.(M)[395]	
hydrotalcite	–	~2.4 ($\eta_Q \approx 1$) (at −97 °C) ~1.5 ($\eta_Q \approx 0$) (at −40 °C) ~1.2 (at room temperature)	Kirkpatrick et al. (M)[396]	Spectra recorded at several temperatures
hydrocalumite	30(5)[d] (at 10–130 °C) 26(5)[d] (<0 °C)	2.87 ($\eta_Q \approx 0$) (at 10 °C) 2.22 ($\eta_Q \approx 0$) (at 130 °C) 3.0 ($\eta_Q = 0.9$) (<0 °C)	Kirkpatrick et al. (M)[396]	Spectra recorded at several relative humidities (R.H.) and temperatures
$CH_3NH_3GeCl_3$	–	~25 (low *T*); approaching zero at 500 K	Yamada et al. (M)[397,398]	^{35}Cl NMR used to confirm disordered perovskite structure ^{35}Cl NMR signal could be detected above 364 K
Cl-doped yttrium ceramics (YBCO-Cl)	Three resonances are observed and assigned to ''three definite positions in the lattice''	Three sites: 1.2 1.4 1.9	Amitin et al.(M)[399]	

(*continued*)

TABLE 7 (*continued*)

Compound	$\delta_{iso}(\pm)$ (ppm)	$C_Q(\pm)$ (MHz)	References (condition)	Additional experiments/comments
$Rb_2Mn_{1-x}Cr_xCl_4$	–	–	Kubo et al.(S)[400,401]	
$(C_3H_7NH_3)_2MnCl_4$	–	–	Muralt et al.(S)[402]	Phase transitions studied
Calcium chloroapatite	–	0.8	Yesinowski and Eckert(M)[184,403]	
ClF_5	–	–	Weulersse et al. (M)[404]	
p-Dichlorobenzene	–	73.96 ($\eta_Q = 0.0712$ (0.0005))	Creel et al.(S)[209]	
Several alkylchlorosilanes	–	–	Kreshkov et al.(M)[405]	
$Ca_{4.99–5.06}(PO_4)_{2.98–3.00}F_{0.51–0.48}Cl_{0.38–0.36}OH_{0.14–0.12}$	~115[b]	~1.6	McCubbin et al. (M)[406]	$^{19}F\{^{35}Cl\}$ TRAPDOR spectrum also collected
$(C_nH_{2n+1}NH_3)_2CuCl_4$ (n= 1~4)	–	–	Kubo et al.(S)[407]	1.75 K zero field experiments also done
$(CH_3)_2CHNH_3CuCl_3$	–	Site 1: 19.5 ($\eta_Q = 0.68$) Site 2: 25.17 ($\eta_Q = 0.5$) Site 3: 21.05 ($\eta_Q = 0.58$)	Saito et al.(S)[408]	Field induced magnetic ordering monitored

Within the references column, the condition of the solid-state sample will be denoted accordingly: S = single crystal, P = polycrystalline, M = microcrystalline powder; if the condition of the sample is unknown, it will not be specified.

[a] With respect to solid NaCl.

[b] With respect to 1M NaCl(aq).

[c] With respect to solid KCl.

[d] No chemical shift reference given.

TABLE 8 Chlorine chemical shift tensor data[f]

Compound	Herzfeld–Berger convention	Haeberlen convention	Standard convention	Euler angles(°)	References
tris Sarcosine $CaCl_2$	$\delta_{iso} = 14.7 \pm 10.0$ ppm[a]; $\Omega < 150$ ppm	$\delta_{iso} = 14.7 \pm 10.0$	–	–	Bryce et al.[181]
$LiAl_2(OH)_6ClO_4 \cdot nH_2O$ Spectra recorded at several relative humidities (R.H.)	$\delta_{iso} = 997.7$[b]; $\Omega = 32$; $\kappa = -1$ at 0% R.H. from static spectrum; $\delta_{iso} = 997.2$ at 0% R.H. from MAS;	$\delta_{iso} = 997.7$; $\Delta\delta = 32$; $\eta = 0$ at 0% R.H. from static spectrum; $\delta_{iso} = 997.2$ at 0% R.H. from MAS;	$\delta_{11} = 1019$; $\delta_{22} = \delta_{33} = 987$ at 0% R.H.; $\delta_{11} = 1007$; $\delta_{22} = \delta_{33} = 994$ at 11% R.H.	–	Hou and Kirkpatrick[387]
	$\delta_{iso} = 998.3$; $\Omega = 13$; $\kappa = -1$ at 11% R.H. from static spectrum; $\delta_{iso} = 998.7$ at 11% R.H. from MAS;	$\delta_{iso} = 998.3$; $\Delta\delta = 13$; $\eta = 0$ at 11% R.H. from static spectrum; $\delta_{iso} = 998.7$ at 11% R.H. from MAS;	$\delta_{11} = 1004$ $\delta_{22} = \delta_{33} = 995$ at 51% R.H.		
	$\delta_{iso} = 998$; $\Omega = 9$; $\kappa = -1$ at 51% R.H. from static spectrum; $\delta_{iso} = 997.8$ at 51% R.H. from MAS	$\delta_{iso} = 998$; $\Delta\delta = 9$; $\eta = 0$ at 51% R.H. from static spectrum; $\delta_{iso} = 997.8$ at 51% R.H. from MAS			

(*continued*)

TABLE 8 (*continued*)

Compound	Herzfeld–Berger convention	Haeberlen convention	Standard convention	Euler angles(°)	References
$Mg_3Al(OH)_6ClO_4 \cdot nH_2O$ Spectra recorded at several relative humidities (R.H.)	$\delta_{iso} = 1002$[b]; $\Omega = 15$; $\kappa = -1$ at 0% R.H. from static spectrum; $\delta_{iso} = 1001.2$ at 0% R.H. from MAS	$\delta_{iso} = 1002$; $\Delta\delta = 15$; $\eta = 0$ at 0% R.H. from static spectrum; $\delta_{iso} = 1001.2$ at 0% R.H. from MAS	$\delta_{11} = 1012$; $\delta_{22} = \delta_{33} = 997$ at 0% R.H.		Hou and Kirkpatrick[387]
$LiAl_2(OH)_6Cl \cdot nH_2O$ (''LiAlCl5''; ''LiAlCl6''; ''LiAlCl8'') Spectra recorded at several relative humidities (R.H.) and temperatures	$\delta_{iso} = 9.3$[b]; $\Omega = 104$; $\kappa = 1$ at 0% R.H. from static spectrum; $\delta_{iso} = 5.3$; $\Omega = -161$; $\kappa = 1$ at room humidity and temperature from static spectrum; $\delta_{iso} = 11$ at room humidity and temperature from MAS	$\delta_{iso} = 9.3$; $\Delta\delta = -104$; $\eta = 0$ at 0% R.H. from static spectrum; $\delta_{iso} = 5.3$; $\Delta\delta = -161$; $\eta = 0$ at room humidity and temperature from static spectrum; $\delta_{iso} = 11$ at room humidity and temperature from MAS	$\delta_{11} = \delta_{22} = 44$; $\delta_{33} = -60$ at 0% R.H. $\delta_{11} = \delta_{22} = 59$ $\delta_{33} = -102$ at room humidity and temperature	–	Hou et al.[388,389]
L-Cysteine ethyl ester hydrochloride	$\delta_{iso} = 53.2 \pm 0.5$[a]; $\Omega = 47 \pm 4$; $\kappa = -0.8 \pm 0.2$	$\delta_{iso} = 53.2 \pm 0.5$; $\Delta\delta = 44.7$; $\eta = 0.158$	$\delta_{11} = 70.4$; $\delta_{22} = 65.7$; $\delta_{33} = 23.4$	–	Bryce et al.[181]

L-Tyrosine hydrochloride	$\delta_{iso} = 49.3 \pm 0.5$[a]; $\Omega < 150$	–	–	–	Bryce et al.[181]
L-Cysteine methyl ester hydrochloride	$\delta_{iso} = 48.2 \pm 0.7$[a]; $\Omega = 45 \pm 15$	–	–	–	Bryce et al.[181]
Quinuclidine hydrochloride	$\delta_{iso} = 9.7 \pm 10.0$[a]; $\Omega = 50 \pm 20$	–	–	–	Bryce et al.[181]
p-Dichlorobenzene	$\delta_{iso} = 666.7$[c]; $\Omega = 4000$; $\kappa = -0.5$ (assuming the PAS of the EFG and CS tensors are coincident)	$\delta_{iso} = 666.7$; $\Delta\delta = 3500$; $\eta = 0.429$ (assuming the PAS of the EFG and CS tensors are coincident)	$\delta_{11} = 3000 \pm 1000$; $\delta_{22} = 0 \pm 1000$; $\delta_{33} = -1000 \pm 1000$ (assuming the PAS of the EFG and CS tensors are coincident)	–	Creel et al.[209]
$NaClO_3$	$\Omega = 40 \pm 7$	–	–	–	Kawamori and Itoh[207]
Alanine hydrochloride	$\delta_{iso} = 106 \pm 5$[d]; $\Omega = 60 \pm 30$; $\kappa = -0.3 \pm 0.5$	$\delta_{iso} = 106 \pm 5$; $\Delta\delta = 49.5$; $\eta = 0.636$	$\delta_{11} = 139$; $\delta_{22} = 100$; $\delta_{33} = 79$	$\alpha = 90 \pm 15$ $\beta = 0 \pm 15$ $\gamma = 0 \pm 15$	Chapman et al.[182]
Aspartic acid hydrochloride	$\delta_{iso} = 102 \pm 5$[d]; $\Omega = 75 \pm 30$; $\kappa = -0.9 \pm 0.1$	$\delta_{iso} = 102 \pm 5$; $\Delta\delta = 73.1$; $\eta = 0.077$	$\delta_{11} = 150.8$; $\delta_{22} = 79.5$; $\delta_{33} = 75.8$	$\alpha = 0 \pm 20$ $\beta = 30 \pm 20$ $\gamma = 93 \pm 20$	Chapman et al.[182]
Cysteine hydrochloride monohydrate	$\delta_{iso} = 104.2 \pm 0.5$[d]; $\Omega = 66 \pm 10$; $\kappa = 0.12 \pm 0.12$	$\delta_{iso} = 104.2 \pm 0.5$; $\Delta\delta = -51.5$; $\eta = 0.846$	$\delta_{11} = 135.9$; $\delta_{22} = 106.8$; $\delta_{33} = 69.9$	$\alpha = 155 \pm 20$ $\beta = 0 \pm 10$ $\gamma = 0 \pm 20$	Chapman et al.[182]
Histidine hydrochloride monohydrate	$\delta_{iso} = 93 \pm 1$[d]; $\Omega < 150$	$\delta_{iso} = 93 \pm 1$	–	–	Chapman et al.[182]
Methionine hydrochloride	$\delta_{iso} = 99 \pm 1$[d]; $\Omega = 100 \pm 20$; $\kappa = 0.3 \pm 0.3$	$\delta_{iso} = 99 \pm 1$; $\Delta\delta = -82.5$; $\eta = 0.636$	$\delta_{11} = 144$; $\delta_{22} = 109$; $\delta_{33} = 44$	$\alpha = 93 \pm 20$ $\beta = 163 \pm 15$ $\gamma = 7 \pm 20$	Chapman et al.[182]

(*continued*)

TABLE 8 (*continued*)

Compound	Herzfeld–Berger convention	Haeberlen convention	Standard convention	Euler angles(°)	References
Threonine hydrochloride	$\delta_{iso} = 99 \pm 10$[d]; $\Omega = 95 \pm 40$; $\kappa = -0.2 \pm 0.5$	$\delta_{iso} = 99 \pm 10$; $\Delta\delta = 76.0$; $\eta = 0.75$	$\delta_{11} = 149.7$; $\delta_{22} = 92.7$; $\delta_{33} = 54.7$	$\alpha = 95 \pm 15$ $\beta = 0 \pm 10$ $\gamma = 0 \pm 15$	Chapman et al.[182]
L-Tryptophan hydrochloride	$\delta_{iso} = 105.0 \pm 1.0$[d]; $\Omega = 72 \pm 5$; $\kappa = 0.10 \pm 0.10$	$\delta_{iso} = 105.0 \pm 1.0$; $\Delta\delta = -55.8$; $\eta = 0.871$	$\delta_{11} = 139.8$; $\delta_{22} = 107.4$; $\delta_{33} = 67.8$	$\alpha = 90 \pm 15$ $\beta = 20 \pm 15$ $\gamma = 2 \pm 20$	Bryce et al.[180]
DL-Arginine hydrochloride monohydrate	$\delta_{iso} = 91.5 \pm 1.0$[d]; $\Omega = 57.5 \pm 3.0$; $\kappa = 0.27 \pm 0.10$	$\delta_{iso} = 91.5 \pm 1.0$; $\Delta\delta = -47.0$; $\eta = 0.670$	$\delta_{11} = 117.7$; $\delta_{22} = 96.7$; $\delta_{33} = 60.2$	$\alpha = 85 \pm 15$ $\beta = 77.5 \pm 12.0$ $\gamma = 30 \pm 30$	Bryce et al.[180]
$MgCl_2 \cdot 6H_2O$	$\delta_{iso} = 75.0 \pm 1.0$[d]; $\Omega < 75$	$\delta_{iso} = 75.0 \pm 1.0$			Bryce et al.[112]
$CaCl_2 \cdot 2H_2O$	$\delta_{iso} = 110.0 \pm 2.0$[d]; $\Omega = 72 \pm 15$; $\kappa = 0.60 \pm 0.2$	$\delta_{iso} = 110.0 \pm 2.0$; $\Delta\delta = -64.8$; $\eta = 0.33$	$\delta_{11} = 138.8$; $\delta_{22} = 124.4$; $\delta_{33} = 66.8$	$\alpha = 90 \pm 10$ $\beta = 82 \pm 5$ $\gamma = 0 \pm 20$	Bryce et al.[112]
$SrCl_2$	$\delta_{iso} = 188.2 \pm 1.0$[d]; $\Omega = 0$	$\delta_{iso} = 188.2 \pm 1.0$;	$\delta_{11} = 188.2$; $\delta_{22} = 188.2$; $\delta_{33} = 188.2$		Bryce et al.[112]
$SrCl_2 \cdot 2H_2O$	$\delta_{iso} = 142.1 \pm 1.0$[d]; $\Omega = 41 \pm 10$; $\kappa = 0.5 \pm 0.2$	$\delta_{iso} = 142.1 \pm 1.0$; $\Delta\delta = -35.9$; $\eta = 0.429$	$\delta_{11} = 159.2$; $\delta_{22} = 148.9$; $\delta_{33} = 118.1$	$\alpha = 86 \pm 15$ $\beta = 75 \pm 5$ $\gamma = 37 \pm 10$	Bryce et al.[112]
$SrCl_2 \cdot 6H_2O$	$\delta_{iso} = 90.4 \pm 1.0$[d]; $\Omega = 45 \pm 20$; $\kappa = -1.0$	$\delta_{iso} = 90.4 \pm 1.0$; $\Delta\delta = 45$; $\eta = 4.737$	$\delta_{11} = 120.4$; $\delta_{22} = 75.4$; $\delta_{33} = 75.4$	$\alpha = 0 \pm 10$ $\beta = 90 \pm 10$ $\gamma = 0 \pm 10$	Bryce et al.[112]
$BaCl_2 \cdot 2H_2O$	Site 1: $\delta_{iso} = 163.4 \pm 2.0$[d]; $\Omega = 50 \pm 25$; $\kappa = -0.8 \pm 0.2$	Site 1: $\delta_{iso} = 163.4 \pm 2.0$; $\Delta\delta = 38.5$; $\eta = 0.896$	Site 1: $\delta_{11} = 189.1$; $\delta_{22} = 162.1$; $\delta_{33} = 139.1$	Site 1: $\alpha = 85 \pm 20$ $\beta = 32 \pm 10$ $\gamma = 60 \pm 20$	Bryce et al.[112]

	Site 2: $\delta_{iso} = 156.6 \pm 2.0$[d]; $\Omega = 50 \pm 25$; $\kappa = 0.20 \pm 0.25$	Site 2: $\delta_{iso} = 156.6 \pm 2.0$; $\Delta\delta = -40$; $\eta = 0.750$	Site 2: $\delta_{11} = 179.9$; $\delta_{22} = 159.9$; $\delta_{33} = 129.9$	Site 2: $\alpha = 20 \pm 15$ $\beta = 8 \pm 10$ $\gamma = 0 \pm 20$	
Procaine hydrochloride	$\delta_{iso} = 96 \pm 6$[d]; $\Omega = 125 \pm 25$; $\kappa = -0.4 \pm 0.3$	$\delta_{iso} = 96 \pm 6$; $\Delta\delta = 106.3$; $\eta = 0.529$	$\delta_{11} = 166.8$; $\delta_{22} = 79.3$; $\delta_{33} = 41.8$	$\alpha = 95 \pm 15$ $\beta = 3 \pm 2$ $\gamma = 32 \pm 8$	Hamaed et al.[183]
Tetracaine hydrochloride	$\delta_{iso} = 71 \pm 6$[d]; $\Omega = 80 \pm 25$; $\kappa = 0.4 \pm 0.3$	$\delta_{iso} = 71 \pm 6$; $\Delta\delta = 68$; $\eta = 0.529$	$\delta_{11} = 106.5$; $\delta_{22} = 81.6$; $\delta_{33} = 25.6$	$\alpha = 60 \pm 8$ $\beta = 8 \pm 5$ $\gamma = 10 \pm 10$	Hamaed et al.[183]
Lidocaine hydrochloride	$\delta_{iso} = 100 \pm 4$[d]; $\Omega = 110 \pm 25$; $\kappa = -0.85 \pm 0.3$	$\delta_{iso} = 100 \pm 4$; $\Delta\delta = 105.9$; $\eta = 0.117$	$\delta_{11} = 170.6$; $\delta_{22} = 68.8$; $\delta_{33} = 60.6$	$\alpha = 12 \pm 3$ $\beta = 40 \pm 10$ $\gamma = 80 \pm 3$	Hamaed et al.[183]
Lidocaine hydrochloride polymorph[e]	Site 1: $\delta_{iso} = 85 \pm 10$[d]; $\Omega = 20 \pm 10$; $\kappa = -0.8 \pm 0.2$	Site 1: $\delta_{iso} = 85 \pm 10$; $\Delta\delta = 19$; $\eta = 0.158$	Site 1: $\delta_{11} = 97.7$; $\delta_{22} = 79.7$; $\delta_{33} = 77.7$	Site 1: $\alpha = 90 \pm 40$ $\beta = 50 \pm 50$ $\gamma = 60 \pm 40$	Hamaed et al.[183]
	Site 2: $\delta_{iso} = 110 \pm 10$[d]; $\Omega = 45 \pm 10$; $\kappa = 0.8 \pm 0.2$	Site 2: $\delta_{iso} = 110 \pm 10$; $\Delta\delta = -42.8$; $\eta = 0.158$	Site 2: $\delta_{11} = 126.5$; $\delta_{22} = 122$; $\delta_{33} = 81.5$	Site 2: $\alpha = 5 \pm 5$ $\beta = 50 \pm 15$ $\gamma = 40 \pm 40$	
Bupivacaine hydrochloride	$\delta_{iso} = 96 \pm 10$[d]; $\Omega = 100 \pm 25$; $\kappa = 0.2 \pm 0.4$	$\delta_{iso} = 96 \pm 10$; $\Delta\delta = -80$; $\eta = 0.750$	$\delta_{11} = 142.7$; $\delta_{22} = 102.7$; $\delta_{33} = 42.7$	$\alpha = 105 \pm 20$ $\beta = 90 \pm 5$ $\gamma = 5 \pm 5$	Hamaed et al.[183]
Bupivacaine hydrochloride heated to 120 °C	Site 1: $\delta_{iso} = 118 \pm 10$[d]; $\Omega = 160 \pm 40$; $\kappa = 0.9 \pm 1.0$	Site 1: $\delta_{iso} = 118 \pm 10$; $\Delta\delta = -156$; $\eta = 0.077$	Site 1: $\delta_{11} = 174$; $\delta_{22} = 166$; $\delta_{33} = 14$	Site 1: $\alpha = 10 \pm 10$ $\beta = 3 \pm 1$ $\gamma = 0 \pm 2$	Hamaed et al.[183]

(*continued*)

TABLE 8 (*continued*)

Compound	Herzfeld–Berger convention	Haeberlen convention	Standard convention	Euler angles(°)	References
	Site 2: $\delta_{iso} = 95 \pm 10$[d]; $\Omega = 160 \pm 40$; $\kappa = -0.2 \pm 1.0$	Site 2: $\delta_{iso} = 95 \pm 10$; $\Delta\delta = 128$; $\eta = 0.750$	Site 2: $\delta_{11} = 180.3$; $\delta_{22} = 84.3$; $\delta_{33} = 20.3$	Site 2: $\alpha = 18 \pm 4$ $\beta = 50 \pm 5$ $\gamma = 80 \pm 5$	
Bupivacaine hydrochloride heated to 170 °C	$\delta_{iso} = 118 \pm 5$[d]; $\Omega = 120 \pm 10$; $\kappa = 0.8 \pm 1.0$	$\delta_{iso} = 118 \pm 5$[d]; $\Delta\delta = 114$; $\eta = 0.157$	$\delta_{11} = 162$; $\delta_{22} = 150$; $\delta_{33} = 42$	$\alpha = 10 \pm 10$ $\beta = 0 \pm 2$ $\gamma = 50 \pm 50$	Hamaed et al.[183]
L-Lysine hydrochloride	$\delta_{iso} = 105 \pm 2$[d]; $\Omega = 26 \pm 10$; $\kappa = -0.4 \pm 0.4$	$\delta_{iso} = 105 \pm 2$; $\Delta\delta = -22.1$; $\eta = 0.529$	$\delta_{11} = 119.7$; $\delta_{22} = 101.5$; $\delta_{33} = 93.7$	$\alpha = 0 \pm 20$ $\beta = 52 \pm 20$ $\gamma = 0 \pm 20$	Bryce et al.[179]
L-Serine hydrochloride	$\delta_{iso} = 120 \pm 30$[d]; $\Omega < 150$				Bryce et al.[179]
L-Glutamic acid hydrochloride	$\delta_{iso} = 102 \pm 1$[d]; $\Omega = 66 \pm 15$; $\kappa = 0.0 \pm 0.3$	$\delta_{iso} = 102 \pm 1$; $\Delta\delta = -49.5$; $\eta = 1$	$\delta_{11} = 135$; $\delta_{22} = 102$; $\delta_{33} = 69$	$\alpha = 9 \pm 20$ $\beta = 77 \pm 20$ $\gamma = 6 \pm 20$	Bryce et al.[179]
L-Proline hydrochloride	$\delta_{iso} = 37 \pm 5$[d]; $\Omega = 63 \pm 5$; $\kappa = -0.54 \pm 0.08$	$\delta_{iso} = 37 \pm 5$; $\Delta\delta = 55.8$; $\eta = 0.390$	$\delta_{11} = 74.2$; $\delta_{22} = 25.7$; $\delta_{33} = 11.2$	$\alpha = 48 \pm 20$ $\beta = 69 \pm 20$ $\gamma = 9 \pm 20$	Bryce et al.[179]
L-Isoleucine hydrochloride	$\delta_{iso} = 96 \pm 20$[d]; $\Omega = 75 \pm 30$; $\kappa < 0.85$	$\delta_{iso} = 96 \pm 20$		$\alpha = 20 \pm 20$ $\beta = 12 \pm 20$ $\gamma = 0 \pm 20$	Bryce et al.[179]
L-Valine hydrochloride	$\delta_{iso} = 90 \pm 10$[d]; $\Omega = 125 \pm 40$; $\kappa = 0.35 \pm 0.5$	$\delta_{iso} = 90 \pm 10$; $\Delta\delta = -104.7$; $\eta = 0.580$	$\delta_{11} = 145.2$; $\delta_{22} = 104.6$; $\delta_{33} = 20.2$	$\alpha = 65 \pm 20$ $\beta = 0 \pm 20$ $\gamma = 0 \pm 20$	Bryce et al.[179]

L-Phenylalanine hydrochloride	$\delta_{iso} = 96 \pm 5$[d];	$\delta_{iso} = 96 \pm 5$;	$\delta_{11} = 154.9$;	$\alpha = 91 \pm 20$	Bryce et al.[179]
	$\Omega = 129 \pm 20$;	$\Delta\delta = -105.1$;	$\delta_{22} = 107.2$;	$\beta = 13 \pm 20$	
	$\kappa = 0.26 \pm 0.25$	$\eta = 0.681$	$\delta_{33} = 25.9$	$\gamma = 10 \pm 20$	
Glycine hydrochloride	$\delta_{iso} = 101 \pm 5$[d];	$\delta_{iso} = 101 \pm 5$;	$\delta_{11} = 146$;	$\alpha = 95 \pm 20$	Bryce et al.[179]
	$\Omega = 100 \pm 20$;	$\Delta\delta = -82.5$;	$\delta_{22} = 111$;	$\beta = 0 \pm 20$	
	$\kappa = 0.3 \pm 0.3$	$\eta = 0.636$	$\delta_{33} = 46$	$\gamma = 0 \pm 20$	

[a] Respect to infinitely dilute NaCl(aq).
[b] With respect to 1M NaCl(aq).
[c] CS reference not given.
[d] With respect to solid NaCl.
[e] See reference 183 for details on preparation.
[f] All CS tensor magnitude values reported in columns 2–4 of this table are in units of ppm, excepting κ and η, which are unitless. All errors are specified immediately following the measured value, if applicable, as done in Tables 2–7.

TABLE 9 Bromine-79/81 solid-state NMR data for simple bromide salts[a]

Compound	$\delta_{iso}(\pm)$ (ppm)	$C_Q(\pm)$ (MHz)	References (condition)	Additional experiments/comments
LiBr	90(25)[b]	–	Kanda(M)[128]	Ngai(M). Temp. dep. of $\delta(^{81}Br)$ over $T = \sim 298–673$ K: $\Delta\delta_{iso}/\Delta T = 1.16$ ppm/K[147]
	93[c]	–	Yamagata(S)[133]	
	109(9)[d,e]	–	Gauß et al.(M)[39]	
	64.74(0.12)[e,f]	–	Hayashi and Hayamizu(M)[137]	
NaBr	–35(20)[b]	–	Kanda(S)[128]	Marsh and Casabella(S). Elastic deformation and effect on ^{79}Br SSNMR spectrum to $p = 6.9$ MPa; measurement of gradient-elastic tensor[148]
	–58(30)[b,e]	–	Bloembergen and Sorokin(M)[131]	
	–24[d]	–	Yamagata(S)[133]	
	–30(10)[e,g]	–	Günther and Hultsch[175]	
	–6(5)[d,e]	–	Gauß et al.(M)[39]	
	–40[e,f]	–	Frye and Maciel (S/M)[146]	Ngai(M). Temp. dep. of $\delta(^{81}Br)$ over $T = \sim 298–553$ K: $\Delta\delta_{iso}/\Delta T = 0.83$ ppm/K[147]
	–52.89(0.08)[e,f]	–	Hayashi and Hayamizu(M)[137]	Campbell and Mackey(P). $NaBr{\cdot}2H_2O$ dehydration observed using $^{79/81}Br$ NMR[410]
	–7[h]	–	Jelinek et al.(M)[349]	Yamanishi et al., Kanashiro et al.(S). Temp. Dep. Of $T_1(^{79/81}Br)$ from $T = 77–700$ K and theoretical interpretation[150–153]
KBr	20(15)[b]	–	Kanda(M)[128]	Otsuka and Kawamura(S). ^{79}Br NMR signal intensity and linewidth as functions of: (i) linear or (ii) circular compression[158]

	22(30)[e,i]	–	Bloembergen and Sorokin(M)[131]	Bonera and Galimberti(S). Phase-dependence of quadrupolar echoes in ^{81}Br NMR.[411]
	27[j]	–	Yamagata(S)[133]	Ngai(M). Temp. dep. of $\delta(^{81}\mathrm{Br})$ over $T = \sim$298–653 K: $\Delta\delta_{iso}/\Delta T = 0.87$ ppm/K[147]
	20(10)[e,g]	–	Günther and Hultsch[175]	Memory and Mathur(S). $^{79/81}$Br SSNMR using FT techniques[412]
	47(2)[d,e]	–	Gauß et al.(M)[39]	Frye and Maciel(S/M). Use full ^{79}Br signal under MAS to set magic-angle; CT linewidth at $\nu_{rot} = 4$ kHz is 70 Hz[146]
	0[e,f]	–	Hayashi and Hayamizu(M)[137]	Hashi et al., Ijima et al.(M) $^{79/81}$Br MAS NMR signal of KBr used to test the field homogeneity of a 30 T hybrid magnet[413–416]
RbBr	105[k]	–	Itoh and Yamagata(S)[41]	Baron(M). $\delta(^{81}\mathrm{Br})$ vs. p; lines of best fit ($\delta_0 = \delta$ at ambient p):
	105[k]	–	Yamagata (S)[133]	NaCl phase ($p <$ 451 MPa): $\delta/\mathrm{ppm} = \delta_0/\mathrm{ppm} + (0.073\ \mathrm{ppm/MPa})(p/\mathrm{MPa})$
	118(3)[d,e]	–	Gauß et al.(M)[39]	CsCl phase (451 MPa $< p <$ 980 MPa): $\delta/\mathrm{ppm} = (\delta_0 + 68)/\mathrm{ppm} + (0.032\ \mathrm{ppm/MPa})(p/\mathrm{MPa})$[42]
	71.66(0.15)[e,f]	–	Hayashi and Hayamizu(M)[137]	Ngai(M). Temp. dep. of $\delta(^{81}\mathrm{Br})$ over $T = \sim$298–553 K: $\Delta\delta_{iso}/\Delta T = 0.75$ ppm/K[147]

(*continued*)

TABLE 9 (*continued*)

Compound	$\delta_{iso}(\pm)$ (ppm)	$C_Q(\pm)$ (MHz)	References (condition)	Additional experiments/comments
CsBr	250(40)[e,l]	–	Bloembergen and Sorokin(S)[131]	Baron(M). $\delta(^{81}Br)$ vs. p; line of best fit ($\delta_0 = \delta$ at ambient p):
	284[m]	–	Yamagata(S)[133]	CsCl phase (p< 980 MPa): δ/ppm = δ_0/ppm + (0.040 ppm/MPa) (p/MPa)[42]
	275(3)[d,e]	–	Gauß et al.(M)[39]	
	227.43(0.08)[e,f]	–	Hayashi and Hayamizu(M)[137]	Ngai(M). Temp. dep. of $\delta(^{81}Br)$ over T = ~298–723 K: $\Delta\delta_{iso}/\Delta T$ = 0.66 ppm/K[147]
AgBr	189(15)[b]	–	Kanda(S)[128]	Höhne(S). ^{79}Br signal intensity and dislocation density as functions of: (i) doping, (ii) plastic deformation, (iii) both (i) and (ii); effects of (i)–(iii) as functions of temperature and time[216]
				Conti et al.(P). ^{81}Br NMR signal intensity as a function of sample aging[417,418]
				Conti(M). Calculations correlating ^{81}Br SSNMR linewidth at high temps. with Br^- vacancy motion[419]
				Zumbulyadis and Marchetti(M). Effect of microcrystal size and pressure on ^{79}Br NMR signal intensity; failed to observe the ^{79}Br signal of $AgBr_xCl_{1-x}$[420]
	169.35(0.07)[e,f]	–	Hayashi and Hayamizu (M)[178]	Hayashi and Hayamizu(M). Temp. dep. of $\delta(^{79}Br)$ over T = 160–320 K:

		208[h]	–	Jelinek et al.(M)[349]	$\delta = (-0.118\ \text{ppm/K})(T/\text{K}) + 203.9$ ppm[178] Yamanishi et al., Kanashiro et al., Michihiro et al.(S). Temp. Dep. Of $T_1(^{79/81}\text{Br})$ from $T = 77$–700 K; theoretical interpretation; calculation of Ag^+ diffusion activation energy[150–153]
TlBr		620(50)[b]	–	Kanda(M)[128]	Saito(S). Comments on $^{79/81}$Br NMR linewidth narrowing in $^{79/81}$Br–$^{203/205}$Tl double-resonance experiments[218] Saito(S). Experimental and theoretical study on spin–spin interactions[219] Ngai(M). Temp. dep. of $\delta(^{81}\text{Br})$ over $T = \sim$453–693 K: $\Delta\delta_{iso}/\Delta T = 1.0$ ppm/K[147]
NH_4Br	Phase II	233(10)[n]	–	Itoh and Yamagata (S/M)[172,212]	Phase labels according to Itoh and Yamagata; ^{79}Br and ^{81}Br NMR signals are observed
	Phase I	132(10)[n]	–		
	Phase III	–	5.5(0.3)		Ueda. ^{81}Br SSNMR linewidth in ND_4Br with respect to temp[174]
		–	5.656(0.01)	Jeffrey et al.(S)[213]	
CuBr		–116(10)[e,g]	–	Günther and Hultsch (M)[175]	Herzog and Richtering(M). Studied $^{79/81}$Br linewidth vs. temp[220] Becker(M). $\delta(^{81}\text{Br})$ vs. temp. from $T = 123$–823 K[177]

(*continued*)

TABLE 9 (*continued*)

Compound	$\delta_{iso}(\pm)$ (ppm)	$C_Q(\pm)$ (MHz)	References (condition)	Additional experiments/comments
				Hayashi and Hayamizu(M). Temp. dep. of $\delta(^{79}Br)$ over $T = 160$–290 K: $\delta = (0.165\ ppm/K)(T/K) - 183.0$ ppm; over $T = 290$–340 K: $\delta = (0.235\ ppm/K)(T/K) - 203.7$ ppm[178]
	–134.14(0.2)[e,f]	–	Hayashi and Hayamizu(M)[178,223]	Kanashiro et al.(M). Temp. Dep. Of $T_1(^{79}Br)$ from $T = 77$–700 K[353]
$BaBr_2$	–	–	Potrepka et al.(M)[421]	$^{79/81}Br$ NMR signals observed; fine structure not resolved; after deoxygenated $YBa_2Cu_3O_y$ is brominated, $BaBr_2$ precipitates result

[a] Unless denoted otherwise, parameters correspond to ^{81}Br measurements at room temperature; within the references column, the condition of the solid-state sample will be denoted accordingly: S = single crystal, P = polycrystalline, M = microcrystalline powder; if the condition of the sample is unknown, it will not be specified.
[b] With respect to NaBr(*aq*).
[c] With respect to dilute LiBr(*aq*)
[d] With respect to dilute NaBr(*aq*).
[e] Denotes a measurement corresponding to the ^{79}Br nuclide.
[f] With respect to KBr(*s*).
[g] With respect to saturated NaBr(*aq*).
[h] With respect to 0.1 M NaBr(*aq*).
[i] With respect to KBr(*aq*).
[j] With respect to dilute KBr(*aq*).
[l] With respect to dilute RbBr(*aq*).
[k] With respect to CsBr(*aq*).
[m] With respect to dilute CsBr(*aq*).
[n] With respect to a dilute aqueous alkali bromide solution.

TABLE 10 Bromine-79/81 solid-state NMR data for the addition of impurities into simple inorganic bromide salts[a]

Principal component	Impurity	maximum doping (mol %)	Temp.dep.[b] T_1	Temp.dep.[b] $S_0/\Delta v$	References (condition)
AgBr	$CdBr_2$	0.1*†	Y	Y	Reif(P)[162]
	NaBr, LiBr, CuBr	0.1*†	N	N	Seifert(P)[214]
	$CaBr_2$, $PbBr_2$, $CdBr_2$	0.06*†	N	Y	
	Ag_2S, Ag_2Se	0.03*†	N	Y	
	Ag_2O	0.04	N	Y	Kluge(P)[215]
	AgCl[c]	~1.3*	N	Y	Fukai(P)[236]
	NaBr	0.5†	N	Y	Höhne(S)[216]
	$FeBr_2$, $CoBr_2$, $NiBr_2$	0.06†	N	Y	Höhne[217]
	CuBr, $CuBr/CdBr_2$, $CdBr_2$	0.1*	N	Y	Kluge(P)[238]
	$CdBr_2$, $MgBr_2$, CuBr, LiBr, NaBr, KBr, RbBr, CsBr, $CuBr/CdBr_2$, $CuBr_2/NaBr$	0.5–1.0*	Y	Y	Becker and Richtering(P)[228]
	$CdBr_2$, CuBr, TlBr, $MgBr_2$	0.005–0.2*	Y	Y	Becker et al.[422]
	$CdBr_2$, $PbBr_2$, $NiBr_2$, $IrBr_3$, $AuBr_3$	0.1†	Y	N	Zumbulyadis and Marchetti (S/M)[420]
LiBr	$MgBr_2$	0.2*	N	Y	Reif(P)[162]
	$MgBr_2$, CuBr	0.01*	N	Y	Becker et al.[422]
NaBr	NaCl[c]	~1.6*	N	N	Fukai(P)[236]
	NaCl[d]	~0.2†	N	N	Andersson(S)[231]
	NaCl	0.1–0.4*†	N	N	Andersson(S)[232]
	Cl^-[e]	0.2*†	N	N	Taki & Satoh(S)[237]

(*continued*)

TABLE 10 (*continued*)

Principal component	Impurity	maximum doping (mol %)	Temp.dep.[b] T_1	Temp.dep.[b] $S_0/\Delta v$	References (condition)
KBr	NaBr	1.87*†	N	N	Otsuka & Kawamura(S)[158]
		1.0*	N	N	Ohlsen & Melich(S)[164]
	KCl	4.66*†	N	N	Andersson & Ödberg(S/P)[227]
	KCl, KI, NaBr, RbBr[c]	0.4	N	N	Andersson(S)[225,226]
	KI[d]	∼0.2†	N	N	Andersson(S)[231]
	RbBr, KOH	0.1–0.4*†	N	N	Andersson(S)[232]
	Cl^-, Na^+, I^-	0.1	N	N	Andersson & Forslind(S)[224]
	KCl[c]	∼1.7*	N	N	Fukai(P)[236]
CuBr	$CdBr_2$	0.002*†	N	Y	Becker et al.(P)[221]

[a] Unless denoted otherwise, measurements were carried out at room temperature. Within the references column, the condition of the solid state sample is denoted accordingly: S = single crystal, P = polycrystalline, M = microcrystalline powder; if the condition of the sample is unknown, it will not be specified. Under the column entitled "doping," the symbols * and † will denote that ^{81}Br and ^{79}Br NMR measurements were carried out, respectively. If the nuclide studied is unknown, it will not be specified.

[b] These two columns disclose if the spin-lattice relaxation and signal intensity (or linewidth) of the doped sample was studied as a function of temperature.

[c] Study to determine gradient-elastic tensor.

[d] Study determined chemical shift effect upon doping.

[e] Nuclear double resonance experiment (with ^{23}Na) at $T = 77$ K.

TABLE 11 Bromine-79/81 solid-state spin-lattice relaxation (T_1) values for simple inorganic systems[h]

Compound		Temp (K)	Field (T)	$T_1(^{81}Br)$ (ms)	$T_1(^{79}Br)$ (ms)	References (condition)
LiBr[a,b]		rt	0.622	34	28	Kanda(M)[128]
NaBr[b]		rt	~1.1	71 ± 7	50 ± 5	Wikner et al.(S)[139]
KBr		rt	~1.1	103 ± 10[c]	72 ± 7[d]	Wikner et al.(S)[139]
		rt	~2.05	96 ± 0.6	67.1 ± 0.7	Halstead et al.(S)[143]
RbBr[e]		rt	–	160	–	Itoh and Yamagata(S)[41]
		rt	~1.1	100 ± 50	65 ± 40	Wikner et al.(S)[139]
		rt	~0.67	100 ± 20	60 ± 5	Niemelä and Tuohi(S)[156]
CsBr		rt	~0.56	105 ± 20	–	Bloembergen and Sorokin(S)[131]
		rt	~1.1	115 ± 12	80 ± 8	Wikner et al.(S)[139]
AgBr		rt	0.622	22	16	Kanda(S)[128]
TlBr		rt	0.622	9.2	6.0	Kanda(M)[128]
CuBr[f,g]		rt	0.934	2.9	2.3	Günther and Hultsch(M)[175]
NH_4Br	Phase I	431	–	33.0	–	Itoh and Yamagama(M/S).[172,212]
	Phase II	377	–	0.245	–	Ueda studied temperature and
		327	–	0.121	–	pressure dependencies of $T_1(^{81}Br)$
		285	–	0.059	–	in ND_4Br up to 0.6 MPa and over $230 < T < 290$ K[174]

[a] Weber and Allen studied the temperature-dependence of $^{79/81}Br$ T_1 ($55\ K < T < 425\ K$) in a single-crystal.[140–142]
[b] Tarr et al. studied the temperature-dependence of $^{79/81}Br$ T_1 ($15\ K < T < 77.3\ K$) in a single-crystal.[155]
[c] $T_1(ms) = (-0.0026\ ms/K^2)(T^2/K^2) + 326/ms$, over the range $T = 195–298$ K.
[d] $T_1(ms) = (-0.0019\ ms/K^2)(T^2/K^2) + 237/ms$, over the range $T = 195–298$ K.
[e] Niemelä and Tuohi studied the temperature-dependence of $^{79/81}Br$ T_1 ($20\ K < T < 300\ K$) in a single-crystal.[156]
[f] Becker et al. studied the temperature-dependence of ^{79}Br T_1 ($223 < T < 393$ K) in a polycrystalline sample.[221]
[g] Andrew et al. studied the temperature-dependence of ^{81}Br T_1 ($78\ K < T < 300\ K$) in a polycrystalline sample.[154]
[h] Within the references column, the condition of the solid state sample is denoted accordingly: S = single crystal, P = polycrystalline, M = microcrystalline powder; if the condition of the sample is unknown, it will not be specified.

TABLE 12 Bromine-79/81 solid-state NMR data for perbromates[a]

Compound	$\delta_{iso}(\pm)$ (ppm)	$C_Q(\pm)$ (MHz)	$\eta_Q(\pm)$	References (condition)	Additional experiments/ comments
$KBrO_4$	–	3.35(0.03)	0.71(0.05)	Tarasov et al.(P)[423]	T= 297 K
$RbBrO_4$	–	2.36(0.04)	0.37	Tarasov et al.(P)[423]	T= 297; VT ^{81}Br NMR experiments conducted from T= 190–300 K
$CsBrO_4$	2400(200)[b]	1.32(0.04) 1.53(0.06)†	0	Tarasov et al.(M)[244]	Tarasov et al. perform $^{79/81}$Br VT NMR experiments[245,423]
NH_4BrO_4	2440(120) 2500(130)†	2.27(0.05) 2.72(0.05)†	0.99	Tarasov et al.(M)[424]	
	–	2.38(0.03)	0.91	Tarasov et al.(P)[423]	T= 297; VT ^{81}Br NMR experiments conducted from T= 180–300 K

[a] Unless noted otherwise, the table denotes ^{81}Br parameters and measurements were taken at room temperature. A dagger (†) will denote a measurement corresponding to the ^{79}Br nuclide. Within the references column, the condition of the solid state sample is denoted accordingly: S = single crystal, P = polycrystalline, M = microcrystalline powder; if the condition of the sample is unknown, it will not be specified.

[b] With respect to 1 M KBr (aq).

TABLE 13 Bromine-81 solid-state NMR data for sodalite systems[a]

Compound		$\delta_{iso}(\pm)$ (ppm)	$P_Q(\pm)$ (MHz)	References (condition)	Additional experiments/ comments
''Mixed Cl/Br sodalites'':	n	–[b]		Trill et al.(M)[94]	MAS and SATRAS experiments; chemical shift trend can be fit to a linear function with respect to the sodium–halogen bond distance
$Na_8[Al_6Si_6O_{24}](Cl_n/Br_{1-n})_2$	0	–220.6(0.4)	0.7(0.2)		
	0.05	–220.8(0.4)	0.3(0.2)		
	0.18	–220.5(0.4)	0.4(0.2)		
	0.38	–219.4(0.4)	0.4(0.2)		
	0.56	–218.6(0.4)	0.4(0.2)		
	0.62	–218.3(0.4)	0.4(0.2)		
	0.76	–217.7(0.4)	0.3(0.2)		
	0.90	–217.3(0.4)	0.3(0.2)		
''Mixed Br/I sodalites'':	n	–[b]		Trill et al.(M)[94]	MAS and SATRAS experiments; chemical shift trend can be fit to a linear function with respect to the sodium–halogen bond distance
$Na_8[Al_6Si_6O_{24}](Br_n/I_{1-n})_2$	0.06	–226.4(0.4)	0.7(0.2)		
	0.25	–225.0(0.4)	1.0(0.2)		
	0.46	–223.7(0.4)	0.9(0.2)		
	0.65	–223.0(0.4)	0.8(0.2)		
	0.77	–222.1(0.4)	0.8(0.2)		
	0.86	–222.0(0.4)	0.3(0.2)		
	0.91	–221.6(0.4)	0.4(0.2)		
	1	–220.6(0.4)	0.7(0.2)		
$Na_8[Al_6Si_6O_{24}]Br_n \cdot$	n	–[b]		Trill et al.(M)[425]	Observed a linear relationship (−86 ppm $Å^{-1}$) between the crystalline lattice constant and $\delta(^{81}Br)$
$(H_3O_2)_{2-n}$	0.98	–221.0	0.5		
	0.78	–220.8	0.6		
	0.67	–220.4	0.6		
	0.61	–219.9	0.7		
	0.45	–219.6	0.8		

(*continued*)

TABLE 13 (*continued*)

Compound		$\delta_{iso}(\pm)$ (ppm)	$P_Q(\pm)$ (MHz)	References (condition)	Additional experiments/ comments
	0.36	–219.2	0.7		
	0.10	–218.0	0.6		
$Na_{6+n}[Al_6Si_6O_{24}]$	n	–[b]		Trill et al.(M)[425]	See comment for
$Br_n \cdot (4H_2O)_{2-n}$	0.98	–221.0	0.5		$Na_8[Al_6Si_6O_{24}]$
	0.78	–221.2	0.5		$Br_n \cdot (H_3O_2)_{2-n}$
	0.67	–221.8	0.7		
	0.61	–223.3	1.1		
	0.45	–225.4	1.5		
	0.36	–227.1	1.7		
	0.10	–230.6	2.2		
$Na_{6+n}[Al_6Si_6O_{24}]$	n	–[b]		Trill et al.(M)[425]	See comment for
$Br_n \cdot \phi_{2-n}(\phi =$ empty	0.98	–221.0	0.5		$Na_8[Al_6Si_6O_{24}]$
sodalite cage)	0.78	–222.4	0.6		$Br_n \cdot (H_3O_2)_{2-n}$
	0.67	–224.4	0.9		
	0.61	–226.4	1.0		
	0.45	–229.5	0.9		
	0.36	–233.3	0.9		
	0.10	–237.8	0.8		
$Na_{8-n-p}Ag_nBr_{2-p}-$	A	214[c]	–	Jelinek et al.	Various n and p values
$Si_6Al_6O_{12}$	B	–219	–	(M)[349]	are studied; sites A, B
	C	–550	–		and C are assigned to AgBr, Na_4Br and Ag_4Br clusters within the sodalite, respectively

[a] The parameters are for ^{81}Br under MAS conditions. Within the references column, the condition of the solid state sample is denoted accordingly: S = single crystal, P = polycrystalline, M = microcrystalline powder; if the condition of the sample is unknown, it will not be specified.
[b] With respect to 1 M NaBr(*aq*).
[c] With respect to 0.1 M NaBr(aq).

TABLE 14 Bromine-81 solid-state NMR data for other inorganic systems[a]

Compound		δ_{iso} (ppm)	C_Q(MHz)	η_Q	References (condition)	Additional experiments/ comments
$K_2Pt(CN)_4Br_{0.3}\cdot 3.2\ H_2O$	Site 1	–	17.6	0	Brenni et al.(S)[242] Brinkmann et al.(S)[241]	Temperature dependence of QI was studied over range 24 $< T <$ 295 K; $C_Q(^{81}Br)$ is found to increase as temp. is decreased
	Site 2	–	15.1	0		Preliminary accounts exist[239,240]
β-Ag_3SBr		–	0	–	Huber et al.(M)[426–428]	$C_Q = 0$ due to Br point symmetry in β phase; temperature and pressure dependence of phase transition (β to γ) studied
BaFBr:O (2%)		–	10.00	0	Bastow et al.(M)[371]	Oxygen doping appears to have little effect on the long range crystalline order
n{HBr}–Na_{56}(zeolite-Y)		–	–	–	Jelinek et al.(M)[349]	Broad (ca. 100 kHz) MAS linewidth is observed

[a] Unless noted otherwise, the table denotes ^{81}Br parameters and measurements were taken at room temperature. Within the references column, the condition of the solid state sample is denoted accordingly: S = single crystal, P = polycrystalline, M = microcrystalline powder; if the condition of the sample is unknown, it will not be specified.

TABLE 15 Bromine-81 solid-state NMR data for other systems[c]

Compound	$\delta_{iso}(\pm)$ (ppm)	$C_Q(\pm)$ (MHz)	$\eta_Q(\pm)$	References (condition)	Additional experiments/comments
C_n-DABCO-C_n-Br_2 (n= 10, 12, 14)[a]	3660[†b]	–	–	Nakayama et al.[429]	Lineshapes and widths amongst series are similar; temperature dependence of $T_1(^{79}Br)$ determined; high-temperature phase only; shift measured at T= 363 K
tris -Sarcosine $CaBr_2$	–	21.9	0.64	Erge et al.(S)[195]	Errors in tensor elements <5%; orientation of EFG tensor PAS determined
	–	–	–	Michel et al.(S)[197]	Temp. dep. of $T_1(^{81}Br)$ studied from T= 128–310 K; onset of partial molecular reorientation is observed at ca. 170 K
Deuterated glycyl-L-alanine $HBr \cdot H_2O$	–	19.750	0.8328	Kehrer et al.(S)[430]	Orientation of EFG tensor determined: V_{ZZ} oriented ca. along shortest H···Br hydrogen bond
L-Leucine hydrobromide	–	49.0[†]	0.59[†]	Persons and Harbison[103]	STREAQI method. CSA not included in fit
L-Tyrosine hydrobromide	–	11.26[†]	0.86[†]	Persons and Harbison[103]	STREAQI method. CSA not included in fit

[a] DABCO = 1,4-diazoniabicyclo[2.2.2]octane.
[b] With respect to NaBr(s).
[c] Unless noted otherwise, the table denotes ^{81}Br parameters and measurements were taken at room temperature. Within the references column, the condition of the solid state sample is denoted accordingly: S = single crystal, P = polycrystalline, M = microcrystalline powder; if the condition of the sample is unknown, it will not be specified.
[†] Represents a measurement corresponding to the ^{79}Br nuclide.

TABLE 16 Bromine-79/81 solid-state NMR data for molecular systems (mainly from Zeeman-perturbed NQR measurements)

Compound	Site labels	C_Q (MHz)[a]	η_Q	References	Additional experiments/ comments
Br_2		756†	0.2 ± 0.02	Kojima et al.[246]	$T = 253$ K
		639.05	''small''	Ege and Negita[307]	$T = 77$ K, polycrystalline sample
$NaBrO_3$		357.8†	0.001 ± 0.001	Bucci et al.[252]	Fusaro and Doane. First known example of bromine CSA: $\delta_{\parallel} = 2620(20)$ ppm; $\delta_{\perp} = 2710(30)$ ppm[313]
					Segel et al.(M). $\delta_{\perp}(^{81}Br) = 2400$ ppm and is temp. indep[312]
					Ege and Negita(P); $T = 77$ K[307]
$KBrO_3$		–	–		Segel et al.(M) $\delta_{\perp}(^{81}Br) = 2400$ ppm and is temp. indep[312]
$KIBr_2 \cdot H_2O$	α	248.34	0.005 ± 0.003	Okuda et al.[282]	$T = 300$ K; labels according to Okuda et al.
	β	256.77	0.034 ± 0.011		
$Mg(BrO_3)_2 \cdot 6H_2O$		352.13†	0.05†	Ramaprabhu and R. Rao[305]	
$Sr(BrO_3)_2 \cdot H_2O$		350.65†	0.07†	Valli and R. Rao[304]	$T = 305$ K
$Ba(BrO_3)_2 \cdot H_2O$		347.15†	0.02†	Valli and R. Rao[304]	$T = 305$ K
BBr_3		339†	0.45 ± 0.05	Chiba[290]	$T = 77$ K; fine structure (~ 24 kHz splitting) is attributed to different isotopomers
		283			
		346.71†	0.26†	Ege and Negita[307]	$T = 77$ K; polycrystalline sample
$Mn(CO)_5Br$		226.7	0.06	Spiess and Sheline[269]	Results are preliminary
		256.8†			
$Ni(BrO_3)_2 \cdot 6H_2O$		354.30†	0.05†	Ramaprabhu and R. Rao[305]	
$CuBr(PPh_3)_2$		105.91 ± 0.02	0.519 ± 0.003	Okuda et al.[291]	
$Cu_2Br_2(PPh_3)_3$	1	82.38	0.997	Negita et al.[286]	Labels according to Negita et al.
	2	86.06	0.987		

(*continued*)

TABLE 16 (*continued*)

Compound	Site labels	C_Q (MHz)[a]	η_Q	References	Additional experiments/ comments
$Zn(BrO_3)_2 \cdot 6H_2O$		353.63†	0.04†	Ramaprabhu and R. Rao[305]	
$ZnBr_2py_2$		–	–	Hiura[293]	py = pyridine; only zero-splitting cone and EFG tensor orientation are reported
$ZnBr_2(4\text{-Me-py})_2$		–	~0.02–0.05	Hiura[293]	py = pyridine
$Cd(BrO_3)_2 \cdot 2H_2O$		349†	0.04†	Valli and R. Rao[285]	$T = 301$ K
	1	349.24†	0.05†	Valli and R. Rao[303]	$T = 305$ K; resolves two sites; calculations highlight inadequacy of point-charge model at calculating the EFG
	2	348.79†	0.02†		
$AlBr_3$	1	189.21†	0.248 ± 0.008†	Okuda et al.[266]	A study on a polycrystalline sample obtains: $\eta_1 = 0.26 \pm 0.02$, η_2 = not obs., $\eta_3 = 0.15 \pm 0.03$.[294]
	2	221.12†	0.073 ± 0.011†		
	3	223.68†	0.106 ± 0.009†		
α-$InBr_3$		167.79	0.387 ± 0.005	Okuda et al.[274]	Low temperature form
β-$InBr_3$	1	168.33	0.362 ± 0.002	Okuda et al.[274]	Labels according to Okuda et al. High temperature form
	2	167.99	0.400 ± 0.007		
$(NH_4)_2InBr_5 \cdot H_2O$	A	146.158 ± 0.01	0.0256 ± 0.020	Yamada et al.[297]	Labels according to Yamada et al.; $T = 303$ K
	B	141.508 ± 0.01	0.0126 ± 0.020		
	C	140.156 ± 0.01	0.1335 ± 0.040		
	D	136.237 ± 0.01	0.1051 ± 0.020		
$SnBr_4$		–	<0.025	Shimomura[248]	Data support the presence of a phase change around $T = 295$ K
$N_3P_3Br_6$		–	<0.01	Ahmad and Porte[289]	Polycrystalline sample

Cs_2CdBr_4—I	1	131.5 157.4†	0.09 ± 0.02	Boguslavskii et al.[306]	Labels according to Boguslavskii et al; polycrystalline sample; anhydrous phase; sites 4 and 5 could not be resolved
	2	119.1 142.5†	0.16 ± 0.03		
	3	114.4 136.9†	0.16 ± 0.03		
Cs_2CdBr_4—II	2	124.5 149.0†	0.15 ± 0.03	Boguslavskii et al.[306]	Labels according to Boguslavskii et al.; polycrystalline sample; surface hydrated phase; sites 1 and 4 could not be resolved
	3	123.2 147.4†	0.07 ± 0.02		
	5	85.4 102.0†	0.25 ± 0.05		
$AsBr_3$		–	0.04 ± 0.02	Shimomura[249]	$T = 283$ K
$TiBr_4$	Cubic-1	77.397	0.020 ± 0.015	Okuda et al.[268]	Labels according to Okuda et al.
	2	78.732	0.025 ± 0.015		
	Monoclinic-1	78.323	0.012 ± 0.010		
	2	78.297	0.046 ± 0.006		
	3	78.850	0.021 ± 0.003		
	4	79.524	0.035 ± 0.006		
α-$SbBr_3$	1	270.01	0.068 ± 0.002	Okuda et al.[267]	Labels according to Okuda et al.
	2	270.53	0.049 ± 0.002		
	3	280.40	0.080 ± 0.004		
$BiBr_3$	1	205.01 ± 0.01	0.077	Furukawa[277]	Labels according to Furukawa
	2	225.39 ± 0.01	0.424		
	3	240.17 ± 0.01	0.152		
$TeBr_4$	1	370.22	0.045 ± 0.003	Okuda et al.[276]	
	2	375.34	<0.05		
	3	375.50	0.044 ± 0.002		
	4	381.74	0.036 ± 0.003		
	5	390.71	0.015 ± 0.005		
	6	394.63	0.027 ± 0.002		

(*continued*)

TABLE 16 (*continued*)

Compound	Site labels	C_Q (MHz)[a]	η_Q	References	Additional experiments/ comments
$PBr_3 \cdot BBr_3$	1	299.48	0.151 ± 0.004	Terao et al.[296]	Labels according to Terao et al.; sites 1, 2 belong to BBr_3; 3,4 to PBr_3; signal intensity (1,2,3,4) is in ratio (1:2:2:1)
	2	302.63	0.120 ± 0.007		
	3	425.01	0.025 ± 0.005		
	4	426.41	0.020 ± 0.004		
$AlBr_3 \cdot SbBr_3$	1	146.5	0.534	Okuda et al.[278,283]	Labels according to Okuda et al. Sites 1–4 are assigned to $[AlBr_4]^-$; sites 5–6 to $[SbBr_2]^+$
	2	152.5	0.477		
	3	161.3	0.307		
	4	164.8	0.141		
	5	287.2	0.024		
	6	300.0	0.011		
$AlBr_3 \cdot BiBr_3$	1	150.3	0.204	Okuda et al.[278,283]	Labels according to Okuda et al. Sites 1–4 are assingned to $[AlBr_4]^-$, site 5 bridges 2 Bi atoms and site 6 is terminally bound to Bi
	2	137.2	0.868		
	3	155.0	0.526		
	4	163.0	0.426		
	5	182.0	0.539		
	6	296.6	0.027		
$AlBr_3 \cdot H_2S$		163.20	0.081 ± 0.008	Okuda et al.[284]	
$AlBr_3 \cdot POBr_3$	a	157.39	0.019 ± 0.007	Okuda et al.[284]	Labels according to Okuda et al; site ''a'' belongs to $AlBr_3$
	b	422.09	0.026 ± 0.006		
$AlBr_3 \cdot KBr$	a	152.60	0.031 ± 0.003	Okuda et al.[284]	Labels according to Okuda et al; sites ''a'' through ''d'' form nearly tetrahedral $[AlBr_4]^+$ unit
	b	153.60	0.244 ± 0.007		
	c	156.23	0.108 ± 0.007		
	d	159.66	0.075 ± 0.007		
$NaAl_2Br_7$	1	158.8	0.161 ± 0.010	Yamada[295]	Labels according to Yamada; Zeeman effect could not be resolved for sites 2, 4 and 5 due to poor S/N; bridging atom assigned to site 6.
	3	160.3	0.188 ± 0.010		
	6	149.7	0.880 ± 0.005		
	7	168.4	0.091 ± 0.010		

KAl_2Br_7	1	164.0	0.100 ± 0.005	Yamada[295]	Labels according to Yamada; bridging atom assigned to site 4
	2	166.7	0.050 ± 0.005		
	3	166.7	0.091 ± 0.010		
	4	149.1	0.902 ± 0.003		
	5	168.1	0.043 ± 0.010		
	6	169.7	0.136 ± 0.010		
	7	175.9	0.104 ± 0.010		
$NH_4Al_2Br_7$	1	168.3	0.119 ± 0.010	Yamada[295]	Labels according to Yamada; bridging atom assigned to site 2
	2	156.3	0.720 ± 0.005		
	3	168.0	0.240 ± 0.010		
	4	169.3	0.144 ± 0.010		
	5	170.0	0.176 ± 0.005		
	6	173.0	0.072 ± 0.005		
	7	177.7	0.112 ± 0.005		
$(CH_3)_4NAl_2Br_7$	1	139.6	0.878 ± 0.002	Yamada[295]	Label according to Yamada; Zeeman effect could not be resolved for any other site; bridging atom assigned to site 1
$2SbBr_3 \cdot C_6H_6$	1	263.04	0.169 ± 0.001	Okuda et al.[267]	Labels according to Okuda et al.
	2	279.23	0.063 ± 0.002		
	3	280.98	0.094 ± 0.002		
$SbBr_3 \cdot (POBr_3)_2$	1	419.29	0.04_0 ± 0.005	Okuda et al.[292]	$T = 77$ K; sites 1–5′ are assigned to $POBr_3$; 6–8 to $SbBr_3$
	2	414.08	0.11 ± 0.01		
	3	414.68	0.05_0 ± 0.005		
	4	409.29	0.02_0 ± 0.005		
	5,5′	409.01	0.04_0 ± 0.005		
	6	280.98	0.04_0 ± 0.005		
	7	267.34	0.05_0 ± 0.005		
	8	222.88	0.21_0 ± 0.005		

(*continued*)

TABLE 16 (*continued*)

Compound	Site labels	C_Q (MHz)[a]	η_Q	References	Additional experiments/ comments
$(NH_4)_4Sb^{III}Sb^{V}Br_{12}$	1	307.8	0.015 ± 0.004	Terao and Okuda.[300]	Labels according to Terao and Okuda; Zeeman-effect for sites 2,4 could not be resolved. Sites 1 and 3 are near Sb(V) and Sb(III), respectively
	3	123.7	0.015 ± 0.005		
$Al_2Br_6 \cdot C_6H_6$	1	157.8	0.289 ± 0.011	Okuda et al.[272]	$T = 301$ K, labels according to Okuda et al.
	2	180.0	0.086 ± 0.010		
	3	182.3	0.060 ± 0.009		
$2AlBr_3 \cdot 4C_5H_5N$	A	139.71	0.040	Okuda et al.[288]	Labels according to Okuda et al; molecular complex consists of $[AlBr_2(C_5H_5N)_4]^+$ (A,B) and $[AlBr_4]^-$ (C–F) species
	B	139.69	0.098		
	C	159.14	0.037		
	D	159.17	0.078		
	E	162.40	0.097		
	F	162.57	0.059		
$AlBr_3 \cdot C_6H_5NH_2$	A	158.11	0.103	Okuda et al.[288]	Labels according to Okuda et al.
	B	159.58	0.090		
	C	169.68	0.032		
Et_2SnBr_2		215.36 ± 0.04	0.132 ± 0.002	Okuda et al.[287]	
$KHgBr_3 \cdot H_2O$	1	228.42	0.005 ± 0.001	Terao et al.[302]	Labels according to Terao et al; sites 1,2 are terminal and site 3 is a bridging bromine
	2	226.24	0.005 ± 0.001		
	3	108.76	0.465 ± 0.001		
$MeNH_3HgBr_3$	1	203.48	0.026	Terao and Okuda[301]	Labels according to Terao and Okuda. Sites 1 and 2 are assigned to terminal and bridging Br atoms, respectively
	2	163.34	0.639		

$(Et_4N)HgBr_3$	1	128.9	0.33	Hiura[293]	$T = 77$ K
	2	219.6	0.06		
	3	234.7	0.03		
$(pyH)(ZnBr_3py)$	1	–	0.231	Hiura[293]	Labels according to Hiura; $T = 77$ K
	2	–	0.123		
	3	–	0.074		
CH_2Br_2		469.59	''very small''	Ege and Negita[307]	$T = 77$ K, polycrystalline sample
EtBr		415.59	''very small''	Ege and Negita[307]	$T = 77$ K, polycrystalline sample
1,4-dibromobutane		501.71†	''small''	Ege and Negita[307]	$T = 77$ K, polycrystalline sample
bromobenzene		538.27†	''very small''	Ege and Negita[307]	$T = 77$ K, polycrystalline sample
p-dibromobenzene		535.19 ± 0.04†	0.12 ± 0.01†	Kojima et al.[247]	$T = 287$ K
		–	0.05 ± 0.01	Shimomura[250]	
		447.4	0.045 ± 0.002[b]	Bucci et al.[252]	
		535.6†			
		447.4	0.0459 ± 0.0006	von Meerwall et al.[319,320]	Powdered sample, quadrupole regime NMR; $\delta_x(^{81}Br) = 1300$ ppm[319]
		447.4	0.0461 ± 0.0004	Griffin et al.[321]	Quadrupole regime NMR; principal components of shift tensor found to be zero within experimental error (±1000 ppm)
		542.24†	''very small''	Ege and Negita[307]	$T = 77$ K; polycrystalline sample
p-Bromophenol		442.20	0.07 ± 0.03	R. Rao and Murty[253,262]	
		528.95†			
		–	0.053_4 ± 0.001	Bucci et al.[263]	

(*continued*)

TABLE 16 (*continued*)

Compound	Site labels	C_Q (MHz)[a]	η_Q	References	Additional experiments/ comments
p-Bromoaniline		–	0.029 ± 0.001	Bucci et al.[255]	Minematsu. Preliminary account of ^{81}Br experiment.[251]
		437.87 523.90†	0.08 ± 0.02	R. Rao and Murty[257,262]	Colligiani et al. Determine relative orientation between ^{81}Br and ^{14}N EFG tensors[271]
2,4-Dibromoaniline	a	446.90	0.047 ± 0.001	Ambrosetti et al.[264]	Labels according to Ambrosetti et al.
	b	449.01	0.053 ± 0.001		
2,6-Dibromoaniline	a	444.38	0.071 ± 0.001	Bucci et al.[255]	Labels according to Bucci et al.
	b	447.16	0.066 ± 0.002		
2,4,6-Tribromoaniline	a	454.66	0.076 ± 0.002	Bucci et al.[255]	Labels according to Bucci et al.
	b	455.25	0.074 ± 0.002		
	c	461.22	0.040 ± 0.001		
2,5-Dibromonitrobenzene	1	493.94 591.18†	0.10†	R. Rao and Murty[258]	Labels according to Rao and Murty
	2	464.98 556.33†	0.08†		
D-3-Bromocamphor		444.34 531.69†	0.10	R. Rao and Murty[256]	
p-Bromoacetophenone		542.48†	0.07 ± 0.02†	K. Rao and Murty[260]	
p-Bromoacetanilide		535.28†	0.06 ± 0.03†	K. Rao and Murty[261]	
1,3,5-Tribromobenzene	1	462.840	0.084_5 ± 0.002	Bucci et al. [254,c]	Labels according to Milledge and Pant
	2	460.401	0.062_5 ± 0.002		
	3	462.651	0.062_5 ± 0.003		

2,4,6-Tribromophenol	1a	551.2†	0.04†	Ramasastry and Premaswarup[279]	Labels according to Ramasastry and Premaswarup; ''a'' and ''b'' labels differentiate between non-equivalent molecules in the unit cell, as identified by their non-equivalent EFG tensor orientations
	1b	551.1†	0.05†		
	2a	553.5†	0.03†		
	2b	553.6†	0.01†		
	3a	568.2†	0.05†		
	3b	568.2†	0.04†		
1-Bromo-2,4-dinitrobenzene	1a	592†	0.18†	Rangacharyulu and Premaswarup[281]	''a'', ''b'', ''c'', ''d'' labels correspond to crystallographically different molecules, as identified by their non-equivalent EFG tensor orientations
	1b	592†	0.18†		
	1c	591†	0.19†		
	1d	592†	0.17†		
Methyl 4-bromobenzoate		453.97	$0.094_5 \pm 0.001$	Angelone et al.[265]	
		460.60	0.094 ± 0.001	Ambrosetti et al.[275]	$T = 77$ K
2,4-Dibromoanisole	1	467.98	0.112 ± 0.003	Ambrosetti et al.[299]	1 is assigned to the 2-bromo position
	2	461.55	0.065 ± 0.003		
2,4,6-Tribromoanisole	1	476.99	0.101 ± 0.001	Ambrosetti et al.[299]	3 is assigned to the 4-bromo position; the 2-, 6-bromo positions are not assigned
	2	467.58	0.096 ± 0.001		
	3	463.04	0.058 ± 0.001		
p-Bromobenzenesulfonyl chloride		557.45†	0.065 ± 0.02†	R. Rao and Rogers[273]	
p-Bromoaniline hydrochloride		546.20†	0.105 ± 0.02†	R. Rao and Rogers[273]	
2,4,6-Tribromophenylacetate	1	569†	0.08 ± 0.03†	Rangacharyulu and Premaswarup[431]	Labels according to Rangacharyulu and Premaswarup; site 3 assigned to the 4-bromo position; sites 1–2 not assigned
	2	568†	0.03 ± 0.03†		
	3	545†	0.02 ± 0.03†		
4,4′-Dibromodiphenylether		456.05	0.064 ± 0.001	Ambrosetti et al.[270]	
		465.01	0.055 ± 0.004	Ambrosetti et al.[275]	$T = 77$ K

(*continued*)

TABLE 16 (*continued*)

Compound	Site labels	C_Q (MHz)[a]	η_Q	References	Additional experiments/ comments
4,4′-Dibromodiphenylsulphide		453.90	0.080 ± 0.001	Ambrosetti et al.[270]	
		459.65	0.078 ± 0.002	Ambrosetti et al.[275]	$T = 77$ K
α-Bromo-*p*-chloroacetophenone		–	~ 0.15–$0.16^{\dagger}$	Ramakrishna[298]	
2,4,6-Tribromophenyl-*p*-toluenesulfonate	1	$561.3^{\dagger}$	$0.11^{\dagger}$	Ramasastry and Premaswarup[280]	Labels according to Ramasastry and Premaswarup
	2	$574.1^{\dagger}$	$0.14^{\dagger}$		
	3	$591.3^{\dagger}$	$0.02 \pm 0.03^{\dagger}$		

[a] Unless noted otherwise, parameters are for ^{81}Br and were measured at room temperature using single crystals. A dagger (†) will denote a measurement corresponding to the ^{79}Br nuclide.
[b] Value is nuclide independent.
[c] Subsequently, K. Rao and Murty measured the ^{79}Br Zeeman-perturbed NQR spectrum, but could not resolve the three sites and assigned all three sites $\eta_Q = 0.12 \pm 0.03$.[259]

TABLE 17 Bromine-79/81 solid-state NMR data for selected non-diamagnetic systems

Compound		State[a]	T (K)	C_Q (MHz)[b]	η_Q	References	Additional experiments/comments
"Fe_8Br_8" $[(C_6H_{15}N_3)_6Fe_8(\mu_3\text{-}O)_2(\mu_2\text{-}OH)_{12}Br_7(H_2O)]Br\cdot 8H_2O$		p	225, 280	–	–	Zipse et al.[432]	$\mathbf{B}_0 = 8.54$ T; measured Fermi contact coupling constant (0.082 MHz) and unpaired electron density on the bromines using ^{81}Br SSNMR experiments
$CrBr_3$ (flakes)		f	<20	200.2[e]	0.293 ± 0.001[e]	Senturia and Benedek[433]	Gossard et al. measure $^{79/81}$Br transition frequencies and T_1 values between 1.3 and 4.2 K[434] Senturia. $^{79/81}$Br experiments conducted between 4.21 and 32.349 K to demonstrate the utility of the sample as a low temp. thermometer[435]
$(NH_4)_2CuBr_4\cdot 2H_2O$	Site I	f	<1.83	12.364[c,d]	0.897 ± 0.003	Renard and Velu[436,437]	Labels according to Klaassen et al. They confirm the parameters of site I in f-state, $\eta_Q = 0.897$ and in p-state, $C_Q(^{81}Br) = 12.322$ MHz; $\eta_Q = 0.917$; parameters of site II in p-state could not be detected[438]
		p	4.215	12.293	0.928 ± 0.002		
	Site II	f	0[d]	151.0[c,e]	0.32[c,e]	Klaassen et al.[438]	
$Rb_2CuBr_4\cdot 2H_2O$	Site I	f	0[d]	22.486	0.640	Klaassen et al.[438,439]	Labels according to Klaassen et al. Parameters of site II in the p-state could not be detected
		p	4.2	22.52	0.628		
	Site II	f	0[d]	163.0[e]	0.22[e]		

(*continued*)

TABLE 17 (*continued*)

Compound		State[a]	T (K)	C_Q (MHz)[b]	η_Q	References	Additional experiments/comments
$(MeNH_3)_2Cu(Cl_{0.75}Br_{0.25})_4$		*f*	1.7	– 170.5 ± 1[e]		Kubo et al.[440]	
$CoBr_2 \cdot 6H_2O$		*af*	1.17	70.9 84.8[e]	0.02	R. Rao et al.[441]	
$CoBr_2 \cdot 6D_2O$		*af*	1.12	71.0 84.9[e]	0.01	Hijmans et al.[442]	
$MnBr_2 \cdot 4H_2O$	I	*af*	0.4	66 79[e]	0.4 ± 0.3	Swüste and Kopinga[443]	Labels according to Swüste and Kopinga
	II			46 55[e]	0.4 ± 0.2		
$CsMnBr_3$		*af*	4.2	–	–	Okada et al.[444]	Also measured ^{81}Br T_1 and signal intensity as functions of temp (1.7–4.2 K)
		af	≤0.9	–	–	Xu et al.[445,446]	Measured ^{81}Br NMR spectra, T_1 and echo intensity between 0.09 and 0.9 K to comment on a low-T phase transition
		af	4.2	–	–	Xu et al.[447]	Br NMR spectrum measured over a large field sweep (0–14 T); 36 resonance peaks observed
$CsMnBr_3 \cdot 2H_2O$	I	*af*	1.1	77.8 93.0[e]	0.35	Swüste et al.[448]	Labels according to Swüste et al.
	II			53.1 63.5[e]	0.70		

$Cs_2MnBr_4 \cdot 2H_2O$	I	*af*	1.1	84.7[e]	0.35	Swüste et al.[448]	Labels according to Swüste et al.
	II			68.8[e]	0.20		
$Rb_2MnBr_4 \cdot 2H_2O$	I	*af*	1.1	80.7[e]	0.36	Swüste et al.[448]	Labels according to Swüste et al.
	II			59.2[e]	0.26		
$CsCoBr_3$		*af*	4.2	92.4	0.53	Uyeda et al.[449]	
				109.2[e]			

[a] *p* corresponds to the paramagnetic state, *f* corresponds to the ferromagnetic state, *af* corresponds to the antiferromagnetic state.
[b] Unless noted otherwise, parameters are for ^{81}Br and were carried out using single crystals and in the absence of an applied magnetic field.
[c] Measured by Klaassen et al.[438]
[d] Measured parameter has been extrapolated to $T = 0$ K.
[e] Denotes a measurement corresponding to the ^{79}Br nuclide.

TABLE 18 Solid-state I-127 NMR data for iodides and hydroiodides[a]

Compound	$\delta_{iso}(\pm)$ (ppm)	$C_Q(\pm)$ (MHz)	References (condition)	Additional experiments/comments
LiI	215.28(0.35)[b]	–	Hayashi and Hayamizu(M)[137]	Ngai(M). Temp. dep. of $\delta(^{127}I)$ over $T = \sim 400$–500 K: $\Delta\delta_{iso}/\Delta T = 0.53$ ppm/K[147] Hayashi and Hayamizu(M). Temp. dep. of $\delta(^{127}I)$ over $T = 294$–400 K: $\delta = (0.097\ \text{ppm/K})(T/\text{K}) + 185.6$ ppm[a,178] Mali et al.(S). Temp. dep. of $T_1(^{127}I)$ from $T = 100$–650 K[450]
NaI	148(15)[c]	–	Kanda(M)[128]	Wikner et al.(S). $T_1(^{127}I) = 12$ ms at $T = 298$ K and $\mathbf{B}_0 = 1.1$ T[139]
	120(30)[d]	–	Bloembergen and Sorokin(S)[131]	Weber(S). Temp. dep. of $T_1(^{127}I)$ over ca. 20–400 K[140]
	200[e]	–	Yamagata(S)[133]	Ngai(M). Temp. dep. of $\delta(^{127}I)$ over $T = \sim 293$–540 K: $\Delta\delta_{iso}/\Delta T = 0.82$ ppm/K[147]
	33.53(0.23)[b]	–	Hayashi and Hayamizu(M)[137]	Hayashi and Hayamizu(M). Temp. dep. of $\delta(^{127}I)$ over $T = 294$–400 K: $\delta = (0.0008\ \text{ppm/K})(T/\text{K}) + 33.8$ ppm[a,178] Kanashiro et al.(S). $T_1(^{127}I)$ temp. dep. from $T = 77$–700 K.[153]
KI	170(20)[c]	–	Kanda(M)[128]	Solomon(S); Butterworth(P). Used ^{127}I SSNMR to study spin echoes[451,452] Wikner et al.(S). $T_1(^{127}I) = 19$ ms at $T = 298$ K and $\mathbf{B}_0 = 1.1$ T.; temp. dep. also studied[139]
	100(30)[c]	–	Bloembergen and Sorokin(S)[131]	Weber(S). Temp. dep. of $T_1(^{127}I)$ over ca. 60–300 K[140]

	180[e]	–	Yamagata(S)[133]	Weisman and Bennett(''fused solid''). Observed T_2 (ST) > T_2 (CT)[453]
	0[b]	–	Hayashi and Hayamizu(M)[137]	Ngai(M). Temp. dep. of $\delta(^{127}\text{I})$ over $T = \sim 293$–555 K: $\Delta\delta_{iso}/\Delta T = 0.70$ ppm/K[147]
				Hayashi and Hayamizu(M). Temp. dep. of $\delta(^{127}\text{I})$ over $T = 294$–400 K: $\delta = (-0.030\ \text{ppm/K})(T/\text{K}) + 8.7$ ppm[a,178]
				Lee et al.(S) Multipole relaxation times determined[454]
RbI	250[e]	–	Yamagata(S)[133]	Ngai(M). Temp. dep. of $\delta(^{127}\text{I})$ over $T = \sim 293$–540 K: $\Delta\delta_{iso}/\Delta T = 0.93$ ppm/K[147]
	76.91(0.12)[b]	–	Hayashi and Hayamizu(M)[137]	
	170(30)[f]	–	Bloembergen and Sorokin(S)[131]	Hayashi and Hayamizu(M). Temp. dep. of $\delta(^{127}\text{I})$ over $T = 294$–400 K: $\delta = (-0.056\ \text{ppm/K})(T/\text{K}) + 94.4$ ppm[a,178]
				Baron(M). $\delta(^{127}\text{I})$ vs. p; line of best fit ($\delta_0 = \delta$ at ambient p): NaCl phase ($p < 397$ MPa): $\delta/\text{ppm} = \delta_0/\text{ppm} + (0.0184\ \text{ppm/MPa})(p/\text{MPa})$
CsI	500(30)[g]	–	Bloembergen and Sorokin(S)[131]	Wikner et al.(S). $T_1(^{127}\text{I}) = 10$ ms at $T = 298$ K and $\mathbf{B}_0 = 1.1$ T[139]
	580[e]	–	Yamagata(S)[133]	Ngai(M). Temp. dep. of $\delta(^{127}\text{I})$ over $T = \sim 293$–600 K: $\Delta\delta_{iso}/\Delta T = 0.76$ ppm/K[147]

(*continued*)

TABLE 18 (*continued*)

Compound	$\delta_{iso}(\pm)$ (ppm)	$C_Q(\pm)$ (MHz)	References (condition)	Additional experiments/comments
	368.69(0.12)[c]	–	Hayashi and Hayamizu(M)[137]	Hayashi and Hayamizu(M). Temp. dep. of $\delta(^{127}I)$ over $T = 294$–400 K: $\delta = (-0.015\ \text{ppm/K})(T/\text{K}) + 374.2$ ppm[a,178] Gerhart and Hooper(S). Uniaxial stress applied to the crystal produced ^{127}I SSNMR lineshape broadening; one component of the gradient-elastic tensor was determined[455] Baron(M). $\delta(^{127}I)$ vs. p; lines of best fit ($\delta_0 = \delta$ at ambient p): CsCl phase ($p < 980$ MPa): $\delta/\text{ppm} = \delta_0/\text{ppm} + (0.093\ \text{ppm/MPa})(p/\text{MPa})$
CuI	–	–	Kanashiro et al.(S)[353]	Becker(M). Chemical shifts measured as a function of temperature ($T = 423$–573 K)[177]
	7.7(0.2)[b]	–	Hayashi and Hayamizu(M)[178]	
	–			
	MAS-rate dependence of chemical shift is investigated	–	Hayashi and Hayamizu(M)[223]	Hayashi and Hayamizu(M). Temperature dependence of chemical shift: $\delta = (0.222\ \text{ppm K}^{-1})(T/\text{K}) - 65.4$ ppm (over the range 200–240 K); $\delta = (0.384\ \text{ppm K}^{-1})(T/\text{K}) - 104.5$ ppm (over the range 240–320 K); $\delta = (0.446\ \text{ppm K}^{-1})(T/\text{K}) - 124.4$ ppm (over the range 320–400 K)[178]

AgI	−232.2(1.0)[b] at 294 K		Hayashi and Hayamizu (M)[178]	$\delta = (0.438\ \text{ppm K}^{-1})\ (T/\text{K}) - 360.6$ ppm (over the range 160–280 K); $\delta = (0.540\ \text{ppm K}^{-1})(T/\text{K}) - 389.0$ ppm (over the range 280–320 K) Wagner(S). Variable temperature experiments on β-AgI[493]
CsI doped with CuI			Budde and Richtering[456]	
LiI/Al_2O_3 mixtures			Ardel et al.(M)[457]	Temperature dependence of chemical shift studied
$(KI)_{0.56}(NH_4I)_{0.44}$			Hinze et al.(S)[458]	
trimethylethyl ammonium iodide			Ishida et al.(M)[459]	
HgI_2			Dzhioev and Kursaev(S)[460]	
glycyl-L-alanine hydroiodide monohydrate		At 274.5 K: 74.04 (η_Q = 0.776) cited from Kehrer et al.[461]	Kehrer et al.(S)[430]	Orientation of iodine EFG tensor determined

[a] Within the references column, the condition of the solid state sample is denoted accordingly: S = single crystal, P = polycrystalline, M = microcrystalline powder; if the condition of the sample is unknown, it will not be specified.
[b] With respect to KI(*s*).
[c] With respect to KI(*aq*).
[d] With respect to NaI(*aq*).
[e] With respect to very dilute aqueous solution.
[f] With respect to RbI(*aq*).
[g] With respect to CsI(*aq*).

TABLE 19 Solid-state I-127 NMR data for periodates, iodates, and other iodo compounds

Compound	$\delta_{iso}(\pm)$ (ppm)	$C_Q(\pm)$ (MHz)	References (condition)	Additional experiments/ comments
KIO_4	–	–	Siegel et al.(M)[87]	Signal-to-noise enhancements using modified QCPMG pulse sequences are demonstrated by Siegel et al.
	3960(10)[a]	20.66(0.01) ($\eta_Q = 0.0$)	Wu and Dong(P)[332]	
	6530(200)[a]	20.73	Segel and Vyas(P)[324]	
NH_4IO_4 ND_4IO_4	–	Temperature dependence of quadrupole coupling reported; C_Q passes through zero and changes sign for ND_4IO_4 at 87 K	Segel et al.(P)[462]	
NH_4IO_4	3960(10)[a]	10.00(0.01) ($\eta_Q = 0.0$)	Wu and Dong(P)[332]	
	–	1.31 to 11.59 over the range 145–440 K	Burkert(M)[325]	
	3810(50)[a]	10.02	Segel and Vyas(P)[324]	
$RbIO_4$	3960(10)[a]	15.65(0.01) ($\eta_Q = 0.0$)	Wu and Dong(P)[332]	
		16.27 to 14.65 over the range 202–433 K	Burkert(M)[325]	
$RbIO_3$	–	–	Segel and Vyas(P)[324]	
$NaIO_4$	3950(10)[a]	42.24(0.01) ($\eta_Q = 0.0$)	Wu and Dong(P)[332]	
	−5370(100)[a]	42.39	Segel and Vyas(P)[324]	
	–	'very large'	Weiss and Weyrich (S)[463]	
$CsIO_4$	3972(2)[a]	1.00(0.01) ($\eta_Q = 0.0$)	Wu and Dong(P)[332]	
	–		Burkert(M)[325]	

		11.45 to 10.45 over the range 202–294 K; 1.8–1.7 over the range 300–315 K		
$CsIO_3$	–	–	Segel and Vyas(P)[324]	
HIO_4	3300(10)[a]	43.00(0.01) ($\eta_Q = 0.75$)	Wu and Dong(P)[332]	
$(CH_3)_4AsIO_4$	–	$\leq$1.8	Grommelt and Burkert (M)[330]	Temperature dependence of shift measured
$(n\text{-}C_4H_9)_4NIO_4$	–	8.07 to 3.35 (over the range 225–310 K) (η_Q ranges from 0.60 to 0.77)	Burkert and Grommelt (M)[329]	Temperature dependence of C_Q and η_Q studied. Several phase transitions studied.
$(n\text{-}C_4H_9)_4PIO_4$	–	5.98 to 3.14 (over the range 150–355 K) (η_Q ranges from 0.08 to 0.30)	Burkert and Grommelt (M)[329]	Temperature dependence of C_Q and η_Q studied. Several phase transitions studied.
$(C_2H_5)_4SbIO_4$	–	5.29 to 5.71 ($\eta_Q = 0.64$ to 0.38) over the range 217–301 K	Klobasa and Burkert (M)[331]	Anomalous increase in C_Q with temperature
$(C_2H_5)_4PIO_4$	–	6.09 to 5.87 over the range 177–302 K	Klobasa et al.(M)[328]	Temperature dependence of C_Q studied.
$(C_2H_5)_4AsIO_4$	–	5.82 to 5.55 over the range 197–299 K	Klobasa et al.(M)[328]	
$(C_6H_5)_4PIO_4$	–	4.12 to 5.71 over the range 228–293 K		Phase transitions and temperature

(*continued*)

TABLE 19 (*continued*)

Compound	δ_{iso}(±) (ppm)	C_Q(±) (MHz)	References (condition)	Additional experiments/ comments
		($\eta_Q \approx 0$)	Burkert and Klobasa; Klobasa et al. (M)[327,328]	dependence of C_Q studied.
$(C_6H_5)_4AsIO_4$	–	3.50 to 7.42 over the range 179–297 K ($\eta_Q \approx 0$)	Burkert and Klobasa; Klobasa et al. (M)[327,328]	
$(C_6H_5)_4SbIO_4$	–	1.37 to 2.76 over the range 228–302 K ($\eta_Q \approx 0$)	Burkert and Klobasa; Klobasa et al. (M)[327,328]	
$(CH_3)_4NIO_4$	–	≈ 20 to 15 over the range 200–300 K	Klobasa and Burkert (M)[331]	
$N(CH_3)_4IO_4$	–	15.46 to 9.07 over the range 301–418 K	Burkert(M)[325]	
$LiIO_3$	–	–	Segel and Vyas(P)[324]	
$AgIO_4$	5410 (50)[a]	29.66	Segel and Vyas(P)[324]	
mixed Br/I sodalites	−255.5(0.8)[c] (0 % Br)	P_Q[†] = 1.0(0.5) (0 % Br)	Trill et al.(M)[94]	
	−255.5(0.8) (6 % Br)	$P_Q = 1.1(0.5)$ (6 % Br)		
	−255.2(0.8) (25 % Br)	$P_Q = 1.3(0.5)$ (25 % Br)		
	−250.4(0.8) (46 % Br)	$P_Q = 2.8(0.5)$ (46 % Br)		
	−250.0(0.8) (65 % Br)	$P_Q = 2.6(0.5)$ (65 % Br)		
	−247.6(0.8) (77 % Br)	$P_Q = 2.1(0.5)$ (77 % Br)		
	−245.5(0.8) (86 % Br)	$P_Q = 1.6(0.5)$ (86 % Br)		
	−245.0(0.8) (91 % Br)	$P_Q = 1.8(0.5)$ (91 % Br)		

mixed Cl/I sodalites	−255.5(0.8)[c] (0 % Cl) −254.6(0.8) (5 % Cl) −254.4(0.8) (6 % Cl) −253.9(0.8) (10 % Cl) −254.8(0.8) (22 % Cl) −228.2(0.8) (89 % Cl) −227.1(0.8) (90 % Cl)	P_Q[†] = 1.0(0.5) (0 % Cl) P_Q = 1.7(0.5) (5 % Cl) P_Q = 1.5(0.5) (6 % Cl) P_Q = 1.8(0.5) (10 % Cl) P_Q = 2.3(0.5) (22 % Cl) P_Q = 4.3(0.5) (89 % Cl) P_Q = 3.9(0.5) (90 % Cl)	Trill et al.(M)[94]	
IF_7	3040(40)[d]	At 77 K: 134.88(0.03) (η_Q = 0.04(0.004)) (from NQR study in same paper)	Weulersse et al.(M)[464]	New solid-solid phase transition discovered; $J(^{127}I, ^{19}F)$ = 2100 Hz (S_1 phase)
$IF_6^+AsF_6^-$	–	2.9 (if $\eta_Q = 0$) 2.32 (if $\eta_Q = 1$)	Hon and Christe(M)[333]	Obtained in a field of 0.936 T
$Ag_xCu_{1-x}I$ (x = 0.05–0.40 and 0.80–0.99)	–	–	Mizuno et al.(M)[465]	
$Mn(CO)_5I$	–	927 (η_Q = 0.03) ('preliminary values')	Spiess and Sheline (S)[269]	
BI_3	–	1190.6(1.1) (η_Q = 0.4518(0.0003))	Okuda et al.(S) [466]	Zeeman-perturbed NQR on a single crystal. Temperature dependence also studied.

(*continued*)

TABLE 19 (*continued*)

Compound	$\delta_{iso}(\pm)$ (ppm)	$C_Q(\pm)$ (MHz)	References (condition)	Additional experiments/ comments
I_2	–	($\eta_Q = 0.16(0.010)$	Kojima and Tsukada (S)[467,468]	Zeeman splitting of the NQR line
^{131}I implanted in Fe crystals	–	–	Visser et al.(S)[469]	^{131}I is a radioactive nucleus with a half-life of about 8 days and nuclear spin of 7/2[470]

Within the references column, the condition of the solid state sample will be denoted accordingly: S = single crystal, P = polycrystalline, M = microcrystalline powder; if the condition of the sample is unknown, it will not be specified.

† $P_Q = C_Q(1+\eta_Q^2/3)^{1/2}$.

[a] with respect to solid NaI.

[b] with respect to solid KI.

[c] with respect to 1M NaI(aq).

[d] with respect to 5M NaI(aq).

TABLE 20 Iodine-127 CSA data from solid-state NMR spectroscopy

Compound	CSA data (ppm)	Reference	Additional information
$CsIO_4$	$\delta_{11} = \delta_{22} = 3978$[a]; $\delta_{33} = 3960$[a] ($\Omega = 18$)	Wu and Dong[332]	This is likely the only reliable report of iodine CSA from solid-state NMR experiments.
NH_4IO_4	$\Omega < 50$	Wu and Dong[332]	This supersedes a value previously reported by Segel and Vyas[324]
KIO_4	$\Omega < 50$	Wu and Dong[332]	This supersedes a value previously reported by Segel and Vyas[324]
$AgIO_4$	$\Omega = 980$	Segel and Vyas[324]	
$NaIO_4$	$\Omega < 50$	Wu and Dong[332]	This supersedes a value previously reported by Segel and Vyas[324]
$LiIO_3$	one component of the CS tensor reported as 5000 ± 400[a]	Segel and Vyas[324]	
$CsIO_3$	one component of the CS tensor reported as 4400 ± 400[a]	Segel and Vyas[324]	
$RbIO_3$	one component of the CS tensor reported as 4900 ± 400[a]	Segel and Vyas[324]	
$CsICl_2$	one component of the CS tensor reported as 3900 ± 200[a]	Segel and Vyas[324]	

[a] with respect to solid NaI.

TABLE 21 Selected gas-phase data measured by molecular beam or microwave methods for quadrupolar halogen nuclei in diatomic molecules

Molecule	C_Q (halogen) (kHz)	c (halogen)[a] (kHz)	c_3 (kHz)	J_{iso} (Hz)	References
$^{1}H^{79}Br$	532 304.1(8)	290.83(8)	10.03(21)	–	Saleck et al., 1996[471]; van Dijk and Dymanus 1969[472]
$^{1}H^{81}Br$	444 679.3(8)	313.25(8)	10.89(21)	–	Saleck et al., 1996[471]; van Dijk and Dymanus 1969[472]
$D^{79}Br$	530 631.5(21)	145.82(24)	1.59(24)	–	Saleck et al., 1996[471]; van Dijk and Dymanus 1974[473]
$D^{81}Br$	443 279.9(21)	157.26(24)	1.74(24)	–	Saleck et al., 1996[471]; van Dijk and Dymanus 1974[473]
$^{1}H^{35}Cl$	−67 617.6(11)	54.00(15)	5.1(4)	–	Cazzoli and Puzzarini, 2004[346]
$^{1}H^{37}Cl$	−53 288.1(17)	44.75(15)	4.4(4)	–	Cazzoli and Puzzarini, 2004[346]
$^{1}H^{127}I$	−1 828 286 ± 9	351.1 ± 0.3	5.49 ± 0.11	−80 ± 70	Van Dijk and Dymanus, 1968[474]
$^{127}I_2$ ($v = 0$, $J = 13$)	−2 452 585.14(45)	3.1536(33)	1.528(18)	3708(22)	Wallerand et al., 1999[475]
$^{7}Li^{79}Br$	38 368.104(36)	7.8816(58)	1.0710(61)	60.4(7.0)	Hilborn et al., 1972[476]
$^{7}Li^{81}Br$	32 050.860(46)	8.4740(74)	1.1789(78)	71.1(8.9)	Hilborn et al., 1972[476]
$^{23}Na^{79}Br$	58 068.90	0.3125	0.3908	78 ± 3	Cederberg et al., 1987[477]
$^{23}Na^{81}Br$	48 508.672	0.3371	0.4248	85.9 ± 1.8	Cederberg et al., 1987[477]
$^{35}Cl^{19}F$	−145 871.82(3)	21.616(2)	2.859(9)	840(6)	Fabricant and Muenter, 1977[478]
$^{37}Cl^{19}F$	−114 961.31(6)	17.649(4)	2.385(17)	710(10)	Fabricant and Muenter, 1977[478]
$^{133}Cs^{35}Cl$ ($v = 0$)	1765.17(6)	0.5872(37)	0.0280(15)	60.5(16)	Cederberg, 1977[479]
$^{133}Cs^{35}Cl$ ($v = 0$)	1392.30(6)	0.4630(37)	0.0318(15)	55.4(16)	Cederberg, 1977[479]
$^{23}Na^{35}Cl$ ($v = 0$)	−5642 ± 50	–	0.22 ± 0.02	50 ± 30	Cederberg and Miller, 1969[480]
$^{23}Na^{35}Cl$ ($v = 0$)	−5646.8 ± 6.0	0.00 ± 0.40	0.24 ± 0.15	0 ± 300	de Leeuw et al., 1970[481]
$^{23}Na^{37}Cl$ ($v = 0$)	−4447.0 ± 1.3	−0.47 ± 0.54	0.25 ± 0.22	90 ± 250	de Leeuw et al., 1970[481]

$^{85}Rb^{35}Cl$	769.45	0.3950	0.033	25.71	Cederberg et al., 2006[482]
$^{85}Rb^{37}Cl$	607.39	0.31615	0.02723	21.64	Cederberg et al., 2006[482]
$^{39}K^{35}Cl$	55.9 ± 0.4	0.435 ± 0.010	0.035 ± 0.012	9 ± 6	Nitz et al., 1984[483]
$^{39}K^{37}Cl$ ($v = 0$, $J = 2$)	44.9 ± 0.3	0.352 ± 0.008	0.030 ± 0.010	7 ± 5	Nitz et al., 1984[483]
$^{39}K^{79}Br$	10 237.8535	1.23695	0.03756	21.89 ± 0.18	Cederberg et al., 2008[342]
$^{39}K^{81}Br$	8550.8901	1.32250	0.04048	23.59 ± 0.19	Cederberg et al., 2008[342]
$^{39}K^{127}I$	−86 896.9856	0.88790	0.01082	24.10	Cederberg et al., 2008[342]
$^{7}Li^{127}I$	−198 478.601	6.80388	0.62584	62.44	Cederberg et al., 1999[341]
$^{79}Br^{19}F$	1 086 891.97(118)	89.051(131)	−7.15(24)	4860(280)	Müller and Gerry 1995[484]
$^{81}Br^{19}F$	907 976.81(116)	95.818(128)	−7.71(26)	5240(300)	Müller and Gerry 1995[484]
$^{127}I^{19}F$	−3 438 176.88 (167)	94.174(89)	−5.202(146)	5730(1050)	Müller and Gerry 1995[484]
$^{175}Lu^{35}Cl$ ($v = 0$)	−647.27(63)	2.141(42)	–	–	Cooke et al., 2005[485]
$^{175}Lu^{37}Cl$ ($v = 0$)	−500.29(92)	1.471(56)	–	–	Cooke et al., 2005[485]
$^{139}La^{35}Cl$ ($v = 0$)	−950.1(24)	2.71(12)	–	–	Rubinoff et al., 2003[486]
$^{139}La^{37}Cl$ ($v = 0$)	−749.6(28)	1.73(15)	–		Rubinoff et al., 2003[486]
$^{139}La^{79}Br$ ($v = 0$)	13 624.2(21)	6.957(57)	–	–	Rubinoff et al., 2003[486]
$^{139}La^{81}Br$ ($v = 0$)	11 375.0(22)	7.405(64)	–	–	Rubinoff et al., 2003[486]

(*continued*)

TABLE 21 (*continued*)

Molecule	C_Q (halogen) (kHz)	c (halogen)[a] (kHz)	c_3 (kHz)	J_{iso} (Hz)	References
$^{139}La^{127}I$ ($v = 0$)	−81 197(23)	5.79(11)	–	–	Rubinoff et al., 2003[486]
$^{45}Sc^{35}Cl$	−3786.1(35)	4.63(24)	−0.65(35)	–	Lin et al., 2000[487]
$^{45}Sc^{37}Cl$	−2982.4(36)	3.69(28)	−0.45(34)	–	Lin et al., 2000[487]
$^{45}Sc^{79}Br$	39 085.7(24)	17.06(16)	–	–	Lin et al., 2000[488]
$^{45}Sc^{81}Br$	32 643.8(19)	18.24(17)	–	–	Lin et al., 2000[488]
$^{89}Y^{35}Cl$	−821.6(43)	2.86(39)	–	–	Hensel and Gerry, 1994[489]
$^{89}Y^{37}Cl$	−621(20)	2.29	–	–	Hensel and Gerry, 1994[489]
$^{63}Cu^{35}Cl$ ($v = 0$)	−32 127.29(59)	−0.250(60)	0.137	–	Low et al.,1993,[345]; Bizzocchi et al., 2007[344]
$^{63}Cu^{79}Br$ ($v = 0$)	261 179.9(23)	0.13(12)	–	–	Low et al., 1993[345]
$^{63}Cu^{127}I$	−938 379.47(73)	0.645(29)	−0.397(47)	298(59)	Bizzocchi et al., 2007[344]
$^{65}Cu^{127}I$	−938 362.8(13)	0.676(53)	–0.460(80)	319	Bizzocchi et al., 2007[344]
$^{107}Ag^{127}I$	−1 062 527.99(66)	0.584(22)	–	–	Bizzocchi et al., 2007[344]
$^{109}Ag^{127}I$	−1 062 522.05(50)	0.599(16)	–	–	Bizzocchi et al., 2007[344]
$^{205}Tl^{35}Cl$ ($v = 0$, $J = 2$)	−15 793.32(50)	1.38(10)	−0.13(10)	−1540(100)	Hammerle et al., 1969[490]
$^{205}Tl^{79}Br$ ($v = 0$, $J = 2$)	126 310.88(10)	3.690(5)	−1.65(5)	−6350(50)	Dickinson et al., 1970[491]
$^{205}Tl^{127}I$ ($v = 0$, $J = 3$)	−438 916.3 ± 0.5	3.05 ± 0.05	−2.48 ± 0.1	−6670 ± 50	Stephenson et al., 1970[492]

Data are for the v = 0, J =1 *rotational-vibrational state unless otherwise stated.*
[a] Spin-rotation constant.

The alkali metal halides which contain half-integer quadrupolar halogen nuclei are amenable to SSNMR experiments primarily because they possess cubic lattice symmetry. They are also particularly convenient to use, since pure samples may be easily prepared and maintained. The first reports of bromine and iodine SSNMR experiments were communicated by Pound and were carried out using single crystals of NaBr[126] and NaI,[127] respectively. The first chlorine SSNMR spectra appear to have been acquired by Kanda in 1955 on powdered samples of NaCl, AgCl, CsCl, and TlCl.[128] Chlorine-35/37, bromine-79/81, and iodine-127 SSNMR experiments on the alkali metal halides were important in furthering the understanding of ionic systems through their: (i) observed isotropic chemical shifts, (ii) quadrupolar relaxation processes, (iii) signal intensities and linewidths, (iv) the temperature and pressure dependence of (i), (ii) and (iii), and (v) effects of lattice perturbations on NMR spectra. Each of these points will now be discussed.

4.1.1. Observed isotropic chemical shifts

Although the crystal structures of the alkali metal halides were determined before the advent of condensed phase NMR spectroscopy, a substantial amount of experimental and theoretical work was required to provide a semi-quantitative model that could rationalize the observed halogen nuclei chemical shifts. Kanda measured bromine chemical shifts for a partial series of alkali metal halides, as well as AgCl, TlCl, AgBr and TlBr, and tentatively concluded that an increase in $\delta_{iso}(X)$ (X = Cl, Br, I) corresponded to an increase in M–X covalent bond character.[128] This study, along with the NMR observations of Gutowsky and McGarvey on the cationic species,[129] motivated Yosida and Moriya (Y–M) to develop a theoretical model which rationalized the chemical shifts between samples as being due to differences in the degree of M–X covalent bond character.[130] This model was used to explain not only observed chemical shifts, but also homonuclear spin–spin coupling (direct and J) and T_1 values. Bloembergen and Sorokin used the Y–M model to explain the $\delta_{iso}(^{79}Br)$ and $T_1(^{81}Br)$ values in a single crystal of CsBr.[131] Following ^{81}Br SSNMR experiments on a single crystal of RbBr, Itoh and Yamagata noted that the Y–M model, as well as the purely ionic model of van Kranendonk,[132] (vK), failed to produce δ(Br) on the order that was being measured and hinted that a more elaborate theory was required.[41] Kondo and Yamashita (K–Y) proposed a model for relaxation and chemical shifts in ionic crystals which assumed that the overlap of ion atomic orbitals of nearest-neighbour atoms was responsible for the observed parameters.[40]

A detailed ^{35}Cl, ^{81}Br, and ^{127}I SSNMR study on all alkali metal halides (except LiI) was carried out by Yamagata in 1964, who concluded that the trend in observed chemical shifts (see Figure 6 for the trend associated with the bromides and iodides; the chlorides are very similar) could not be qualitatively understood by any model proposed up to that date. Taking the K–Y model as a starting point, it was shown that M–X bond covalence, lattice vibrations and electrostatic effects were only of minor importance in differentiating the shifts of the alkali metal halides. It was concluded that the dominating halogen chemical shift effect was due to orbital overlap between the halogen ion with both its nearest (NN) and next-nearest neighbours (NNN).[133]

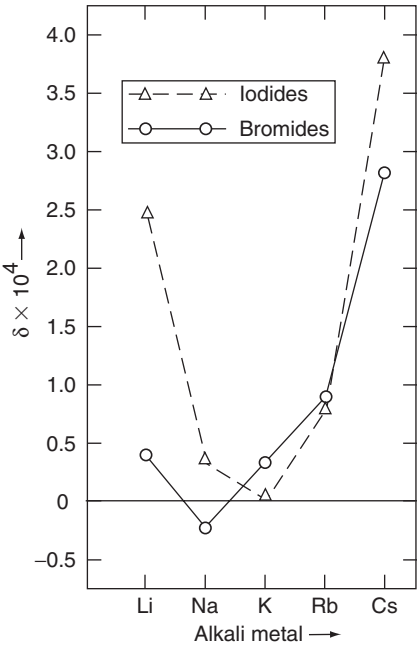

Figure 6 Experimental chemical shifts of the halogen nuclei versus the identity of the alkali metal ion (room temperature). Modified from Ref. 147. Reproduced by permission of *Elsevier Ltd.*

The calculation of magnetic shielding parameters in the alkali metal halides using Hartree–Fock wavefunctions was carried out by Ikenberry and Das, but their approach did not reproduce the observed halogen shift values of the systems studied (chemical shifts were in error by about 200–300 ppm).[45] The pressure dependence of the shifts of several alkali halides was calculated by Hafemeister and Flygare.[134]

Using MAS $^{35/37}$Cl SSNMR experiments on powdered samples of NaCl, KCl, RbCl, and CsCl, Weeding and Veeman[135] observed that the chlorine chemical shifts were nearly isotope independent. They also observed that two properties correlated with the observed shifts, namely the M–X bond distance and the Sanderson electronegativity of the cation, with the latter exhibiting a stronger correlation. This correlation between Sanderson electronegativity and chlorine shift was confirmed by Lefebvre,[136] with the exception of LiCl. The possibility that the $Li(H_2O)_x^+$ ion was the true counterion in solid samples of LiCl was proposed as an explanation for this anomalous shift given the hygroscopic nature of this material.

Hayashi and Hayamizu carried out a comprehensive SSNMR study on the alkali metal halides.[137] All shifts were determined from MAS experiments at $\mathbf{B}_0 =$ 9.4 T with $\nu_{rot} =$ 2–5 kHz. By performing ^{7}Li, ^{23}Na, ^{87}Rb, ^{133}Cs, ^{35}Cl, ^{79}Br, and ^{127}I MAS SSNMR experiments (and static ^{39}K NMR experiments) on microcrystalline powders for all 15 alkali metal halides, they determined very precise chemical shifts for the halide nuclei relative to solid KX salts. They also measured the static

and MAS linewidths for all the halide nuclei noted above. They found solid KX salts to be ideal for setting the X nucleus shift reference, a point to which we will return later. They also attempted to relate their observations to structural parameters, although they did not find a simple explanation. They finished by rationalizing the halogen chemical shifts in a manner similar to that of Yamagata[133] by taking into account the orbital overlap between the halogen ion and its NN and NNN.

4.1.2. Understanding quadrupolar relaxation processes in solids

After observing the ^{81}Br and ^{127}I NMR signals for single crystals of NaBr and KI,[126] as well as the $^{79/81}$Br NMR signals of crystalline and powdered KBr,[138] it was suggested by Watkins and Pound that the rapid relaxation ($T_1 << 1$ s) in these systems arose from the coupling between Q and a time-dependent EFG due to crystal lattice strain and thermal vibrations. The quadrupolar mechanism dominates the relaxation processes in the alkali halides and for the bromides it is generally observed that $[T_1(^{81}\text{Br})/T_1(^{79}\text{Br})] = [Q(^{79}\text{Br})/Q(^{81}\text{Br})]^2 \approx 1.43$.[139] As long as the temperature is greater than about 1/2 of the Debye temperature, θ_D, there is roughly a $1/T^2$ dependence of T_1(X), (X = $^{35/37}$Cl, $^{79/81}$Br, ^{127}I).[139] Kanda observed a correlation between decreasing $^{79/81}$Br T_1 values and increasing δ(Br) (Figure 7) and concluded that the data were suggestive of a common origin, although a source was not provided.[128]

Several theories were developed to explain the remarkably short halogen T_1 values. While it was clear that a time-dependent EFG was present at the relevant nuclear site, early consensus regarding the origin was not found. As mentioned earlier, Y–M proposed that the time-dependent EFG was generated by the distorted ions (due to M–X covalent bonding) coupling to thermal lattice

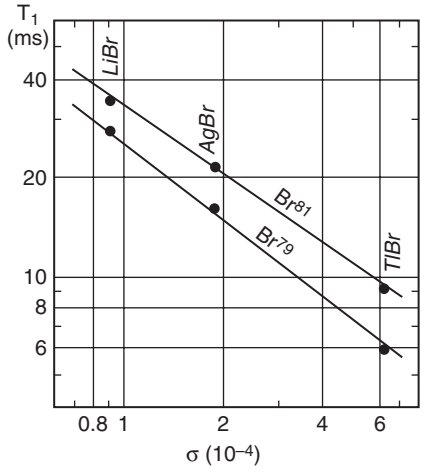

Figure 7 Relation between T_1 and bromine chemical shift of LiBr, AgBr and TlBr. From Ref. 128. Reproduced by permission of the *Institute of Pure and Applied Physics*.

vibrations.[130] Bloembergen and Sorokin agreed this would cause a reduction, but did not quantitate this statement for the CsBr single crystal used in their study.[131] The observed $T_1(^{81}Br)$ value of RbBr was not well accounted for using the covalent Y–M model.[41] It was discovered, however, that van Kranendonk's model,[132] while still yielding T_1 values too large by a factor of 10, was preferred.

Wikner et al. performed a detailed study of relaxation using single crystals of many alkali halides (see Table 11) and concluded that neither the Y–M nor the vK model performed very well at rationalizing halide T_1 values. The authors proposed a model which took the vK model and augmented it with the anti-shielding factor proposed by Sternheimer,[115] as well as an additional consideration regarding induced dipole polarization (which is associated with optical lattice vibrations). This model still did not account fully for all measured T_1 values. A possible explanation for this discrepancy is outlined below and involves an inadequate description of the lattice vibrational spectrum.[140–142] As well, the K–Y (ion overlap) model[40] was shown[133] to not reproduce the measured T_1s for all halogen nuclei in the alkali metal halides. Yamagata proposed that the vK electrostatic model could describe the halogen relaxation of the light metal halides, but the model was required to include overlap effects to properly treat the heavier metal halides. A semi-quantitative model was eventually arrived at after considering the temperature and pressure dependencies of the measured T_1 values (*vide infra*).

The multipole NMR approach has also been used to calculate the quadrupolar spin echo time response for a variety of pulse sequences for a single crystal of KBr.[143] The findings were experimentally verified using ^{81}Br SSNMR experiments.

4.1.3. Signal intensities and linewidths

For the cubic alkali bromides and iodides, the observed signal intensities of the $^{79/81}$Br and ^{127}I resonances were less than would be expected, even if a ''perfect'' single crystal was used.[138,144] The lack of signal intensity was explained as being due to the interaction between the large Q and the EFG generated at that point arising primarily from dislocations and thermal lattice vibrations. This interaction causes the ST to be broadened such that they are not detectable. The observed signal is from the CT only, as it is not affected by the QI to first order. It was not until the advent of pulsed techniques that the ST could be observed directly without difficulty, although it was noted by Bonera et al. that upon plastically deforming KBr and NaBr single crystals, they could no longer observe the ST even when using pulsed techniques.[145]

Under MAS conditions, it has been observed that as long as the magic angle is set correctly,[146] the NMR linewidth of the halogen decreases relative to the static case in microcrystalline powders without exception.[137] The reduction in linewidth does not appear to depend strongly on the relative magnetogyric ratios, but rather on the combined atomic masses of the atoms in the sample. For example, the ^{35}Cl linewidth of LiCl is reduced by a factor of about 18, while the ^{127}I linewidth of CsI is reduced by 1.5. The average reduction due to MAS is ca. 5–10.

4.1.4. Pressure and temperature dependence of δ_{iso}(X), T_1(X), and linewidth

Using powdered samples of RbX (X = Cl, Br, I) and CsX (X = Br, I) and ^{35}Cl, ^{81}Br and ^{127}I SSNMR experiments, it was demonstrated by Baron that a positive halogen δ_{iso} results when alkali metal halides are subjected to a uniform pressure at constant temperature.[42] Baron also studied the phase transitions for the RbX series and concluded from the data that the covalent (Y–M) model for rationalizing chemical shifts was inadequate. It was seen that the K–Y model fared better at predicting the trend in halogen chemical shifts, once NNN effects were included. This mirrors the conclusions of Hafemeister and Flygare during their computational study of chemical shifts of many alkali metal halides as a function of pressure.[134] Baron also noted that while the Y–M model improved the results of the K–Y model, it could not account for the observations alone. Lastly, it was observed that the NMR line shapes (^{35}Cl, ^{81}Br, ^{87}Rb, and ^{127}I), widths and intensities changed only upon the initial application of pressure, or when a sample was passing through a phase transition, and remained constant otherwise.

Ngai measured the temperature dependence of δ_{iso}(^{81}Br, ^{127}I) for the full series of alkali metal bromide and iodide powders, as well as the corresponding thallium salts.[147] The author observed a consistent positive shift with respect to increasing temperature and devised a reasonable model to account for the anion chemical shift trend of the alkali metal halides at room temperature (recall Figure 6). For the room temperature trend, it was reasoned that the ion overlap model of K–Y, with the inclusion of NN and NNN, satisfactorily explained the halogen shift trends for light alkali metal halides (i.e. LiX, NaX, KX). As one goes from LiX to CsX, the effects denoted by Y–M (covalent model) become increasingly important, but are not expected to dominate the ion orbital overlap effect in the alkali metal halides (Figure 8). Ngai reasoned that the systematic positive chemical shift of the halogen nuclei as a function of increasing temperature was due primarily to increased thermal lattice vibrations which enhanced the orbital overlap and hence the paramagnetic contribution to shielding.

Marsh and Casabella induced elastic strain upon single crystals of NaCl and NaBr by applying static pressure (up to 6.9 MPa) and noted, as expected, that the ^{35}Cl and ^{79}Br NMR lineshapes broadened and became less intense. The authors determined that the purely ionic model of vK was inadequate to describe the changing field gradients at the chlorine and bromine nuclei with respect to changing pressure. It was concluded that ion orbital overlap between nearest and NNN atoms was a satisfactory model to rationalize their observations and that pure covalent effects did not need to be included.[148] The effects of static elastic strain on chlorine SSNMR spectra were observed to determine the gradient-elastic tensors for LiCl and RbCl by Hackeloer and Kanert.[149]

Allen and Weber demonstrated that increasing temperature will enhance the likelihood of cationic vacancies diffusing through the lattice.[141] This is typically observed by a deviation in the T_1 versus T plot from the T^{-2} behaviour noted earlier. This change in behaviour is accompanied by a decrease in the halogen NMR signal linewidth (Figures 9 and 10).[141] This characteristic temperature

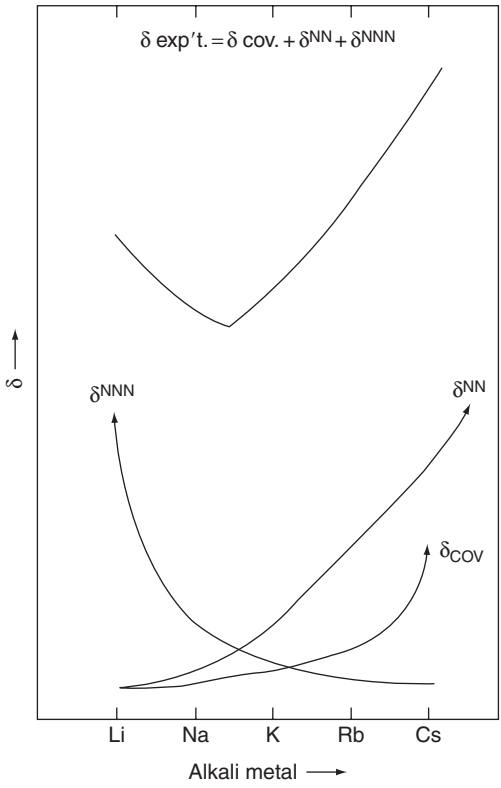

Figure 8 A schematic plot showing the dominant effects on the bromine chemical shifts as one changes the alkali metal from Li to Cs in the alkali metal bromides. See text for discussion (NN = nearest neighbours; NNN = next nearest neighbours). From: Ref. 147. Reproduced by permission of *Elsevier Ltd*.

dependence of T_1 at higher temperatures may be used to determine lattice defect migration activation energies, as demonstrated in single crystals of NaCl and NaBr.[150–153]

At low temperatures, assuming the effects of paramagnetic impurities to be negligible, the temperature dependence of halogen T_1 values will also no longer be described by a T^{-2} dependence, although the mechanism behind the origin is different than outlined above (at low temperatures ($\sim 0.02\theta_D$) the T_1 dependence is roughly T^{-7}).[154] Tarr et al. observed this low temperature deviation using $^{79/81}$Br and ^{127}I SSNMR experiments on single crystals of NaBr, LiBr, NaI, and RbI.[155] Niemelä and Tuohi also observed this deviation using single crystals of RbBr.[156] What was strikingly different in each of the above cases was the conclusion that each group arrived at regarding the origin. Of the three theoretical models (i.e. vK, Y–M, K–Y), the electrostatic vK model was the best at describing the temperature-dependent relaxation in RbBr, but was completely inadequate at describing the observations in all other systems. The shortcoming of the vK model is likely the assumption that acoustic-phonon relaxation dominates optical-phonon relaxation

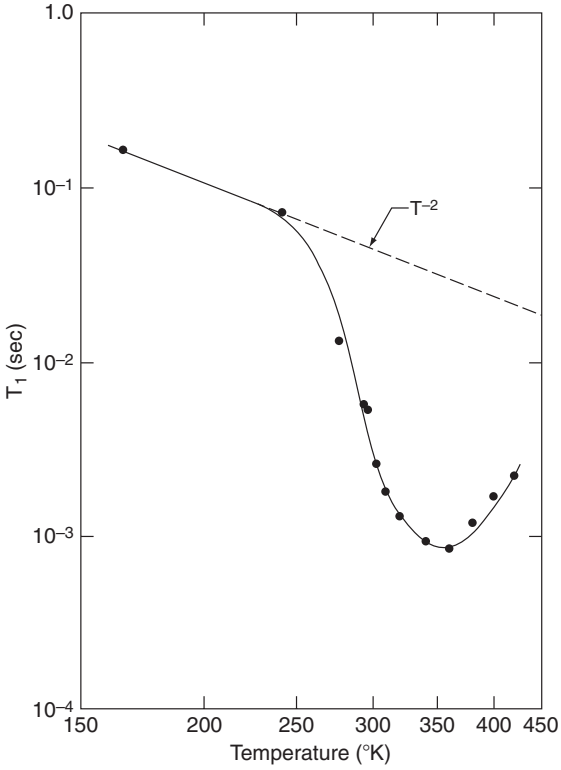

Figure 9 Temperature dependence of the relaxation time T_1 for ^{81}Br in a single crystal of LiBr. From Ref. 141. Reproduced by permission of the *American Institute of Physics.*

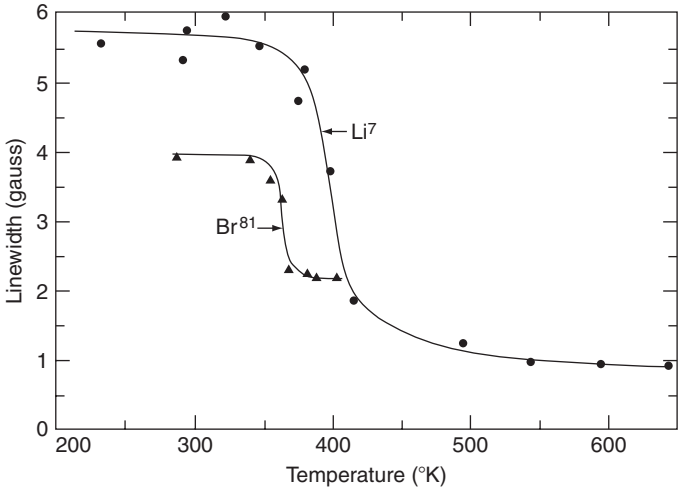

Figure 10 Narrowing of ^{7}Li and ^{81}Br resonances in a single crystal of LiBr as a function of temperature due to translational diffusion of lithium nuclei. From Ref. 141. Reproduced by permission of the *American Institute of Physics*.

at all temperatures (in fact, the vK model made no reference to optical lattice vibrations). It is postulated that even at low temperatures, relaxation via the coupling of Q to optical-phonons is of importance.[157] It was first pointed out by Wikner et al.[139] and expanded upon by Weber and Allen in their studies on the temperature dependence of the ^{7}Li and $^{79/81}$Br T_1s of LiBr (they also studied KF, NaF, KI, and NaI) that accurate descriptions of relaxation as a function of temperature are not likely when one uses a poor description of the lattice vibrational spectrum.[140–142] It was tentatively concluded that a reasonable (but not overly detailed) description of the optic vibrational branch is needed to describe the T_1 behaviour as a function of temperature when the mass ratio between the metal and halogen deviates greatly (ca. > 3) from unity, but would not be required when the mass ratio was near one.

4.1.5. Effects of lattice perturbations

It was established early that $^{79/81}$Br and ^{127}I SSNMR experiments on alkali halide single crystals and microcrystalline powders were extremely sensitive probes of crystal lattice imperfections. It was demonstrated by Watkins and Pound that KBr and KI single crystals of the highest possible quality possessed enough lattice strain to diminish the intensity of the CT significantly and either completely obscure (KBr) or greatly diminish (KI) the signal intensity due to the STs.[138,144] The lattice strain was attributed largely to the presence of dislocations, rather than the presence of vacancies or intrinsic impurities.[158] Induced lattice imperfections may result from: (i) deformations, which could be either elastic[148] or plastic[138,144,158–161] in nature; (ii) doping, which may give rise to any combination of lattice vacancies, interstitials and foreign atoms;[158,162–164] and (iii) increasing temperature, which as mentioned before typically serves to increase cation vacancy diffusion rates.[141,162] It has generally been established that a deformed or doped sample will exhibit a decreased halogen T_1, as well as decreased signal intensity and increased linewidth. The mechanism responsible for the changing parameters can be attributed to an increase in the quadrupolar interaction at the nuclear site, an effect which is usually enhanced by a partial deformation of the ion.

By measuring the shape of the quadrupolar echo in single crystals of RbBr and RbI, Mehring and Kanert showed that a quadrupolar distribution function could be determined.[161] Once this function was known, the authors could quantitate the dislocation density as a function of shear stress[160] and presented a model to determine the density of point defects and dislocations in the lattice.[165] It was concluded that the EFG in undeformed RbBr single crystals was due to point defects, while plastic deformation induced dislocations. Discussion pertaining to sample doping is delayed to Section 4.3.2.

Hon and Bray discussed the effects of neutron irradiation damage in cubic lattices using ^{81}Br SSNMR experiments on a KBr single crystal and ^{127}I SSNMR (as well as ^{7}Li and ^{23}Na) experiments on LiI, NaI, and KI.[166–168] They provided detailed descriptions of the line broadening mechanisms that would be present, their origins, their effects on resonance linewidths and T_1 values and established that lattice defects after neutron irradiation are clustered rather than random.[169]

4.2. Solid-state chlorine-35/37 nuclear magnetic resonance

As mentioned above, the alkali metal chlorides have cubic symmetry about the chlorine nucleus which requires that the EFG to be essentially zero in a perfect crystal. This results in CT NMR spectra with narrow lines that are free of quadrupolar effects. As the environment around the chlorine nucleus is transformed to lower symmetry, second-order quadrupolar effects begin to be observed, leading to broadened CT lines with quadrupolar line shapes. The broadening of the signals in chlorine CT NMR spectra as the quadrupolar effects become more significant is the most serious limitation to the types of materials which can be studied with typical SSNMR methods.

In the sections that follow, we discuss in detail specific applications of chlorine SSNMR to a range of compounds. For example, recent studies have demonstrated the utility of chlorine SSNMR as a materials characterization tool. Brinkmann et al.[170] used the technique, along with ^{109}Ag and ^{125}Te SSNMR to study ion dynamics in three polymorphs of Ag_5Te_2Cl while Czupiński et al.[171] used chlorine SSNMR along with a variety of other techniques, including differential scanning calorimetry, dilatometry, and infrared measurements, to study the dynamic properties and phase changes in 2-cyanopyridinium perchlorate. Chlorine SSNMR has also found applications in the study of materials such as sodalites and glasses (Tables 3 and 5).

4.2.1. Simple salts

In addition to the alkali metal salts, there are other simple salts which have been popular materials to study by chlorine SSNMR (Table 2). Ammonium chloride, for example, also has an EFG of essentially zero at the chlorine nucleus and has been examined in multiple studies. The salt was a subject of one of the very early halogen SSNMR studies, carried out by Itoh and Yamagata, in 1962.[172] In their study, the temperature dependence of the ^{35}Cl chemical shift and T_1 times of ammonium chloride powder were monitored. The chemical shift at room temperature was found to be 76 ppm (w.r.t. dilute NaCl(aq)) and the T_1 trend was found to change sharply at the temperatures where the structure undergoes a phase change. Study of this salt continued throughout the late 1960s and early 1970s with multiple publications discussing the pressure dependence of T_1.[173,174] Ammonium chloride was also studied by Weeding and Veeman, and Lefebvre,[135,136] with both groups noting a ^{35}Cl chemical shift of ca. 74 ppm (w.r.t. 1 M NaCl(aq)).

Solid-state chlorine NMR data are available for several other simple metal salts. Silver chloride was studied by Kanda;[128] its chemical shift was reported as intermediate between that of sodium and cesium chlorides. Hayashi and Hayamizu also included this compound in a study along with alkali metal and cuprous halides, reporting $\delta_{iso}(^{35}Cl)$ as −12.82 ppm (w.r.t. solid KCl), and found a negative temperature dependence of the chemical shift. Several studies in the mid-1990s by Yamanishi, Michihiro, and co-workers[150–153] reported how the temperature dependence of T_1 was used to determine the activation energy of the Ag^+ defect migration in AgCl.

Chlorine NMR parameters for thallium chloride were also measured by Kanda,[128] who reported a chemical shift of −2.5 ppm (w.r.t. saturated NaCl (aq)). This chemical shift was confirmed by Günther and Hultsch[175] in their 1969 study of cuprous halides, which included the salt for comparison purposes. The chlorine vacancy diffusion within salts was also examined in the early 1970s by Samuelson and Ailion,[176] through measurement of the temperature dependence of the chlorine T_1 and T_2^* relaxation times.

Copper chloride was first studied by chlorine SSNMR in 1968 by Günther and Hultsch[175] at 1.0 T. Although the study was focused primarily on the ^{63}Cu SSNMR of cuprous halides, several ^{35}Cl isotropic shifts were reported, including that of CuCl as −93 ppm (w.r.t. saturated NaCl(aq)). In the late 1970s, Becker[177] re-examined this material, and found that the chlorine chemical shift decreased linearly with increasing temperature. The material was also included in Hayashi and Hayamizu's comprehensive 1992 study of alkali metal, cuprous, and silver halides.[178] Magic angle spinning experiments were used to accurately determine a ^{35}Cl chemical shift of −127.23 ppm (w.r.t. solid KCl) for CuCl, and the temperature dependence of the chemical shift was confirmed.

4.2.2. Hydrochloride salts

Hydrochloride salts have been popular materials to study, particularly in recent years, as evidenced by the reports of Bryce et al.,[179–181] Chapman and Bryce,[182] and Hamaed et al.[183] (see Figure 11 for an example). Data are summarized in Table 4. To the best of our knowledge, the first chlorine SSNMR report for a powdered hydrochloride salt appears to be that of Pines and co-workers, who studied cocaine hydrochloride in 1995.[184] The study utilized multiple techniques to study the hydrochloride salt, including ^{14}N NQR. The chlorine-35 SSNMR experiment was carried out at 7.0 T using a Hahn-echo pulse sequence, and a chlorine-35 C_Q of 5.027 MHz was reported. To avoid the intensity distortions that result from a finite pulse applied to a broad line shape, a variable frequency offset approach, in which the frequency was stepped in 2 or 4 kHz increments over the entire spectral width, was used to acquire the spectrum.

Several organic hydrochloride salts were included in a 2001 study by Bryce et al.[181] and the utility of chlorine SSNMR in examining hydrogen bonding environments was demonstrated. The study examined both the chlorine-35 and chlorine-37 SSNMR spectra of L-tyrosine hydrochloride, L-cysteine methyl ester hydrochloride, L-cysteine ethyl ester hydrochloride and quinuclidine hydrochloride obtained at 18.8 and 9.4 T. Several methods were used for acquisition of the spectra including Hahn-echoes for both MAS and stationary experiments and QCPMG experiments on stationary samples. Complete EFG data were reported for all four compounds, while complete CSA data were also provided for L-cysteine ethyl ester hydrochloride (Tables 4 and 8). The parameters were extracted through simulation of the spectra using the WSolids package,[185] which is currently one of the programs of choice for quadrupolar line shape simulations.

Gervais et al.[111] also studied selected amino acid hydrochlorides, using ^{13}C, ^{14}N, ^{15}N, ^{17}O, and ^{35}Cl SSNMR spectroscopy in 2005. EFG and isotropic chemical shift data were reported for glycine hydrochloride, L-valine hydrochloride and

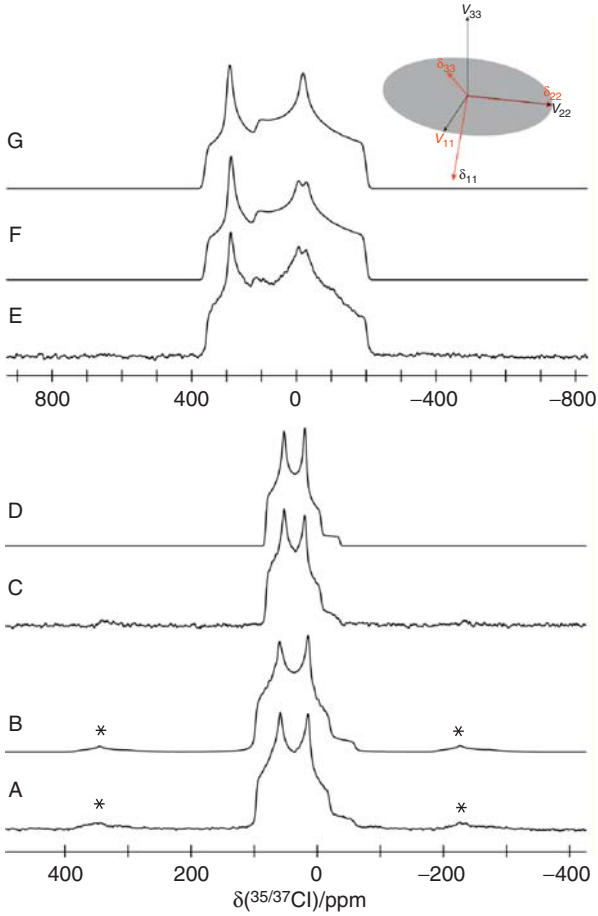

Figure 11 Solid-state chlorine NMR spectra of L-lysine hydrochloride. Experimental spectra are shown in (A) ^{35}Cl at 11.75 T and (C) ^{37}Cl at 11.75 T. The ^{35}Cl NMR spectrum of a stationary sample obtained at 11.75 T is shown in (E). A hyperbolic secant spin-echo sequence was used to acquire the spectra. Simulated spectra are shown above each experimental spectrum. The effects of CSA are evident in the spectrum of the stationary sample (E); shown in trace (G) is the simulated spectrum obtained with an isotropic CS tensor. The relative orientation of the EFG and CS tensor PASs are shown in the inset. From Ref. 179. Reproduced by permission of the *American Chemical Society.*

L-glutamic acid hydrochloride, as determined through fits of the static and MAS spectra, done using the DMFIT program.[186] In addition, the authors[111] reconfirmed the values obtained previously[181] for L-tyrosine hydrochloride. While no experimental CSA data were reported, first principles calculations were done, predicting small CS tensor spans ranging between 78 and 157 ppm.[111]

The recent interest in applying chlorine-35/37 SSNMR spectroscopy to amino acid hydrochlorides stems from their biological importance, as they serve as simple models for chloride ion binding sites in ion channels. We have reported

and analysed the NMR spectra for most of these hydrochloride salts (see Figure 11 for an example).[179,180,182] In previous studies, complete CS tensor parameters were not given in most cases. The chlorine CS tensor data which have been reported more recently were reliably extracted in large part due to the 21.1 T magnetic field used.[179,182] Despite the structural similarities within the amino acid family, the sensitivity of both the EFG and the CS parameters to the small changes in chloride bonding environments was demonstrated by the range of parameters observed. For example, the magnitudes of chlorine-35 quadrupolar coupling constants range from 7.1 to 2.03 MHz, as summarized, along with the CS span data, in Figure 12.[179–182] The value of −7.1 MHz reported by Chapman and Bryce[182] for aspartic acid hydrochloride is the largest chlorine-35 C_Q observed for an organic hydrochloride. The chlorine isotropic chemical shifts for these salts, summarized in Figure 13, were found to lie in the range of 90–106 ppm with only proline hydrochloride and serine hydrochloride as exceptions.[179,180,182] A correlation between the magnitude of $C_Q(^{35}Cl)$ in amino acid hydrochlorides and the hydropathy of the amino acid has been reported.[179] Chlorine SSNMR could potentially provide insight into the chloride hydrogen bonding environment in peptide hydrochlorides for which crystal structures are unavailable.

Hamaed et al.[183] have also utilized ^{35}Cl SSNMR as a method to study biologically important systems, in their study of hydrochloride salts of four local anaesthetic pharmaceuticals. Complete CSA and EFG data were reported for these materials, and subtle changes in structure were found to drastically change both sets of parameters. In addition, the authors demonstrated that chlorine-35 SSNMR is sensitive enough to distinguish between polymorphs of the same material. Polymorphs of both monohydrated lidocaine and monohydrated bupivacaine could be easily distinguished due to significant differences in their chlorine NMR spectra. The authors propose that chlorine NMR could be used as a method to rapidly identify and distinguish polymorphs of these types of materials. Impressively, the authors demonstrate cases where the ^{35}Cl NMR experiments are more useful than X-ray diffraction and ^{13}C NMR for characterizing the materials. One potential limitation of the technique for identifying polymorphic impurities is that its sensitivity depends on the line width (and therefore the QI) of the impurity, a factor which cannot be controlled. For example, a small fraction of an impurity with a chloride ion in a cubic or near-cubic site will be easily detected by ^{35}Cl NMR; however, if the chlorine is subject to strong quadrupolar coupling, it will be more difficult to detect in the NMR experiment.

In 2003, Frydman and co-workers[187] studied a mixture of L-ornithine/L-lysine hydrochloride using chlorine SSNMR to demonstrate the potential of using differences in relaxation properties to resolve non-equivalent chlorine sites in solid samples. The relaxation-assisted separation (RAS) technique was shown to distinguish between the overlapping ^{35}Cl SSNMR signals of a 1:1 mixture of the two hydrochlorides at 14.1 T. The method is therefore valuable in distinguishing between different chlorine sites, provided they have sufficiently different relaxation properties. The technique could be particularly useful in cases where MAS experiments are not feasible due to large line widths.

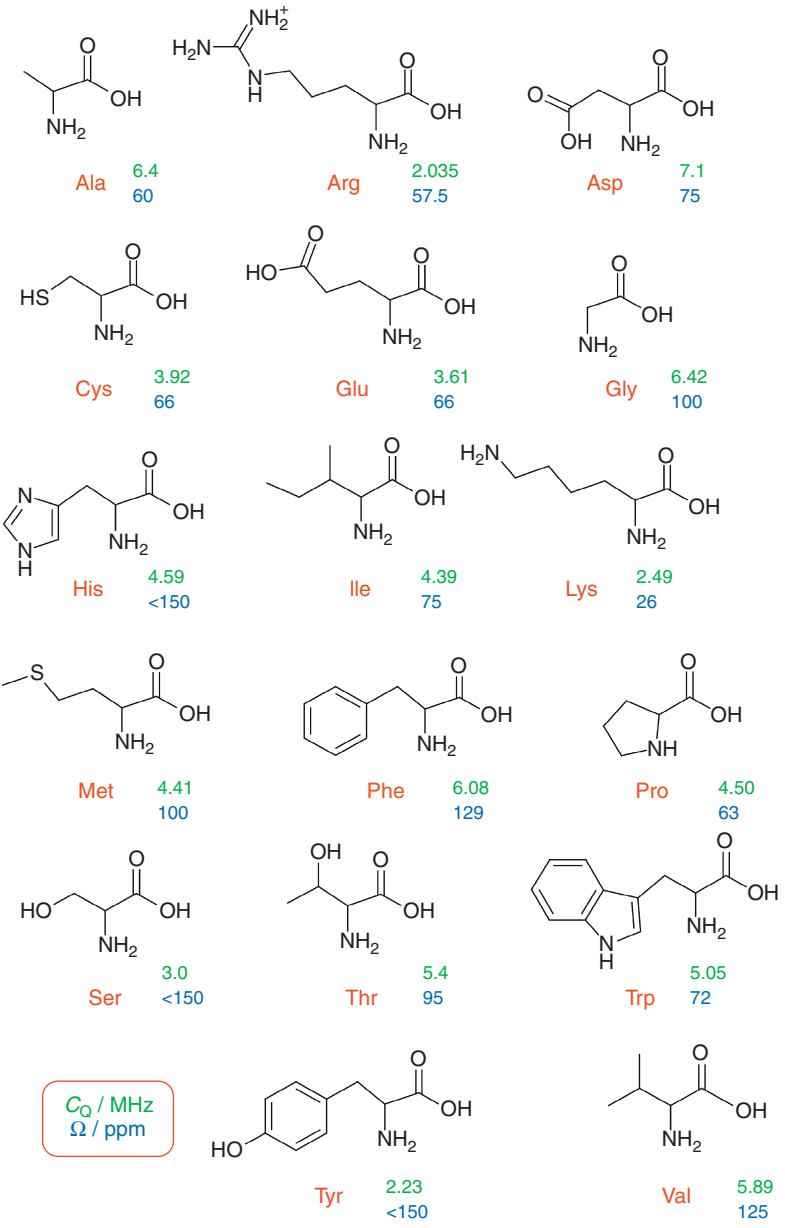

Figure 12 Summary of ^{35}Cl C_Q and Ω data for the amino acid hydrochlorides. Data from Refs. 179–182.

Several alkylammonium chlorides have been analysed using chlorine SSNMR. In 1994, Hattori et al.[188] observed the temperature dependence of the ^{35}Cl quadrupolar coupling constant of $C_4H_9NH_3Cl$, which ranged from 0.85 to 1.2 MHz over a temperature range of 300–480 K. In 2003, Honda[189] published a study

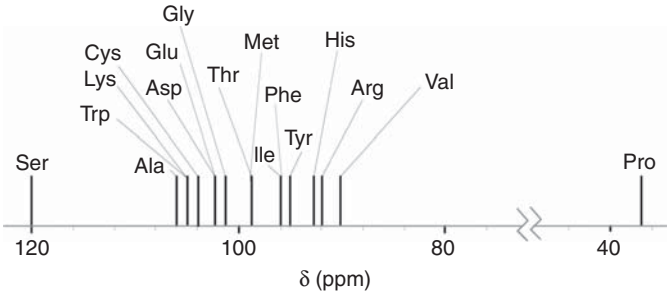

Figure 13 Summary of the chlorine-35 isotropic chemical shifts for solid amino acid hydrochlorides. Reproduced from Ref. 182 by permission of the *PCCP Owner Societies.*

examining seven *n*-alkylammonium chlorides. Selected deuterated samples of the *n*-alkylammonium salts were also studied, and it was found that the ^{35}Cl C_Q was consistently lower in these salts, compared to their non-deuterated counterparts. In addition, the chlorine-35 quadrupolar coupling constant was found to follow an ''even–odd'' trend in the highest temperature phase of these salts of general formula n-$C_xH_{(2x\ +\ 1)}NH_3Cl$. The ''even'' salts ($x = 8$ and 10) had significantly larger coupling constants compared to those of the ''odd'' salts ($x = 5, 7, 9$), with all falling in the range 1.0–1.5 MHz. Point charge EFG calculations, based on known crystal structures, were used to explain this trend.

4.2.3. Alkaline earth chlorides

The alkaline earth chlorides, and their pseudo-polymorphs (i.e., their hydrates), have been studied by chlorine SSNMR. The first study of these salts was carried out by Lefebvre[136] in 1992. While several isotropic chlorine chemical shifts were reported, corresponding EFG data were not provided. The only anhydrous sample to have its chemical shift reported was $SrCl_2$ ($\delta_{iso}(^{35}Cl) = 140.8$ ppm w.r.t. 1.0 M NaCl(aq)), in which the chloride is at a site of cubic symmetry. Multiple apparent chemical shifts were reported for several of the hydrate salts; however, it is now clear that there were problems with the interpretation of these spectra. It was hypothesized, in our previous review,[11] that the reported chlorine chemical shifts for the alkaline earth metal chloride hydrates studied, $MgCl_2{\cdot}6H_2O$, $CaCl_2{\cdot}2H_2O$, $SrCl_2{\cdot}6H_2O$ and $BaCl_2{\cdot}2H_2O$, actually refer to the two peak maxima from the second-order quadrupolar powder patterns and are not true chemical shifts. This hypothesis was confirmed by Bryce and Bultz[112] in a 2007 study, which analysed many of the hydrates. In that study, $^{35/37}$Cl SSNMR spectroscopy was applied at 11.75 and 21.1 T to study a series of alkaline earth chloride hydrates. Complete CS and EFG tensor parameters were reported (see Tables 2 and 8). Chlorine-35 quadrupolar coupling constants range from zero in $SrCl_2$ to 4.26 ± 0.03 MHz in calcium chloride dihydrate. Shown in Figure 14 is an example of the spectra obtained for barium chloride dihydrate, which features two crystallographically distinct chlorine sites. In addition, Bryce and Bultz demonstrated the sensitivity of chlorine SSNMR to pseudo-polymorphism through the acquisition of spectra corresponding to different hydration states of

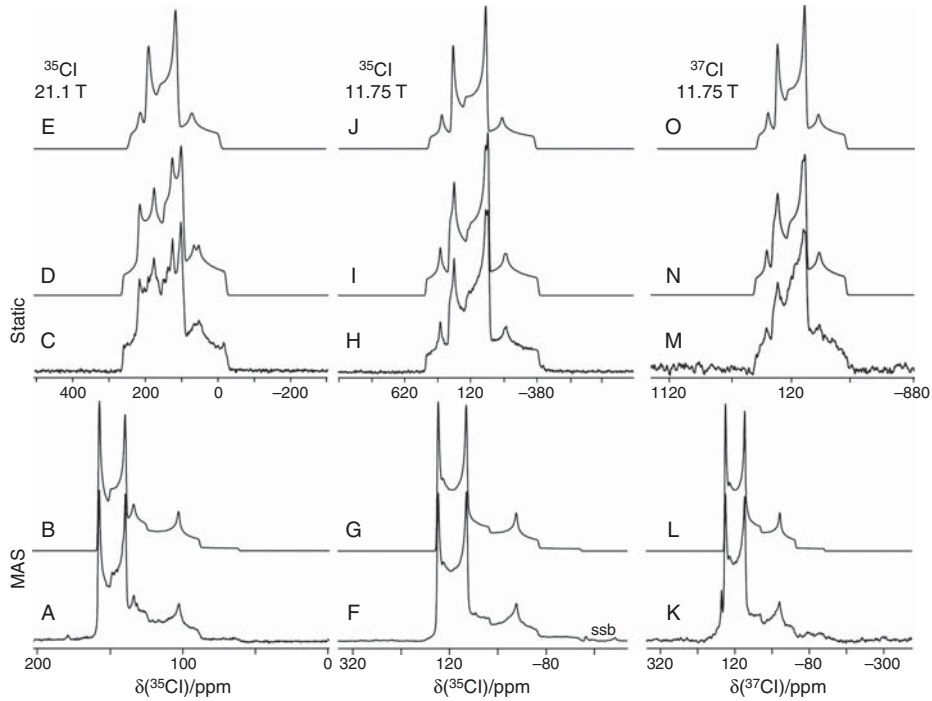

Figure 14 Chlorine NMR spectra of solid powdered $BaCl_2 \cdot 2H_2O$ obtained at 11.75 and 21.1 T. Spectra acquired under MAS and static conditions for both ^{35}Cl and ^{37}Cl are shown. Simulated spectra are shown above the experimental spectra. Also, spectra of stationary samples (top) have been simulated with the span of the CS tensor set to zero (see parts E, J and O) to demonstrate the importance of the anisotropy of the chemical shift tensor in obtaining accurate fits. Reproduced by permission of *Wiley-VCH* from Ref. 112.

strontium chloride. The spectra of the anhydrous, dihydrate, and hexahydrates of this salt were shown to be easily distinguishable using chlorine SSNMR, as each pseudo-polymorph is characterized by significantly different EFG and CS parameters. This may be seen in Figure 15, which depicts the ^{35}Cl SSNMR spectra of a mixture of the dihydrate and hexahydrate pseudo-polymorphs. The spectra also demonstrate how the kinetics of a reaction, in this case the interconversion of hydrates due to MAS sample heating, could be monitored using chlorine SSNMR.

Chlorine SSNMR parameters have been reported for other selected anhydrous alkaline earth chlorides. Stebbins and Du[190] acquired a ^{35}Cl NMR spectrum of $BaCl_2$ in their study of chlorine-containing glasses, and reported two chlorine sites with chemical shifts of 124 and 219 ppm (w.r.t. 1 M NaCl(aq)) and C_Q values of 3.5 and 3.95 MHz, respectively. In a similar glass study, Stebbins and co-workers[191] analysed $CaCl_2$, reporting a chemical shift of 122 ppm (w.r.t. 1 M NaCl(aq)) and a C_Q of 2.1 MHz. On the basis of the chemical shifts now known for chloride ions,[112] it seems likely that the chemical shift of 2880 ppm reported[190] for $AlCl_3$ is erroneous.

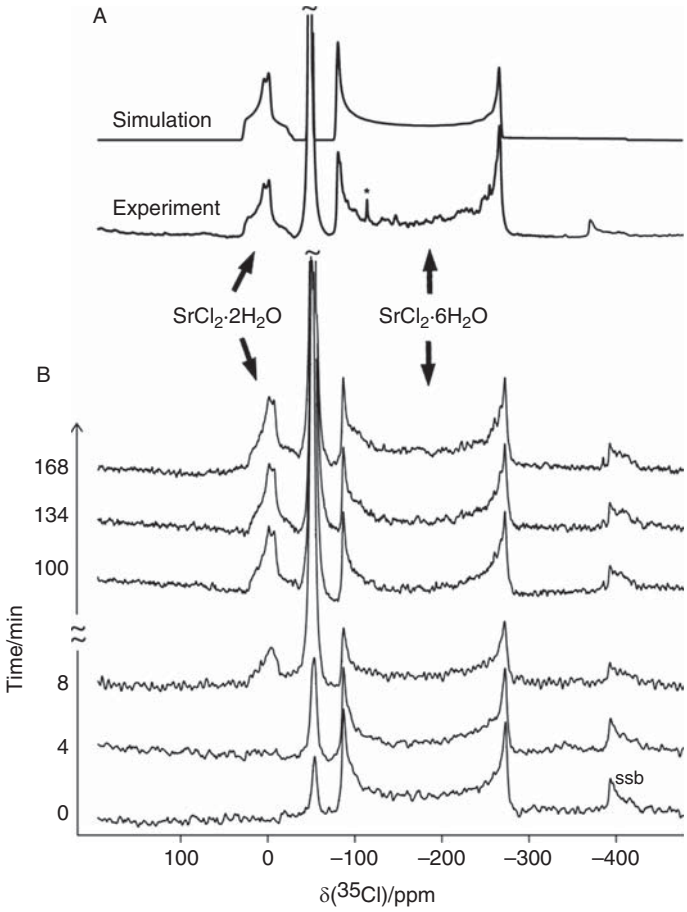

Figure 15 (A) Experimental and simulated chlorine-35 solid-state MAS NMR spectra of a mixture of the hydrates of $SrCl_2$. (B) ^{35}Cl MAS NMR spectra of the mixture as a function of time. The sample is heated due to the MAS and the hexahydrate gradually loses water to form the dihydrate. $\mathbf{B}_0 =$ 11.75 T.

Multiple studies on *tris*-sarcosine calcium chloride ($(CH_3NHCH_2COOH)_3{\cdot}CaCl_2$) have been performed due to its use as a model compound for the study of a second-order ferroelectric phase transition. The majority of the studies were carried out by Michel and co-workers[193–197] in the late 1980s and early 1990s. In their first report, ^{35}Cl single-crystal NMR studies were performed and EFG tensor data reported, with a C_Q value of 4.10 MHz at room temperature. Later reports, using both single crystal and powdered samples, described the temperature dependence of C_Q and T_1 for both the paramagnetic and ferroelectric phases, with the transition to the latter occurring at a temperature of 131.5 K. The variation in the ^{35}Cl quadrupolar frequency over the range of 120–260 K was reported to be 0.75 kHz K^{-1}. The authors emphasized the importance of N–H$\cdots$Cl hydrogen

bonds in determining the EFG. Bryce et al.[181] later studied this material using $^{35/37}$Cl SSNMR, finding a slightly smaller $C_Q(^{35}Cl)$ of 4.04 MHz.

4.2.4. Perchlorates and Chlorates

The perchlorates (ClO_4^-) became the subject of analysis by chlorine SSNMR in the late 1980s (see Table 6). Although the chlorine atom in perchlorates lies in a high-symmetry pseudo-tetrahedral environment, the EFG is not required to be zero at Cl if the salts are non-cubic. The first study was published in 1986 by Jurga et al.[198] and included static and MAS chlorine NMR spectra of some multimethylammonium perchlorates. See also the associated NQR study by the same group.[199] Three alkali metal perchlorates were studied under stationary conditions at 7.04 T by Tarasov et al.[200,201] in the early 1990s. This is an impressive study which has been overlooked in subsequent chlorine SSNMR work. Complete quadrupolar data were reported with $C_Q(^{35}Cl)$ values of ~0.63, 0.60, and 0.51 MHz for cesium, rubidium, and potassium perchlorates, respectively, at room temperature. Variable temperature experiments were also reported, and a particularly detailed account was provided for $CsClO_4$.[200] Chemical shift anisotropy, however, was not included in the analysis. In 1999, Skibsted and Jakobsen[202] published an extensive study of solid perchlorates, which included those compounds studied by Tarasov and co-workers along with several others. The study was carried out on powdered samples, using static, MAS and SATRAS techniques (see Figure 16). Precise C_Q, η_Q and δ_{iso} values were determined for a total of 13 different perchlorates via simulation of the MAS spectra (Table 6). The $C_Q(^{35}Cl)$ values reported in this study for three perchlorates differed slightly from those previously reported by Tarasov,[200,201] with values of 0.585, 0.537, and 0.440 MHz for cesium, rubidium, and potassium perchlorate, respectively. These latter values are more reliable due to the fact that the satellite transitions were fit. Chemical shifts for the perchlorates are approximately 900–1000 ppm larger than for chlorides due to increased paramagnetic contributions to the shielding tensor in the former.

The only chlorate which has been significantly studied using chlorine SSNMR is sodium chlorate. Many early Zeeman-perturbed chlorine NQR studies feature analyses of this salt.[192,203–206] It is not surprising therefore, that one of the early chlorine-35 SSNMR studies was on this material, carried out by Kawamori and Itoh[204,207] in 1963. The authors studied a single crystal and reported the resonance frequency for multiple orientations. Bain and co-workers[208] re-examined a single crystal of $NaClO_3$ recently to confirm the validity of their theoretical approach for the exact calculation of combined Zeeman and quadrupolar interactions.

4.2.5. Chlorine chemical shift tensors

Chlorine chemical shift tensor information is summarized in Table 8. In the past decade, several reports of CSA measured using powdered samples have been published for chloride ions and some perchlorates. Although Creel reported a span of 4000 ppm for *p*-dichlorobenzene, there are large errors associated with the principal components (1000 ppm) and it was assumed that the EFG and CS

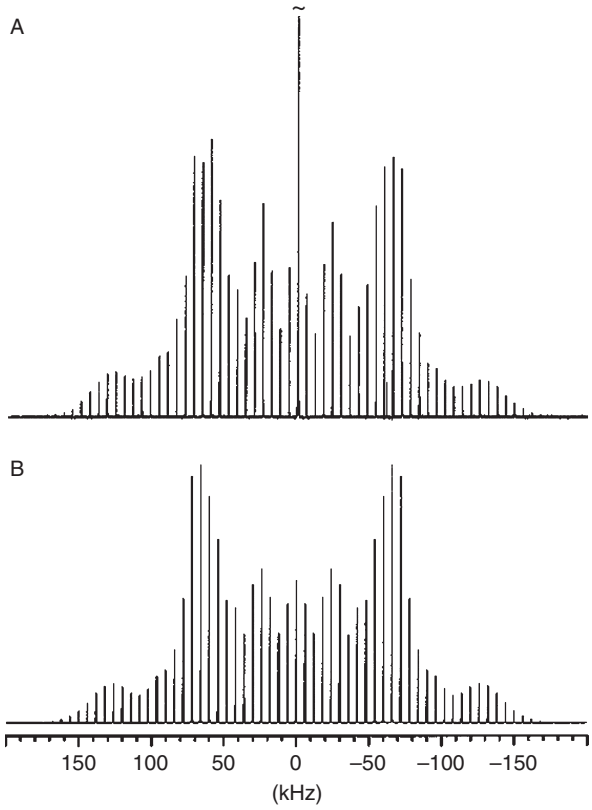

Figure 16 (A) Experimental ^{35}Cl MAS NMR spectrum of the central and satellite transitions for $(CH_3)_4NClO_4$ shown with the central transition cut off at 1/10 of its total height. (B) Simulated spectrum of the satellite transitions. From Ref. 202. Reproduced by permission of the *American Chemical Society*.

tensors were coincident.[209] The largest precisely measured span is 160(40) ppm for a polymorph of bupivacaine hydrochloride.[183] For other hydrochloride salts, spans range from, for example 26 ± 10 ppm for L-lysine hydrochloride to 129 ± 20 ppm for L-phenylalanine hydrochloride.[179] Accurate measurements of CS tensor magnitudes require consideration of the relative orientation of the EFG and CS tensors, and where this angular information is available, it is presented in Table 8. The large majority of recent CSA measurements were enabled by recording the $^{35/37}$Cl SSNMR spectra in magnetic fields of 18.8 or 21.1 T. Most reports also benefit from having acquired and simulated spectra at more than one magnetic field strength. This is important given the large number of parameters required to fit the spectra. A tentative correlation between the span of the chlorine CS tensor and the hydropathy of the amino acid in amino acid hydrochlorides has been proposed;[180] spans for the more hydrophilic salts tend to be smaller than those of hydrophobic salts. This may be qualitatively rationalized by considering

that the hydrophilic amino acids have more potential hydrogen bond donors, thereby creating a more symmetric environment at the chloride ion.

For alkaline earth metal chlorides, the chlorine CS tensor spans range from zero for cubic strontium chloride to 72 ± 15 ppm for calcium chloride dihydrate.[112] Shown in Figure 14 is an example of the effect of including CSA on line shape simulations of ^{35}Cl and ^{37}Cl SSNMR spectra of barium chloride dihydrate, which has two crystallographically non-equivalent chloride sites. Again, the successful determination of the chemical shift tensor magnitudes and orientations depended critically in this case on the use of two magnetic field strengths (one of them 21.1 T) and the simulation of line shapes for both isotopes.

Since there is generally no correlation between chlorine quadrupolar coupling constants and CSA, it is recommended that CS parameters be reported whenever possible since these carry additional information on electronic structure.

4.2.6. Applications of quantum chemistry

The use of quantum chemical calculations in concert with $^{35/37}$Cl NMR studies has also become increasingly prevalent in recent years, due to the improved accuracy of such calculations and the increasing availability of suitable software. In particular, standard methods for treating isolated molecules have been used in many studies (e.g. RHF or B3LYP based calculations using localized basis sets). In 2006, Bryce et al.[179] determined an optimal method and basis set combination for calculations of chlorine NMR parameters for amino acid hydrochlorides. The RHF method with the cc-pVTZ basis set on chlorine and the cc-pVDZ basis set on all other atoms in the system was found to produce excellent agreement with experimental quadrupolar coupling constants. Importantly, neutron diffraction structures were used to calibrate the methods, since knowledge of the proton positions around the chlorine atoms is very important in obtaining the best possible results. The B3LYP method with the aug-cc-pVDZ method on chlorine and the cc-pVDZ basis set on all other atoms produced chlorine CS tensor spans within experimental error. These optimized methods were subsequently applied to provide insights into polymorphic hydrochloride salts of pharmaceutical importance.[183] We emphasize the importance of accurate structures in such calculations.[179,180,182,183]

The above-mentioned optimal methods were also used in combination with experimental chlorine NMR data to refine the hydrogen-bonded proton positions in some amino acid hydrochlorides for which neutron diffraction data are unavailable.[180] The combined experimental–theoretical procedure provided proton positions which resulted in back-calculated values of the chlorine quadrupolar coupling constant typically within 15% of experiment. The values of Ω were found to be less sensitive to the proton positions.

For purely inorganic systems, such as alkaline earth metal chlorides, however, isolated molecule methods have been found to give poor agreement with experiment,[107] likely due to the extended ionic nature of the systems. Recently, the GIPAW method has become available in the CASTEP program,[108,109] which performs calculations using planewaves and can therefore mimic the crystal lattice environment in the solid state, and was found to yield excellent agreement

with experiment in a study of the ionic alkaline earth chlorides.[112] The trend in the chlorine-35 quadrupolar coupling constants was accurately reproduced by these calculations, although a systematic overestimation was noted, consistent with the results found by Gervais et al.[111] in their study of selected amino acid hydrochlorides. Given that most of the applications of chlorine, bromine, and iodine SSNMR will be for systems in which these elements exist as ions (rather than covalently bound), planewave methods will likely be a popular choice for calculating the relevant NMR parameters.

4.3. Solid-state bromine-79/81 nuclear magnetic resonance

Molecular beam resonance experiments performed on CsBr and LiBr resulted in a coarse determination of the $^{79/81}$Br nuclear magnetic moments.[210] Pound subsequently used solution-state $^{79/81}$Br NMR experiments (a negative solid-state experiment was attempted on a single crystal of KBr) to improve the precision of both magnetic moments by nearly an order of magnitude.[211] The first bromine SSNMR spectrum (^{81}Br) was acquired by Pound using a single crystal of NaBr.[126] Relative to $^{35/37}$Cl, far fewer literature reports contain $^{79/81}$Br SSNMR experiments. This can be attributed in large part to the increased relative line width of $^{79/81}$Br SSNMR spectra for a given EFG (Table 1). As greater external magnetic fields become available, the applications of $^{79/81}$Br SSNMR experiments should become more substantial. This section reports on the chemical and structural insights that have been gained as a result of $^{79/81}$Br NMR experiments, with a focus on solid-state experiments on diamagnetic systems.

4.3.1. Simple inorganic bromide salts, NH_4Br, AgBr, CuBr, TlBr

A highly detailed $^{79/81}$Br SSNMR study was carried out by Itoh and Yamagata.[172,212] They conducted variable-temperature (VT) $^{79/81}$Br SSNMR experiments to comment upon the structure and dynamics in three crystalline phases of NH_4Br (using both the powder and single-crystal forms). It was clearly demonstrated that the phase changes could be monitored by observing changes in bromine δ_{iso} and T_1 values. Using simple calculations, they connected changing NMR observables to structural change. For example, upon heating the sample through 411 K, the crystal structure undergoes a phase transition from a CsCl type lattice (phase II) to a NaCl type lattice (phase I). This transition does not alter the cubic crystal symmetry and the value of C_Q remains zero; however, the observed chemical shift decreases by about 100 ppm, while the T_1 value increases considerably. It was reasoned that the average number of covalent bonding interactions between the bromide and ammonium ions had decreased, a finding consistent with the changing crystal structure and Ramsey's theory of magnetic shielding.[30–33] The structural change likely enabled additional high-frequency ammonium ion re-orientational motions, thus averaging the $^{79/81}$Br–^{1}H dipolar interaction and leading to an increased T_1.

Upon cooling the sample through 235 K, a tetragonal phase is formed (phase III). The phase change was clearly quantified by the presence of a non-zero ^{81}Br C_Q value (5.5 $\pm$ 0.3 MHz); the first measured by a conventional high-field bromine

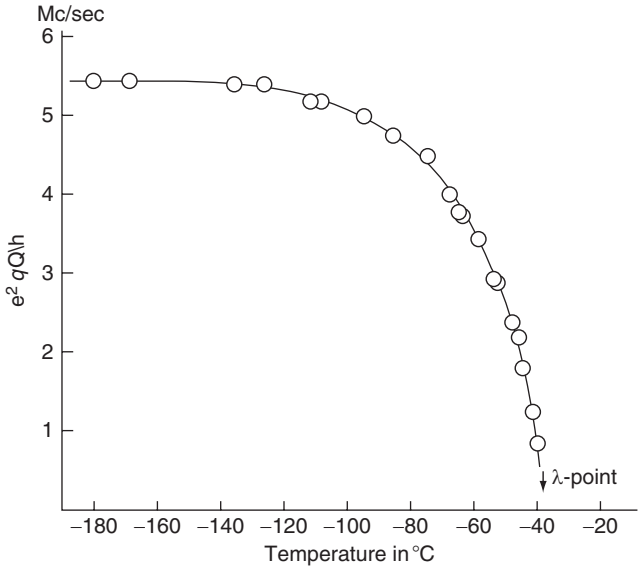

Figure 17 C_Q for ^{81}Br nuclei as a function of temperature for ammonium bromide in the ordered phase. From Ref. 172. Reproduced by permission of the *Institute of Pure and Applied Physics.*

SSNMR experiment. They also determine the temperature dependence of $C_Q(^{81}Br)$ in this phase (Figure 17) and attribute the dependence to the degree of crystalline ordering. They also provide a very detailed discussion pertaining to the origin of the quadrupolar relaxation and observed shifts. A subsequent study redetermined $C_Q(^{81}Br)$ and the ordering parameter in the tetragonal phase with increased precision.[213] A study on the deuterated version of this compound highlights the pressure and temperature dependencies of both the linewidth and spin–lattice relaxation time.[174]

Numerous $^{79/81}$Br SSNMR studies have been carried out on AgBr, many of which focused on the addition of dopants and their effects on the bromine SSNMR spectra (see below).[162,214–217] The temperature and time dependence of the ^{79}Br NMR signal of plastically deformed AgBr (both pure and NaBr doped) have also been discussed and related to the density of lattice dislocations.[216] The reader is referred to Table 9 for additional information on AgBr.

A single crystal of AgBr and powdered TlBr were amongst the samples used by Kanda[128] when establishing his covalent model for rationalizing observed shifts and T_1 values. TlBr was often used during formative double-resonance experiments.[218] Using single crystals of TlBr and TlCl, both isotropic J and dipolar-coupling constants have been measured through $^{79/81}$Br and $^{35/37}$Cl NMR experiments.[219] It was observed by Saito that the K–Y model does a very poor job at describing the observed chemical shift values in these types of systems. This conclusion was also reached by Ngai during a study of the temperature-dependence of the ^{81}Br chemical shift.[147] Ngai argued that covalent effects would have a significant impact

on the chemical shift and that the temperature-dependence of the bromine shift in these compounds is explained by considering the lattice vibrations that would induce lower degrees of orbital overlap as the temperature is increased.

Using ^{63}Cu, $^{79/81}$Br, and ^{127}I SSNMR on powdered CuBr, CuI and CuS, Herzog and Richtering determined the temperature dependence of the copper, bromine, and iodine linewidths.[220] In all cases, as the temperature was increased, the linewidth associated with the anionic species was found to increase, while that of the copper decreased. This was interpreted by the authors as being due to the onset of Cu^+ lattice mobility and enabled them to determine the activation energies for this process. Günther and Hultsch were the first to report the highly shielded shift and short $T_1(^{79/81}\text{Br})$ of this compound when they studied $T_1(^{63}\text{Cu})$ temperature dependence in CuX (X = Cl, Br, I) systems.[175] Spin–lattice relaxation values for lower temperatures (T = 78–300 K) in polycrystalline samples of CuBr were studied using ^{81}Br NMR and found to obey the expected T^{-2} temperature dependence while near or above θ_D, in accord with the pure ionic vK model.[154]

Becker and co-workers carried out a detailed study of the temperature dependence of the linewidth and T_1 values for the solid CuX series, using ^{35}Cl, $^{63/65}$Cu, $^{79/81}$Br, and ^{127}I SSNMR experiments.[221] The linewidths were also studied as functions of the addition of impurities (Table 10). The frequency jumping of Cu^+ interstitials was shown to behave very similarly to the Ag^+ interstitials in AgBr. This motion created maximum line-narrowing of the signals at around 373 K, was found to be similar for each salt, and did not depend significantly on impurities.

The CuX series was also looked at by Hayashi and Hayamizu, who used $^{63/65}$Cu, ^{79}Br, and ^{127}I SSNMR experiments on powders to address the issue of MAS rotation frequency dependent chemical shifts.[222,223] For ^{79}Br, the MAS frequency dependent shift is modest (ca. +1 ppm at ν_{rot} = 4 kHz, relative to the corresponding non-spinning sample), while it is quite substantial for ^{127}I under the same sample conditions (ca. +12 ppm). After ruling out numerous possibilities as to the cause, it was concluded that the shift as a function of MAS frequency was due to a Lorentz type force acting on the Cu^+ ions.

4.3.2. Doping alkali metal bromides and other simple salts

A number of studies involved doping inorganic bromides, followed by $^{79/81}$Br SSNMR experiments.[158,214,215,221,224–228] Generally, it is expected that as one increases the impurity fraction, the bromine NMR signal intensity decreases and the signal breadth increases (Figures 18 and 19). The reasons for the trend are obvious: the impurity introduces crystalline strain, which results in a larger EFG at the bromine nuclear site. The source of this strain is postulated by Das and Dick to be due to subtle lattice displacements, which cause ions around the impurity site to become polarized and thus destroy the cubic electric field symmetry and significantly alter the local EFG.[229,230] Studies have also been carried out which link the decreasing NMR signal that is observed upon the introduction of impurities with the creation of lattice dislocations.[216]

Using ^{79}Br, ^{127}I, ^{23}Na, and ^{87}Rb SSNMR experiments, Andersson tested the lattice displacement theory in the framework of the ion overlap model of K–Y by observing the chemical shift change upon doping a variety of alkali halide

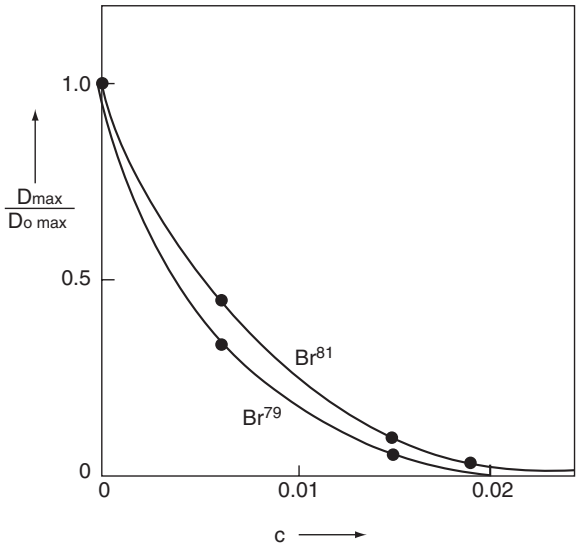

Figure 18 Normalized signal strengths of both ^{79}Br and ^{81}Br in single crystals of (1-*c*)KBr-*c*NaBr plotted against the relative concentration *c* of the minority species. From: Ref. 158. Reproduced by permission of the *Institute of Pure and Applied Physics.*

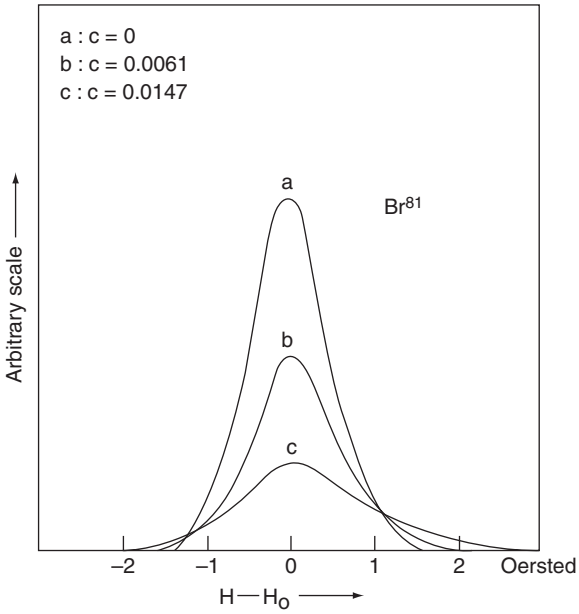

Figure 19 Integrated absorption curves for ^{81}Br magnetic resonance in a series of mixed single crystals (1-*c*)KBr-*c*NaBr. From: Ref. 158. Reproduced by permission of the *Institute of Pure and Applied Physics*.

crystals.[231] The author found good agreement between theory and experiment. The general trend established experimentally is as follows: a substitution with a smaller lattice cation results in a positive chemical shift, while substitution with a larger lattice cation resulted in a negative chemical shift. The author argued that a smaller lattice cation substitution results in slightly greater orbital overlap with the adjacent ions, and thus creates a slightly larger negative paramagnetic shielding effect.

Andersson and co-workers also carried out several studies which involved doping single crystals (primarily NaBr, KBr, and KI) with a variety of impurities and measuring the first- and/or second-order quadrupolar shifts in the SSNMR spectra (^{23}Na, $^{79/81}$Br, ^{127}I, as appropriate) that were induced by the substitution; they determined the EFG tensor at several crystal lattice sites and then estimated the distance to the impurity site.[224–227,232] A similar study on a reagent grade specimen of KBr was carried out by Ohlsen and Melich, who introduced NaBr into the lattice up to 0.1 mol %.[164] What is interesting in their study is that while they observed the location of and EFG at the bromine atoms with respect to the impurity Na^+, they also managed to determine these same parameters for bromine atoms near inadvertent Cl^- impurity sites, which were estimated to make up no more than 0.2 mol %.

Several reasonably simple models have been proposed to determine the EFGs at the sites of the halogen atoms in systems where cubic symmetry was lost to the presence of some form of lattice strain, typically an impurity, although they were not quantitative and in some cases were off by more than one order of magnitude.[229,230,233–235] Although the initial demonstrations were not good at quantitatively reproducing the experimental observations, it was abundantly clear that the inclusion of only NN effects was not adequate to describe either shielding or EFG parameters.

A number of studies have involved the doping of simple inorganic systems, followed by bromine NMR to determine the gradient-elastic tensor of various alkali halide crystals, which provides another way for determining the EFG tensor at the halogen site.[226,236] Pulsed double-resonance experiments have also been used to establish the presence of impurity ions in alkali halide crystals.[237]

There are many cases where complicated temperature-dependent behaviour has been observed. As an example, upon heating a polycrystalline sample of AgBr doped with 3×10^{-4} mol % $CdBr_2$, Reif observed the $^{79/81}$Br NMR signal intensity to be a minimum at room temperature over the temperature range of about 150–550 K.[162] Initially, one might expect that the signal intensity would decrease consistently with increasing temperature, as the crystal lattice should become increasingly strained with increasing temperature, which would lead to an increasing EFG at the bromine and hence broaden the signal. Reif attributed the minimum signal intensity to a matching of the Ag^+ vacancy jump frequency with $1.83\omega_0$. This would lead to an efficient relaxation process and hence greatly reduce the T_1, perhaps even to the extent that lifetime broadening is observed. Further heating eventually removes this relaxation process and corresponds to a slight increase in T_1 (the increasing lattice strains with increasing temperature competes with this process and hence the initial bromine T_1 increase is only slight),

an increase in signal intensity and decrease in linewidth. At higher temperatures ($T > 450$ K), the lineshape is primarily determined by Br–Br magnetic dipole interactions. These observations have been confirmed in subsequent studies[221] and similar temperature-dependent behaviour was observed upon doping AgBr with CuBr,[238] as well as with $FeBr_2$, $CoBr_2$ and $NiBr_2$,[217] and in a variety of other cases (Table 10).

4.3.3. Other bromide ion-containing systems

Several papers have been published which comment upon the Br^- anion in two pesudo-polymorphs of $K_2Pt(CN)_4Br_{0.3} \cdot xH_2O$ ($x = 2.6$, 3.2). Although initially attributed to a dynamic motion of the bromine atoms,[239] the sharp ^{81}Br signal observed in studies of the $x = 2.6$ pseudo-polymorph interestingly highlights that $^{79/81}Br$ SSNMR experiments may be used to detect liquid inclusions within polycrystalline materials.[240] It was also established that the true signals associated with the bromine nuclei within the compound were likely beneath detection limits. With the introduction of greater NMR magnetic field strengths (at that time, 5.17 T), VT ^{81}Br SSNMR studies were able to detect two bromine sites with moderately large QI parameters (Table 14).[241,242]

4.3.4. Alkali metal and ammonium perbromates ($MBrO_4$, M = K, Rb, Cs, NH_4)

As is the case with the perchlorates, the bromine atom in the perbromate series is in a nearly tetrahedral environment and hence the EFG at the bromine will be nearly zero. Therefore, it should be possible to observe $^{79/81}Br$ SSNMR signals in these systems. The cesium member of this series, $CsBrO_4$,[243] belongs to the tetragonal $I4_1/a$ space group, while the others (M = K, Rb, NH_4) belong to the orthorhombic group *Pnma*.

In $CsBrO_4$, all the Br–O bond lengths are equivalent and there is only a slight distortion of the O–Br–O angles from that of an ideal tetrahedron (ca. 2–3°). As the bromine atoms are located on $\bar{4}$ sites, it is therefore not surprising that the observed C_Q is very small ($C_Q(^{81}Br) = 1.32 \pm 0.04$ MHz) and axially symmetric ($\eta_Q = 0$).[244] Variable-temperature $^{79/81}Br$ NMR experiments were also carried out on this compound and show a highly temperature-dependent QI (Figure 20).[245] The authors reasoned that this was due to rotational oscillation of the bromate tetrahedra about their equilibrium position.

For the other members of this group, the orthorhombic crystalline lattice appears to have only a very slight effect upon the measured spectra, and it is seen that the intramolecular symmetry is the dominant factor when considering the contributions to the EFG at the bromine atom (Table 12). Some of the observations made suggest that further experiments are in order. For example, there appears to be a significant Br isotope dependent shift of over 60 ppm in NH_4BrO_4. This seems to be several orders of magnitude too large. In addition, these studies never considered CSA, an effect which is expected by symmetry to be present in all the perbromates.

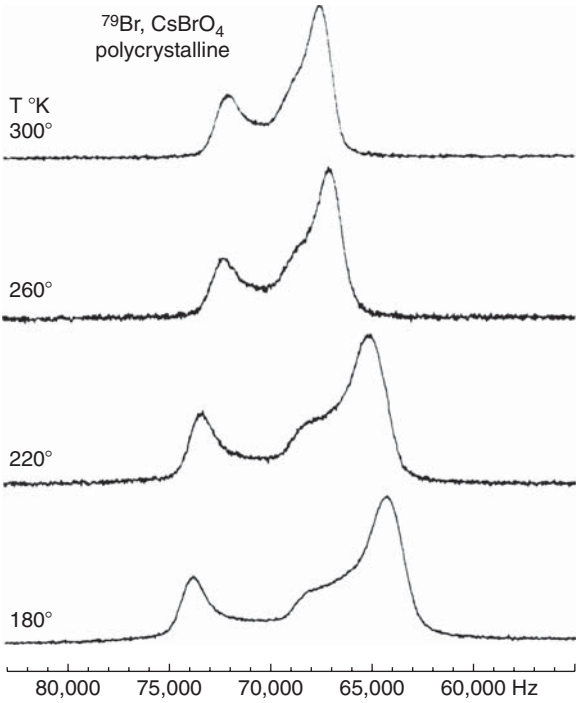

Figure 20 Temperature dependence of the ^{79}Br CT NMR line shape for polycrystalline $CsBrO_4$ (static sample); $\mathbf{B}_0 = 7.04$ T, $\nu_0 = 75.2$ MHz. From: Ref. 245. Reproduced by permission of *Verlag der Zeitschrift für Naturforschung*.

4.3.5. Molecular systems

Although this review is aimed at covering high-field NMR experiments on diamagnetic solids, a great number of studies have been published which serve to highlight the complimentary nature between Zeeman-perturbed $^{79/81}$Br NQR and standard NMR and NQR experiments on single crystals (Table 16).[246–305,431] Experiments involving polycrystalline samples are increasingly rare,[294,306] but a detailed study was carried out by Ege and Negita in 1990.[307] They observed Zeeman-perturbed bromine NQR signals in a variety of samples, although they could not quantitatively measure the asymmetry parameter in any case except BBr_3. Their value, however, differed significantly from the value determined by single-crystal experiments.

The first reports of Zeeman-perturbed bromine NQR, both using single crystals of $NaBrO_3$, confirmed prior measurements of the ^{79}Br magnetic dipole moment[204] and also highlighted the fact that Krüger's[308] Zeeman-perturbed NQR theory was valid for both bromine isotopes.[309]

Subsequent Zeeman-perturbed NQR experiments were generally used to determine η_Q (which is not possible using a pure NQR spectrum of an $I = 3/2$ nucleus), the orientation of the EFG tensor in the crystal frame, and could also be used to determine the bond character for the atoms directly bound to the bromine

(see Table 16). For example, using Zeeman-perturbed $^{79/81}$Br NQR, Kojima et al. determined η_Q values for molecular bromine[246] and *p*-dibromobenzene[247] and made reasonable arguments regarding the degree of C–Br double bond character in the latter using the method of Townes and Dailey.[310,311] It was found that compared to the C–Cl bonds in *p*-dichlorobenzene, the double bond character of the C–Br bond was 50% greater. The authors also found that the difference in double bond character contributed directly to an increase in the η_Q value.

It should be noted that the Zeeman-perturbed $^{79/81}$Br NQR experiment is also amenable to measure bromine chemical shifts, as demonstrated by Segel et al. using powdered samples of $KBrO_3$ and $NaBrO_3$ and the measurement of the ^{81}Br signal as a function of applied magnetic field strength.[312] In fact, to the best of our knowledge, the Zeeman-perturbed NQR experiment was the first experiment to measure bromine chemical shift anisotropy. Fusaro and Doane, using a single crystal of $NaBrO_3$, made very convincing arguments that the anomalous ^{81}Br shift they observed as a crystal was rotated about θ (the angle between V_{33} and $\mathbf{B}_0$) was due to chemical shift anisotropy.[313] This can be done with rotation about only one axis since η_Q had been determined to be zero. They measured $\delta_{\|} = 2620 \pm 20$ ppm and $\delta_{\perp} = 2710 \pm 30$ ppm; hence, $\Omega = 90$ ppm.

Doane and Hultsch used a single crystal of $NaBrO_3$ to demonstrate the interesting possibility of using the Zeeman-perturbed NQR transitions to modify the signal intensity associated with the ^{79}Br Zeeman transitions by irradiating the sample at NQR transition frequencies while in a weak magnetic field.[314] This information was subsequently used to determine quadrupolar relaxation transition probabilities.[315]

For characterizing the $^{79/81}$Br EFG and magnetic shielding tensors in systems where the QI dominates the Zeeman interaction, an additional experiment, known as quadrupolar regime NMR, has been suggested.[316–318] It relies upon the observation of the slightly perturbed $m = \pm 1/2$ transition. Compared to the more conventional Zeeman-perturbed experiments, similar information is obtained, and the chemical shift tensor may be characterized in addition to the EFG tensor. This experiment has been carried out on powdered and single crystalline samples of *p*-dibromobenzene.[319–321] The authors reported chemical shift tensor parameters for ^{81}Br, although the error bounds are too large to conclude that shift anisotropy was observed.

Further reports of $^{79/81}$Br SSNMR have been tabulated and can be found in Tables 9–17. Very brief summaries are provided within the tables, where appropriate. Although not discussed explicitly here, some $^{79/81}$Br SSNMR experiments have been carried out upon sodalite solid solutions (Table 13), as well as paramagnetic, ferromagnetic and antiferromagnetic materials (Table 17). In the latter systems, the NMR experiments have been largely carried out below liquid helium temperature using single crystals.

4.4. Solid-state iodine-127 nuclear magnetic resonance

Iodine-127 SSNMR data and references are summarized in Tables 18-20. Although ^{127}I has a good NMR receptivity, its applicability as an NMR probe is limited due to its large Q value and the resulting broad line shapes when symmetry at the

nucleus deviates from T_d or O_h. For this reason, there have been few developments since the 2006 review.[11] Bieroń et al. have described how the quadrupole moments for bromine and iodine were derived from combined atomic and molecular data.[322] However, since our previous review, the recommended value of $Q(^{127}I)$ has been altered by Pyykkö from −710(10) mb to −696(12) mb (see Table 1).[323]

Reported ^{127}I SSNMR studies of diamagnetic solids are mainly restricted to periodate (IO_4^-) salts in addition to the cubic alkali metal iodides discussed in Section 4.1. ^{127}I SSNMR spectra of sodalites have also been acquired (see Figure 5).[94] The ^{127}I quadrupolar coupling constants and CS tensors for NH_4IO_4, KIO_4, $AgIO_4$, and $NaIO_4$ were reported by Segel and Vyas.[324] Burkert et al. also reported on ^{127}I quadrupolar coupling constants as a function of temperature in various periodates.[325–331] The ^{127}I nuclear quadrupolar coupling constants for periodates range from 1.31 MHz at 145 K in NH_4IO_4 to about 43 MHz at 300 K in $NaIO_4$.

Wu and Dong[332] revisited the ^{127}I SSNMR spectroscopy of the periodates as a result of the anomalously large span of the iodine CS tensor reported for $NaIO_4$, 59 000 ppm.[324] Wu and Dong showed that the anisotropy of the iodine CS tensor is essentially negligible (< 50 ppm) in the periodates ($NaIO_4$, KIO_4, $RbIO_4$, NH_4IO_4, HIO_4) and a span of just 18 ppm was determined for $CsIO_4$. The ^{127}I SSNMR spectra of NH_4IO_4 and KIO_4 are presented in Figure 21. These results are more consistent with the high symmetry at iodine in periodiates. It is difficult to speculate on the reason that such large spans were reported previously, as no spectra are shown in the paper of Segel and Vyas. Recording of the broad ^{127}I resonances in stationary powdered samples of $NaIO_4$ ($C_Q = 42.24$ MHz; $\eta_Q = 0.0$) and HIO_4 ($C_Q = 43.00$ MHz; $\eta_Q = 0.75$) was facilitated by acquiring the whole echo rather than a half-echo.[332]

Zeeman-perturbed NQR was applied by Kehrer et al.[461] to determine the ^{127}I EFG tensor in glycyl-L-alanine hydroiodide monohydrate. Although this is not a typical solid-state NMR study, it is interesting to quote the quadrupolar parameters, $C_Q(^{127}I) = 74.04$ MHz and $\eta_Q = 0.776$ (at 274.5 K) since the corresponding hydrobromide salt is isomorphous and could be of interest for further study.

Hon and Christe reported a ^{127}I NMR study of polycrystalline $IF_6^+AsF_6^-$.[333] This early study did not benefit from modern pulse sequences and spectrometer electronics; nevertheless, the spectrum was interpreted to provide reasonable bounds on the ^{127}I quadrupolar coupling constant, 2.32–2.9 MHz, depending on the value of the asymmetry parameter (which could not be determined). Given the high symmetry at iodine in the IF_6^+ cation, this small value of C_Q seems plausible. Lehmann et al. have reported solution $^{35/37}Cl$, $^{79/81}Br$, and ^{127}I NMR studies of $ClF_6^+AsF_6^-$, $BrF_6^+AsF_6^-$, and $IF_6^+Sb_3F_{19}^-$ and obtained valuable chemical shift and *J*-coupling information.[334] It would be very interesting to apply solid-state NMR methods to these and analogous systems, particularly in the case of ^{127}I SSNMR of the IF_6^+ cation since the large quadrupole moment of this isotope so severely limits the types of bonding environments which may be easily probed.

Additional examples of ^{127}I SSNMR are scarce, as evidenced by the entries in Tables 18–20. In terms of modern pulsed high-field NMR applications, it seems

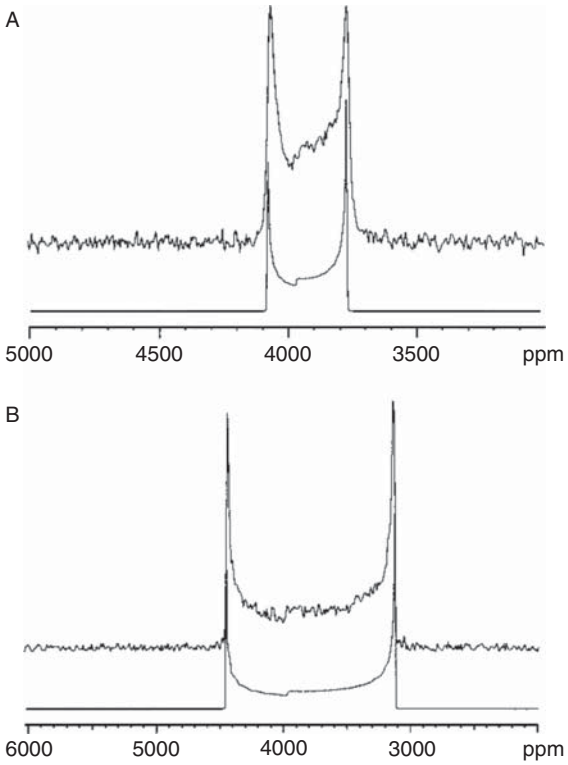

Figure 21 Iodine-127 NMR spectra of solid (A) NH_4IO_4 and (B) KIO_4 (static powders). Simulations are shown below each of the experimental spectra. $\nu_0 = 100.36$ MHz. From Ref. 332. Reproduced by permission of *Elsevier.*

clear that studies will remain limited to iodine atoms in high-symmetry environments including, e.g., iodides and periodates.

4.5. Chemical shift references for solids: Bromine

It was discussed in Section 4.1 that Weeding and Veeman have presented reliable chlorine chemical shifts obtained under MAS conditions for the solid alkali metal chlorides.[135] Hayashi and Hayamizu reported analogous data for bromine and iodine.[137] Here, we establish the bromine chemical shifts with respect to the IUPAC standard solution (0.01 M NaBr in D_2O). While carrying out these experiments, it was found that the recommended IUPAC standard solution (Table 1) was not a practical SSNMR reference sample. Our experiments were carried out at $\mathbf{B}_0 =$ 11.75 T using 4 mm o.d. MAS rotors (a common experimental configuration for SSNMR). Therefore, only 0.1–0.15 mL of solution is in the rotor and hence the mass of solute within the rotor is maximally about 150 μg for NaBr. The solution was so dilute that no signal could observed within 15 min of experimental time, using a 1 s

interacquisition delay. For comparison purposes, strong $^{79/81}$Br signals can be seen in one scan using a 4 mm MAS rotor filled with solid NaBr.

Therefore, for $^{79/81}$Br NMR experiments, a slightly more concentrated solution was prepared (~0.03 M). Using this solution still required nearly 1 h of experiment time to achieve a signal-to-noise ratio of about 16 (Figure 22C). A similar observation was made for iodine. While it is known that the halogen nuclei can exhibit significant concentration dependant shifts, the shift difference between very dilute (< 0.05 M) solutions is not expected to be particularly significant. Previous bromine NMR studies on alkali bromide solutions have been carried out where aqueous solution concentrations up to 0.2 M were used without measurable shifts from those that were ''infinitely'' dilute.[335] Very small concentration-dependent shifts have been measured using ^{35}Cl and ^{81}Br NMR experiments for solutions of NaCl and KBr in D_2O.[336] To the best of our knowledge, concentration-dependent shift data do not exist for NaBr in D_2O; however, using the data for KBr in D_2O, it is estimated that the shift difference between the 0.03 M NaBr solution used here

Compound	$\delta(^{81}Br)(\pm)$/ppm	$\delta(^{79}Br)(\pm)$/ppm
LiBr	64.82(0.15)	64.75(0.22)
NaBr	–52.94(0.09)	–53.02(0.09)
NaBr(D_2O)	–54.51(0.30)	–54.31(0.50)
KBr	0.0	0.0
RBr	71.62(0.11)	71.58(0.15)
CsBr	228.25(0.25)	228.35(0.35)

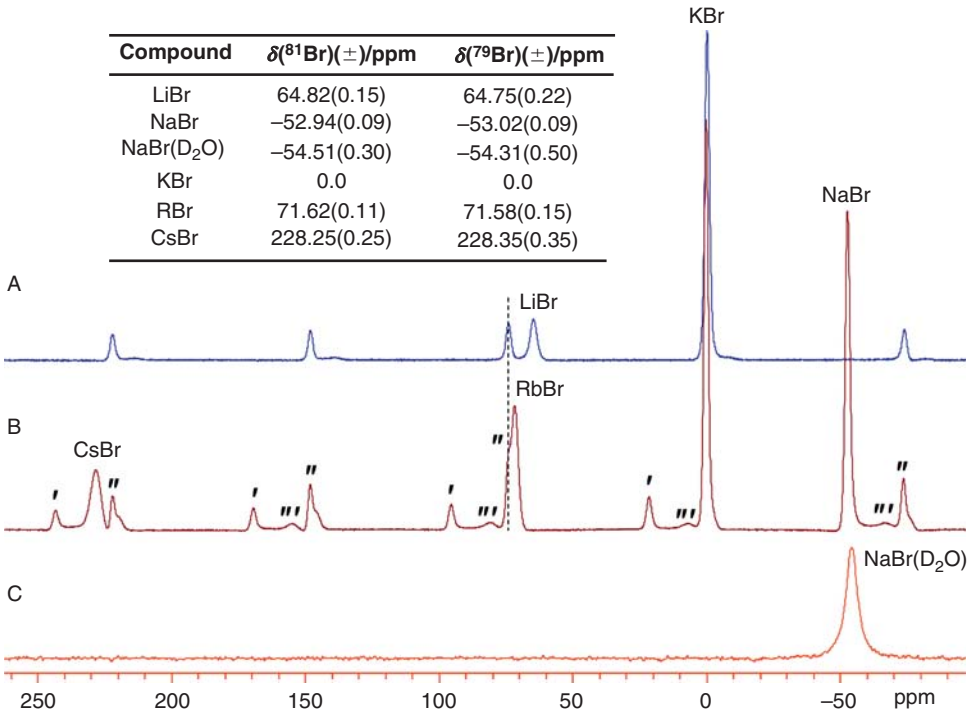

Figure 22 ^{81}Br MAS NMR spectra of powdered alkali metal bromides. All experiments were carried out at $\mathbf{B}_0 = 11.7$ T and used $\nu_{rot} = 10$ kHz. (A) a mixture of LiBr and KBr; (B) a mixture of CsBr, RbBr, KBr and NaBr; (C) 0.03 M NaBr in D_2O. For (B), the single, double and triple primes correspond to the rotational sidebands of NaBr, KBr and CsBr, respectively. The sidebands for RbBr were not fully resolved due to overlap with the KBr sidebands, which are shown for comparison in (A). Inset: measured bromine chemical shift values (errors).

and the 0.01 M NaBr IUPAC recommended solution would be at most ±0.3 ppm, which is of the same order of magnitude as the reproducibility in the bromine shift measurement of the solution sample in an unlocked widebore magnet.

The collected data for $^{79/81}$Br MAS SSNMR experiments on the alkali metal bromides are shown in Figure 22. All experiments, even for the solution, were carried out using 10 kHz MAS in cylindrical MAS rotors to minimize the errors due to temperature and bulk susceptibility differences. It is noted that the shift values for all the salts (except CsBr) measured by us agree with the findings of Hayashi and Hayamizu,[137] within experimental error. It is unclear why our value for only CsBr is different. It could potentially be due to a frictional heating effect since the spectra were acquired under MAS conditions: after considering the effects of MAS heating, our experiments were at a slightly different temperature than Hayashi and Hayamizu, who spun their samples at 2–5 kHz. The bromine chemical shift dependence with respect to temperature is known,[147] but we cannot comment on this further, as we do not know the precise temperature at which the experiments of Hayashi and Hayamizu were carried out.

We did not observe an isotope-dependent chemical shift: under our experimental conditions, if a shift is measured for one of the bromine isotopes, it will be the same, within experimental error, for the other isotope. This is consistent with expected isotope effects on chemical shifts. Based upon our preliminary findings, we suggest that the IUPAC chemical shift scale for both bromine isotopes may be converted to an equivalent scale for solids and that the solid-state bromine standard may be either NaBr(*s*) or KBr(*s*). If KBr(*s*) is used,

$$\delta_{\mathrm{KBr}(s),^{79/81}\mathrm{Br}}(\mathrm{ppm}) = \delta_{\mathrm{IUPAC},^{79/81}\mathrm{Br}}(\mathrm{ppm}) - 54.41(\mathrm{ppm}),$$

while if NaBr(*s*) is used,

$$\delta_{\mathrm{NaBr}(s),^{79/81}\mathrm{Br}}(\mathrm{ppm}) = \delta_{\mathrm{IUPAC},^{79/81}\mathrm{Br}}(\mathrm{ppm}) - 1.43(\mathrm{ppm}).$$

4.6. Gas-phase data for diatomics

We tabulate and briefly consider here the wealth of NMR data available from molecular beam and high-resolution microwave spectroscopy experiments carried out on diatomic molecules (Table 21). Under favourable conditions, these experiments can provide quadrupolar coupling constants, spin-rotation constants, effective dipolar coupling constants ($c_3 = R_{\mathrm{eff}} = R_{\mathrm{DD}} - \Delta J/3$, where R_{DD} is the direct dipolar coupling constant and ΔJ is the anisotropy of the **J** tensor[337]), and isotropic *J*-coupling constants for diatomic molecules in various rotational-vibrational states.[49,338] As a result, the experimental data are very valuable for testing various approaches for calculating NMR parameters including their anisotropies. Since the molecules are essentially isolated in the experiments, the comparisons with ''gas-phase'' calculations (where a single molecule is in a vacuum environment) can be particularly fruitful.[104,116] The experimental dependencies of the parameters on the rotational and vibrational quantum states are also valuable for assessing the utility of computational approaches. Cederberg has contributed a great deal to this field over the past several decades, having

reported hyperfine parameters for many diatomics in addition to those containing halogens. In the limit where relativistic effects are unimportant (only the case perhaps for chlorine; although, even in HCl the relativistic correction is not entirely negligible for the chlorine EFG[117]), information on the magnetic shielding tensor and its anisotropy may be extracted from the spin-rotation constants. Many of the original references cited in Table 21 feature much more detailed information on the rotational-vibrational dependence of the NMR parameters than what is presented here. One of the early high-resolution studies of the hydrogen halides was by Gordy and co-workers;[339] Gierke and Flygare subsequently interpreted their data to obtain information on the halogen shielding tensors.[340]

Mentioned briefly here are some highlights of the most recent developments relating to the quadrupolar halogens. Cederberg has investigated the potential evidence for a non-zero ^{127}I nuclear electric hexadecapole interaction by analysing high-resolution molecular beam electric resonance spectra of LiI and KI.[341,342] Although evidence for the hexadecapole interaction was found in both cases (the ^{127}I coupling constant was found to be -0.0102 ± 0.0015 kHz in ^{39}K^{127}I and ^{41}K^{127}I, and -0.0151 ± 0.0030 kHz in ^{7}Li^{127}I), the coupling constants are three orders of magnitude larger than those calculated for lithium iodide by Thyssen et al.[343] Their values ranged from +6 to +20 mHz. It has been suggested by Cederberg and Pyykkö that the spectral effect, while real, is probably not due a true hexadecapole interaction and is rather a ''pseudo-hexadecapole effect''.[341,342] No experimental evidence was found for a ^{127}I nuclear magnetic octupole effect in the study of LiI.

Bizzocchi et al. have carried out a detailed analysis of the hyperfine spectra of AgI and CuI using high-resolution microwave FT spectroscopy.[344] They reported hyperfine parameters for ^{63}Cu^{127}I, ^{65}Cu^{127}I, ^{107}Ag^{127}I, and ^{109}Ag^{127}I isotopomers, and extracted information on the shielding tensors for both nuclei on the basis of the measured spin-rotation constants. They observed an increase in the anisotropy of the reduced spin–spin coupling tensor (ΔK) and in the value of $\Delta J/(3R_{DD})$ with the atomic number of the halogen within the series CuF, CuCl, CuBr, and CuI, in agreement with previously proposed trends.[104] Interestingly, Bizzocchi et al.[344] resolve the issue of why the effective coupling constant c_3 (equivalent to R_{eff}) was not previously observed for ^{63}Cu^{79}Br; it is found by interpolation of the values of ΔK across the copper halide series that the values of the direct coupling constant and one-third the anisotropy in the **J** tensor are fortuitously approximately equal, yielding an R_{eff} of very close to zero.[345]

Finally, we point out the recent Lamb-dip spectroscopic study of H^{35}Cl and H^{37}Cl, which has yielded what are very likely the most accurate and precise hyperfine constants for these molecules to date.[346] The most accurate ground state rotational constants for hydrogen chloride are also reported. The study is complemented with a large series of ab initio calculations of the spin-rotation and quadrupolar coupling constants for HCl. The final results are in good agreement with experiment; the best vibrationally corrected CASSCF computed values of the spin-rotation constants are 54.31 kHz (^{1}H) and -42.18 kHz (^{35}Cl) while the experimental values are 54.00(15) and $-42.32(70)$ kHz. Similarly, the values for C_Q(^{35}Cl) are -67.72 MHz (calc) and $-67.6176(11)$ (expt).

5. CONCLUDING REMARKS

One question which frequently arises when discussing Cl, Br, and I NMR spectroscopy is whether covalently bound halogens will ever be amenable to study using conventional techniques on powdered samples. In principle, as long as the T_2 values are not too short, a stepped-frequency approach could be used to acquire such spectra in many parts. If we consider a $C_Q(^{35}Cl)$ of 73 MHz (a typical value for a covalently bound chlorine[61]), the breadth of the CT due to second-order quadrupolar effects would be almost 8 MHz at 21.1 T. This would require 80 sub-spectra if 100 kHz steps were used. Of course the situation becomes even worse for bromine and iodine. So, observing covalently bound chlorine is probably possible but one must decide what information one is seeking and whether it is worth the effort. One must keep in mind the availability of techniques such as NQR and the ability to obtain information through the NMR spectra of nearby nuclei which exhibit residual dipolar coupling to the halogen nucleus. In the context of this discussion, the STREAQI experiment[103] may be useful.

The most exciting recent developments in the field of SSNMR of the quadrupolar halogens, in our opinion, relate to studies of the chlorine-35/37 nuclides. This is largely due to the more moderate quadrupole moments of these nuclides when compared with $^{79/81}$Br and ^{127}I. Important advances in $^{35/37}$Cl SSNMR studies of hydrochloride salts of biochemical and pharmaceutical importance have been reported in the past few years. This work has shown that there are useful relationships between the chlorine NMR interaction tensors and the local environment at chlorine, specifically pertaining to hydrogen bonding involving Cl^-, thereby opening the door to using chlorine SSNMR as a new tool for characterizing materials for which diffraction data are not available or are limited. Examples include pharmaceutical polymorphs and hydrates, as well as peptide hydrochlorides or small ion channels. Chloride and perchlorate ions in purely inorganic materials have also yielded valuable information from $^{35/37}$Cl SSNMR experiments; the sensitivity of the chlorine EFG and CS tensors to hydration state (pseudo-polymorphism) has been demonstrated. Taken together, the $^{35/37}$Cl SSNMR experiments from the last decade have shown that there is great potential to study chlorine in high symmetry environments in a variety of materials.

Recent developments in bromine and iodine NMR spectroscopy in the last decade are scarce. Based upon our review of the literature, it is clear that $^{79/81}$Br and ^{127}I SSNMR applications lie predominantly in systems where the nucleus finds itself in an ionic and highly symmetric (i.e. tetrahedral or octahedral) environment. The recent success of high-field pulsed $^{35/37}$Cl SSNMR methods in systems where the geometry at the halogen deviates slightly from ideally symmetric cases indicates that $^{79/81}$Br and ^{127}I SSNMR should be also applicable to such systems. Our group is currently exploring the possibility of using $^{79/81}$Br and ^{127}I SSNMR experiments to characterize Br^- and I^- environments with reduced symmetry. Systems of this sort should enable additional chemical shift tensors and quadrupolar coupling parameters to be determined, thereby adding to our understanding of the relationships between the NMR observables and the local

nuclear environment. Further applications of bromine and iodine SSNMR experiments will likely remain relatively limited; however, as commercially available magnetic fields continue to increase in strength, we anticipate that new opportunities will become available.

ACKNOWLEDGEMENTS

DLB thanks the Natural Sciences and Engineering Research Council (NSERC) of Canada for funding. We are grateful to Prof. R. Schurko (University of Windsor) for providing a preprint of Ref. 183 prior to publication, and to Prof. A. Bain (McMaster University) for providing a copy of his program for calculating exact transition frequencies.

REFERENCES

1. T. M. Trnka, J. P. Morgan, M. S. Sanford, T. E. Wilhelm, M. Scholl, T.-L. Choi, S. Ding, M. W. Day and R. H. Grubbs, *J. Am. Chem. Soc.*, 2002, **125,** 2546.
2. K. Mikami, M. Terada and H. Matsuzawa, *Angew. Chem. Int. Ed.*, 2002, **41,** 3554.
3. F. M. Ashcroft, *Ion Channels and Disease*. Academic Press, San Diego, 2000.
4. M. E. Loewen and G. W. Forsyth, *Physiol. Rev.*, 2005, **85,** 1061.
5. R. Dutzler, E. B. Campbell, M. Cadene, B. T. Chait and R. MacKinnon, *Nature*, 2002, **415,** 287.
6. R. Dutzler, E. B. Campbell and R. MacKinnon, *Science*, 2003, **300,** 108.
7. N. Iwase, S. Tadaki, S. Hidaka and N. Koshino, *J. Lumin.*, 1994, **60–61,** 618.
8. G. Corradi, M. Secu, S. Schweizer and J.-M. Spaeth, *J. Phys.: Condens. Matter*, 2004, **16,** 1489.
9. J. Selling, M. D. Birowosuto, P. Dorenbos and S. Schweizer, *J. Appl. Phys.*, 2007, **101,** 034901-1.
10. J. Selling, S. Schweizer, M. D. Birowosuto and P. Dorenbos, *J. Appl. Phys.*, 2007, **102,** 074915-1.
11. D. L. Bryce and G. D. Sward, *Magn. Reson. Chem.*, 2006, **44,** 409.
12. T. Drakenberg and S. Forsén, *NATO ASI Series, Series C: Mathematical and Physical Sciences: Multinucl. Approach, NMR Spectrosc.*, 1983, **103,** 405.
13. B. Lindman and S. Forsén, *NMR Basic Princ. Prog.*, 1976, **12,** 1.

13a. B. Lindman and S. Forsén, *The Halogens-Chlorine, Bromine and Iodine*, chapter 13 in NMR and the Periodic Table, R. K. Harris and B. E. Mann (Eds.), Academic Press, London, 1978.

13b. B. Lindman, *Chlorine, Bromine and Iodine,* chapter 9 *in NMR of Newly Accessible Nuclei, Volume 1: Chemical and Biochemical Applications*, P. Laszlo (Ed.), Academic Press, London, 1983.

14. E. A. C. Lucken, *Nuclear Quadrupole Coupling Constants*. Academic Press, London, 1969.
15. A. Abragam, *Principles of Nuclear Magnetism*. Oxford University Press, New York, 1961.
16. C. P. Slichter, *Principles of Magnetic Resonance*. Springer-Verlag, New York, 1990.
17. K. Schmidt-Rohr and H. W. Spiess, *Multidimensional Solid-State NMR and Polymers*. Academic Press, San Diego, 1994.
18. K. J. D. MacKenzie and M. E. Smith, *Multinuclear Solid-State NMR of Inorganic Materials*. Pergamon, Amsterdam, 2002.
19. M. J. Duer, *Solid-State NMR Spectroscopy*. Blackwell Publishing, Oxford, 2004.
20. M. H. Cohen and F. Reif, *Solid State Phys.*, 1957, **5,** 321.
21. A. D. Bain, *Mol. Phys.*, 2003, **101,** 3163.
22. R. B. Creel, *J. Magn. Reson.*, 1983, **52,** 515.
23. R. B. Creel and D. A. Drabold, *J. Mol. Struct.*, 1983, **111,** 85.
24. G. M. Muha, *J. Magn. Reson.*, 1983, **53,** 85.
25. B. C. Sanctuary, T. K. Halstead and P. A. Osment, *Mol. Phys.*, 1983, **49,** 753.
26. S. Ding and C. A. McDowell, *J. Chem. Phys.*, 1997, **107,** 7762.
27. A. D. Bain, Beta software, private communication.
28. C. M. Widdifield and D. L. Bryce, *Manuscript in preparation.*
29. W. E. Lamb Jr., *Phys. Rev.*, 1941, **60,** 817.
30. N. F. Ramsey, *Phys. Rev.*, 1950, **77,** 567.

31. N. F. Ramsey, *Phys. Rev.*, 1950, **78,** 699.
32. N. F. Ramsey, *Phys. Rev.*, 1951, **83,** 540.
33. N. F. Ramsey, *Physica (The Hague)*, 1951, **17,** 303.
34. R. K. Harris, E. D. Becker, S. M. Cabral De Menezes, P. Granger, R. E. Hoffman and K. W. Zilm, *Pure Appl. Chem.*, 2008, **80,** 59.
35. A. Loewnstein, M. Shporer, P. C. Lauterbur and J. E. Ramirez, *J. Chem. Soc., Chem. Commun. (London)*, 1968, 214.
36. J. Blaser, O. Lutz and W. Steinkilberg, *Phys. Lett. A*, 1970, **32,** 403. [Errata: ibid., 1972, **38**, 458].
37. M. Gee, R. E. Wasylishen and A. Laaksonen, *J. Phys. Chem. A*, 1999, **103,** 10805.
38. C. Y. Lee and C. D. Cornwell, *Magnetic Resonance and Related Phenomena*, Groupement Ampere, Heidelberg, 1976, 261.
39. W. Gauß, S. Gunther, A. R. Haase, M. Kerber, D. Kessler, J. Kronenbitter, H. Kruger, O. Lutz, A. Nolle, P. Schrade, M. Schule and G. E. Siegloch, *Z. Naturforsch. A*, 1978, **33,** 934.
40. J. Kondo and J. Yamashita, *J. Phys. Chem. Solids*, 1959, **10,** 245.
41. J. Itoh and Y. Yamagata, *J. Phys. Soc. Jpn.*, 1959, **14,** 225.
42. R. Baron, *J. Chem. Phys.*, 1963, **38,** 173.
43. D. Ikenberry and T. P. Das, *Phys. Rev.*, 1965, **138,** A822.
44. J. Itoh and Y. Yamagata, *J. Phys. Soc. Jpn.*, 1958, **13,** 1182.
45. D. Ikenberry and T. P. Das, *J. Chem. Phys.*, 1966, **45,** 1361.
46. J. Demaison, A. Dubrulle, D. Boucher and J. Burie, *J. Chem. Phys.*, 1977, **67,** 254.
47. A. D. Buckingham and R. M. Olegário, *Mol. Phys.*, 1997, **92,** 773.
48. K. Kudo, H. Maeda, T. Kawakubo, Y. Ootani, M. Funaki and H. Fukui, *J. Chem. Phys.*, 2006, **124,** 224106-1.
49. N. F. Ramsey, *Molecular Beams*. Oxford University Press, Oxford, 1956.
50. W. H. Flygare and J. Goodisman, *J. Chem. Phys.*, 1968, **49,** 3122.
51. M. A. M. Forgeron, R. E. Wasylishen and G. H. Penner, *J. Phys. Chem. A*, 2004, **108,** 4751.
52. A. D. Buckingham and S. M. Malm, *Mol. Phys.*, 1971, **22,** 1127.
53. J. B. Robert and L. Wiesenfeld, *Phys. Rep.*, 1982, **86,** 363.
54. F. A. L. Anet and D. J. O'Leary, *Concepts Magn. Reson.*, 1991, **3,** 193.
55. U. Haeberlen, *Advances in Magnetic Resonance, Supplement 1*. Academic Press, New York, 1976.
56. J. Mason, *Solid State Nucl. Magn. Reson.*, 1993, **2,** 285.
57. J. Herzfeld and A. E. Berger, *J. Chem. Phys.*, 1980, **73,** 6021.
58. G. B. Arfken, *Mathematical Methods for Physicists*. Academic Press, New York, 1985.
59. R. K. Harris and A. C. Olivieri, *Prog. NMR Spectrosc.*, 1992, **24,** 435.
60. A. C. Olivieri, J. Elguero, I. Sobrados, P. Cabildo and R. M. Claramunt, *J. Phys. Chem.*, 1994, **98,** 5207.
61. K. Eichele, R. E. Wasylishen, J. S. Grossert and A. C. Olivieri, *J. Phys. Chem.*, 1995, **99,** 10110.
62. B. Thomas, S. Paasch, S. Steuernagel and K. Eichele, *Solid State Nucl. Magn. Reson.*, 2001, **20,** 108.
63. S. H. Alarcón, A. C. Olivieri and R. K. Harris, *Solid State Nucl. Magn. Reson.*, 1993, **2,** 325.
64. A. S. Batsanov, S. M. Cornet, L. A. Crowe, K. B. Dillon, R. K. Harris, P. Hazendonk and M. D. Roden, *Eur. J. Inorg. Chem.*, **2001**, 1729.
65. R. K. Harris, M. M. Sünnetçioğlu, K. S. Cameron and F. G. Riddell, *Magn. Reson. Chem.*, 1993, **31,** 963.
66. D. C. Apperley, B. Haiping and R. K. Harris, *Mol. Phys.*, 1989, **68,** 1277.
67. A. E. Aliev, K. D. M. Harris, P. J. Barrie and S. Camus, *J. Chem. Soc., Faraday Trans.*, 1994, **90,** 3729.
68. B. Nagasaka, S. Takeda and N. Nakamura, *Chem. Phys. Lett.*, 1994, **222,** 486.
69. S. H. Alarcón, A. C. Olivieri, S. A. Carss and R. K. Harris, *Angew. Chem., Int. Ed. Engl.*, 1994, **33,** 1624.
70. M. Strohmeier, A. M. Orendt, D. W. Alderman and D. M. Grant, *J. Am. Chem. Soc.*, 2001, **123,** 1713.
71. D. Rentsch, R. Hany and W. von Philipsborn, *Magn. Reson. Chem.*, 1997, **35,** 832.
72. R. K. Harris, A. Sebald, D. Furlani and G. Tagliavini, *Organometallics*, 1988, **7,** 388.
73. W. W. Fleming, C. A. Fyfe, J. R. Lyerla, H. Vanni and C. S. Yannoni, *Macromolecules*, 1980, **13,** 460.
74. R. C. Crosby and J. F. Haw, *Macromolecules*, 1987, **20,** 2326.
75. A. Lyčka, J. Holeček, A. Sebald and I. Tkáč, *J. Organomet. Chem.*, 1991, **409,** 331.
76. R. K. Harris and A. Root, *Mol. Phys.*, 1989, **66,** 993.
77. S. Hayashi and K. Hayamizu, *Magn. Reson. Chem.*, 1992, **30,** 658.
78. J. Böhm, D. Fenzke and H. Pfeifer, *J. Magn. Reson.*, 1983, **55,** 197.

79. C. Aubauer, G. Engelhardt, T. M. Klapötke, H. Nöth, A. Schulz and M. Warchhold, *Eur. J. Inorg. Chem.*, **2000**, 2245.
80. S. H. Alarcón, A. C. Olivieri, S. A. Carss and R. K. Harris, *Magn. Reson. Chem.*, 1995, **33,** 603.
81. A. E. Aliev, L. Elizabé, B. M. Kariuki, H. Kirschnick, J. M. Thomas, M. Epple and K. D. M. Harris, *Chem. Eur. J.*, 2000, **6,** 1120.
82. S. H. Alarcón, A. C. Olivieri, S. A. Carss, R. K. Harris, M. J. Zuriaga and G. A. Monti, *J. Magn. Reson., Ser. A*, 1995, **116,** 244.
83. Z. Luz, L. Olivier, R. Poupko, K. Müller, C. Krieger and H. Zimmermann, *J. Am. Chem. Soc.*, 1998, **120,** 5526.
84. M. A. Kennedy and P. D. Ellis, *Concepts Magn. Reson.*, 1989, **1,** 109.
85. M. A. Kennedy and P. D. Ellis, *Concepts Magn. Reson.*, 1989, **1,** 35.
86. T. Vosegaard, E. Hald, P. Daugaard and H. J. Jakobsen, *Rev. Sci. Instrum.*, 1999, **70,** 1771.
87. R. Siegel, T. T. Nakashima and R. E. Wasylishen, *Concepts Magn. Reson. A*, 2005, **26A,** 47.
88. Z. Yao, H. T. Kwak, D. Sakellariou, L. Emsley and P. J. Grandinetti, *Chem. Phys. Lett.*, 2000, **327,** 85.
89. A. P. M. Kentgens and R. Verhagen, *Chem. Phys. Lett.*, 1999, **300,** 435.
90. R. Siegel, T. T. Nakashima and R. E. Wasylishen, *Chem. Phys. Lett.*, 2004, **388,** 441.
91. A. Samoson, *Chem. Phys. Lett.*, 1985, **119,** 29.
92. C. Jäger, *NMR Basic Princ. Prog*, 1994, **31,** 133.
93. J. Skibsted, N. C. Nielsen, H. Bildsøe and H. J. Jakobsen, *J. Magn. Reson.*, 1991, **95,** 88.
94. H. Trill, H. Eckert and V. I. Srdanov, *J. Phys. Chem. B*, 2003, **107,** 8779.
95. F. H. Larsen, H. J. Jakobsen, P. D. Ellis and N. C. Nielsen, *J. Phys. Chem. A*, 1997, **101,** 8597.
96. R. Siegel, T. T. Nakashima and R. E. Wasylishen, *Concepts Magn. Reson. A*, 2005, **26A,** 62.
97. J. T. Ash, N. M. Trease and P. J. Grandinetti, *J. Am. Chem. Soc.*, 2008, **130,** 10858.
98. J. A. Tang, J. D. Masuda, T. J. Boyle and R. W. Schurko, *ChemPhysChem*, 2006, **7,** 117.
99. I. J. F. Poplett and M. E. Smith, *Solid State Nucl. Magn. Reson.*, 1998, **11,** 211.
100. L. A. O'Dell and R. W. Schurko, *Chem. Phys. Lett.*, 2008, **464,** 97.
101. L. Frydman and J. S. Harwood, *J. Am. Chem. Soc.*, 1995, **117,** 5367.
102. Z. Gan, *J. Am. Chem. Soc.*, 2000, **122,** 3242.
103. J. Persons and G. S. Harbison, *J. Magn. Reson.*, 2007, **186,** 347.
104. D. L. Bryce and R. E. Wasylishen, *J. Am. Chem. Soc.*, 2000, **122,** 3197.
105. J. Autschbach and T. Ziegler, *J. Chem. Phys.*, 2000, **113,** 9410.
106. Y. Zhang, S. Mukherjee and E. Oldfield, *J. Am. Chem. Soc.*, 2005, **127,** 2370.
107. S. Adiga, D. Aebi and D. L. Bryce, *Can. J. Chem.*, 2007, **85,** 496.
108. M. D. Segall, P. J. D. Lindan, M. J. Probert, C. J. Pickard, P. J. Hasnip, S. J. Clark and M. C. Payne, *J. Phys.: Condens. Matter*, 2002, **14,** 2717.
109. S. J. Clark, M. D. Segall, C. J. Pickard, P. J. Hasnip, M. I. J. Probert, K. Refson and M. C. Payne, *Z. Kristallogr.*, 2005, **220,** 567.
110. C. J. Pickard and F. Mauri, *Phys. Rev. B*, 2001, **63,** 245101.
111. C. Gervais, R. Dupree, K. J. Pike, C. Bonhomme, M. Profeta, C. J. Pickard and F. Mauri, *J. Phys. Chem. A.*, 2005, **109,** 6960.
112. D. L. Bryce and E. B. Bultz, *Chem. Eur. J.*, 2007, **13,** 4786.
113. J. W. Zwanziger and M. Torrent, *Appl. Magn. Reson.*, 2008, **33,** 447.
114. R. G. Barnes, S. L. Segel and W. H. Jones, *J. Appl. Phys.*, 1962, **S33,** 296.
115. R. Sternheimer, *Phys. Rev.*, 1950, **80,** 102.
116. D. L. Bryce, R. E. Wasylishen, J. Autschbach and T. Ziegler, *J. Am. Chem. Soc.*, 2002, **124,** 4894.
117. V. Kellö and A. J. Sadlej, *Chem. Phys. Lett.*, 1990, **174,** 641.
118. V. Kellö and A. J. Sadlej, *Mol. Phys.*, 1996, **89,** 127.
119. V. Kellö and A. J. Sadlej, *Int. J. Quantum Chem.*, 1998, **68,** 159.
120. P. Manninen, P. Lantto, J. Vaara and K. Ruud, *J. Chem. Phys.*, 2003, **119,** 2623.
121. R. Fukuda, M. Hada and H. Nakatsuji, *J. Chem. Phys.*, 2003, **118,** 1027.
122. J. Autschbach and T. Ziegler, *Encyclopedia of Magnetic Resonance*, Volume 9, D. M. Grant and R. K. Harris (eds.), Wiley, 2002, pp. 306–323.
123. M. Kaupp, O. L. Malkina, V. G. Malkin and P. Pyykkö, *Chem. Eur. J.*, 1998, **4,** 118.
124. P. Pyykkö, *Chem. Phys.*, 1983, **74,** 1.
125. J. W. Akitt, *In Multinuclear NMR*, (J. Mason, ed.), Plenum Press, New York, 1987, Chapter 17.

126. R. V. Pound, *Phys. Rev.*, 1950, **79,** 685.
127. R. V. Pound, *Phys. Rev.*, 1948, **73,** 1112.
128. T. Kanda, *J. Phys. Soc. Jpn.*, 1955, **10,** 85.
129. H. S. Gutowsky and B. R. McGarvey, *J. Chem. Phys.*, 1953, **21,** 1423.
130. K. Yosida and T. Moriya, *J. Phys. Soc. Jpn.*, 1956, **11,** 33.
131. N. Bloembergen and P. P. Sorokin, *Phys. Rev.*, 1958, **110,** 865.
132. J. van Kranendonk, *Physica*, 1954, **20,** 781.
133. Y. Yamagata, *J. Phys. Soc. Jpn.*, 1964, **19,** 10.
134. D. W. Hafemeister and W. H. Flygare, *J. Chem. Phys.*, 1966, **44,** 3584.
135. T. L. Weeding and W. S. Veeman, *J. Chem. Soc., Chem. Commun*, 1989, 946.
136. F. Lefebvre, *J. Chim. Phys.*, 1992, **89,** 1767.
137. S. Hayashi and K. Hayamizu, *Bull. Chem. Soc. Jpn.*, 1990, **63,** 913.
138. G. D. Watkins and R. V. Pound, *Phys. Rev.*, 1953, **89,** 658.
139. E. G. Wikner, W. E. Blumberg and E. L. Hahn, *Phys. Rev.*, 1960, **118,** 631.
140. M. J. Weber, *Phys. Rev.*, 1963, **130,** 1.
141. R. R. Allen and M. J. Weber, *J. Chem. Phys.*, 1963, **38,** 2970.
142. M. J. Weber and R. R. Allen, *Proc. Coll. AMPERE*, 1963, **11,** 177.
143. T. K. Halstead, P. A. Osment, B. C. Sanctuary, J. Tegenfeldt and I. J. Lowe, *J. Magn. Reson.*, 1986, **67,** 267.
144. R. V. Pound, *J. Phys. Chem.*, 1953, **57,** 743.
145. G. Bonera, A. Avogadro and F. Borsa, *Phys. Rev.*, 1968, **165,** 391.
146. J. S. Frye and G. E. Maciel, *J. Magn. Reson.*, 1982, **48,** 125.
147. L. H. Ngai, *J. Phys. Chem. Solids*, 1969, **30,** 571.
148. J. L. Marsh Jr. and P. A. Casabella, *Phys. Rev.*, 1966, **150,** 546.
149. H. J. Hackeloer and O. Kanert, *Z. Naturforsch*, 1972, **27a,** 1235.
150. T. Yamanishi, T. Kanashiro, A. Itabashi, Y. Michihiro, Y. Kishimoto and T. Ohno, *J. Phys. Soc. Jpn.*, 1994, **63,** 3903.
151. T. Yamanishi, T. Kanashiro, Y. Michihiro, Y. Kishimoto and T. Ohno, *J. Phys. Soc. Jpn.*, 1995, **64,** 643.
152. Y. Michihiro, T. Yamanishi, T. Kanashiro and Y. Kishimoto, *Solid State Ionics*, 1995, **79,** 40.
153. T. Kanashiro, Y. Michihiro, K. Kitahara, T. Yamanishi, Y. Kishimoto and T. Ohno, *Solid State Ionics*, 1996, **86–88,** 223.
154. E. R. Andrew, W. S. Hinshaw and R. S. Tiffen, *J. Phys. C Solid State*, 1973, **6,** 2217.
155. C. E. Tarr, L. M. Stacey and C. V. Briscoe, *Phys. Rev.*, 1967, **155,** 272.
156. L. Niemelä and J. Tuohi, *Ann. Acad. Sci. Fenn., Ser. A6*, 1970, **338**.
157. B. I. Kochelaev, *Sov. Phys. JETP-USSR*, 1960, **10,** 171. [Translated from: *Zh. Eskperim. i Teor. Fiz.*, 1959, **37**, 242]
158. E. Otsuka and H. Kawamura, *J. Phys. Soc. Jpn.*, 1957, **12,** 1071.
159. O. Kanert, *Phys. Status Solidi*, 1964, **7,** 791.
160. M. Mehring and O. Kanert, *Z. Naturforsch. A*, 1969, **24,** 332.
161. M. Mehring and O. Kanert, *Z. Naturforsch. A*, 1969, **24,** 768.
162. F. Reif, *Phys. Rev.*, 1955, **100,** 1597.
163. M. E. Melich and W. D. Ohlsen, *B. Am. Phys. Soc. Ser. 2*, 1963, **8,** 468.
164. W. D. Ohlsen and M. E. Melich, *Phys. Rev.*, 1966, **144,** 240.
165. O. Kanert, D. Kotzur and M. Mehring, *Phys. Status Solidi*, 1969, **36,** 291.
166. J. F. Hon and P. J. Bray, *B. Am. Phys. Soc. Ser. 2*, 1957, **2,** 267.
167. J. F. Hon and P. J. Bray, *B. Am. Phys. Soc. Ser. 2*, 1957, **2,** 344.
168. P. J. Bray and J. F. Hon, *B. Am. Phys. Soc. Ser. 2*, 1958, **3,** 22.
169. J. F. Hon and P. J. Bray, *J. Phys. Chem. Solids*, 1959, **11,** 149.
170. C. Brinkmann, S. Faske, M. Vogel, T. Nilges, A. Heuer and H. Eckert, *Phys. Chem. Chem. Phys.*, 2006, **8,** 369.
171. O. Czupiński, M. Wojtaś, J. Zaleski, R. Jakubas and W. Medycki, *J. Phys.: Condens. Matter*, 2006, **18,** 3307.
172. J. Itoh and Y. Yamagata, *J. Phys. Soc. Jpn.*, 1962, **17,** 481.
173. S. Ueda and J. Itoh, *J. Phys. Soc. Jpn.*, 1967, **22,** 927.

174. S. Ueda, *Kanazawa Kaigaku Kogakubu Kiyo*, 1973, **7,** 167.
175. B. D. Günther and R. A. Hultsch, *J. Magn. Reson.*, 1969, **1,** 609.
176. G. L. Samuelson and C. Ailion, *Phys. Rev. B*, 1972, **5,** 2488.
177. K. D. Becker, *J. Chem. Phys.*, 1978, **68,** 3785.
178. S. Hayashi and K. Hayamizu, *J. Phys. Chem. Solids*, 1992, **53,** 239.
179. D. L. Bryce, G. D. Sward and S. Adiga, *J. Am. Chem. Soc.*, 2006, **128,** 2121.
180. D. L. Bryce and G. D. Sward, *J. Phys. Chem. B.*, 2006, **110,** 26461.
181. D. L. Bryce, M. Gee and R. E. Wasylishen, *J. Phys. Chem. A*, 2001, **105,** 10413.
182. R. P. Chapman and D. L. Bryce, *Phys. Chem. Chem. Phys.*, 2007, **9,** 6219.
183. H. Hamaed, J. M. Pawlowski, B. F. T. Cooper, R. Fu, S. H. Eichhorn and R. W. Schurko, *J. Am. Chem. Soc.*, 2008, **130,** 11056.
184. J. P. Yesinowski, M. L. Buess, A. N. Garroway, M. Ziegeweld and A. Pines, *Anal. Chem.*, 1995, **67,** 2256.
185. K. Eichele and R. E. Wasylishen, *WSolids*, version 1.17.30.
186. D. Massiot, F. Fayon, M. Capron, I. King, S. Le Calvé, B. Alonso, J. -O. Durand, B. Bujoli, Z. Gan and G. Hoatson, *Magn. Reson. Chem.*, 2002, **40,** 70.
187. A. Lupulescu, M. Kotecha and L. Frydman, *J. Am. Chem. Soc.*, 2003, **125,** 3376.
188. M. Hattori, Y. Onoda, T. Erata, M. E. Smith, M. Hattori, H. Ohki and R. Ikeda, *Z. Naturforsch*, 1994, **49a,** 291.
189. H. Honda, *Z. Naturforsch*, 2003, **58a,** 623.
190. J. F. Stebbins and L. S. Du, *Am. Mineral.*, 2002, **87,** 359.
191. T. O. Sandland, L. S. Du, J. F. Stebbins and J. D. Webster, *Geochem. Cosmochim. Acta*, 2004, **68,** 5059.
192. E. L. Hahn and B. Herzog, *Phys. Rev.*, 1954, **93,** 639.
193. T. Erge, D. Michel, J. Petersson and W. Windsch, *Phys. Status Solidi A*, 1989, **114,** 705.
194. T. Erge, F. Engelke, D. Michel, W. Windsch and J. Petersson, *Ferroelectrics*, 1990, **108,** 331.
195. T. Erge, D. Michel, J. Petersson and F. Engelke, *Phys. Status Solidi A*, 1991, **123,** 325.
196. F. Engelke, D. Michel, W. Windsch, P. Sarv and E. Lippmaa, *Ferroelectrics*, 1990, **108,** 337.
197. D. Michel, U. Häcker, T. Erge and J. Petersson, *Phys. Status Solidi B*, 1994, **185,** 257.
198. S. Jurga, G. S. Harbison, B. Blümich, H. W. Spiess, F. Fujara and A. Olinger, *Ber. Bunsen-Ges. Phys. Chem.*, 1986, **90,** 1153.
199. S. Jurga, J. Seliger, R. Blinc and H. W. Spiess, *Phys. Lett. A.*, 1986, **116,** 295.
200. V. P. Tarasov, M. A. Meladze, G. A. Kirakosyan, A. E. Shvelashvili and Y. A. Buslaev, *Phys. Status Solidi B*, 1991, **167,** 271.
201. V. P. Tarasov, M. A. Meladze and G. A. Kirakosyan, *Russ. J. Coord. Chem.*, 1992, **18,** 823.
202. J. Skibsted and H. J. Jakobsen, *Inorg. Chem.*, 1999, **38,** 1806.
203. M. Bloom, E. L. Hahn and B. Herzog, *Phys. Rev.*, 1955, **97,** 1699.
204. J. Itoh and R. Kusaka, *J. Phys. Soc. Jpn.*, 1954, **9,** 434.
205. M. Bloom and R. E. Norberg, *Phys. Rev.*, 1954, **93,** 638.
206. B. Herzog and E. L. Hahn, *Phys. Rev.*, 1956, **103,** 148.
207. A. Kawamori and J. Itoh, *J. Phys. Soc. Jpn.*, 1963, **18,** 1614.
208. M. Khasawneh, J. S. Hartman and A. D. Bain, *Mol. Phys.*, 2004, **102,** 975.
209. R. B. Creel, E. von Meerwall, C. F. Griffin and R. G. Barnes, *J. Chem. Phys.*, 1973, **58,** 4930.
210. S. B. Brody, W. A. Nierenberg and N. F. Ramsey, *Phys. Rev.*, 1947, **72,** 258.
211. R. V. Pound, *Phys. Rev.*, 1947, **72,** 1273.
212. J. Itoh and Y. Yamagata, *J. Chem. Phys.*, 1956, **24,** 621.
213. K. R. Jeffrey, A. G. Brown and R. L. Armstrong, *Phys. Rev. B*, 1973, **8,** 3071.
214. G. Seifert, *Z. Phys.*, 1961, **161,** 132.
215. J. Kluge, *Phys. Status Solidi*, 1962, **2,** K133.
216. M. Höhne, *Phys. Status Solidi*, 1964, **7,** 869.
217. M. Höhne, *Phys. Status Solidi*, 1964, **7,** K167.
218. Y. Saito, *J. Phys. Soc. Jpn.*, 1958, **13,** 72.
219. Y. Saito, *J. Phys. Soc. Jpn.*, 1966, **21,** 1072.
220. G. W. Herzog and H. Richtering, *Z. Phys. Chem. Neue Fol.*, 1967, **56,** 109.
221. K. D. Becker, G. W. Herzog, D. Kanne, H. Richtering and E. Stadler, *Ber. Bunsen-Gesell.*, 1970, **74,** 527.
222. S. Hayashi and K. Hayamizu, *Chem. Lett.*, 1989, 1419.

223. S. Hayashi and K. Hayamizu, *J. Chem. Phys.*, 1990, **92,** 2818.
224. L. O. Andersson and E. Forslind, *J. Chem. Phys.*, 1963, **38,** 2303.
225. L. O. Andersson, *Proc. Coll. AMPERE*, 1967, **14,** 1101.
226. L. O. Andersson, *Proc. Brit. Ceramic Soc.*, 1967, **No. 9,** 83.
227. L. O. Andersson and L. Ödberg, *Ark. Fys.*, 1967, **35,** 85.
228. K. D. Becker and H. Richtering, *Ber. Bunsen-Gesell.*, 1974, **78,** 461.
229. T. P. Das and B. G. Dick, *Phys. Rev.*, 1962, **127,** 1063.
230. B. G. Dick, Jr and T. P. Das, *J. Appl. Phys.*, 1962, **33,** 2815.
231. L. O. Andersson, *Phys. Lett. A*, 1968, **27,** 383.
232. L. O. Andersson, *Ark. Fys.*, 1969, **40,** 71.
233. B. G. Dick, *Phys. Rev.*, 1966, **145,** 609.
234. D. Ikenberry and T. P. Das, *B. Am. Phys. Soc. Ser. 2*, 1968, **13,** 466.
235. D. Ikenberry and T. P. Das, *Phys. Rev.*, 1969, **184,** 989.
236. Y. Fukai, *J. Phys. Soc. Jpn.*, 1964, **19,** 175.
237. T. Taki and M. Satoh, *Phys. Status Solidi B*, 1975, **71,** K21.
238. J. Kluge, *Phys. Status Solidi*, 1966, **13,** 401.
239. H. Nagasawa and N. Miyauchi, *Phys. Status Solidi B*, 1975, **71,** 671.
240. D. Brinkmann, G. Finger and H. Arend, *Phys. Status Solidi B*, 1977, **83,** K45.
241. D. Brinkmann, H. Huber, M. Mali, J. Roos and H. Arend, *Helv. Phys. Acta*, 1982, **55,** 568.
242. P. Brenni, D. Brinkmann, H. Huber, M. Mali, J. Roos and H. Arend, *Solid State Commun.*, 1983, **47,** 415.
243. E. Gebert, S. W. Peterson, A. H. Reis and E. H. Appelman, *J. Inorg. Nucl. Chem.*, 1981, **43,** 3085.
244. V. P. Tarasov, S. A. Petrushin and Y. K. Gusev, *Dokl. Akad. Nauk SSSR*, 1987, **293,** 1423.
245. V. P. Tarasov, V. I. Privalov, Y. A. Buslaev and U. Eichhoff, *Z. Naturforsch. B*, 1990, **45,** 1005.
246. S. Kojima, K. Tsukada, A. Shimauchi and Y. Hinaga, *J. Phys. Soc. Jpn.*, 1954, **9,** 795.
247. S. Kojima, K. Tsukada and Y. Hinaga, *J. Phys. Soc. Jpn.*, 1955, **10,** 498. [Errata: *ibid.*, **10**, 828.]
248. K. Shimomura, *J. Phys. Soc. Jpn.*, 1957, **12,** 657.
249. K. Shimomura, *J. Phys. Soc. Jpn.*, 1957, **12,** 1386.
250. K. Shimomura, *J. Phys. Soc. Jpn.*, 1959, **14,** 235.
251. M. Minematsu, *J. Phys. Soc. Jpn.*, 1959, **14,** 1030.
252. P. Bucci, P. Cecchi and A. Colligiani, *J. Am. Chem. Soc.*, 1964, **86,** 2513.
253. K. V. S. R. Rao and C. R. K. Murty, *Curr. Sci.*, 1965, **34,** 660.
254. P. Bucci, P. Cecchi, A. Colligiani and M. Landucci, *Ric. Sci., Rend., Sez. A*, 1965, **8,** 1144.
255. P. Bucci, P. Cecchi, A. Colligiani and R. Meschia, *Bollettino Scientifico della Facolta di Chimica Industriale di Bologna*, 1965, **23,** 307.
256. K. V. S. R. Rao and C. R. K. Murty, *Phys. Lett.*, 1966, **23,** 404.
257. K. V. S. R. Rao and C. R. K. Murty, *Curr. Sci.*, 1966, **35,** 252.
258. K. V. S. R. Rao and C. R. K. Murty, *J. Phys. Soc. Jpn.*, 1966, **21,** 1627.
259. K. K. Rao and C. R. K. Murty, *J. Phys. Soc. Jpn.*, 1966, **21,** 2725.
260. K. K. Rao and C. R. K. Murty, *Curr. Sci.*, 1966, **35,** 591.
261. K. K. Rao and C. R. K. Murty, *Chem. Phys. Lett.*, 1967, **1,** 323.
262. K. V. S. R. Rao and C. R. K. Murty, *J. Phys. Soc. Jpn.*, 1968, **25,** 1423.
263. P. Bucci, P. Cecchi and A. Colligiani, *J. Chem. Phys.*, 1969, **50,** 530.
264. R. Ambrosetti, P. Bucci, P. Cecchi and A. Colligiani, *J. Chem. Phys.*, 1969, **51,** 852.
265. R. Angelone, P. Cecchi and A. Colligiani, *J. Chem. Phys.*, 1970, **53,** 4096.
266. T. Okuda, H. Terao, O. Ege and H. Negita, *J. Chem. Phys.*, 1970, **52,** 5489.
267. T. Okuda, H. Terao, O. Ege and H. Negita, *Bull. Chem. Soc. Jpn.*, 1970, **43,** 2398.
268. T. Okuda, Y. Furukawa and H. Negita, *Bull. Chem. Soc. Jpn.*, 1971, **44,** 2083.
269. H. W. Spiess and R. K. Sheline, *J. Chem. Phys.*, 1971, **54,** 1099.
270. R. Ambrosetti, R. Angelone, P. Cecchi and A. Colligiani, *J. Chem. Phys.*, 1971, **54,** 2915.
271. A. Colligiani, R. Ambrosetti and P. Cecchi, *J. Chem. Phys.*, 1971, **55,** 4400.
272. T. Okuda, Y. Furukawa and H. Negita, *Bull. Chem. Soc. Jpn.*, 1972, **45,** 2245.
273. K. V. S. R. Rao and M. T. Rogers, *J. Magn. Reson.*, 1972, **8,** 392.
274. T. Okuda, Y. Furukawa, H. Shigemoto and H. Negita, *Bull. Chem. Soc. Jpn.*, 1973, **46,** 741.
275. R. Ambrosetti, R. Angelone, A. Colligiani and P. Cecchi, *Mol. Phys.*, 1974, **28,** 551.

276. T. Okuda, K. Yamada, Y. Furukawa and H. Negita, *Bull. Chem. Soc. Jpn.*, 1975, **48,** 392.
277. Y. Furukawa, *J. Sci. Hiroshima Univ., Ser. A*, 1973, **37,** 357.
278. T. Okuda, K. Yamada, H. Ishihara and H. Negita, *Chem. Lett.* 1975, 785.
279. K. S. Ramasastry and D. Premaswarup, *J. Phys. Soc. Jpn.*, 1976, **41,** 338.
280. K. S. Ramasastry and D. Premaswarup, *J. Phys. Soc. Jpn.*, 1976, **41,** 997.
281. M. Rangacharyulu and D. Premaswarup, *Indian J. Pure Appl. Phys.*, 1977, **15,** 518.
282. T. Okuda, I. Tomoyasu, K. Yamada and H. Negita, *Bull. Chem. Soc. Jpn.*, 1977, **50,** 1695.
283. T. Okuda, K. Yamada, H. Ishihara and H. Negita, *Bull. Chem. Soc. Jpn.*, 1977, **50,** 3136.
284. T. Okuda, H. Ishihara, K. Yamada and H. Negita, *Bull. Chem. Soc. Jpn.*, 1978, **51,** 1273.
285. R. Valli and K. V. S. R. Rao, *Proc. Nuc. Phys. Sol. State Phys. Symp.*, 1978, **21C,** 685.
286. H. Negita, M. Hiura, K. Yamada and T. Okuda, *J. Mol. Struct.*, 1980, **58,** 205.
287. T. Okuda, M. Hiura, R. Boku, K. Yamada and H. Negita, *Chem. Lett.*, 1980, 1049.
288. T. Okuda, H. Ohta, H. Ishihara, K. Yamada and H. Negita, *Bull. Chem. Soc. Jpn.*, 1980, **53,** 2721.
289. K. S. Ahmad and A. L. Porte, *J. Mol. Struct.*, 1980, **58,** 459.
290. T. Chiba, *J. Phys. Soc. Jpn.*, 1958, **13,** 860.
291. T. Okuda, M. Hiura and H. Negita, *Bull. Chem. Soc. Jpn.*, 1981, **54,** 1920.
292. T. Okuda, H. Ishihara, K. Yamada, M. Hiura and H. Negita, *J. Mol. Struct.*, 1981, **74,** 347.
293. M. Hiura, *J. Sci. Hiroshima Univ., Ser. A*, 1982, **45,** 383.
294. O. Ege, *J. Sci. Hiroshima Univ., Ser. A*, 1982, **46,** 21.
295. K. Yamada, *J. Sci. Hiroshima Univ., Ser. A*, 1977, **41,** 77.
296. H. Terao, M. Fukura, T. Okuda and H. Negita, *Bull. Chem. Soc. Jpn.*, 1983, **56,** 1728.
297. K. Yamada, N. Weiden and A. Weiss, *J. Mol. Struct.*, 1983, **111,** 217.
298. V. Ramakrishna, D. K. Rao, G. Satyanandam and C. R. K. Murty, *Org. Magn. Reson.*, 1983, **21,** 205.
299. R. Ambrosetti, R. Angelone, A. Colligiani and P. Cecchi, *Mol. Phys.*, 1971, **22,** 619.
300. H. Terao and T. Okuda, *Chem. Lett.*, 1989, 649.
301. H. Terao and T. Okuda, *J. Mol. Struct.*, 1995, **372,** 49.
302. H. Terao, T. Okuda, S. Uyama, H. Negita, S. Q. Dou, H. Fuess and A. Weiss, *Z. Naturforsch. A*, 1996, **51,** 1197.
303. R. Valli and K. V. S. R. Rao, *J. Chem. Phys.*, 1983, **79,** 4113.
304. R. Valli and K. V. S. R. Rao, *J. Mol. Struct.*, 1983, **102,** 365.
305. S. Ramaprabhu and K. V. S. R. Rao, *Cryst. Latt. Def. Amorph. Mat.*, 1984, **10,** 229.
306. A. A. Boguslavskii, R. S. Lotfullin and E. Y. Peresh, *Sov. Phys. Solid State*, 1988, **30,** 903. [Translated from: *Fiz. Tverd. Tela.*, 1988, **30**, 1558].
307. O. Ege and H. Negita, *Z. Naturforsch. A*, 1990, **45,** 599.
308. H. Krüger, *Z. Physik*, 1951, **130,** 371.
309. T. Kushida, Y. Koi and Y. Imaeda, *J. Phys. Soc. Jpn.*, 1954, **9,** 809.
310. C. H. Townes and B. P. Dailey, *J. Chem. Phys.*, 1949, **17,** 782.
311. C. H. Townes and B. P. Dailey, *J. Chem. Phys.*, 1952, **20,** 35.
312. S. L. Segel, R. G. Barnes and R. B. Creel, *Chem. Phys. Lett.*, 1968, **2,** 613.
313. R. Fusaro and J. W. Doane, *J. Chem. Phys.*, 1967, **47,** 5446.
314. J. W. Doane and R. A. Hultsch, *Phys. Rev.*, 1964, **133,** A1085.
315. J. W. Doane and R. A. Hultsch, *Phys. Rev.*, 1966, **143,** 172.
316. E. von Meerwall, J. Worth, R. B. Creel and C. F. Griffin, *B. Am. Phys. Soc. Ser. 2*, 1973, **18,** 86.
317. J. Worth, C. F. Griffin and E. von Meerwall, *B. Am. Phys. Soc. Ser. 2*, 1973, **18,** 245.
318. C. F. Griffin, E. von Meerwall, J. Worth and R. B. Creel, *B. Am. Phys. Soc. Ser. 2*, 1974, **19**.
319. R. B. Creel and S. L. Segel, *B. Am. Phys. Soc. Ser. 2*, 1973, **18,** 245.
320. E. D. von Meerwall, R. B. Creel, C. F. Griffin and S. L. Segel, *J. Chem. Phys.*, 1973, **59,** 5350.
321. C. F. Griffin, R. B. Creel, J. Worth and E. von Meerwall, *J. Phys. Chem. Solids*, 1974, **35,** 71.
322. J. Bieroń, P. Pyykkö, D. Sundholm, V. Kellö and A. J. Sadlej, *Phys. Rev. A*, 2001, **64,** 052507.
323. P. Pyykkö, *Mol. Phys.*, 2008, **106**, 1965.
324. S. L. Segel and H. M. Vyas, *J. Chem. Phys.*, 1980, **72,** 1406.
325. P. K. Burkert, *Z. Naturforsch*, 1980, **35b,** 1349.
326. D. G. Klobasa and P. K. Burkert, *Z. Naturforsch*, 1984, **39a,** 1222.
327. P. K. Burkert and D. G. Klobasa, *Z. Naturforsch*, 1985, **40a,** 274.
328. D. G. Klobasa, P. K. Burkert and G. Müller, *Z. Naturforsch*, 1986, **41a,** 330.

329. P. K. Burkert and M. Grommelt, *Z. Naturforsch*, 1988, **43b,** 1381.
330. M. Grommelt and P. K. Burkert, *Z. Naturforsch*, 1989, **44b,** 1053.
331. D. G. Klobasa and P. K. Burkert, *Z. Naturforsch*, 1987, **42a,** 275.
332. G. Wu and S. Dong, *Solid State Nucl. Magn. Reson.*, 2001, **20,** 100.
333. J. F. Hon and K. O. Christe, *J. Chem. Phys.*, 1970, **52,** 1960.
334. J. F. Lehmann, G. J. Schrobilgen, K. O. Christe, A. Kornath and R. J. Suontamo, *Inorg. Chem.*, 2004, **43,** 6905.
335. T. R. Stengle, Y. E. Pan and C. H. Langford, *J. Am. Chem. Soc.*, 1972, **94,** 9037.
336. J. Blaser, O. Lutz and W. Steinkilberg, *Z. Naturforsch. A*, 1972, **27,** 72.
337. J. Vaara, J. Jokisaari, R. E. Wasylishen and D. L. Bryce, *Prog. Nucl. Magn. Reson. Spectrosc.*, 2002, **41,** 233.
338. D. L. Bryce and R. E. Wasylishen, *Acc. Chem. Res.*, 2003, **36,** 327.
339. F. C. De Lucia, P. Helminger and W. Gordy, *Phys. Rev. A*, 1971, **3,** 1849.
340. T. D. Gierke and W. H. Flygare, *J. Am. Chem. Soc.*, 1972, **94,** 7277.
341. J. Cederberg, D. Olson, A. Nelson, D. Laine, P. Zimmer, M. Welge, M. Feig, T. Höft and N. London, *J. Chem. Phys.*, 1999, **110,** 2431.
342. J. Cederberg, J. Randolph, B. McDonald, B. Paulson and C. McEachern, *J. Mol. Spectrosc.*, 2008, **250,** 114.
343. J. Thyssen, P. Schwerdtfeger, M. Bender, W. Nazarewicz and P. B. Semmes, *Phys. Rev. A*, 2001, **63,** 022505.
344. L. Bizzocchi, B. M. Giuliano and J.-U. Grabow, *J. Mol. Struct.*, 2007, **833,** 175.
345. R. J. Low, T. D. Varberg, J. P. Connelly, A. R. Auty, B. J. Howard and J. M. Brown, *J. Mol. Spectrosc.*, 1993, **161,** 499.
346. G. Cazzoli and C. Puzzarini, *J. Mol. Spectrosc.*, 2004, **226,** 161.
347. P. P. Man, *J. Chim. Phys.*, 1992, **89,** 335.
348. O. Kanert, *Z. Phys.*, 1965, **184,** 92.
349. R. Jelinek, A. Stein and G. A. Ozin, *J. Am. Chem. Soc.*, 1993, **115,** 2390.
350. K. Saito, K. Kanehashi and I. Komaki, *Annu. Rep. Nucl. Magn. Reson. Spectrosc.*, 2001, **44,** 23.
351. H. Yun, M. E. Patton, J. H. Garrett, Jr., G. K. Fedder, K. M. Frederick, J. J. Hsu, I. J. Lowe, I. J. Oppenheim and P. J. Sides, *Cem. Concr. Res.*, 2004, **34,** 379.
352. F. Barberon, V. Baroghel-Bouny, H. Zanni, B. Bresson, J. B. d'Espinose de la Caillerie, L. Malosse and Z. Gan, *Magn. Reson. Imaging*, 2005, **23,** 267.
353. T. Kanashiro, R. M. Mahbubar, Y. Michihiro, K. Nakamura, T. Ohno and Y. Kishimoto, *J. Phys. Soc. Jpn.*, 2001, **70,** 3322.
354. F. Tabak, A. Lascialfari and A. Rigamonti, *J. Phys: Conden. Matter*, 1993, **5,** B31.
355. F. V. Bragin and S. M. Ryabchenko, *Fiz. Tverd. Tela*, 1973, **15,** 1050.
356. T. Tsuda, H. Yasuoka and M. Suzuki, *Synth. Met.*, 1985, **12,** 461.
357. A. Narath, *Phys. Rev.*, 1965, **140,** A552.
358. H. Rinneberg, H. Haas and H. Hartmann, *J. Chem. Phys.*, 1969, **50,** 3064.
359. R. H. Clark and W. G. Moulton, *J. Appl. Phys.*, 1971, **42,** 1308.
360. R. H. Clark and W. G. Moulton, *Phys. Rev. B*, 1972, **5,** 788.
361. H. Rinneberg and H. Hartmann, *J. Chem. Phys.*, 1970, **52,** 5814.
362. W. B. Euler, C. Long, W. G. Moulton and B. B. Garrett, *J. Magn. Reson.*, 1978, **32,** 33.
363. K. P. Holzer, U. Häcker, J. Petersson, D. Michel and S. Kluthe, *Solid State Commun.*, 1995, **94,** 275.
364. O. Ofer, A. Keren, E. A. Nytko, M. P. Shores, B. M. Bartlett, D. G. Nocera, C. Baines and A. Amato, *Arch. Conden. Matter*, 2006, 1. DOI: arXiv:cond-mat/0610540.
365. T. Imai, E. A. Nytko, B. M. Bartlett, M. P. Shores and D. G. Nocera, *Phys. Rev. Lett.*, 2008, **100,** 077203.
366. J. P. Hessler, *B. Am. Phys. Soc. Ser. 2*, 1973, **18,** 113.
367. W. J. O'Sullivan, W. W. Simmons and W. A. Robinson, *Phys. Rev.*, 1965, **140,** A1759.
368. R. G. Barnes and S. L. Segel, *J. Chem. Phys.*, 1962, **37,** 1895.
369. W. H. Jones and S. L. Segel, *Phys. Rev. Lett.*, 1964, **13,** 528.
370. S. H. Choh and C. V. Stager, *Can. J. Phys.*, 1971, **49,** 144.
371. T. J. Bastow, S. N. Stuart, W. G. McDugle, R. S. Eachus and J. M. Spaeth, *J. Phys.: Condens. Matter*, 1994, **6,** 8633.

372. A. G. Brown, R. L. Armstrong and K. R. Jeffrey, *J. Phys. C: Solid State Phys.*, 1973, **6,** 532.
373. S. L. Segel and R. G. Barnes, *Phys. Rev. Lett.*, 1965, **15,** 886.
374. H. Trill, H. Eckert and V. I. Srdanov, *Phys. Rev. B*, 2005, **71,** 014412-1.
375. S. Elschner and J. Petersson, *Z. Naturforsch*, 1986, **41a,** 343.
376a. T. J. Bastow and S. N. Stuart, *J. Phys.: Condens. Matter*, 1989, **1,** 4649.
376b. T. J. Bastow, R. J. C. Brown and S. L. Segel, *J. Chem. Phys.*, 1988, **89,** 1203.
377. S. L. Segel, S. Maxwell, R. D. Heyding, P. Ingman, E. Ylinen and M. Punkkinen, *Solid State Commun.*, 1988, **66,** 1039.
378. N. Binesh and S. V. Bhat, *Solid State Ionics*, 1996, **92,** 261.
379. H. Ono, S. Ishimaru, R. Ikeda and H. Ishida, *Bull. Chem. Soc. Jpn.*, 1999, **72,** 2049.
380. H. Ono, S. Ishimaru, R. Ikeda and H. Ishida, *Chem. Phys. Lett.*, 1997, **275,** 485.
381. A. Taye, D. Michel and J. Petersson, *Phys. Rev. B*, 2002, **66,** 174102-1.
382. A. Taye and D. Michel, *Phys. Status Solidi B*, 2002, **233,** 519.
383. A. Taye, D. Michel and J. Petersson, *Phys. Rev. B*, 2004, **69,** 224206-1.
384. A. Taye and D. Michel, *Phys. Status Solidi B*, 2004, **241,** 1333.
385. H. Tou, Y. Maniwa, S. Yamanaka and M. Sera, *Physica B*, 2003, **329–333,** 1323.
386. T. Azaïs, C. Bonhomme and M. E. Smith, *Solid State Nucl. Magn. Reson.*, 2003, **23,** 14.
387. X. Hou and R. J. Kirkpatrick, *Chem. Mater.*, 2002, **14,** 1195.
388. X. Hou and R. J. Kirkpatrick, *Inorg. Chem.*, 2001, **40,** 6397.
389. X. Hou, A. G. Kalinichev and R. J. Kirkpatrick, *Chem. Mater.*, 2002, **14,** 2078.
390. S. Mulla-Osman, D. Michel, Z. Czapla and W. D. Hoffman, *J. Phys: Condens. Matter*, 1998, **10,** 2465.
391. S. Mulla-Osman, D. Michel, G. Völkel and Z. Czapla, *Phys. Status Solidi B*, 2000, **219,** 9.
392. S. Mulla-Osman, D. Michel, G. Völkel, I. Peral and G. Madariaga, *J. Phys: Condens. Matter*, 2001, **13,** 1119.
393. B. J. Suh, F. Borsa, L. L. Miller, D. C. Johnston, D. R. Torgeson and M. Corti, *J. Appl. Phys.*, 1996, **79,** 5084.
394. B. J. Suh, *J. Korean Phys. Soc.*, 2000, **36,** 387.
395. S. D. Goren, L. F. Ben-Yakar, A. Shames, B. Pandyopadhayay, C. Korn, H. Shaked, P. Massiot, C. Perrin, J. Gallier and A. Privalov, *Physica C*, 1999, **313,** 127.
396. R. J. Kirkpatrick, P. Yu, X. Hou and Y. Kim, *Am. Mineral.*, 1999, **84,** 1186.
397. K. Yamada, K. Isobe, T. Okuda and Y. Furukawa, *Z. Naturforsch*, 1994, **49a,** 258.
398. K. Yamada, K. Isobe, E. Tsuyama, T. Okuda and Y. Furukawa, *Solid State Ionics*, 1995, **79,** 152.
399. E. B. Amitin, N. V. Bausck, S. A. Gromilov, S. G. Kozlova, N. K. Moroz, L. N. Mazalov, V. N. Naumov, P. P. Samoilov, S. A. Slobodjan, M. A. Starikov, V. E. Fedorov, G. I. Frolova and S. B. Erenburg, *Physica C*, 1993, **209,** 407.
400. H. Kubo, T. Hamasaki, K. Takeda, N. Uryû, M. Tanimoto and K. Katsumata, *Technol. Rep. Kyushu Univ.*, 1986, **59,** 647.
401. H. Kubo, T. Hamasaki, M. Tanimoto and K. Katsumata, *J. Phys. Soc. Jpn.*, 1986, **55,** 3301.
402. P. Muralt, P. Caravatti, R. Kind and J. Roos, *J. Phys. C: Solid State Phys.*, 1986, **19,** 1705.
403. J. P. Yesinowski and H. Eckert, California Institute of Technology, Unpublished data, 1985.
404. J. M. Weulersse, P. Rigny and J. Virlet, *J. Chem. Phys.*, 1975, **63,** 5190.
405. A. P. Kreshkov, V. F. Andronov and V. A. Drozdov, *Zh. Fiz. Khim.*, 1972, **46,** 309.
406. F. M. McCubbin, H. E. Mason, H. Park, B. L. Phillips, J. B. Parise, H. Nekvasil and D. H. Lindsley, *Am. Mineral.*, 2008, **93,** 210.
407. H. Kubo, N. Kaneshima, Y. Hashimoto, K. Tsuru and K. Hirakawa, *J. Phys. Soc. Jpn.*, 1977, **42,** 484.
408. T. Saito, H. Inoue, J. Tonisi, A. Oosawa, T. Goto, T. Sasaki, N. Kobayasi, S. Awaji and K. Watanabe, *J. Phys: Conf. Ser.*, 2006, **51,** 203.
409. W. Gauβ, S. Günther, A. R. Haase, M. Kerber, D. Kessler, J. Kronenbitter, H. Krüger, O. Lutz, A. Nolle, P. Schrade, M. Schüle and G. E. Siegloch, *Z. Naturforsch. A*, 1978, **33a,** 934.
410. I. D. Campbell and D. J. Mackey, *Aust. J. Chem.*, 1971, **24,** 45.
411. G. Bonera and M. Galimberti, *Solid State Commun.*, 1966, **4,** 589.
412. J. D. Memory and J. Mathur, *B. Am. Phys. Soc., Ser. 2*, 1971, **16,** 521.
413. K. Hashi, T. Shimizu, A. Goto, T. Iijima and S. Ohki, *Jpn. J. Appl. Phys. 1*, 2005, **44,** 4194.
414. K. Hashi, T. Shimizu, T. Fujito, A. Goto and S. Ohki, *J. Phys.: Conf. Ser.*, 2006, **51,** 573.
415. T. Iijima, K. Takegoshi, K. Hashi, T. Fujito and T. Shimizu, *J. Magn. Reson.*, 2007, **184,** 258.

416. K. Hashi, T. Shimizu, T. Fujito, A. Goto, S. Ohki, K. Shimoda, Y. Tobu and K. Saito, *Chem. Lett.*, 2007, **36,** 884.
417. L. G. Conti, R. D'Alessandro and V. Di Napoli, *J. Phys. Chem. Solids*, 1971, **32,** 1092, [Erratum: *ibid.*, 1972, **33**, 767].
418. L. G. Conti and F. Di Piro, *Magn. Reson. Relat. Phenom., Proc. Congr. AMPERE, 18th*, 1975, **2,** 571.
419. L. G. Conti, *Gazz. Chim. Ital.*, 1976, **106,** 393.
420. N. Zumbulyadis and A. P. Marchetti, *Colloids Surf.*, 1990, **45,** 335.
421. D. M. Potrepka, J. I. Budnick, D. B. Fenner, W. A. Hines, M. Balasubramanian and A. R. Moodenbaugh, *Phys. Rev. B*, 1999, **60,** 10489.
422. K. D. Becker, H. Hamann, N. Kozubek and H. Richtering, *Ber. Bunsen-Gesell.*, 1975, **79,** 1124.
423. V. P. Tarasov, V. I. Privalov, K. S. Gavrichev, V. E. Gorbunov, Y. K. Gusev and Y. A. Buslaev, *Russ. J. Coord. Chem*, 1990, **16,** 854, [Translated from: *Koordinats. Khim.*, 1990, **16**, 1603].
424. V. P. Tarasov, S. A. Petrushin and Y. K. Gusev, *Russ. J. Inorg. Chem.*, 1988, **33,** 452, [Translated from: *Zh. Neorg. Khim.*, 1988, **33**, 804].
425. H. Trill, H. Eckert and V. I. Srdanov, *J. Am. Chem. Soc.*, 2002, **124,** 8361.
426. H. Huber, M. Mali, J. Roos and D. Brinkmann, *Helv. Phys. Acta*, 1984, **57,** 738.
427. H. Huber, M. Mali, J. Roos and D. Brinkmann, *Solid State Ionics*, 1986, **18 & 19,** 1188.
428. H. Huber, M. Mali, J. Roos and D. Brinkmann, *Physica B + C*, 1986, **139–140,** 289.
429. H. Nakayama, T. Eguchi, N. Nakamura, H. Chihara, T. Nogami, K. Imamura and Y. Shirota, *Bull. Chem. Soc. Jpn.*, 1989, **62,** 399.
430. A. Kehrer, N. Weiden and A. Weiss, *Z. Phys. Chem.*, 1992, **178,** 1.
431. M. Rangacharyulu and D. Premaswarup, *Indian J. Pure Appl. Phys.*, 1976, **14,** 160.
432. D. Zipse, N. S. Dalal, R. M. Achey, J. M. North, S. Hill and R. S. Edwards, *Appl. Magn. Reson.*, 2004, **27,** 151.
433. S. D. Senturia and G. B. Benedek, *Phys. Rev. Lett.*, 1966, **17,** 475.
434. A. C. Gossard, V. Jaccarino, E. D. Jones, J. P. Remeika and R. Slusher, *Phys. Rev.*, 1964, **135,** A1051.
435. S. D. Senturia, *J. Appl. Phys.*, 1970, **41,** 644.
436. J. P. Renard and E. Velu, *Solid State Commun.*, 1970, **8,** 1945.
437. J. P. Renard and E. Velu, *J. Phys.-Paris, Colloque*, 1971, **32,** C1, 1154.
438. T. O. Klaassen, A. Gevers and N. J. Poulis, *Physica (Amsterdam)*, 1972, **61,** 95.
439. T. O. Klaassen and N. J. Poulis, *J. Phys.-Paris, Colloque*, 1971, **32,** C1, 1157.
440. H. Kubo, Y. Suzuki and T. Akitomi, *J. Phys. Soc. Jpn.*, 1979, **47,** 2029.
441. K. V. S. R. Rao, W. J. M. De Jonge and C. H. W. Swüste, *Physica (Amsterdam)*, 1971, **53,** 621.
442. J. P. A. M. Hijmans, W. J. M. DeJonge, P. Van der Leeden and M. J. Steenland, *Physica (Amsterdam)*, 1973, **69,** 76.
443. C. H. W. Swüste and K. Kopinga, *Physica (Amsterdam)*, 1972, **60,** 415.
444. K. Okada, X. Xu and M. Fujii, *Czech. J. Phys.*, 1996, **46**(Suppl. S4), 2045.
445. X. Xu, K. Okada, M. Fujii and Y. Ajiro, *J. Phys: Conden. Matter*, 1996, **8,** L675.
446. X. Xu, K. Okada and M. Fujii, *Czech. J. Phys.*, 1996, **46**(Suppl. S4), 2047.
447. X. Xu, K. Okada, T. Shimamoto, M. Chiba, M. Fujii and Y. Ajiro, *Physica B*, 1997, **239,** 131.
448. C. H. W. Swüste, W. J. M. De Jonge and J. A. G. W. Van Meijel, *Physica (Amsterdam)*, 1974, **76,** 21.
449. M. Uyeda, T. Kubo, M. Chiba, Y. Ajiro and T. Asano, *J. Magn. Magn. Mater.*, 1998, **177–181,** 833.
450. M. Mali, J. Roos, D. Brinkmann, J. B. Phipps and P. M. Skarstad, *Solid State Ionics*, 1988, **28–30,** 1089.
451. I. Solomon, *Phys. Rev.*, 1958, **110,** 61.
452. J. Butterworth, *Proc. Phys. Soc.*, 1965, **86,** 297.
453. I. D. Weisman and L. H. Bennett, *Phys. Rev.*, 1969, **181,** 1341.
454. N. Lee, B. C. Sanctuary and T. K. Halstead, *J. Magn. Reson.*, 1992, **98,** 534.
455. G. R. Gerhart and H. O. Hooper, *Phys. Rev. B*, 1974, **10,** 4413.
456. K. Budde and H. Richtering, *Phys. Stat. Sol. B*, 1983, **120,** 595.
457. G. Ardel, D. Golodnitsky, E. Peled, Y. Wang, G. Wang, S. Bajue and S. Greenbaum, *Solid State Ionics*, 1998, **113–115,** 477.
458. G. Hinze, R. Böhmer, B. Zalar and R. Blinc, *J. Phys: Conden. Matter*, 1997, **9,** 117.
459. H. Ishida, Y. Furukawa, S. Kashino, S. Sato and R. Ikeda, *Ber. Bunsen-Ges. Phys. Chem.*, 1996, **100,** 433.
460. R. I. Dzhioev and Y. G. Kursaev, *Fiz. Tverd. Tela*, 1996, **38,** 2148.

461. A. Kehrer, S. Q. Dou and A. Weiss, *Z. Naturforsch*, 1989, **44a,** 659.
462. S. L. Segel, R. J. C. Brown, E. E. Ylinen, L. P. Ingman and T. J. Bastow, *Z. Naturforsch*, 2002, **57a,** 661.
463. A. Weiss and W. Weyrich, *Z. Naturforsch*, 1969, **24a,** 474.
464. J. M. Weulersse, J. Virlet and P. Rigny, *Mol. Phys.*, 1979, **38,** 923.
465a. M. Mizuno, A. Hirai, H. Matsuzawa, K. Endo and M. Suhara, *Phys. Chem. Chem. Phys.*, 2001, **3,** 107.
465b. M. Mizuno, T. Iijima, J. Kimura, K. Endo and M. Suhara, *J. Mol. Struct.*, 2002, **602–603,** 239.
466. T. Okuda, H. Ishihara, K. Yamada and H. Negita, *Bull. Chem. Soc. Jpn.*, 1977, **50,** 1007.
467. K. Tsukada, *J. Phys. Soc. Jpn.*, 1956, **11,** 956.
468. S. Kojima and K. Tsukada, *J. Phys. Soc. Jpn.*, 1955, **10,** 591.
469. D. Visser, L. Niesen and H. de Waard, *J. Phys. F: Met. Phys.*, 1984, **14,** 2419.
470. R. Livingston, B. M. Benjamin, J. T. Cox and W. Gordy, *Phys. Rev.*, 1953, **92,** 1271.
471. A. H. Saleck, T. Klaus, S. P. Belov and G. Winnewisser, *Z. Naturforsch.* 1996, **51a,** 898.
472. F. A. van Dijk and A. Dymanus, *Chem. Phys. Lett.*, 1969, **4,** 170.
473. F. A. van Dijk and A. Dymanus, *Chem. Phys.*, 1974, **6,** 474.
474. F. A. Van Dijk and A. Dymanus, *Chem. Phys. Lett.*, 1968, **2,** 235.
475. J. -P. Wallerand, F. du Burck, B. Mercier, A. N. Goncharov, M. Himbert and C. J. Bordé, *Eur. Phys. J. D*, 1999, **6,** 63.
476. R. C. Hilborn, T. F. Gallagher, Jr. and N. F. Ramsey, *J. Chem. Phys.*, 1972, **56,** 855.
477. J. Cederberg, D. Nitz, A. Kolan, T. Rasmusson, K. Hoffman and S. Tufte, *J. Mol. Spectrosc.*, 1987, **122,** 171.
478. B. Fabricant and J. S. Muenter, *J. Chem. Phys.*, 1977, **66,** 5274.
479. J. Cederberg, *J. Chem. Phys.*, 1977, **66,** 5247.
480. J. W. Cederberg and C. E. Miller, *J. Chem. Phys.*, 1969, **50,** 3547.
481. F. H. De Leeuw, R. van Wachem and A. Dymanus, *J. Chem. Phys.*, 1970, **53,** 981.
482. J. Cederberg, S. Fortman, B. Porter, M. Etten, M. Feig, M. Bongard and L. Langer, *J. Chem. Phys.*, 2006, **124,** 244305.
483. D. Nitz, J. Cederberg, A. Kotz, K. Hetzler, T. Aakre and T. Walhout, *J. Mol. Spectrosc.*, 1984, **108,** 6.
484. H. S. P. Müller and M. C. L. Gerry, *J. Chem. Phys.*, 1995, **103,** 577.
485. S. A. Cooke, C. Krumrey and M. C. L. Gerry, *Phys. Chem. Chem. Phys.*, 2005, **7,** 2570.
486. D. S. Rubinoff, C. J. Evans and M. C. L. Gerry, *J. Mol. Spectrosc.*, 2003, **218,** 169.
487. W. Lin, S. A. Beaton, C. J. Evans and M. C. L. Gerry, *J. Mol. Spectrosc.*, 2000, **199,** 275.
488. W. Lin, C. J. Evans and M. C. L. Gerry, *Phys. Chem. Chem. Phys.*, 2000, **2,** 43.
489. K. D. Hensel and M. C. L. Gerry, *J. Mol. Spectrosc.*, 1994, **166,** 304.
490. R. H. Hammerle, J. T. Dickinson, R. G. VanAusdal, D. A. Stephenson and J. C. Zorn, *J. Chem. Phys.*, 1969, **50,** 2086.
491. J. T. Dickinson, D. A. Stephenson and J. C. Zorn, *J. Chem. Phys.*, 1970, **53,** 1525.
492. D. A. Stephenson, J. T. Dickinson and J. C. Zorn, *J. Chem. Phys.*, 1970, **53,** 1529.
493. G. W. Wagner, *Solid State Ionics*, 1991, **47,** 143.

SUBJECT INDEX

Page numbers followed by f indicate figures, t indicate tables.

D

T